

International Review of Mechanical Engineering (IREME)

Contents

| | |
|---|-----|
| Performance Study of Reference Height Control Algorithm for Tripod Hopping Robot <i>by A. M. Kassim, T. Yasuno, N. Abas, M. S. M. Aras, M. Z. A. Rashid</i> | 784 |
| UTeM's Amphibious Hybrid Vehicle: Development of Hybrid Electric Propulsion System <i>by Muhammad Zahir Hassan, Amjad Saddar Md Isa, Syahibudil Ikhwan Abdul Kudus, Muhammad Zaidan Abdul Manaf</i> | 790 |
| Motorcycle Handlebar Dynamic Response: Theoretical and Experimental Investigation <i>by D. De Falco, G. Di Massa, S. Pagano, S. Strano</i> | 795 |
| Optimal Solution for Gear Drive Design Using Population Based Algorithm <i>by Padmanabhan S., M. Chandrasekaran, P. Asokan, V. Srinivasa Raman</i> | 802 |
| Geometry Based Recursive Algorithm to Control the End Effector of Coordinated TRRLR Manipulators <i>by Seetharaman N., R. Sivaramakrishnan, Abin John Thomas</i> | 807 |
| Modeling of Dynamic Response of Beam-Type Vibration Absorbing System Excited by a Moving Mass <i>by Mothanna Y. Abd, Azma Putra, Nawal A. A. Jalil, Sidik Susilo</i> | 813 |
| Research on Dynamics Simulation of CNC Milling Machine Based on Virtual Prototyping <i>by Yixuan Wang, Yanli Guo, Ying Wang</i> | 821 |
| Comparison of Contact Stress of Helical Gear for Steel C45 with AGMA Standard and FEA Model <i>by S. Prabhakaran, S. Ramachandran</i> | 828 |
| Hamessing Energy from Mechanical Vibration Using Non-Adaptive Circuit and Smart Structure <i>by Intan Z. Mat Darus, Ameirul A. Mustadza, Hanim Mohd Yatim</i> | 832 |
| A Full Scale Test Rig to Characterize Pneumatic Tyre Mechanical Behaviour <i>by Flavio Farroni, Ernesto Rocca, Francesco Timpone</i> | 841 |
| Transient Wave Propagation in Non-Homogeneous Viscoelastic Media <i>by Shahin Nayyeri Amiri, Asad Esmaeily</i> | 847 |
| Study on the Heat Transfer of the Rectangular Fin with Dehumidification: Temperature Distribution and Fin Efficiency <i>by Abdenour Bourabaa, Mohamed Saighi, Malika Fekih, Brahim Belal</i> | 857 |
| Theoretical, Experimental and Finite Element Analysis of Heat Loss for Designing a Parabolic Concentrator <i>by Abhijeet B. Auti, T. P. Singh, Mandar S. Sapre</i> | 864 |
| Instant Hot Water Generation System for Domestic Utility in Rural Areas <i>by P. Selvakumar, P. Somasundaram</i> | 869 |
| Numerical Study of Ice Melting Inside a Rectangular Cavity and a Horizontal Cylinder Including Convective Effects <i>by Christiano G. S. Santim, Luiz Fernando Milanez</i> | 874 |

(continued)



Praise Worthy Prize

| | |
|--|-----|
| Effect of the Flow Field Design and Gas Flow Configuration on the Performance of the Polymer Electrolyte Membrane Fuel Cell - An Experimental Analysis <i>by V. Savithiri, G. Nagarajan</i> | 882 |
| Cycle Efficiency Optimization for ORC Solar Plants <i>by A. Amoresano, G. Langella, S. Meo</i> | 888 |
| Integrated Oil Palm Fruit Digester-Separator-Screw Press Machine <i>by Nwankwojike, B. Nduka</i> | 895 |
| Machinability Study of Biocomposite: Palm Oil Based Wax/LLDPE/Palm Oil Fiber Blends for Prototype Application <i>by A. N. M. Khalil, M. F. M. A. Hamzas, M. S. Hussin, Z. A. Zailani, A. B. Sanuddin</i> | 903 |
| An Effect of Boric Acid Mixture as Solid Lubricant Towards Machining Processes <i>by Z. A. Zailani, A. B. Sanuddin, M. S. Hussin, A. N. M. Khalil, M. F. M. A. Hamzas, Nurliana Ahmad Mustafa</i> | 912 |
| Experimental Investigation on the Performance, Emission and Combustion Characteristics of a Diesel Engine Fuelled with Polymer Oil - Ethanol Blends <i>by Ganapathi P., Robinson Y.</i> | 919 |
| Biodiesel Blend, Fuel Properties and its Emission Characteristics Sterculia Oil in Diesel Engine <i>by P. P. Sethusundaram, K. P. Arulshri, K. Mysamy</i> | 925 |
| Experimental Investigations of Silicon Carbide - Fly Ash Reinforced Aluminium Metal Matrix Composite <i>by Vivekanandan P., Arunachalam V. P.</i> | 930 |
| Development of Empirical Models of Polyfelt Fibrous Materials for Acoustical Applications <i>by L. Egab, X. Wang, S. K. Mazlan, M. L. Choo</i> | 939 |
| Workability Behaviour of Al-SiC Matrix P/M Composite Under Triaxial Stress State Condition <i>by J. Bensam Raj, P. Marimuthu, M. Prabhakar, V. Anandkrishnan</i> | 947 |
| Experimental and Emission Analysis of Rubber Seed Oil and Jatropha Oil Blends with Diesel in Compression Ignition Engine <i>by S. Mahalingam, B. R. Ramesh Babu</i> | 955 |
| A Review of Localised Time-Frequency Features Classification Associated to Fatigue Data Analysis <i>by M. F. M. Yunoh, S. Abdullah, Z. M. Nopiah, M. Z. Nuawi</i> | 960 |
| Strength of the Weld Line and Warpage Defects on the Molded Parts in Injection Molding Process <i>by S. M. Nasir, K. A. Ismail, Z. Shayfull, N. A. Shuaib</i> | 977 |
| Design of a Fuzzy Logic Approach for Optimization of Fracture Length in Hydrofracturing Technique <i>by B. Guruprasad, A. Ragupathy, T. S. Badrinarayanan, E. Sambath</i> | 991 |



Performance Study of Reference Height Control Algorithm for Tripod Hopping Robot

A. M. Kassim, T. Yasuno, N. Abas, M. S. M. Aras, M. Z. A. Rashid

Abstract – Central Pattern Generator (CPG) algorithm enables to produce rhythmic patterned outputs where this neural networks underlie the production of most rhythmic motor patterns. In this paper, the generation of vertical jumping motion for tripod hopping robot by applying the Central Pattern Generator networks with reference height control algorithm in order to achieve reference height for each leg of tripod hopping robot is discussed. The proposed algorithm is designed using MATLAB/ Simulink which is consisted of maximum height detector, PI controller in the system of Central Pattern Generator (CPG). By using the proposed algorithm, the developed tripod hopping robot can achieve the reference height and maintain the hopping motion respectively. As the result, the effectiveness of proposed reference height control algorithm in order to achieve the reference height is confirmed. **Copyright © 2013 Praise Worthy Prize S.r.l. - All rights reserved.**

Keywords: Tripod Hopping Robot, Reference Height Control Algorithm, Central Pattern Generator

I. Introduction

Physiological experiments suggest that basic locomotor patterns of most living bodies such as walking, flapping, flying and swimming are generated by CPGs which generates rhythmic activities [1].

CPG is neural networks that can endogenously produce rhythmic patterned outputs; these networks underlie the production of most rhythmic motor patterns. The periodic activities of the CPG which are initiated by a burst from the higher motor centre induce the muscle activities. After the initiation of the locomotion, the activities of the CPG are affected by sensory signals which show the bending of the body and so on [2].

The proactive sensory feedback plays an important role in the shaping and coordination of the neural activity with the mechanical activity. Moreover, neurophysiologic studies of insect locomotion suggest that sensory feedback is involved in patterning motor activities and that is more than modulation of the centrally generated pattern [3].

The construction of useful legged type locomotion comes from the system which able to control joint motion, monitor and manipulate balance, generate motions to use known footholds, sense the terrain to find good footholds and calculate negotiable foothold sequences. Meanwhile, M. H. Raibert who has done research on one-legged hopping robot is the main contributor of hopping robot research [4]-[5].

It is consisted body and leg which is equipped with a pair of pneumatic actuators to exert torque between the leg and the body about to hip. In addition, discrete dynamic system theory has been discovered by Koditscheck and Buhler which analyze the dynamics of a simplified hopping robot that focused only on the vertical movement

[6]-[7]. On the other hand, Son et al. proposed a CPG model including the motor dynamic characteristic of an actuator for the purpose of implementing generation adaptive gait patterns for quadruped robot under various environments [8]-[9]. Besides, for application on quadruped hopping robot, Kondo et. al proposed the CPG networks to generate continuous jumping motion patterns [10]-[11]. The contribution of the proposal in this paper is to generate a vertical hopping motion rhythmically by applying the CPG network and reference height control algorithm.

The CPG network with reference height control algorithm is succeed when applied with quadruped hopping robot by achieving the reference height which has been set while jumping continuously [12]-[14]. The proposed reference height control algorithm also evaluated for tripod hopping robot in order to converge the steady state error which existed on each jump according to the reference height for each leg of the developed tripod hopping robot. Therefore, the approved reference height control algorithm also can be applied in moving motion of tripod hopping robot in the future.

II. Developed Hopping Robot

II.1. Robot Modeling

This section focused towards hopping robot modeling.

The hopping robot consists of two part modeling where covered on electrical and mechanical modeling.

The electrical modeling is included the Direct Current (DC) motor modeling. Besides, the mechanical design and dynamical modeling of the hopping robot structure is covered the mechanical dynamic modeling.

Electrical Modeling

A DC motor is the main electrical part in producing hopping mechanism. Refer to Fig. 1, the motor applies a torque, τ which the maximum torque is 0.098 Nm at 12 Volt to the platform. The voltage to torque model of the motor determined by System Identification method:

$$\frac{\tau(s)}{V(s)} = \frac{(K_{mf} / L_f)}{s + (R_f / L_f)} = \frac{8.258}{s + 10.34} \quad (1)$$

where R_f is field resistor and L_f is field inductor of the motor. The hopping height of the robot is controlled by regulating the voltage supply to the motor. Different speed of the motor produced different hopping height of the robot. The voltage to speed transfer function of the motor:

$$\frac{\omega(s)}{V(s)} = \frac{7.13s + 538.4}{s^2 + 27.98s + 459.7} \quad (2)$$

where the output of the motor speed within range of 0% and 100% depend on the voltage input as follows:

Clockwise:

$$\omega = \begin{cases} \omega_{max} & \text{if } V = 12V \\ 0 < \omega < \omega_{max} & \text{if } 0 < V < 12V \\ 0 & \text{if } V = 0V \end{cases}$$

Counter clockwise:

$$\omega = \begin{cases} 0 & \text{if } V = 0V \\ 0 < \omega < \omega_{max} & \text{if } 0V > V > -12V \\ \omega_{max} & \text{if } V = -12V \end{cases}$$

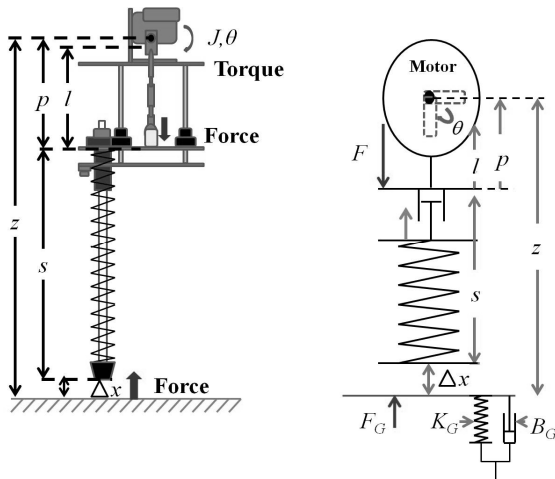


Fig. 1. One legged hopping robot

Mechanical Design And Modeling

1) One Legged Hopping Robot

The mechanical structure and component of one legged hopping robot is designed as illustrated in Fig. 1. A stand

is attached to the one legged hopping robot to ensure the vertical hopping dynamic produced. The one legged hopping robot is designed based on 'passive dynamic' of mass-spring-damper model.

TABLE I
PARAMETER USED IN ONE LEGGED HOPPING ROBOT

| Parameter | Description |
|-----------|-------------------------------|
| z | Body height |
| p | Distance length |
| l | Rod end bearing length |
| l_o | Motor to platform free length |
| s | Spring length |
| s_o | Spring free length |
| θ | Motor angle |
| J | Motor inertia |
| k | Spring stiffness |
| c | Viscous damping coefficient |
| τ | Motor torque |
| m_m | Spring mass |
| m_b | Unspring mass |
| m_p | Sliding mass |
| m_t | Total mass |

2) Motor Crank

The force react on the spring is produced by a motor with crank which inspired from piston mechanism. The rotation angle of the motor is model as follows:

$$\theta = \sin^{-1} \left(\frac{\dot{p} + l\dot{\phi} \sin \phi}{-r\Omega} \right) \quad (3)$$

The distance from the motor to the platform is rise continuously until the angle of the motor reach 180° and ease to the initial distance at 360° as follows:

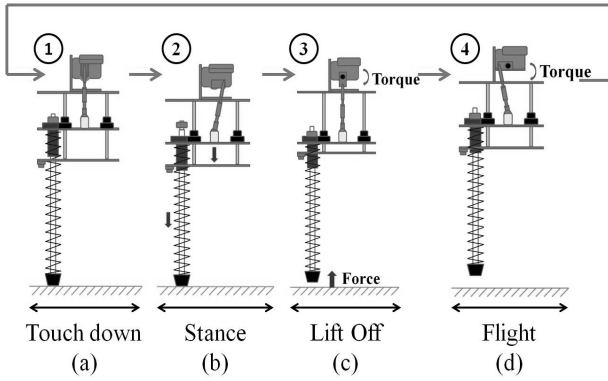
$$\dot{l}(t) = \begin{cases} l_o < l \leq l_{max} & \text{if } 0 < \theta < 180^\circ \\ l_{max} > l \geq l_o & \text{if } 180^\circ < \theta < 360^\circ \end{cases} \quad (4)$$

$$\dot{l} = -r\Omega \sin \theta - l\dot{\phi} \sin \phi$$

3) Hopping Mechanism

The hopping mechanism of one legged hopping robot is illustrated in Figs. 2. The mechanism consists of four states as follows:

- i. Touch down: The moment of the base makes contact to the ground.
- ii. Stance: The cranks are installed at the motor operates the same mechanism to convert the motor torque as the conservation energy into the spring.
- iii. Lift-off: The moment when the base losses contact with the ground. This phase occurs caused by the conservation energy of the depressed spring and ground repulsive force that excited the robot to hop.
- iv. Flight: The moment that the robot has peak altitude and vertical position/motion changes from downward to upward or otherwise.



Figs. 2. Crank mechanism

4) Stance Phase

Fig. 2(b) represents the stance phase mechanism. By using Lagrangian Method equation as follows:

$$L = T - V \tag{5}$$

where T is total kinetic energy and V is potential energy, the stance mechanism dynamic model is derived in state-space as follows:

$$\dot{x} = Ax + B\tau + E \tag{6}$$

$$A = \begin{bmatrix} 0 & 1 & 0 & 0 \\ 0 & \frac{-Jc}{r^2\beta} & 0 & \frac{Jc}{r^2\beta} \\ 0 & 0 & 0 & 1 \\ 0 & \frac{m_m c}{\beta} & 0 & \frac{-m_m c}{\beta} \end{bmatrix}$$

$$B = \frac{\eta}{\beta r} \begin{bmatrix} 0 \\ m_p \\ 0 \\ m_m + m_p \end{bmatrix}; x = \begin{bmatrix} z \\ \dot{z} \\ p \\ \dot{p} \end{bmatrix}$$

$$E = \frac{1}{\beta} \begin{bmatrix} 0 \\ \alpha \left(-(m_m + m_p)g + k(s_o - z + p) + \right. \\ \left. -(F_{fr,p} + F_{fr,z}) \text{sign}(\dot{z}) \right) + \\ + m_p(m_p g - k(s_o - z + p)) \\ 0 \\ m_p \left(-(m_m + m_p)g + k(s_o - z + p) + \right. \\ \left. -(F_{fr,p} + F_{fr,z}) \text{sign}(\dot{z}) \right) + \\ \left. + (m_m + m_p)(m_p g - k(s_o - z + p)) \right) \end{bmatrix}$$

5) Flight Phase

Fig. 2(d) represents the flight phase mechanism. The final state equation of the flight mechanism dynamic model is derived as follows:

$$A = \begin{bmatrix} 0 & 1 & 0 & 0 \\ 0 & 0 & 0 & \frac{-m_p c}{\gamma} \\ 0 & 0 & 0 & 1 \\ 0 & 0 & 0 & \frac{-m_t c}{\gamma} \end{bmatrix}; B = \frac{\eta}{\gamma r} \begin{bmatrix} 0 \\ m_p \\ 0 \\ m_t \end{bmatrix}; x = \begin{bmatrix} z \\ \dot{z} \\ p \\ \dot{p} \end{bmatrix}$$

$$E = \frac{1}{\gamma} \begin{bmatrix} 0 \\ \alpha \left(-m_t g - F_{fr,p} \text{sign}(\dot{z}) + \right. \\ \left. + m_p(m_p g - k(s_o - l_o + p)) \right) \\ 0 \\ m_p \left(-m_t g - F_{fr,p} \text{sign}(\dot{z}) + \right. \\ \left. + m_t(m_p g - k(s_o - l_o + p)) \right) \end{bmatrix}$$

II.2. Robot Construction

Fig. 3 shows the developed tripod hopping robot which its overall length and width is 26cm, overall height is 40cm and its weight is 4.59 kg.

The robot is consisted of three legs which are connected to a shared platform. A DC geared motor (12V, 200min⁻¹, 0.098Nm), a crank and a spring are joined together to form a leg which is attached to the crankshaft.

DC geared motor plays as the main role of the tripod hopping robot performance. DC amplifier is used to drive the DC geared motor to provide torque through the crank to push the platform.

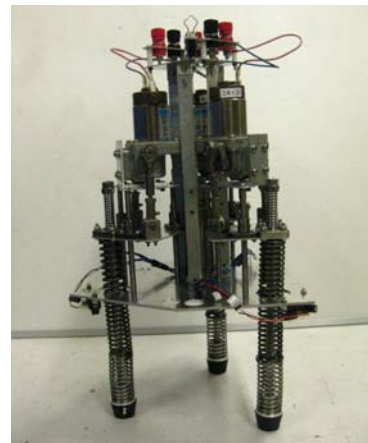


Fig. 3. Developed tripod hopping robot

II.3. Experimental Setup

Fig. 4 shows the experimental setup for evaluation of the tripod hopping robot. The system needs two different computers which is connected through Ethernet to each other.

One of the computers is included with MATLAB/Simulink model functions as the host computer while the other one plays as xPC target computer. The model which built by realtime workshop is downloaded to

the xPC target computer and run by using realtime OS. The measurement of sensor on each leg will be send to the A/D converter and input to the xPC Target Computer as the experimental results.

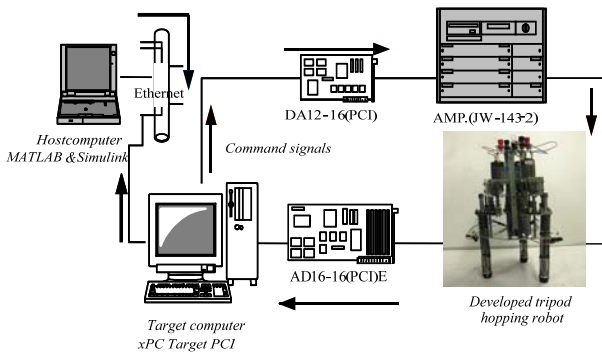


Fig. 4. Experimental Setup

III. System Configuration

III.1. CPG Model

Fig. 5 shows the block diagram of the CPG model which is used for the tripod hopping robot. Mechanical dynamics of the leg is included into the inhibitory unit.

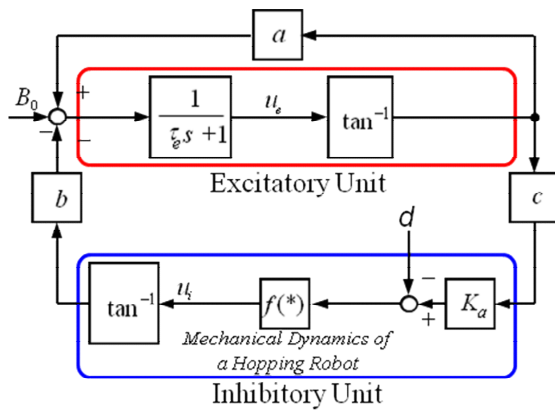


Fig. 5. Block diagram of CPG model

Parameters u_e and u_i denotes the internal state of the excitatory unit and inhibitory unit, b and c denotes the intrinsic excitatory and inhibitory coupling parameter, a denotes the excitatory coupling factor while B_0 denotes the constant bias input.

The output of the inhibitory unit corresponds to the platform position of each leg and is applied to the excitatory unit through a nonlinear function $\tan^{-1}(u_i)$ and the feedback gain b which is formulated as

$$\tau_e \frac{du_e}{dt} = -u_e + a \tan^{-1}(u_e) - b \tan^{-1}(u_i) - B_0$$

$$u_i = f(K_a c \tan^{-1}(u_e) - d)$$

where $f(*)$ is the mechanical dynamics of the hopping robot's leg, K_a is the gain constant of the DC amplifier and

d is the external disturbances which is the floor repulsive force for this case. CPG may change the amplitude and frequency of internal states u_e and u_i by only hanging the coupling parameters a, b, c , the time constant τ_e and the mechanical dynamics of the hopping robot arbitrarily.

III.2. Reference Height Control Algorithm

Fig. 6 shows the block diagram of the reference height control algorithm for one leg of developed tripod hopping robot. This block diagram is built by using MATLAB/Simulink tool. This system consists of maximum height detector, the PI controller and the CPG.

By using the proposed control algorithm, the tripod hopping robot can keep the hopping motion and control the hopping height to achieve the reference hopping height by adding a feedback loop through a fixed gain PI controller. The joint actuator is driven by the control system in order to realize the reference hopping position generated by the PI controller on each leg.

Deduction of sensory feedback signal h_{max} of the ultrasonic sensors on each legs from the reference height h_{ref} gives the value of steady state error h_{diff} which represents the command signal. In control engineering, a PI controller is a feedback controller which drives the plant to be controlled with a weighted sum of error h_{diff} and integral of that value. The integral term in PI controller causes the steady state error to be zero for a step input.

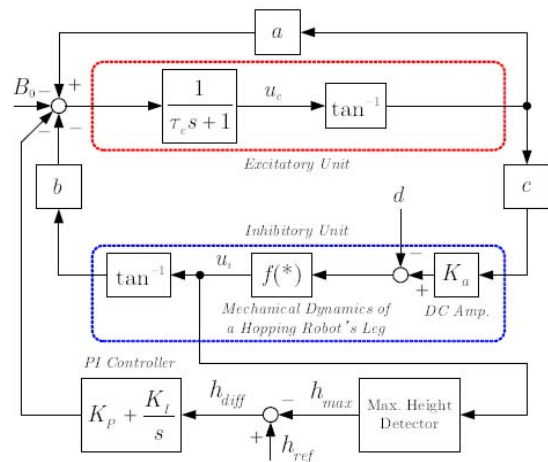


Fig. 6. Block diagram of reference height control system

III.3. CPG Networks

Configuration of typical CPG network is shown in Fig. 7. Cooperative oscillations among the CPG is required and continuous hopping performance of the tripod hopping robot is achievable by applying the same periodic force to the spring of the robot.

IV. Experimental Results

In order to evaluate the validity and the performances

of the proposed reference height control system for the tripod hopping robot, the experiment was conducted.

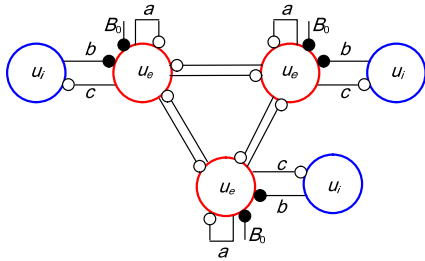


Fig. 7. CPG networks for tripod hopping robot

At the same time, these experiments also to adjust the best value of PI gain from the PI controller system according to the changes of size and weight of developed tripod hopping robot from the developed quadruped hopping robot. These experiments are conducted to evaluate the maximum height detector system and PI controller system which included in the proposed system.

The values of CPG networks coupling parameters proposed for the experiments are $a = 0.1$, $b = 2$, $c = 1$, $B_0 = 0.01$ and $\tau_e = 0.1$.

The first experiment is conducted for reference height control system by using P controller only. This method is approached in order to adjust the best value of P gain in order to generate the continuous hopping performances while achieving the reference height which has been set. In other words, this experiment is conducted to evaluate the effectiveness of P controller for the tripod hopping robot to achieve the reference hopping height.

P gain value is tuned manually from $K_p = 0.5$ to the best value while $K_I = 0$. The best jumping performances are observed and the jumping height data is analyzed. The best value of gain P will be remained for the second experiment. As the result, the best value of P gain which is acquired is $K = 1.0$. Fig. 8 shows the experimental results for leg 1 and center of the platform for developed tripod hopping robot using P controller only.

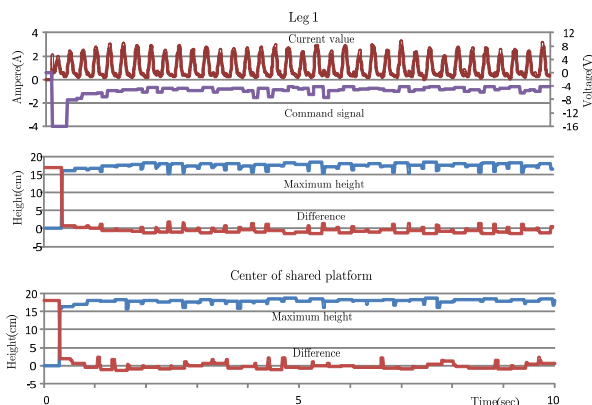


Fig. 8. Experimental result on using P control only ($K_p=1.0$)

The experimental results shows the data of jumping height, command signal, difference (steady state error),

feedback signal, and center jumping height for leg 1 while conducting the experiments.

The whole experiment for evaluating the stability of the proposed reference hopping height control system is conducted in 10s.

The evaluation of PI controller in order to converge the remained steady state error to zero is conducted as the second step of experiment. The best value for I gain is evaluated by setting P and I gain from $K_p = 1.0$ and $K_I = 0$ in order to converge steady state error to zero.

Analyzing whether the steady state error is converged into zero or not help to determine the best value of I gain. Then, the similar method which used to determine the P gain is conducted to acquire the best value of gain I by increasing the value $K_I = 0.1$ each experiment.

Fig. 9 shows the experimental results of using PI controller system for the developed tripod hopping robot.

From the experimental result, it is proved that the developed tripod hopping robot can achieve the reference height which is set to each leg by using PI controller.

The tripod hopping robot jumped with synchronizes and the same frequency of each jumping can be seen in result of current value at Fig. 9.

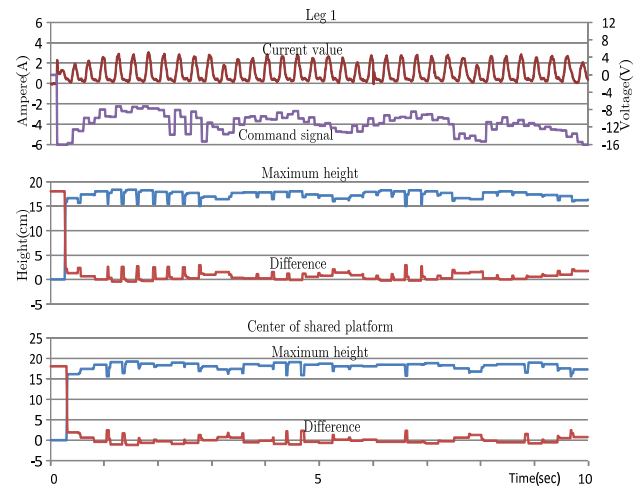


Fig. 9. Experimental result of reference height control system (PI controller $K_p=1.0$, $K_i=0.2$)

From the result, it can be seen that the frequency for each jumping is same on all legs except some current value is not detected from leg 1.

This condition represents that leg 1 is floating while leg 2 and leg 3 are on the floor. At this condition, higher voltage is sent to leg 2 and leg 3 so that higher jumping performance can be done in order to stable the body balances of the developed tripod hopping robot from tumble. Therefore, the effectiveness of leg 2 and leg 3 to balance the body of the developed tripod hopping robot is confirmed.

V. Conclusion

In this paper, the proposed reference height control algorithm with CPG networks is confirmed in order to

achieve the desired reference height while generating continuous hopping motion. By using the collaboration of CPG networks and PI controller, the successful continuous hopping performances also is obtained and the desired hopping height is achieved. However, the collaboration of CPG and PI controller was to optimize the parameter for each controller.

In future, we aim to investigate the moving motion control system of the tripod hopping robot for better moving motion performance. Besides that, we would like to build simulation model for the tripod hopping robot and by using learning algorithm we aim to acquire the CPGs parameters and coupling parameters of CPG networks for hopping at arbitrary place.

Acknowledgements

This work is supported in part by a Grant-in -Aid for Ministry of Higher Education Malaysia FRGS/2012/FKE/TK02/03/2/F00124 and also technically support from Yasuno laboratory member, The University of Tokushima, Japan.

References

- [1] Grillner S, "Neurobiological Bases of Rhythmic Motor Acts Invertebrates", *Science*, Vol.228, pp.143-149, 1985.
- [2] Shahir Hasanzadeh, Alireza Akbarzadeh, "Development of a new spinning gait for a planar snake robot using central pattern generators", *Intelligent Service Robotics*, Volume 6, Issue 2, pp 109-120, 2003
- [3] Bässler U; "On the Definition of the Central Pattern Generator and its Sensory Control", *Biol. Cybernetics*, No.54, pp 65-69, 1986.
- [4] M.H Raibert; *Legged Robot That Balance*, MIT Press, Cambridge, Massachusetts, 1986
- [5] M.S.M, Aras, S.S. Abdullah, A.A. Rahman, M.A.A.Aziz, "Thruster Modelling for Underwater Vehicle Using System Identification Method", *International Journal Advance Robotic System*, Vol.10, Issue 252, pp. 1-12, 2013.
- [6] R. Mellah, R. Toumi, Adaptive Neuro-fuzzy Control With Fast Learning Algorithm of PUMA560 Robot Manipulator, (2007) *International Review of Mechanical Engineering (IREME)*, 1 (4), pp. 347-355.
- [7] D.E Koditscheck and M. Buhler; Analysis of a Simplified Hopping Robot, *Int. Journal of Robotics Res.*, Vol.10(6), pp.587-605,1991.
- [8] Y. Son, T. Kamano, T. Yasuno, T. Suzuki, and H. Harada: Generation of adaptive gait patterns for quadruped robot Using CPG Network, *Electrical Eng. Jpn.*, Vol.115, No.1, pp. 35-43, 2006.
- [9] N, Abas and A, Legowo and Z, Ibrahim and A.M. Kassim and N. Rahim, "Modeling and System Identification using Extended Kalman Filter for a Quadrotor System". *Machinery Electronics and Control Engineering II, Periodical of Applied Mechanics and Materials*, Vol. 313-314, pp. 976-981, 2013.
- [10] K. Kondo, T. Yasuno and H. Harada: Generation of jumping motion patterns for quadruped hopping robot using CPG network, *Journal of Signal Processing*, Vol.11, No.11, pp. 321-324, 2007.
- [11] Jebelli, A., Yagoub, M.C.E., Abdul Rahim, R.H.J., Kazemi, H., Design and construction of an underwater robot based fuzzy logic controller, (2013) *International Review of Mechanical Engineering (IREME)*, 7 (1), pp. 147-153.
- [12] A. M. Kassim, M. Z. A. Rashid, M. R. Yaacob, N. Abas, and T. Yasuno, "Effect of Reference Height Control System on CPG Networks for Quadruped Hopping Robot," *Machinery Electronics and Control Engineering II, Periodical of Applied Mechanics and Materials*, Vol. 313-314, pp. 498-502, 2013.

- [13] M.Z.A Rashid, M.S.M, Aras, A.M Kassim, Z. Ibrahim, A. Jamali, "Dynamic Mathematical Modeling and Simulation Study of Small Scale Autonomous Hovercraft", *International Journal of Advanced Science and Technology* 46, pp. 95-114, 2012
- [14] N.H.A Rahim, A.M. Kassim, M.F. Miskon, A.H. Azahar, "Effectiveness of central pattern generator model on developed one legged hopping robot", 2011 *IEEE Student Conference on Research and Development (SCoReD)*, 85-88, 2011.

Authors' information



Anuar Mohamed Kassim received his B.Eng. degree in Electrical and Electronic Engineering from the Ehime University, Japan in 2006. He was engineer in Panasonic Communication Co. Ltd, Japan from 2006 to 2008 at Blu-ray disc (BD) drive department. He finished his M. Eng. degree in the Department of Electrical and Electronic Engineering, Graduate School of Advanced Technology and Science, The University of Tokushima, Japan in 2010. Currently, he serve as lecturer in Universiti Teknikal Malaysia Melaka. His current research interests include the motion control of multi-legged type hopping robot.



Takashi Yasuno received his B.E. degree in Electrical Engineering, M.E. degree in Electrical and Electronic Engineering, and D.Eng degree in System Engineering from The University of Tokushima in 1991, 1993, and 1998, the respectively. He is currently working at Faculty and School of Engineering, The University of Tokushima, where he has served as an Associate Professor since 2003. His current research interests include intelligent motion control systems. He is a member of the Society of Instrument and Control Engineers, the Institute of Systems, Control and Information Engineers, the Japan Society for Fuzzy Theory and Intelligent Informatics, the Robotics Society of Japan, and the Institute of Electrical Engineers of Japan.



Norafizah Abas received her B.Eng. degree in Mechatronics from the International Islamic University Malaysia in 2008, and she completed her M.Sc. degree in Mechatronics from the International Islamic University Malaysia in 2012. Currently, she served as lecturer in Universiti Teknikal Malaysia Melaka. Her current research interests include the motion control of multi-legged type hopping robot, system identification and nonlinear control system of UAV.



Mohd Zamzuri Ab. Rashid received his B.Eng degree in Mechatronics from International Islamic University in 2005. He finished his MSc. in Mechatronics from International Islamic University in 2012. Currently, he serves as lecturer in Universiti Teknikal Malaysia Melaka. His current research interests include unmanned system and underactuated nonlinear system. He is an associate member of Universal Association of Computer and Electronics Engineers (UACEE)



Mohd Shahrieel b Mohd Aras is a lecturer at Faculty of Electrical Engineering, Universiti Teknikal Malaysia Melaka UTeM. He currently pursues his PhD in Control and Automation, Faculty of Electrical Engineering, Universiti Teknologi Malaysia. His currently research is focusing on control system design of underwater technology.

UTeM's Amphibious Hybrid Vehicle: Development of Hybrid Electric Propulsion System

Muhammad Zahir Hassan, Amjad Saddar Md Isa, Syahibudil Ikhwan Abdul Kudus,
Muhammad Zaidan Abdul Manaf

Abstract – This paper presents the preliminary development of hybrid electric propulsion system for amphibious hybrid vehicle (AHV). AHV is developed as a transportation vehicle that can operate both on land and water to be used by the rescue team in rescue operations. AHV is driven by motor electric on the land, while on the water, AHV is propelled by the internal combustion engine (ICE). At the same time, ICE is used as generator to generate the electricity to recharge the battery pack. The main factors that need to be considered in order to develop a hybrid electric propulsion system is the power required by batteries to transmit to the motor electric to move the vehicle. An optimum hybrid electric propulsion system should have minimum fuel consumption, simple to develop and high reliability. Matlab Simulink Analysis based on the mathematical modelling is conducted to determine the power required before the fabrication take place. The design of hybrid electric propulsion is then fabricated by combination of ICE and electric motor. Finally experimental analysis is conducted to determine its reliability and durability. **Copyright © 2013 Praise Worthy Prize S.r.l. - All rights reserved.**

Keywords: Hybrid Electric Propulsion System, Amphibious Hybrid Vehicle

Nomenclature

| | |
|----------|--|
| F_{ad} | Aerodynamic resistance force |
| F_{rr} | Rolling resistance force |
| F_{hc} | Rolling resistance force |
| F_{la} | Acceleration force |
| F_{te} | Tractive force |
| ρ | Air density |
| C_d | Coefficient of drag (depends on body design) |
| A | Frontal area of vehicle |
| v | Velocity |
| m_t | Total mass |
| g | Acceleration of gravity |
| θ | Angle of slope |
| P | Power required |

I. Introduction

Hybrid vehicle means combination of two or more power source to increase the overall efficiency [1]-[16].

The types of hybrid can be classified based on driveline configuration. There are three common types of hybrid design configuration which are series, parallel, and series-parallel. Although further improvements on vehicle fuel economy since the last 40 years have been conducted, the average efficiency in the use of gasoline ICE normal operation is only at 15%. While other 85% is lost to the environment as engine heat, exhaust gas heat, aerodynamic drag, rolling resistance of the tires, losses at the driveline and during braking [2].

Addition of an electric motor and electric energy storage from ICE can increase diversity of efficiency significantly, depends on the system design.

Common features of most hybrids that improve fuel economy are:

(i) *Idle stop*

The average vehicle idle time is around 20% of the total driving operation. During this time, turning off the engine can reduce the fuel consumption by 5 to 8% [2].

While during others time, fuel can be saved by turning off the engine when the vehicle is under deceleration, thus CO_2 emissions is not released. The idle stop is possible because restarting the engine happen at very low engine speed. The mix of air-fuel is combust at crank speed of 400 rpm. [1].

(ii) *Regenerative braking*

During deceleration or braking driving phase, the system will absorb the braking energy and store it in an energy storage device such battery or other components for future use, and it is also helps in charging the battery [3].

(iii) *Power-assist*

The electric motor gives additional power to the ICE when the vehicle is accelerated. Assistance from the power-assist module can reduce the size of the engine and improve the fuel efficiency without reducing the overall performance of the vehicle. Application of power-assist in Toyota Prius shows that the performance of 1800cc ICE is comparable to 2400cc performance with power-assist. [4]

(iv) Engine efficiency

The ICE efficiency is low during low speed and low load operation. Therefore, to increase the system efficiency at this condition, the electric motor can be used as alternative power supply. Hence, the fuel consumption and emission is can be set to zero at this particular time.

II. Development Process

In development of the hybrid electric propulsion system, the following considerations need to be adhered:

- i. Design of hybrid configuration.
- ii. Power requirement.
- iii. Component selection and arrangement.
- iv. Vehicle size.

The first two criteria are very important parameters in order to design a hybrid electric propulsion system. Apart from that, the following assumptions are required in conducting the analysis:

- i. Vehicle moving in constant velocity without acceleration.
- ii. There is no energy loss from ICE.

II.1. Design Process

Firstly, to design the hybrid electric propulsion system is to come up with a power flow planning in the AHV. A series hybrid configuration type is applicable in the vehicle as the propulsion system. The power flow plan is presented as in the Fig. 1.

II.1.1. Determining Hybrid Configuration

The AHV hybrid system in Fig. 1 consists of seven main components as correlation in the hybrid system of vehicle. When the ICE is running, the alternator that be linked to the crankshaft of ICE will generate the electricity according to the rotation of the crankshaft.

The increasing speed of the crankshaft rotation will increase the production of Alternating Current (AC).

Then, the regulator will regulate the unstable rectified AC to the steady at 12Volt of direct current (DC).

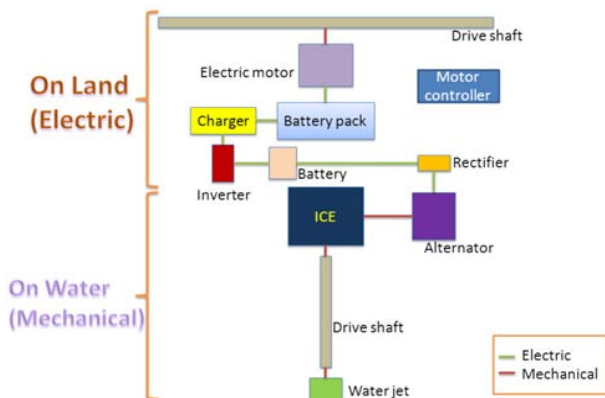


Fig. 1. Planning of the power flow in a AHV

The 12Volt DC from regulator is recharged the 12 Volt batteries which is used as a power bank. Next, the inverter will amplify the 12Volt DC to the 240Volt DC.

The amplified current is then use to run the charger. Charger is used to charge the 60 Volt DC battery packs that are required by the electric motor to operate. AHV also come with plug-in charging system to charge power bank as an alternative to ICE charging system.

Both power sources have specific operation environment. On the water surface, AHV is propelled by water jet which is connected to ICE driveshaft. While on the land, AHV is driven by the tyre which is connected to the drive shaft that powered by the electric motor.

The factors that determine the amount of the power from batteries which can transmit to motor electric are: tractive force. It is a summation of aerodynamic resistance force, rolling resistance force, hill climbing force, and acceleration force [5]. As shown in Fig. 2, the vehicle with mass, m moving at velocity, v on the slope with an angle, θ should overcome all the opposing force.

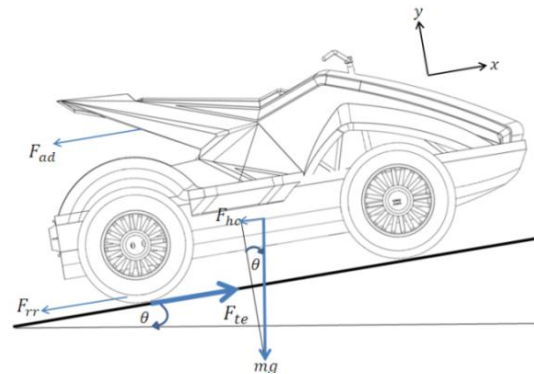


Fig. 2. Mathematical model of vehicle

II.1.2. Determining the Tractive Force

Based on the mathematical model of vehicle as shown in the Fig. 2, aerodynamics force is a friction force acting on the body surface area with the air when the vehicle is on the move. The corresponding mass density of air may be taken as $1.25 \text{ kg} \cdot \text{m}^{-3}$ [6]. The common value of drag coefficient C_d is determined from the Table I [7].

Rolling resistance force is due to the friction between tyre and the road surface. The typical value of rolling coefficient μ_{rr} is 0,015 [8]. Hill climbing force is required for vehicle to move along incline road. Based on the Newton's Second law of motion, the inertia force is increasing if acceleration is increase [9].

Therefore, the tractive force is increasing proportional to inertial force [10]. As mentioned earlier in previous section, vehicle will move on constant velocity. This is to simplify the analysis as the vehicle is in equilibrium condition due to summation of all forces is zero.

II.1.3. Determining Power

Assuming that vehicle does not stop until the fully charged batteries is exhausted.

TABLE I
COMMON VALUE OF C_d

| | C_d | | C_d |
|-------------------------|---------|------------------------|---------|
| Sport car, sloping rear | 0.2-0.3 | Truck | 0.8-1.0 |
| Saloon, stepped rear | 0.4-0.5 | Motorcycle and rider | 1.8 |
| Convertible, open top | 0.6-0.7 | Sphere | 0.47 |
| Bus | 0.6-0.8 | Long stream-lined body | 1.2 |

The required power of batteries to operate the electric motor at any given constant velocity can be calculated using Eq. (6):

The aerodynamics resistance force:

$$F_{ad} = \frac{1}{2} \rho C_d A v^2 \tag{1}$$

The rolling resistance force:

$$F_{rr} = \mu_{rr} m_t g \tag{2}$$

Hill climbing force:

$$F_{hc} = m_t g \sin \theta \tag{3}$$

Inertial force:

$$F_{la} = m a \tag{4}$$

Total tractive force:

$$F_{te} = F_{ad} + F_{rr} + F_{hc} + F_{la} \tag{5}$$

Power required by batteries for motor electric:

$$P_{b-m} = (F_{te} \times gear\ ratio) + \frac{1}{\eta} \tag{6}$$

Units:

| | |
|-----------------|---------------------|
| Force, F | N |
| Density, ρ | $kg \cdot m^{-3}$ |
| Area, A | m^2 |
| Velocity, v | $m \cdot s^{-1}$ |
| Mass, m | kg |
| Acceleration | $m \cdot s^{-2}$ |
| Angle | degree ^o |
| Power, P | W |

The power analysis is done for each constant velocity ranging from 0 km/h to 40 km/h with different gradient of 0°, 5°, and 10°.

II.1.4. Analysis Results

The analysis is focus only on electric motor and the result of analysis is determined by equations (1)-(6). The equation parameter is shown in Table II [11].

From Fig. 2, the frontal area of vehicle is calculated as stated in Table II. From Table I, there is no common value of drag coefficient for this type of vehicle, so the

value is assumed as in Table II. Total of mass is 273.2 kg where the mass of rider is to be assumed with typical weight around 60 kg. The vehicle is assumed moving on incline road surface gradient of 0°, 5° and 10° degrees. With all parameters and assumptions, the result for analysis on power required for vehicle is shown on the graph in Fig. 3. The analysis is conducted by using Matlab Simulink Analysis and the block diagram is shown in Appendix (Figs. 1A(a) and 1(b)).

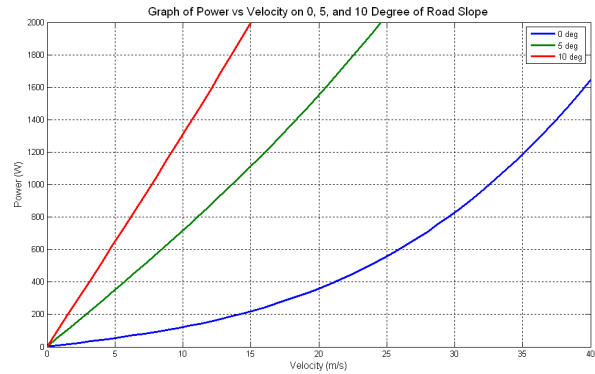


Fig. 3. Graph of Power vs. Velocity on 0, 5 and 10 Degree of Road Slope

Fig. 3 shows that the required power of the vehicle to move at different slope subjected to constant velocity. Power required by battery is proportional with the vehicle speed. Therefore, the speed of the vehicle is depends on the capacity of the power bank [12].

According to the graph, when the vehicle is move on a flat road at speed of 35 km/h, the battery need to supply the power of 1200W to the electric motor. By using the same battery power, if the vehicle move along the slope of 5°, the vehicle can speed up is up to 16 km/h. The speed of vehicle is up to 9.2 km/h when vehicle move along 10° of slope.

TABLE II
ASSUMPTION AND PARAMETER

| Parameter | Value | Parameter | Value |
|---------------------------------|------------------------|------------------------|----------|
| Density of air, ρ | 1.25 $kg \cdot m^{-3}$ | Mass of vehicle, m_v | 213.2 kg |
| Drag Coefficient, C_d | 1.3 | Mass of rider, m_r | 60 kg |
| Surface are, A | 0.98 m^2 | Efficiency, η | 0.98 |
| Gravity acceleration, g | 9.81 $m \cdot s^{-2}$ | Gear ratio | 14/60 |
| Rolling Coefficient, μ_{rr} | 0.015 | | |

The result shows that the power requires are proportional to the vehicle speed and the climb angle.

The selection of battery sizing and performance is based on the maximum power required to move the vehicle on flat surface which is 1600W.

II.2. Fabrication of the Hybrid Electric Propulsion System

The next step of this research is the fabrication of the hybrid electric propulsion system. The hybrid electric propulsion system was fabricated by installing the 150cc ICE which is used as a power source for water jet propulsion and it is also use to generate electricity by using the alternator that is built-in inside the engine.

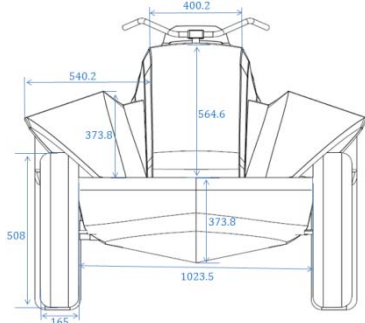


Fig. 4. Front view of the vehicle

AHV is installed with Brushless DC motor with 1kW to 3kW of rated power. Brushless DC Motor is more efficient, more compact and lightweight [2]. Lead Acid with Nano Gel technology is used as battery pack for the vehicle. Lead Acid is cheaper compared to Lithium-Ion or Nickel-Metal Hydride and this type of battery is suitable for mild level of hybrid. Five of batteries is used

which is 12V, 20Ah each make the total of voltage is 60 Volt. Motor controller with 60Volt of working voltage is used to control the voltage and current supply to electric motor. Throttle voltage for motor controller is 1.2 Volt to 4.3 Volt and the maximum current through motor controller is 70 Ampere. An intelligent charger with 240V is installed into the vehicle. As shown in Fig. 2A, the components are mounted to the chassis of the vehicle.

The component placement follows the suitability of the chassis and the component function. The hybrid electric propulsion system in amphibious hybrid vehicle is completely developed as shown in Fig. 3A.

III. Conclusion

In this paper, the development process of the hybrid electric propulsion system is properly demonstrated. It started with proper power planning, then the components integration and finally system testing and analysis.

Maximum 3kW rated power of the electric motor capable to propel the vehicle more than 40 km/h. However due to safety factor, the maximum speed of the vehicle is limited to 40 km/h. The installation of electric motor really assists in reduction of fuel consumption and vehicle emission.

Appendix

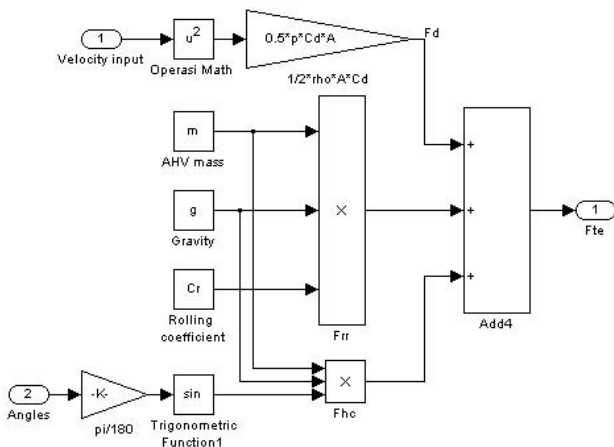


Fig. 1A(a). Block diagram for tractive force

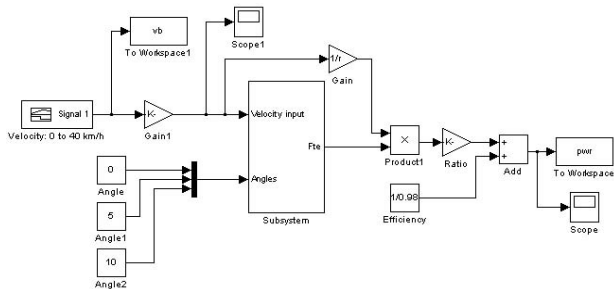


Fig. 1A(b). Block diagram for power

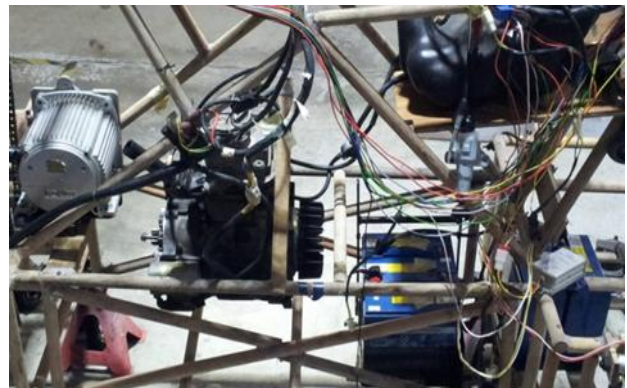


Fig. 2A. Hybrid propulsion system [12]



Fig. 3A. Complete AHV with hybrid propulsion system [12]

Acknowledgements

The authors would like to acknowledge Universiti Teknikal Malaysia Melaka for supporting this work through a short term grant title "Development of Hybrid Amphibious Vehicle Propulsion System for Marine Safety and Rescue Operation" (PJP/2012/FKM(17C)/S01109).

References

- [1] Ogawa H., Matsuki M., Eguchi T. (2003). "Development of Power Train for the Hybrid Automobile - the Civic Hybrid". Hybrid Gasoline-Electric Vehicle Development. pp 35-46.
- [2] Germen J. M. (2003). "Hybrid Powered Vehicle". USA: SAE International. pp. 17-67.
- [3] Halderman J. D. (2009). "Automotive Technology: Principles, Diagnosis, and Service". 3rd Edition Upper Saddle River: Pearson Prentice Hall.
- [4] UMW Toyota Motor (2012). "Introducing Sophisticated Intelligence and a New Hybrid Style". Malaysia: Sales brochure
- [5] Rozaini, O. (2011). "Design and Fabricate Propulsion System of UTeM Personal Electric Vehicle (PEV)": Thesis Bachelor
- [6] Rajamani, R. (2006). "Vehicle Dynamics and Control." New York: Springer. pp 97.
- [7] Carvill, J. (2003). "Mechanical Engineer's Data Handbook." Burlington: Butterworth-Heinemann. pp 77.
- [8] Larminie, J. and Lowry, J. (2003), "Electric Vehicle Technology Explained." West Sussex, England: John Wiley & Sons, Ltd. pp 221.
- [9] Gillespie, T. D. (1992) "Fundamentals of Vehicle Dynamics" USA: SAE International.
- [10] Zakaria, M.A. (2010) "I-Scoot: Intelligent Mobility Scooter": Master Thesis, Universiti Teknologi Malaysia.
- [11] Dukkupati, R.V., Pang, J., Qatu, M.S., Sheng, G. and Shuguang, Z. (2008) "Road Vehicle Dynamics", USA: SAE International.
- [12] Md. Isa, A.S. (2013). "Development of Hybrid Electric Propulsion System for UTeM's Amphibious Hybrid Vehicle": Thesis Bachelor.
- [13] Esposito, F., Isastia, V., Meo, S., Energy management strategy for automotive electric power system, (2006) *Przeglad Elektrotechniczny*, 82 (2), pp. 26-31.
- [14] Isastia, V., Meo, S., Esposito, F., An optimization technique for the choice of advanced automotive electrical systems, 5th *IATED International Conference on POWER AND ENERGY SYSTEMS (EuroPES 2005)*, June 15-17, 2005, Benalmádena, Spain, art. no. 468-150, pp. 251-256.
- [15] Ebadian, M., Mowlaie, V., Shafiee, F., Farshad, M., Mir Seyedi Anbaran, M., Study and simulation of PMBLDC motors as the proper choice for electric and hybrid electric vehicles, (2012) *International Review on Modelling and Simulations (IREMOS)*, 5 (4), pp. 1500-1509.
- [16] Ebadpour, M., Sharifian, M.B.B., Cascade H-bridge multilevel inverter with low output harmonics for electric/hybrid electric vehicle applications, (2012) *International Review of Electrical Engineering (IREE)*, 7 (1), pp. 3248-3256.

Authors' information



Muhammad Zahir Hassan is currently a Senior Lecturer at University Teknikal Malaysia Melaka. He graduated with the degree in Mechanical and Aerospace Engineering from Seoul National University, M.Sc. in Automotive Engineering from Coventry University and PhD in Mechanical Engineering from The University of Leeds. He has published more than 50 papers in refereed journals, proceeding and book chapter.



Amjad Saddar Bin Md. Isa received a Matriculation certificate from Johor Matriculation College on 2008. He graduated from Universiti Teknikal Malaysia Melaka with the degree of Bachelor of Mechanical Engineering (Automotive) with Honours in 2013.



Syahibudil Ikhwan bin Abdul Kudus is a lecturer at Faculty of Mechanical Engineering, Universiti Teknikal Malaysia Melaka, Malaysia. He graduated from Universiti Teknologi Malaysia in BSc. (Hons.) Industrial Design in 2003. In 2008, he finished his MSc. Design Innovation in Product Design from De Monfort University, UK. His expertise is in design and product development.



Muhammad Zaidan Bin Abdul Manaf is currently a lecturer at University Teknikal Malaysia Melaka. He received his first degree from Universiti Sains Malaysia in Aerospace Engineering in 2005. He then pursues his Master degree in Mechanical Engineering at Universiti Kebangsaan Malaysia in 2012. During his Masters, he is focusing on the mechanical hybrid propulsion systems.

Motorcycle Handlebar Dynamic Response: Theoretical and Experimental Investigation

D. De Falco¹, G. Di Massa², S. Pagano², S. Strano²

Abstract – *Motorcycle driver interacts with the vehicle through the hands, feet and buttocks. Through these parts of the body, the driver perceives vibrations due to engine and road roughness. A good level of comfort would require that handlebar and foot pegs natural frequencies should not line up with the operating range frequencies. In this paper the results of experimental tests direct to investigate the handlebar dynamic response is reported; the investigation is adopted to evaluate the possibility of adopting a vibration exciter placed in correspondence of the grips that could provide an alarm signal when a danger situation occur. This type of active assistance has already been used for cars and has proved effective in the accidents prevention. Copyright © 2013 Praise Worthy Prize S.r.l. - All rights reserved.*

Keywords: *Drive Assistant System, Vibration, Handlebar, Motorcycle*

I. Introduction

The drive assistant systems (DAS) are safety devices that provide active assistance to the vehicle drivers to avoid potentially dangerous situations and are a very effective form of accident prevention.

The DAS define the risk level by means of a comparison between the expected and the monitored vehicle conditions and inform the driver about a possible risk situation.

As the driver receives much information in visual or acoustic manner, it could be convenient to give an alert signal through vibrations so that it may result well distinguishable from other kind of information. The human body is very sensible to the periodic haptic stimuli and is able to appreciate vibrations until frequencies of about 1000 Hz.

The ISO2631-1 states that the maximum probability of vibration perception is comprised in the frequency range 0.5-80 Hz, with a maximum at about 40 Hz [1]. Motorcycle handlebar vibrations are influenced by the presence of the driver hands; in [2] the perception of vibrations transmitted to a rider's hands, through a motorcycle handlebar, is discussed.

Motor-vehicles have many sources of vibrations and the warning signals are perceived to be weaker [3]. Anyway DAS with vibrating alert have been already adopted for cars; in several commercial applications the system warns the driver by making the steering wheel or the seat vibrate in particular danger situations as, for example, in cases such as unintentionally overcoming of the lane lines, possible collision with the ahead vehicle, overcoming of the speed limit, etc.

The paper does not deal with road situation analysis for driver assistance and safety warning, that is an interdisciplinary endeavor involving many research fields

as vehicle engineering, cognitive science, computer science and psychology [4]; it focuses on the possibility to adopt vibrating alert signals acting on motorcycle handlebars that, with respect to the steering wheel of the cars, are less insulated against vibrations.

For this reason vibrating alert signals may be less perceivable as it could be not distinguishable from vibrations due to engine, wheels unbalance, road roughness or front assembly oscillations around the steering axis.

This last phenomenon was theoretically [5] [6] [7] and experimentally [8][9] investigated and involves oscillations with frequencies ranging from about 5 to 12 Hz, depending on the tyre-road interaction [10] [11] [12]. Wheel unbalance excitation covers the 0-40 Hz range; engine vibrations are characterized by a wide range of possible frequencies (about 10-500 Hz) and overlap the previous ones. To reduce the driver vibration exposure and annoying tingling in the hands, an handlebar should be designed to avoid resonances due to the engine. Usually this is not possible because of the wide range of frequencies covered by the engine.

It may be convenient to tune the handlebar first natural frequency at a sufficient low value that is not frequently excited by the engine. To achieve this goal, calibrated masses are often placed at the extremities of the handlebar. In reference [13], the use of a multi-dof tuned mass damper, to reduce handlebar vibrations, is proposed.

In the following, motorcycle handlebar dynamic response is experimentally investigated. Several tests were performed to evaluate handlebar vibrations excited by the engine and by a rotating shaker placed at the extremities of the grips; the exciter could be used to generate a warning signal of a DAS system.

II. Description of the Test Rig

The experimental investigation on the motorcycle handlebar vibrations was conducted on two different motorcycles: a sport-touring and a scooter. The two motorcycles are characterized by different handlebar type and by different frequency range excitations due to the engine:

- the sport-touring motorcycle has two straight semi-handlebar and is powered with a 900 cc, V-90° two cylinders engine with six gear ratios; the engine operates with a significant torque values in the rotating speed range comprised between 3500 rpm and 10000 rpm;
- the scooter has a single steering tube, a 150 cc single cylinder engine, operating between 4000 and 7500 rpm, with a CVT transmission.

For both motorcycles, the front wheel radius is equal to about 0.28 m; according to the maximum velocity the wheel unbalance force can achieve the maximum frequency of 40 Hz for the sport touring and 20 Hz for the scooter.

The two motorcycles were tested on the FSMDR flat track (Fig. 1) [14], [15], equipped with an adjustable hydraulic brake to simulate the forces opposing the vehicle motion. In this way it is possible to conduct experimental tests with actual vibrations due to engine and wheels unbalance in every operational condition. The system cannot replicate the on-road loads.

A remote control system allows to control a set of actuators placed on the motorcycles; it is so possible to simulate and execute the main driving commands via a PC. In particular, the throttle is actuated by a stepper motor, having an angular resolution of 0.225° , that drives a pulley on which is wound the throttle wire while the clutch and the gearshift levers are driven by pneumatic actuators. A sequence of commands can be recorded and controlled by the PC in order to run repeatable tests.

It can be noted that, according to the common natural frequency of the handlebars, the maximum wheel unbalance frequency is too low to cause handlebar resonance. Furthermore, road loads can result severe only in presence of particular roads pavements and, in any case they are filtered by the suspension. So, large handlebar vibration can be excited only the engine.

The tested motorcycles handlebars were equipped with a shaker (Fig. 2), constituted of an unbalanced rotating mass (Fig. 3), adjustable until 6000 rpm (100 Hz), connected at the extremity of the grip; the shaker can exert a rotating force of about 16N at the maximum angular speed. On the shaker case, two accelerometers with the sensitivity axis disposed along vertical and horizontal direction respectively, are mounted.

The motorcycles are instrumented even with gyroscopic sensors, placed on the triple clamp, and with an angular position transducer to detect front assembly rotations with respect to the rear frame (steer angle). The experimental tests were carried out without taking into account the presence of the driver hands.

III. Test Results

III.1. The Sport-Touring Motorcycle

The handlebar natural frequencies were evaluated by hitting the handlebar and performing an FFT on the free vibration accelerometer signals; for the sport-touring motorcycle the first two natural frequencies are 110 and 120 Hz, respectively.

So, the engine inertia forces cause handlebar resonance at about 3300/3600 rpm (resonance due to the second order reciprocating inertia forces) and at 6600/7200 rpm (resonance due to the inertia forces synchronous with the engine rotating speed).



Fig. 1. Motorcycle on the FSMDR rig



Fig. 2. Handlebar shaker/accelerometers



Fig. 3. Shaker and case

The frequency analysis response of the accelerometer signals, detected with the engine rotating at 4800 rpm (80 Hz), in neutral gear and with the shaker at rest, evidences harmonic components (Fig. 4) due to:

- rotating and first order reciprocating inertia forces (1x component);
- second order reciprocating inertia forces (2x component);
- inertia forces generated by the distribution bodies ($1/2$ x component);
- horizontal and vertical handlebar natural frequencies (F_{no} , F_{nv}).

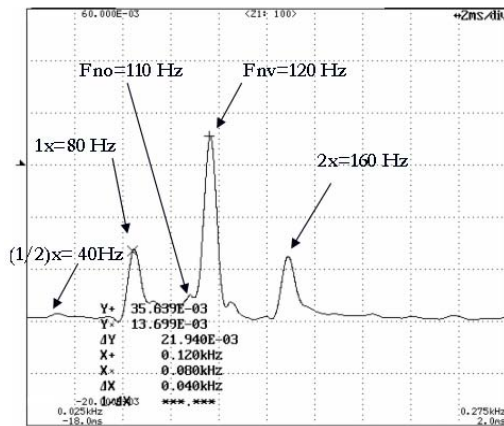


Fig. 4. FFT at 4800rpm and V=0

Fig. 5 reports the front assembly yaw rate FFT, detected with the gyroscopic sensor; the test was performed at the forward speed of 29.6 m/s, with the IV gear level and with the engine rotating at 5185 rpm (86 Hz). The figure puts in evidence the harmonic components caused by the above said forcing actions; furthermore a harmonic component at a frequency synchronous with front wheel rotating speed (16 Hz) mainly due to the wheel unbalance and to the front assembly oscillation (wobble) natural frequency at 9 Hz are present. The dynamic wheel unbalance couple excites the motorcycle front assembly to rotate around the steering axis; when the couple frequency is equal to the wobble natural one, the front assembly rotation amplitude is maximum.

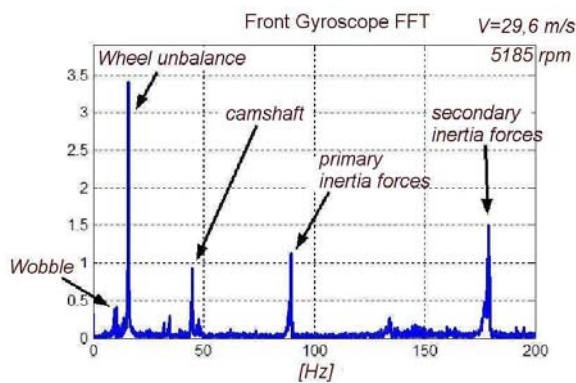
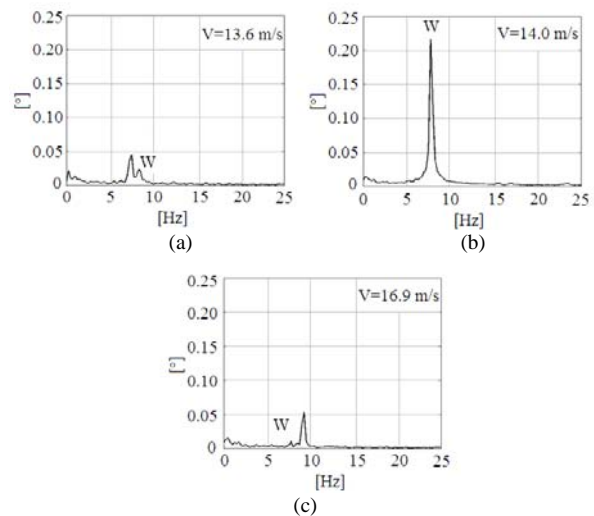


Fig. 5. FFT of the front assembly rotation speed

Figs. 6 report the FFT of the steer angular position for three different values of the forward speed; in particular, in Fig. 6(a) (13.6 m/s) the forcing moment has a frequency slightly smaller than the wobble one.

A resonance condition occurs at the speed of 14 m/s, for which the two frequencies are equal and the rotation amplitude achieves the maximum amplitude (Fig. 6(b)).

Then, for further increases of the forward speed (16.9m/s) the front assembly rotation amplitude decrease (Fig. 6(c)). The engine angular speed of the tested sport-touring motorcycle ranges between 3500rpm and 10000rpm; in Fig. 7, driving the handlebar exciter at a frequency of 90 Hz, the FFTs of the signal detected by the horizontal accelerometer, for several engine rotation speed, in neutral gear, are reported.



Figs. 6. FFT of the steer angle

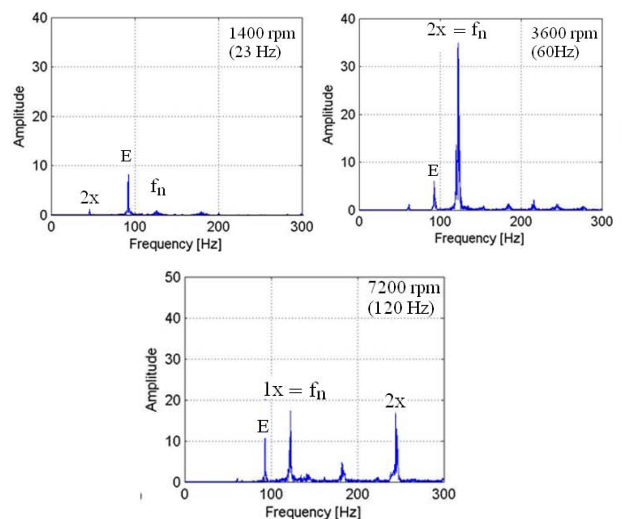


Fig. 7. Accelerometer signal FFT

Fig. 7 shows that for low engine rotating speed, only the exciter frequency component (E) is present. At 3600 rpm (60 Hz) the handlebar resonance is due to the not-balanced second order reciprocating inertia forces.

Another resonance condition arises at 7200 rpm due to the inertia forces synchronous with the engine rotating speed; it is also evident the second order harmonic component at 240 Hz. In these cases the exciter signal has a small amplitude with respect to those due the engine that are quite outside the maximum probability of vibration perception.

III.2. The Scooter

Analogous tests were performed on the scooter; for the presence of a CVT transmission the engine angular speed varies in the range of 4000-7500rpm so that the inertia forces have a frequency ranging in the interval 66-250Hz.

The scooter handlebar is constituted by a single tube 22x2.5 whose geometry (Figs. 8, 9) is characterized by the following dimensions: tube height (or rise) = 98 mm; pullback = 85 mm; centre width = 80 mm; width: 650 mm. The modal shape and the natural frequencies have been evaluated by means of a FEM simulation (Fig. 10) schematizing the handlebar components (grips, levers, brake oil tank, grip end masses) with lumped masses.

The first two vibrating modes (78 Hz, 86 Hz) involve the handlebar vertical bending while the third and the fourth modes (110 Hz, 112 Hz) regard the bars horizontal bending. The subsequent modes are characterized by natural frequencies greater than 460Hz.

Detecting the handlebar accelerations due to an impulsive excitation, the experimental values of the handlebar natural frequencies were determined. The accelerometers FFTs (Fig. 11) shows that:

- Two peaks at 82 and 88Hz, associable to the bending vertical modes;
- A wide peak at about 120Hz corresponding to the two bending horizontal modes;
- Two frequencies at 54 and 58Hz, not previewed by the FEM model, that mainly consists of a rigid rotation of the front assembly involving the tire flexibility and the headstock torsional stiffness.

Same tests were conducted exciting the handlebar with the shaker rotating force (with the reciprocating engine at rest) and detecting the acceleration orbits described by the grip extremity for several forcing frequencies.

The results, reported in Fig. 12, shows that, only in few cases, the acceleration orbits have a rounded shape.

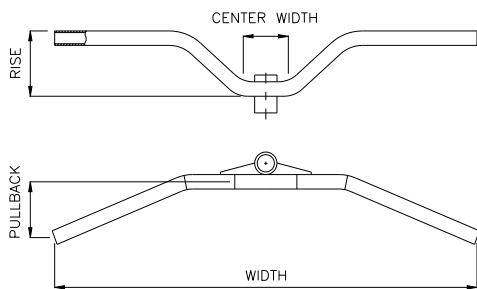


Fig. 8. Handlebar geometric characteristics



Fig. 9. Scooter handlebar

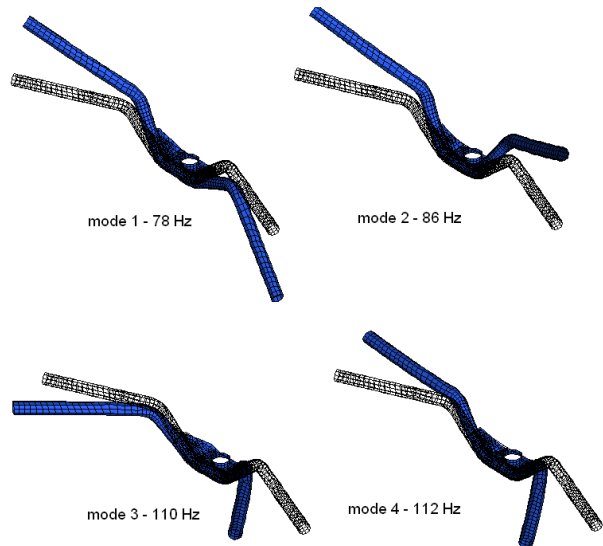


Fig. 10. Handlebar vibrating modes

At the frequency of 57 Hz, the irregular shapes is due to overlap of the forcing vibration with the lowest handlebar natural frequencies; in the interval 87-93Hz the orbits are mostly elongated in the vertical direction as the forcing frequency is close to the natural vertical frequencies while in the range 100-110Hz the orbits are elongated in the horizontal direction, according to the corresponding values of the natural frequencies.

IV. Handlebar Excitation

To excite handlebar vibration it could be convenient to choose the shaker angular speed so that the handlebar is in resonance condition. In this way it is possible to have a large enough vibrations with low power supply and so with very small shakers.

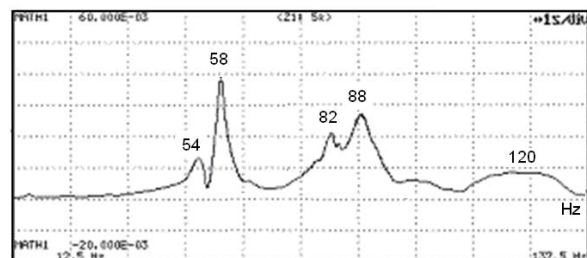


Fig. 11. Accelerometer signal FFT

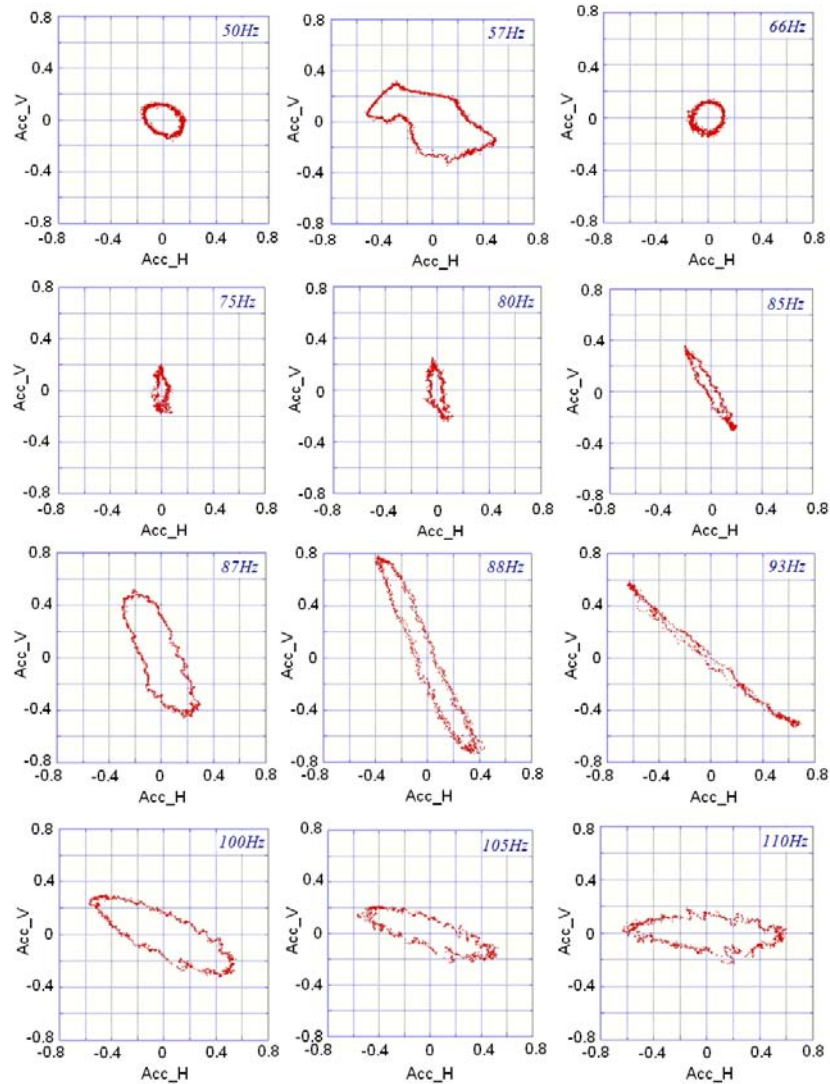


Fig. 12. Acceleration (ms^{-2}) orbits for several values of the forcing frequency

In particular it would be convenient to excite the handlebar with a frequency close to the first natural one and design the handlebar so that the other natural frequencies are over the range excited by the engine.

The handlebar sport-touring motorcycle has the first two natural frequencies very close each other (110 and 120 Hz) involving the bending flexibility of the two semi-bars; the upper modes have frequencies that are over the engine range.

The single tube handlebar of the scooter has several frequencies in the engine range; it can be noted that the modes involving the bending vertical flexibility can be shifted over the engine range stiffening the handlebar with a cross-bar and clamping the tube in correspondence of two tube sections (Fig. 13); with a suitable choice it is possible to make the first three natural frequency very close each other. Several tests were conducted setting the rotating speed of the shaker at 5280 rpm (88 Hz) and for several engine angular speed, the FFTs of the detected accelerometer signals are reported (Fig. 14). With the engine at rest ($n=0$ rpm), only the shaker vibration component is present in the diagrams.

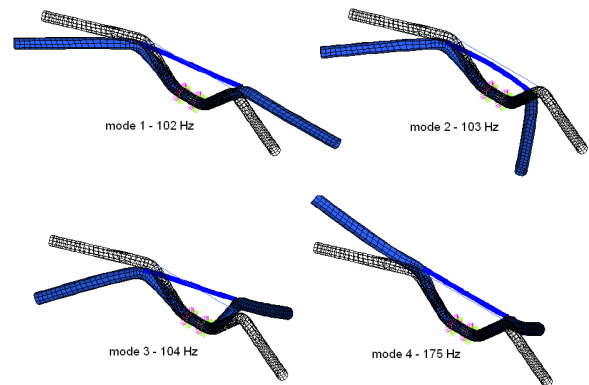


Fig. 13. Vibrating modes of the handlebar with the cross-bar

For $n=3500$ rpm the engine frequency excitation is equal to the natural frequency at 58 Hz but the relative acceleration component has an amplitude negligible with respect to the shaker one.

For $n=5300$ rpm (88 Hz), a resonance condition occurs and the FFT diagram shows one peak having an amplitude equal to those detected in the previous cases.

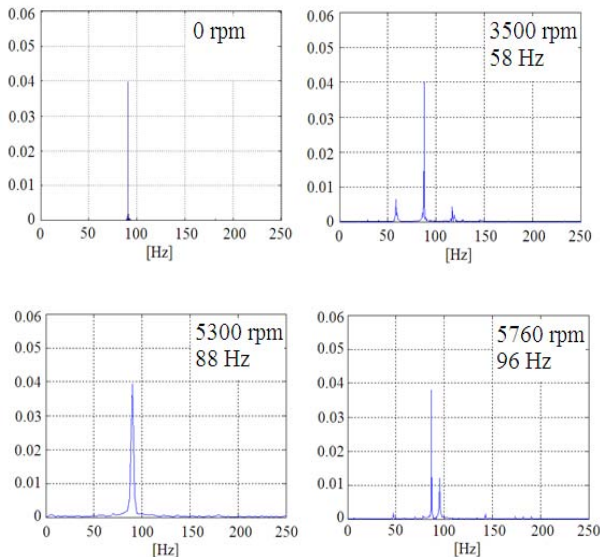


Fig. 14. Accelerometers FFT for shaker excitation frequency of 88Hz

The last FFT was detected for $n=5760\text{rpm}$ (96Hz) above the resonance condition and the harmonic component excited by the engine has a smaller amplitude with respect to that excited by the shaker.

Conclusively it seems that a vibrating alert signal may have a frequency very close to the first handlebar natural mode that it is not excited by the engine; in this case even a small shaker is able to generate a signal having a sufficient amplitude to alert the driver.

V. Conclusion

Some experimental and numerical investigations have been reported to investigate the handlebar motorcycle dynamic response and to evaluate the possibility to adopt a drive assistant systems on motorcycles, based on mechanical vibrations of the grips.

The handlebar should be designed to have only two quite coincident natural frequency in the range excited by the engine; to warn the driver about a particular danger event, the shaker should excite the grips at this frequency to have a well perceivable vibration with a small exciting force.

In this way the driver should distinguish the warning vibrating signal from those coming from the engine or due to other causes occurring during operation.

To avoid the effect of underlying vibration frequency and to let well distinguishable the warning signal perceived by the human hand in all the operating conditions, as outlined in [16], the signal should be frequency modulated. Furthermore, pulsed vibration signals are useful to combat adaptation effects [3].

Acknowledgements

The authors are very grateful to *Ducati Motor* and *Aprilia* for supplying the motorcycle and the scooter used in the tests.

References

- [1] H. Muijser, The influence of spatial contrast on the frequency-dependent nature of vibration sensitivity, *Attention, Perception & Psychophysics*, September 1990, Volume 48, Issue 5, pp 431-435.
- [2] Ali Israr, Hong Z. Tan, James Mynderse George T.C. Chiu - A psychophysical model of motorcycle handlebar vibrations - *Proceedings of IMECE2007, ASME Int. Mech. Eng. Congr. and Exposition* -, Seattle, Washington, USA IMECE2007-41504 , November 11-15, 2007.
- [3] Yao, H.S., Grant, D., Cruz, M.: Perceived Vibration Strength in Mobile Devices: the Effect of Weight and Frequency. *IEEE Transaction on Haptics*, 2009.
- [4] S. Kannan, A. Thangavelu, R. Kalivaradhan, An Intelligent Driver Assistance System for Vehicle Safety Modelling using Ontology, *Int. Journal Of UbiComp (IJU)*, Vol.1, No.3, July 2010.
- [5] D. de Falco, G. Di Massa, S. Pagano, On the castor dynamic behavior, *Journal of the Franklin Institute* n.347 , pp. 116–129, ISSN 0016-0032 – 2010;
- [6] G. Di Massa, S. Pagano, S. Strano, M. Terzo, A stability analysis of the wheel shimmy, *ASME 2012 , 11th Biennial Conference on Engineering systems Design and Analysis (ESDA) – Vol.1*, pp.669-678- Nantes, France, July 2-4, 2012.
- [7] D. de Falco, S. della Valle, G. di Massa, S. Pagano, The influence of the tyre profile on motorcycle behaviour, *Vehicle Systems Dynamics*, vol.43; pp.179–186, 2005.
- [8] D. de Falco, G. Di Massa, S. Pagano, Wheel shimmy experimental investigation – *ASME 2012, 11th Biennial Conference on Engineering systems Design and Analysis (ESDA) – Vol.1*, pp. 717-726, Nantes, France, July 2-4, 2012.
- [9] De Falco, D., Di Massa, G., Pagano, S., Castor dynamic investigation, (2013) *International Review of Mechanical Engineering (IREME)*, 7 (3), pp. 527-533.
- [10] F. Farroni, M. Russo, R. Russo, F. Timpone, Tyre-Road Interaction: Experimental Investigations About the Friction Coefficient Dependence on Contact Pressure, Road Roughness, Slide Velocity and Temperature. *Proceedings of the ASME 11th Biennial Conference on Engineering Systems Design and Analysis (ESDA2012)*, 2012
- [11] Capone, G., Giordano, D., Russo, M., Terzo, M., Timpone, F., "Ph.An.Ty.M.H.A.: A physical analytical tyre model for handling analysis, The normal interaction", *Vehicle System Dynamics*, 47 (1) , pp. 15-27, 2009.
- [12] Brancati, R., Strano, S., Timpone, F., "An analytical model of dissipated viscous and hysteretic energy due to interaction forces in a pneumatic tire: Theory and experiments", *Mechanical Systems and Signal Processing*, 25 (7), 2785–2795, 2011.
- [13] S. Agostoni, F. Cheli, E. Leo, M. Pezzola , An innovative multi dof TMD system for motorcycle handlebars designed to reduce structural vibrations and human exposure, *Mechanical Systems and Signal Processing – vol. 31*, pp. 298–315, August 2012.
- [14] De Falco, D., Di Massa, G., Pagano, S., A full scale motorcycle dynamic rig, (2013) *International Review of Mechanical Engineering (IREME)*, 7 (3), pp. 519-526.
- [15] G. Di Massa, S. Pagano, S. Strano, M. Terzo - A mono-axial wheel force transducer for the study of the shimmy phenomenon - *World Congress on Engineering*, - London, U.K., 3-5 July, 2013.
- [16] Westling G., Johansson R., Vallbo A.B. – *A Method for Mechanical Stimulation of Skin Receptors – Sensory Function of the Skin – Edited J.Zotterman – Pergamon Press – Oxford and NewYork*, 1986.

Authors' information

¹Dipartimento di Ingegneria Industriale ed Informatica, Seconda Università di Napoli, Napoli, Italy.

²Dipartimento di Ingegneria Industriale (DII), Università di Napoli Federico II Napoli, via Claudio 21, 80125, Italy.



Domenico de Falco is professor of mechanics of machinery at the Second University of Naples, Italy. His theoretical and experimental activities especially regards kinematics and dynamics of motorcycles, modelling and simulation of mechanical systems using bond graph, mechanical vibrations, the analytical dynamics.



Giandomenico Di Massa is professor of mechanics of machinery at the University of Naples Federico II, Italy. His theoretical and experimental activities regards: motorcycle dynamics, shimmy phenomenon, modelling and simulation of mechanical systems, mechanical vibrations, analytical dynamics, seismic insulation.



Stefano Pagano is professor of mechanics of machinery at the University of Naples Federico II, Italy. His theoretical and experimental researches regards: Coriolis mass flow-meters, lubricated bearings, motorcycle dynamics, shimmy phenomenon, seismic insulation.



Salvatore Strano received the M.S. degree in Mechanical Engineering and the Ph.D. degree in Mechanical Systems Engineering from the Università degli Studi di Napoli Federico II, Napoli, Italy, in 2005 and 2009, respectively. He is currently a postdoctoral researcher. His research interests include modelling and control of mechatronic systems, vision systems, robotics, rotordynamics and seismic base isolation.

Optimal Solution for Gear Drive Design Using Population Based Algorithm

Padmanabhan S.¹, M. Chandrasekaran², P. Asokan³, V. Srinivasa Raman⁴

Abstract – Optimization plays a fundamental role in numerous engineering applications such as process design, product design, re-engineering, new product development etc. In engineering, a best answer is achieved by comparison of some completely different solutions through utilization of previous downside information. Optimization algorithms provide systematic associated economical ways of constructing and comparing new design solutions. This enables us to understand a best trend, in order to boost solution efficiency and acquire the foremost optimal design impact. In this paper, a new Evolutionary Algorithm based Modified Artificial Immune System (MAIS) algorithm is used to optimize a gear drive design. The results are compared with an existing design. Copyright © 2013 Praise Worthy Prize S.r.l. - All rights reserved.

Keywords: Design Optimization, Helical Gear Drive, Modified Artificial Immune System and Multi-Objective Optimization

Nomenclature

| | |
|----------|---|
| H_s | Specific sliding velocity at start of approach action |
| H_r | Specific sliding velocity at end of recess action |
| P | Power transmitted in kW |
| Z_1 | Number of teeth in pinion |
| m_n | Normal Module in mm |
| b | Thickness of gear and pinion in mm |
| η | Percentage Efficiency |
| P_L | Percentage of power loss |
| N_C | The number of clones to be generated |
| x' | Mutated variable |
| α | A random number between (0,1) |

I. Introduction

Most engineering optimization problems normally have continuous and discrete design variables with usually conflicting with each other. These problems with several objectives, are called “multi objective” optimization problems, and were initially studied as nonlinear objective functions. Constraints are extremely vital in engineering design problems with nonlinear constraints, usually obligatory on the statement of the issues and generally are terribly exhausting to satisfy, that makes the search tough and inefficient.

A computational paradigms system called Artificial Immune System (AIS) which is inspired by biological immune system. It is based on the principal of natural system. This system is based on the general Immune system as in our body. This system find application in the future computerized industries, Robotics, Aerospace, automotive etc., because of its immune system which develops its own anti bodies for the virus or foreign

bodies which will harm the system and also because of its identification system which identifies the previous attack or problem and produce solution for that .These are the main reason for the attraction towards the system AIS.

David F. W. Yap et al. [1] proposed the clonal selection algorithm was modified using the best solutions for each iteration namely Single Best Remainder and the proposed algorithm was able to improve the conventional results in terms of accuracy and stability for single and multi objective functions.

Deb et al. [2] discussed immune system for the first-generation algorithms use simplistic models of immunology as the initial inspiration, for example negative and clonal selection.

Coello and Cortes [3] developed multiobjective immune system algorithm (MISA) for its employment of an AIS in a multiobjective evolutionary algorithm context. Woldemariam and Yen [4] his research exploits the fact embedded in immune system to communicate between innate immune response and adaptive immune response levels. Luh et al. [5] proposed a Multi-objective Immune Algorithm (MOIA), MO-AIS (Multi-objective Artificial Immune System) research grew into maturity, following that tens of algorithms were proposed. Garrett [6] developed Adaptive Clonal Selection (ACS) by improving a number of processes and parameters initialization.

Juan Carlos Herrera et al. [7] proposed a new cloning system and for the maturation stage of the clones, two simple and fast mutation operators are used in a nominal convergence that works together with a re-initialization process to preserve the diversity. Padmanabhan et al. [8] made an attempt to optimize bevel gear pair design using a non-linear programming optimizing software LINGO

and meta-heuristics. The efficiency of the proposed algorithms is validated through gear design problems and the comparative results were studied.

Quancai Li et al. [9] developed a multi-objective for gear transmission with design variables and choice restrictive constraints. Deb and Jain [10] has proposed a Non-Sorted Genetic Algorithm II for optimizing multi speed gear box which consider multi objectives such as maximizing the power and minimizing the total volume of the gear. In this paper, a new immune clonal system based Modified Artificial Immune System (MAIS) algorithm used to optimize the helical gear drive design.

II. Artificial Immune System Algorithm

The Artificial Immune Systems design new intelligent determination techniques that getting used in varied engineering optimization issues. AIS are outlined as procedure systems impressed by theoretical medicine, ascertained immune functions, principles and mechanisms so as to resolve issues. Because the biological process algorithms, artificial system has been with success applied to a range of optimization issues. AIS have a procedure intelligence paradigm impressed by the biological system that has found application in pattern recognition and machine learning. Alternative ways of AIS for optimization because the immune network theory and therefore the organism choice principle are projected and enforced by totally different researchers.

The steps of Modified Artificial Immune System as followed:

1. Generate randomly a population of “N” size with design variables. In the initial generation, these variables are copied directly to the working population and nominal convergence is controlled by the number of generation.
2. Find the Objective Function for those strings and continued for sorting and ranking.
3. Use selection based on ranking. The string with the highest affinity will be the best individual.
4. Perform the cloning of the antibodies using equation (1) was adopted from Juan Carlos Herrera et al. [7]:

$$N_c = \sum (n - (i - 1)) \quad (1)$$

where, N_c is the number of clones to be generated for each string, n is the total number of strings in the population and i is the current string starting from the strings with the highest affinity.

5. All the clones in the set of clones which are the copies of variables with good affinity degrees undergo a mutation process. Here two phased mutation process carried out using the Eqs. (2), Juan Carlos Herrera et al. [7]:

$$x' = x + \frac{(\alpha \times range \times generation)}{N_c} \quad (2a)$$

$$x' = x + \frac{(\alpha \times range)}{(N_c \times generation)} \quad (2b)$$

where, x' is mutated variable, α is a random number between (0,1), range is variables between upper and lower limit and generation is current generation cycle.

6. After the first mutation operator, In the case of having a better solution in mutated string, then the clone is replace with the new one, else the second operator is used.
7. In the second mutation method, if there is no improvement in the mutated string, then the original solution remains with no change.
8. A model of receptor editing mechanism of the immune system was used, i.e., a proportion of the worst solution eliminated and new ones are generated in placed after predefined iterations.
9. Again find the objective function for the clones and sort it, rank it mutate it then extract first best 10 solutions from the list for the further design process and visualization.

III. Gear Drive Design

In this paper, an engineering design problem has been adopted from Jayakumar [11]. The gear design problem states that, Design a pair of helical gears to transmit 12.5 kW at 1200 rpm. The transmission ratio is 3.5 and material adapted as Alloy steel material 40Ni 2Cr1Mo28. The helix angle is 15° and pressure angle is 20°. The above helical gear design is to be solved with two different gear materials, such as Carbon Steel C40 and Alloy Steel (40Ni 2Cr1Mo28). The material properties of gear drive are tabulated in Table I.

TABLE I
MATERIAL PROPERTIES OF HELICAL GEAR DRIVE

| Components | C-40 | Alloy Steel |
|--|----------------------|------------------------|
| Density(ρ) kg/mm ³ | 7.7×10^{-6} | 8.839×10^{-6} |
| Bending Stress (σ_b) kg/mm ² | 111.23 | 173.133 |
| Compressive Stress (σ_c) kg/mm ² | 852.64 | 852.64 |
| Young's Modulus (E) N/mm ² | 2×10^5 | 2.15×10^5 |

III.1. Optimal Helical Gear Drive Design

The design variable such as Power (P), Normal module (m_n), gear thickness (b) and number of teeth on pinion (Z_1) are determined in order to optimize the helical gear drive design and number of objective functions include: Maximization of Power transmitted (f_1), Minimization of Weight (f_2), Maximization of Efficiency (f_3) and Minimization of Centre distance (f_4).

The above gear drive objectives should satisfies with the design constraints of allowable bending stress, allowable compressive stress, minimum module and minimum centre distance. The complete optimized problem of helical gear drive in terms of design variables P , m_n , b and Z_1 for the above problem with Alloy steel material, after simplification the helical gear design

problem is in terms of non linear objective function with constraint equation as follows:

$$\text{Maximize } f_1 = P \tag{3}$$

$$\text{Minimize } f_2 = 98.58 \times 10^{-6} \times b \times (m_n Z_1)^2 \tag{4}$$

$$\text{Maximize } f_3 = 100 - P_L \tag{5}$$

where:

$$P_L = 3.97 \times \frac{(H_s^2 + H_t^2)}{(H_s + H_t)} \tag{6}$$

$$H_s = 4.5 \times \left\{ \left[\left(1 + \frac{0.552}{Z_1} \right)^2 - 0.883 \right]^{0.5} - 0.342 \right\} \tag{7}$$

$$H_t = 1.286 \times \left\{ \left[\left(1 + \frac{1.931}{Z_1} \right)^2 - 0.883 \right]^{0.5} - 0.342 \right\} \tag{8}$$

$$\text{Minimize } f_4 = 2.33 m_n Z_1 \tag{9}$$

subject to:

$$m_n Z_1 b^{0.5} P^{-0.5} \geq 65.741 \tag{10}$$

$$m_n^2 (3.5 Z_1 + 20) b P^{-1} \geq 250.51 \tag{11}$$

$$m_n Z_1 P^{-0.333} \geq 18.35 \tag{12}$$

$$m_n^3 (3.5 Z_1 + 20)^{0.333} P^{-0.333} \geq 2.94 \tag{13}$$

The efficiency Eq. (6) has been adopted from Dudley [12] and all other equations adopted from Design Data book [13].

Since these entire objective functions are on different scales, these factors are to be normalized to the same scale. The normalized objective function is obtained by Combined Objective Function (COF) as in the following Eq. (14):

$$COF = \left[\left(\frac{power}{max.power} \times NW_1 \right) + \left(\frac{min.weight}{weight} \times NW_2 \right) + \left(\frac{efficiency}{max.efficiency} \times NW_3 \right) + \left(\frac{min.cent.dist}{cent.dist} \times NW_4 \right) \right]$$

where, $NW =$ Normalized weight of criterion:

$$NW_1, NW_2, NW_3 \text{ and } NW_4 = 0.25$$

IV. Results and Discussion

The Modified Artificial Immune System algorithm was developed using Microsoft Visual C#, with design

parameters (P, m_n, b and $Z1$) boundary values as inputs.

This program was designed to solve any gear ratio, driver speed, pressure angle and gear material properties.

The window developed by visual C# for the gear drive with Artificial Immune System algorithm is shown in Fig. 1.

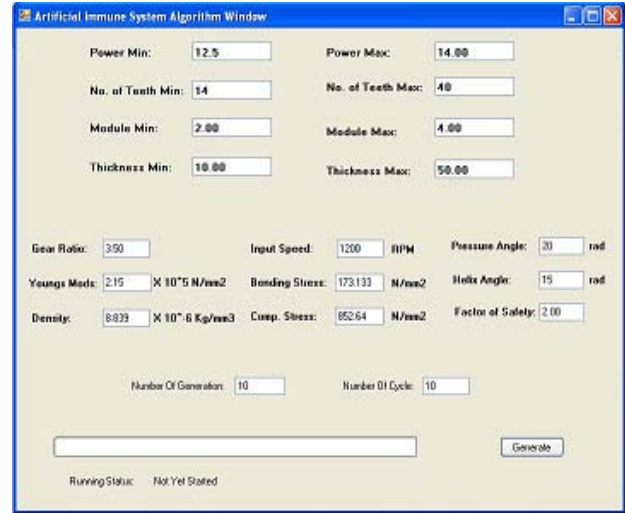


Fig. 1. Window of Modified Artificial Immune System algorithm

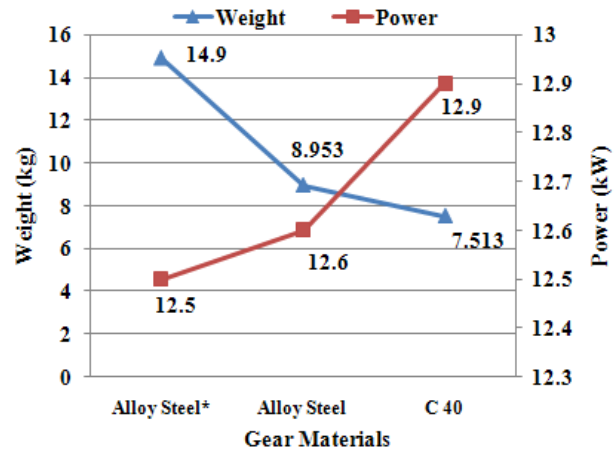


Fig. 2. Comparison of Helical Gear results

The above Fig. 2 shows, a slight increase in power and 39.91% of weight reduction for the existing Alloy material with respect to MAIS results.

After number of iteration performed by MAIS, for the two different gear materials for the specified helical gear drive, the optimized results were tabulated in Table II in compared with existing design by Jayakumar [11].

The MAIS result shows, significantly enhanced values with respect to power and weight reduction for the helical gear drive.

Power increased about 3.2% and 49.57% of weight reduction for the carbon steel 40 in compared with existing Alloy steel material by conventional design.

From the results, MAIS shows a significant improvement in its optimal design values to its objectives.

TABLE II
COMPARISON OF HELICAL GEAR DRIVE OPTIMIZED RESULTS
BY MAIS

| Parameters / Material | MAIS | | |
|-------------------------------------|--------------------|-------------|--------|
| | Existing System | Alloy Steel | C-40 |
| Power (P) kW | 12.5 | 12.6 | 12.9 |
| Normal Module (m_n) mm | 3.00 | 2.80 | 3.00 |
| Gear Thickness (b) mm | 42.00 | 35.75 | 30.00 |
| No. of teeth on pinion (Z_1) | 20 | 18 | 18 |
| Centre Distance (a) mm | 139.76 | 117.40 | 125.79 |
| Gear Weight (kg) | 14.9 | 8.953 | 7.513 |
| Efficiency (%) | 98.67 | 98.54 | 98.54 |

V. Conclusion

In this paper, a helical gear reducer was taken with two gear materials and optimized results were obtained by MAIS. In the designing of machinery gear drive and automobiles takes the advantage of evolutionary algorithm, the gear manufacturers can strongly face the adequate atmosphere of producing at sensible cost by reduction of weight.

The above stated gear design problem result shows that, by using the AIS algorithm we can get the modified better solution for the practical problem and also for the theoretical problem.

In future, AIS will play the major role in the industries like automotive, aerospace, robotics, manufacturing etc., and it's also easy to understand and explain to the followers as it contains the natural human immune system as its base.

And also by using AIS we can also solve the multi objective problems which contains different nonlinear, non-differentiable and multi variables objective functions. By using AIS we can assure that the better solution are extracted using better values for the betterment of the design.

This work can be extended to experimental investigation to check power and efficiency in real time environment by the optimized results. As a future work, the immune system can be used to evaluate the range of engineering design application like multispeed gear box, steering gear box, springs and bearings etc.

References

- [1] David F. W. Yap, and Koh, S. P. and Tiong, S. K., Mathematical function optimization using AIS antibody remainder method, *International Journal of Machine Learning and Computing*, Vol. 1, n.1, pp. 13-19, 2011.
- [2] Deb.K, J. Sundar, N. Udaya Bhaskara Roa and S. Chaudhuri, Reference point based multi-objective optimization using evolutionary algorithms, *Int. Journal of computational Intelligence Research*, Vol. 2, n. 3, pp. 273-286, 2006.
- [3] Coello, C., Cortés, N., Solving Multiobjective Optimization Problems Using an Artificial Immune System, *Genetic Programming and Evolvable Machines*, Vol. 6, pp.163-190, 2002.

- [4] Woldemariam, K.M. and Yen, G.G, *Constrained optimization using artificial immune system*, IEEE Congress on Evolutionary Computation (CEC), Spain, 2010, pp. 1-8.
- [5] Luh, G.C., Chueh, C. H., and Liu W.W. MOIA, Multi-objective Immune Algorithm, *Engineering Optimization*, Vol. 35, n. 2, pp. 143-164, 2003.
- [6] Garrett, S.M., Parameter-free, adaptive clonal selection, In Proc of Congress on Evolutionary Computing, Portland Oregon, USA, Vol. 1, 2004, pp. 1052-1058.
- [7] Juan Carlos Herrera-Lozada, Hiram Calvo and Hind Taud, A Micro Artificial Immune system, *Polibits no.43 México ene./jun. 2011*.
- [8] Padmanabhan, S., Srinivasa Raman, V., Asokan, P., Arunachalam, S. and Page, T., Design optimisation of bevel gear pair, *Int. J. Design Engineering*, Vol. 4, n. 4, pp.364-393, 2011.
- [9] Quancai Li; Xuetao Qiao; Cuirong Wu and Xingxing Wang, The study on gear transmission multi-objective optimum design based on SQP algorithm, Proc. SPIE 8350, Fourth International Conference on Machine Vision (ICMV 2011): Computer Vision and Image Analysis; Pattern Recognition and Basic Technologies, Singapore (January 12, 2012); doi:10.1117/12.920249.
- [10] Deb. K and Jain, S, Multi-Speed Gearbox Design Using Multi-Objective Evolutionary Algorithms, *Journal of Mechanical design*, Vol.125, n.3, pp.609-619, 2002.
- [11] Dr.V.Jayakumar, Design of transmission Systems (Fourth Edition, Lakshmi Publications, 2012).
- [12] Dudley.D.W, Handbook of Practical Gear Design (McGraw-Hill Book Co: New York, 1994).
- [13] Faculty of Mechanical Engineering, PSG College of Technology, Design Data Book (PSG College of Technology, 2008, Coimbatore- 641004, Tamilnadu, India).

Authors' information

¹Research Scholar, Department of Mechanical and Production Engineering, Sathyabama University, Chennai, India.
E-mail: padmanabhan.ks@gmail.com

²Professor and Director, Faculty of Mechanical Engineering, Vels University, Chennai, India.

³Professor, Department of Production Engineering, NIT, Trichy, India.

⁴ Professor and Head, Department of Mechanical Engineering, R.V.S. College of Engineering and Technology, Dindigul, India.



Padmanabhan S. is a research scholar in the Faculty of Mechanical Engineering at Sathyabama University, Chennai, India. He received his Engineering Master degree on Automobile Engineering from MIT, Anna University, Chennai. He also obtained his MBA in Operation Management. His field of interest is design optimization and in particular the design optimization of gears. He published more than 10 research papers in journals and conference proceedings.

Chandrasekaran M. received his Engineering Master degree on Industrial Engineering from National Institute of Technology, Trichy, India in 2002. He received his Doctorate degree in 2007 in Scheduling from National Institute of Technology, Trichy, India. He is a Professor and Director for Faculty of Mechanical engineering at Vels University, Chennai. His research interests include combinatorial optimization and scheduling. He is author of nearly 30 publications in refereed journals, conferences. He is in the Editorial Boards of IJPTM, IJAMT, IJPR, IJINS etc.

Asokan P. received his Engineering Master degree on Manufacturing Technology from National Institute of Technology, Trichy, India in 1990. He received his PhD degree in 1998 from Bharathidasan University, Trichy, India. He is a Full time Professor at National Institute of Technology, Trichy, India. His research interests include

Operation Management and Optimization in Manufacturing. He till date guided more than fifteen PhD research scholars and he is the author of more than 50 publications in refereed journals and conferences.

Srinivasa Raman V. received his Doctorate degree in 2009 in Gearbox design Optimization from National Institute of Technology, Trichy, India. He is a Professor and Head of Mechanical engineering department at R.V.S. College of Engineering and Technology, Dindigul, India. His research interests include combinatorial optimization and gearbox design. He published many research papers in journals and conference proceedings.

Geometry Based Recursive Algorithm to Control the End Effector of Coordinated TRRLR Manipulators

Seetharaman N., R. Sivaramakrishnan, Abin John Thomas

Abstract – This paper focuses on a mobile manipulator which is the combination of a mobile platform and a manipulator, with a highly flexible system, which can be used in hazardous application. One of the challenges with mobile manipulators is the construction of control systems, enabling the robot to operate safely in potentially dynamic and all terrain environments. In this paper we will present work in which a mobile manipulator is controlled using the hybrid approach. The method presented is a real time approach in which geometry of the arm with onboard sensor data processing are used both for the overall coordination of the mobile platform and the manipulator as well as the trajectory planning along a straight line parallel to two planes. Copyright © 2013 Praise Worthy Prize S.r.l. - All rights reserved.

Keywords: Forward Kinematics, Trajectory Planning, Robotics Toolbox

Nomenclature

| | |
|-----------------|---|
| θ_i | Joint angle |
| a_i | Angle of link |
| α_i | Link twist |
| d_i | Link offset |
| L | Maximum stroke of linear actuator |
| θ_{step} | Step angle to turret motor |
| α | Angle rotation of Back arm motor |
| δz | Change in gap along z- axis of end effector |
| L_0 | Length of back arm |
| L_1 | Length of fore arm with prismatic joint |

I. Introduction

The mobile manipulator systems comprising of a mobile platform with one or more manipulators are of great interest in number of applications. This paper presents a planning and control methodology for such systems allowing them to follow a desired end-effector trajectories.

Robotic manipulators are being considered for a wide variety of applications outside of their traditional factory settings. These applications, such as fire-fighting, toxic waste cleanup, hazardous explosive material handling and planetary exploration will require the manipulators to operate from moving vehicles, with the mobile manipulators. A mobile manipulator, composed of a manipulator arm mounted on a mobile platform, is far more versatile than a conventional manipulator whose base is fixed, as a consequence of its enlarged operational space.

Typically, a mobile manipulator's vehicle will have significant dynamic behavior, particularly due to suspension compliance, in contrast to factory manipulators generally mounted on rigid bases.

As a result, a mobile manipulator's motions will dynamically interact with those of its vehicle on its suspension to degrade the manipulator's performance. Such problems as excessive end-effector errors and poor system stability can result. The control problems for these systems are further exacerbated by highly variable system characteristics.

Hybrid approach is a technique combining the kinematic model of the manipulator and sensor data of platform disturbances with real time closed loop control system. This paper, describes the construction of TRRLR mobile manipulator for uneven and unknown terrain application. Precise control is required to deploy the arm for hazardous mission from folding condition to the mission position.

During the mission it is mandatory to maintain a constant gap between the ground and sensor intended to carry out the mission. Also the sensor should always be at a constant distance from vehicle so that it can scan along a straight line. Then, it represents the kinematics of the system and also the envelope of the manipulator without disturbing the other system. With geometry based principle, a method to control the servo angles of all arm joints to get the desired tip position is discussed.

II. System Description and Methodology

II.1. Unmanned System with Mobile Manipulator

Unmanned tracked vehicle carrying mine detection sensors fitted on robotic arm controlled from a base station must poses automatic control and tele-operation control to successfully complete the mission. The serial arm has to carry the mine detection sensor which is meant to detect buried land mines in unstructured and unknown terrain.

It has to be deployed from the frontal edge of the vehicle with adequate standoff distance from the hazardous objects. The manipulator arm has to maintain the constant distance in between the ground surface and mine detection sensor for different orientation of the vehicle and sensor together or separately during the movement of the vehicle on undulated terrain. Precise control is required to protect the expensive sensor from obstacles in the path of unmanned vehicle which carries the robotic arm with sensor.

II.2. Methodology

There is a serial arm manipulator fitted in front of the unmanned tracked vehicle. The remote vehicle is controlled from a base vehicle through wireless LAN. The manipulator arm will carry the sensor to detect the buried object under the ground is also remotely operated.

But the closed loop control of the end effectors position has to be carried out by an electronic controller system. The suitable control loop to carry out the position control based on the signals from onboard sensors like ultrasonic distance sensors, Inertial Measurement Unit and array of accelerometer will reside in the embedded controller. The each arm has five degree of freedom such as base turret twist (T), back arm rotation (R), fore arm rotation (R), fore arm linear actuation (L) and rotation of end effectors (R).

The configuration of this arm is TRRLR and is represented in Fig. 1. The gap between the ground surface and the sensor is maintained by measuring the distance with ultrasonic sensors. When any presence of mines is detected the arm will scan the area to identify the exact location of the mine so that the area over which mine is present can be found out. A geometry based recursive algorithm is used for trajectory control of the sensor attached to the manipulator. When the back arm is rotated through an angle θ , the x and y coordinates varies with the z axis remaining constant. Now to bring the x axis back to the desired position, fore arm has to be rotated through an angle α which depends on the variation in x -axis, δx . When fore arm rotates there will be variations along x , y and z directions. The end effector lifts up by δz . Now the linear actuator extends by a length δz bringing it back. The algorithm is continued till the y -axis reaches the desired limit.

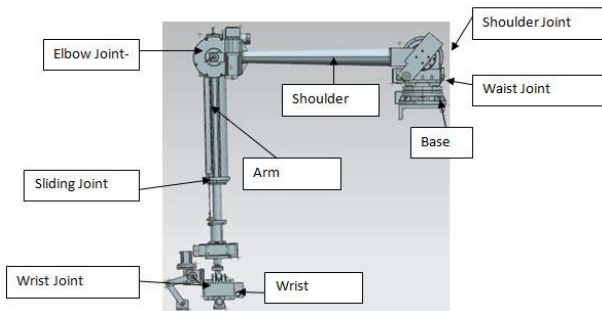


Fig. 1. TRRLR mobile manipulator

The complete manipulator structure with sensor is shown in Fig. 2.

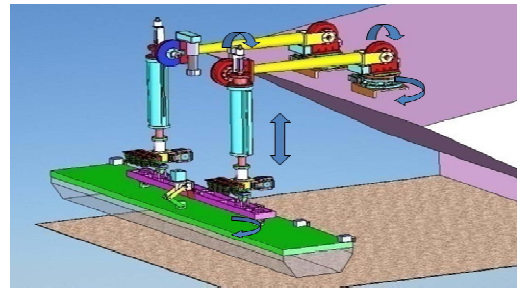


Fig. 2. TRRLR manipulators with Sensor

Based on these results the corresponding joint actuators are rotated to make the mine detection sensor optimally parallel to the ground undulations.

The geometry based analysis of the arm is utilized to ensure the safety of the sensor mounted on the arm from unknown terrain obstacle when the unmanned vehicle is deployed for the mine detection mission. Obstacle detection sensor is mounted on the frame carried by the robotic arm along with the sensor.

III. Kinematics of Manipulator

III.1. Forward Kinematics

In manipulator system, five Degree of freedom jointed arm configuration (Twist-Revolute-Revolute-Linear-Revolute) TRRLR is designed to carry the sensor and marking unit at the end effectors. The forward kinematics of the single arm is represented as given below in Table I. The Denavit - Hartenberg parameters have been found out for this configuration as shown in Table I. It represents the link parameters like joint angle θ_i , angle of link a_i , link twist α_i and link offset d_i .

TABLE I
D-H PARAMETERS OF MANIPULATOR

| Joint | θ_i | α_i | a_i | d_i |
|-------|------------|------------|-------|---------|
| 1 | θ_1 | 90 | 0 | 0 |
| 2 | θ_2 | 0 | a_2 | 0 |
| 3 | θ_3 | 90 | 0 | 0 |
| 4 | θ_4 | 0 | 0 | d_4+L |
| 5 | θ_5 | -90 | 0 | 0 |

By multiplying sequentially the transformation matrices from the initial frame to the end-effectors frame, the transform matrix for the four joint as arrived in Eqs. (1) to (6):

$$T_5^0 = T_1^0 * T_2^1 * T_3^2 * T_4^3 * T_5^4 \tag{1}$$

$$T_1^0 = \begin{bmatrix} \cos\theta_1 & 0 & \sin\theta_1 & 0 \\ \sin\theta_1 & 0 & -\cos\theta_1 & 0 \\ 0 & 1 & 0 & 0 \\ 0 & 0 & 0 & 1 \end{bmatrix} \tag{2}$$

$$T_2^1 = \begin{bmatrix} \cos\theta_2 & -\sin\theta_2 & 0 & \cos\theta_2 \\ \sin\theta_2 & \cos\theta_2 & 0 & \sin\theta_2 \\ 0 & 0 & 1 & 0 \\ 0 & 0 & 0 & 1 \end{bmatrix} \quad (3)$$

$$T_3^2 = \begin{bmatrix} \cos\theta_3 & 0 & \sin\theta_3 & 0 \\ \sin\theta_3 & 0 & -\cos\theta_3 & 0 \\ 0 & 1 & 0 & 0 \\ 0 & 0 & 0 & 1 \end{bmatrix} \quad (4)$$

$$T_4^3 = \begin{bmatrix} 1 & 0 & 0 & 0 \\ 0 & 1 & 0 & 0 \\ 0 & 0 & 1 & d_4 + L \\ 0 & 0 & 0 & 1 \end{bmatrix} \quad (5)$$

$$T_5^4 = \begin{bmatrix} \cos\theta_5 & 0 & -\sin\theta_5 & 0 \\ \sin\theta_5 & 0 & \cos\theta_5 & 0 \\ 0 & -1 & 0 & 0 \\ 0 & 0 & 0 & 1 \end{bmatrix} \quad (6)$$

The position of the end effector is found after multiplying the above matrices and is given in the following equations:

$$X = (\cos(\theta_1) \cdot \cos(\theta_2) \cdot \sin(\theta_3) \cdot (d_4 + L) + (\cos(\theta_1) \cdot \cos(\theta_3) \cdot \sin(\theta_2) \cdot (d_4 + L) + (\cos(\theta_1) \cdot \cos(\theta_2))) \quad (7)$$

$$Y = (\sin(\theta_1) \cdot \sin(\theta_3) \cdot \cos(\theta_2) \cdot (d_4 + L) + (\sin(\theta_1) \cdot \sin(\theta_2) \cdot \cos(\theta_3) \cdot (d_4 + L)) \quad (8)$$

$$Z = (\sin(\theta_2) \cdot \sin(\theta_3) \cdot (d_4 + L) - (\cos(\theta_2) \cdot \cos(\theta_3) \cdot (d_4 + L) + \sin(\theta_2)) \quad (9)$$

IV. Geometrical Algorithm

IV.1. Geometry Based Recursive Algorithm Scheme

The flowchart of the algorithm is given in the Fig. 3 and the explanation is also given below. It is essential to move the mine detection sensor in the straight line like moving the sensor only in y direction alone and similarly, move the sensor only in z direction. It can be achieved by means of the geometrical algorithm that the joint coordinates can be calculated. It is possible to dictate the manipulator movement in a straight line by specifying the x, y and z distance. Once the final target is known, further work out the angle of rotation for rotary joints and displacement for linear joints are arriving by means of the equations as given below:

$$\begin{aligned} &\text{Clockwise motion } y=0 \text{ to } y=.750 \\ \theta_{step} &= (180/\pi) \cdot (\sin^{-1}((\text{displacement}) / (L_0 + L_1 \cdot \sin(\alpha)))) \end{aligned} \quad (10)$$

$$x_0 = (L_0 + d \cdot \sin(\alpha_{n-1})) \cdot \cos(\theta_n) \quad (11)$$

$$y_0 = (L_0 + d \cdot \sin(\alpha_{n-1})) \cdot \sin(\theta_n) \quad (12)$$

$$z_0 = z \quad (13)$$

where displacement is the step size along y axis.

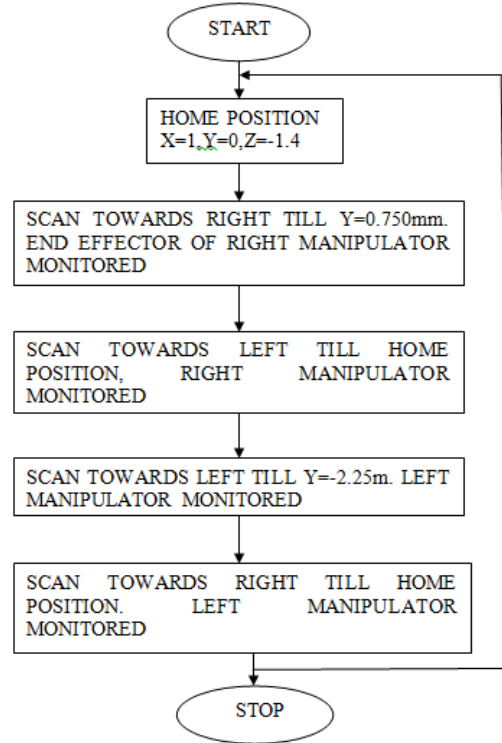


Fig. 3. Flowchart of the Algorithm Implemented

Now when forearm is rotated:

$$\alpha_n = \sin^{-1}((L_0/L_1) \cdot (1 - \cos(\theta_n)) / \cos(\theta_n)) \quad (14)$$

$$x_1 = (L_0 + (L_1 \cdot \sin(\alpha_{n-1}))) \cdot \cos(\theta_n) \quad (15)$$

$$y_1 = (L_0 + (L_1 \cdot \sin(\alpha_{n-1}))) \cdot \sin(\theta_n) \quad (16)$$

$$z_1 = -L_1 \cdot \cos(\alpha_n) \quad (17)$$

with the rotation of forearm, the end effector rises up by δz . So to bring it back linear actuator is used.

The linear actuator is extended by δz :

$$\delta z = |(z(n)) - z(n-1)| \quad (18)$$

$$x_2 = (L_0 + (L_1 \cdot \sin(\alpha_n))) \cdot \cos(\theta_n) \quad (19)$$

$$y_2 = (L_0 + (L_1 \cdot \sin(\alpha_n))) \cdot \sin(\theta_n) \quad (20)$$

$$z_2 = -L_1 \cdot \cos(\alpha_n) \quad (21)$$

Counter clockwise $y=.750$ to $y=0$:

$$\theta_n = \theta_n - \theta_{step} \quad (22)$$

$$x_1 = (L_1 + d \cdot \sin(\alpha_{n-1})) \cdot \cos(\theta_n) \quad (23)$$

$$y_1 = (L_1 + d \cdot \sin(\alpha_{n-1})) \cdot \sin(\theta_n) \quad (24)$$

$$z_1 = z_0 \quad (25)$$

Forearm rotation:

$$\alpha_n = \text{asin}((L0/L1) \cdot (1 - \cos(\theta_n)) / \cos(\theta_n)) \quad (26)$$

$$x1 = (L0 + (L1 \cdot \sin(\alpha_n))) \cdot \cos(\theta_n) \quad (27)$$

$$y1 = (L0 + (L1 \cdot \sin(\alpha_n))) \cdot \sin(\theta_n) \quad (28)$$

$$z1 = -L1 \cdot \cos(\alpha_n) \quad (29)$$

$$L1 = L1 - (\delta z / \cos(\alpha_n)) \quad (30)$$

Linear actuator actuation:

$$x2 = (L0 + (L1 \cdot \sin(\alpha_n))) \cdot \cos(\theta_n) \quad (31)$$

$$y2 = (L0 + (L1 \cdot \sin(\alpha_n))) \cdot \sin(\theta_n) \quad (32)$$

$$z2 = -L1 \cdot \cos(\alpha_n) \quad (33)$$

Scanning anticlockwise $0 < y > 2.25$:

$$X0 = (L0 + d \cdot \sin(\alpha_{n-1})) \cdot \cos(\theta_n) \quad (34)$$

$$Y0 = (L0 + d \cdot \sin(\alpha_{n-1})) \cdot \sin(\theta_n) \quad (35)$$

$$Z0 = z0 \quad (36)$$

$$\alpha_n = \text{asin}((L0/L1) \cdot (1 - \cos(\theta_n)) / \cos(\theta_n)) \quad (37)$$

$$x1 = (L0 + (L1 \cdot \sin(\alpha_n))) \cdot \cos(\theta_n) \quad (38)$$

$$y1 = (L0 + (L1 \cdot \sin(\alpha_n))) \cdot \sin(\theta_n) \quad (39)$$

$$z1 = -L1 \cdot \cos(\alpha_n) \quad (40)$$

Linear actuator:

$$\delta z = |(z(n) - z(n-1))| \quad (41)$$

$$L1 = L1 + (\delta z / \cos(\alpha_n)) \quad (42)$$

$$x2 = (L0 + (L1 \cdot \sin(\alpha_n))) \cdot \cos(\theta_n) \quad (43)$$

$$y2 = (L0 + (L1 \cdot \sin(\alpha_n))) \cdot \sin(\theta_n) \quad (44)$$

$$z2 = -L1 \cdot \cos(\alpha_n) \quad (45)$$

Scanning clockwise $-0.225 < y < -1.5$:

$$\theta_n = \theta_n + \theta_{step} \quad (46)$$

$$x0 = (L0 + d \cdot \sin(\alpha_{n-1})) \cdot \cos(\theta_n) \quad (47)$$

$$y0 = (L0 + d \cdot \sin(\alpha_{n-1})) \cdot \sin(\theta_n) \quad (48)$$

$$z0 = z0 \quad (49)$$

Forearm movement:

$$\alpha_n = \text{asin}((L0/L1) \cdot (1 - \cos(\theta_n)) / \cos(\theta_n)) \quad (50)$$

$$x1 = (L0 + (L1 \cdot \sin(\alpha_n))) \cdot \cos(\theta_n) \quad (51)$$

$$y1 = (L0 + (L1 \cdot \sin(\alpha_n))) \cdot \sin(\theta_n) \quad (52)$$

$$z1 = -L1 \cdot \cos(\alpha_n) \quad (53)$$

Linear Actuator:

$$\delta z = |(z0 - z1)| \quad (54)$$

$$L1 = L1 - (\delta z / \cos(\alpha_n)) \quad (55)$$

$$x2 = L0 + (L1 \cdot \sin(\alpha_n)) \cdot \cos(\theta_n) \quad (56)$$

$$y2 = L0 + (L1 \cdot \sin(\alpha_n)) \cdot \sin(\theta_n) \quad (57)$$

$$z2 = -L1 \cdot \cos(\alpha_n) \quad (58)$$

V. Results and Discussion

During the mission mode of mine detection if the sensor identifies land mine in front of the UGV it becomes inevitable to scan the ground for ensuring clear way without any buried land mine like object.

To carry out this task precisely the recursive geometry approach makes the Turret motor to rotate in desired step angle followed by fore arm rotation and prismatic joint displacement to ensure desired trajectory with constant 300mm gap between the radar and ground surface.

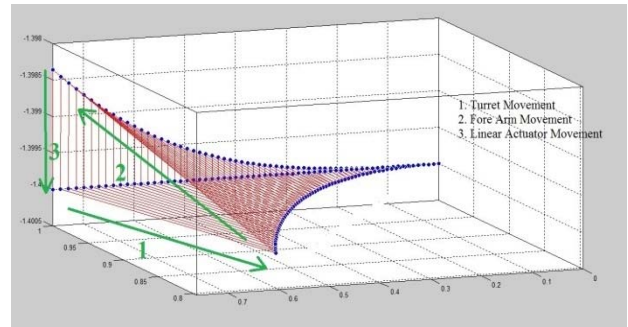


Fig. 4. Principle of Scanning from Origin to Positive maximum

Fig. 5 to Fig. 10 show sequentially the methodological control of the independent and combined arm and controlled trajectories by mean of geometrically worked out spatial movement of the arms.

The principle based on which the manipulator scans from the centre to either direction is given in Fig. 5.

As the desired end effect or coordinate moves towards either side, the joint coordinates θ , α , L increases. First θ_{n-1} incremented to θ_n .

The end effect or moves out of the desired trajectory depicted by movement 1 in the figure.

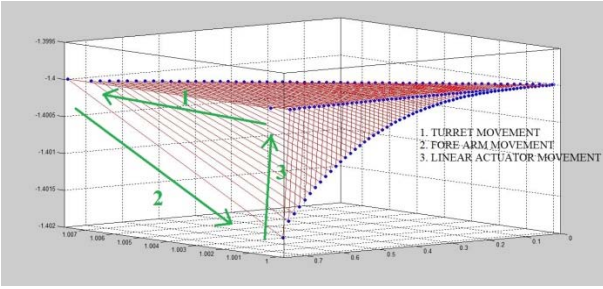


Fig. 5. Principle of Scanning from Positive maximum to origin

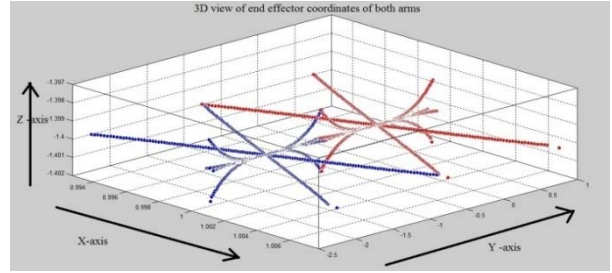


Fig. 10. 3D view of both arms

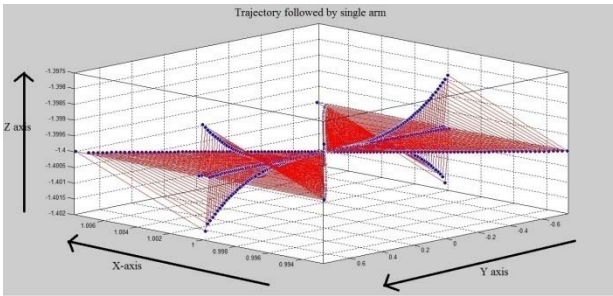


Fig. 6. Trajectory Followed by single arm

Finally step 3, the linear actuator brings down the end effector to desired z axis coordinate, where the end effector meets the required coordinate. The three steps are repeated till it reaches the required width.

After reaching the maximum on either side, the arm has to come to home position.

The sequence of operation are shown in Fig. 6. The sequence starts by decreasing the turret joint by step angle, at which the fore arm parameter and linear joint parameters are higher than required. The end effector will at a point $(x+\delta x, y, z)$ which has to be brought to x, y, z .

The fore arm joint parameter and linear actuator parameters are calculated and applied. Step 1 represents the movement due to forearm, step 2 the fore arm joint due to which the end effector comes to $(x, y, z+\delta z)$. Step 3 the linear actuator motion takes it back to (x, y, z) . The process is repeated till y becomes zero. Fig. 7 shows the maximum error along X axis which occurs after the turret movement. The maximum error is $\pm 5\text{mm}$. Each point indicates the end effector position after turret movement in each iteration. The end effect or position after the fore arm movement is indicated in Fig. 8. The maximum error induced will be $\pm 2.5 \text{ mm}$. When moving from origin to any of the maximum position, the end effector will be moving upwards from required line. When coming back the end effector will be moving downwards from where it is brought to straight line using linear actuator. The complete trajectory of the end effector of a manipulator is given in Fig. 9. The end effector position while scanning in the either direction is indicated. The blue points shows the end effector points and the red lines indicates the path along which the end effector moves from one point to other. The trajectory of both manipulators is given in Fig. 10. Two colors indicate the two arms. The coordinated manipulator positions at different instances are given in Figs. 7, 8 and 9. In Fig. 7, both arms will be at home positions. When scanned in left direction the control variable will be monitoring the movement till it reaches 750mm. It is shown in Fig. 8.

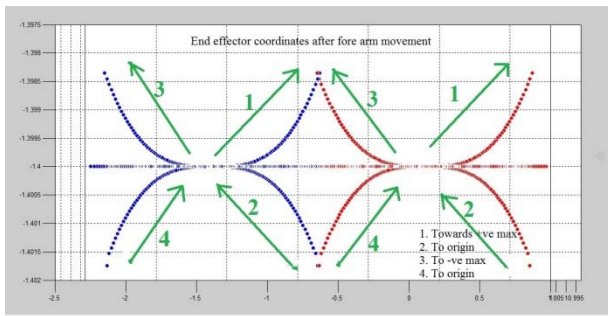


Fig. 7. Maximum error along X axis

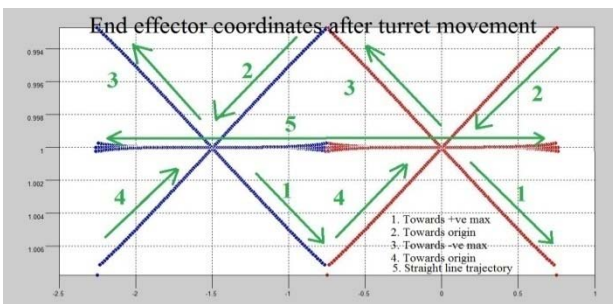


Fig. 8. Top View In Either Direction

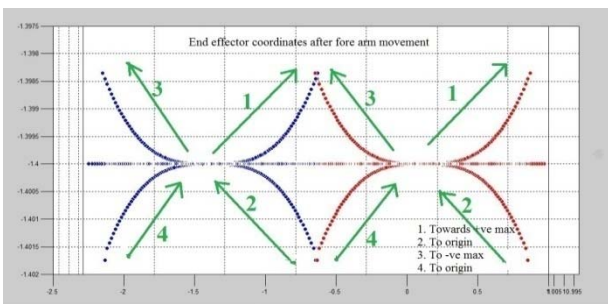


Fig. 9. Front view of end effector movement

Now it will scan in opposite direction till it reaches home and then continue scanning in right direction till it reaches 750mm towards right. The manipulators at right maximum is shown in Fig. 10.

VI. Conclusion

This paper exhaustively addresses the issues related to the control scheme of the mobile manipulator arm to be

used on an unmanned tracked vehicle for carrying out hazardous roles in unstructured terrains. The geometry of the single arm is used to control the end effector position.

The concept has been developed and simulated in MATLAB. This algorithm is implemented to a custom designed robotic arm for specific tasks like scanning the surrounding area once land mine is detected by the sensor in front of the unmanned vehicle.

The processing is near real time for controlling back arm motor, fore arm motor and linear joint motor.

To execute in real time MATLAB code to be converted to embedded 'C' code. This scheme has to be implemented for the real time control of the multiple axes of the arm with hybrid methodology. Different control system methods to be analysed for closed loop precise control of the arm for unstructured environment.



Dr. **R. Sivaramakrishnan** received his B.E. degree in Mechanical Engineering and M.E. in Production Engineering from College of Engineering, Anna University, India, in 1992 and 1994 respectively. He is currently employed as Associate Professor and heading the Division of Mechatronics in the Department of Production Technology, Madras Institute of Technology campus of Anna University. His research interests include Parallel Manipulators, Mechatronics and Computer Integrated Manufacturing.



Abin John Thomas received B.Tech degree in Electronics and Communication from Amal Jyothi College of Engineering Kanjirappally, Kerala and doing M.E Mechatronics in Anna University Chennai. Area of interests are embedded systems and robotics.

References

- [1] Dubowsky, S., Paul, I. and West, H., An Analytical and Experimental Program to Develop Control Algorithms for Mobile Manipulators, *Proc. of the VII Symp on Theory and Practice of Robots and Manipulators*.
- [2] Seraji H., A Unified Approach to Motion Control of Mobile Manipulators, *Int. J. Robotics Research*, Vol. 17, No. 2.
- [3] Norbert A. M. Hootsmans *The Experimental Performance of a Mobile Manipulator Control Algorithm* Proceedings 1992 IEEE International Conference on Robotics and Automation.
- [4] Evangelos Papadopoulos and John Poulakakis, *Planning and Model-Based Control for Mobile Manipulators*, Proceedings IROS 2000 Conference on Intelligent Robots and Systems
- [5] De Xu†‡, Carlos A. Acosta Calderon, John Q. Gan, Huosheng Hu An Analysis of the Inverse Kinematics for a 5-DOF Manipulator, *International Journal of Automation and Computing* 2 (2005) 114-124
- [6] N. Seetharaman, G.Kannan, N.Babu, and R. Alexander, Unmanned Armoured Vehicle for Hazardous Roles, *Proc. International Conference on Emerging Challenge in Design and Manufacturing Technologies (ECHDEM 2007)*
- [7] N.Babu, G.Kannan, N.Seetharaman and R.Alexander, Mine detection manipulator for uneven terrain mounted on unmanned tracked vehicle, *IURS JOURNAL OF Unmanned Robotic Vehicle & Intelligent Systems*, vol.1, pp 92-96, Sep. 2007

Authors' information



Seetharaman N. (Corresponding Author) received B.Tech degree in Automobile Engineering from Madras Institute of Technology, Anna University, India in 1987 and MTech degree in Modelling and Computer Simulation from University of Poona, India in 1992. Working as Scientist in Defence Research and Development Organization.

Awarded Best innovative and futuristic Technology award, 2009 of DRDO. Area of specialization design, development, of systems in Robotics, Unmanned vehicles, Drive By Wire, Mine detection systems.
E-mail: roboraman2007@gmail.com

Modeling of Dynamic Response of Beam-Type Vibration Absorbing System Excited by a Moving Mass

Azma Putra¹, Mothanna Y. Abd², Nawal A. A. Jalil², Sidik Susilo¹

Abstract – A numerical simulation to calculate the dynamic response of a beam attached with beam vibration absorber through a viscoelastic layer subjected to a moving load is presented in this paper. The mathematical model is formulated by using Euler-Bernoulli theory to calculate the vertical response of the system. The effect of the inertia of the moving load is included in the model to study its effect on the beam response at the mid span. The viscoelastic layer is introduced as uniformly distributed stiffness and damping and the concept of mixed damping ratio is implemented which allows the system to be modeled for different rigidity ratio. The response is calculated using time integration method for different moving mass inertia, rigidity ratio of the beams and the stiffness and damping of the visco-elastic layer. The effect is investigated for different values of mass and speed of the moving load. **Copyright © 2013 Praise Worthy Prize S.r.l. - All rights reserved.**

Keywords: Vibration Absorber, Beam, Moving Mass, Dynamic Response

Nomenclature

| | |
|---------------|---|
| E | Modulus of elasticity of the beam (N/m ²) |
| I | Area moment of inertia of the beam (m ⁴) |
| w | Vertical displacement of the beam (m) |
| x | Position coordinate (m) |
| t | Time (s) |
| m | Mass per unit length of the beam (kg/m) |
| k | Layer stiffness (N/m ²) |
| β | Layer stiffness non-dimensional parameter |
| ω_n | Natural frequency of the single beam system (rad/s) |
| n | Integer number, 1,2... |
| μ | Absorber to main beam mass ratio |
| ζ | Layer damping ratio |
| e | Absorber to main beam rigidity ratio |
| M_v | Moving mass (kg) |
| ε | Load parameter |
| σ | Eigenvalue of the mode shape function |
| $X(x)$ | Beam shape function |
| q | Generalized beam time function |
| v | Moving mass velocity(m/s) |
| L | Beam length (m) |

I. Introduction

Beam absorber has been known as one type of absorbers among many types of dynamic absorber used to reduce undesirable vibration in vibrating structures, such as in synchronous machine. Application is also possible to suppress the vibration from beam structures by using an auxiliary beam as the absorbing system.

The auxiliary beam is usually attached through stiffness and damping layers to the main vibrating beam.

Several works have therefore been established to model the dynamics of this double-beam system.

Yamaguchi (1985) first studied the vibration of a double-cantilever beam connected by a spring and a viscous damper where a sinusoidal load is acting at the edge of the main beam [1]. It was found that the response of the main beam is sensitive to the stiffness and mass of the absorbing beam.

Tadayoshi et al. [2] also proposed a theoretical framework for solving the dynamics of a vibration absorber in the case of stationary harmonic load. Chen and Lin [3] analyzed the structural parameters of an absorber system to find an optimum design by using dynamic stiffness matrix method.

In the study, two beams made from the same material have been used and the analysis was carried out for different values of thickness of the absorber beam. It was found that optimum reduction of vibration response can be achieved when the absorber and main beams have the same thickness. However, this case leads to an unacceptable solution for heavy main beam structures, because it requires an identical and heavy absorber beam.

Recently, Abd et al. [4] proposed a mixed damping ratio model for a double-beam system where distributed lumped parameter of the visco-elastic layer stiffness and damping components is assumed.

The model allows calculation with different rigidity and mass ratio of the beams. Some works have been presented emphasizing on the development of the algorithm to calculate the dynamic response of the beam with beam absorber.

Rosa and Lippiello [5] presented the Differential Quadrature Method (DQM) to study the free vibration of a double-beam system.

Sadek et al. [6] implemented legendry wavelets approach for solving optimal control of transverse vibration of two-parallel beam system. Their findings show that the reduction of the beam vibration energy depends on the spring location on the beam.

Again, their methods are also limited for ‘identical beam’ assumption. This assumption is proposed for mathematical convenience from which the two equations of motion can be easily decoupled. Oniszczuk [7] studied free vibration of identical parallel simply supported beams attached by continuous elastic layer. The author then continued the study for a forced vibration case by applying modal summation technique to solve the eigen frequencies [8].

The effect of loading on the dynamic response of a double-beam system was also studied by several authors. Among others are Zhang et al. [9] which studied the vibration characteristics of the double-beam system under axial compressive load. The studies were limited for two identical simply supported double beams and the effect of the axial load on the beams vibration amplitude was reported. Abu-Hilal [10] studied the effect of a moving constant load on the dynamic response of the beams for different parameter values of speed, damping ratio and stiffness.

This paper proposes similar study as from Abu-Hilal [10] but applying the effect of inertia of the moving mass in the model. Previous model of a double-beam system by Abd et al. [4] is also implemented here to conveniently perform calculation for different rigidity ratios. The model is useful to provide a design guide for beam-like structures subjected to moving mass such as bridge or building structure supported by beams frequently excited by a moving object.

II. Mathematical Model

Consider an absorbing beam system compounded of two linearized and isotropic parallel, uniform one-dimensional continuous beams as shown in Fig. 1.

The main and absorber beams are assumed to have simply supported edges. The two beams are connected by visco-elastic layer which is represented by an evenly discrete damper and linear spring components. The transverse forced vibration of the absorbing system can be described by Bernoulli-Euler theory.

For the system with length L along the x -axis, this can be written as [10]:

$$E_1 I_1 \frac{\partial^4 w_1}{\partial x^4} + m_1 \frac{\partial^2 w_1}{\partial t^2} + c \left(\frac{\partial w_1}{\partial t} - \frac{\partial w_2}{\partial t} \right) + k (w_1 - w_2) = f(x, t) \tag{1}$$

$$E_2 I_2 \frac{\partial^4 w_2}{\partial x^4} + m_2 \frac{\partial^2 w_2}{\partial t^2} + c \left(\frac{\partial w_2}{\partial t} - \frac{\partial w_1}{\partial t} \right) + k (w_2 - w_1) = 0 \tag{2}$$

where w is the vertical displacement of the beam, E is the modulus elasticity, m is the mass per unit length, c and k are the damping and the stiffness constants of the visco-elastic layer, t is the time, $K = EI$ is the flexural rigidity and subscripts 1 and 2 refer to the main and the absorbing beams, respectively. A general force $f(t)$ has been assumed here to excite the main beam structure.

The displacement of the beams can be expressed as a summation modal response of the beams as:

$$w_1(x, t) = \sum_{n=1}^{\infty} X_n(x) q_{1n}(t) \tag{3}$$

$$w_2(x, t) = \sum_{n=1}^{\infty} X_n(x) q_{2n}(t) \tag{4}$$

where X_n is the mode shape function which for the simply supported edges is expressed by:

$$X_n = \sin(\sigma_n x) \tag{5}$$

with $q(t)$ is the time function. The eigenvalue σ_n is given by:

$$\sigma_n = \frac{n\pi}{L} \tag{6}$$

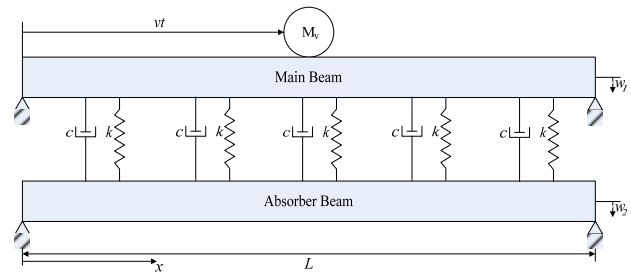


Fig. 1. Two visco-elastically connected simply supported double-beams

The damping of the layer between the main beam and the absorbing beam can be approached by using the concept of “mixed damping ratio” in discrete dynamic vibration absorber [11]. The damping ratio of visco-elastic layer can be formulated by:

$$\zeta = \frac{c}{2\mu m_1 \omega_n} \tag{7}$$

where $\mu = m_2/m_1$ and ω_n is the principle natural frequency of the main beam before the absorber beam is attached defined as:

$$\omega_n = \sqrt{\frac{E_1 I_1 \sigma_n^4}{m_1}} \tag{8}$$

For Eq. (8) to be valid the layer is assumed to have uniformly distributed stiffness and damping.

Substituting Eqs. (3), (4) and (7) into Eqs. (1) and (2) and multiplying both sides of Eqs. (1) and (2) with mode shape function X_n and integrating from 0 to L yields:

$$\ddot{q}_{1n}(t) + 2\zeta\omega_n \dot{q}_{1n}(t) + \omega_n^2(1+k_r)q_{1n}(t) - 2\zeta\mu\omega_n \dot{q}_{2n}(t) - \Omega^2 q_{2n}(t) = \frac{2}{Lm_1} \int_0^L f(x,t) X_n(x) dx \quad (9)$$

$$\ddot{q}_{2n}(t) + 2\zeta\omega_n \dot{q}_{2n}(t) + \frac{\omega_m^2}{\mu}(e+k_r)q_{2n}(t) - 2\zeta\mu\omega_n \dot{q}_{1n}(t) - \frac{\Omega^2}{\mu}q_{2n}(t) = 0 \quad (10)$$

where:

$$k_r = \frac{k}{E_1 I_1 \sigma_n} \quad (11)$$

$$e = \frac{E_2 I_2}{E_1 I_1} \quad (12)$$

$$\Omega^2 = \frac{k}{m_1} \quad (13)$$

Note that in Eqs. (9) and (10), the orthogonality condition has been implemented where:

$$\int_0^L X_n(x) X_m(x) dx = 0, \quad n \neq m \quad (14)$$

II.1. Moving Mass Model

In the previous established model from [10], the load function was represented as a concentrated load and ignores the effect of inertia of the moving mass.

The right hand side of Eq. (9) in the case of moving mass by including the effect of inertia is given:

$$\int_0^L \frac{2}{Lm_1} f(x,t) X_n(x) dx = \frac{2M_v}{Lm_1} (g - \lambda) \int_0^L X_n(x) \delta(x-vt) dx \quad (15)$$

where M_v the mass of the load, v is the speed of the moving mass, g is the gravity acceleration, δ is the Dirac delta function and λ is the term of moving mass inertia given by:

$$\lambda = \frac{d^2 w_1(vt,t)}{dt^2} \quad (16)$$

For the inclusion of mass inertia effect to be valid, it is assumed that the moving mass keeps in contact with the main beam, which means that the displacement of the moving mass is equal to that of the main beam at the contact point. The right-hand side Eq. (13) can be expanded to give:

$$\frac{2M_v}{Lm_1} \left(g - \frac{d^2 w_1(vt,t)}{dt^2} \right) \int_0^L X_n(x) \delta(x-vt) dx = \frac{2M_v}{Lm_1} \left(g - \frac{d^2 w_1}{dt^2} - 2v \frac{\partial^2 w_1}{\partial t \partial x} - v^2 \frac{\partial^2 w_1}{\partial x^2} \right)_{x=vt} X_n(vt) \quad (17)$$

where:

$$\int_0^L X_n(x) \delta(x-vt) dx = X_n(vt) \quad (18)$$

Substituting Eq. (3) into Eq. (15), then Eq. (9) yields:

$$S_{1n} \frac{d^2 q_{1n}(t)}{dt^2} + S_{2n} \frac{dq_{1n}(t)}{dt} + S_{3n} q_{1n}(t) - 2\zeta\mu\omega_n \frac{dq_{2n}(t)}{dt} - \Omega_1^2 q_{2n}(t) = F_n(t) \quad (19)$$

where:

$$S_{1n} = 1 + 2\varepsilon \sin^2(\sigma_n vt) \quad (20)$$

$$S_{2n} = 2\zeta\mu\omega_m + 4\varepsilon v \sigma_n \sin(\sigma_n vt) \cos(\sigma vt) \quad (21)$$

$$S_{3n} = \omega_m^2 (1+k_r) - \alpha_n \quad (22)$$

$$F_n(t) = 2\varepsilon g \sin(\sigma_n vt) \quad (23)$$

$$\varepsilon = \frac{M_v}{Lm_1} \quad (24)$$

$$\alpha = 2\varepsilon v^2 \sigma_n^2 \sin^2(\sigma_n vt) \quad (25)$$

where ε is defined as the load parameter. Eqs. (17) and (10) can be written in matrix form as:

$$[M] \begin{bmatrix} \frac{d^2 q_{1n}(t)}{dt^2} \\ \frac{d^2 q_{2n}(t)}{dt^2} \end{bmatrix} + [C] \begin{bmatrix} \frac{dq_{1n}(t)}{dt} \\ \frac{dq_{2n}(t)}{dt} \end{bmatrix} + [K] \begin{bmatrix} q_{1n(t)} \\ q_{2n(t)} \end{bmatrix} = R(t) \quad (26)$$

where the mass matrix $[M]$, the damping matrix $[C]$, the stiffness matrix $[K]$ and the force vector are given by:

$$[M] = \begin{bmatrix} S_{1n} & 0 \\ 0 & 1 \end{bmatrix} \quad (27)$$

$$[C] = \begin{bmatrix} S_{2n} & -2\zeta\mu\omega_m \\ -2\zeta\mu\omega_m & 2\zeta\mu\omega_m \end{bmatrix} \quad (28)$$

$$[K] = \begin{bmatrix} S_{3n} & \Omega \\ -\frac{\Omega^2}{\mu} & \frac{\omega_m^2}{\mu}(e+k_r) \end{bmatrix} \quad (29)$$

$$R(t) = \begin{bmatrix} F_n(t) \\ 0 \end{bmatrix} \quad (30)$$

These matrices (Eqs. (18) to (21)) are ready to be solved and the dynamic response of the system can be numerically simulated. The calculation for the remaining of this paper considers only the first fundamental mode of the simply supported beam at very low frequency of which its maximum displacement occurs at the middle of the structure (mid span).

II.2. Model Validation

In this section, the proposed model is validated with the existing model from Oniszczuk [8]. The properties of the main beam are listed in Table I.

TABLE I
PARAMETERS OF THE MAIN BEAM USED FOR SIMULATION

| Modulus of elasticity, E_1 (Pa) | Mass, m_1 (kg/m) | Length, L (m) | Area moment of inertia, I_1 (m^4) |
|-----------------------------------|--------------------|-----------------|---|
| 1×10^{10} | 100 | 10 | 4×10^{-4} |

The non-dimensional parameters namely the layer stiffness β , time parameter T , and speed parameter s of the system used in the simulation are defined as follows:

$$\beta = \frac{kL^4}{E_1 I_1} \quad (31)$$

$$T = \frac{vt}{L} \quad (32)$$

$$s = \frac{v}{v_{cr}} \quad (33)$$

where v_{cr} is the critical frequency given by:

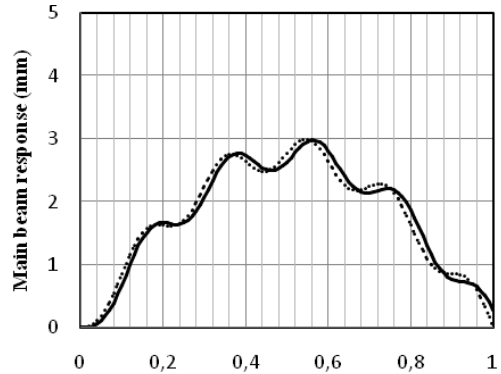
$$v_{cr} = \frac{\gamma L}{\pi} \quad (34)$$

with:

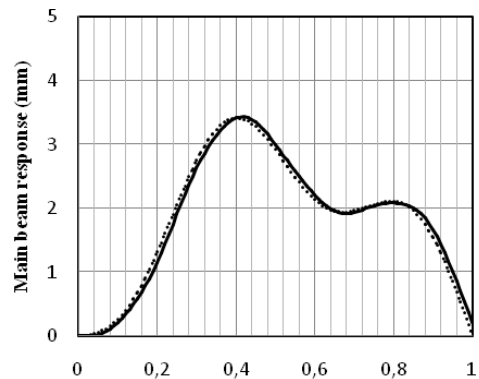
$$\gamma = \left(\frac{\pi}{L}\right)^2 \sqrt{\frac{E_1 I_1}{m_1}} \quad (35)$$

The dimensionless time T represents the location of the moving mass on the main beam. i.e. when $T = 0$, the position of the moving mass is at the edge of the main beam at $x = 0$ (see Fig. 1) and for $T = 1$ is at the other edge of the beam. The numerical main beam response is calculated by using time integration method (Wilson- θ) and using MATLAB software for 100 time steps.

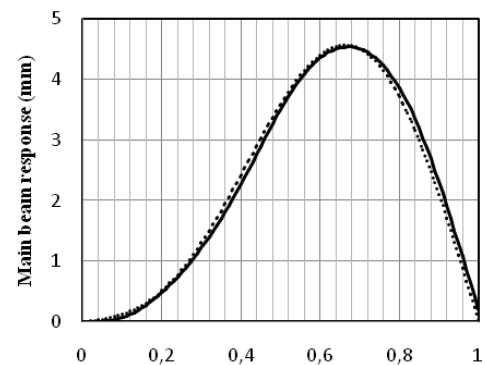
For this validation, the beams are assumed to be identical and the inertia of the moving mass is neglected. Figs. 2 show the results of the displacement at the mid span of the main beam for different values of the speed parameter.



(a)



(b)



(c)

Figs. 2. Displacement of the main beam as a function of dimensionless time T for different speed parameters: (a) $s = 0.1$, (b) $s = 0.25$ and (c) $s = 0.5$ (proposed model, — [8])

It can be observed that the results of the current study are in good agreement with those obtained from the model of Oniszczuk [8].

It is noticeable from Figs. 2 that the speed of the moving load affects the displacement of the beam. For $s = 0.1$, the mid span reaches its maximum displacement when the load is close to the mid span. For $s = 0.25$, the maximum displacement occurs when the load is at 40% of the main beam length and for $s = 0.5$ is when the load has travelled 60% of the beam length.

Fig. 3 plots together the results for different speed parameters. It can be observed that as the moving load speed increases, the distance of the load from the origin ($x = 0$) also increases to generate maximum displacement at the mid span of the beam structure.

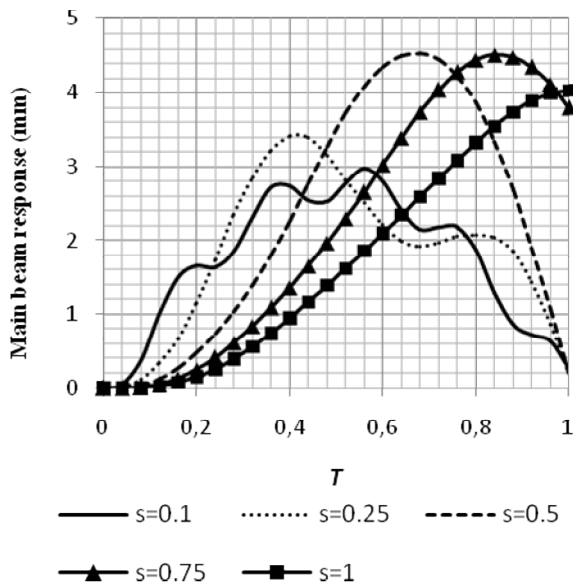


Fig. 3. Displacement of the main beam for different values of the speed parameter

III. Numerical Results

III.1. Effect of Moving Mass Inertia

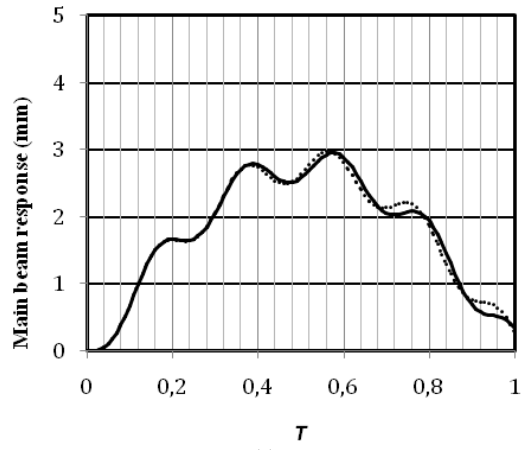
The previous existing studies considered the moving mass as a concentrated load by ignoring its inertia effect [10]-[12].

In the real case, however, the moving mass exhibits two types of load; one due to moving mass gravity i.e. concentrated load and the second due to the moving mass vibration i.e. inertia load. As long as the moving mass is in contact with the beam, the vibration of the beam is transferred to the moving mass at the contact point ($x = vt$) causing the vibration of the loading mass.

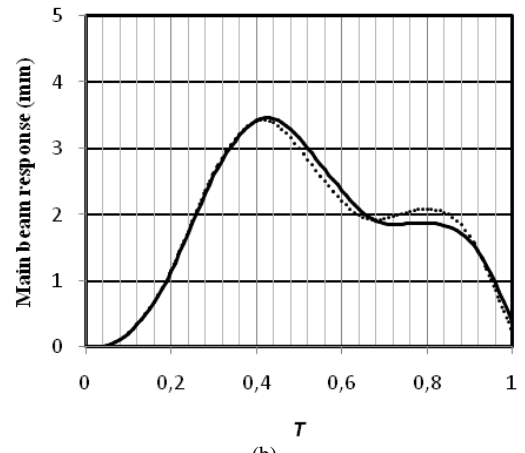
The moving mass then generates inertia force to the beam besides its gravity force.

In this paper, the inertia effect has been investigated for different values of the load parameter and the speed parameter.

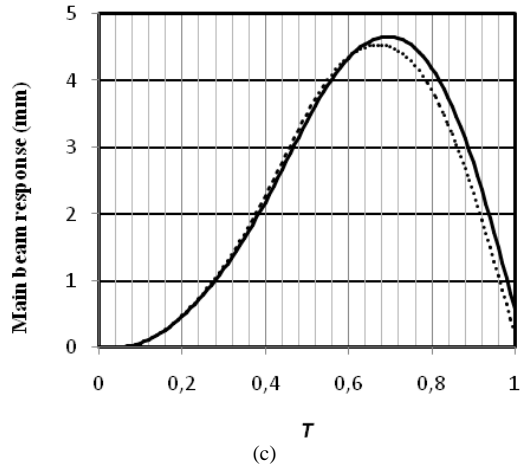
Figs. 4 show that the effect of inertia for the corresponding load parameter ($\epsilon = 0.1$) can be neglected.



(a)



(b)

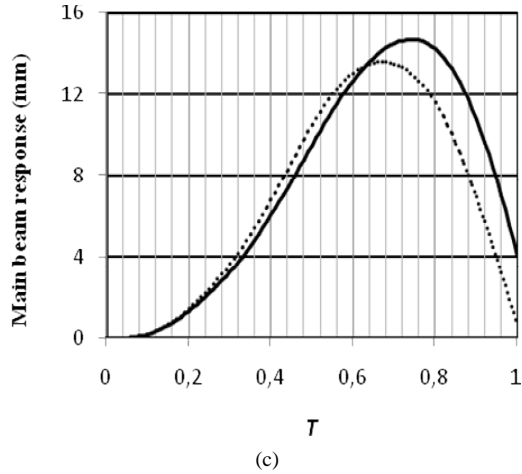
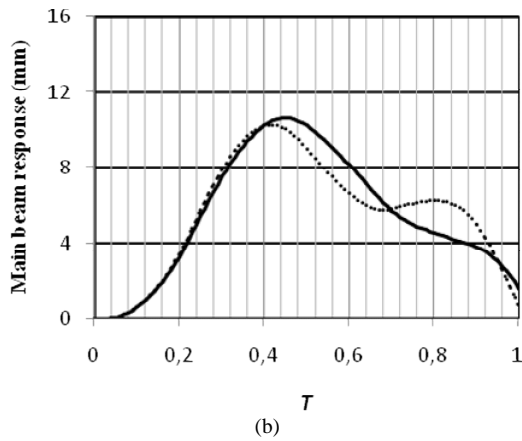
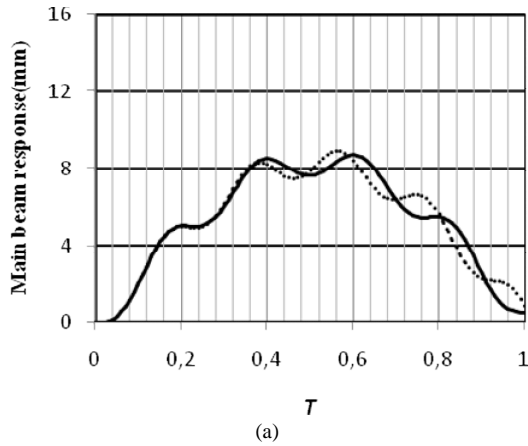


(c)

Figs. 4. Effect of moving mass inertia on main beam mid span displacement for load parameter $\epsilon = 0.1$: (a) $s = 0.1$, (b) $s = 0.25$ and (c) $s = 0.5$ (··· inertia neglected, — inertia included)

However, as the load parameter increases ($\epsilon = 0.3$), the effect of the inertia can be observed particularly above $T = 0.5$. As seen in Figs. 5, the effect becomes greater as the speed parameter increases. As the moving mass is increased, the energy kinetic transferred to the beam also increases.

As the energy kinetic is proportional to the squared velocity, this effect becomes much greater at high speed.

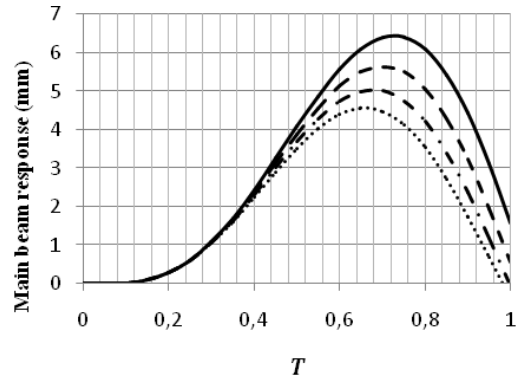


Figs. 5. Effect of moving mass inertia on main beam mid span displacement for load parameter $\epsilon = 0.3$: (a) $s = 0.1$, (b) $s = 0.25$ and (c) $s = 0.5$ (··· inertia neglected, — inertia included)

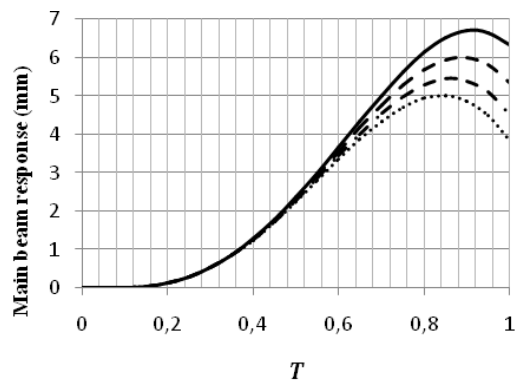
III.2. Effect of Rigidity Ratio and Stiffness and Damping of the Layer

Figs. 6 show the response of the main beam for different values of rigidity ratio e . It can be seen that the response reduces as e increases.

In other words, absorber with stiffness approaches the stiffness of the main beam is preferred to effectively reduce the vibration.



(a)



(b)

Figs. 6. Effect of rigidity ratio on the main beam mid span displacement for $\mu = 0.2$, $\epsilon = 0.1$ and $\beta = 500$: (a) $s = 0.5$ and $s = 0.75$

Fig. 7 shows the effect of the layer stiffness parameter β at speed parameter $s = 0.5$. It can be observed that increasing the stiffness parameter of the layer decreases the main beam displacement.

With constant force acting on the system, increasing the layer stiffness reduces the displacement.

However, this is only valid at low frequency and is true for this case as the calculation is made for the fundamental mode of the beam.

Figs. 8 show that the damping factor of the layer has no significant effect on the vibration response for the case of moving mass load.

Small effect can be seen with small layer stiffness as in Fig. 8(b), but this requires large damping factor.

IV. Conclusion

The dynamic response of a beam absorbing system at the mid span subjected to a moving mass loading has been modeled by including the effect of inertia. The previous mixed damping model is also implemented to enable calculation for different rigidity ratios.

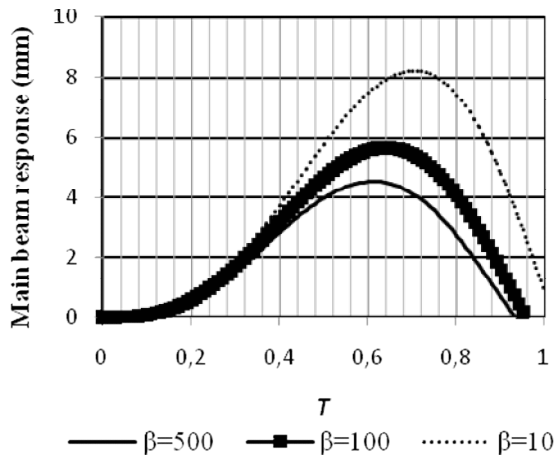
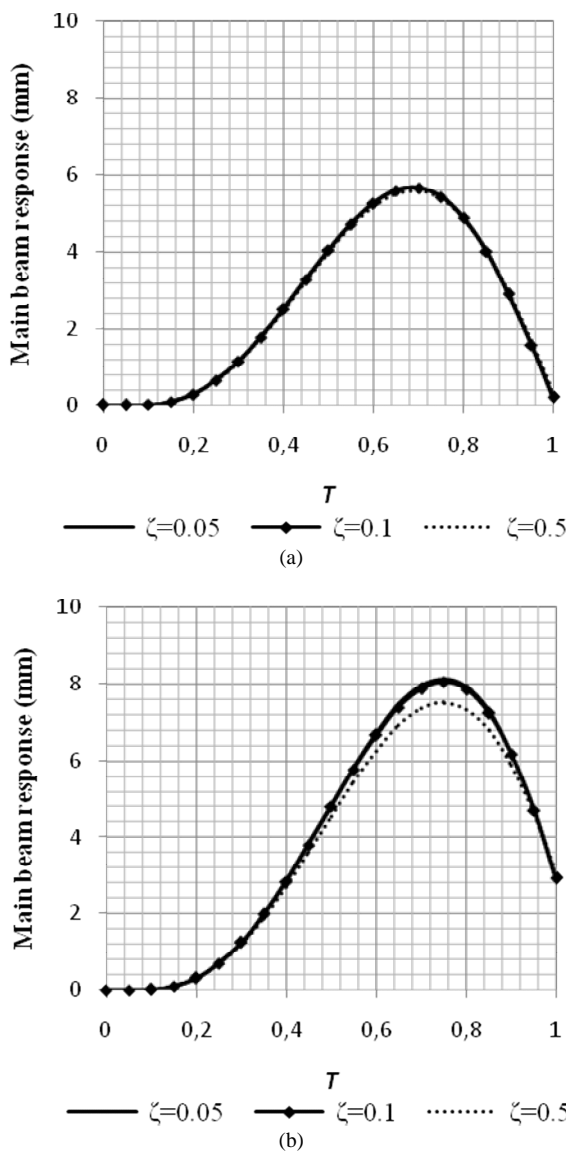


Fig. 7. Effect of viscoelastic layer stiffness on the displacement of the main beam at mid span for $\zeta = 0, s = 0.5$



Figs. 8. Main beam displacement at mid span for different damping factor: $s = 0.5$; (a) $\beta = 100$ and (b) $\beta = 10$

The effect of inertia is found to have significant effect as the mass of the load and the speed are increased.

Large rigidity ratio is also found to reduce the displacement.

The increase of the viscoelastic layer stiffness can reduce the displacement, while negligible effect can be seen by changing its damping factor.

The calculation is made for the fundamental of mode of the beam which dominates the vibration response at very low frequency.

However, it is also of interest to study the results for multi-modal responses for flexible beam structure to observe the phenomena for high frequency.

References

- [1] H. Yamaguchi, Vibrations of a beam with an absorber consisting of a viscoelastic beam and a spring-viscous damper, *Journal of Sound and Vibration*. 103(3): 417-425, 1985.
- [2] A. Tadayoshi, T. Siisumu, O. Norio, I. Yasuo, Vibration control of beams by beam-type dynamic vibration absorbers, *ASCE Journal of Engineering Mechanics*. 118: 248-258, 1992.
- [3] Y. H. Chen, C.Y. Lin, Structural analysis and optimal design of a dynamic absorbing beam, *Journal of Sound and Vibration*. 212(5): 759-769, 1998.
- [4] Y.M.Abd, A.Putra, N.A. Jalil and J.Noorzaei, Effects of structural parameters on the dynamics of a beam structure with a beam-type vibration absorber, *Advances in Acoustics and Vibration*. doi:10.1155/2012/268964.2012.
- [5] D. Rosa, M. Lippiello, Non-classical boundary conditions and DQM for double-beam, *Mechanics Research Communications*. 34: 538-544, 2007.
- [6] T. A. Sadek and M. Abukhaled, A computational method for solving optimal control of a system of parallel beams using Legendre Wavelets, *Mathematical and Computer Modelling*. 45: 1253-1264, 2007.
- [7] Z. Oniszczuk, Free transverse vibration of elastically connected simply supported double-beam complex system, *Journal of Sound and Vibration*. 232(2): 387-403, 2000.
- [8] Z. Oniszczuk, Forced transverse vibrations of an elastically connected complex simply supported double-beam system, *Journal of Sound and Vibration*. 264: 273-286, 2003.
- [9] Y.Q. Zhang, Y.Lu, S.L. Wang and X.Liu, Vibration and buckling of a double-beam system under compressive axial loading, *Journal of Sound and Vibration*. 318: 341-352, 2008.
- [10] Abu-Hilal. Dynamic response of a double Euler-Bernoulli beam due to a moving constant load, *Journal of Sound and Vibration*. 297: 477-491, 2006.
- [11] D.J. Inman, *Engineering Vibration*. (Pearson Education, 2008).
- [12] M.F.M.Hussein and H.E.M.Hunt, Modeling of Floating-Slab Tracks With Continuous Slabs Under Oscillating Moving Loads, *Journal of Sound and Vibration*. 297: 37-54, 2006.

Authors' information

¹Department of Structure and Material, Faculty of Mechanical Engineering, Universiti Teknikal Malaysia Melaka, Hang Tuah Jaya, 76100 Durian Tunggal, Melaka, Malaysia.
Tel: +606 234 6891
Fax: +60 234 6884

²Department of Mechanical and Manufacturing Engineering, Faculty of Engineering, Universiti Putra Malaysia, 43400 UPM Serdang, Selangor, Malaysia.
Tel: +603 8946 4422
Fax: +603 8656 7122



Azma Putra was born in Perth, Australia on 30 September 1978. He received his Ph.D in 2008 from the Institute of Sound and Vibration Research (ISVR), University of Southampton, United Kingdom. He is now a senior lecturer in Universiti Teknikal Malaysia Melaka (UTeM), Malaysia. His current interests are engineering acoustics and noise control, vibro-acoustics and structural dynamics. Dr. Putra is a member of Institute of Noise Control Engineering (INCE), USA and the Society of Vibration and Acoustics Malaysia (SVAM).



Mothanna Y. Abd was born in 2 June 1980 in Babylon, Iraq. He finished his degree in mechanical engineering at Babylon University, Iraq in 2003. In 2010, he has been awarded master of science in mechanical engineering from Universiti Putra Malaysia (UPM), Malaysia. His research interest is vibration and structural dynamics. He worked from August 2010 until October 2012 in The Institute of Noise and Vibration, University Technology Malaysia as a researcher officer.



Nawal A. A. Jalil (Corresponding author) was born on 13 August 1978. He received his Ph.D in 2006 from the Institute of Sound and Vibration Research (ISVR), University of Southampton, United Kingdom. He is now Senior Lecturer at the Department of Mechanical and Manufacturing Engineering, Faculty of Engineering, Universiti Putra Malaysia (UPM). His research interests are biodynamics, structural vibration and machine health monitoring. He is currently the head of Sound and Vibration Research Group at the faculty. Dr. Nawal is a Certified Vibration Analyst from Mobius Institute, Australia and currently the Secretary General of Society of Vibration and Acoustics Malaysia.



Sidik Susilo was born in Sukoharjo, Indonesia on 5 June 1988. He finished his degree in mechanical engineering at Sebelas Maret University, Indonesia in 2012. He is now a postgraduate student in Universiti Teknikal Malaysia Melaka (UTeM), Malaysia. His current interests are engineering acoustics, dynamics and energy harvesting.

Research on Dynamics Simulation of CNC Milling Machine Based on Virtual Prototyping

Yixuan Wang, Yanli Guo, Ying Wang

Abstract – In this paper, design and analysis of the main structure of milling machine has been done. In order to obtain the parameters of servo control system, the automatic control theory, system modeling, simulation, and virtual prototyping technology and so on are used in this paper. It has built 3D virtual prototype model and control systems of the CNC milling machine on ADAMS and MATLAB platform respectively, as well as processed united simulation on ADAMS and MATLAB. Through the control of workbench's speed simulations, simulation results are obtained, by which the reasonability and validity have been testified. The method can be applied to the design and adjustment of NC milling machine. **Copyright** © 2013 Praise Worthy Prize S.r.l. - All rights reserved.

Keywords: NC Milling Machine, Virtual Prototype, Workbench, Servo Control System, ADAMS / MATLAB United Simulation

Nomenclature

| | |
|-------------|---|
| J_e | Equivalent inertia of load system |
| J_y | Rotation inertia of screws in Y-direction |
| M_x | Mass of workbench in X-direction |
| M_{screw} | Mass of screw in X-direction |
| M_y | Mass of workbench in Y-direction |
| ω_l | Angular velocity of screw in Y-direction |
| V | Movement speed of workbench |

I. Introduction

In the modern manufacturing technology system, CNC technology, which integrates microelectronics and computers, information processing, automatic detection, automatic control and some other high-techs, and has many characteristics that including high precision, high efficiency and flexible automation and so on, is the key technology. It plays a prominent role in the implementation of flexible automation, integration and intelligence in the manufacture [1], [2].

Since Seventh Five-Year Plan of China, the research on the CNC technology has been highly supported by government, enterprises and experts and scholars, and gained greater development, but comparing with advanced level in the world, there is still a big gap.

As the development of the machine to high-precision, high surface quality and high productivity direction, engineering and technical experts have been plagued by the debugging of CNC servo control system, on many occasions, they only use the method of simplifying models and experiences to adjust the parameter, which

makes parameters adjustment complicated and makes that most servo-control system of CNC machines do not work in the optimal condition [3]. In this paper, the virtual prototype technology is used to establish an entire CNC milling machine model in Pro/E software, and build virtual prototype of milling machine and realize its motion simulation in ADAMS software.

Then three control schemes for CNC milling machine, the simulation of servo control system based on ADAMS/View, and MATLAB, and the united simulation of servo control system based on ADAMS and MATLAB, have been established. ADAMS / Controls module is used to establish the appropriate state variables, through the state variables, and data exchange is processed between the virtual prototype in ADAMS and control system established in the MATLAB, so as to achieve co-simulation control system based on ADAMS and MATLAB platform.

By comparing these three methods, the co-simulation control do not need to create a mathematical model of the servo control system of the CNC milling machine, the calculation of the transfer function, but output the parameters of the system equations in the ADAMS to MATLAB. Thus the united simulation of ADAMS and MATLAB provides a brand-new method for us to get the parameters of the CNC servo control system.

II. Parameterized Modeling (Virtual Prototype) and Movement Simulation of CNC Milling Machine

Virtual Prototyping (VT), also known as the System Dynamic Simulation Technology, takes mechanical system kinematics, dynamics and control theory as the

core, and integrates the distributed development and design with analysis of the product by means of three-dimensional calculation graphics technology, the graphical user interface technology, information technology, integrated technology and so on [4].

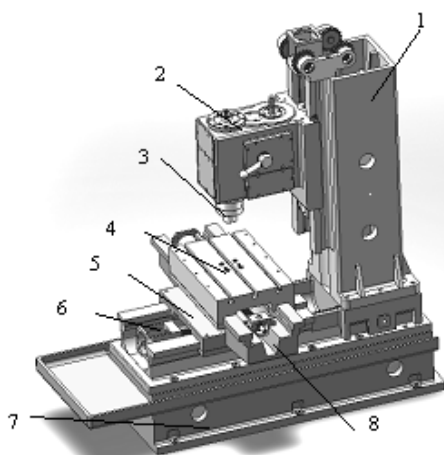
II.1. Vertical Drilling and Milling Machine

The mechanism of CNC milling machine is complicated, according to the different functions of main components, it can be divided into several parts which include basic components, transmissions and accessories and so on [7], [8]. Basic components basically include foundations, columns, worktables, guide rails, etc.

Transmissions mainly include the feed system of lead screw in three directions of X, Y, Z, and counterweight devices.

Accessories mainly include the protective covers of the guide rail, excluding chip device, headlamps, cooling equipments and other auxiliary equipments. NC milling machine is different from ordinary milling machine, its main motion and feed motion of each axes are respectively drove by the servo motor, so NC milling machine' drive chain is short, and the structure is quite simple. In order to ensure the rapid response characteristic and processing precision of NC milling machine, precision ball screws and linear rolling guide rail pairs is widely used. The NC milling machine in this paper is vertical milling machine with the function of the three axial associated motion, which its moving parts can move along the direction of x, y, z. The detailed structure model in Pro/E is shown in Fig. 1.

Using the data interface provided by ADAMS/view, the assembly imported from Pro/E to ADAMS is re-edited, and the kinematic pair and drive motor are added in ADAMS, and then the motion simulation is done in ADAMS/view. The simulation model of NC milling machines is showed in Fig. 2, and simulation graph of displacement of the X-axis workbench is showed in Fig. 3.



1-column 2-gear box 3-main axis 4- X worktable 5- Y worktable 6-screw in Y-direction 7-foundation 8- screw in X-direction

Fig. 1. Assembly model of drilling and milling machine in Pro/E

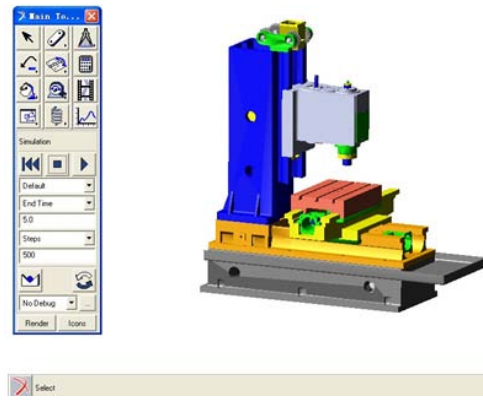


Fig. 2. Simulation model of drilling and milling machine in the ADAMS

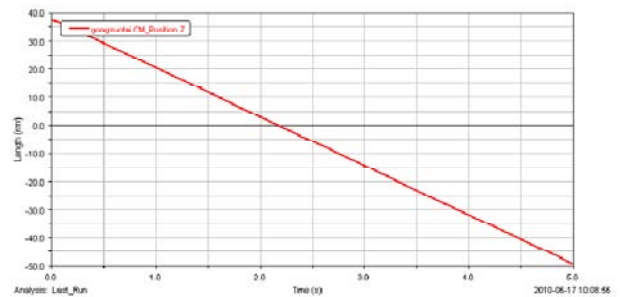


Fig. 3. Simulation of displacement of the X-axis workbench

II.2. Large Portal-Type Milling Machine

The Fig. 4 is the assembly model of large portal-type milling machine in Pro/E. The gantry structure is composed of columns and beams, large structure component of gantry milling machine. The two columns were fixed on both sides of the sliding seat. The slide is driven by the ball screw along the longitudinal direction movement (X direction). Tray is driven through a roller screw along the transverse movement (Y direction). The Ram is driven through the ball screw along vertical direction reciprocating motion (Z direction) relative to the tray. The simulation model of NC large portal-type milling machines in ADAMS is showed in Fig. 5, and simulation graph of displacement of the three-axis is showed in Fig. 6.

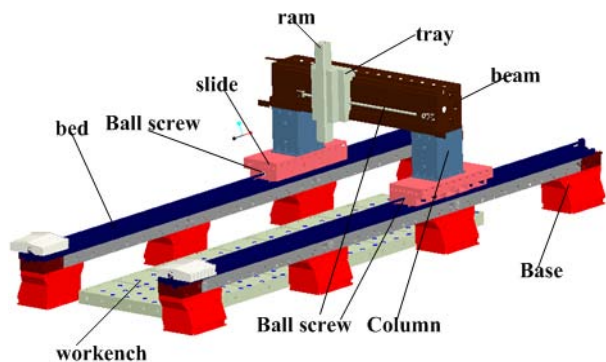


Fig. 4. Assembly model of large portal-type milling machine in Pro/E

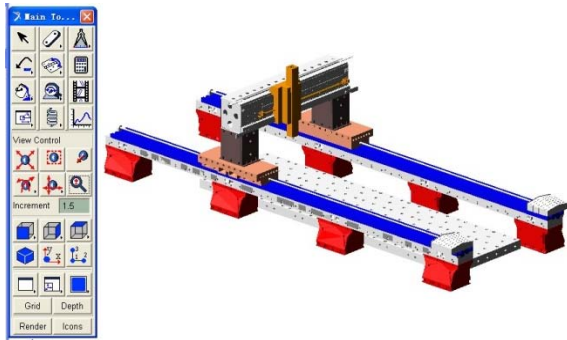


Fig. 5. Simulation model of large portal-type milling machine in the ADAMS

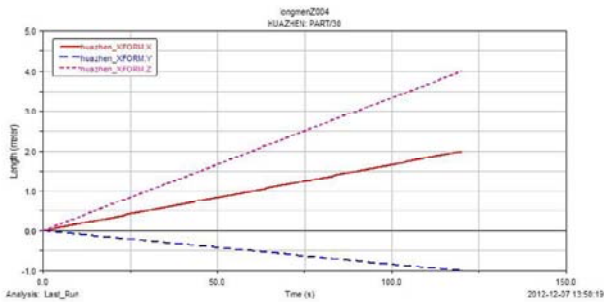


Fig. 6. Three axis displacement simulation of large portal-type milling machine in the ADAMS

II.3. Dynamic Design of Main Structural

(1) Uprights of vertical drilling and milling machine [5], [8].

The column of drilling and milling machine is an important structural cast, and the main force component of the machine. The cross section of column is rectangular, and the height is much larger than the dimensions of cross section. The inner wall of column is provided with vertical and horizontal stiffened plate. If the column structure design is unreasonable, the stiffness of the bed is insufficient, and it will produce a variety of deformation and vibration, so that the machining accuracy is reduced. Parameterized column model with strip ribs and cross ribs is shown in Fig. 7 and Fig. 8 respectively.

The first 20 natural frequencies and mode shapes of the column (material is gray cast iron, and the bottom is fixed) is calculated on ANSYS / Workbench 14.0 platform, and the calculation results are shown in Table I.

The results show that drilling and milling work frequency must be less than 200HZ, that is, the rotation speed of the spindle and the main drive shaft shall not be greater than 12000rpm in order to ensure good dynamic characteristics and stiffness of the machine.

(2) Gantry of portal-type milling machine [6].

Gantry frame structure is composed of columns and beams, as the parameterized models are shown in Fig. 9.

In this paper three types of gantry structure parameters are shown in Table II. The natural frequency and modal shapes are calculated and shown in Table III and Fig. 10.

These results provide an important basis for the drive system design and control.

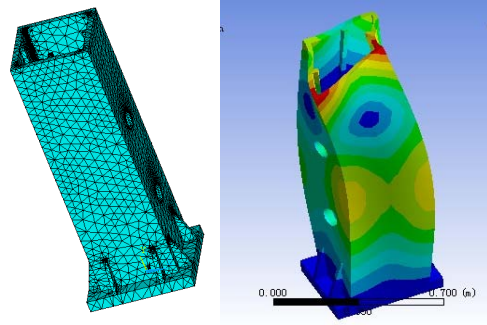


Fig. 7. Finite element model and 9th mode shape of upright with strip ribs

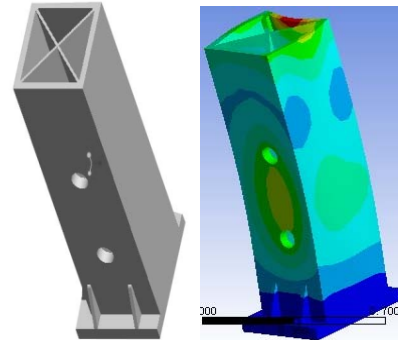


Fig. 8. 3D model and 6th mode shape of upright with cross ribs

TABLE I
FIRST 20 NATURAL FREQUENCY OF THE COLUMN (HZ)

| Order | The column with strip ribs | The column with Cross ribs |
|-------|----------------------------|----------------------------|
| 1. | 222.91 | 209.74 |
| 2. | 231.27 | 216.31 |
| 3. | 400.22 | 529.72 |
| 4. | 573.87 | 786.47 |
| 5. | 574.87 | 848.59 |
| 6. | 702.68 | 865.71 |
| 7. | 752.52 | 940.75 |
| 8. | 818.82 | 1067.1 |
| 9. | 867.76 | 1148.7 |
| 10. | 928.83 | 1294.1 |
| 11. | 1061.6 | 1377.1 |
| 12. | 1161.1 | 1393.2 |
| 13. | 1201.8 | 1435.7 |
| 14. | 1222.6 | 1442.2 |
| 15. | 1272.8 | 1559.7 |
| 16. | 1337.3 | 1574.8 |
| 17. | 1438.7 | 1625.7 |
| 18. | 1488.3 | 1742.4 |
| 19. | 1497.9 | 1751.4 |
| 20. | 1588.7 | 1774.8 |

TABLE II
GANTRY FRAME STRUCTURE DIMENSIONS (Unit: mm)

| Gantry parameter | Model 1 | Model 2 | Model 3 |
|------------------------|-----------|-----------|-----------|
| Column cross section | 1500×1280 | 1300×1000 | 2000×1600 |
| Column height | 1675 | 1200 | 2500 |
| Beam cross section | 1500×1530 | 1000×700 | 2000×1500 |
| Beam length | 8560 | 5500 | 4000 |
| Wall thick | 25 | 30 | 70 |
| Cross ribs thick | 25 | 50 | 60 |
| Inner sides ribs thick | 30 | 50 | 70 |

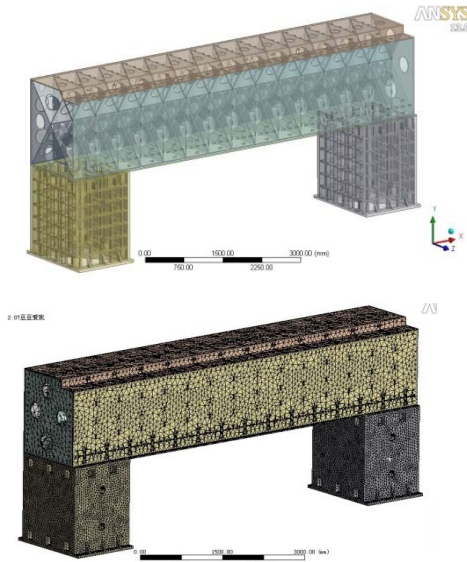


Fig. 9. 3D model and Finite element model of gantry framework

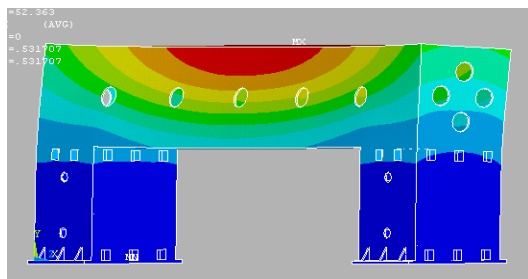


Fig. 10. 1st mode shape of Model 1(gantry frame)

TABLE III
FIRST 20 NATURAL FREQUENCY OF GANTRY FRAME (HZ)

| Order | Model 1 | Model 2 | Model 3 |
|-------|---------|---------|---------|
| 1. | 52.313 | 127.95 | 110.77 |
| 2. | 88.905 | 164.17 | 127.44 |
| 3. | 96.733 | 174.98 | 163.49 |
| 4. | 103.80 | 204.01 | 174.82 |
| 5. | 105.40 | 223.86 | 222.91 |
| 6. | 116.94 | 265.10 | 222.91 |
| 7. | 131.39 | 293.74 | 284.81 |
| 8. | 136.20 | 309.28 | 292.15 |
| 9. | 160.13 | 334.51 | 293.59 |
| 10. | 169.05 | 356.52 | 294.86 |
| 11. | 181.56 | 365.06 | 298.25 |
| 12. | 183.67 | 376.33 | 320.88 |
| 13. | 186.53 | 383.06 | 325.02 |
| 14. | 192.62 | 386.72 | 325.75 |
| 15. | 203.44 | 396.67 | 337.63 |
| 16. | 214.90 | 403.88 | 342.14 |
| 17. | 226.72 | 407.99 | 361.95 |
| 18. | 232.50 | 410.41 | 385.46 |
| 19. | 237.23 | 430.08 | 408.42 |
| 20. | 239.16 | 446.55 | 422.47 |

III. The Simulation of Servo Control System Based on ADAMS/View

The control system design module of ADAMS software is a basic aspect to model, simulate and analyze the complex mechanical systems [9]. For the general control links, we can use the control toolbox provided by

ADAMS/View to deal, which can directly add control modules into the ADAMS/View prototype models, and complete the simulation analysis of mechatronics integration system.

The workbench speed control system established in ADAMS/View, takes the angular velocity of the screw in X-direction as control object, and associates the speed variation produced by comparing given angular velocity with actual angular velocity, with the control torque in screws through control modules, thereby we can control the actual speed of screws in virtual prototypes. And then by constantly comparing the feedback part with the given speed, eventually it makes the speed of ball screws reach the given speed. The control principle is shown in Fig. 11.

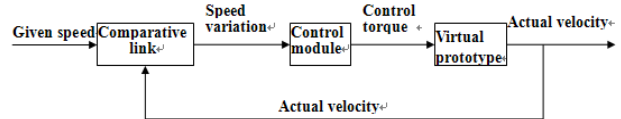


Fig. 11. Control principle diagram in ADAMS/View

The main steps to establish the workbench speed control system in ADAMS/View: 1) Open models, and add Control Torque into screws in the direction X; 2) Establish the input link in Controls Toolkit, which include the given speed -input_vdesired and the angular velocity of screws input_vactual of screws, because that given revolving speed of servo motors is the 3,000 rpm, which is equivalent to 18000d/s and 314 rad/s; 3) Establish comparative links; 4) Establish gain links; 5) Associate torque; 6) simulate, setting the simulation time in 5S, and the simulation step in 50 steps, the results of the simulation is showed in Fig. 12.

IV. The Simulation of Servo Control System Based on the MATLAB

Simulink toolbox of Matlab is a kind of computational simulation tool based on transfer functions of Control System.

Simulink can be modularized, packaged, reloaded, programmed oriented structure chart and highly visualization, etc., and so it can greatly improve the efficiency and reliability of System Simulation [10]. Simulink includes Sinks (output), Source (input source), receiver, linear and nonlinear components of Connections (Connection and Interface) and other sub-module libraries. Each sub-module library also contains corresponding function modules; one can easily create your own modules.

After defined one model, one can input commands to simulate it through the menu of Simulink or the command window of Matlab.

Workbench servo system is a high-precision and closed loop servo system to angle, which consists of drive modules and servo motors and so on. Its input is the instruction pulse given by CNC system and the output is the rotation of Motor.

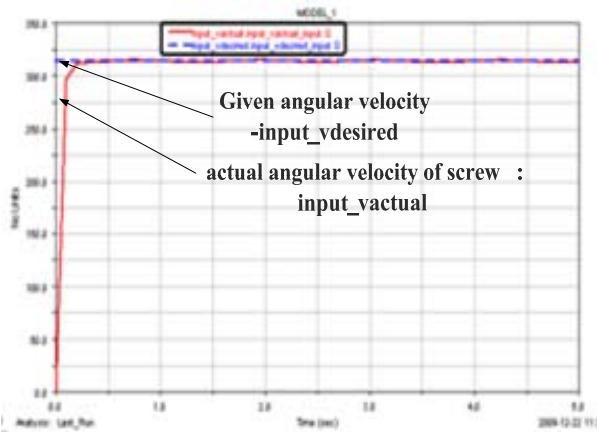


Fig. 12. Speed simulation in ADAMS / View

Under the closed-loops control which realized by the detection feedback loop that composed of Grating and Pulse Coder and so on, Motor rotation will change with numerical orders.

Through the transmission of high-precision screw-nut pairs, the angular displacement of Motor is converted to the required linear displacement of Worktable.

The control system Schematics is shown in Fig. 13. In fact, the semi-closed loop control is used, and the detecting elements added into Servo Motor to detect the speed and displacement of Motor. Under the condition of general accuracy requirement, the feedback of electric current is not required and one can directly use a single closed-loop speed regulation system, in addition can add a position loop, but in this paper, the speed control system is only researched.

When Servo control system of workbench in Y-direction is simulated in Matlab software, firstly, one need to establish the mathematical model of the Y-direction workbench, and then the energy conservation method is used to equate the rotary inertia of the load to the motor shaft side:

$$\frac{1}{2} J_e \omega_1^2 = \frac{1}{2} J_y \omega_1^2 + \frac{1}{2} (M_y + M_{screw} + M_x) V^2$$

Arrange and obtain that:

$$J_e = J_y + (M_y + M_{screw} + M_x) \frac{V^2}{\omega_1^2}$$

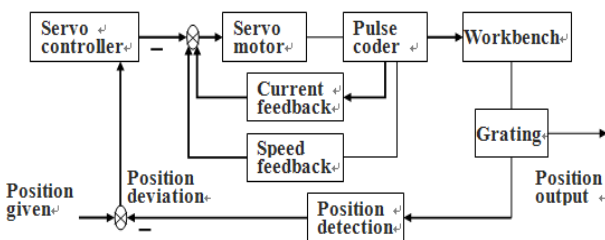


Fig. 13. Control system theory frame

By means of simulation models established in ADAMS/View software, we may obtain the following parameters:

$$J_y = 0.182 \quad M_x = 136.3 \quad M_{screw} = 4.974$$

$$M_y = 262.818 \quad \omega_1 = 100\pi / 3 \text{ rad/s} \quad V = 16.67 \text{ mm/s,}$$

get the solution:

$$J_e = 0.284 \text{ kg/m}^2$$

The significance of each symbol is as follows: J_e is the equivalent inertia of load system; J_y is the rotation inertia of screws in Y-direction; M_x is the mass of workbench in X-direction; M_{screw} is the mass of screw in X-direction; M_y is the mass of workbench in Y-direction; ω_1 is the angular velocity of screw in Y-direction; V is the movement speed of workbench.

After establishing mathematical models, the control simulation model of the feed system of Y-direction workbench is established in Matlab, as shown in Fig. 14.

The model is simulated, and the simulation result is shown in Fig. 15. From the results curve, the system is stable.

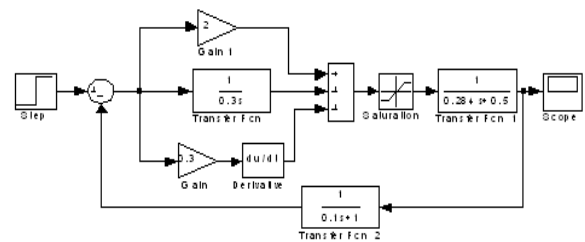


Fig. 14. Simulation model of workbench in Y direction

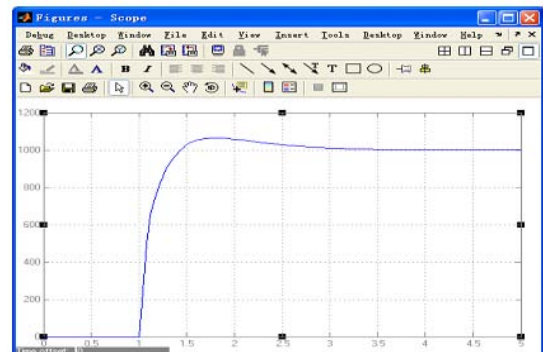


Fig. 15. Step response curve

V. United Simulation of Servo Control System Based on ADAMS and MATLAB

The joint control of Adams and Matlab is to establish the virtual prototype of mechanical movement parts in Adams, and then output the relevant parameters described

system equations by Adams. Lastly, to read the information outputted by Adams in Matlab and establish control schemes. In the process of simulation calculating, Adams exchanges data with Matlab, and solves system equations in Adams and control equations in Matlab [11].

Main steps to establish a joint simulation are as following: 1) Open the virtual prototyping model of CNC milling machine in Adams; 2) Determine the input and output variables of virtual prototyping model. Input variables are control torque variables, which is used to accept the input signal of Adams transferred from Control System. The input signal is also the output signal of Control System, and the output variable is the angular velocity of screw in X-direction, which is used to input the real-time speed signal for control system, and feeds back to control system at the same time; 3) Load ADAMS/Controls modules, and export the control parameters the torque and the velocity. The built models have been successfully converted into the form that MATLAB can read, ADAMS/Control stores the input and output information in m files (Matlab), and meanwhile produces a model file (.adm) and a command file (.cmd) that will be used to conduct the joint simulation analysis; 4) Start MATLAB, and point the working directory of MATLAB to the working directory of ADAMS, and set the adams sub module showed in MATLAB/Simulink; 5) Establish the control scheme in MATLAB, which is as shown in Fig. 16; 6) Simulate and calculate, and then respectively obtained simulation results in MATLAB showed in Fig. 17 and in ADAMS showed in Fig. 18.

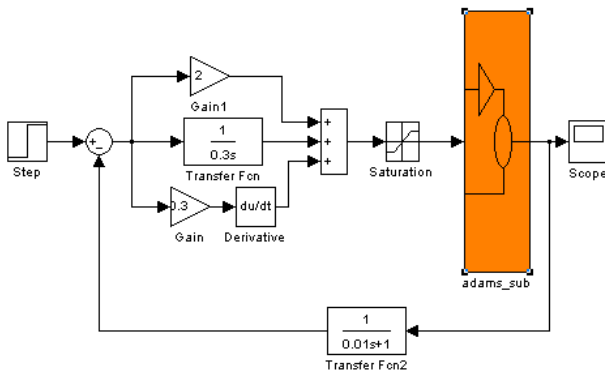


Fig. 16. Control scheme of joint simulation

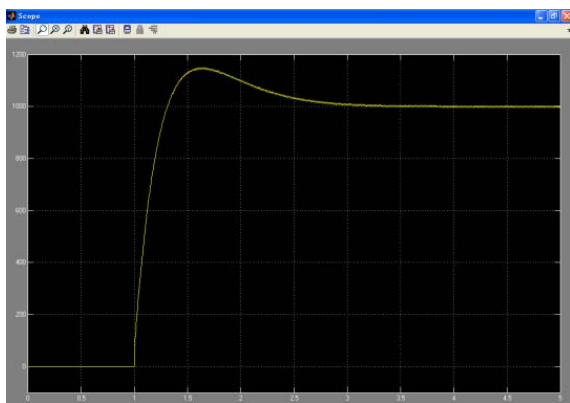


Fig. 17. Result of MATLAB simulation

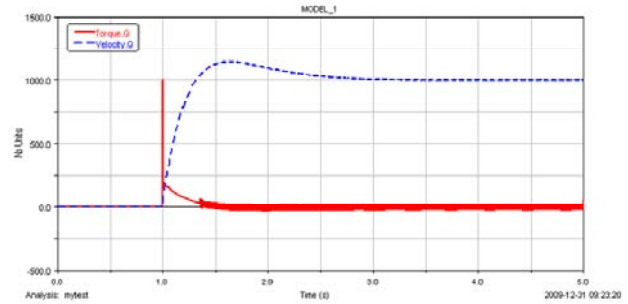


Fig. 18. Result of ADAMS simulation

From the union simulation results, it can be seen that the system has a good stability. In the future, in addition to further improving virtual prototyping models of CNC milling machine, the key point is to study the parameterization of the virtual prototype to make the virtual prototype performance really close to the actual physical prototype and can be more convenient to consider the effects of the guide friction, thermal deformation and the high-speed cutting of main axis. On this basis, we will achieve more satisfactory results, when synchronously conducting control in three directions of X, Y, Z.

VI. Conclusion

In this paper, we mainly design and analyze main structure of milling machine, and simulate the servo control system of CNC milling machine's workbench, and determine the best parameters of the controller through repeated simulations. In addition, by analyzing and comparing three kinds of control projects, it can be seen that the joint simulation based on ADAMS and MATLAB has following advantages:

- (1) Add complex control systems into mechanical system virtual prototype models, and then make the conjoint simulation analysis of mechatronics system.
- (2) It can directly use ADAMS software to establish mechanical system simulation models in Control System analysis, and need not model mathematical formulas.
- (3) The mechanical designers and control engineers can share a virtual prototype model to process the same design verification and experiment, and this make the mechanical system design and control system design sync consistent, meanwhile amend synchronously to achieve optimal design of mechatronics system.

Acknowledgements

This work supported by Natural Science Foundation of Shaanxi Province Colleges and Universities Science Fund (07JK260, 11JK0882), China.

References

- [1] Zhang Jun, Wei Hong-gen, CNC Technology Development

- Trend—Intelligent NC System , *Manufacturing Technology and Machine Tools(Chinese)*, vol.10 n.4, August 2000, pp.7-9.
- [2] Ge Bao-Ming, Jiang Jing-Ping. Model Algorithm Control of Permanent Magnet Synchronous Motor Drive System, *Journal of China Electrical Engineering (Chinese)*, vol.19 n.10, October 1999, pp.67-69.
- [3] Wang Xiao-Dong, Wang Da-Cheng, Modeling Simulation of CNC Servo System Based on Matlab/Smiulink, *Combination Machine Tools and Automatic Processing Technology(Chinese)*. Vol.15 n.8, August 2006, pp.67-69
- [4] Zheng Jian-Rong. *Introduction and Improve of Virtual Prototype Technology* (Mechanic industry press, Beijing, China, 2001).
- [5] Yixuan Wang, Duan Li ,Ying Wang ,Yanli Guo,Xu Chen, The Dynamic Design of Mechanical Structures of CNC Milling Machine Based on Virtual Prototyping, *Applied Mechanics and Materials Vols. 220-223 (2012)*, 2012, pp 410-413.
- [6] CHEN Xu,WANG Yixuan,LI Duan,GUO Yanli, The Dynamic Analysis of the Large Portal-type CNC Filament Winding / Laying Molding Machine, *Journal of Xi'an Polytechnic University(Chinese)*,Vol.27 n.2,2013,pp.215-218.
- [7] YU Yongji,WANG Yixuan,LIU Xin , WANG Xuche, Servo Control System of CNC Milling Machine Based on Virtual Prototyping, *Journal of Xi'an Polytechnic University (Chinese)*,Vol.25 n.1,2011,pp.73-77.
- [8] WANG Xuchen,WANG Yixuan,YU Yongji,WEI Zhongxuan, The Dynamic Analysis of Mechanical Structures of CNC Milling Machine Based on Virtual Prototyping, *Journal of Xi'an Polytechnic University(Chinese)*,Vol.25 n.2,2011,pp.163-167.
- [9] Guo Wei-Dong, *Virtual Prototype Technology and ADAMS Application Example Tutorial* (Beijing aerospace university press, China, 2008).
- [10] Xue Ding-Yu, *Control System Simulation and Computer Aided Design*,(Beijing: Mechanic industry press, China,2005).
- [11] Li Zeng-Gang, *ADAM Introductory Explanation and Examples* (China National Defence Industry Press, Beijing, 2006).

Authors' information



Yixuan Wang, was born in Shaanxi Province China in 16 August 1957, obtained a bachelor's degree in the Department of Mechanical Engineering, Donghua University(in Shanghai, China) in January 1982, received his M.S. degree in Mechanical Engineering in 'Mechanical dynamics systems' from Shanghai Science and Technology University, China in March 1989. He was an assistant from January 1982 to August 1986, a lecturer from September 1986 to October 1994 (The period from September 1986 to March 1989 to pursue his M.S. degree), an associate professor from November 1994 to November 2000, and since December 2000 he has been a professor in CAD/CAE/CAM at the College of Mechanical and Electrical Engineering at the Xi'an Polytechnic University. His major field of study includes finite element analysis of mechanical and electrical structure, electromagnetic and structural design of large-capacity generator, virtual prototyping, and CAD/CAE/CAM and dynamics design. Since as a professor; he has published more than fifty in important international conferences and academic journals, including 10 papers on the large turbo-generator. Previous publications on the large turbo-generator can be found in the references. His Current and previous research interests includes the design and analysis of large turbine generators and wind turbine structure and electromagnetic systems, the structure and control system design of CNC 3D loom and CNC filament winding laying molding machine. Professor Wang is currently a member of the Committee for China Standardization Technical Committee for Textile machinery and accessories, an executive director of China's Shaanxi Province Vibration Engineering Society, and a professor of Xi'an Polytechnic University.
E-mail: wyingping886@126.com



Yanli Guo was born in Shaanxi Province China in 25 June 1987, obtained a bachelor's degree in the Department of Mechanical Engineering, Xian Polytechnic University (in Xian, China) in July 2010, and gained master degree in mechanical design and theory in April 2013 at mechanical school at Xian Polytechnic University. His major field of study includes finite element analysis of mechanical and electrical structure, virtual prototyping.
E-mail: gyl872526@126.com



Ying Wang, was born in Shaanxi Province China in 27 January 1986, obtained a bachelor's degree in the Department of computer science, Xian Jiaotong University(in Xian, China) in July 2008, gained master degree in computer science in July 2010 at computing school at National University of Singapore. She is a researcher and IT analyst in imaging processing and computing vision at National University Health System of Singapore, from March, 2010 to Feb.2011. She is currently a Ph.D. candidate in School of Information Technologies at the University of Sydney. Her major field of study includes imaging processing and computing vision. She has published more than ten in important international conferences and academic journals, including four papers on the large turbo-generator. Her current and previous research interests includes imaging processing and computing vision, and Her Skills & Specialties includes Computer Programming(C, C++, Java, MatLab, C#); Database: SQL (mySQL, ORACLE); Web Development: ASP.NET PHP & HTML, JavaScript, SVG, smil, Dreamweaver, Flash, Photoshop, Adobe audition (Cool Edit Pro) & Video editing: Adobe Premier. She is currently a Ph.D. candidate in School of Information Technologies at the University of Sydney.
E-mail: ywan7763@uni.sydney.edu.au

Comparison of Contact Stress of Helical Gear for Steel C45 with AGMA Standard and FEA Model

S. Prabhakaran¹, S. Ramachandran²

Abstract – In helical gears teeth are at an angle with the axis of the gears. A helical gear is termed right handed or left handed. This paper explains about the geometry of helical gears by mathematical equations, load distribution at various positions of the contact line and the stress analysis of helical gears using three-dimensional finite element method. The contact stress in the tooth root was examined for steel C45 using three-dimensional finite element model. Root stresses are evaluated for different positions of the contact line when it moves from the root to the tip. These stresses were compared with the theoretical values. Both results agree very well. This indicates that the finite element method model is accurate. **Copyright** © 2013 Praise Worthy Prize S.r.l. - All rights reserved.

Keywords: Gearing, Transmission System, Bending Stresses, Root Stresses

Nomenclature

| | |
|--------------|--|
| mn | Normal Module (helical gear) in mm |
| N_1, N_2 | Speed of Gear, Pinion in rpm |
| P | Power transmitted in kW |
| i | Gear (or) transmission ratio Gear in mm |
| b | Thickness of gear and pinion in mm |
| a | Centre distance between shafts in mm |
| z_1, z_2 | Number of teeth in pinion, gear |
| d_1, d_2 | Pitch circle diameter of pinion, |
| β | Helix angle in degrees |
| α | Normal Pressure angle (helical gear) |
| ρ | Density of the material in kg/mm^3 |
| E | Young's modulus in N/mm^2 |
| V_1 | Pitch Line Velocity |
| $[Mt]$ | Design twisting moment in N/mm |
| y | Form factor |
| fo | Height factor |
| k | Load concentration factor |
| kd | Dynamic load factor |
| kb_1 | Life factor for bending |
| $k\sigma$ | Stress concentration factor for the fillet |
| n | Factor of safety |
| σ_b | Induced bending stress in N/mm^2 |
| $[\sigma_b]$ | Allowable bending stress in N/mm^2 |
| σ_c | Induced contact stress in N/mm^2 |
| $[\sigma_b]$ | Allowable contact stress in N/mm^2 |

I. Introduction

Helical gears are similar to spur gears except that the gears teeth are at an angle with the axis of the gears [1].

A helical gear is termed right handed or left handed as determined by the direction the teeth slope away from the viewer looking at the top gear surface along the axis of the gear Meshing helical gears must be of opposite hand.

Meshed helical gears can be at an angle to each other (up to 90°). The helical gear provides a smoother mesh and can be operated at greater speeds than a straight spur gear. In operation helical gears generate axial shaft forces in addition to the radial shaft force generated by normal spur gears. In operation the initial tooth contact of a helical gear is a point which develops into a full line contact as the gear rotates. This is a smoother cycle than a spur which has an initial line contact.

The helix angle of helical gears β is generally selected from the range 6,8,10,12,15,20 degrees. The larger the angle the smoother the motion and the higher speed possible however the thrust loadings on the supporting bearings also increases. In case of a double or herringbone gear β values 25, 30, 35, 40 degrees can also be used. These large angles can be used because the side thrusts on the two sets of teeth cancel each other allowing larger angles with no penalty

When two helical gears are used to transmit power between non parallel, non-intersecting shafts, they are generally called crossed helical gears. These are simply normal helical gears with non-parallel shafts. For crossed helical gears to operate successfully they must have the same pressure angle and the same normal pitch.

They need not have the same helix angle and they do not need to be opposite hand. The contact is not a good line contact as for parallel helical gears and is often little more than a point contact. Running in crossed helical gears tend to marginally improve the area of contact. For instance, in automobile industry highly reliable and lightweight gears are essential. Cockerham, G. [2] has said the finite element method is proficient to supply this information but the time required to generate proper model is a large. Therefore to reduce the modeling time a pre-processor method that builds up the geometry required for finite element analysis may be used, such as

Pro/Engineer. Pro/Engineer can generate three dimensional models of gears. In Pro/Engineer the generated model geometry is opened in ANSYS for analysis. Application of finite element analysis allows investigating the formation of bearing contact during the cycle of meshing and performing the stress analysis. The design of finite element models and the settings of boundary conditions are automatized.

II. Helical gear Design

II.1. Design Objectives

The objective functions are obtained in terms of design variables Normal module (m_n), material selection and Thickness of the gear (b) with the input parameters tabulated in Table I.

Lewis considered gear tooth as a cantilever beam with static normal force F applied at the tip.

Assumptions made are:

1. The full load is applied to the tip of a single tooth in static condition.
2. The radial component is negligible.
3. The load is distributed uniformly across the full face width.
4. Forces due to tooth sliding friction are negligible.
5. Stress concentration in the tooth fillet is negligible.

TABLE I
REQUIRED INPUT DATA FOR HELICAL GEAR DESIGN
(STEEL C45 MATERIAL)

| Description | Gear | Pinion |
|-----------------------------------|----------------------|----------------------|
| Material | Steel C45 | Steel C45 |
| No of Teeth (Z) | 47 | 18 |
| Speed (N) | 635rpm | 1500 rpm |
| Young's Modulus(E) | 2.10×10^5 | 2.10×10^5 |
| | N/mm ² | N/mm ² |
| Poisson Ratio | 0.3 | 0.3 |
| Density of the material(ρ) | 7.8×10^{-6} | 7.8×10^{-6} |
| | kg/mm ³ | kg/mm ³ |

TABLE II
COMPARISON OF RESULTS BETWEEN AGMA AND EXPERIMENTAL
VALUE FOR C45 HELICAL GEAR

| Description | Formula Used | AGMA Results | Experimental Results |
|-------------------------------|---|--------------|----------------------|
| Pitch Diameter (d_1) | $(m_n / \cos\beta) \cdot z_1$ | 92.01mm | 92.05mm |
| Centre Distance (a) | $\left(\frac{m_n}{\cos\beta}\right) \left(\frac{Z_1 + Z_2}{2}\right)$ | 166.13mm | 166.45mm |
| Addendum | $0.8m_n$ | 4mm | 4mm |
| Dedendum | $1 m_n$ | 5mm | 5mm |
| Tooth depth | $2.25 m_n m_n$ | 11.25mm | 11.20mm |
| Minimum Clearance | $0.2 m_n m_n$ | 1mm | 1mm |
| Thickness of the Tooth | $1.5708 m_n$ | 7.854mm | 7.9mm |
| Transverse Circular Pitch(Pt) | $\pi * m_t$ | 16.05 mm | 16.10 mm |
| Normal Circular Pitch(Pn) | $\pi * m_n$ | 15.70 mm | 15.80 mm |
| Axial Pitch(Pa) | $(\pi * m_n) / \sin\beta$ | 75.55 mm | 75.67 mm |
| Tip Diameter (d_a) | $\left(\left(\frac{Z_1}{\cos\beta}\right) + 2fo\right) m$ | 102.01mm | 102.11mm |
| Root Diameter (d_f) | $\left(\left(\frac{Z_1}{\cos\beta}\right) - 2fo\right) m - 2c$ | 80.01mm | 80.13mm |
| Face Width (b) | Ψ_a | 49.83mm | 49.79mm |

TABLE III
RESULTS OBTAINED AS PER AGMA STANDARDS FOR HELICAL GEAR

| Description | Formula Used | Steel C45 |
|--|---|-------------------------|
| Gear Ratio (i) | Z_2/Z_1 | 2.611 |
| Pitch Line Velocity (V1) | $\frac{\pi d_1 N_1}{60}$ | 7.226m/s |
| Tangential Force(Ft) | $\frac{P}{v} * k_o$ | 3459N |
| Radial Force (Fr) | $F_t * \left(\frac{\tan\alpha}{\cos\beta}\right)$ | 1287N |
| Axial Force (Fa) | $F_t * (\tan\beta)$ | 735N |
| Axial Pitch(Pa) | $(\pi * m_n) / \sin\beta$ | 75.55 mm |
| Initial Dynamic Load (Fd) | F_t / C_v | 7623N |
| Velocity factor Cv | $6 / (6 + v)$ | 0.4538 |
| Beam Strength (Fs) | $\pi * m_n * b * [\sigma_b] * y$ | 15324 N |
| Accurate Dynamic Factor (Fd) | $F_t + \frac{21v(b * c * \cos^2\beta + Ft)}{(21v + \sqrt{b * c * \cos^2\beta + Ft})}$ | 8298N |
| Wear Load(Fw) | $(d_1 * b * q * k_w) / \cos^2\beta$ | 17406N |
| Design Torque [Mt] | $M_t * K * K_d$ | 159.15N-m |
| Contact Stress [σ_c] | $C_R * HRC * k_{cl}$ | 852.64N/mm ² |
| Revision of design torque of gear [Mt] | $M_t * K * K_d$ | 196.70N-m |
| Contact stress σ_c | $\sigma_c = 0.74 (i + 1) / a \sqrt{\left(\frac{i + 1}{ib}\right) * E_{eq} [M_t]}$ | 497.33N/mm ² |

Each of these factors can be obtained from the books on machine design such as [1]. This analysis considers only the component of the tangential force acting on the tooth, and does not consider effects of the radial force, which will cause a compressive stress over the cross section on the root of the tooth. Suppose that the greatest stress occurs when the force is exerted at top of tooth, which is the worst case.

When the load is at top of the tooth, usually there are at least two tooth pairs in contact. In fact, the maximum stress at the root of tooth occurs when the contact point moves near the pitch circle because there is only one tooth pair in contact and this teeth pairs carries the entire torque.

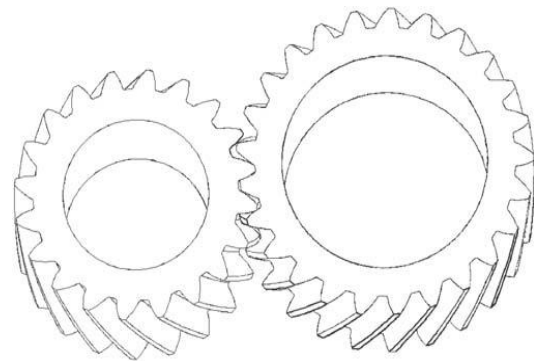


Fig. 1. Helical gears with asymmetric involutes teeth

When the load is moving at the top of the tooth, two teeth pairs share the whole load if the ratio is larger than one and less than two. If one tooth pair was considered to carry the whole load and it acts on the top of the tooth this is adequate for gear bending stress fatigue.

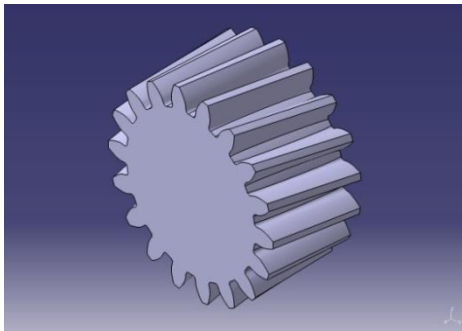


Fig. 2. Helical gear model for Steel C45



Fig. 3. Helical gear and Pinion for Steel C45

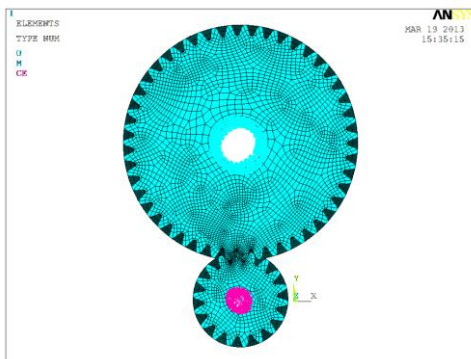


Fig. 4. Meshing of Helical gear for Steel C45

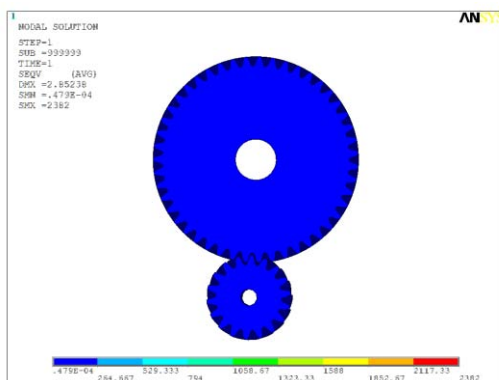


Fig. 5. Contact stress model of Helical gear for Steel C45

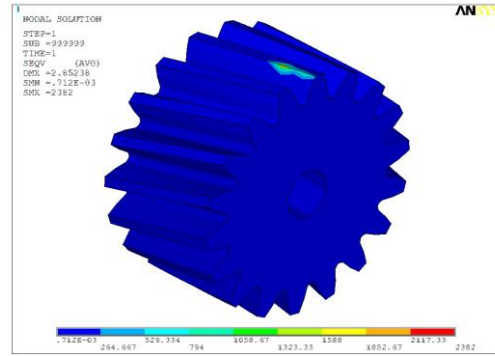


Fig. 6. Contact stress model of Helical gear for Steel C45

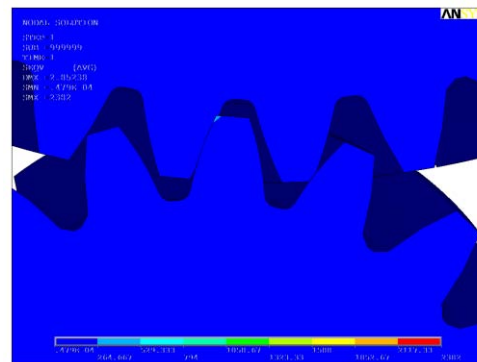


Fig. 7. Contact stress model of Helical gear for Steel C45

FEA- Finite Element Analysis

AGMA- American Gear Manufacturing Association

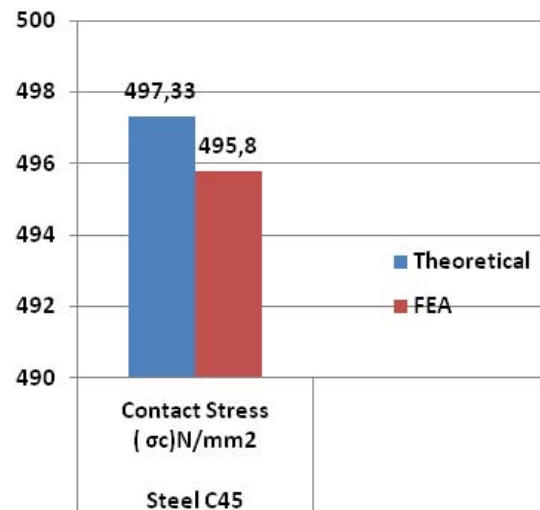


Fig. 9. Comparison between Theoretical value and FEA for Steel C45

TABLE IV
COMPARISON BETWEEN THEORETICAL VALUE AND FEA FOR SPUR GEAR DESIGN

| Description | Theoretical | FEA |
|---------------------------|-------------------------|-------------------------|
| Material | Steel C45 | Steel C45 |
| Contact stress σ_c | 497.33N/mm ² | 495.80N/mm ² |

III. Conclusion

In the present study, effective methods to estimate the contact stress by the three-dimensional finite element method are proposed. To determine the accuracy of the present method for the contact stress the three dimensional method were built in this paper using finite element method.

The contact stress results for steel C45 are compared between the theoretical value and finite element method.

Both results agree very well. This indicates that the finite element method model is accurate. However the present study gives the accurate results by finite element method for contact stress, it can be analysed with the experimental study for the material steel C45, thus remains another scope of this study.

References

- [1] Ch.Rama Mohana Rao, G. Muthuveerappan "Finite element modelling and stress analysis of helical gear teeth" *Department of Mechanical Engineering, Indian Institute of Technology, Madras-600 036, India.*
- [2] Hamrock, B. J., Jacobson, S. R., "Fundamentals of Machine Elements".
- [3] S.Padmanabhan, Dr.M.Chandrasekaran, Dr. P.Asokan and Dr. V.Srinivasa RamanA "Performance Study of Real Coded Genetic Algorithm on Gear Design Optimization" *Advanced Materials Research Vols. 622-623 (2013) pp 64-68*
- [4] Chong, T. H., Bar, I., 2001, "Multiobjective optimal Design of Cylindrical Gear Pairs for the Reduction of Gear Size and Meshing Vibration", *JSME International Journal*, Vol.44, No. 1, pp 291-292
- [5] Buckingham, E., 1949, "Analytical Mechanics of Gears", *McGraw-Hill, New York.*
- [6] Prof. K.Gopinath & Prof. M.M.Mayuram "*Machine Design II*"
- [7] Cockerham, G., 1967, "Computer-Aided Design of Spur or Helical Gear Train", *Computer-Aided Design*, Vol.8 No. 2, pp. 84-88.

Authors' information

¹Research Scholar, Department of Mechanical Engineering, Sathyabama University, Chennai, India.

²Sathyabama University /Professor, Head Of the Department, Department Of Mechanical Engineering, Chennai, India.



Prabhakaran S. is a research scholar in the Faculty of Mechanical Engineering at Sathyabama University, Chennai, India. I am working as a Associate Professor in the department of Mechanical Engineering, Anand Institute of Higher Technology, Chennai. I have completed my Bachelor degree in Mechanical Engineering in the year 2001 and Master degree in CAD in the year Dec 2002. I have more than 10 years of experience in the teaching field. I have more than 8 papers in journals and conference proceedings. Dr. S. Ramachandran is working as a professor and Head in the department of Mechanical Engineering, Sathyabama University, Chennai, India. He is author of nearly 20 publications in refereed journals, conferences. He has written more than 8 books.

E-mail: prabhakaran.sk1980@gmail.com

Harnessing Energy from Mechanical Vibration Using Non-Adaptive Circuit and Smart Structure

Intan Z. Mat Darus¹, Ameirul A. Mustadza², Hanim Mohd Yatim³

Abstract – Energy harnessing for the purpose of powering low power electronic devices has received much attention in the last few years. By harnessing ambient energy from the environment it will eliminate the need for batteries and supplying the portable electronic devices such as cell phones, laptops and MP3 players with infinite amount of energy. The ambient energy that can be harnessed to generate electricity comes from a wide range of sources but vibration energy shows a promising amount of power generation. This paper present the integration of instrumentation for conversion of mechanical vibration into electricity using piezoelectric vibration-to-electricity converter, quantification of the amount of power that can be generated and identification of electronic devices that can fully utilize this power. The research is conducted on the laboratory experiment on vibrating mechanical equipment such as turbine and centrifugal pump. The experimental result shows that for the turbine, as the speed of the turbine increases from 1150 rpm to 1450 rpm, the average power produced increases from 1.63 μ W to 2.02 μ W. Also, for the centrifugal pump, as the speed increases from 1700 rpm to 1900 rpm, the average power produced increases from 3.02 μ W to 3.06 μ W. The experimental results also revealed that within 30 minutes, 1.84 μ W of energy could be harnessed from the vibration of the turbine at speed of 1450 rpm while 3.06 μ W of energy could be harnessed from the vibration of the centrifugal pump at speed of 1900 rpm. This power output is sufficient for low-powered wireless sensor networks in silent mode which can be used in variety of applications as indicated in the previous literature. Copyright © 2013 Praise Worthy Prize S.r.l. - All rights reserved.

Keywords: Energy Harnessing, Mechanical Vibration, Non-Adaptive Circuit, Piezoelectric, Vibration-To-Electric Energy Conversion

I. Introduction

Over the last 20 years, the continuous development of technology has significantly reduced the size and increased the function of electronic devices and in parallel decreased their power consumption [1].

Nowadays hand held and portable electronic devices such as cell phones, laptops and MP3 players provide users with comprehensive functions which include communication, computing and audio functions. Batteries are commonly used to power the electronic devices.

However, due to its limited capacity, batteries could possibly supply power only for short lifetime of about one to three years and its significant size and weight has caused problem to the present hand held and portable devices. This problem has then led to the rising demand for self-powered electronic devices because the usage of current battery technology to power electronic devices has become impractical. The advancement of current technology has helped to fulfill the demand for self-powered electronics devices by harnessing ambient energy from the environment, thus eliminating the need for batteries and supplying these electronic devices with infinite amount of energy.

The ambient energy that can be harnessed to generate electricity is coming from a wide range of sources such as human body temperature gradient [2], [3], [4].

Another form of energy sources that has received attention from researchers for energy harnessing is vibration which can be observed in buildings, factories, vehicles, industrial machineries and household appliances [5]-[13]. Typically, vibration energy can be converted into electric energy by three methods, namely electromagnetic (inductive), electrostatic (capacitive) and piezoelectric conversion. Table I shows a comparison of potential energy sources with a fixed level of power generation and a fixed amount of energy storage where all power density values are normalized to the size of 1 cm³ based on the size of typical wireless sensor nodes [14]. The driving force to harness ambient energy from the environment is mostly due to the development of wireless sensor and actuator networks where particular research has been conducted for a project named Pico Radios [14]. This project aims to develop a small and flexible wireless platform for ubiquitous wireless data acquisition that minimizes power dissipation. The important specifications for the power system developed by PicoRadios project researchers are the total size and average power dissipation of an individual node.

The size of a node must not be larger than 1 cm³ and the target average power dissipation of a completed node is 100 μW. The previous research also showed a promising amount of power density about 50 to 200 μW/cm³ that can be harnessed from vibration energy as illustrates in Table I. Therefore, the measure of acceptability of an energy harnessing solution will be its ability to provide 100 μW of power in less than 1cm³. However, this does not mean that solutions which do not meet this criterion are not worthy of further exploration but simply that they will not meet the needs of the Pico Radios project. Thus, the primary criterion to evaluate power sources in this research is power per volume with a target of at least 100 μW/cm³.

TABLE I
COMPARISON OF POTENTIAL ENERGY SOURCES WITH A FIXED LEVEL OF POWER GENERATION AND A FIXED AMOUNT OF ENERGY STORAGE

| Sources | Power Density (μW/cm ³) | Power Density (μW/cm ³) |
|---|---|---|
| | 1 year lifetime | 10 year lifetime |
| Solar (outdoors) | 15,000 – direct sun 150 – cloudy day | 15,000 – direct sun 150 – cloudy day |
| Solar (indoors) | 6 – office desk | 6 – office desk |
| Shoe inserts | 330 | 330 |
| Temperature gradient | 15 at 10°C gradient | 15 at 10°C gradient |
| Vibration (electromagnetic conversion) | 100 | 100 |
| Vibration (electrostatic conversion) | 50 | 50 |
| Vibration (piezoelectric conversion) | 200 | 200 |
| Batteries (non-rechargeable lithium) | 45 | 3.5 |
| Batteries (rechargeable lithium) | 7 | 0 |
| Hydrocarbon fuel (micro heat engine) | 333 | 33 |
| Fuel cells | 280 | 28 |

Batteries are type of energy storage devices that commonly used to power hand held and portable electronic devices as well as implanted biomedical systems. However, due to its limited capacity, batteries could possibly supply power only for short lifetime of about one to three years and its significant size and weight has caused problem to the present hand held and portable devices as well as implanted biomedical systems. While researchers continuously developed the technology to increase the energy of storage devices, the solutions are still going to have finite lifetime.

This problem has led to the rising demand for self-powered devices and systems which can be solved by harnessing energy from a wide range of sources using a few technique that have been proven can supply infinite amount of power. In this study, conversion of mechanical vibration into electricity using piezoelectric material is undertaken with a focus to quantify the amount of power that can be generated and identify electronic devices that can fully utilize this power.

The objective of this research is to design, simulate and develop an instrumentation system to harness energy

from mechanical vibration using smart materials. Based on the research conducted, piezoelectric energy harnessing circuit selection process was made in order to get the suitable circuit followed by the selection of a few types of energy storage devices to be used in this paper.

II. Literature Review

The development of technology has significantly decreased the power consumption of electronic devices thus it becomes possible to power the electronic devices by harnessing ambient energy from the environment.

The ambient energy that can be harnessed to generate electricity is coming from a wide range of sources such as human body, solar, temperature gradient, air flow, acoustic noise and vibration.

The piezoelectricity phenomenon happened when certain crystals were subjected to mechanical strain, they become electrically polarized and the degree of polarization was proportional to the applied strain. On the other hand, these materials deformed when they are exposed to an electric field. There are quite a number of different piezoelectric materials that have been developed thus far, available in many forms including single crystal such as quartz, piezoceramic such as lead zirconate tinate (PZT), thin film such as sputtered zinc oxide and polymer materials such as polyvinylidene fluoride (PVDF). There are a few important fundamental material properties when comparing different piezoelectric materials. The piezoelectric strain coefficient, *d* relates strain to electric field.

The coupling coefficient, *k* is an indication of the material's ability to convert mechanical energy to electrical energy or vice versa. It is functionally related to the strain coefficient by (1):

$$k = \sqrt{\frac{Y}{\epsilon}} d \tag{1}$$

From (1), it is clearly shown that materials with larger strain and coupling coefficients have a higher potential for energy conversion. The strain and coupling coefficients are different in 33 mode than in 31 mode which generally much higher in 33 mode. The tensile strength of the material is also very important.

As mentioned earlier, the power output is related to the average strain developed. In certain cases, the design will be limited by the maximum strain that a bender can withstand.

The piezoelectric constants for common materials such as hard lead zirconate tinate (PZT-5A), barium tinate (BaTiO₃) and polyvinylidene fluoride (PVDF) are provided in Table II. In conclusion, the maximum available piezoelectric generators electromechanical efficiency is approximately 50% which corresponds to parallel mode and PZT material. Harnessing energy using piezoelectric materials convert wasted vibration energy from surrounding into electrical energy that could be useful to power electronic devices.

The concept of vibration energy harnessing using piezoelectric materials is shown in Fig. 1.

Ottman *et al.* (2003) presented an optimized method of harnessing vibration energy with a piezoelectric element using a step-down converter. In this configuration, the converter regulates the power flow from the piezoelectric element to the desired electronic load. The experimental results show that the converter could increase the power output by approximately almost 325% [15].

Roundy *et al.* (2003) made a qualitative comparison for the three basic vibration energy harnessing methods which then focus only on electrostatic and piezoelectric power harnessing methods. The experimental results showed that the PZT bimorph are capable of producing a power density of $70 \mu\text{W}/\text{cm}^3$ [10]. Roundy and Wright (2004) developed a small piezoelectric cantilever generator that was used to power a custom radio transmitter. Their study demonstrated that, for a vibration source of 2.5 m/s^2 at 120 Hz, the piezoelectric generator was capable in producing a power output of $375 \mu\text{W}/\text{cm}^3$ [8].

In his study, Sodano *et al.* (2004) developed a mathematical model to predict the energy generated from a piezoelectric bimorph cantilever beam. A maximum error of 4.61% was found upon validation of the model through an experimental testing [16]. In a later study, Sodano *et al.* (2005) compared the efficiencies of three types of piezoelectric materials which include the commonly used PZT, the bimorph Quick Pack (QP) actuator and the macro-fiber composite (MFC). Each specimen was excited at resonance, subjected to a 0 until 500 Hz chirp and lastly exposed to random vibrations with frequencies of 0 to 500 Hz.

TABLE II
COMPARISON OF PIEZOELECTRIC MATERIALS [1]

| Property | Units | PZT-5A | BaTiO ₃ | PVDF |
|-----------------------|--------------------------------------|--------|--------------------|------|
| d ₃₃ | 10 ⁻¹² C N ⁻¹ | 374 | 149 | -33 |
| d ₃₁ | 10 ⁻¹² C N ⁻¹ | -171 | 78 | 23 |
| g ₃₃ | 10 ⁻³ V m N ⁻¹ | 24.8 | 14.1 | 330 |
| g ₃₁ | 10 ⁻³ V m N ⁻¹ | -11.4 | 5 | 216 |
| k ₃₃ | | 0.71 | 0.48 | 0.15 |
| k ₃₁ | | 0.31 | 0.21 | 0.12 |
| Relative permittivity | ε/ε ₀ | 1700 | 1700 | 12 |

The efficiency of the PZT was quite consistent with 4.5% at resonance, 3.0% for a chirp and 6.8% for random vibrations and was higher than the other two devices.

The QP had efficiencies of 0.6% at resonance, 1.4% for a chirp, and 3% under random vibrations.

The MFC had efficiencies of 1.75% at resonance, 0.3% for a chirp, and 1.3% for random vibrations. It was concluded that the PZT is the most efficient of all three materials [17].

In another study, Ward and Behrens (2008) have demonstrated a new approach in harvesting energy from vibration where a reinforced learning algorithm is used to maximize the extraction of vibration energy from different disturbance scenarios. Experimental results

showed that efficiencies of 27 - 34% could be achieved for mechanical vibration to electrical energy conversion [18]. In a more recent study, Adhikari *et al.* (2009) analyzed the possibility of harvesting energy under broadband random excitations. Two cases of harvesting circuit with and without an inductor have been considered. It was highlighted that for harvesting circuit with an inductor as a function of α for $\beta = 1$, $\zeta = 0.1$ and $\kappa = 0.6$, the maximum mean harvested power corresponds to the optimal value of $\alpha = 1.667$. The mathematical expressions derived in this study are useful in quantifying the power that could be harvested under broadband random vibrations [19].

The amount of energy generated by piezoelectric materials is far smaller than required for the normal operations of most electronic devices.

Therefore, the method of accumulating and storing the energy generated until sufficient power has been captured is the key in developing completely self-powered systems. Starner (1996) investigated the possibility of harnessing energy from the human body for the use of wearable electronic devices [3]. Based on the study, it was proposed that capacitors and rechargeable batteries could be used as the storage devices. Sodano *et al.* (2002) have investigated the amount of power generated through the vibration of a composite piezoelectric aluminium plate and compared two methods of power storage. It was found that a maximum power of 2 mW could be generated when the plate was excited at its resonant frequency.

It was also demonstrated that the power output of a piezoelectric material was able to recharge a fully discharged battery in one hour and suggests that batteries are the superior option for storing electrical energy for continuous power supply applications [20]. Roundy and Wright (2004) developed a small piezoelectric cantilever generator that was used to power a custom radio transmitter. A piezoelectric generator of 1 cm³ total volume was used based on the size of most wireless sensor nodes. Their study showed that, for a vibration source of 2.5 m/s^2 at 120 Hz, the piezoelectric generator was capable of charging a storage capacitor to a sufficient level at which the transmitter could be turned on [8].

The energy sources such as human body, solar, temperature gradient, air flow, acoustic noise and vibration that can be used for energy harnessing are discussed. From the wide range of energy sources, vibration energy is chosen for its potential as a viable power source for applications where vibration is present.

Piezoelectric conversion mechanism is chosen as a method to convert vibration into electricity because piezoelectric converter produces the highest energy density. The basic concept of piezoelectricity is studied and the previous related works on harnessing energy from vibration using piezoelectric materials are also discussed. The amount of energy generated by piezoelectric materials is far smaller than required for the normal operations of most electronic devices; therefore,

capacitor is chosen as the storage device for this study as the method of accumulating and storing the energy generated until sufficient power is captured.

In the following chapter, the instrumentation system used to harness energy from micro vibration using piezoelectric materials is presented.

III. Methodology

The flow of the process and technique used to harness energy from vibration using piezoelectric materials is as illustrated in Fig. 1. The study on piezoelectric energy harnessing has been divided into two main parts which are (1) simulation of the vibration environment and (2) laboratory experiment on vibrating mechanical equipments.

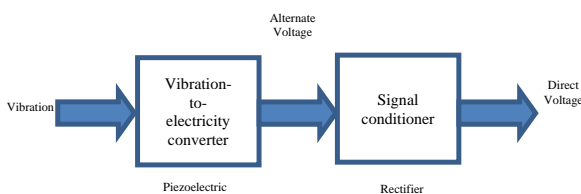


Fig. 1. Concept of vibration energy harnessing using piezoelectric materials

Both simulation and laboratory experiment will undergo the same process such as piezoelectric vibration to electricity conversion, rectification and energy storage.

The simulation in Matlab SIMULINK has been done using vibration data acquired from experimental study by previous researcher in order to determine the possible amount of power density output that can be produced for the specific acceleration input.

With the promising amount of power density output produced during simulation, the laboratory experiment on vibrating mechanical equipment were conducted for the purpose of quantifying the amount of power that can be generated by vibrating mechanical equipment and identifying electronic devices that can fully utilize this power.

III.1. Simulation Setup

A piezoelectric behavior can be modeled in terms of acceleration and voltage as given by (2):

$$V = k \times L^2 \times a \tag{2}$$

where k is a piezoelectric constant [21]. Sensing element modeled in Matlab SIMULINK as shown in Fig. 2 was used to evaluate the output voltage from the piezoelectric vibration-to-electricity converter based on (2).

The acceleration input used for the sensing element is adapted from the vibrational data acquired experimentally by previous researcher and the ideal gain of transfer function for piezoelectric element is taken as one. It is worth to note that piezoelectric material

produces alternate voltage and current when it is mechanically deformed.

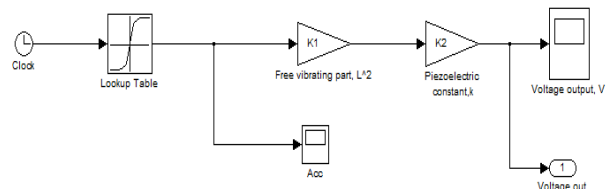


Fig. 2. Sensing element of piezoelectric accelerometer developed using Matlab SIMULINK

This alternate voltage and current are not so much useful because most of the electronic devices nowadays operate on direct current.

Therefore, harnessing circuit is utilized to rectify this alternate voltage and current as well as to optimize the energy harnessed from vibration environment. In this paper, non-adaptive circuit presented by Mingjie and Wei-Hsin (2005) is used as the harnessing circuit because it has been proved that more power can be harnessed as compared with adaptive circuit proposed by Ottman *et al.* (2002) [22], [23]. The non-adaptive circuit is illustrated in Fig. 3 which includes a conventional diode bridge rectifier and a passive circuit. Diodes are used in this circuit and it is assumed that there is no voltage drop across it. Capacitance value, C for the filtering capacitor is calculated by using (3) where i is the load current across the capacitor, V_p is the bridge rectifier output peak voltage and f is the frequency of the AC supply where in this experiment, the value of frequency was taken at 10 Hz:

$$C = \frac{5i}{V_p f} \tag{3}$$

The value of load resistance, R is determined by using the basic electric law which is Ohm's Law as given by (4), where V is the voltage across it and I is the current.

The non-adaptive harnessing circuit that was simulated in Matlab SIMULINK environment is shown in Fig. 4. Data for voltage input was taken from piezoelectric sensing element simulated in the Matlab SIMULINK environment earlier:

$$V = IR \tag{4}$$

III.2. Integration of Instrumentation System

The integration of instrumentation used in this research is as shown in Fig. 5. The piezoelectric sensor (P-876.A12 DuraAct) was considered to sense physical signals and translate it into electric signals [24].

This transducer acts as a vibration-to-electricity convertor. Electrical signals are later conditioned in such a way that they can be used by an analog input board [25]. In this research, the required signal conditioning circuits have been incorporated into the National Instrumentation (NI) Compact-Data Acquisition unit

equipped with NI-9234 module which also includes an analog-to-digital converter (A/D). Intel Core TM Duo Processor with LabVIEW environment is used to process, analyze, store, and display the acquired data.

The test equipment that have been used in this research are as listed in Table III.

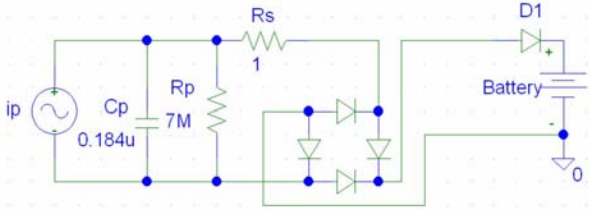


Fig. 3. Non-adaptive harnessing circuit (Mingjie and Wei-Hsin, 2005)

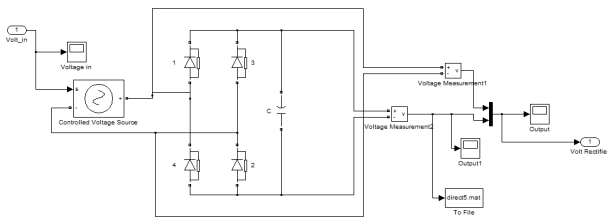


Fig. 4. Matlab SIMULINK diagram for the non-adaptive harnessing circuit

III.3. Experimental Setup

The experiment was conducted on two vibrating mechanical equipment which are turbine and centrifugal pump as shown in Figs. 6 and 7. The experimental setup is shown in Fig. 8. The piezoelectric sensor P-876.A12 DuraAct was attached to the vibrating mechanical equipment i.e., turbine and centrifugal pump. When the equipment vibrate, piezoelectric sensor produced alternate current and alternate voltage.

TABLE III
EXPERIMENTAL INSTRUMENTATION

| Instrument | Specification |
|---------------------------------|--|
| Piezoelectric P-876.A12 DuraAct | <ul style="list-style-type: none"> 61 mm x 35 mm x 0.5 mm weight 0.0072kg -100 V to +400 V (with amplifier) -100 V to ±3 V (without amplifier) |
| NI cDAQ-9172 data acquisition | <ul style="list-style-type: none"> 8-slot NI Compact DAQ chassis 11 to 30 VDC an AC/DC power converter 32-bit counter/timer chips |
| NI-9234 (24-bit resolution) | <ul style="list-style-type: none"> digital I/O module is installed in slot 5 or 6 delivers 102 dB of dynamic range 4-Channel, ±5 V, 51.2 kS/s per Channel, 24-Bit IEPE 51.2 kS/s per-channel maximum sampling rate; ±5 V input 24-bit resolution; 102 dB dynamic range; ant aliasing filters Software-selectable AC/DC coupling; AC-coupled (0.5 Hz) Software-selectable IEPE signals conditioning (0 or 2 mA) Smart TEDS sensor compatibility |
| Processor | Intel Core TM Duo with LabVIEW software |
| Storage | Capacitor |

The non-adaptive circuit connected directly to the piezoelectric sensor then rectified the signal into direct current and direct voltage.

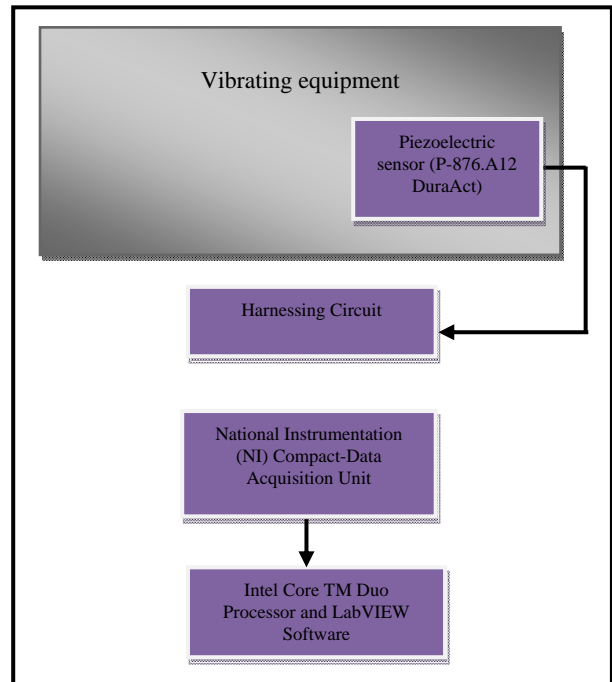


Fig. 5. Experimental setup layout



Fig. 6. Turbine



Fig. 7. Centrifugal pump

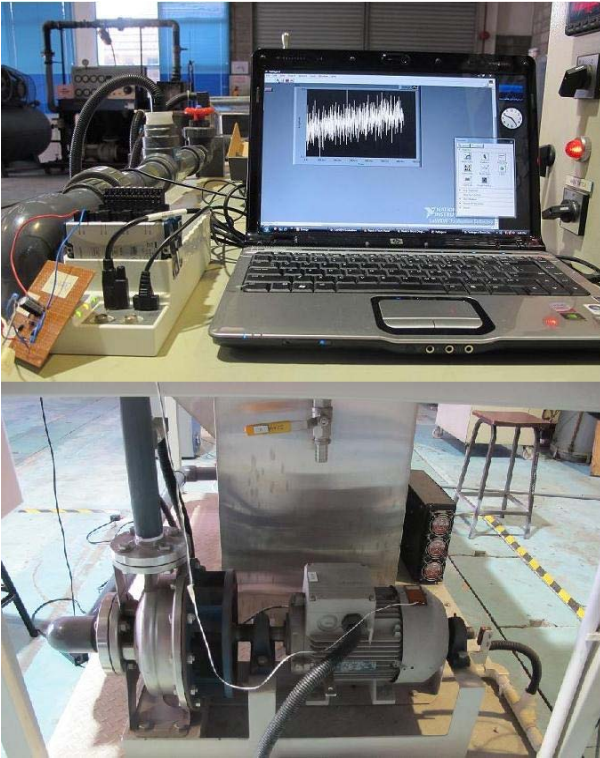


Fig. 8. Experimental setup

The direct current and direct voltage signal were acquired through a NI compact-data acquisition unit equipped with NI-9234 module and the acquired signal was analyzed, stored and displayed using Intel Core TM Duo Processor with LabVIEW software.

IV. Results and Discussion

The actual experiments were conducted on two vibrating mechanical equipments which are turbine and centrifugal pump.

The results of the experiments conducted which includes direct voltage and direct current generated from centrifugal pump and turbine as well as the amount of voltage accumulated and stored in the capacitor are presented as follow.

IV.1. Turbine

The experiment was conducted on the turbine at two different speeds of 1150 rpm and 1450 rpm. The sampling time was set at 40 seconds.

Figs. 9 and 10 show the results of direct voltage and direct current obtained for the turbine at speed of 1150 rpm while Figs. 11 and 12 show the results of direct voltage and direct current obtained for the turbine at speed of 1450 rpm. From these Figs. 9 – 12, it shows that as the acceleration magnitude of the turbine increases from 1150 rpm to 1450 rpm, the direct voltage and direct current produce are also increasing.

As shown in Fig. 13, for the turbine at speed of 1450 rpm, the amount of voltage accumulated and stored in the

capacitor is around 0.173 V for time duration of 30 minutes. This result shows that within 30 minutes, 1.84 μW of energy could be harnessed from the turbine at speed of 1450 rpm.

IV.2. Centrifugal Pump

The experiment was conducted on the centrifugal pump at two different speeds of 1700 rpm and 1900 rpm.

The sampling time was set at 40 seconds. Figs. 14 and 15 show the results of direct voltage and direct current obtained for the centrifugal pump at speed of 1700 rpm while Figs. 16 and 17 show the results of direct voltage and direct current obtained for the centrifugal pump at speed of 1900 rpm.

From the Figs., it shows that as the acceleration magnitude of the centrifugal pump increases from 1700 rpm to 1900 rpm, the direct voltage and direct current produced are also increased. For the centrifugal pump at speed of 1900 rpm, the amount of voltage accumulated and stored in the capacitor is around 0.23 V for sampling time of 30 minutes as shown in Fig. 18.

This result indicates that within 30 minutes, 3.06 μW of energy could be harnessed from the centrifugal pump at speed of 1900 rpm.

Table IV summarizes the actual experimental results conducted on the two vibrating mechanical equipment which are the turbine and the centrifugal pump. It can be seen that, as the speed of equipment increase which directly reflects to the acceleration magnitude of vibrating mechanical equipment, the direct voltage and direct current produced are also increased. For the turbine, as the speed increases from 1150 rpm to 1450 rpm, the average voltage increases from 0.17 V to 0.19 V while the average current increases from 9.56 μA to 10.65 μA . The average power produced is also increasing from 1.63 μW to 2.02 μW . For the centrifugal pump, as the speed increases from 1700 rpm to 1900 rpm, the average voltage remains at 0.23 V while the average current increases from 13.12 μA to 13.32 μA . The average power produced is also increased from 3.02 μW to 3.06 μW .

From these results, it shows that a higher average power could be produced if the experiment is conducted on vibrating mechanical equipment with larger acceleration magnitude.

For example, the sources of vibration that can produce a higher vibration are vehicles on the road as well as mechanical vibration from motors, compressors and pumps with larger capacity.

As for the accumulation of energy, the result shows that within 30 minutes, 1.84 μW of energy could be harnessed from the turbine at speed of 1450 rpm while 3.06 μW of energy could be harnessed from the centrifugal pump at speed of 1900 rpm.

From the previous literature, the power output ranging from 1.84 μW to 3.06 μW are sufficient for low-powered wireless sensor networks although it is smaller compared to the power produced by Roundy *et al.* (2003).

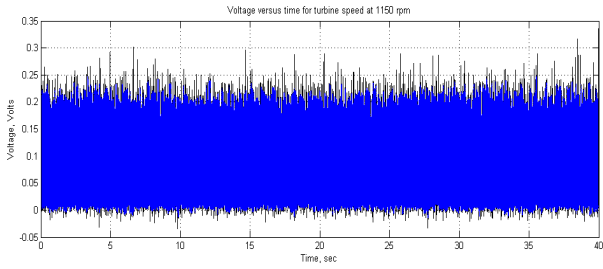


Fig. 9. Voltage versus time for the turbine at speed of 1150 rpm

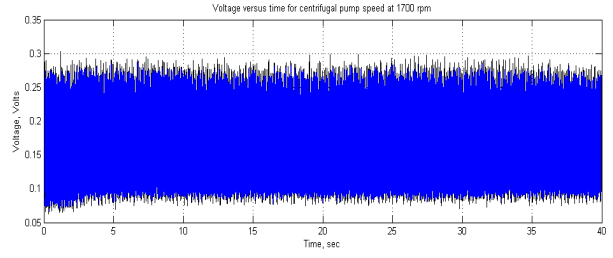


Fig. 14. Voltage versus time for the centrifugal pump at speed of 1700 rpm

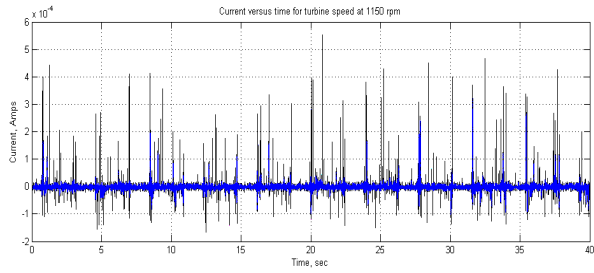


Fig. 10. Current versus time for the turbine at speed of 1150 rpm

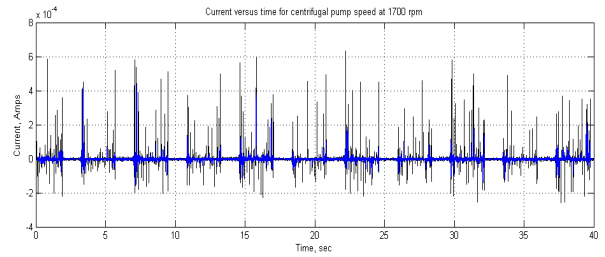


Fig. 15. Current versus time for the centrifugal pump at speed of 1700 rpm

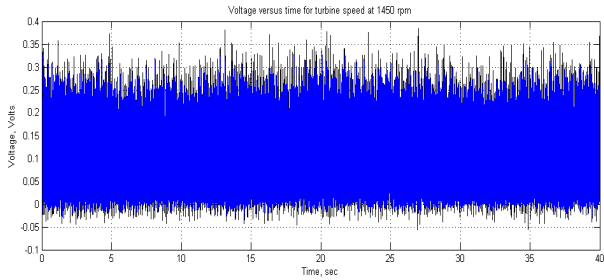


Fig. 11. Voltage versus time for the turbine at speed of 1450 rpm

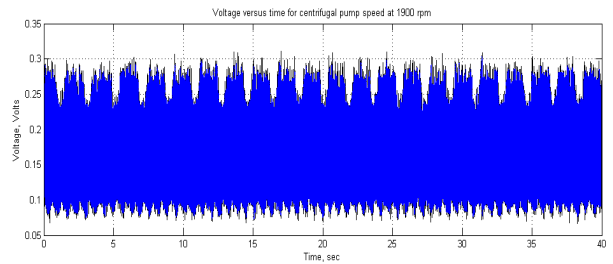


Fig. 16. Voltage versus time for the centrifugal pump at speed of 1900 rpm

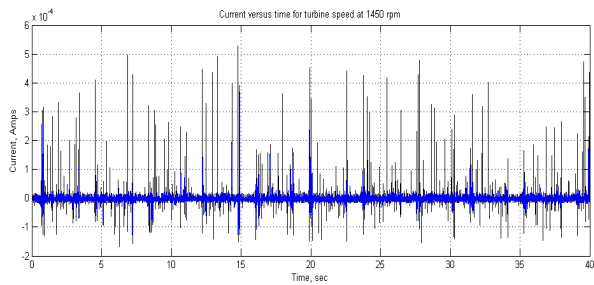


Fig. 12. Current versus time for the turbine at speed of 1450 rpm

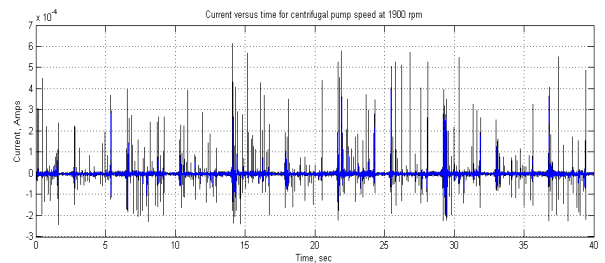


Fig. 17. Current versus time for the centrifugal pump at speed of 1900 rpm

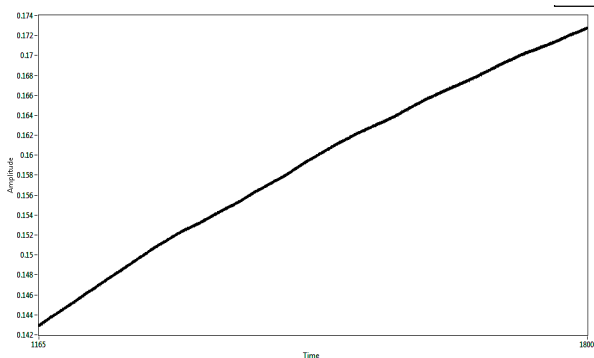


Fig. 13. Voltage accumulated and stored in the capacitor for the turbine at speed of 1450 rpm

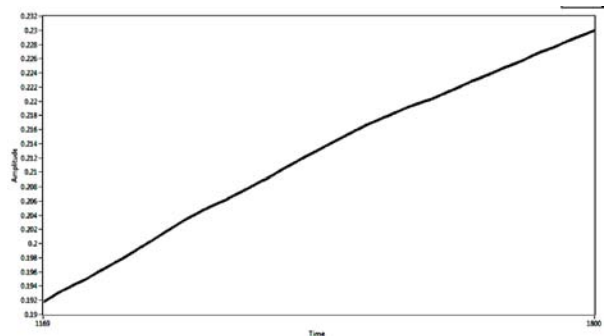


Fig. 18. Voltage accumulated and stored in the capacitor for the centrifugal pump speed at 1900 rpm

TABLE IV
SUMMARY OF ACTUAL EXPERIMENT RESULTS

| Equipment | Speed (rpm) | Average Voltage (V) | Average Current (μ A) | Average Power (μ Watt) |
|------------------|-------------|---------------------|----------------------------|-----------------------------|
| Turbine | 1150 | 0.17 | 9.56 | 1.63 |
| Turbine | 1450 | 0.19 | 10.65 | 2.02 |
| Centrifugal Pump | 1700 | 0.23 | 13.12 | 3.02 |
| Centrifugal Pump | 1900 | 0.23 | 13.32 | 3.06 |

V. Conclusion

Based on the experimental results obtained, it can be concluded that as the speed of equipment increase which directly reflects to the acceleration magnitude of vibrating mechanical equipment, the direct voltage and direct current produce are also increased which means more power could also be produced. The objective of this research to design, simulate and develop an instrumentation system to harness energy from mechanical vibration using smart materials has been achieved where piezoelectric vibration-to-electricity converter is used throughout this project in both simulation and experimental setup. As stated in the problem statement, the amount of power that can be generated has been successfully quantified in which it is sufficient to be used for low-powered wireless sensor networks.

Acknowledgements

The authors wish to thank the Ministry of Higher Education (MOHE) and Universiti Teknologi Malaysia (UTM) for providing the research grant and facilities. This research is supported using UTM Research University grant, Vote No. 04H17.

References

- [1] Gonzalez, J. L., Rubio, A. and Moll, F. (2002). Human Powered Piezoelectric Batteries to Supply Power to Wearable Electronic Devices. *International Journal of the Society of Materials Engineering for Resources*, 10(1), 34-40.
- [2] Shenck, N. S. and Paradiso, J. A. (2001). Energy Scavenging with Shoe-Mounted Piezoelectrics. *Micro, IEEE* 21(3), 30-42.
- [3] Starner, T. (1996). Human Powered Wearable Computing. *IBM Systems Journal* 35(3.4), 618-629.
- [4] Stordeur, M. and Stark, I. (1997). Low Power Thermoelectric Generator - Self-Sufficient Energy Supply for Micro Systems. *Proceedings of the 1997 16th International Conference on Thermoelectrics Dresden*, Germany 575-577.
- [5] Chiu, Y. and Tseng, V. F. G. (2008). A Capacitive Vibration-to-Electricity Energy Converter with Integrated Mechanical Switches. *Journal of Micromechanics and Microengineering*, 18(10), 1-8.
- [6] Glynne-Jones, P., Tudor, M. J., Beeby, S. P. and White, N. M. (2004). An Electromagnetic, Vibration-Powered Generator for Intelligent Sensor Systems. *Sensors and Actuators A: Physical*, 110(1-3), 344-349
- [7] Lefeuvre, E., Badel, A., Richard, C., Petit, L. and Guyomar, D. (2006). A Comparison between Several Vibration-Powered Piezoelectric Generators for Standalone Systems. *Sensors and Actuators A: Physical*, 126(2), 405-416. Roundy and Wright, 2004;
- [8] Roundy, S., Wright, P. and Pister, K. (2002). Micro-Electrostatic Vibration-to-Electricity Converters. *Proceedings of the 2002 IMECE New Orleans, Louisiana*, 1-10.
- [9] Roundy, S., Wright, P. and Rabaey, J. M. (2003). A Study of Low Level Vibrations as a Power Source for Wireless Sensor Nodes. *Computer Communications*, 26(11), 1131-1144.
- [10] Williams, C. B., Shearwood, C., Harradine, M. A., Mellor, P. H., Birch, T. S. and Yates, R. B. (2001). Development of an Electromagnetic Micro-Generator. *Proceedings of the 2001 IEE - Circuits, Devices and Systems*, 337-342.
- [11] Williams, C. B. and Yates, R. B. (1996). Analysis of a Micro-Electric Generator for Microsystems. *Sensors and Actuators A: Physical*, 52(1-3), 8-11.
- [12] Yen, B. C. and Lang, J. H. (2006). A Variable-Capacitance Vibration-to-Electric Energy Harvester. *IEEE Transactions on Circuits and Systems I: Regular Papers*, 53(2), 288-295.
- [13] Rabaey, J. M., Ammer, J., Karalar, T., Li, S., Otis, B., Sheets, M., et al. (2002). PicoRadios for Wireless Sensor Networks: The Next Challenge in Ultra-Low Power Design. *Proceeding of the 2002 IEEE International Solid-State Circuits Conference*.
- [14] Ottman, G. K., Hofmann, H. F. and Lesieutre, G. A. (2003). Optimized Piezoelectric Energy Harvesting Circuit using Step-Down Converter in Discontinuous Conduction Mode. *IEEE Transactions on Power Electronics*, 18(2), 696-703.
- [15] Sodano, H. A., Park, G. and Inman, D. J. (2004). Estimation of Electric Charge Output for Piezoelectric Energy Harvesting. *Strain*, 40(2), 49-58.
- [16] Sodano, H. A., Inman, D. J. and Park, G. (2005). Comparison of Piezoelectric Energy Harvesting Devices for Recharging Batteries. *Journal of Intelligent Material Systems and Structures*, 16(10), 799-807
- [17] Ward, J. K. and Behrens, S. (2008). Adaptive Learning Algorithms for Vibration Energy Harvesting. *Smart Materials and Structures*, 17(3), 1-9.
- [18] Adhikari, S., Friswell, M. I. and Inman, D. J. (2009). Piezoelectric Energy Harvesting from Broadband Random Vibrations. *Smart Materials and Structures*, 18(11), 1-7.
- [19] Sodano, H. A., Magliula, E. A., Park, G. and Inman, D. J. (2002). Electric Power Generation using Piezoelectric Materials. *Proceedings of the 2002 13th International Conference on Adaptive Structures and Technologies Potsdam/Berlin, Germany*, 153-161
- [20] Mohd Yatim, H. (2011). Harnessing Energy from Micro-Vibration. Degree Thesis, Universiti Teknologi Malaysia, Skudai.
- [21] Mingjie, G. and Wei-Hsin, L. (2005). Comparative Analysis of Piezoelectric Power Harvesting Circuits for Rechargeable Batteries. *Proceedings of the 2005 IEEE International Conference on Information Acquisition*. 27 June-3 July 2005. Hong Kong and Macau, China, 243-246.
- [22] Ottman, G. K., Hofmann, H. F., Bhatt, A. C. and Lesieutre, G. A. (2002). Adaptive Piezoelectric Energy Harvesting Circuit for Wireless Remote Power Supply. *IEEE Transactions on Power Electronics*
- [23] Darus, I.Z.M., Zahidi Rahman, T.A., Mailah, M., Experimental evaluation of active force vibration control of a flexible structure using smart material, (2011) *International Review of Mechanical Engineering (IREME)*, 5 (6), pp. 1088-1094.
- [24] Saad, M.S., Jamaluddin, H., Darus, I.Z.M., Iterative algorithm for active vibration control of flexible beam, (2012) *International Review of Mechanical Engineering (IREME)*, 6 (1), pp. 61-73.
- [25] Bronstein, S., Abramovitz, A., An approach to simulation of Piezoelectric Transformers, (2011) *International Review on Modelling and Simulations (IREMOS)*, 4 (3), pp. 1190-1193.

Authors' information

^{1,2}Department of Applied Mechanics and Design,
Faculty of Mechanical Engineering,
Universiti Teknologi Malaysia.



Intan Z. M. Darus was born in Melaka, Malaysia, in September 16th, 1976. She received her First Class B.Eng (Hons.) degree in Mechanical Engineering from the University of Wales College Cardiff, Wales, United Kingdom in 1998 and later her Ph.D in Automatic Control and Systems Engineering from the University of Sheffield, United Kingdom in 2004. Currently, she is an Associate Professor in the Department of Applied Mechanics and Design, Faculty of Mechanical Engineering, Universiti Teknologi Malaysia. Her current research interests are active vibration control, modeling and simulation of dynamical system, soft computing and artificial intelligent techniques for system identification and control.



Ameirul A. Mustadza was born in Melaka, Malaysia, in March 21st, 1986. He received his B.E. (Hons) Mechanical from Universiti Teknologi PETRONAS (UTP), Tronoh, Perak, Malaysia in 2009 and later his Master of Engineering (Mechanical) from Universiti Teknologi Malaysia (UTM), Skudai, Johor, Malaysia in 2012. Currently, he works at SapuraKencana Petroleum Berhad as a Senior Executive at Senior Vice President Office, Offshore Construction and Subsea Services Division. He is registered as a graduate engineer with Board of Engineers Malaysia (BEM), a graduate member with The Institution of Engineers Malaysia (IEM) and a member of Society of Petroleum Engineers (SPE). He also serves Young Engineers Section (YES) of The Institution of Engineers Malaysia (IEM) as the Vice Chairman II for Session 2012/2013. His current research interests include vibration-to-electric energy harnessing using piezoelectric materials.



Hanim Mohd Yatim was born in Johor, Malaysia, in September 27th, 1988. She graduated from Universiti Teknologi Malaysia (UTM), Malaysia in First Class B.Eng Degree of Mechanical Engineering in the year 2011. Her field of research interests are in active vibration control, modeling and simulation of dynamical system and artificial intelligent techniques for system identification and control. Currently, she extending her knowledge by undergoing Ph.D studies in Automatic Control and Systems Engineering from the Universiti Teknologi Malaysia (UTM), Malaysia.

A Full Scale Test Rig to Characterize Pneumatic Tyre Mechanical Behaviour

Flavio Farroni, Ernesto Rocca, Francesco Timpone

Abstract – In this paper an experimental test rig aimed to characterize mechanical properties of a pneumatic tyre, together with some results, is presented. The objective is to determine tyre mechanical characteristics useful to physically model its behaviour; in particular: the normal interaction characteristic, the radial stiffness, the total stiffness and the longitudinal hysteretic cycles. To this aim two different kind of tests have been executed: radial and longitudinal. In the radial test the load is statically applied to the tyre, along the vertical direction, by means of an hydraulic press and it is measured together with the consequent radial deformation, so allowing the estimation of the tyre normal interaction characteristic and of its radial stiffness. Different radial tests can be conducted for an assigned tyre varying the inflation pressure. The longitudinal tests are conducted applying, under an assigned constant vertical load, a variable horizontal strain to the tyre by means of a linear actuator, two profile rail guides and a system to transfer the horizontal motion to the contact patch of the tyre, opportunely placed on a moving steel plate placed on the two linear guide rails. During the tests the horizontal load and the resulting deformations are measured and acquired so allowing the estimation of tyre total stiffness and of its longitudinal hysteretic cycles. Longitudinal tests can be conducted varying the assigned vertical load, the horizontal displacement law in terms of frequency and amplitude, the tyre inflation pressure. All the different types of rim can be mounted on the test rig thanks to a universal quick flange. **Copyright** © 2013 Praise Worthy Prize S.r.l. - All rights reserved.

Keywords: Tyre, Stiffness, Hysteresis, Experimental Test Rig

Nomenclature

| | |
|----------|---|
| σ | Damping coefficient [Ns/m] |
| ω | Frequency [Hz] |
| X | Tyre deformation [m] |
| ρ | First Dahl's model cycle parameter [1/m] |
| k_w | Second Dahl's model cycle parameter [N] |
| a | First damping parameter [[Ns ^b /m] |
| b | First damping parameter [-] |

I. Introduction

As concerns vehicle dynamics, and particularly control systems [1], [2], [3], [4], [5], tyre-road interaction modeling is of fundamental importance.

At present, models of empirical or semi-empirical nature [6], [7], [8], [9] are widely available in literature to simulate the vehicle dynamic behaviour, while physical models [10], [11] of tyre-road interaction, useful in the design phase as they are predictive of the tyre behaviour, are not very diffused, due both to the physical complexity and to the difficulty in the estimation of static and dynamic tyre characteristics.

To make operative physical models both stiffness parameters, along proper directions, and damping and hysteresis phenomena need to be estimated and taken into account.

The hysteresis phenomena could be analytically modelled according to some specific theories [12], [13], [14], [15] although such models require knowledge of some parameters rather difficult to estimate, to be instead experimentally identified. This work falls just in this context concerning the experimental characterization of automotive tyres with the aim to determine the parameters to adopt in physical analytical models of tyre-road interaction.

The present research activity first idea was to design and to build a test rig to carry on experimental tests useful to measure and to estimate some of the mechanical properties of an automotive pneumatic tyre necessary in a physical analytical modeling of its behaviour.

Currently, the rig allows quasi-static tests along radial direction to determine the radial load-strain curve and so the radial stiffness diagram, as well as static and dynamic tests along the longitudinal direction, through which it is possible to obtain the longitudinal load-strain curve, the relative stiffness (total stiffness, involving both a radial component and a torsional one) and the longitudinal hysteresis cycles (present during braking/accelerating maneuvers). The tyre during its working is subject to cyclic deformations generating hysteresis. Its deforming cycle develops in a revolution and it is composed of two phases which are almost equal in duration: a first phase characterized by an increase in the strain (loading phase)

starting from zero, and a second phase related to a decrease in the deformation (unloading phase), ending with zero; the period T is equal to the sum of the two time intervals referring to the loading and unloading phases. The energy loss due to this phenomenon influences the tyre temperature and consequently the friction coefficient [16], [17].

In the following the test rig is described, highlighting its main operative properties, as well as all the measurement equipment and the experimental methodology adopted in the tests. Finally some results are reported and analyzed.

II. Test Rig Description

The tyre test rig is essentially composed by:

- A system for applying the vertical load to the tyre consisting of:
 - A manually actuated hydraulic press (Fig. 1 (1));
 - A fixed frame integral with the press fixed structure (Fig. 1 (2));
 - A vertically mobile frame (Fig. 1 (3)) in contact with a press actuator on which a universal quick flange (Fig. 1 (4)) to lock the wheel is mounted;
 - A system with manually variable weights (Fig. 1 (5)) to balance the weights of the mobile frame and the wheel so that the tyre has no initial vertical load;
 - Two linear guide rails (Fig. 1 (6)) placed along the vertical direction between the fixed and the mobile frame;
- A system to apply the horizontal load to the tyre, consisting of:
 - A linear actuator (Fig. 1 (7)) whose fixed part is integral with the press fixed frame;
 - A plate (Fig. 1 (8) and Fig. 3), on which the tyre is vertically loaded, which can be moved horizontally and is directly connected to the linear actuator;
 - A fixed plate (Fig. 1 (9) and Fig. 3) integral with the press fixed frame;
 - Two linear guide rails (Fig. 1 (10) and Fig. 3) placed along the longitudinal direction between the fixed and the mobile plate.

The test rig is also equipped with the following measurement instruments:

- A strain gauge load cell (Fig. 1 (11)) to measure the vertical load applied by the press;
- A draw-wire sensor (Fig. 1 (12)) to evaluate tyre deformation along the vertical direction;
- A quartz force sensor (Fig. 1 (13) and Fig. 3) to measure the horizontal load applied by the linear actuator;
- A position transducer with restoring spring (Fig. 1 (14) and Fig. 3) to evaluate tyre deformation along the horizontal direction.

The horizontal linear actuator (Fig. 1 (7)) converts the rotary motion, imposed by an electric motor coupled to a gearbox with a transmission ratio equal to 20, into the

alternative rectilinear motion of the mobile plate (Fig. 1 (8)). The actuator includes an innovative rotary crank mechanism in which the crank consists of a double eccentric as shown in Fig. 2.

The drive mechanism consists of three elements: a disc eccentrically fixed on the transmission shaft placed inside a second disc (collar) which is also eccentric, and finally a connecting rod, linked to the collar by a rolling bearing, which moves the plate by means of a bar.

The offline relative rotation of the two eccentric elements provides the change of the crank radius, thus allowing the drive system to achieve different values of the movable plate stroke and different values of tyre strain amplitude; this operation should be done before starting each test campaign.

The range of plate stroke can vary from 0 to 40 mm since each of the eccentric parts has an eccentricity of 10 mm.

The driving rod is fixed to the connecting rod on one side by flanges and bolts, the other side is articulated to the plate through a universal joint. The eccentric inner disc has been fixed on the transmission shaft through a self-centering friction device (sit-lock).

Alternative fixing systems of the universal quick flange on the vertically mobile frame, suitably inclined, allow to conduct tests with nonzero camber and/or toe angles.

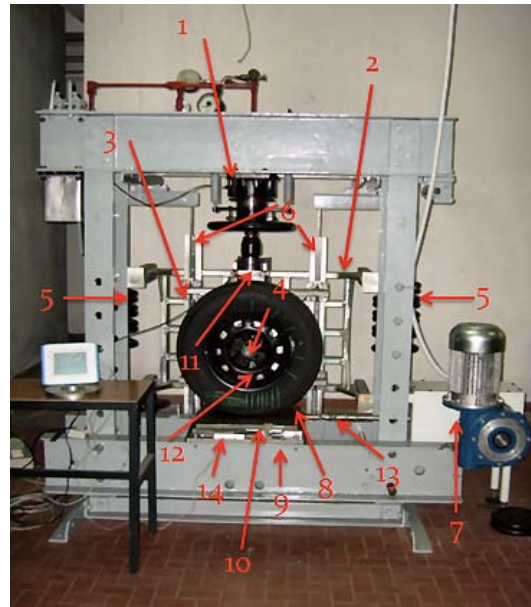


Fig. 1. The test rig



Fig. 2. Crank-rod drive mechanism

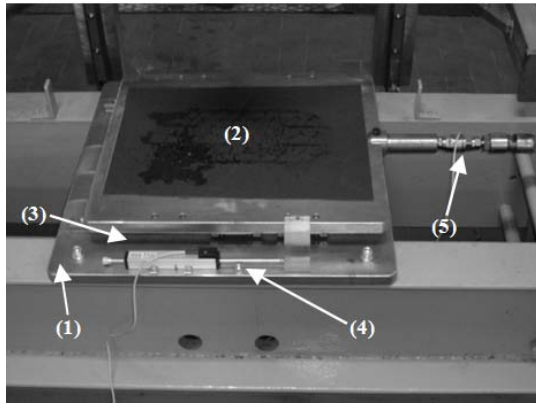


Fig. 3. Test rig detail – (1) Frame; (2) Mobile plate; (3) Linear guide rail; (4) Longitudinal position transducer; (5) Load Cell

III. Tests Procedures

Opportune tests carried on the described test rig allow to determine the following mechanical characteristics of an automotive pneumatic tyre: the normal interaction characteristic, the radial stiffness, the total stiffness, the longitudinal hysteretic cycles and the consequent strain energy loss [18].

In particular, to this aim, two different test procedures have been developed: radial and longitudinal tests. To execute these tests the tyre has been locked to the universal quick flange.

III.1. Radial Test

This kind of test consists in a quasi-static tyre radial compression; it is realized manually actuating the press while the horizontal movable plate is kept stopped, and it is conducted with different values of the inflation pressure. During this kind of test the vertical load and the corresponding strain are acquired, and consequently it is possible to determine the normal interaction characteristic and the radial stiffness.

III.2. Horizontal Test

To perform this kind of test, first of all, it is necessary to move the plate to one of the ends of its stroke. Then the tyre is positioned so that its midplane, orthogonal to its axis, contains the crank-rod mechanism axis. Subsequently a prescribed vertical load is applied, greater than the one necessary to avoid tyre sliding. After this the linear actuator is activated with fixed values of its motion amplitude and frequency.

So all the available stroke is used to strain the tyre along a unique direction (unilateral test), as occurs usually during its working in pure longitudinal interaction conditions. The linear actuator imposes the stroke and hence the tyre strain in the contact patch.

This kind of test can be conducted, for a fixed tyre, varying the inflation pressure, the vertical load, the stroke magnitude, the linear actuator motion frequency.

At the end of this test it is possible to determine the total stiffness and the longitudinal hysteretic cycles.

IV. Normal Interaction Characteristic and Radial Stiffness

The radial tests, as said, allow to determine the normal interaction characteristic and the radial stiffness of a tyre.

The first one is obtained measuring the vertical load applied to the tyre and its deformation along the same direction and representing the first as function of the second, while the radial stiffness is the discrete derivative of the normal interaction curve as a function of the vertical strain. This measure can be repeated varying the tyre radial direction unlocking the tyre, after having rotated it of a fixed angle, and locking it again to the universal quick flange (the radial stiffness should be the same along each radial direction considering the tyre axial symmetry). It is possible to see how the considered quantities vary with the inflation pressure.

In Fig. 4 different normal interaction characteristics, obtained varying the inflation pressure, together with the relative mean values of the radial stiffness, for a Firestone 195/65 R 15 91T Tubeless pneumatic tyre, are reported.

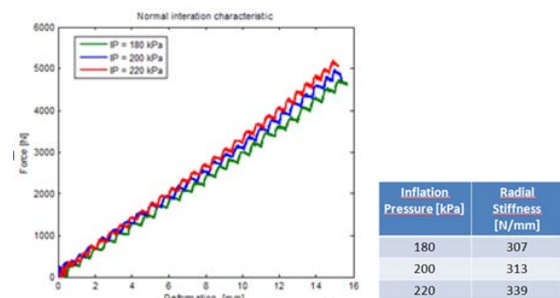


Fig. 4. Normal interaction characteristic and radial stiffness

As expected the tyre becomes more stiff in radial direction increasing the inflation pressure. Oscillations in the curves are due to the fact that vertical load is manually applied acting on the press; after each load increase, the tyre exhibits an elastic release, that causes the visible oscillations.

V. Hysteresis Cycles and Total Stiffness

The horizontal tests allow to determine the tyre total stiffness and its hysteretic cycles. The total stiffness is the one involved in the longitudinal test due to the vertical load and the horizontal tyre strain. It is called “total” because it includes both a radial and a torsional contribution. This parameter is adopted in multi degree of freedom tyre-carcass models [18], [19], [20].

To determine this quantity the horizontal test is performed at a very low frequency of the linear actuator motion. The tyre hysteresis cycles come out plotting the horizontal load as a function of the horizontal strain.

A test campaign has been conducted, on a predetermined tyre, varying the amplitude and the frequency of the linear actuator motion, the vertical load, the tyre inflation pressure and the toe angle.

In particular the values adopted for the above parameters are reported in Table I. All the possible combinations have been tested and for each of them at least 5 cycles have been acquired. The measured cycles showed irregularities due to backlash in the test rig, so, during the elaboration process the force-displacement diagrams have been “reconstructed” by means of a moving average based procedure in order to reduce these irregularities. In Fig. 5 a measured hysteric cycle is reported together with the correspondent reconstructed one. Figs. 6(a), 6(b) and 7 show some results about the influence of actuator stroke, motion frequency and vertical load on hysteric cycles shape and position. In all showed hysteresis cycles diagrams tyre inflation pressure is equal to 200 kPa and toe angle is equal to 0°.

As expected increasing the linear actuator stroke the energy loss (hysteresis cycles area) rapidly increases (Fig. 6(a)), while linear actuator motion frequency seems not influent on position and extension of cycles (Fig. 6(b)). As concerns the vertical load (Fig. 7) and the angle (Fig. 8) they seem directly influent mainly on total stiffness (increasing the two parameters, increases this stiffness).

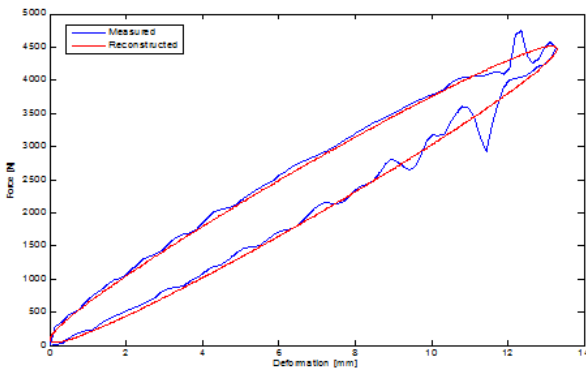


Fig. 5. Measured and reconstructed hysteric cycles

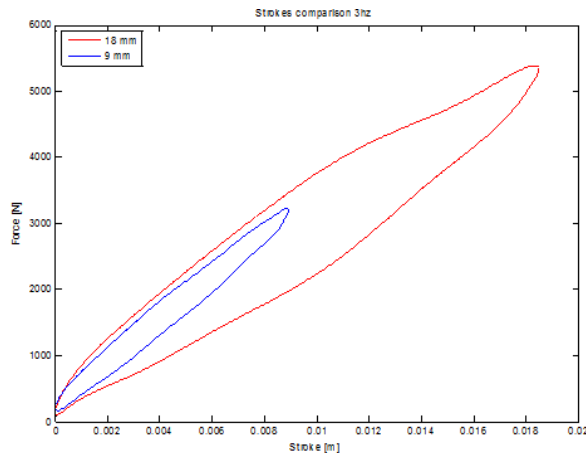


Fig. 6(a). Hysteresis cycles: Linear actuator stroke influence
Vertical load: 5500 N, Motion frequency: 3 Hz

| Amplitude of the linear actuator motion [mm] | 9, 18 |
|--|------------|
| Frequency of the linear actuator motion [Hz] | 1, 3, 5 |
| Vertical load [N] | 5500, 6000 |
| Tyre inflating pressure [kPa] | 160, 200 |
| Toe angle [°] | 0, 5 |

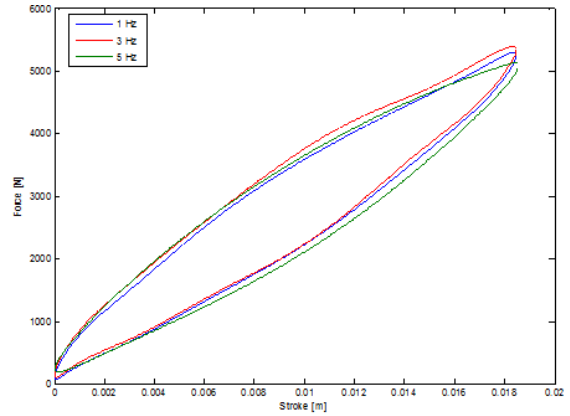


Fig. 6(b). Hysteresis cycles: Motion frequency influence
Vertical load: 5500 N, Actuator stroke: 18 mm

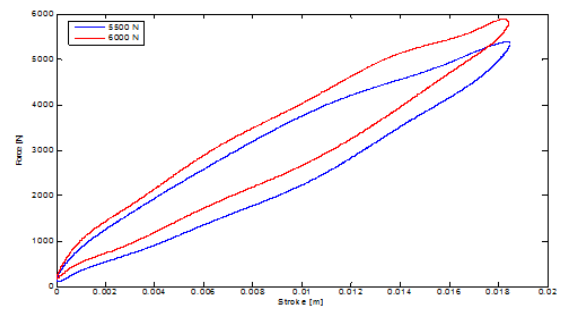


Fig. 7. Hysteresis cycles: Vertical load influence
Motion frequency: 1 Hz; Actuator stroke: 18 mm

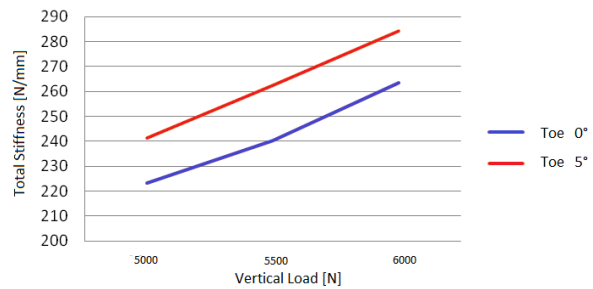


Fig. 8. Toe angle influence on total stiffness
Motion frequency: 1 Hz; Actuator stroke: 18 mm

VI. Pneumatic Tyre Energy Loss

The longitudinal tests have been also used to identify the parameters of an explicit expression of total dissipated energy for a pneumatic tyre for each cycle, based on the Dahl model [21]:

$$E = 4k_w \left(X - \frac{\tanh(\rho X)}{\rho} \right) + \pi \cdot \sigma(\omega) \cdot \omega \cdot X^2 \quad (1)$$

where X is the strain amplitude and k_w , ρ are the parameters to be identified.

Assuming a power law dependency between the viscous dissipated energy and frequency ω [22], the expression of damping is obtained:

$$\sigma(\omega) = \frac{a\omega^{b-1}}{\pi} \quad (2)$$

where a and b are two parameters to be identified.

Other longitudinal tests have been carried out with several vertical loads using various amplitudes and frequencies for deformation laws. For the identification have been used the tests relative to the vertical load of 4000 N and a deformation of 1.5 cm that supplied the values of energy reported in Table II

TABLE II
VALUES OF ENERGY OF TESTS RELATIVE TO THE VERTICAL LOAD OF 4000 N AND A DEFORMATION OF 1.5 CM

| Frequency [Hz] | Energy loss [J] |
|----------------|-----------------|
| .05 | 6.9 |
| .5 | 7.3 |
| 1 | 7.7 |
| 2 | 8.5 |
| 3 | 8.7 |
| 4 | 9.1 |
| 5 | 9.2 |

By applying an identification procedure, the following parameters of the damping expression were determined (Table III):

TABLE III
PARAMETERS OF THE DAMPING EXPRESSION APPLYING AN IDENTIFICATION PROCEDURE

| $\sigma(\omega) = \frac{a\omega^{b-1}}{\pi}$ | |
|---|--------|
| $a = \left[\frac{\text{N} \cdot \text{s}^b}{\text{m}} \right]$ | b |
| 25970 | 0.5234 |

From Eq. (1), the explicit expression of total dissipated energy parameters can be obtained, and the results are reported in Table IV

TABLE IV
RESULTS OF THE EXPLICIT EXPRESSION TOTAL DISSIPATED ENERGY PARAMETERS

| Vertical load [N] | k_w [N] | ρ [1/m] |
|-------------------|-----------|--------------|
| 4000 | 500 | 400 |

The model with the identified parameters therefore allows to calculate the energy loss by means of Eq. (1) for the tyre in question. Fig. 9 shows the comparison between calculated energy loss with 4000 N of vertical load and the measured values assigning harmonic strain law with 5 Hz frequency.

The procedure has been repeated for other values of the vertical load, always showing the same good level of agreement as the one noticeable in Fig. 9.

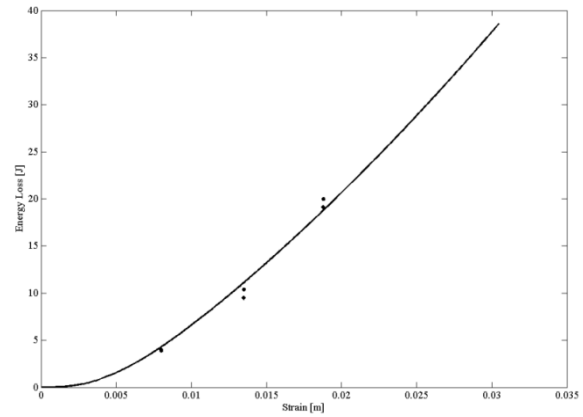


Fig. 9. Energy – strain diagram: (■) measured value; (line) calculated.

VII. Conclusion

In this paper an experimental test rig useful to characterize a pneumatic tyre, together with the some experimental results, has been presented.

It has been used adopting two different test procedures: radial and longitudinal tests.

By means of the measures on the test rig some tyre mechanical characteristics as the normal interaction characteristic, the radial stiffness, the total stiffness and the longitudinal hysteretic cycles have been determined, together with some considerations about their sensitivity to some test parameters.

The longitudinal test results have also been used to identify the parameters of an explicit expression of total dissipated energy for a pneumatic tyre.

The results are useful to be used in physical tyre road interaction models, in thermal tyre models and in physical hysteresis models.

References

- [1] F. Farroni, M. Russo, R. Russo, M. Terzo, F. Timpone – “A combined use of phase plane and handling diagram method to study the influence of tyre and vehicle characteristics on stability” - *Vehicle System Dynamics*, DOI: 10.1080/00423114.2013.797590, 2013.
- [2] Terzo, M., Timpone, F., The control of the handling of a front wheel drive vehicle by means of a magnetorheological differential, (2013) *International Review of Mechanical Engineering (IREME)*, 7 (3), pp. 395-401.
- [3] R. Russo, M. Terzo, F. Timpone - "Software in the loop development and validation of a cornering brake control logic" - *Vehicle System Dynamics*, 45 (2) , pp. 149-163, 2007.
- [4] R. Russo, M. Terzo, F. Timpone – “Software-in-the-loop development and experimental testing of a semi-active magnetorheological coupling for 4WD on demand vehicles” - 11th VSDIA, Mini Conference on Vehicle System Dynamics, Identification and Anomalies, 2008.
- [5] Carro, M., Russo, M., Timpone, F. - "A Modern Approach to Design Optimization and Development of Vehicle Control Systems" - 8th VSDIA, Mini Conference on Vehicle System Dynamics, Identification and Anomalies, 2002.
- [6] Pacejka, H. B. *Tire and Vehicle Dynamics*, Butterworth-Heinemann, Oxford, 2006.
- [7] H.B. Pacejka, E. Bakker, and L. Nyborg, *Tyre modeling for use in vehicle dynamics studies*, SAE 870421, 1987.

- [8] Canudas de Wit, C., H. Olson, K. J. Astrom, and P. Lischinsky, "A New Model for Control of Systems with Friction," *IEEE TAG*, Vol. 40, No. 3, pp. 419-425, 1995.
- [9] E. Velenis, P. Tsiotras, C. Canudas de Wit and M. Sorine, Dynamic tyre friction models for combined longitudinal and lateral vehicle motion, *Vehicle System Dynamics*, Vol. 43, No. 1, January 2005, 3 – 29.
- [10] G. Capone, D. Giordano, M. Russo, M. Terzo and F. Timpone, Ph.An.Ty.M.H.A.: a physical analytical tyre model for handling analysis – the normal interaction, *Vehicle System Dynamics* Vol. 47, No. 1, January 2009, 15–27.
- [11] R. Hedekel, The mechanical characteristics of pneumatic tyres, S&T Memo 10/52, *British Ministry of Supply*, TPA 3/TIB, 1952.
- [12] Dahl P.A., A solid friction model, technical report TOR-0158H3107, *The Aerospace Corporation, el Segundo*, CA, 1968.
- [13] Y.K. Wen, Method for Random Vibration of Hysteretic Systems, *Journal of the Engineering Mechanics Division*, Vol. 102, No. 2, pp. 249-263, 1976.
- [14] Ikhouane F and Rodellar J, On the hysteretic Bouc–Wen model. Part I: forced limit cycle characterization *Nonlinear Dynamics*, 42, 63–78, 2005.
- [15] Brancati, R., Strano, S., Timpone, F., "An analytical model of dissipated viscous and hysteretic energy due to interaction forces in a pneumatic tire: Theory and experiments" - *Mechanical Systems and Signal Processing*, 25 (7), 2785–2795, 2011, doi: 10.1016/j.ymssp.2011.04.007.
- [16] Allouis, C., Amoresano, A., Giordano, D., Russo, M., Timpone, F., Measurement of the thermal diffusivity of a tire compound by mean of infrared optical technique, (2012) *International Review of Mechanical Engineering (IREME)*, 6 (6), pp. 1104-1108.
- [17] Farroni, F., Russo, M., Russo, R., Timpone, F. - "Tyre - Road Interaction: Experimental Investigations about the Friction Coefficient Dependence on Contact Pressure, Road Roughness, Slide Velocity and Temperature" - Proceedings of the ASME 2012 11th Biennial Conference On Engineering Systems Design And Analysis, 2012.
- [18] *The Pneumatic Tire*, J. D. Walter and A. N. Gent, editors, National Highway Traffic Safety Administration, Washington, D.C..
- [19] P. W. Anton Zegelaar, *The Dynamic Response of Tyres to Brake Torque Variations and Road Unevennesses*, 1998, Delft University of Technology.
- [20] J.P. Pauwelussena, L. Gootjesb, C. Schröderb, K.-U. Kohnb, S. Jansenc, A. Schmeitzd, Full vehicle ABS braking using the SWIFT rigid ring tyre model, *Control Engineering Practice*, Volume 11, Issue 2, February 2003, Pages 199-207.
- [21] Dupont P. et al. Single state elastoplastic friction models, *IEEE Transactions on Automatic Control*, 47, 12, pp. 787-792, 2002
- [22] Pritz P., Frequency power law of material damping, *Applied Acoustics* 65, pp. 1027–1036, 2004.



Ernesto Rocca received a "laurea" degree in Mechanical Engineering in 1991 and a PhD in Thermo-Mechanical Systems Engineering in 1995, both from the "Federico II" University of Naples. He was appointed "Researcher" (Assistant professor) in 1999 at the University of Naples and currently he is Associate professor of Applied Mechanics at the same University. His research fields of interest regarded both theoretical and experimental aspects of the following arguments: nonlinear dynamics of rotors on hydrodynamic journal bearings; vehicle suspensions elasto-kinematics analysis; the dynamic behaviour of the vehicle driveline.



F. Timpone (Corresponding author) was born in Naples (Italy) the 5th of September 1974. He received the M.Sc. degree in Mechanical Engineering in 1999 and the Ph.D. degree in Thermomechanical System Engineering in 2004 both from the University of Naples "Federico II". He is Assistant Professor at the University of Naples "Federico II" and his research interests include the dynamics and the control of mechanical systems.

Tel: +39 081 7683263
 Fax: +39 081 2394165
 E-mail: francesco.timpone@unina.it

Authors' information

Department of Industrial Engineering, University of Naples Federico II, Via Claudio 21, 80125 Naples, Italy.



F. Farroni (Naples, 7th of March 1985) received his M.Sc. degree in Mechanical Engineering in 2010 at University of Naples "Federico II" where is actually Ph.D. bursary holder in Mechanical System Engineering. He is technical consultant for vehicle dynamics at Ferrari S.p.A. and tyre modeler at GES racing department. His recent work has focused on the development of interaction models accounting friction and thermodynamics phenomena and on experimental activities in the field of contact mechanics for the optimization of dry and wet grip performances.

Transient Wave Propagation in Non-Homogeneous Viscoelastic Media

Shahin Nayyeri Amiri, Asad Esmaily

Abstract – Propagation of transient pressure waves in nonhomogeneous viscoelastic media with a cylindrical hole of circular cross section is investigated by employing the theory of propagating surfaces of discontinuities. The non-homogeneities are assumed to depend on the radial distance from the axis of the cylindrical hole. The solutions for the normal stress components and the radial particle velocity are expressed as Taylor series expansions about the time of arrival of the wave front. Two types of boundary conditions are considered. The wall of the cylindrical hole is either subjected to uniform pressure or to uniform radial particle velocity both of which have arbitrary dependence on time. Then the solutions are reduced to the special case of homogeneous viscoelastic media. Numerical computations are carried out for a homogeneous standard linear solid and for a uniform pressure with a step distribution in time applied at the wall of the hole. These numerical results are compared with those obtained previously by other investigators who have employed the method of characteristics. **Copyright © 2013 Praise Worthy Prize S.r.l. - All rights reserved.**

Keywords: Transient Wave Propagation, Non Homogeneous, Viscoelastic Media

Nomenclature

| | |
|---------------------|----------------------------|
| u | Displacement vector |
| ε | Infinitesimal strain |
| σ | Cauchy stress tensor |
| $G_1(r,t)$ | Shear relaxation functions |
| $G_2(r,t)$ | Bulk relaxation functions |
| σ'_{ij} | Stress deviators |
| ε'_{ij} | Strain deviators |
| δ_{ij} | Kronecker delta |
| ρ | Mass density material |
| t | Time |

I. Introduction

The propagation of transient waves in nonhomogeneous elastic media has recently attracted the attention of many researchers. Sternberg and Chakravorty [1] investigated the propagation of shock waves in a nonhomogeneous isotropic plate of infinite extent with a cylindrical hole at the wall of which uniform shearing tractions were suddenly applied and there, after steadily maintained.

The Laplace transform technique was employed in their research in obtaining the solution. Later, Chou and Schaller [2] applied the method of characteristics to solve the same problem. The latter method, of course, involved numerical integration and was suitable for wider class of non-homogeneities.

Reddy and Marietta [3] investigated an analogous problem of radial propagation of axial shear waves in a nonhomogeneous elastic medium with a cylindrical cavity by employing the theory of propagating surfaces of discontinuity. Longitudinal wave propagation in non-homogeneous elastic rods of finite and semi-infinite lengths was also investigated in considerable detail by several authors [4]-[7].

Transient wave propagation in nonhomogeneous viscoelastic media has received less attention. An important contribution in this field was made by Sun [8] who examined axi-symmetrical transient rotary shear waves in nonhomogeneous viscoelastic media with a cylindrical hole.

Sun [8] employed the theory of propagating surfaces of discontinuity which, previously, was applied by Achenbach and Reddy [9], Reddy and Marietta [3] to investigate the longitudinal wave propagation in a homogeneous semi-infinite viscoelastic rod, in a nonhomogeneous semi-infinite elastic rod and the axial shear wave propagation in a nonhomogeneous elastic medium, respectively.

The work of Avtar Singh and Kishan Chand Gupt [10] who used studied the propagation of one – dimensional stress discontinuities in one-dimensional propagation of discontinuities in non-homogeneous linear viscoelastic semi-infinite media should also be mentioned.

In this study, the propagation of transient cylindrical pressure waves in a nonhomogeneous viscoelastic medium with a cylindrical cavity is investigated.

The theory of propagating surfaces of discontinuity, as used by Sun [8] and others such as Achenbach and

Reddy [9] is employed. The solutions for the radial and circumferential stresses and the radial particle velocity are expanded as Taylor series about the time of arrival of the wave front. Two types of boundary conditions are considered. The wall of the cylindrical hole is either subjected to uniform pressure or to uniform radial particle velocity both of which have arbitrary dependence on time. By employing the equation of motion, the stress-strain relations and the kinematical condition of compatibility, the coefficients of the Taylor series for the radial particle velocity are obtained as the solutions of linear ordinary differential equations of the first order.

Using the solution for the radial particle velocity together with the constitutive equations and the kinematical condition of compatibility, the solutions for the radial and circumferential stresses are computed.

The solutions are reduced to the special case of homogeneous viscoelastic media by disregarding the nonhomogeneous. In the numerical examples, for purposes of comparison, stress prescribed boundary condition is considered and the time variation of the pressure applied on the wall of the cylindrical cavity is assumed to be stepwise. Furthermore, the homogeneous viscoelastic medium is modeled as a standard linear solid.

In the special case of the homogeneous viscoelastic medium, the wave profiles for radial particle velocity and radial stress distributions at two stations are obtained and are compared with those of McNiven and Mengi [11] who employed the method of characteristics in their analyses. Good agreement is found over the time range that is close to the time of arrival of the wave front by taking only a few terms in the Taylor series expansions.

II. Formulation of the Problem

We consider a nonhomogeneous, linearly viscoelastic infinite medium with an infinitely long circular cylindrical cavity of radius a . The medium is initially at rest and the material properties are assumed to depend solely on the radial distance from the center of the cavity. A uniform pressure or a uniform radial particle velocity with arbitrary dependence on time is applied on the wall of the cylindrical hole.

The body is referred to a cylindrical coordinate system (r, θ, z) in which the z axis coincides with the axis of the hole. In the development that follows, indicial notation and all of the rules associated with it are used when it is appropriate. Due to the axi-symmetry of the problem, the displacement field can be written as:

$$u_r = u_r(r, t); \quad u_\theta = 0, \quad u_z = 0 \quad (1)$$

Using the strain – displacement relations in a cylindrical coordinate system, we get:

$$\varepsilon_{rr} = u_{r,r}; \quad \varepsilon_{\theta\theta} = \frac{u_r}{r}; \quad \varepsilon_{zz} = \varepsilon_{r\theta} = \varepsilon_{rz} = \varepsilon_{\theta z} = 0 \quad (2)$$

If the medium is at rest prior to $t = 0$, the stress-strain relations for a linear isotropic non-homogeneous viscoelastic material can be expressed as

$$\sigma'_{ij}(r, t) = G_{10} \varepsilon'_{ij}(r, t) + \int_0^t G_1^{(1)}(r, t - \tau) \varepsilon'_{ij}(r, \tau) d\tau \quad (3)$$

$$\sigma_{kk} = G_{20} \varepsilon_{kk}(r, t) + \int_0^t G_2^{(1)}(r, t - \tau) \varepsilon_{kk}(r, \tau) d\tau \quad (4)$$

where $G_1(r, t)$ and $G_2(r, t)$ are the shear and bulk relaxation functions, respectively, and $\sigma'_{ij}, \varepsilon'_{ij}$ are the components of the stress and strain deviators defined as:

$$\begin{aligned} \sigma'_{ij} &= \sigma_{ij} - \frac{1}{3} \delta_{ij} \sigma_{kk} \\ \varepsilon'_{ij} &= \varepsilon_{ij} - \frac{1}{3} \delta_{ij} \varepsilon_{kk} \end{aligned} \quad (5)$$

where δ_{ij} is the Kronecker delta. From Eq. (2) the second of Eqs. (5), we can write:

$$\begin{aligned} \varepsilon'_{rr} &= \frac{2}{3} \frac{\partial u_r}{\partial r} - \frac{1}{3} \frac{u_r}{r} \\ \varepsilon'_{\theta\theta} &= \frac{2}{3} \frac{u_r}{r} - \frac{1}{3} \frac{\partial u_r}{\partial r} \\ \varepsilon_{kk} &= \varepsilon_{rr} + \varepsilon_{\theta\theta} + \varepsilon_{zz} = \frac{\partial u_r}{\partial r} + \frac{u_r}{r} \end{aligned} \quad (6)$$

In Eqs. (3)-(4) we also define:

$$\begin{aligned} G_{10} &= G_1(r, 0); \quad G_1^{(n)}(r, t) = \frac{\partial^n G_1(r, t)}{\partial t^n} \\ G_{10}^{(n)} &= \left. \frac{\partial^n G_1(r, t)}{\partial t^n} \right|_{t=0} \\ G_{20} &= G_2(r, 0); \quad G_2^{(n)}(r, t) = \frac{\partial^n G_2(r, t)}{\partial t^n} \\ G_{20}^{(n)} &= \left. \frac{\partial^n G_2(r, t)}{\partial t^n} \right|_{t=0} \end{aligned} \quad (7)$$

In view of Eqs. (1)-(4), it is clear that only $\sigma_{rr}, \sigma_{\theta\theta}$ and σ_{zz} are non-vanishing and that they are functions of r and t only. Then, the stress equation of motion becomes:

$$\frac{\partial \sigma_{rr}}{\partial r} + \frac{\sigma_{rr} - \sigma_{\theta\theta}}{r} = \rho \frac{\partial^2 u_r}{\partial t^2} \quad (8)$$

where $\rho(r)$ is the mass density of the medium. In terms of stress deviators Eq. (8) can be written as:

$$\frac{\partial \sigma'_{rr}}{\partial r} + \frac{1}{3} \frac{\partial \sigma'_{kk}}{\partial r} + \frac{\sigma'_{rr} - \sigma'_{\theta\theta}}{r} = \rho \frac{\partial^2 u_r}{\partial t^2} \quad (9)$$

The other two stress equations of motion are satisfied identically. In this study, two types of boundary conditions are considered:

- a) At time $t = 0$ a time – dependent uniform pressure is applied at $r = a$, i.e. on the surface of the cylindrical hole, and it is assumed that this pressure can be represented by a Maclaurin series:

$$\sigma_{rr}(a, t) = \sum_{n=0}^{\infty} \sigma_n \frac{t_n}{n!} \quad (10a)$$

- b) The radial particle velocity at $r = a$, $v(a, t)$, is prescribed and can be expanded as:

$$v(a, t) = \sum_{n=0}^{\infty} v_n \frac{t_n}{n!} \quad (10b)$$

In Eq. (10b), we have used the notation $v = \partial u_r / \partial t$. As for the initial condition, the medium is assumed to be at rest prior to $t = 0$.

Thus, the problem, which is completely described now, is to determine the solutions of Eqs. (8) and (2)-(4) subject to quiescent initial conditions and boundary condition as give by Eqs. (10a), (10b). It should be noted that the constitutive Eqs. (3)-(4) are expressed in terms of the components of the stress and strain deviators for simplicity.

The solutions, however, will be found for the stress components $\sigma_{rr}, \sigma_{\theta\theta}$ and σ_{zz} .

III. Solution of the Problem

The theory of propagating surfaces of discontinuity will be employed here in obtaining the solutions. A basic equation in the study of propagating discontinuities is the kinematical condition of compatibility which is discussed in general by Thomas [12]. Consider a function $f(r, t)$ which is discontinuous and has radial discontinuous derivatives across the wave front that moves in the radial direction with velocity c .

The kinematical condition of compatibility for this function takes the form:

$$\frac{d_D}{dt} [f] = \left[\frac{\partial f}{\partial t} \right] + c \left[\frac{\partial f}{\partial r} \right] \quad (11)$$

where finite jumps across the wave front are denoted by square brackets and the notation d_D / dt is introduced for the time – rate of change of a quantity as observed by an observer who moves with the propagating surface.

In this paper, it is assumed that the displacement remains continuous throughout the process and therefore:

$$[u_r] = 0 \quad (12)$$

Across the wave front. If the kinematical condition of compatibility given by Eq. (11) is applied to the displacement u_r , with Eq. (12) in consideration, we obtain:

$$\left[\frac{\partial u_r}{\partial r} \right] = -\frac{1}{c} \left[\frac{\partial u_r}{\partial t} \right] \quad (13)$$

Conservation of liner momentum, which is discussed in a general form by Thomas [12], can be expressed for the present problem in the form:

$$[\sigma_{rr}] = -\rho c \left[\frac{\partial u_r}{\partial t} \right] \quad (14)$$

In terms of the components of the stress deviator, Eq. (14) can be written as:

$$[\sigma'_{rr}] + \frac{1}{3} [\sigma'_{kk}] = -\rho c \left[\frac{\partial u_r}{\partial t} \right] \quad (15)$$

Since the integrals in Eqs. (3) and (4) are continuous at the wave front, we have the relations:

$$\begin{aligned} [\sigma'_{rr}] &= G_{10} [\varepsilon'_{rr}]; [\sigma'_{\theta\theta}] = G_{10} [\varepsilon'_{\theta\theta}] \\ [\sigma'_{kk}] &= G_{20} [\varepsilon'_{kk}] \end{aligned} \quad (16)$$

Now, substituting Eqs. (16) together with Eqs. (6) into Eq. (15) and taking into account Eq. (12), we get:

$$\frac{(2G_{10} + G_{20})}{3} \left[\frac{\partial u_r}{\partial r} \right] = -\rho c \left[\frac{\partial u_r}{\partial t} \right] \quad (17)$$

Comparing Eqs. (13) and (17), we obtain:

$$c^2 = \frac{2G_{10} + G_{20}}{3\rho} \quad (18)$$

Thus, the wave front propagates with a velocity which, depends on G_{10}, G_{20} and the mass density, and may vary as it penetrates into the medium.

At a cylindrical surface defined by a fixed r , the material is at rest until the wave front arrives. The time it takes for the wave front to arrive at this position can be computed as:

$$t = \phi(r) = \int_a^r \frac{dr}{c} \quad (19)$$

where a is the radius of the cylindrical cavity and c is the wave velocity given by Eq. (18).

Now following Sun [8], and also [9], we seek the solutions for the radial particle and the stress components $\sigma_{rr}, \sigma_{\theta\theta}$ and σ_{zz} as Taylor's expansions about the time of arrival of the wave front:

$$v(r, t) = \sum_{n=0}^{\infty} \frac{1}{n!} \{t - \phi(r)\}^n \left[\frac{\partial^n v}{\partial t^n} \right]_{t=\phi(r)} \quad t \geq \phi(r) \quad (20)$$

$$\sigma_{rr}(r, t) = \sum_{n=0}^{\infty} \frac{1}{n!} \{t - \phi(r)\}^n \left[\frac{\partial^n \sigma_{rr}}{\partial t^n} \right]_{t=\phi(r)} \quad t \geq \phi(r) \quad (21)$$

$$\sigma_{\theta\theta}(r, t) = \sum_{n=0}^{\infty} \frac{1}{n!} \{t - \phi(r)\}^n \left[\frac{\partial^n \sigma_{\theta\theta}}{\partial t^n} \right]_{t=\phi(r)} \quad t \geq \phi(r) \quad (22)$$

$$\sigma_{zz}(r, t) = \sum_{n=0}^{\infty} \frac{1}{n!} \{t - \phi(r)\}^n \left[\frac{\partial^n \sigma_{zz}}{\partial t^n} \right]_{t=\phi(r)} \quad t \geq \phi(r) \quad (23)$$

The coefficients of expansions in Eqs. (20)-(23) represent propagating discontinuities and the problem reduces to the determination of these coefficients.

We shall first find the solutions for the coefficients in the expansion for radial particle velocity given by Eq. (20).

Then, using the solutions for these coefficients together with the constitutive equations and the kinematical condition of compatibility, the coefficients of the expansions given in Eqs. (21)-(23) will be computed.

For this purpose, we first differentiate Eqs. (3) and (4) $n + p$ times with respect to time to obtain:

$$\frac{\partial^{n+p} \sigma'_{rr}}{\partial t^{n+p}} = G_{10} \frac{\partial^{n+p} \varepsilon'_{rr}}{\partial t^{n+p}} + \sum_{i=1}^{n+p} G_{10}^{(i)} \frac{\partial^{n+p-i} \varepsilon'_{rr}}{\partial t^{n+p-i}} + \int_0^t G_1^{(n+p)}(r, t - \tau) \varepsilon'_{rr} d\tau \quad (24)$$

$$\frac{\partial^{n+p} \sigma'_{\theta\theta}}{\partial t^{n+p}} = G_{10} \frac{\partial^{n+p} \varepsilon'_{\theta\theta}}{\partial t^{n+p}} + \sum_{i=1}^{n+p} G_{10}^{(i)} \frac{\partial^{n+p-i} \varepsilon'_{\theta\theta}}{\partial t^{n+p-i}} + \int_0^t G_1^{(n+p)}(r, t - \tau) \varepsilon'_{\theta\theta} d\tau \quad (25)$$

$$\frac{\partial^{n+p} \sigma_{kk}}{\partial t^{n+p}} = G_{20} \frac{\partial^{n+p} \varepsilon_{kk}}{\partial t^{n+p}} + \sum_{i=1}^{n+p} G_{20}^{(i)} \frac{\partial^{n+p-i} \varepsilon_{kk}}{\partial t^{n+p-i}} + \int_0^t G_2^{(n+p)}(r, t - \tau) \varepsilon'_{kk} d\tau, \quad (26)$$

where for p we shall consider only the values 0 and 1.

Since the integrals in Eqs. (24)-(26) are continuous at the wave front, we have the following relations between the discontinuities:

$$\left[\frac{\partial^{n+p} \sigma'_{rr}}{\partial t^{n+p}} \right] = G_{10} \left[\frac{\partial^{n+p} \varepsilon'_{rr}}{\partial t^{n+p}} \right] + \sum_{i=1}^{n+p} G_{10}^{(i)} \left[\frac{\partial^{n+p-i} \varepsilon'_{rr}}{\partial t^{n+p-i}} \right] \quad (27)$$

$$\left[\frac{\partial^{n+p} \sigma'_{\theta\theta}}{\partial t^{n+p}} \right] = G_{10} \left[\frac{\partial^{n+p} \varepsilon'_{\theta\theta}}{\partial t^{n+p}} \right] + \sum_{i=1}^{n+p} G_{10}^{(i)} \left[\frac{\partial^{n+p-i} \varepsilon'_{\theta\theta}}{\partial t^{n+p-i}} \right] \quad (28)$$

$$\left[\frac{\partial^{n+p} \sigma_{kk}}{\partial t^{n+p}} \right] = G_{20} \left[\frac{\partial^{n+p} \varepsilon_{kk}}{\partial t^{n+p}} \right] + \sum_{i=1}^{n+p} G_{20}^{(i)} \left[\frac{\partial^{n+p-i} \varepsilon_{kk}}{\partial t^{n+p-i}} \right] \quad (29)$$

From Eq. (9) we have:

$$\left[\frac{\partial \sigma'_{rr}}{\partial r} \right] + \frac{1}{3} \left[\frac{\partial \sigma_{kk}}{\partial r} \right] + \frac{1}{r} [\sigma'_{rr}] - \frac{1}{r} [\sigma'_{\theta\theta}] = \rho \left[\frac{\partial^2 u_r}{\partial t^2} \right] \quad (30)$$

By writing the kinematical condition of compatibility given by Eq. (11) for $\sigma'_{rr}, \sigma_{kk}$ and $\partial u_r / \partial t$, we get:

$$\frac{d_D}{dt} [\sigma'_{rr}] = \left[\frac{\partial \sigma'_{rr}}{\partial t} \right] + c \left[\frac{\partial \sigma'_{rr}}{\partial r} \right] \quad (31)$$

$$\frac{d_D}{dt} [\sigma_{kk}] = \left[\frac{\partial \sigma_{kk}}{\partial t} \right] + c \left[\frac{\partial \sigma_{kk}}{\partial r} \right] \quad (32)$$

$$\frac{d_D}{dt} \left[\frac{\partial u_r}{\partial t} \right] = \left[\frac{\partial^2 u_r}{\partial t^2} \right] + c \left[\frac{\partial^2 u_r}{\partial r \partial t} \right] \quad (33)$$

Employing relations (31)-(32) in Eq. (30) and rearranging the terms, we get:

$$\frac{1}{c} \frac{d_D}{dt} \left\{ [\sigma'_{rr}] + \frac{1}{3} [\sigma_{kk}] \right\} - \frac{1}{c} \left[\frac{\partial \sigma'_{rr}}{\partial t} \right] - \frac{1}{3c} \left[\frac{\partial \sigma_{kk}}{\partial t} \right] + \frac{1}{r} [\sigma'_{rr}] - \frac{1}{r} [\sigma'_{\theta\theta}] = \rho \left[\frac{\partial^2 u_r}{\partial t^2} \right] \quad (34)$$

For $n = 0$ and $p = 1$, Eqs. (27) and (29) become:

$$\left[\frac{\partial \sigma'_{rr}}{\partial t} \right] = G_{10} \left[\frac{\partial \varepsilon'_{rr}}{\partial t} \right] + G_{10}^{(1)} [\varepsilon'_{rr}] \quad (35)$$

$$\left[\frac{\partial \sigma_{kk}}{\partial t} \right] = G_{20} \left[\frac{\partial \varepsilon_{kk}}{\partial t} \right] + G_{20}^{(1)} [\varepsilon_{kk}] \quad (36)$$

From Eqs. (6) and their time derivatives, the following relations between the discontinuities can be written:

$$\begin{aligned} [\varepsilon'_{rr}] &= \frac{2}{3} \left[\frac{\partial u_r}{\partial r} \right]; [\varepsilon'_{\theta\theta}] = -\frac{1}{3} \left[\frac{\partial u_r}{\partial r} \right] \\ [\varepsilon_{kk}] &= \left[\frac{\partial u_r}{\partial r} \right] \end{aligned} \quad (37)$$

$$\left[\frac{\partial \varepsilon'_{rr}}{\partial t} \right] = \frac{2}{3} \left[\frac{\partial^2 u_r}{\partial r \partial t} \right] - \frac{1}{3r} \left[\frac{\partial u_r}{\partial t} \right] \quad (38)$$

$$\left[\frac{\partial \varepsilon_{kk}}{\partial t} \right] = \left[\frac{\partial^2 u_r}{\partial r \partial t} \right] + \frac{1}{r} \left[\frac{\partial u_r}{\partial t} \right] \quad (39)$$

In writing Eqs. (37), Eq. (12) is taken into account.

Now substituting Eqs. (15), (16), (35)-(36) into Eq. (34) and then employing Eqs. (37)-(39), we obtain:

$$\begin{aligned} -\rho \frac{d_D}{dt} \left[\frac{\partial u_r}{\partial t} \right] - \frac{1}{c} \frac{d_D}{dt} (\rho c) \left[\frac{\partial u_r}{\partial t} \right] + \\ - \frac{2G_{10} + G_{20}}{3c} \left[\frac{\partial^2 u_r}{\partial r \partial t} \right] - \frac{2G_{10}^{(1)} + G_{20}^{(1)}}{3c} \left[\frac{\partial u_r}{\partial r} \right] + \\ + \frac{G_{10}}{3cr} \left[\frac{\partial u_r}{\partial t} \right] - \frac{G_{20}}{3cr} \left[\frac{\partial u_r}{\partial t} \right] + \frac{G_{10}}{r} \left[\frac{\partial u_r}{\partial r} \right] = \rho \left[\frac{\partial^2 u_r}{\partial t^2} \right] \end{aligned} \quad (40)$$

Now, using Eqs. (13), (33) and (18) in Eq. (40), we get, after some manipulation:

$$\frac{d_D}{dt} \left[\frac{\partial u_r}{\partial t} \right] + \alpha(t) \left[\frac{\partial u_r}{\partial t} \right] = 0 \quad (41)$$

where:

$$\alpha(t) = \left\{ \frac{c}{2r} + \frac{1}{2\rho c} \frac{d_D}{dt} (\rho c) - \frac{m_1}{2} \right\} \quad (42)$$

and:

$$m_1 = \left\{ \frac{2G_{10}^{(1)} + G_{20}^{(1)}}{2G_{10} + G_{20}} \right\} \quad (43)$$

Eq. (41) is a liner ordinary differential equation of the first order whose solution give $[v] = [\partial u_r / \partial t]$, the coefficient corresponding to $n=0$ in the Taylor's expansion in Eq. (20). To determine the coefficients for $n \geq 1$, we differentiate the equation of motion (9) with respect to time for n times to obtain:

$$\begin{aligned} \left[\frac{\partial^{n+1} \sigma'_{rr}}{\partial r \partial t^n} \right] + \frac{1}{3} \left[\frac{\partial^{n+1} \sigma_{kk}}{\partial r \partial t^n} \right] + \frac{1}{r} \left[\frac{\partial^n \sigma'_{rr}}{\partial t^n} \right] + \\ - \frac{1}{r} \left[\frac{\partial^n \sigma'_{\theta\theta}}{\partial t^n} \right] = \rho \left[\frac{\partial^{n+2} u_r}{\partial t^{n+2}} \right] \end{aligned} \quad (44)$$

By writing the kinematical condition of compatibility for $\partial^n \sigma'_{rr} / \partial t^n$ and $\partial^n \sigma_{kk} / \partial t^n$, and employing these relations in Eq. (44), we obtain:

$$\begin{aligned} \frac{1}{c} \frac{d_D}{dt} \left[\frac{\partial^n \sigma'_{rr}}{\partial t^n} \right] - \frac{1}{c} \left[\frac{\partial^{n+1} \sigma'_{rr}}{\partial t^{n+1}} \right] + \frac{1}{3c} \frac{d_D}{dt} \left[\frac{\partial^n \sigma_{kk}}{\partial t^n} \right] + \\ - \frac{1}{3c} \left[\frac{\partial^{n+1} \sigma_{kk}}{\partial t^{n+1}} \right] + \frac{1}{r} \left[\frac{\partial^n \sigma'_{rr}}{\partial t^n} \right] - \frac{1}{r} \left[\frac{\partial^n \sigma'_{\theta\theta}}{\partial t^n} \right] = \\ = \rho \left[\frac{\partial^{n+2} u_r}{\partial t^{n+2}} \right] \end{aligned} \quad (45)$$

Differentiation of the strain – displacement relations (6) with respect to time for $n+p$ times yields between the discontinuities the following relations:

$$\left[\frac{\partial^{n+p} \varepsilon'_{rr}}{\partial t^{n+p}} \right] = \frac{2}{3} \left[\frac{\partial^{n+p+1} u_r}{\partial r \partial t^{n+p}} \right] - \frac{1}{3r} \left[\frac{\partial^{n+p} u_r}{\partial t^{n+p}} \right] \quad (46)$$

$$\left[\frac{\partial^{n+p} \varepsilon'_{\theta\theta}}{\partial t^{n+p}} \right] = \frac{2}{3r} \left[\frac{\partial^{n+p} u_r}{\partial t^{n+p}} \right] - \frac{1}{3} \left[\frac{\partial^{n+p+1} u_r}{\partial r \partial t^{n+p}} \right] \quad (47)$$

$$\left[\frac{\partial^{n+p} \varepsilon_{kk}}{\partial t^{n+p}} \right] = \left[\frac{\partial^{n+p+1} u_r}{\partial r \partial t^{n+p}} \right] + \frac{1}{r} \left[\frac{\partial^{n+p} u_r}{\partial t^{n+p}} \right] \quad (48)$$

where, again, only the values 0 and 1 will be considered for p .

Applying the kinematical condition of compatibility given by Eq. (11) to $\partial^{n+p} u_r / \partial t^{n+p}$ and $\partial^{n+p-i} u_r / \partial t^{n+p-i}$, we obtain:

$$\frac{d_D}{dt} \left[\frac{\partial^{n+p} u_r}{\partial t^{n+p}} \right] = \left[\frac{\partial^{n+p+1} u_r}{\partial t^{n+p+1}} \right] + c \left[\frac{\partial^{n+p+1} u_r}{\partial r \partial t^{n+p}} \right] \quad (49)$$

$$\frac{d_D}{dt} \left[\frac{\partial^{n+p-i} u_r}{\partial t^{n+p-i}} \right] = \left[\frac{\partial^{n+p+1-i} u_r}{\partial t^{n+p+1-i}} \right] + c \left[\frac{\partial^{n+p+1-i} u_r}{\partial r \partial t^{n+p-i}} \right] \quad (50)$$

Now, substituting Eqs. (27-29) into Eq. (45) and then employing first Eqs. (46)-(48) then Eqs. (49)-(50) and (18) with the values 0 or 1 chosen appropriately for p , we get, after some manipulations:

$$\frac{d_D}{dt} \left[\frac{\partial^n v}{\partial t^n} \right] + \alpha(t) \left[\frac{\partial^n v}{\partial t^n} \right] = F_n(t) \quad (51)$$

$n \geq 1$

where $\alpha(t)$ is defined by Eq. (42) and:

$$\begin{aligned}
 F_n(t) &= \frac{1}{2} \frac{d^2_D}{dt^2} \left[\frac{\partial^{n-1} v}{\partial t^{n-1}} \right] + \alpha(t) \frac{d_D}{dt} \left[\frac{\partial^{n-1} v}{\partial t^{n-1}} \right] + \\
 &+ \left\{ \frac{1}{2r} \left(\frac{c}{2G_{10} + G_{20}} \right) \left(\frac{d_D}{dt} (G_{20} - G_{10}) \right) + \left[\frac{\partial^{n-1} v}{\partial t^{n-1}} \right] + \right. \\
 &\left. - \frac{c^2}{2r^2} - \frac{m_1 c}{2r} \right\} \\
 &+ \sum_{i=1}^n \left\{ \frac{m_i}{2} \frac{d^2_D}{dt^2} \left[\frac{\partial^{n-i-1} v}{\partial t^{n-i-1}} \right] + \left(\frac{1}{2\rho c} \frac{d_D}{dt} (m_i c \rho) + \frac{m_i c}{2r} \right) \frac{d_D}{dt} \left[\frac{\partial^{n-1-i} v}{\partial t^{n-1-i}} \right] + \right. \\
 &\left. - \left(\frac{1}{2} \frac{m_i c^2}{r^2} - \frac{1}{2r} \left(\frac{c}{2G_{10} + G_{20}} \right) \right) \left[\frac{\partial^{n-1-i} v}{\partial t^{n-1-i}} \right] - \left(\frac{d_D}{dt} (G_{20}^{(i)} - G_{10}^{(i)}) \right) \left[\frac{\partial^{n-1-i} v}{\partial t^{n-1-i}} \right] \right\} \\
 &- \sum_{i=2}^{n+1} \left\{ m_i \frac{d_D}{dt} \left[\frac{\partial^{n-i} v}{\partial t^{n-i}} \right] + \left(\frac{1}{2\rho c} \frac{d_D}{dt} (c\rho) + \frac{m_i c}{2r} \right) \left[\frac{\partial^{n-i} v}{\partial t^{n-i}} \right] - \frac{m_i}{2} \left[\frac{\partial^{n+1-i} v}{\partial t^{n+1-i}} \right] \right\}
 \end{aligned} \tag{52}$$

In eq. (52), m_i is defined as:

$$m_i = \left\{ \frac{2G_{10}^{(i)} + G_{20}^{(i)}}{2G_{10} + G_{20}} \right\} \tag{53}$$

and m_1 is given by Eq. (43). It should be noted once again that in writing Eqs. (51) and (52), the relation $v = \partial u_r / \partial t$ is used. If we define $F_n(t) = 0$ for $n = 0$, the general solutions for the linear ordinary differential Eqs. (41) and (51) can be written in a single expression as:

$$\left[\frac{\partial^n v}{\partial t^n} \right] = e^{-\beta(t)} \left\{ \int_0^t F_n(s) e^{\beta(s)} ds + A_n \right\} \quad n \geq 0 \tag{54}$$

where:

$$\beta(t) = \int_0^t \alpha(s) ds \tag{55}$$

and $A_n (n \geq 0)$ are integration constants to be determined from the boundary conditions.

Before we determine the integration constants, A_n , we shall proceed to determine, $[\partial^n \sigma_{rr} / \partial t^n]$, the coefficients of the Taylor's expansion for radial as give by Eq. (21).

Since the solutions for the coefficients, $[\partial^n v / \partial t^n]$, have been obtained, Eq. (54), we shall attempt to express

$[\partial^n \sigma_{rr} / \partial t^n]$ in terms of $[\partial^n v / \partial t^n]$ and their time derivatives. Form Eq. (14), we have:

$$[\sigma_{rr}] = -\rho c [v] \tag{56}$$

where, of course, the relation $v = \partial u_r / \partial t$ is used.

For $n \geq 1$, we make use of the constitutive equation for the radial stress written at the wave front, Eq. (27). Employing Eqs. (46)-(48) in Eq. (27), with p taken as 0, and considering Eqs. (5) together with eq. (29), we find:

$$\begin{aligned}
 \left[\frac{\partial^n \sigma_{rr}}{\partial t^n} \right] &= \frac{G_{20}}{3} \left\{ \left[\frac{\partial^{n+1} u_r}{\partial r \partial t^n} \right] + \frac{1}{r} \left[\frac{\partial^n u_r}{\partial t^n} \right] \right\} + \\
 &+ \sum_{i=1}^n \frac{G_{20}^{(i)}}{3} \left\{ \left[\frac{\partial^{n+1-i} u_r}{\partial r \partial t^{n-i}} \right] + \frac{1}{r} \left[\frac{\partial^{n-i} u_r}{\partial t^{n-i}} \right] \right\} + \\
 &+ G_{10} \left\{ \left[\frac{\partial^{n+1-i} u_r}{\partial r \partial t^n} \right] - \frac{G_{10}}{3} \left\{ \left[\frac{\partial^{n+1} u_r}{\partial r \partial t^n} \right] + \frac{1}{r} \left[\frac{\partial^n u_r}{\partial t^n} \right] \right\} + \right. \\
 &\left. + \sum_{i=1}^n G_{10}^{(i)} \left\{ \left[\frac{\partial^{n+1-i} u_r}{\partial r \partial t^{n-i}} \right] - \frac{1}{3} \left(\left[\frac{\partial^{n+1-i} u_r}{\partial r \partial t^{n-i}} \right] + \frac{1}{r} \left[\frac{\partial^{n-i} u_r}{\partial t^{n-i}} \right] \right) \right\} \right\}
 \end{aligned} \tag{57}$$

Now, applying Eqs. (49) and (50), with $p = 0$, in Eq. (57) and using the relation $v = \partial u_r / \partial t$, we get:

$$\begin{aligned}
 \left[\frac{\partial^n \sigma_{rr}}{\partial t^n} \right] &= c\rho \frac{d_D}{dt} \left[\frac{\partial^{n-1} v}{\partial t^{n-1}} \right] - c\rho \left[\frac{\partial^n v}{\partial t^n} \right] + \\
 &+ \frac{1}{3r} (G_{20} - G_{10}) \left[\frac{\partial^{n-1} v}{\partial t^{n-1}} \right] + \\
 &+ \sum_{i=1}^n \left\{ c\rho m_i \left(\frac{d_D}{dt} \left[\frac{\partial^{n-1-i} v}{\partial t^{n-1-i}} \right] - \left[\frac{\partial^{n-i} v}{\partial t^{n-i}} \right] \right) + \right. \\
 &\left. + \frac{1}{3r} (G_{20}^{(i)} - G_{10}^{(i)}) \left[\frac{\partial^{n-1-i} v}{\partial t^{n-1-i}} \right] \right\}
 \end{aligned} \tag{58}$$

In view of Eqs. (56) and (58), the Taylor's expansion for the radial stress σ_{rr} can be written as:

$$\begin{aligned}
 \sigma_{rr}(r,t) &= \sum_{n=0}^{\infty} \frac{1}{n!} \{t - \phi(r)\}^n \left\{ c\rho \frac{d_D}{dt} \left[\frac{\partial^{n-1} v}{\partial t^{n-1}} \right] + \right. \\
 &- c\rho \left[\frac{\partial^n v}{\partial t^n} \right] + \frac{1}{3r} (G_{20} - G_{10}) \left[\frac{\partial^{n-1} v}{\partial t^{n-1}} \right] + \\
 &+ \sum_{i=1}^n \left\{ c\rho m_i \left(\frac{d_D}{dt} \left[\frac{\partial^{n-1-i} v}{\partial t^{n-1-i}} \right] - \left[\frac{\partial^{n-i} v}{\partial t^{n-i}} \right] \right) + \right. \\
 &\left. + \frac{1}{3r} (G_{20}^{(i)} - G_{10}^{(i)}) \left[\frac{\partial^{n-1-i} v}{\partial t^{n-1-i}} \right] \right\} \Bigg|_{t=\phi(r)} \quad t \geq \phi(r)
 \end{aligned} \tag{59}$$

In which we set:

$$\left[\frac{\partial^{n-1} v}{\partial t^{n-1}} \right] \equiv 0 \quad \text{if } n = 0 \quad (60)$$

The two types of boundary conditions as described by Eqs. (10a) and (10b) are now employed to determine the integration constants A_n which appear in the solutions through Eq. (54).

For type *A* of the boundary conditions the radial stress is prescribed at $r = a$.

Noting that the relation $t = \phi(r)$ at the wave front becomes $t = \phi(r) = 0$ at the surface of the cylindrical cavity, we compare in this case Eq. (59) with Eq. (10a) at $r = a$ to obtain:

$$\begin{aligned} \sigma_n = & \left\{ c\rho \frac{d_D}{dt} \left[\frac{\partial^{n-1} v}{\partial t^{n-1}} \right] - c\rho \left[\frac{\partial^n v}{\partial t^n} \right] + \right. \\ & + \frac{1}{3r} (G_{20} - G_{10}) \left[\frac{\partial^{n-1} v}{\partial t^{n-1}} \right] + \\ & + \sum_{i=1}^n \left\{ c\rho m_i \left(\frac{d_D}{dt} \left[\frac{\partial^{n-1-i} v}{\partial t^{n-1-i}} \right] - \left[\frac{\partial^{n-i} v}{\partial t^{n-i}} \right] \right) + \right. \\ & \left. \left. + \frac{1}{3r} (G_{20}^{(i)} - G_{10}^{(i)}) \left[\frac{\partial^{n-1-i} v}{\partial t^{n-1-i}} \right] \right\} \right\}_{t=0} \end{aligned} \quad (61)$$

From Eq. (54), we have:

$$A_n = \left[\frac{\partial^n v}{\partial t^n} \right]_{t=0} \quad (62)$$

Substituting Eq. (62) in Eq. (61) give:

$$\begin{aligned} A_n = & \left\{ \frac{d_D}{dt} \left[\frac{\partial^{n-1} v}{\partial t^{n-1}} \right] - \frac{\sigma_n}{c\rho} + \frac{c}{r} \left(\frac{G_{20} - G_{10}}{2G_{10} + G_{20}} \right) \left[\frac{\partial^{n-1} v}{\partial t^{n-1}} \right] + \right. \\ & + \sum_{i=1}^n \left\{ m_i \left(\frac{d_D}{dt} \left[\frac{\partial^{n-1-i} v}{\partial t^{n-1-i}} \right] - \left[\frac{\partial^{n-i} v}{\partial t^{n-i}} \right] \right) + \right. \\ & \left. \left. + \frac{c}{r} \left(\frac{G_{20}^{(i)} - G_{10}^{(i)}}{2G_{10} + G_{20}} \right) \left[\frac{\partial^{n-1-i} v}{\partial t^{n-1-i}} \right] \right\} \right\}_{t=0} \quad n \geq 0 \end{aligned} \quad (63)$$

It is noted that Eq. (60) should be considered when Eq. (63) is used to compute A_0 . It is observed from eq. (54) together with Eq. (52) that the solution for $\left[\frac{\partial^{n-1} v}{\partial t^{n-1}} \right]$ involves only the constants A_i ($i \leq n-1$).

Therefore, all the constants A_n can be determined successively from Eq. (63) once the first constant A_0 is known. This completes the solutions for the radial

particle velocity and radial stress when boundary conditions of type *A* are considered.

For type *B* of the boundary conditions the radial particle velocity is prescribed at the cylindrical surface $r = a$ as given by Eq. (10b).

A comparison between Eq. (10b) and Eq. (20) in conjunction with Eq. (54) yields:

$$A_n = v_n \quad (64)$$

The coefficients of the Taylor's expansions for the stress components $\sigma_{\theta\theta}$ and σ_{zz} as given by Eqs. (22)-

(23) can be computed in terms of $\left[\frac{\partial^n v}{\partial t^n} \right]$ in an exactly analogous manner by employing the constitutive equations, the strain-displacement relations and the kinematical condition of compatibility. We give here the result for the circumferential stress $\sigma_{\theta\theta}$:

$$\begin{aligned} \sigma_{\theta\theta}(r,t) = & \sum_{n=0}^{\infty} \frac{1}{n!} \{ t - \phi(r) \}^n \\ & \left\{ \left(\frac{2G_{10} + G_{20}}{3r} \right) \left[\frac{\partial^{n-1} v}{\partial t^{n-1}} \right] + \right. \\ & + \frac{1}{3c} (G_{20} - G_{10}) \left(\frac{d_D}{dt} \left[\frac{\partial^{n-1} v}{\partial t^{n-1}} \right] - \left[\frac{\partial^n v}{\partial t^n} \right] \right) + \\ & + \sum_{i=1}^n \left\{ \frac{1}{3c} (G_{20}^{(i)} - G_{10}^{(i)}) \left(\frac{d_D}{dt} \left[\frac{\partial^{n-1-i} v}{\partial t^{n-1-i}} \right] - \left[\frac{\partial^{n-i} v}{\partial t^{n-i}} \right] \right) + \right. \\ & \left. \left. + \frac{2(G_{10}^{(i)} - G_{20}^{(i)})}{3r} \left[\frac{\partial^{n-1-i} v}{\partial t^{n-1-i}} \right] \right\} \right\}_{t=\phi(r)} \end{aligned} \quad (65)$$

For the special case of homogeneous viscoelastic medium the shear and bulk relaxation functions and the mass density are independent of the spatial coordinate r , i.e.:

$$G_1 = G_1(t); G_2 = G_2(t); \rho = const \quad (66)$$

The solutions for this special case can be derived from the solutions obtained above for the nonhomogeneous viscoelastic medium by considering relations (66). The propagation velocity becomes $c^2 = (2G_{10} + G_{20})/3\rho = \text{constant}$ and the time it takes for the disturbance to arrive at a position r is computed as $t = \phi(r) = (r - a)/c$ in this case.

The radial particle velocity, the radial stress and the circumferential stress are computed Eqs. (20), (59) and (65), respectively, in view of Eqs (66). The coefficients $\left[\frac{\partial^n v}{\partial t^n} \right]$ have the same form as in equation (54), but $\beta(t)$ and $F_n(t)$ for this case are obtained from Eqs.

(55) and (42), and Eq. (52), respectively, in the forms:

$$\beta(t) = \int_0^t \frac{1}{2} \left(\frac{c}{r} - m_1 \right) ds \quad (67)$$

$$\begin{aligned} F_n(t) = & \frac{1}{2} \frac{d^2_D}{dt^2} \left[\frac{\partial^{n-1} v}{\partial t^{n-1}} \right] + \left(\frac{c}{2r} - m_1 \right) \frac{d_D}{dt} \left[\frac{\partial^{n-1} v}{\partial t^{n-1}} \right] + \\ & - \left(\frac{c^2}{2r^2} + \frac{m_1 c}{2r} \right) \left[\frac{\partial^{n-1} v}{\partial t^{n-1}} \right] + \sum_{i=1}^n \left\{ \frac{m_i}{2} \frac{d^2_D}{dt^2} \left[\frac{\partial^{n-1-i} v}{\partial t^{n-1-i}} \right] + \right. \\ & + \frac{m_i c}{2r} \frac{d_D}{dt} \left[\frac{\partial^{n-1-i} v}{\partial t^{n-1-i}} \right] - \frac{m_i c^2}{2r^2} \left[\frac{\partial^{n-1-i} v}{\partial t^{n-1-i}} \right] \left. \right\} + \quad (68) \\ & + \sum_{i=2}^n \left\{ -m_i \frac{d_D}{dt} \left[\frac{\partial^{n-i} v}{\partial t^{n-i}} \right] - \frac{m_i c}{2r} \left[\frac{\partial^{n-i} v}{\partial t^{n-i}} \right] + \right. \\ & \left. + \frac{m_i}{2} \left[\frac{\partial^{n+1-i} v}{\partial t^{n+1-i}} \right] \right\} \end{aligned}$$

where m_1 and m_i are given by Eqs. (43) and (53), respectively, and they, of course, should be interpreted in view of Eqs. (66).

The integration constants A_n are determined from Eq. (63) or (64) depending upon whether stress or particle velocity is prescribed at the boundary surface with necessary considerations given for homogeneity.

For simplicity and for purposes of comparison with McNiven and Mengi [11], standard liner solid is chosen as the specific viscoelastic model and radial stress is prescribed at the wall the cylindrical cavity $r = a$.

The shear and bulk moduli for the standard liner solid are:

$$\begin{aligned} G_1(t) &= G_{1F} + (G_{10} - G_{1F}) e^{-t/\tau_1} \\ G_2(t) &= G_{2F} + (G_{20} - G_{2F}) e^{-t/\tau_2} \end{aligned} \quad (69)$$

respectively. In Eqs. (69), the constants τ_1 and τ_2 are the relaxation times of the shear and bulk moduli, respectively, and:

$$\begin{aligned} G_{1F} &= G_1(\infty) ; G_{2F} = G_2(\infty) ; G_{10} = G_1(0) \\ G_{20} &= G_2(0) \end{aligned} \quad (70)$$

For material constants and relaxation times, we take the same numerical values as considered by McNiven and Mengi [11] for what they called "material one".

These are:

$$\begin{aligned} \frac{G_{1F}}{G_{10}} &= 0.40 ; \frac{G_{20}}{G_{10}} = 2.28571 \\ \frac{G_{2F}}{G_{10}} &= 1.142852 ; \frac{c\tau_1}{a} = 3.0 ; \frac{c\tau_2}{a} = 5.0 \end{aligned} \quad (71)$$

The coefficients $\left[\frac{\partial^n v}{\partial t^n} \right]$ of the Taylor's expansion for radial particle velocity as given by Eq. (20) can be obtained from Eq. (54) together with Eqs. (66)-(68). The integration constants A_n can be computed from eq. (63) with Eq. (66) taken in to account.

As for the boundary condition, we assume specifically that a radial pressure of magnitude P_0 is suddenly applied at $r = a$ and maintained constant thereafter.

The boundary condition, then, is given by eq. (10a) with:

$$\sigma_0 = -P_0 ; \sigma^n = 0 \quad (72)$$

$$\text{for } n \geq 1$$

Now, to compute the coefficient $[v]$, we carry out the integration of Eq. (67) to obtain:

$$\beta(t) = \ln \left(\frac{r}{a} \right)^{1/2} - \frac{m_1}{2c} (r - a) \quad (73)$$

where m_1 is given by Eq. (43), and the wave front $t = \phi(r) = (r - a) / c$ From Eq. (63) we obtain, in view of Eq. (72):

$$A_0 = P_0 / (\rho c) \quad (74)$$

For $n = 0$, Eq. (54) gives:

$$[v] = A_0 e^{-\beta(t)} \quad (75)$$

Substituting Eqs. (73) and (74) into Eq. (75) and using the numerical values given by Eq. (71), we get:

$$[v] = \left(\frac{a}{r} \right)^{1/2} \frac{P_0}{\rho c} e^{-0.0733 \left(\frac{r}{a} - 1 \right)} \quad (76)$$

The integrations to be carried out in obtaining $\left[\frac{\partial^n v}{\partial t^n} \right]$ for $n \geq 1$ are simple and these coefficients can be calculated as described above in a straightforward manner without difficulty. We give here only the next two coefficients:

$$\begin{aligned} \left[\frac{\partial v}{\partial t} \right] = & \left\{ 0.375 \left(\frac{r}{a} \right)^{-3/2} - 0.012826 \left(\frac{r}{a} \right)^{1/2} + \right. \\ & \left. - 0.4888 \left(\frac{r}{a} \right)^{-1/2} \right\} \frac{cP_0}{a\rho c} e^{-0.0733 \left(\frac{r}{a} - 1 \right)} \end{aligned} \quad (77)$$

$$\left[\frac{\partial^2 v}{\partial t^2} \right] = \left\{ -0.117712 \left(\frac{r}{a} \right)^{-5/2} - 0.21032 \left(\frac{r}{a} \right)^{-3/2} + \right. \\ \left. -0.00604 \left(\frac{r}{a} \right)^{-1/2} \ln \left(\frac{r}{a} \right) + 0.003376 \left(\frac{r}{a} \right)^{1/2} + \right. \\ \left. +0.00018 \left(\frac{r}{a} \right)^{3/2} + \right. \\ \left. -0.011623 \left(\frac{r}{a} \right)^{-1/2} \right\} \frac{c^2 P_0}{a^2 \rho c} e^{-0.0733 \left(\frac{r}{a} - 1 \right)} \quad (78)$$

In obtaining Eqs. (77) and (78), the numerical values given in Eq. (71) are employed.

The first seven coefficients thus computed, we have plotted the dimensionless radial velocity $\frac{v}{P_0 / \rho c}$ against

the dimensionless time $\frac{ct}{a}$ for two stations $\frac{r}{a} = 1$ and

$\frac{r}{a} = 2.5$ in Figs. 1 and 2. For comparison, the solution

obtained by McNiven and Mengi [11] is also plotted. In the same figures. It is seen from the figures that the present solution with seven terms taken compares well with the solution of McNiven [11] over the time range that is close to the time of arrival of wave front.

In an analogous manner, the coefficients $\left[\frac{\partial^n \sigma_{rr}}{\partial t^n} \right]$ of the Taylor's expansion for radial stress can be calculated in terms of the already computed coefficients $\left[\frac{\partial^n v}{\partial t^n} \right]$ according to Eq. (58) which should be interpreted in view of Eqs. (66). The first seven coefficients thus found, the radial stress σ_{rr} is computed from Eq. (59), with Eqs. (66) taken into consideration, and the dimensionless radial stress

σ_{rr} / P_0 is plotted against the dimensionless time $\frac{ct}{a}$ at

station $\frac{r}{a} = 2.5$, together with the solution obtained by

McNiven and Mengi [11], in Fig. 3. It is found that the present 7-term solution agrees favorably with the solution of McNiven [11] up till the dimensionless time

$\frac{ct}{a} = 4$. As $\frac{ct}{a}$ increases, the discrepancy between the

two solutions increases and the convergence of the series solution presented here slows down considerably. Thus for long times after the time of arrival of the wave front the present method loses its effectiveness and advantages.

IV. Conclusion

The theory of propagating surfaces of discontinuity was employed to study the propagation of transient pressure waves in an extended non-homogenous

viscoelastic medium with a cylindrical cavity.

The solutions were obtained for viscoelastic materials with in homogeneities depending arbitrarily on the radial coordinate r , only, and satisfying, otherwise, the most general linear stress-strain relations. Both stress-prescribed and velocity-prescribed boundary conditions were considered. By disregarding the non-homogeneities, the solutions for the homogeneous viscoelastic medium were, then, obtained. The solutions for the special case of non-homogenous elastic media can also be found easily by neglecting the viscoelastic effects in the solutions already obtained for the non-homogenous viscoelastic media. It was shown that the method presented here yielded good results for short times after the time of arrival of the wave front.

This makes the method useful for transient wave propagation problems. However, over the time range that is far to the time of arrival of the wave front, the method loses its advantages.

The present method may also prove to be useful for solving nonlinear wave propagation problems in nonhomogeneous viscoelastic materials.

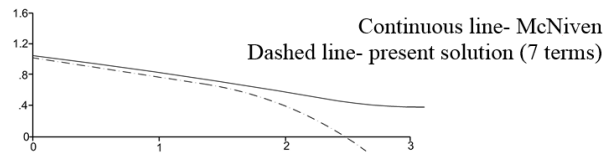


Fig. 1. Radial velocity as a function of a time at the station $r=a$

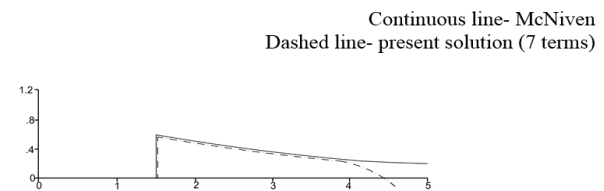


Fig. 2. Radial velocity as a function of time at the station $r=2.5a$

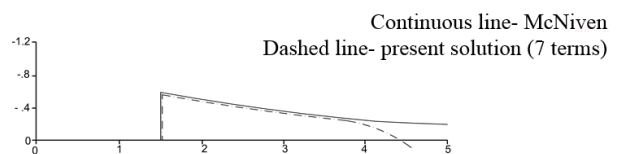
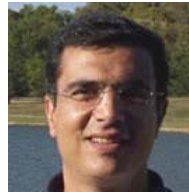


Fig. 3. Radial stress as a function of time at the station $r=2.5a$

References

- [1] Sternberg, E., Chakravorty, J. G." On the propagation of shock waves in a non- homogeneous elastic medium". J. Appl. Mech. 26, , 528, 1959, 528.
- [2] Chou, P. C. and Schaller, R. J., " Propagation of cylindrical waves in a non-homogeneous elastic medium" AIAA Journal, 6, 4 (1966).
- [3] Reddy, D. P. and Marietta, M. G., "Propagation of Shear-Stress Waves in an Infinite Nonhomogeneous Elastic Medium with Cylindrical Cavity "Soc. Amer., 46, 1381 (1969).
- [4] Lindholm, U. S. and Doshi, K. D., "Wave propagation in an elastic nonhomogeneous bar of finite length "J. Applied Mech., 32, 135 (1965).

- [5] Han Zhao and Gérard Gary, "A three dimensional analytical solution of the longitudinal wave propagation in an infinite linear viscoelastic cylindrical bar. Application to experimental techniques" *Journal of the Mechanics and Physics of Solids*, Volume 43, Issue 8, (1995).
- [6] Zhang, J.; Shen, Y. P.; Du, J. K." The effect of inhomogeneous initial stress on Love wave propagation in layered magneto-electro-elastic structures" *Smart Materials and Structures*, Volume 17, Issue 2, pp. 250-260 (2008).
- [7] Yang, Ke . "A unified solution for longitudinal wave propagation in an elastic rod" *Journal of Sound and Vibration*, Volume 314, Issue 1-2, p. 307-329 (2008).
- [8] S. Chin-Teh. Transient rotary shear waves in nonhomogeneous viscoelastic media. *Int. J. Solids Struct*, 7:25{37, 1971.
- [9] Achenbach, J. D. and Reddy, D. P., *Z. Angew. "Wave Propagation in Linearly Viscoelastic Media"* *Math. Phys.*, 18, 141 (1967).
- [10] Avtar Singh and Kishan Chand Gupt."One-dimensional propagation of discontinuities in non-homogeneous linear viscoelastic semi-infinite media" *Sadhana*, Volume 9, (1986).
- [11] McNiven, H. D. and Mengi, Y., " Propagation of transient waves in elastic laminated composites " *int. J. Solids Structures*, 15 (1979c), pp. 303–318.
- [12] T. Y. Thomas, *Plastic Flow and Fracture in Solids*, Academic Press, New York, 1961.



Asad Esmaeily is an associate professor of structural engineering at the Kansas State University, Civil Engineering Department. He earned his PhD in civil engineering from the University of Southern California (USC) in 2001. He also holds an MS in structural engineering and an MS in electrical engineering from the same university. He had an MSc and BS in civil engineering from Tehran University before joining USC graduate school.

Authors' information

Kansas State University.



Shahin Nayyeri Amiri received his Ph.D., M. Phil, and M.Sc degrees in Structural Engineering, second M.Sc. in Geotechnical Engineering, and B.Sc in Civil Engineering. Currently he is lecturer in Civil Engineering department as well as he is research associate in Mechanical and Nuclear Engineering department at Kansas State University. He is teaching theory of Plates and Shells, Vibration, Advanced Dynamics, Design of Tall Buildings for graduate students at Kansas State University. Shahin is a registered professional engineer. His research interest includes Buckling of Plates and Shells, Structural Dynamics, Vibration of Plates and Shells, Beam on Elastic Foundation, Finite Element Method, Biomechanics, Damage detection and Health Monitoring of the Structures, Sustainable Design of Structures, Geotechnical and Earthquake Engineering, Numerical Modeling of Soil Structure Interaction, Slope Stability, field and laboratory soil testing, Bridge Engineering and air bleeding in jet engines.

Study on the Heat Transfer of the Rectangular Fin with Dehumidification: Temperature Distribution and Fin Efficiency

Abdenour Bourabaa¹, Mohamed Saighi², Malika Fekih², Brahim Belal¹

Abstract – This study presents a numerical investigation of the fin efficiency and temperature distribution of a plain fin with combined heat and mass transfer. Using the finite difference scheme the differential equation results from an energy balance on an element of the fin has been solved to obtain temperature distribution along the fin surface. The effects of variations in relative humidity, dry air and fin base temperatures, atmospheric pressure, and fin pitch on temperature distribution and also on fin efficiency are discussed. **Copyright © 2013 Praise Worthy Prize S.r.l. - All rights reserved.**

Keywords: Dehumidification, Fin Analysis, Heat and Mass Transfer, Heat Exchangers, Wet Fin Efficiency

Nomenclature

| | | | | | |
|-----------|---|------------------------------------|----------|---|-------------------------------|
| a_2 | Parameter defined by Eq (6) | (kg_w/kg_a) | T_s | Surface temperature | ($^{\circ}\text{C}$) |
| A_f | Fin heat transfer surface | (m^2) | t | Fin thickness | (m) |
| b_2 | Parameter defined by Eq (7) | (kg_w/kg_a) | u_{fr} | Frontal air speed | (m/s) |
| B | Parameter defined by Eq (10) | (K) | w_a | Humidity ratio of moist air | (kg_w/kg_a) |
| c_{pm} | Isobaric specific heat | (J/kg K) | w_a | Humidity ratio of saturated air | (kg_w/kg_a) |
| F_p | Fin pitch | (mm) | x | Distance from the fin base | (m) |
| h_{hta} | Air-side sensible heat transfer coefficient | ($\text{W}/\text{m}^2\text{K}$) | X | Dimensionless distance | x/L (-) |
| h_{mta} | Mass transfer coefficient on the air-side | ($\text{kg}/\text{m}^2\text{s}$) | η | Fin efficiency | (-) |
| i_{fg} | Enthalpy of vaporization | (J/kg) | θ | Dimensionless fin surface temperature defined by Eq (9) | (-) |
| k | Thermal conductivity of the fin material | ($\text{W}/\text{m K}$) | | | |
| L | Fin length | (m) | | | |
| Le | Lewis number | (-) | | | |
| m | Wet fin parameter defined by Eq (12) | (m^{-1}) | | | |
| m_o | Dry fin parameter defined by Eq (11) | (m^{-1}) | | | |
| N | Number of the nodal points | | | | |
| P | Fin perimeter | (m) | | | |
| P_a | Atmospheric pressure | (Pa) | | | |
| q | Heat transfer rate | (W) | | | |
| RH | Relative humidity | (%) | | | |
| T_a | Bulk air temperature | ($^{\circ}\text{C}$) | | | |
| T_b | Fin base temperature | ($^{\circ}\text{C}$) | | | |
| T_{dew} | Dew point temperature | ($^{\circ}\text{C}$) | | | |

I. Introduction

Heat exchangers are widely used in many applications such as heating, refrigeration and air conditioning systems. In general, they consist of expanded round tubes in a block of continuous fins. Extended surfaces are commonly used as fins to enhance heat transfer between the coil surface and the ambient air by increasing the surface area available for convection. Under dehumidification process the surface temperature is below the dew point temperature of the air being cooled.

This application involves condensation of humid air on the cooled surface. As a result, simultaneous heat and mass transfer occurs along the fin surface.

The change of temperature from the tip to the base of fin is governed by a non-homogeneous second order differential equation. Several solutions to the problem of steady conduction within annular fins or straight fin with different profiles of constant thickness have been presented in the open literature. Under fully wet circular fin, Elmahdy and Biggs [1] presented a numerical study to get an overall fin efficiency.

They assumed a linear relationship between the humidity ratio of the saturated air on the fin surface and its corresponding temperature. Their results show a decrease in the fin efficiency with the increase in relative humidity. Kazeminejad [2] obtained a numerical solution to the differential equation for fully wet rectangular fin using the concept of sensible to total heat ratio. His differential equations are solved numerically using a shooting method which combines the Runge-Kutta method and the Newton-Raphson iteration.

The effects of variations in the relative humidity, dry air temperature and cold fluid temperature on the temperature distribution are investigated and compared with those under fully dry fin surface. Rosario and Rahman [3] studied a radial fin assembly under partially wet, fully wet and fully dry modes. Their fin efficiency depends on the fin surface conditions. Similar to the work by Elmahdy and Biggs [1], Sharqawy and Zubair [4], [5] proposed another relationship between the humidity ratio of the saturated air on the fin surface and its corresponding temperature. They suggested that the maximum temperature at the fin tip for wet condition is the dew point temperature of the air stream. An analytical model and a numerical model have been made by Liang et al [6] to investigate one-dimensional and two-dimensional models for wet fin efficiency of a rectangular fin profile. Their relationship between the saturated specific humidity on the fin surface and its temperature is given by a third degree polynomial expression. Using this polynomial correlation, Naphon [7] carried out a numerical analysis to investigate annular fin under different fin conditions. He used the central finite difference method to obtain temperature distribution along the fin surface in which the effects of inlet conditions of hot and cold fluids and the fin dimensions on the fin surface temperature are presented. Kundu [8] studied analytically longitudinal and pin fins of uniform thickness when combined heat and mass transfer occurs. For the same thermo-geometric and psychrometric conditions, he reported that longitudinal fin gives higher efficiency than the corresponding pin fin. McQuiston and Parker [9] determined that the fin efficiency is strongly influenced by the presence of condensate on the surface.

They studied analytically the fin efficiency of a straight longitudinal fin. Their fin efficiency is believed by many researchers [6] to be more accurate and simply to use. Over a small range of temperatures, McQuiston and his co-author [9] introduced a C parameter to take into account the effect of moisture on fin efficiency. This method is more convenient because it is based on the modified dry fin efficiency formula. In the present work the fin surface temperature over a rectangular fin have been obtained by solving the second order differential equation using finite difference scheme in which the effects of relative humidity, dry air and fin base temperatures, face velocity, fin pitch and atmospheric pressure on the efficiency and temperature distribution under dehumidifying process are investigated.

II. Mathematical Formulas

II.1. Wet Fin Analysis

Fig. 1 shows a schematic diagram of a rectangular fin profile exposed to moving air stream. When the fin surface temperature is below the dew point temperature condensation of humid air on the cold fin surface occurs. In this situation, the total heat transfer from moist air to a surface may be expressed as follows:

$$dq_f = h_{hta} dA_f (T_a - T_s) + h_{mta} dA_f (w_a - w_s) \quad (1)$$

where; A_f , the fin heat transfer surface; h_{hta} and h_{mta} , the sensible heat and mass transfer coefficients, respectively; T_a and T_s , the bulk air and fin surface temperatures, respectively; w_a and w_s , the humidity ratio of moist air and the humidity ratio of saturated air at temperature T_s , respectively; and i_{fg} , the enthalpy of vaporization evaluated at the fin base temperature.

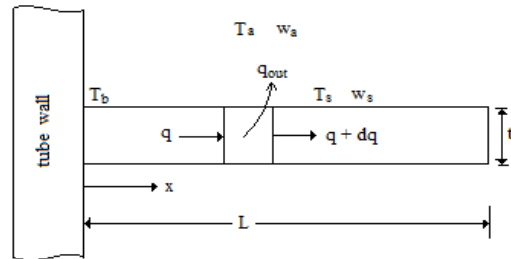


Fig. 1. Schematic diagram of rectangular fin

Introducing the Lewis analogy between heat transfer and mass transfer, Eq. (1) becomes:

$$dq_f = h_{hta} dA_f \left(1 + \frac{i_{fg}}{c_{pm} Le} \frac{w_a - w_s}{T_a - T_s} \right) (T_a - T_s) \quad (2)$$

here, c_{pm} is the isobaric specific heat. The second term on the right side of Eq. (2) describes the effect of mass transfer due to the vapor condensation from humid air.

The Lewis analogy can be expressed as:

$$Le = \frac{h_{hta}}{c_{pm} h_{mta}} \quad (3)$$

hence, the temperature and the corresponding humidity ratio at any location over a wet fin surface are necessary to have the heat transfer rate for wet fin surface, Eq. (2).

The usual assumption is that heat conduction along the fin surface is in one-dimension. In that regard, the following differential equation derived from a simple energy balance on a differential element of a rectangular fin of uniform thickness, shown in Fig. 1, can be obtained: where, k is the thermal conductivity of the fin material and p is the fin parameter

$$\frac{d^2 T_f}{dx^2} + \frac{ph_{hta}}{kA_f} \left[(T_a - T_s) + \frac{i_{fg}(w_a - w_s)}{c_{pm}Le} \right] = 0 \quad (4)$$

The humidity ratio of saturated air at fin temperature can be calculated from the correlation by Sharqawy and Zubair [5]:

$$w_s = a_2 + b_2 T_s \quad (5)$$

where:

$$a_2 = w_{sb} - \frac{w_{sdp} - w_{sb}}{T_{dp} - T_b} T_b \quad (6)$$

$$b_2 = \frac{w_{sdp} - w_{sb}}{T_{dp} - T_b} \quad (7)$$

here, subscripts b and dp referred to base and dew point, respectively.

Following to the work by Elmahdy and Biggs [1], the one-dimensional temperature distribution described by Eq. (4) can be transformed to:

$$\frac{d^2 \theta}{dX^2} - m^2 L^2 \theta = m_o^2 B L^2 C_o \quad (8)$$

where:

$$\theta = \frac{T_a - T_s}{T_a - T_b} \quad (9)$$

$$B = \frac{i_{fg}}{c_{pm}Le} \quad (10)$$

$$m_o^2 = \frac{2h_{hta}}{kt} \quad (11)$$

$$m^2 = m_o^2 (1 + Bb_2) \quad (12)$$

$$X = \frac{x}{L} \quad (13)$$

$$C_o = \frac{w_a - a_2 - b_2 T_a}{T_a - T_b} \quad (14)$$

In the previous equations, L is the fin length, t is the fin thickness and x is the distance from the fin base. The non-homogeneous differential equation can be solved with the following boundary conditions:

$$\text{fin base } X = 0 \quad \theta = \theta_b \quad (15)$$

$$\text{fin tip } X = 1 \quad \frac{d\theta}{dX} = 0 \quad (16)$$

II.2. Analytical Solution

Since Eq. (8) is non-homogeneous, we assume a solution of the form:

$$\theta = \theta_h + \theta_{pt} \quad (17)$$

where; θ_h and θ_{pt} are the homogeneous and the particular solutions, respectively. The use of the boundary conditions, Eqs. (15) and (16), gives us the dimensionless fin temperature in terms of dimensionless distance, X , and the fin parameter, m :

$$\frac{\theta + \theta_p}{\theta_b + \theta_p} = \cosh(mLX) - \tanh(mL) \sinh(mLX) \quad (18)$$

where:

$$\theta_p = \frac{BC_o}{1 + Bb_2} \quad (19)$$

II.3. Fin Efficiency

The fin efficiency is defined as the ratio of the actual heat rate transferred to the fin surface to the maximum possible heat transfer rate if the entire fin surface was at the base temperature.

The actual heat transfer rate can be calculated from: where A_c is the cross section area:

$$q_{fin} = -k \frac{A_c (T_a - T_b)}{L} \frac{d\theta}{dX} \Big|_{X=0} \quad (20)$$

This leads to:

$$q_{fin} = kA_c m (\theta_b + \theta_p) (T_a - T_b) \tanh(mL) \quad (21)$$

The maximum possible heat transfer rate in which the entire fin surface is at the base temperature can be expressed as:

$$q_{max} = \frac{2h_{hta}}{t} (1 + Bb_2) A_c L (T_a - T_b) (\theta_b + \theta_p) \quad (22)$$

The expression of fin efficiency can be now obtained from Eqs (21) and (22), thus:

$$\eta = \frac{q_{fin}}{q_{max}} = \frac{\tanh(mL)}{mL} \quad (23)$$

II.4. Finite Difference Scheme

To obtain a solution to the second order differential equation describing the temperature distribution over the fin surface, we develop here a simple numerical method

using the finite difference scheme. The discrete spatial increment can be computed as:

$$\Delta X = \frac{1}{N} \quad (24)$$

here, N is the number of the nodal points where the fin surface temperature is to be determined, see Fig. 2.

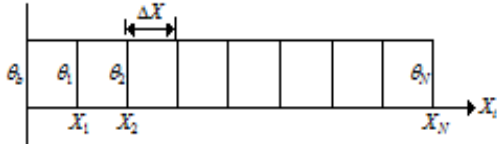


Fig. 2. Finite difference method for 1-D fin

The non-homogeneous second order differential equation, Eq. (8), can be discretized using the central difference for second derivative as follows:

$$\frac{\theta_{i-1} - 2\theta_i + \theta_{i+1}}{\Delta X^2} - m^2 L^2 \theta_i = m_o^2 BL^2 C_o \quad (25)$$

Since we used the central difference approximation, the temperature distribution at first node and at the end node must be known as special cases.

Note that for $i=1$ we have $\theta_0 = \theta_b$ and Eq. (25) can be used directly, thus:

$$-(2 + m^2 L^2 \Delta X) \theta_1 + \theta_2 = m_o^2 BL^2 C_o \Delta X^2 - \theta_b \quad (26)$$

For the end node, at $i=N$, we can generate a backward approximation and, to do this, let's write:

$$\begin{aligned} \frac{d^2\theta}{dx^2} &= \theta'' \text{ and } \theta''|_N = \theta''_N = \\ &= \frac{d}{dx}(\theta')|_N \approx \frac{\theta'_N - \theta'_{N-1}}{\Delta X} \end{aligned} \quad (27)$$

The first derivative at point $N-1$ can be written as:

$$\theta'_{N-1} = \frac{\theta_N - \theta_{N-2}}{2\Delta X} \quad (28)$$

Together, Eqs. (16), (27) and (28) give us:

$$\theta''_N = \frac{\theta_{N-2}}{2\Delta X^2} - \frac{\theta_N}{2\Delta X^2} \quad (29)$$

Putting, now, this expression into Eq. (8), for $i=N$ we get:

$$\begin{aligned} \theta_{N-2} - (1 + 2m^2 L^2 \Delta X^2) \theta_N &= \\ &= 2m_o^2 BL^2 C_o \Delta X^2 \end{aligned} \quad (30)$$

Finally, a system of N equations can be obtained with the combination of Eqs (25), (26) and (30). The fin surface temperature can be easily found by solving this system.

III. Results and Discussion

In this paper, the dimensionless fin surface temperature is plotted against the non-dimensional fin distance measured from the fin base. Firstly, the fin surface temperature resulted from both the analytical and the finite difference methods of the present work are compared with analytical results obtained by Liang et al [6] and Kundu [8] for two values of relative humidity (50% and 90%). The results showed in Fig. 3 demonstrate that the dimensionless temperature decreases with the increase in the non-dimensional distance. This decrease in the dimensionless temperature indicates that the fin temperature increases from the fin base to the fin tip in which reaches its maximum value.

By comparison, the present results obtained from both analytical and numerical methods matched satisfactory even at higher relative humidity. As can be seen, there is a deviation between the results of the present work and those from Liang et al [6] and Kundu [8] especially at higher values of the non-dimensional distance.

The difference decreases with the increase of the relative humidity.

The causes of this deviation can be associated with the temperature/humidity ratio relationships employed before solving the second differential equation that describes the temperature distribution along the fin surface. In the work by Liang et al [6] the driving force for the mass transfer is calculated by a cubic relationship between the humidity ratio of the saturated air and its corresponding temperature in which parameters a, b, c and d are constants. This correlation leads to a higher deviation with the present results particularly at lower relative humidity and higher non-dimensional distance from the fin base. Kundu [8] assumed a linear temperature/humidity ratio relationship over the temperature range between fin base temperature and fin tip temperature. Similar to the work by Sharqawy and Zubair [4] we assumed that the maximum temperature at the fin tip is the dew point temperature of the air stream.

As is known in evaporator applications, the surface is fully wet when its temperature is below the in-coming dew point temperature of the airflow. Therefore, at higher relative humidity value the difference between the fin tip and dew point temperature will be lowered.

Another comparison on the fin efficiency for rectangular fin is shown in Fig. 4. It is clear that the fin efficiency gives good agreement with that of McQuiston and Parker [9] at higher value of relative humidity.

However, deviation between the present fin efficiency with that of McQuiston and Parker [9] can be seen at lower relative humidity (RH=50%). For given fin geometric parameters and flow conditions the fin surface is partially wet for 50% relative humidity.

Thus, in the analytical model presented by McQuiston and his co-author the wet fin efficiency calculation is based on a modified formula obtained from a dry fin.

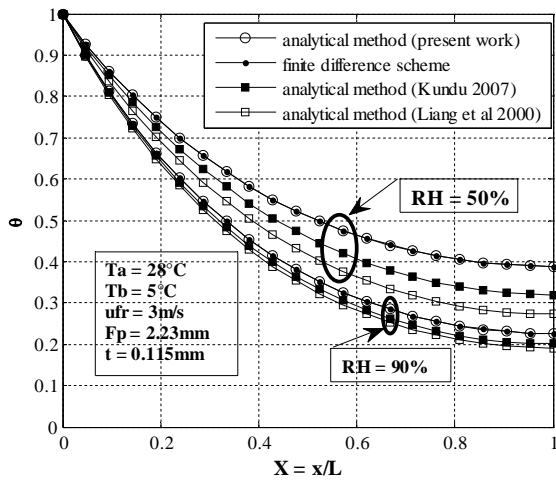


Fig. 3. Fin surface temperature comparison

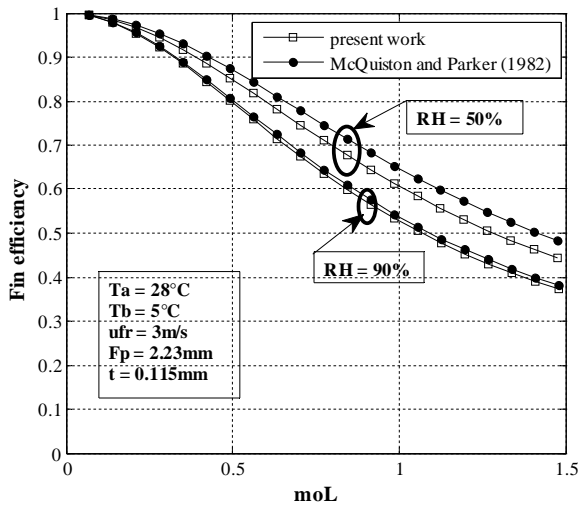


Fig. 4. Fin efficiency comparison

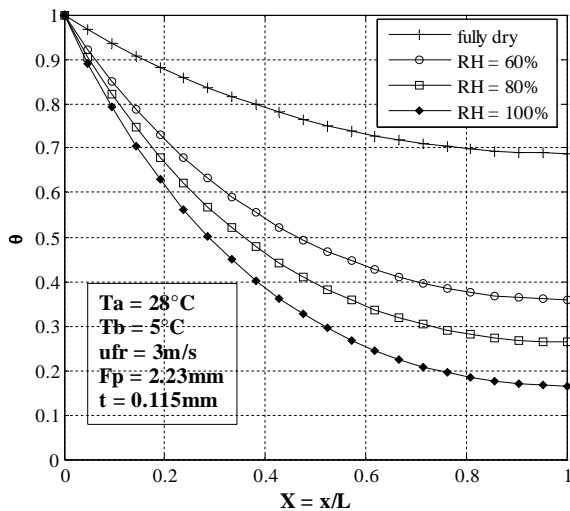


Fig. 5. Effect of relative humidity on fin surface temperature

As reported by Liang et al [6], the McQuiston model fails to distinguish the difference between a partially wet and a fully wet fin and gives higher fin efficiency for partially wet fin.

The effect of relative humidity on the dimensionless temperature is illustrated in Fig. 5. As can be seen, the curves with dehumidification lie below that of dry surface fin. By increasing relative humidity the departure of the fin surface temperature curves from the dry surface becomes greater. This is because more droplets accumulation can be found for higher relative humidity values.

Higher relative humidity translates into a larger amount of droplets on the fin surface. This results in higher amount of heat and mass transfer. On the other hand, higher amount of latent heat transfer can cause higher fin temperature.

The effect of relative humidity on the fin efficiency of rectangular profile is shown in Fig. 6. The fin efficiency decreases with increasing relative humidity. This implies that the fin efficiency is influenced by the amount of moisture on the fin surface.

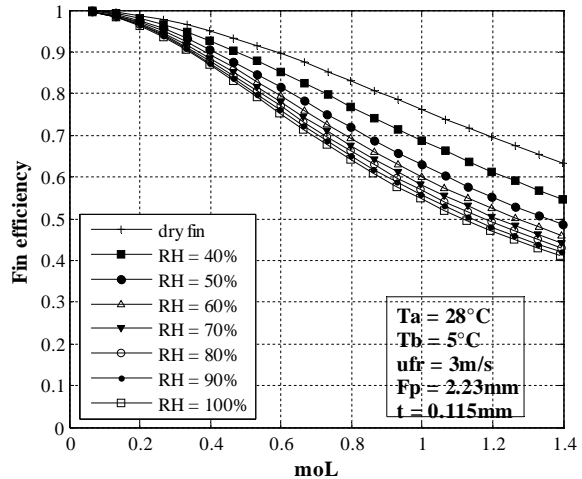


Fig. 6. Effect of relative humidity on fin efficiency

For 40%, 50% and 60% relative humidity values the fin efficiency decreases rapidly with the increase in relative humidity. This means that the fin surface is in partially wet condition. In this situation, the maximum heat transfer through the fin base and the corresponding actual heat transfer through the fin surface do not increase by the same amount and a significant reduction in fin efficiency is seen when relative humidity increased.

Moreover, the width of wet surface region increases with increasing relative humidity and the fin surface becomes in fully wet condition for relative humidity values above 70%.

Here, the ratio of actual heat transfer rate to the maximum heat transfer rate remains approximately constant. However, it can be seen that the effect of relative humidity on the fin efficiency is comparatively small for totally wet fin surface.

The effect of atmospheric pressure on fin efficiency is shown in Fig. 7. As can be seen the fin efficiency increased with increasing atmospheric pressure. When the atmospheric pressure increases the humidity ratio of air also increases.

This makes the moisture content between the bulk air and the fin surface to increase which leads to a higher amount of latent energy. By consequence, actual heat transfer enhancement is seen for higher atmospheric pressure.

Fig. 8 depicts the effect of fin pitch on the fin surface temperature, other conditions being kept constant. The dimensionless temperature increases when the fin pitch increases. Apparently it is attributed to the condensate adhered phenomenon.

The condensate is easier to adhere between fin surfaces when the fin spacing is small. Therefore, the condensate may be blowing off the fin surface when the fin spacing increased. On the other hand, when the fin pitch increase a large amount of condensate water may suspend between fins and this leading to a higher fin surface temperature.

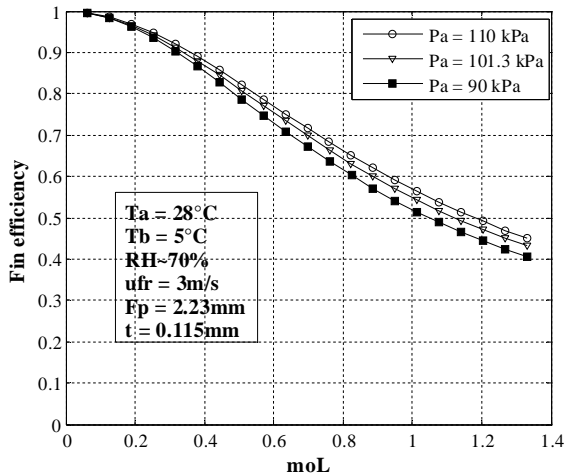


Fig. 7. Effect of atmospheric pressure on fin efficiency

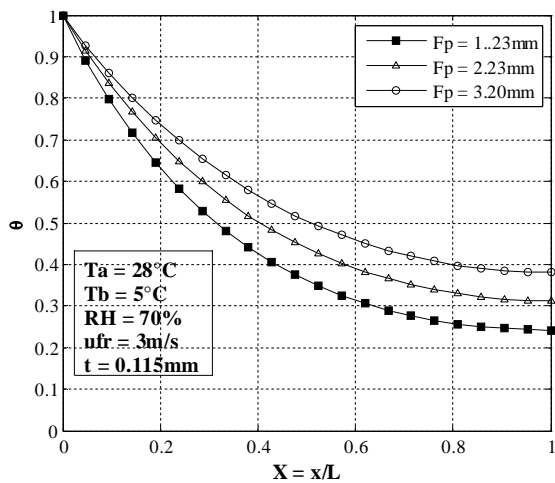


Fig. 8. Effect of fin pitch on fin surface temperature

Fig. 9 illustrates the effect of dry bulb temperature on fin surface temperature. For a given thermal-geometric fin parameters the temperature distribution curves at higher dry temperature are lower. It is known that the dew point temperature increases with the increase of dry temperature. Thus, the potential of heat and mass transfer increases as the dew point temperature increases.

For the influence of fin base temperature variations on the temperature distribution, Fig. 10 shows the variation of fin surface temperature with variation in fin base temperature. For a constant non-dimensional distance lower curve is seen for lower fin base temperature. When the fin base temperature increases the fin temperature also increases. Therefore, the difference between the dew point and the fin temperature increases.

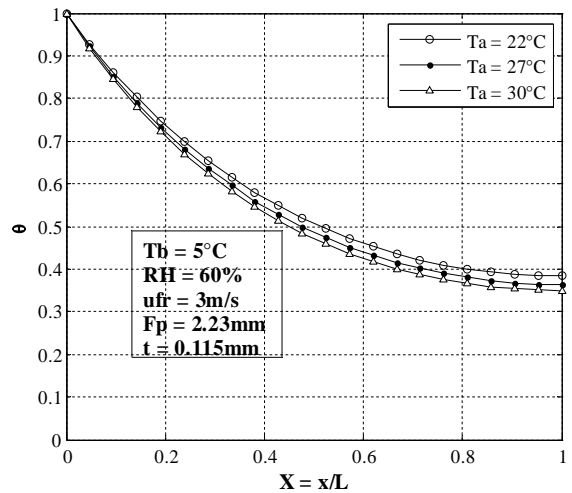


Fig. 9. Effect of dry temperature on fin surface temperature

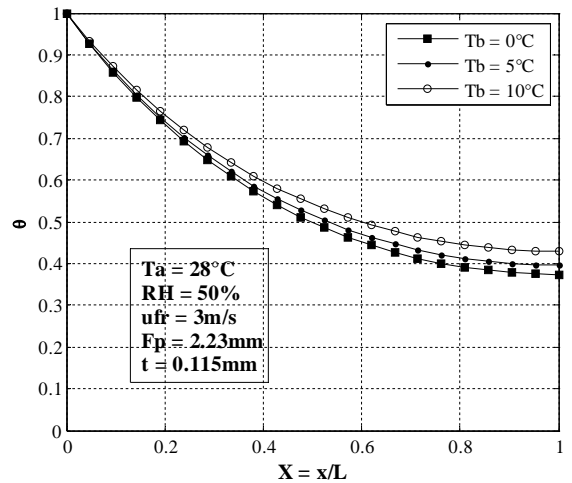


Fig. 10. Effect of base temperature on the fin surface temperature

IV. Conclusion

In this paper, an investigation of the heat transfer characteristics of the rectangular fin with a constant thermal conductivity under dehumidification has been presented. The second order differential equation

describing the temperature distribution over the fin has been solved using an analytical method and a simple finite difference method.

Effects of variations in relative humidity, dry air and fin base temperatures, atmospheric pressure and fin pitch on the temperature distribution and also on the fin efficiency are investigated.

References

- [1] A. H. Elamhdy, R. C. Biggs, Efficiency of extended surfaces with simultaneous heat and mass transfer, *ASHRAE Transaction*, Vol.89, Part.1A, pp. 135-143, 1979.
- [2] H. Kazeminejad, Analysis of one-dimensional fin assembly heat transfer with dehumidification, *International Journal of Heat and Mass Transfe*, Vol. 38, n.3, pp. 455-462, 1995.
- [3] L. Rosario, M. M. Rahman, Analysis of heat transfer in a partially wet radial fin assembly during dehumidification, *International Journal of Heat and Fluid Flows*, Vol. 20, pp. 642-648, 1999.
- [4] M. H. Sharqawy, S. M. Zubair, Efficiency and optimization of an annular fin with combined heat and mass transfer - An analytical solution, *International Journal of Refrigeration*, Vol. 30, pp. 751-757, 2007.
- [5] M. H. Sharqawy, S. M. Zubair, Efficiency and optimization of straight fins with combined heat and mass transfer - An analytical solution, *Applied Thermal Engineering*, Vol. 28, pp. 2279-2288, 2008.
- [6] S. Y. Liang, T. N. Wong, G. K. Nathan, Comparison of one-dimensional and two dimensional models for wet-surface fin efficiency of a plate-fin-and-tube heat exchanger, *Applied Thermal Engineering*, Vol. 20, pp. 941-962, 2000.
- [7] P. Naphon, Study on the heat transfer characteristics of the annular fin under dry-surface, partially wet-surface and fully wet-surface conditions, *International Communication in Heat and Mass Transfer*, Vol. 33, pp. 112-121, 2006.
- [8] Balaram. Kundu, Performance and optimum design analysis of longitudinal and pin fins with simultaneous heat and mass transfer: Unified and comparative investigations, *Applied Thermal and Engineering*, Vol. 27, p. 976-987, 2007.
- [9] F. C. McQuiston, J. D. Parker, *Heating, ventilating and air conditioning: Analysis and design*, (2nd edition, Wiley and Sons, 1982).

Authors' information

¹Centre de Développement des Energies Renouvelables, CDER, 16340, Algiers, Algeria.

²University of Science and Technology, 16111, Algiers, Algeria.



A. Bourabaa was with Thermodynamics and Energetically Systems Laboratory, Faculty of Physics, USTHB, Bab Ezzouar, Al Alia 16111, Algiers, Algeria. He is now a researcher in the "Centre de Developpement des Energies Renouvelables, 16340, Algiers, Algeria.
E-mails: abdenourbourabaa@yahoo.fr
a.bourabaa@cderr.dz



M. Fekih, Researcher with University of Science and Technology Houari Boumediene, USTHB, Faculty of Physics, Laboratory of Thermodynamics and Energetically Systems, LTSE, Bab Ezzouar 16111, Algiers, Algeria.
E-mail: Fekih.mali2005@yahoo.fr

Theoretical, Experimental and Finite Element Analysis of Heat Loss for Designing a Parabolic Concentrator

Abhijeet B. Auti, T. P. Singh, Mandar S. Sapre

Abstract – Parabolic solar concentrators are used for cooking to reduce the burden on conventional fuels. More efficient design of concentrator is possible when utilization of solar energy is known. The paper explains the heat analysis by solar concentrator. The heat input received by the solar radiation is divided for heat utilization, heat loss through convection and radiation and loss through transmission in air medium. All these losses are calculated theoretically and experimentally and verified with finite element analysis using ANSYS. Copyright © 2013 Praise Worthy Prize S.r.l. - All rights reserved.

Keywords: Absorber, Focal Area

Nomenclature

| | |
|---------------|---|
| A | Surface area(m ²) |
| A_c | Aperture area of concentrator (m ²) |
| β | Coefficient of thermal expansion (K ⁻¹) |
| C | Concentration ratio (dimensionless) |
| C_p | Specific heat (J/kgK) |
| d | Aperture diameter of concentrator (m) |
| d_a | Diameter of absorber (m) |
| ε | Emissivity of the black coating (dimensionless) |
| f | Focal length of the concentrator (m) |
| g | Acceleration due to gravity (m/s ²) |
| h | Heat transfer coefficient (W/m ² K) |
| I | Solar irradiance (W/m ²) |
| K | Thermal conductivity (W/m K) |
| L | Characteristic length(m) |
| m | The mass of water (kg) |
| Nu | Nusselt's Number (dimensionless) |
| ρ | Density (kg/m ³) |
| ρ_r | Reflectivity of material of concentrator (dimensionless) |
| Q_1 | Net solar radiation available (W) |
| Q_2 | The utilized heat at the absorber (W) |
| Q_3 | The heat loss through convection and radiation (W) |
| Q_4 | The heat loss while reflection (W) |
| Q_c | Heat loss from convection (W) |
| Q_r | Heat loss from radiation (W) |
| Ra | Rayleigh's number (dimensionless) |
| r | Focal spot radius (m) |
| σ | Stefan Boltzmann constant (J/m ² sK ⁴) |
| t | Time of experiment(s) |
| ΔT | Rise in temperature (°C) |
| T_i | Initial Temperature (°C) |
| T_s | Surface temperature (°C) |
| T_a | Atmospheric temperature (°C) |

| | |
|----------|--|
| ϕ | Rim angle of the concentrator (degrees) |
| θ | Half the angle made by the solar radiations with the axis of the absorber at a particular time (degrees) |
| ν | Kinematic viscosity (m ² /s) |
| % | Percentage |

I. Introduction

The sun has produced abundant energy for billions of years and humanity has been able to utilize only a small fraction of it. [1] The conventional sources of energy are limited and costly. Using solar energy has been proved as the simplest, safest and the most convenient system for cooking food without using traditional fuels.

Two types of solar collectors generally used for cooking are, flat plate collectors and the concentrating collectors. Studies have shown that high performance is achieved with concentrating systems for a major part of the day. Higher temperatures at focus are observed in concentrating collectors by point focussing as, compared with flat plate collectors of same size. [2] Concentrated solar radiation is directed using a collector onto an absorber of smaller area placed within the focal region of the concentrator. [1]

The efficiency of concentrator depends on available solar radiations, reflectivity of material, absorber material and heat loss that takes place during the process. Paper aims to discuss distribution of heat input to concentrator and to the surroundings.

Heat is lost as the reflected radiations are transmitted through the air. Heat is also lost from the surface of the absorber by convection and radiation.

The numerical value of convection coefficient is dependent on the surface geometry, and also on the physical as well as thermal properties of the system [3].

The paper aims to analyze and review the heat losses in the parabolic concentrator and helps to design it for

purpose of cooking; as per the desired heat input.

II. Experimental Heat Analysis

If Q_1 be the net solar radiation available to the concentrator and Q_2 be the utilized heat at the absorber then, if Q_3 is the heat loss through convection and radiation and Q_4 is the heat loss while the radiation is transmitted through the air medium, then the relation between them is given by the equation:

$$Q_1 = Q_2 + Q_3 + Q_4 \quad (1)$$

II.1. Experimental Analysis for Q_2

Experimental setup consists of parabolic dish concentrator with aperture diameter 2.3 m manufactured with aluminum plates of reflectivity, ρ as 0.88.

The experiment is carried out to determine the rise in the temperature of the surface of absorber of size 30 cm \times 30 cm which is made of stainless steel SS 304 L. The experiment is conducted in summer when the average solar irradiance (I) measured using a pyranometer is 800 W/m².

Heat input available at the concentrator of aperture area A_c is calculated as:

$$Q_1 = A_c \times \rho_r \times I = \frac{\pi}{4} 2.3^2 \times 0.88 \times 800 = 2925W \quad (2)$$

Water of different quantities is kept in an absorber and temperature of water after 5 minutes is measured.

The heat utilized, Q_2 is then calculated as:

$$Q_2 = \frac{(m \times C_p \times \Delta T)}{t} \quad (3)$$

where, m is the mass of water in kg, C_p is the specific heat of water, and ΔT is the temperature difference measured over a period of time, t . The results are tabulated below in Table I.

TABLE I
HEAT UTILIZED BY WATER IN THE ABSORBER

| Sr. no | Time Interval [min] | Final temperature of Water T_{wf} [°C] | | | Heat utilized[Watts] | | |
|--------|---------------------|--|------|------|----------------------|---------|--------|
| | | 9 kg | 6 kg | 4 kg | 9 kg | 6 kg | 4 kg |
| 1 | 0-5 | 45 | 48.9 | 48.2 | 859.76 | 1139.34 | 919.26 |
| 2 | 5-10 | 56.9 | 57 | 65.2 | 1162.63 | 904.77 | 1186.6 |
| 3 | 10-15 | 68 | 66.6 | 80.2 | 1084.47 | 1072.32 | 1047 |
| 4 | 15-20 | 78.4 | 72.8 | 87 | 1016.08 | 692.54 | 474.64 |

From the experiment it is found that the average value of heat utilized Q_2 , is in the range of 900 [watts] which is nearly 31%.

Various solar dish concentrators have been tested with operational efficiency ranging from 30% to 35%. [4] Thermal and graphical tests have been performed on the present concentrator to find variation in the optical

efficiency and heat loss factor. From both the analysis, value of optical efficiency obtained ranges from 30 to 35%. [5] As the experimental analysis also shows the value of Q_2 as 30 to 35 % of Q_1 .

The value of efficiency varies due to continuous variation in the solar radiations

For heat loss analysis, the maximum temperature attained by the absorber is measured. The initial temperature of surface is measured as T_i °C. After a period of 40 minutes it is observed that, the temperature of surface of absorber becomes almost steady and is found to be 102-105°C. The result is tabulated below in Table II.

TABLE II
TEMPERATURE AT THE SURFACE OF ABSORBER

| Time | Temperature (°C) | ΔT (°C) |
|------|------------------|-----------------|
| 0 | 35 | - |
| 5 | 38 | 3 |
| 10 | 45 | 7 |
| 15 | 52 | 7 |
| 20 | 61 | 9 |
| 25 | 70 | 9 |
| 30 | 77 | 7 |
| 35 | 84 | 7 |
| 40 | 89 | 5 |
| 45 | 94 | 5 |
| 50 | 97 | 3 |
| 55 | 100 | 3 |
| 60 | 102 | 2 |
| 65 | 104 | 2 |
| 70 | 105 | 1 |
| 75 | 105 | 0 |
| 80 | 105 | 0 |

III. Theoretical Heat Analysis

Absorber loses heat to surrounding by convection and radiation when heat is given to it. Maximum heat loss takes place when steady state temperature is reached. So heat losses are calculated for 105°C.

The overall heat loss rate, is calculated by considering the heat loss from convection, Q_c and heat loss from radiation, Q_r as:

$$Q_3 = Q_c + Q_r \quad (4)$$

III.1. Theoretical Heat Loss through Convection

Heat loss to surroundings occurs from top, bottom and vertical sides by natural convection. Heat flow by convection is calculated as:

$$Q = h \times A \times \Delta T \quad (5)$$

$$\therefore Q_c = \text{Heat loss from vertical surface} + \text{Heat loss from top surface} + \text{Heat loss from bottom surface}$$

a) Heat transfer coefficients are calculated using the formulae given below [5]:

1) Rayleigh's number:

$$Ra = \frac{g\beta\rho C_p}{\nu K} \Delta T L^3 \quad (6)$$

where β , ρ , K , ν are calculated for air at mean temperature. ΔT is rise in temperature and L is the characteristic length:

For vertical cylinder:

$$L = d_a \quad (7)$$

For top and bottom circular plates:

$$L = d_a/4 \quad (8)$$

2) Nusselt's Number, Nu :

For vertical cylinder:

$$Nu = 0.56 \times (Ra)^{1/4} \quad (9)$$

For top surface

$$Nu = 0.54 \times (Ra)^{1/4} \quad (10)$$

For bottom flat surface

$$Nu = 0.27 \times (Ra)^{1/4} \quad (11)$$

3) Heat transfer coefficient:

$$h = \frac{K \times Nu}{L} \quad (12)$$

Properties of absorber selected are having specification as density of steel $\rho = 8000 \text{ kg/m}^3$, C_p for steel = 500 J/kgK, surface temperature $T_s = 105^\circ\text{C}$, atmospheric temperature $T_a = 35^\circ\text{C}$, emissivity ϵ of the black coating = 0.88 [1] [3].

Similarly, Properties of air taken at mean temperature, are having specification as density $\rho = 1.029 \text{ kg/m}^3$, thermal conductivity $k = 0.0297 \text{ W/mK}$, specific heat $C_p = 1009 \text{ J/kgK}$, kinematic viscosity, $\nu = 20.02 \times 10^{-6} \text{ m}^2/\text{s}$, coefficient of thermal expansion, $\beta = 2.915 \times 10^{-3} \text{ K}^{-1}$ [1][3].

b) Convection loss from various surfaces

Values of Ra , Nu , and value of h for all the surfaces are calculated by substituting input parameters in Eqs. (6) to (12). These are used to determine convection losses at various surfaces as shown in the Table III below.

III.2. Heat loss by Radiation

Heat also radiates from the vertical cylindrical surface,

top and bottom circular areas of the absorber to the surroundings which is computed using standard formula (13) Radiation losses are given by:

$$Q_r = \epsilon \times \sigma \times A \times (T_s^4 - T_a^4) \quad (13)$$

where T_s is final surface temperature 105°C and T_a is ambient temperature 35°C :

$$Q_r = .88 \times 5.67 \times 10^{-8} \times \left[(\pi \times .3 \times .3) + 2 \times \frac{\pi}{4} \times (.3)^2 \right] \times (378^4 - 308^4) = 241.48 \text{ W}$$

TABLE III
CONVECTION HEAT LOSSES

| Surface | L | Ra | Nu | h (W/m ² K) | Heat Loss (W) |
|----------|-----|--------------------|--------|------------------------|---------------|
| Vertical | d | 9.44×10^7 | 55.197 | 5.465 | 108.15 |
| Bottom | d/4 | 1.63×10^6 | 9.64 | 3.82 | 18.89 |
| Top | d/4 | 1.63×10^6 | 19.28 | 7.64 | 37.78 |
| | | | | Total | 164.82 |

\therefore Total heat loss through Convection, $Q_c = 164.82 \text{ W}$

Hence the total heat flow by convection and radiation is calculated by substituting value of Q_c and Q_r in (4):

$$Q_3 = 164.82 + 241.48 = 406.30 \text{ W}$$

Considering $Q_1 = 2925 \text{ W}$ shows that 14% of heat is lost through convection and radiation.

IV. Finite Element (FE) Analysis and Verification of Experimental Result

The surface temperatures obtained from experimental analysis are taken as reference for ANSYS analysis. The temperature rise determined experimentally is compared using ANSYS. The model of the absorber of SS 304 L is prepared using ANSYS workbench 12.

IV.1. Input to ANSYS

(1) The properties of absorber

Following properties of steel are entered in the Engineering data [6]:

1. Density 8000 kg/m^3 and specific heat 502 J/kgK
2. Thermal Conductivity (W/mC) and coefficient of thermal expansion variation with Temperature (C) is as shown in the Table IV.

(2) Available heat input – quantity and location

(1) Quantity: The absorber has three faces – top, bottom and vertical cylindrical to which convection and radiation loads have been applied. Total surface area of absorber is 0.424 m^2 . Considering 35% utilized heat [5] and 14% losses, total available heat flux at the focal region can be estimated as:

$$Q_{tot} = \frac{2925 \times [35 + 14]\%}{0.424} = 3380 \text{ W/m}^2$$

TABLE IV
PROPERTIES OF MATERIAL OF ABSORBER

| Temperature | Thermal Conductivity (W m ⁻¹ C ⁻¹) | coefficient of thermal expansion (× 10 ⁶) |
|-------------|---|---|
| 20 | 14.8 | 15.3 |
| 50 | 15.3 | 16.0 |
| 75 | 15.8 | 16.5 |
| 100 | 16.2 | 17.0 |
| 125 | 16.6 | 17.4 |
| 150 | 17 | 18.9 |

(2) Location: According to Stine and Harrigan (1985), the reflected rays from the concentrator do not form a point but a circular image of finite size centred about the focal point of the parabola. Two major reasons for this effect are that the sun’s rays not being truly parallel and due to concentrator errors [4]. The given concentrator has focal length $f = 500$ mm, If $d = 2.3$ m is the aperture diameter, then, the rim angle ϕ of the concentrator and the focal spot radius are calculated as [7] [8]:

$$\phi = 2 \tan^{-1} \left[\frac{d}{4f} \right] = 97.98^\circ \quad (14)$$

$$r = \frac{2f \tan \theta}{\cos \phi (1 + \cos \phi)} \quad (15)$$

Here 2θ is the angle made by the sun radiations with the axis of the absorber at a particular time. It is found that in 20 minutes, sun’s position (zenith angle) will change by 4° on an average [9].

So the concentrator is tracked after every 20 min and axis of concentrator is aligned with the sun direction. Still there are non-parallel rays which travel at a maximum angle of $32'$. [Sun is not a point but has an apparent arc of $32'$.][10]

So with $\theta = 16'$, it can be found that the value of r is, $r = -0.04$ m. Negative sign indicates that focal point is in the interior of the concentrator volume. This focal radius is due to non-parallel rays. Due to errors in concentrator geometry, actual radius will be still lesser.

Analysis with same input applied at the region was done by varying radii. Thus it was concluded that average radius of focal region for the present configuration is 0.02 m. The heat input of 3380 W/m^2 is applied at circular region of this radius.

IV.2. Analysis

Solar flux as calculated is applied. The heat transfer coefficients are taken as calculated in the previous section. Convection and radiation loads are applied at the surface of the absorber as shown in Figs. 1.

Initial temperature is taken as 35°C . The temperature change is measured for every 1 min for 20 min using the

probe in ANSYS. [11] The temperature distribution after every 5 minutes is shown in the Figs. 2.

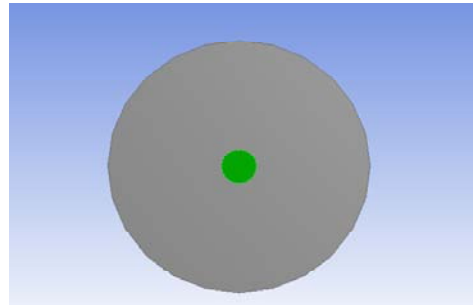
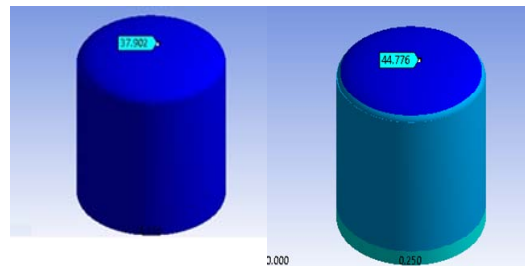


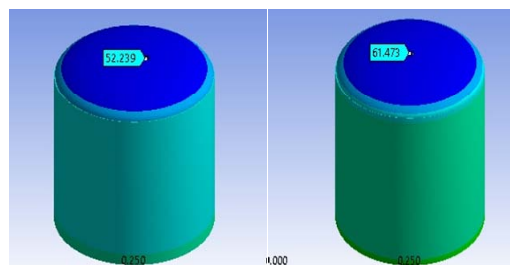
Fig. 1(a). Location of focal radius



Fig. 1(b). Convection and radiation loads in thermal analysis



(a) After 5 min (b) After 10 min



(c) After 15 min (d) After 20 min

Figs. 2. Temperature variation in ANSYS

Results in Table V and Fig. 3 show the same readings of surface temperature in ANSYS. This shows that theoretical heat loss calculations and heat utilized calculations seem to be right.

Considering the heat loss Q_3 as 406.30 W, heat input Q_1 as 2925 W, Q_2 as 35% and using Eq. (1), the distribution of heat input Q_1 is shown in Fig. 4.

TABLE V
TEMPERATURE VARIATION WITH TIME

| Time | Temperature Experimental (°C) | Temperature ANSYS (°C) | Error (%) |
|------|-------------------------------|------------------------|-----------|
| 0 | 35 | 35 | - |
| 5 | 38 | 37.902 | -0.25 |
| 10 | 45 | 44.776 | -0.498 |
| 15 | 52 | 52.24 | 0.462 |
| 20 | 61 | 61.473 | 0.775 |

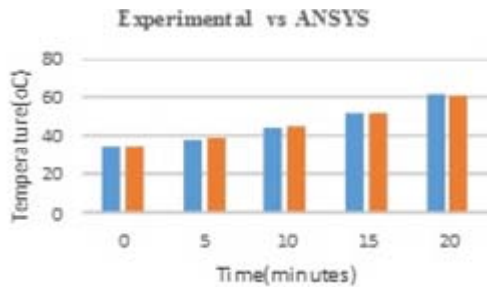


Fig. 3. Temperature – Experimental vs ANSYS – Graphical comparison

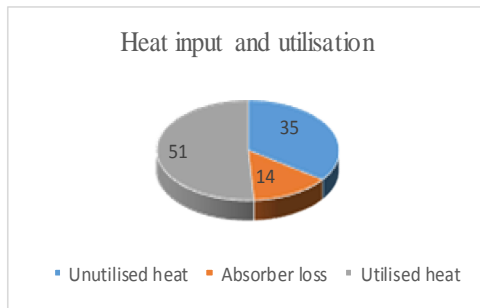


Fig. 4. Proportion of heat utilized

V. Conclusion

It has been observed through experimental and FE analysis that 14% of the heat is lost by convection and radiation at the surface of the absorber. Also the heat utilized value is in the range of 30 to 35% of the total input. 50% of the heat remains unutilized.

The analysis shows that value of unutilized heat can be reduced by designing exact shape of parabolic concentrator and with minimum manufacturing error. Similarly, heat loss to surrounding can be reduced by using minimum size of absorber. Concentrator can be designed as per the requirement of heat at the focal area and can be decided using this analysis.

Acknowledgements

I am extremely thankful to Prof. Nitin Solke, Prof. Ashok Chavan, Dr. Abhijit Bhattacharya, and Prof. Laxman Bhargava for their timely guidance.

References

[1] Sukatme S.P., *Solar Energy* (2nd edition Tata McGraw-Hill Publishing Company Ltd.) pp(197-200)

[2] Socrates Kaplanis, George Barakos, Flat plate and concentrating collectors: a comparison of their performances. first results, *Simpozionul national cu participare international, PROiectarea ASIstat, de Calculator, PRASIC '02, Vol. III – Design de Prodis 7-8 November ,Brasov, România, ISBN 973-635-076-2*

[3] Frank Keith, Mark S. Bohn, Principles of Heat Transfer (6th edition,Cengage Learning, 2001)

[4] W.G. le Roux, Solar tracking for a parabolic dish used in a solar thermal Brayton cycle ,*centre for renewable and sustainable energy studies*

[5] Abhijeet Auti , Dr. T. P. Singh , Dr. Dilip R. Pangavhane., Thermal analysis of parabolic concentrator for finding optical efficiency by different methods with varying parameters, *International Journal of Engineering and Technology, Vol 5 No 2 Apr-May 2013*

[6] *ASME Boiler and Pressure Vessel Code 2010 ,Part D Properties (Metric)*

[7] .B.Stine and R.W.Harrigan "*Solar Energy Systems Design*" (John Wiley and Sons, Inc. 1986)

[8] Qiao Xu ; Qiancheng Zhao ; Yejun Qin ; Youduo Peng, Concentrating performance analysis for large dish solar concentrator, *Proc. SPIE 7997, Fourth International Seminar on Modern Cutting and Measurement Engineering, 799725 (May 26, 2011); doi:10.1117/12.891271*

[9] Spencer, J.W., "*Fourier Series Representations of the Position of the Sun*" *Search, Vol 2 1971, p.172*

[10] Micheal Seeds , *Foundations of Astronomy, Cengage learning, 12th edition ,2013*

[11] *ANSYS thermal analysis guide, Release 12.0; ANSYS, Inc. website: http://www1.ansys.com/customer/content/documentation/120/ans_the.pdf.*

Authors' information

Symbiosis International University, Lavale, Pune 412 115, India.



Abhijeet B. Auti He has completed Bachelor of Mechanical Engineering and M.E. in Heat Power from Pune University. He has a teaching experience of 13 years. He is working as Assistant Professor at Symbiosis Institute of Technology and pursuing Ph.D at Symbiosis International University. He is the Author of 12 Engineering books which have been published for different universities of India.



Dr. T. P. Singh, Director, Symbiosis Institute of Technology, Symbiosis International University; Pune received his B.E. Degree in Mechanical Engineering, M.E. and Ph. D in Industrial Engineering from Thapar University, Patiala. He has more than 24 years of teaching experience. He has supervised M.E. and Ph.D research and has worked on many sponsored research and consultancy projects. His specialization areas include Waste Minimization, Lean Manufacturing, Flexibility, Technology Management and Electric Discharge Machining.



Mandar S. Sapre He has completed Bachelor of Production Engineering from Mumbai University with First Class from Fr. Conceicao Rodrigues college of Engineering and currently pursuing M.Tech. in CAD/CAM from Symbiosis Institute of Technology. Also He is working as faculty in the Mechanical Engineering department.

Instant Hot Water Generation System for Domestic Utility in Rural Areas

P. Selvakumar¹, P. Somasundaram²

Abstract – Hot water is required for bathing and cleaning of utensils in the morning and evening hours in Indian homes. People in rural areas use fossil fuels, cooking gas and rarely electricity for hot water production. Present day solar collectors cannot help in instant hot water generation. A system involving a parabolic trough, an evacuated tube and Therminol D-12 oil is developed and studied for instant hot water generation. The developed system works satisfactorily during low incident solar radiation. Experiments on the developed new system show that Therminol D-12 helps to generate hot water at a temperature of 60°C within 10 minutes of time with low solar radiation. **Copyright © 2013 Praise Worthy Prize S.r.l. - All rights reserved.**

Keywords: Instant Hot Water, Therminol, Domestic Water Heating

Nomenclature

| | |
|--------|---|
| Cp_o | Specific heat of oil in J/kg K |
| Cp_w | Specific heat of water in J/kg K |
| m_o | Mass flow rate of oil in kg/s |
| m_w | Mass flow rate of water in kg/s |
| Tf_o | Temperature of oil at the heating coil outlet in °C |
| Ti_o | Temperature of oil at the heating coil inlet in °C |
| Tf_w | Temperature of water at the storage tank outlet in °C |
| Ti_w | Temperature of water at the storage tank inlet in °C |

I. Introduction

Flat plate collector and evacuated tube collector are widely used in India for domestic hot water generation.

One of the problems is the time required for producing hot water by solar energy is greater than that of LPG and electrical energy. So, a solar water heater with better heat transfer methodology need to be devised to produce the required hot water in short period of time.

In India, research on domestic solar water heater seems to be saturated after started using ETC water heaters.

Quite a large number of literatures and practical implications are made towards industrial hot water generation and steam production. Goswami [1], [2] had studied and presented the technological developments in the field of solar thermal applications.

Literatures pertaining to the heat transfer fluids are reviewed and some of the significant findings are discussed. Use of alternate heat transfer fluid for solar applications is studied by many researchers.

But all of them are related to high temperature applications like steam generation and industrial process heat generation.

Cheng et al. [3] used syltherm800 liquid oil in an experiment to study the heat transfer characteristics in the receiver tube of parabolic trough solar collector. Zang and Yamaguchi [4] used supercritical carbon dioxide to study the heat transfer phenomenon in evacuated tubes.

Roberto Grena and Pietro Tarquini [5] used molten nitrate as heat transfer fluid and conducted experiments on solar linear Fresnel collector. Lin Lu et al. [6] used nanofluids as heat transfer fluid for studying the open thermosyphon effect on high temperature evacuated tube collector. Glycol/Water mixture, synthetic hydrocarbon oils, paraffin hydrocarbon oils and aromatic hydrocarbon oils are used as heat transfer fluid in different applications.

Syltherm800 hydrocarbon oil is used in many parts of the world for steam generation using solar energy. Glycol/water mixtures and aromatic hydrocarbon oils are suggested for domestic applications. Therminol is aromatic hydrocarbon oil which can be used for medium and high temperature applications. Evacuated tube collectors (ETC) are widely used in domestic hot water generation because of high performance, low cost and easy maintenance. High temperatures can be obtained in solar water heaters with evacuated tube fitted with parabolic trough collector compared to flat plate collector based solar water heaters. Water is used as heat transfer fluid in these collectors. When water with hardness greater than 300ppm is used in evacuated tubes, scale forms along the tube walls at higher temperature.

The performance of the evacuated tube gets decreased because of scale deposits.

By using an alternate heat transfer fluid, the problem of scale formation can be eliminated. At higher temperatures water starts to boil inside the tubes which lead to evaporative energy loss. When a fluid with boiling point higher than that of water is used as a heat transfer fluid, the problem of boiling can be eliminated.

The present day solar water heaters seem to be a luxurious need for the lower middle class people.

Most of the upper middle class people purchased solar water heaters because of government subsidy and many of them are not in use because of proper maintenance. For a country like India which is dominated by lower income group and villages, a cost effective and energy efficient system can only make them to think of buying solar water heater. Global warming can be reduced when the villages shift over from using fossil fuels to solar water heaters. An experimental model is developed with the help of a parabolic trough and an evacuated tube with therminol oil as heat transfer fluid for instant hot water generation.

II. Therminol D-12 as Heat Transfer Fluid

Different kinds of heat transfer fluids are used in large scale hot water generation and steam generation. One among those fluids has to be identified for domestic usage. In large solar power plants synthetic and mineral oils are used as heat transfer fluids. The flow path is too long in large scale applications and the flow path is short in domestic applications. Selvakumar et al. [7] studied the heat transfer and fluid flow characteristics of various heat transfer fluids like helium, therminol, calfo, duratherm, exceltherm, molten salt, dynalene and vegetable oil. Therminol is suggested as the best heat transfer fluid for short flow length applications.

Therminol is available in different grades and its selection depends on the safe operating temperature limits. Different grades of therminol and their working temperatures are shown in Fig. 1. Therminol-D12 which has flash point of 260°C and fire point of 267°C is an inexpensive and easily available heat transfer fluid. The other fluid properties like density and viscosity are close to that of water. The comparison of fluid properties of Therminol-D12 with that of water is shown in Table I.

III. Parabolic Trough Collector

Parabolic trough collectors (PTC) are used in high temperature applications. However, their usage in domestic sector is studied by Valanarasu and Sornakumar [8].

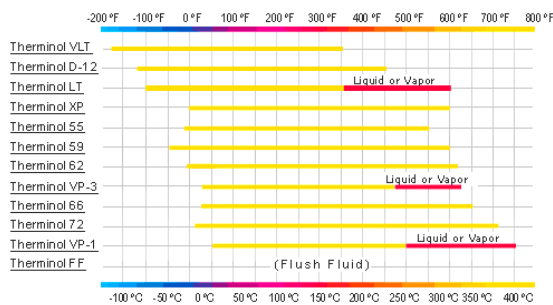


Fig. 1. Therminol grades and operating temperature limits (Source:www.therminol.com)

TABLE I
COMPARISON OF THERMINOL D-12 AND WATER

| Properties | Therminol-D12 | Water |
|---------------|-----------------------|------------------------|
| Density | 927 kg/m ³ | 1000 kg/m ³ |
| Specific heat | 2.5 kJ/kg K | 4.186 kJ/kg K |
| Kinematic | 145.5 centi Stoke @ | 0.801 centi Stoke |
| Viscosity | 33°C | @ 30°C |
| | 8.14 centi Stoke @ | 0.294 centi Stoke |
| | 120°C | @ 100°C |

In that work, the parabolic trough is constructed of fibre glass and the collector tube is made of copper enclosed by a glass cover. Water is used as heat transfer fluid and forced circulation system is adopted. The system's performance is good but the compactness criterion is not achieved. After studying several literatures [1]-[12], the idea for present work is developed. In the present work parabolic trough made of aluminium sheet with polished aluminium reflector is used. The collector tube is the simple water-in-glass evacuated tube which is used in present day evacuated tube solar water heaters. The parabolic trough profile is generated in CAD software and fabricated with the help of wooden templates. Use of aluminium sheet and aluminium reflector considerably reduced the cost of the system which is one of the prime objectives of this work.

The evacuated tube is made of borosilicate glass and its length and diameter are 1500 mm and 47 mm respectively. Only one parabolic trough with single evacuated tube at the focal axis is used in this system.

The picture of those two are shown in Fig. 2.

IV. Header and Passive Heating Coil

Therminol-D12 is chosen as the heat transfer fluid for the new system. So, passive heating of water in the storage tank is going to take place.

The specific heat of therminol is less than that of water. So, the amount of heat required to raise the temperature of therminol is comparatively less than that of water. Also, the scaling problem in the tube is completely eliminated by using therminol as heat transfer fluid. For transferring heat from therminol to water, a passive heating coil is required in the storage tank.

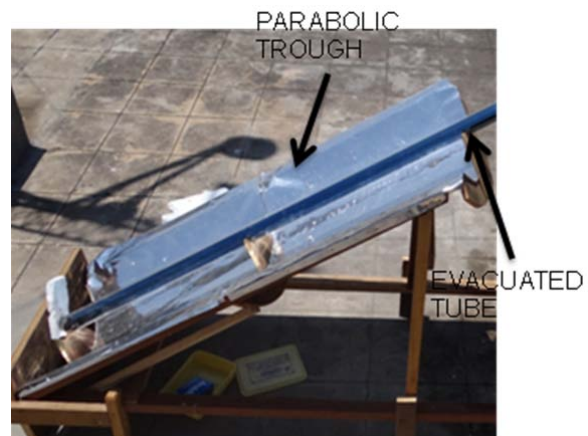


Fig. 2. Parabolic trough with evacuated tube

Copper tube of diameter 6 mm and length 4 m is used as a passive heating coil. The dimensions of the copper tube are based on heat transfer calculations. Using NTU method of heat exchanger design the length of the copper tube is determined as 4 m. The heating coil is shown in Fig. 3. For recirculation of therminol into the evacuated tube, the ends of the heating coil are connected to a header.

The header is coupled to the evacuated tube such that leakage of oil does not occur.

The header is specially designed for this particular type of system. The header made of aluminium comprises of two cylindrical parts, one with 50 mm outer diameter, 47 mm inner diameter and internal thread of pitch 1.5 mm.

The other cylindrical part is of 47mm inner diameter, 55 mm outer diameter with an external thread of pitch 1.5 mm. The inlet and outlet of the heating coil are connected to the header and a dummy hole is provided on the header to fill the heat transfer fluid initially. The model of the header and real picture of the header are shown in Fig. 4 and Fig. 5 respectively.



Fig. 3. Heating Coil

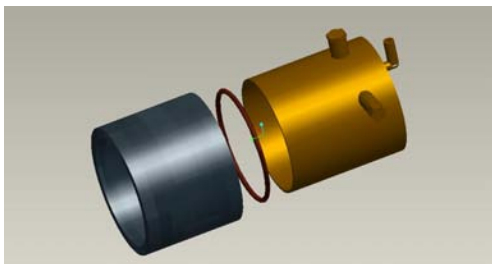


Fig. 4. Model of the Header



Fig. 5. Header in experimental set up

V. Experimentation

Experiment is conducted on a sunny day to find the hot water generation rate of the newly designed system. Solar radiation is measured by pyrheliometer which is available in the Solar Radiation Monitoring Station of Kongu Engineering College. The experimental setup is kept along north-south direction with parabolic trough and ETC facing south direction.

The temperature of therminol oil at inlet and outlet, temperature of water at inlet and outlet, parabolic trough temperature and evacuated tube temperature are noted using standard thermocouples. The readings are taken at every 15 minutes of interval from 10am to 12.15pm. The experimental set-up is shown in Fig. 6.

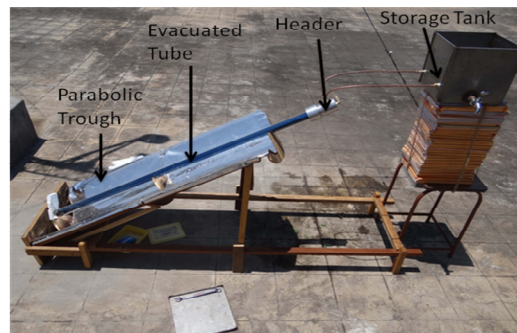


Fig. 6. Experimental set up

VI. Results and Discussion

Direct radiation, diffuse radiation and global radiation are measured with the help of pyrheliometer. Direct radiation varied between 600 W/m^2 to 700 W/m^2 .

Diffused radiation varied between 290 W/m^2 to 350 W/m^2 . Global radiation varied between 750 W/m^2 to 1000 W/m^2 . Direct radiation and global radiation reached minimum during 10.15am to 10.30am because of passing clouds. The variations in the radiation are plotted and shown in Fig. 7. The temperatures of the oil entering and leaving the passive heating coil are plotted against time in Fig. 8. After 15 minutes of the exposure of experimental setup to solar radiation, the inlet temperature of oil reached 87°C . Gradually the oil temperature increased to 168.2°C .

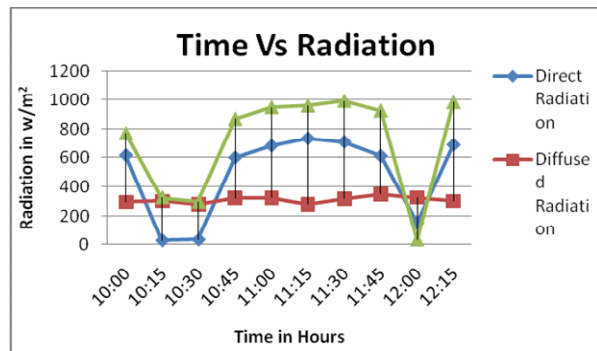


Fig. 7. Time Vs Solar Radiation

The water temperature at the inlet of the storage tank is 35°C and by taking the heat from oil, water attains a temperature of 57°C within 15 minutes. Hot water temperature drops down during 10.15am to 10.30am because of drop in oil temperature. This variation happened due to passing clouds. The capacity of the storage tank used in this experiment is of 15 litres. For a maximum oil inlet temperature of 168.2°C, the hot water temperature reaches 88.6°C. Even though the capacity of the tank is increased, the newly designed system can supply a hot water of temperature around 40°C to 45°C in a shorter period of time. Also, there is no need for the equipment to be kept in sunlight throughout the day. The system is a compact structure with only one parabolic trough and one evacuated tube. The temperature profiles recorded during the experiment is shown in Fig. 8.

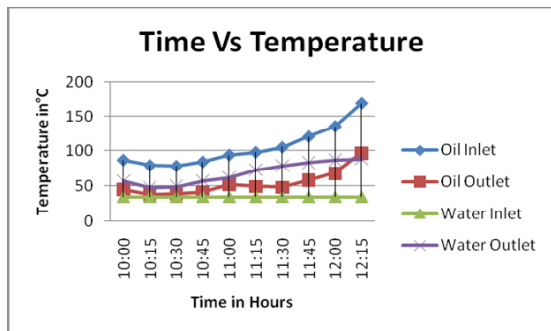


Fig. 8. Time Vs Temperature

The performance of the system is indicated by the effective heat transfer in the passive heating coil. Heat rejected by the oil and heat absorbed the water are calculated using the formula. The ratio of heat absorbed by the water to heat lost by the oil gives the efficiency of hot water generation:

$$\text{Heat rejected by oil} = m_o \times C_{p_o} \times (T_{i_o} - T_{f_o})$$

where m_o = mass flow rate of the oil:

$$\text{Heat absorbed by water} = m_w \times C_{p_w} \times (T_{i_w} - T_{f_w})$$

$$\text{Efficiency of hot water generation} = \frac{\text{Heat absorbed by water}}{\text{Heat rejected by oil}}$$

The hot water generation efficiency is plotted against time in Fig. 9. Maximum efficiency of 94.5% is achieved at 12 noon. This efficiency gives clear idea that therminol D-12 can be used as a heat transfer fluid to produce hot water in short duration of time. The safety aspects in using therminol oil are also discussed in the following paragraph.

VII. Safety Aspects in using Therminol D-12

Hot water is generated within 10 to 15 minutes by exposing the water heater to solar radiation.

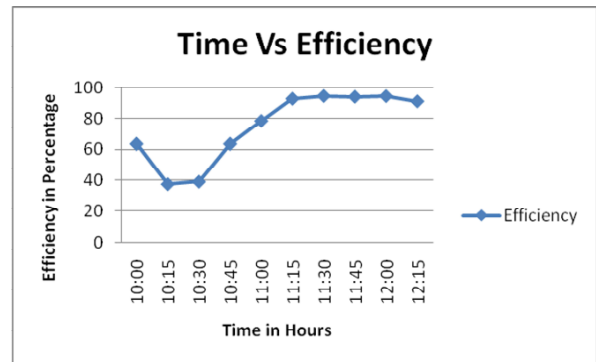


Fig. 9. Time Vs Efficiency

It is not necessary for the entire system to be kept all through the day in the sunlight.

The fire point of Therminol-D12 is 267°C and the operating temperature of oil inside the water heater is 80°C to 150°C. So, there is no chance of fire accidents to occur. Therminol-D12 is suited to applications where a low odor and low toxicity are desired. Therminol-D12 is an FDA recognized fluid and has excellent industrial hygiene properties. This product meets the requirements established by the FDA at 21 CFR 172.882, 172.884, 178.3530, and 178.3650. The user is not going to have direct contact with therminol. Passive heating of water is done by circulating hot therminol in closed copper coils.

There is no possibility for miscibility of therminol with water. The boiling point of Therminol-D12 is 192°C and the possibility of increase in pressure of the fluid inside the pipe is also restricted.

VIII. Conclusion

From the experimental results, it is clear that the newly designed solar water heating system with Therminol-D12 as heat transfer fluid can be used for producing instant hot water in homes.

Within 15 minutes of time, hot water at a temperature of 60°C is produced by the system. This will also help the Indian homes in saving their fuel bills. Commercial evacuated tube water heaters which seem to be expensive for middle class and rural population can be replaced by this new system.

The evacuated tube and parabolic trough are the readily available components whereas the header and passive heating coil are designed for the new system. Also, the new system will contribute to the nation's campaign on reduction in fossil fuel burning which leads to global warming.

The behavior of this newly developed system under various climatic conditions, cost benefits and the life of the Therminol D-12 oil are being studied.

Acknowledgements

I sincerely thank Mr. Christo K. George, Managing Director, Hykon Solar Energy Private Limited for

supporting the project financially and morally. I also thank Automatic Solar Radiation Monitoring Station, Kongu Engineering College for providing solar radiation data.

References

- [1] D.Y. Goswami, Solar thermal power technology: present status and ideas for the future, *Energy Sources Vol. 20*, pp. 137-145, 1998.
- [2] D.Y. Goswami, S. Vijayaraghavan, S. Lu, G. Tamm, New and emerging developments in solar energy, *Solar Energy Vol.76*, pp. 33-43, 2004
- [3] Z.D. Cheng, L.Y. He, J. Xiao, Y.B. Tao, R.J. Xu, Three-dimensional numerical study of heat transfer characteristics in the receiver tube of parabolic trough solar collector, *International Communications in Heat and Mass Transfer, Vol. 37*, pp. 782-787, 2010
- [4] X.R. Zhang, H. Yamaguchi, An experimental study on evacuated tube solar collector using supercritical CO₂, *Applied Thermal Engineering, Vol. 28*, pp. 1225-1233, 2008.
- [5] Roberto Grena, Pietro Tarquini, Solar linear Fresnel collector using molten nitrates as heat transfer fluid, *Energy, Vol. 36*, pp. 1048-1056, 2011.
- [6] Lin Lu, Zhen-Hua Liu, Hong-Sheng Xiao, Thermal performance of an open thermosyphon using nanofluids for high-temperature evacuated tubular solar collectors: Part 1: Indoor experiment, *Solar Energy, Vol.85*, pp. 379-387, 2011.
- [7] P. Selvakumar, S.A. Prasanth, N. Rakesh, A. Vignesh, Fluid flow and heat transfer analysis on multiple parabolic trough collectors by varying heat transfer fluids, B.E. dissertation, Dept. Mech. Eng., Anna University of Technology Coimbatore, India, 2011
- [8] A. Valan Arasu, T. Sornakumar, Performance characteristics of parabolic trough solar collector system for hot water generation, *International Energy Journal Vol.7*, pp.137-145, 2006.
- [9] I. Budihardjo, GL Morrison, M.Behnia, Natural circulation flow through water-in-glass evacuated tube solar collectors, *Solar Energy Vol. 81*, pp. 1460-1472, 2007
- [10] I. Budihardjo, GL Morrison, Performance of water-in-glass evacuated tube solar water heaters, *Solar Energy Vol.83*, pp. 49-56, 2009
- [11] E Azad, Theoretical and experimental investigation of heat pipe solar collector, *Experimental Thermal Fluid Sciences Vol.32*, pp. 1666-1672, 2008
- [12] D.R. Mills, Advances in solar thermal electricity technology, *Solar Energy Vol.76*, pp. 19-31, 2004

Authors' information

¹Dept Mechanical Engineering, Kongu engineering College, Perundurai-638052, Erode, TN, India.
E-mail: selva_vit@yahoo.co.in

²Dept. Mechanical Engineering, EBET Group of Institutions, Kangeyam, Erode, TN, India.
E-mail: somuannauniv@hotmail.com



P. Selvakumar is working as Assistant Professor in the Department of Mechanical Engineering, Kongu Engineering College, Perundurai, Erode, India. He had his Bachelor Degree in Mechanical Engineering from M.S.University and Master Degree in Energy Systems Engineering from VIT University. Currently, he is pursuing his research degree in Anna University, Chennai. He is a member in the Society of Automotive Engineers. He has published two papers in International Journal. He has executed various projects in the field of solar energy, computational fluid dynamics and biomass gasification.



Dr. P. Somasundaram is working as Professor and Head in the Department of Mechanical Engineering, EBET Group of Institutions, Kangeyam, Erode, India. He had his Bachelor and Master degree in Mechanical Engineering and Ph.D. degree from Anna University, Chennai. He has 15 years of teaching experience and 2 years of industrial experience. He is guiding 8 research scholars and his area of expertise is low temperature applications. He has executed various projects in the fields of refrigeration and solar energy.

Numerical Study of Ice Melting Inside a Rectangular Cavity and a Horizontal Cylinder Including Convective Effects

Christiano G. S. Santim, Luiz Fernando Milanez

Abstract – The present work deals with the numerical study of ice melting inside a rectangular cavity with all isothermally heated walls and inside a horizontal cylinder with isothermally heated wall, utilizing a CFD code. Initially the solid material is sub-cooled. The objective is to verify the influence of the heating in the melting process as well as the sub-cooling effect. Some simplifying hypotheses were assumed in the mathematical model. The thermophysical properties of phase change material were considered constants, except for the density where the relation proposed by Gebhart and Mollendorf [1] was used. The problem was solved by using a mathematical formulation based on the enthalpy-porosity method, which allows the use of a fixed spatial grid. The total heat flux in the inner surfaces was obtained for the systems, as well as several temperature profiles, streamlines and melting front positions. Correlations for the total ice melting time as a function of the Stefan number was presented. It was found that the convective effects directly influences the melting front profiles, the heat transfer in the systems and the melting rates. **Copyright © 2013 Praise Worthy Prize S.r.l. - All rights reserved.**

Keywords: Horizontal Cylinder, Ice Melting, Natural Convection, PCM, Simulation

Nomenclature

| | |
|-----------|--|
| T | Temperature, K |
| T_m | Temperature of melting, K |
| T_r | Reference temperature, K |
| T_{ref} | Reference temperature at $T = 277\text{K}$ |
| T_{hot} | Heating temperature, K |
| H | Total enthalpy, J kg^{-1} |
| h | Sensible enthalpy, J kg^{-1} |
| L | Latent heat, J kg^{-1} |
| c_p | Specific heat, $\text{J kg}^{-1} \text{K}^{-1}$ |
| k | Thermal conductivity, $\text{W m}^{-1} \text{K}^{-1}$ |
| x, y | Cartesian coordinates, m |
| t | Time, s |
| S | Porosity function |
| S_e | Source term for energy equation |
| S_b | Buoyancy source term |
| P | Effective pressure, $\text{kg m}^{-1} \text{s}^{-2}$ |
| C | Morphology constant, $\text{kg m}^{-3} \text{s}^{-1}$ |
| V_l | Volume of liquid, m^3 |
| V_o | Total volume of the systems, m^3 |
| g | Gravity, m s^{-2} |
| Ste | Stefan number |
| f | Liquid fraction of the system |
| r_{sp} | Temperature coefficient at $T = 277 \text{K}$ |
| u | Velocity component in x direction, m s^{-1} |
| v | Velocity component in y direction, m s^{-1} |
| ρ | Density, kg m^{-3} |

| | |
|---------------|---|
| \mathbf{v} | Velocity vector, $\mathbf{v} = (u, v)$ |
| μ | Dynamic viscosity, $\text{kg m}^{-1} \text{s}^{-1}$ |
| γ | Porosity of computational cell |
| τ_{melt} | Total ice melting time, s |
| β | Thermal expansion coefficient, K^{-1} |

I. Introduction

Melting and solidification have great influence on nature and modern applications such as in metal purification and processing, in the latent heat thermal energy storage systems, as well as in many other technologies. Problems involving phase change are non-linear due to the presence of natural convection, which affects directly the morphology of interface solid-liquid.

This work deals with melting processes, utilizing ice as the phase change material (PCM).

There are basically two methods to formulate phase change problems, one utilizes the temperature as a dependent variable in the energy equation, and the other utilizes the enthalpy. The first experimental studies of melting inside rectangular geometries considering the convective effects were conducted by Hale and Viskanta [2]. Gau and Viskanta [3] conducted experiments regarding melting and solidification processes of gallium inside a rectangular recipient with one of the vertical walls heated.

Brent et al. [4] applied the mathematical formulation based on the enthalpy-porosity method in the melting of pure gallium, inside a rectangular cavity. The rectangular cavity had an aspect ratio (height/ width) of 0.714, the

same applied in the present work.

The numerical results were compared with those obtained experimentally by Gau and Viskanta [3] and showed good agreement. Ghasemi and Molki [5] studied numerically the melting of an unfixed solid in a square cavity using the fixed-grid enthalpy formulation.

The authors considered a square cavity with all isothermal heated walls for the Rayleigh number range $0-10^8$. They concluded that for the Rayleigh number equal to zero, there was no liquid motion and the melting progressed by conduction. Natural convection appears as the Ra increases, forcing the solid to move downwards.

They also observed that the flow is more active in the upper region and more melting of the solid surface was observed there. Hannoun et al. [6] tried to clarify the controversy over tin and gallium melting inside a rectangular cavity heated from the side. Several issues were discussed about the influence of some parameters (grid sizes, discretization schemes, grid-converged solution) on the flow structure of melting process in this geometry. Previous experimental studies were discussed.

In the numerical analysis, three common discretization schemes (upwind, hybrid and centered) and several grid sizes were tested. The authors stated that the flow structure must be multicellular in this case. Ygit [7] solved analytically a two-dimensional problem with phase-change considering only conduction as mechanism of heat transfer by using a linear perturbation method.

As results the author obtained several melting fronts as function of time. Temperature profiles were also presented in the shell and mold.

The melting process of PCMs inside a horizontal cylinder was studied numerically and experimentally by several authors. This problem constitutes an interesting subject of study due to the differences observed in the results that have been reported in the literature.

The review presented here considers only papers that utilized ice as PCM. Rieger and Beer [8] studied experimentally and numerically the fixed ice melting inside a horizontal cylinder, considering the tube wall heated isothermally. In their experiments, the authors employed a radius of 0.030m and temperatures of 279, 281, 283 and 288K of the isothermally heated cylinder wall. In the numerical study, two radii were used: 0.032m and 0.016m. The same values of temperatures were employed for the heating.

The results obtained numerically for the radius of 0.032m were compared with the experimental results and were found to be in good agreement.

They concluded that the lower heat transfer on the ice melting process occurred around 281K. Riviere and Beer [9] conducted an experimental investigation of melting of unfixed ice in an isothermal horizontal cylinder and compared the melting rates obtained with an analytical solution, showing good agreement.

The authors concluded that for bottom wall temperatures $\leq 281.4K$ a thermally stable zone exists in the region beneath the ice bulk. For wall temperatures slightly above this value, this zones extends up to the

tube wall. For temperatures above 284.6K, stable zone vanishes and this behavior affected directly the interface shape.

Fukusako and Yamada [10] conducted a comprehensive review about ice melting and water freezing problems under a variety of conditions. They presented a review of relations for thermophysical properties of pure and sea ice. Souza and Vielmo [11] analyzed numerically the same problem studied by Rieger and Beer [8], but in their analysis they considered only the radius of 0.032m. The enthalpy formulation was employed. The results obtained were compared with those presented by Rieger and Beer [8] and were in good agreement. The spatial grid utilized consisted of 40×40 nodes. The results included the phase change interface position, temperature, density and streamlines profiles for heating of the cylinder wall at temperatures of 277 and 281K.

In the present work, the melting of ice within a rectangular cavity and a horizontal cylinder were considered. The CFD ANSYS Fluent12.0 code was used for the numerical simulation and the software ANSYS ICEM CFD was employed for the generation of the computational grids.

The problem formulation was based on the enthalpy-porosity method. The main objective of this work is to analyze the influence of the isothermal heating applied to the walls in both geometries considered, as well as the initial ice sub-cooling effect in the melting process inside a rectangular cavity.

II. Mathematical Formulation

This work consists of two cases. Case I deals with the ice melting inside a rectangular cavity with all walls heated and case II analyzes the melting of ice within a horizontal cylinder. Three different temperatures (T_{hot}) were used on the isothermal heating of the geometries: 279, 281 and 283K. At instant $t = 0$, all the phase change material is in the solid state, with uniform temperature. It should be noted that at this instant the solid is considered sub-cooled of 1K. Such assumption was adopted for all simulations, except when verifying the influence of the degree of the initial ice sub-cooling for case I, where sub-cooling of 1 and 5K were used for two values of the Stefan number: 0.076 and 0.126.

The cavity aspect ratio was taken as 0.714. The horizontal cylinder with a radius of 0.016m was utilized in case II. Simplifying hypotheses were made in the development of the mathematical model.

The model was considered two-dimensional and transient. The flow in the melting process was assumed laminar and incompressible. The thermophysical properties of the material were considered constants at mean temperature utilizing the relation proposed by Silva [12]. For the density, the relation proposed by Gebhart and Mollendorf [1] was used, equation (1), by implementation of an UDF (User Defined Function).

This non-linear relation takes into account the anomalous behavior of the water density around 277K:

$$\rho = \rho_{ref} \left(1 - rsp |T - T_{ref}|^{1.894816} \right) \quad (1)$$

where ρ_{ref} represents the density at $T_{ref} = 277$ K and rsp means the temperature coefficient ($rsp = 9 \times 10^{-6}$ / K).

The numerical simulation was performed with the aid of a CFD code (ANSYS Fluent12.0), utilizing the Solidification/Melting model, which employs a mathematical formulation based on the enthalpy-porosity. This formulation allows the use of a fixed spatial grid. The governing equations are presented below, in rectangular coordinates.

The energy conservation equation can be written as:

$$\frac{\partial(\rho H)}{\partial t} + \nabla \cdot (\rho \mathbf{v} H) = \nabla \cdot (k \nabla T) + S_e \quad (2)$$

The source term S_e can be calculated as:

$$S_e = \frac{\partial(\rho \Delta H)}{\partial t} + \nabla \cdot (\rho \mathbf{v} \Delta H) \quad (3)$$

and the enthalpy of the material is computed as being the sum of the sensible enthalpy, h , and the latent heat, ΔH :

$$H = h + \Delta H \quad (4)$$

where the sensible enthalpy can be presented by:

$$h = h_r + \int_{T_r}^T c_p dT \quad (5)$$

In the case of an isothermal phase change (T_s [solidus temperature] = T_l [liquidus temperature] = T_m), the last term of Eq. (3) vanishes and ΔH can be defined as a function of temperature:

$$f(T) = L \quad T > T_m \quad (6)$$

$$f(T) = 0 \quad T < T_m \quad (7)$$

In the regions where the liquid state is present, it is necessary to write equations for the flow.

Assuming that the fluid is Newtonian and the flow is laminar, Eq. (8) is obtained for the mass conservation, Eq. (9) for the flow in the x direction, and Eq. (10) for the flow in the y direction, the last two equations representing the conservation of momentum (Navier-Stokes equations):

$$\frac{\partial \rho}{\partial t} + \nabla \cdot (\rho \mathbf{v}) = 0 \quad (8)$$

$$\begin{aligned} \frac{\partial(\rho u)}{\partial t} + \nabla \cdot (\rho \mathbf{v} u) &= \\ &= \nabla \cdot (\mu \nabla u) - \frac{\partial P}{\partial x} + S_u \end{aligned} \quad (9)$$

$$\begin{aligned} \frac{\partial(\rho v)}{\partial t} + \nabla \cdot (\rho \mathbf{v} v) &= \\ &= \nabla \cdot (\mu \nabla v) - \frac{\partial P}{\partial y} + S_v + S_b \end{aligned} \quad (10)$$

The porosity function (S), present in Eq. (9) and Eq. (10), is defined as:

$$S = -C \frac{(1-\gamma)^2}{\gamma^3 + \varepsilon} \quad (11)$$

where C is a constant reflecting the morphology of the melting front (this constant is a large number, usually $10^4 - 10^7$) and ε is a small number (0.001) to prevent division by zero. The S_b source term (Eq. (12)), present in the Eq. (10), is a buoyancy term used to induce natural convection in the cavity (assuming the Boussinesq approximation):

$$S_b = \rho_r g \beta (T - T_r) \quad (12)$$

The mathematical formulation in cylindrical coordinates is analogous to that described for rectangular coordinates. It should be cited that in the cylindrical coordinates, the buoyancy term appears in the radial and angular directions.

The solver model utilized in the numerical simulation was pressure-based. The coupling pressure-velocity was solved by the SIMPLE method. The scheme used in the discretization of momentum and energy equations was the Power-Law, and the scheme used for the pressure was the PRESTO!. Considering the symmetry of the problems, the computational grids used were of 44×63 nodes in directions x and y , respectively (case I), and of 50×50 for case II. The grid sizes were selected after verification that the results were invariant with more refinement. The convergence criterion for the energy equation was 10^{-8} and for the velocities and continuity was 10^{-5} and 10^{-4} respectively.

III. Validation of the CFD Code

To validate the code ANSYS Fluent12.0 for the proposed work, the results obtained experimentally by Rieger and Beer [8] served for comparison, presented in Fig. 1. Fig. 1 shows that the numerical analysis is in good agreement with the experimental results. It should be cited that in experimental analysis, Rieger and Beer [8] used a cylinder with radius equal to 0.030m whereas the present numerical result was achieved with a radius equal to 0.032m. Therefore, the use of the CFD ANSYS Fluent12.0 code in this problem can be considered satisfactory.

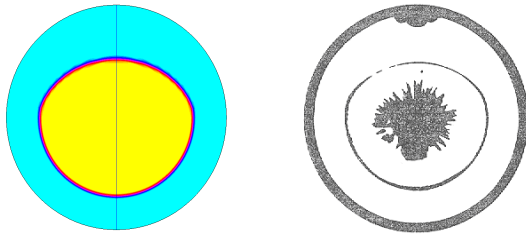


Fig. 1. Comparison of numerical analysis and experimental melting front obtained by Rieger and Beer [8] with $T_{hot} = 283K$ for τ (dimensionless time) = 0.045

IV. Results and Discussion

This work consists of two cases as previously mentioned. Case I considers ice melting inside a rectangular cavity and case II deals with ice melting within a horizontal cylinder

IV.1. Case I: Ice Melting Inside a Rectangular Cavity

Figs. 2, 3 and 4 show the isotherms and streamlines with an isothermal heating of 279, 281 and 283K, respectively, for two stages of the melting process.

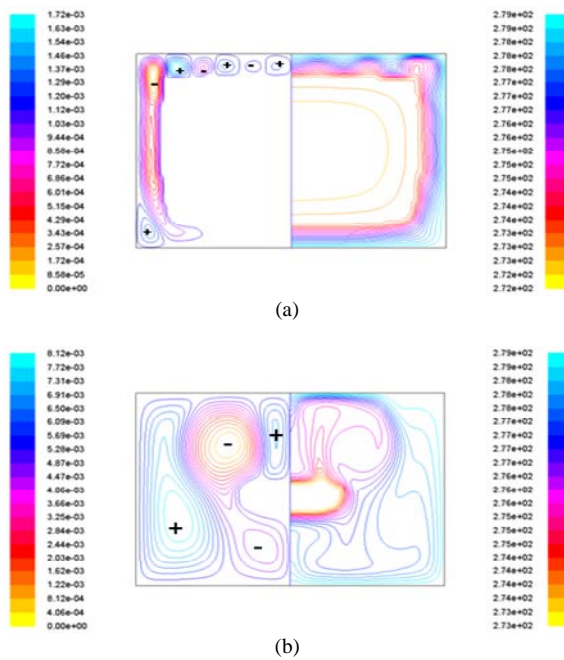


Fig. 2. Streamlines at left side and isotherms at right for $Ste = 0.076$. (a) $t = 2510s$; (b) $t = 8676s$

By analyzing Fig. 2, it may be noticed a complex flow at all stages of the melting process for $Ste = 0.076$. The higher heat transfer rate occurs at the lower region and the clockwise vortex (in blue) located at the bottom cavity corner is the main responsible for it. The positive sign means clockwise direction, whereas the negative means counter clockwise direction. This representation was considered for all streamlines. A complex flow structure also can be noted in Figs. 3 and 4.

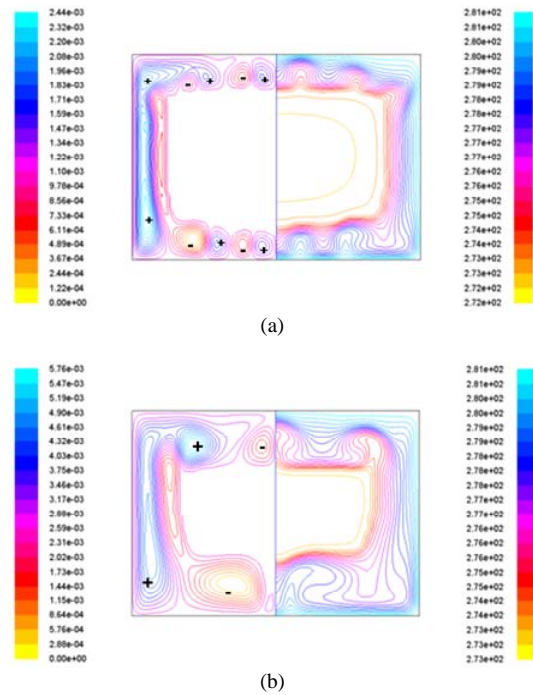


Fig. 3. Streamlines at left side and isotherms at right for $Ste = 0.100$. (a) $t = 3350 s$; (b) $t = 5182s$

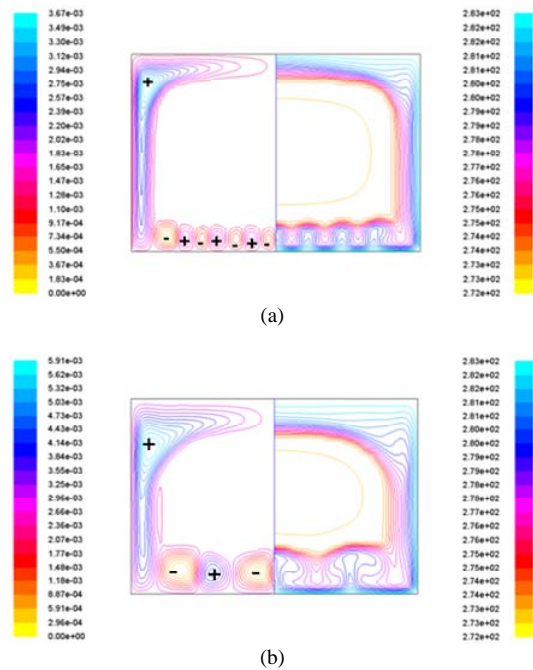


Fig. 4. Streamlines at left side and isotherms at right for $Ste = 0.126$ (a) $t = 1604s$; (b) $t = 2604s$

For $Ste = 0.100$ the same amount of the vortices are observed at the upper and lower regions for the two stages of the melting process, showing that the heat transfer in this case is almost the same in these zones while for $Ste = 0.126$ the heat transfer rate is higher at the upper region. It is important to mention that, in this paper, the ice was considered constrained. Therefore, heat conduction is predominant only at the beginning of the melting process.

With the increase of the liquid layer, the convection takes a dominant role, directly influencing the heat transfer, melting rates and melting front shapes. It should be noted that the Stefan number (Ste) is defined as:

$$Ste = \frac{c_p (T_{hot} - T_m)}{L} \quad (13)$$

The liquid fraction in the system f can be represented by:

$$f = \frac{V_l}{V_o} \quad (14)$$

where V_l is the volume of liquid and V_o is the total volume of the geometries considered. Fig. 5 presents the liquid fraction as function of dimensional time, for several values of the Stefan numbers.

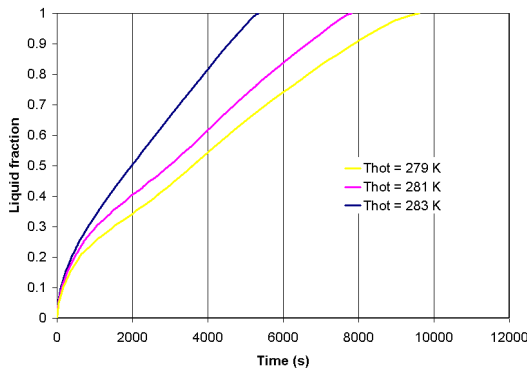


Fig. 5. Liquid fraction versus time for several wall temperatures

It may be observed that the higher the wall heating, the lower the total melting time.

Fig. 6 shows the sub-cooling effect for two values of the Stefan number. It can be seen that the sub-cooling effect is higher as Ste decreases and the lower the degree of sub-cooling, the lower the total melting time (for the same Stefan number). This effect can be verified more clearly by the analysis of the heat flux in the internal surfaces.

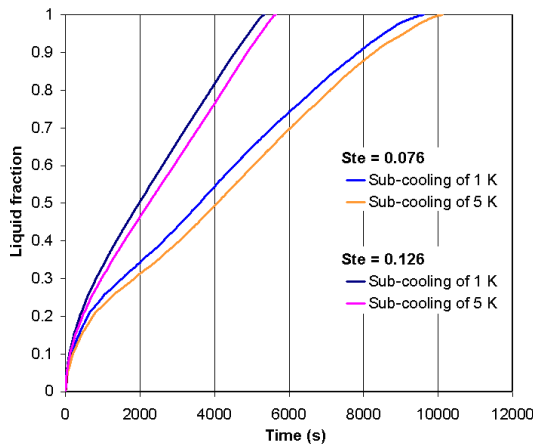
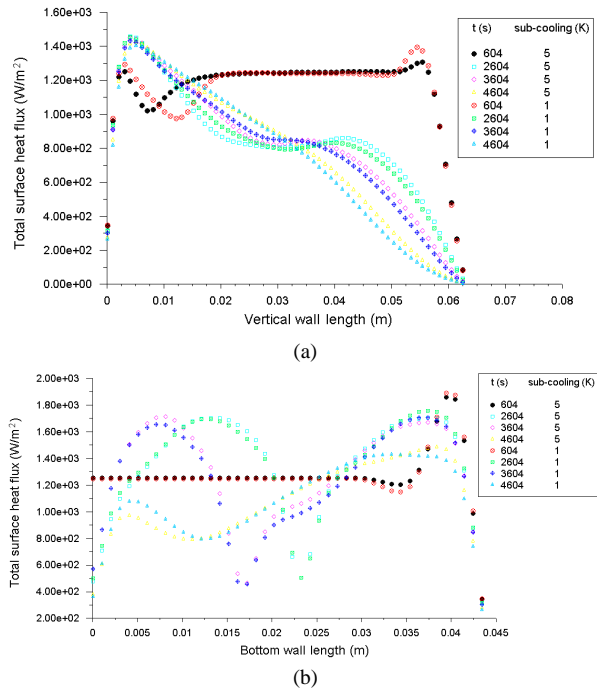


Fig. 6. Sub-cooling effect for two values of the Stefan number

Figs. 7 show the heat flux in the internal surface of the vertical and bottom walls of the rectangular cavity for $Ste = 0.126$ and for two degrees of sub-cooling and Figs. 8 present the inner surface heat flux in the vertical and top walls for $Ste = 0.076$, also showing the effects of two different degrees of sub-cooling.

Due to the horizontal symmetry of the problem, the results can be obtained for just half of the cavity. It is important to know the direction in which the internal heat flux was plotted in each wall. For the vertical wall, it was considered from south to north, whereas for the other walls, west to east direction was applied.



Figs. 7. Heat flux on the inner surfaces for two degrees of sub-cooling for $Ste = 0.126$. (a) Vertical wall length; (b) Bottom wall length

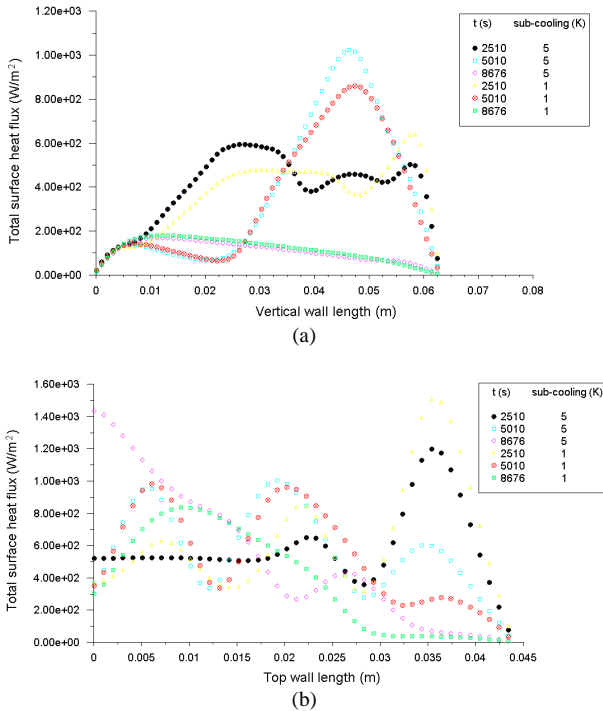
Analyzing Fig. 7(a) it may be noticed that the internal surface heat flux is greater at the lower region.

In the Fig. 7(b), can be verified the vortices influence on the inner surface heat flux of the bottom wall. Figs. 8 shows that, contrary to what was observed in Figs. 7, the heat flux at the inner surface of the cavity walls is higher in the upper region.

Besides, it may be noticed that the degree of the sub-cooling for $Ste = 0.076$ affects significantly the heat flux at the walls, a behavior expected by the analysis of Fig. 6. The discrepancy observed in Fig. 8(b) at the final stage of the melting process, due to the upper morphology of the melting front, which is concave for sub-cooling of 1K and convex (not presented in this work) for sub-cooling of 5K.

IV.2. Case II: Ice Melting Within a Horizontal Cylinder

This case deals with ice melting inside a horizontal cylinder.



Figs. 8. Heat flux on the inner surfaces for two degrees of sub-cooling for $Ste = 0.076$. (a) Vertical wall length; (b) Top wall length

Three different temperatures were used in the isothermal heating wall of the cylinder with radius 0.016m. Figs. 9 show the streamlines (left side of the cylinder) and isotherms (right side) for a wall heating of 279K and two stages of the melting process.

It may be noted the anomalous behavior of the water density causing a flow movement different from that in normal fluids. As the process develops a second vortex appears. This vortex is the major responsible for the heat transfer from the heated wall to the ice and it can be noted by the isotherms.

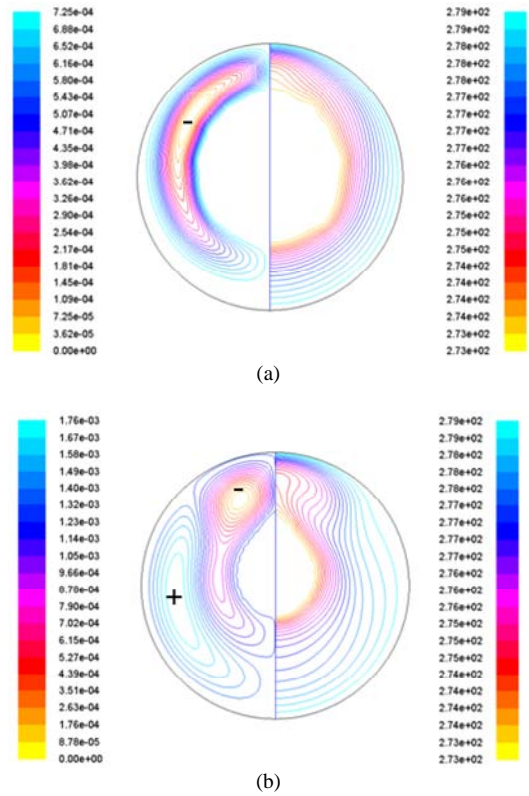
Therefore, for $Ste = 0.076$, the higher heat transfer inside a horizontal cylinder occurs at the lower region. As noticed in Figs. 2, which presents results for the same wall heating, the solid would move upwards, if not fixed.

It should be cited that, for $Ste = 0.126$, the heat transfer is higher at the upper region of the cylinder, being very slightly at the upper zone for the $Ste = 0.100$ (streamlines and isotherms of these two values of Stefan number were not presented in this work).

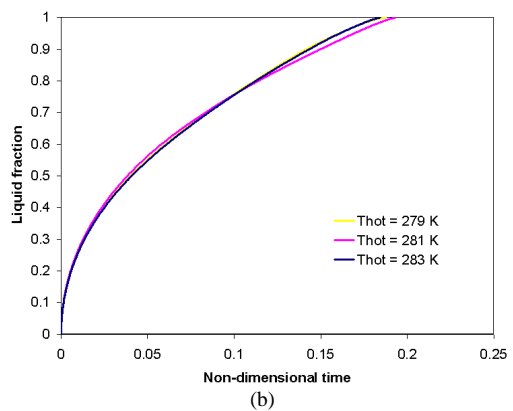
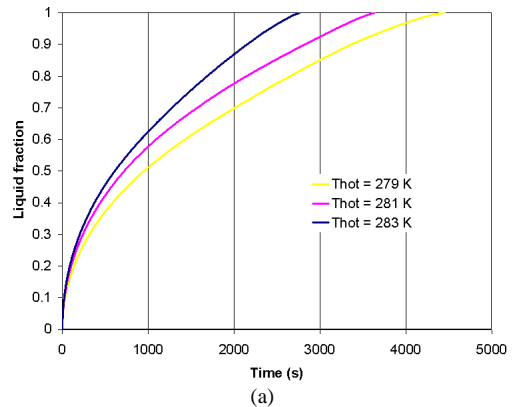
Fig. 10(a) presents the liquid fraction versus time for three different isothermal heating wall temperatures. It may be noticed that, although the blue curve is not so close of the others, the slope of the curves are similar indicating that the melting rates are almost the same, as the melting process develops.

Fig. 10(b) shows the liquid fraction versus dimensionless time, for a better analysis. It may be verified that the lower melting rate is achieved by a wall heating temperature of 281K.

Rieger and Beer [8] also reported that the heat transfer becomes minimum utilizing a heating temperature of 281K, being in good agreement with the present study.



Figs. 9. Streamlines at left side and isotherms at right for $Ste = 0.076$. (a) $t = 2077s$; (b) $t = 3505s$



Figs. 10. Liquid fraction versus time for various wall temperatures. (a) Liquid fraction versus dimensional time; (b) Liquid fraction versus dimensionless time

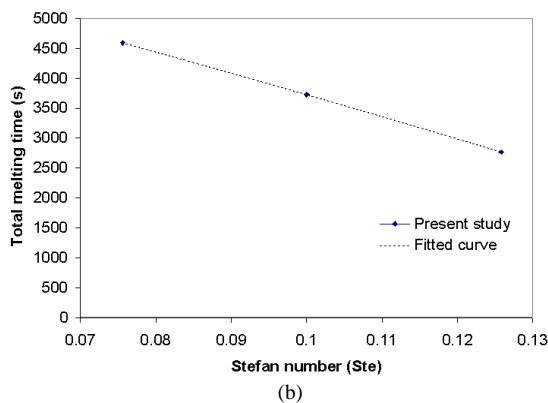
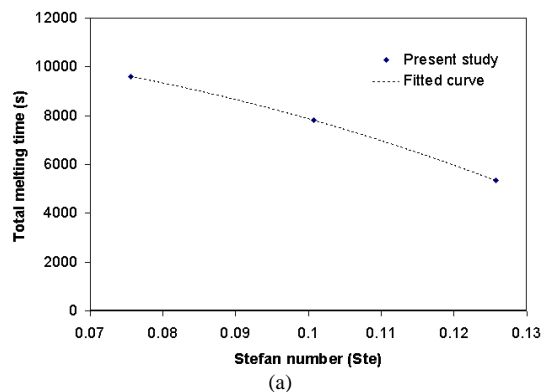
Fig. 11(a) shows the total melting time of ice versus Stefan number for case I and Fig. 11(b) presents the total ice melting time versus Stefan number for case II.

It can be stated that, the higher Stefan number, the lower will be the total melting time.

Correlations for the total ice melting time as a function of the Stefan number are presented below, being the Eq. (15) for the case I and the Eq. (16) for the case II:

$$\tau_{melt} = -551123(Ste)^2 + 25945(Ste) + 10795 \quad (15)$$

$$\tau_{melt} = -33158(Ste)^2 - 29684(Ste) + 7025.9 \quad (16)$$



Figs. 11. Total melting time in terms of Stefan number. (a) Rectangular cavity (case I); (b) Horizontal cylinder (case II)

V. Conclusion

In this study the melting process of constrained ice was analyzed numerically, in two situations. It was observed that in the initial stages of the melting process, the dominant heat transfer mechanism is conduction. As the melting process develops, the convection becomes the main mechanism of heat transfer in the system.

The profiles of the streamlines, isotherms and melting fronts stressed the importance of the influence of natural convection during the process and, from these results, it can be noted the anomalous behavior of water density around 277K and concluded that, for $T_{hot} > 281K$, the ice body tends to drop (higher heat transfer at the upper zone) whereas for $T_{hot} < 281K$, the solid tends to an

upward movement once the higher heat transfer in this case occurs at the lower region.

The total ice melting time decreases as the Stefan number increases, for all wall heating temperature values tested, for the two cases.

The sub-cooling effect was studied for the ice melting inside a rectangular cavity, showing that the higher the Stefan number, the lower will be the sub-cooling influence, as long as, for the same Stefan number, the lower initial sub-cooling of the ice body, the faster will be the melting process.

Acknowledgements

The authors would like to thanks CAPES for the financial support.

References

- [1] B. Gebhart, J. Mollendorf, A New Density Relation for Pure and Saline Water, *Deep-Sea Research*, Vol. 124, n. 1, pp. 831-848, 1977.
- [2] N. Hale Jr., R. Viskanta, Photographic Observation of the Solid-Liquid Interface Motion During Melting of a Solid Heated from an Isothermal Vertical Wall. *Lett. Heat Mass Transfer*, Vol. 5, pp. 329-337, 1978.
- [3] C. Gau, R. Viskanta, Melting and Solidification of a Pure Metal on a Vertical Wall. *Journal of Heat Transfer*, Vol. 108, 174-181, 1986.
- [4] D. Brent., V. Voller, K. Reid, Enthalpy-Porosity Technique for Modeling Convection Diffusion Phase Change: Application to the Melting of a Pure Metal. *Numerical Heat Transfer*, Vol. 13, pp. 297-318., 1988.
- [5] B. Ghasemi, M. Molki, Melting of Unfixed Solids in Square Cavities. *International Journal of Heat and Fluid Flow*, Vol. 20, pp. 446-452, 1999.
- [6] N. Hannoun, V. Alexiades, T. Mai, Resolving the Controversy Over Tin and Gallium Melting in a Rectangular Cavity Heated from the Side. *Numerical Heat Transfer, Part B*, Vol. 44, pp. 253-276, 2003.
- [7] F. Ygit, A Simplified Analytical Solution of a Two-Dimensional Stefan Problem with a Periodic Boundary Condition. (2007) *International Review of Mechanical Engineering (IREME)*, 1 (6), pp. 703-714.
- [8] H. Rieger, H. Beer, The Melting Process of Ice Inside a Horizontal Cylinder: Effects of Density Anomaly. *Journal of Heat Transfer*, Vol. 108, pp. 166-173, 1986.
- [9] P. Riviere, H. Beer, Experimental Investigation of Melting of Unfixed Ice in an Isothermal Horizontal Cylinder. *Int. Comm. Heat Mass Transfer*, Vol. 14, pp. 155-165, 1987.
- [10] S. Fukusako, M. Yamada, Recent Advances in Research on Water-Freezing and Ice-Melting Problems. *Experimental Thermal and Fluid Science*, Vol. 6, pp. 90-105, 1993.
- [11] S. Souza, H. Vielmo, Numerical Analysis of Water Melting and Solidification in the Interior of Tubes. *J. of the Braz. Soc. of Mech. Sci. & Eng.*, Vol. 27, pp. 119-131, 2005.
- [12] M. Silva, *Numerical study of melting around a horizontal cylinder including convective effects*, Ph. D. thesis, University of Campinas, Campinas, SP, 2001.

Authors' information

Department of Energy,
Faculty of Mechanical Engineering,
University of Campinas, 13083-970,
Campinas – SP – Brazil.



Christiano G. S. Santim was born in Brazil in 1987 and received his B.Sc. degree in chemical engineering from University of São Paulo (Brazil) in 2009 and his M.Sc. in mechanical engineering from the University of Campinas (Brazil).

His research interests include heat transfer, energy storage and multiphase flows. M.Sc

Christiano Santim is currently a Ph.D. student in mechanical engineering at the University of Campinas.



Luiz F. Milanez was born in Brazil in 1950 and received his B.Sc. degree in mechanical engineering from the University of Campinas in 1973, his M.Sc. by research from the University of Salford (England) in 1976 and his Ph.D. in mechanical engineering from the University of Campinas in 1982. His research interests include thermodynamics, conduction and convection

heat transfer. Prof. Milanez is currently a Professor at the University of Campinas and is the Brazilian Delegate to the Assembly for International Heat Transfer Conferences and also a Member of the Scientific Council of the International Centre for Heat and Mass Transfer.

Effect of the Flow Field Design and Gas Flow Configuration on the Performance of the Polymer Electrolyte Membrane Fuel Cell - An Experimental Analysis

V. Savithiri, G. Nagarajan

Abstract – Fuel cells are electrochemical devices that convert chemical energy in fuels into electrical energy directly, promising power generation with high efficiency and low environmental impact. The most predominantly used fuel cell is proton exchange membrane (PEM) fuel cell because of its wide range of applications. The performance of PEM fuel cells strongly depend on many factors including operating conditions, transport phenomena in the cells, electrochemical reaction kinetics, flow field design and manufacturing process. This experimental research aims to study the effect of different gas flow field designs on the PEM fuel cell's performance. A new flow field design was established and its performance was compared with the serpentine flow field and convection enhanced serpentine flow field. It was observed that at lower reactant flow rates, the new design showed better performance. Different reactant flow configurations were also studied and the results reveal that the gas flow configuration has a significant effect on the cell performance. **Copyright** © 2013 Praise Worthy Prize S.r.l. - All rights reserved.

Keywords: PEM Fuel Cell, Water Management, Flow Field Design, Gas Flow Configuration, Under Rib Convection

I. Introduction

Fuel cells are electrochemical devices that convert the chemical energy in the fuel into electrical energy directly, with high efficiency and low environmental impact. Among different types of fuel cells, the PEMFC is attractive for many applications, because of its low operating temperature, fuel compatibility, high power density and possible modular design as per power requirements [1]. However, significant technical challenges have to be resolved before wide spread commercialization can occur, including cost reduction and better performance (including reliability and durability). These technical challenges are closely related to the two critical issues of water and heat management for PEM fuel cells, that mandate the use of complex flow channels on bipolar plates [2]. Bipolar plates are one of the most important and expensive components of the PEMFC, because they account for more than 60% of the total weight and 30% of the total cost of the system. Therefore, improving or addressing a novel flow field design seems to be workable for improving these issues with respect to the weight, volume and cost [3].

The main tasks of these flow-field plates are to act as current-collectors, and to guarantee the distribution of the fuel or oxidant over the reaction surface area as well as the removal of products from the cell [4]. Towards this end, different flow field designs have been developed, and tested under different operating conditions, experimentally and numerically.

T. S. Zhao *et al.* [5] designed a new flow field called as Convection Enhanced Serpentine flow field (CESFF), and compared the performance with the conventional Serpentine Flow Field (SFF). They have demonstrated experimentally that the new CESFF resulted in substantial improvement in both the cell performance and operating stability, as opposed to the conventional serpentine flow field design. Dongmei Zhou and Jeremy W. Dabel [6] studied a self-hydrating, proton exchange membrane (PEM) fuel cell system with a coupled cathode air and cooling air supply.

Their results reveals that the relationships between reactant flow rates, cell temperature, relative humidity, and membrane conductivity suggests that an additional performance improvement in current density and protonic conductivity could be achieved by placing an impermeable boundary between the porous transport layer and the gas channel on the cathode side of the cell to uncouple the cathode air from the cooling air in current fuel cell design.

J. Scholta *et al.* [7] have tested a stack with different flow field variations using co-flow, cross flow and counter flow directions.

They found that the performance dependency on the flow directions for partially humidified gas streams, increased from co to cross to counter flow. S. Jayanti *et al.* [8] through CFD simulation, established a link between the cross flow between adjacent channels in a serpentine flow field and water vapour distribution in the electrode. If the electrode permeability on the pressure

drop is high, then a significant cross flow i.e. under the rib can be established, and will lead to more effective evacuation of water vapour.

The superior performance of the CESFF of T. S. Zhao *et al.* may also be attributed to this. Hence, they concluded that the cross flow (under rib convection) can be used as an additional parameter in arriving at the optimum design of the flow field. Sarit K. Das *et al.* [1] have demonstrated that the effect of the flow distribution pattern has a significant impact on the cell performance, by comparing the performance of the three distributors, namely parallel, serpentine, and mixed. It was evident from a phenomenal improvement in the cell performance for the mixed distributor over the parallel and the serpentine distributors in the middle region of the polarization curve, i.e., the ohmic loss controlled region. Also, the loss in voltage was quite gradual for the mixed flow distributor in this region.

The flow field structures in fuel cells have to meet several requirements, such as homogeneous fluid distribution, product water removal, good current transport, good under-rib convection, and high conductivity.

Each factor can considerably influence the performance of the fuel cells. From the literature, it was found that the uniformity of oxygen distribution in cathode channels and high quantity of product water removal from the cathode flow path are imperative, for good cell performance. Based on this, a new flow field, named Convection Enhanced Uniformly Distributing Flow Field (CEUDFF) has been designed, and the performance was compared with that of the conventional serpentine flow field and CESFF of T. S. Zhao *et al.*

II. Experimental Setup

The PEMFC usually has a seven layer structure, that is, an anode flow field, an anode gas diffuser layer, an anode catalyst layer, a proton exchange membrane, a cathode catalyst layer, a cathode gas diffuser layer and a cathode flow field. The material of the end plate used in this work was aluminum alloy. The nickel coated copper plate was used as the current collector. The bipolar plate used in the experiments is of pure graphite, 8 cm × 8 cm, with a depth of 1 cm and a surface size of 5 cm × 5 cm, for flow field machining.

The width, depth of channel and rib width are 1mm each. The bipolar plate is used to fabricate the flow field on its surface, which provides paths for the anode and cathode gases to the MEA.

The MEA used was a three-layer combination of Nafion 117 as the electrolyte and carbon cloth as electrodes, the Pt alloy between the anode and the cathode.

The size of the catalyst coated layer is 5 cm × 5 cm, that is, a reactive area of 25 cm², which has a direct influence on the fuel cell power produced by the electrochemical reaction.

The test bench included four parts: the gas supply,

flow rate control, temperature control and electric load systems. The gas supply system supplied hydrogen, oxygen / air as the anode and cathode reactant gas to the fuel cell, and supplied nitrogen for removing the residual gas in the pipeline before and after the experiments. The flow rate control system controlled the gas inlet flow rate following stoichiometry and the minimum flow mode.

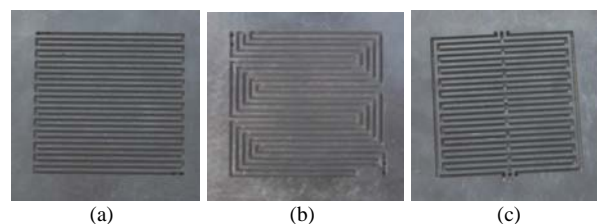
In the temperature control system, a plate type heater, T-type thermocouple and temperature controller were employed to control and measure the cell temperature.

The electric load system had a maximum current of 50A and a maximum voltage of 2 V. The three different flow field designs SFF, CESFF and CEUDFF shown in Figs. 1 were used on the cathode side. The anode side flow field did not have much impact on water management [9], hence, only the SFF was used for all three types of cathode flow fields.

III. Flow Field Design

The flow field is one of the key components of a PEMFC, which serves as both the current collector and the reactant distributor. The reactants, as well as the products, are transported to and from the cell through the flow channels.

The essential requirements for the flow field are uniform distribution of reactants over the entire electrode surface and effective removal of products from the cell, to minimize the concentration polarization. The channel-to-channel convection under ribs can facilitate both mass transport into the electrode and removal of water flooding. Therefore, enhancing convection through the GDL by optimizing the flow field is an effective way to reduce water flooding at the cathode, enhance the mass transport, and thus improve both cell performance and operating stability [4].



Figs. 1. Cathode side flow field designs (a) Serpentine flow field (b) convection enhanced serpentine flow field (c) convection enhanced uniformly distributing flow field

Based on this a new flow field named Convection Enhanced Uniformly Distributing Flow Field (CEUDFF) was developed which is shown in Fig. 1(c). The pressure difference between adjacent channel may improve the in-plane flow through the gas diffusion layer due to which the area under the ribs also get exposed to reactant, which can eliminate the water accumulation under the ribs. Fig. 2 shows the pressure distribution along the flow path of CEUDFF from simulation. There exists pressure difference adjacent to the bends and the channel length, which will enhance the under rib convection.

IV. Results and Discussion

IV.1. Effect of Flow Field Design

The fuel cell performance in the form of the polarization and power density curves is shown in Figs. 3. The cell temperature was maintained at 50°C. The inlet conditions of the reactants were dry. The hydrogen flow rate was fixed at 200 cc/min and oxygen flow rates used were 275 cc/min and 350 cc/min.

The performance of the cell is low at lower oxygen flow rates with the SFF. The voltage drop is sharp in the ohmic region of the SFF, under lower oxygen flow rate conditions. But the voltage drop is gradual at higher flow rates. At lower flow rates of oxygen the product water blocks the flow path and the flow velocity may not be sufficient to remove the product water. Also, the blocking of the reaction sites for the oxidant increases the concentration losses leading to lower cell performance. In the case of the CESFF and the CEUDFF at lower oxygen flow rates, because of the flow field design more uniform distribution of the reactant over the electrode area occurs, which leads to better cell performance. Moreover, in both the cases because of the pressure difference in the adjacent channels, under the rib, convection is increased; this eliminates the accumulation of water under the ribs, which leads to better cell performance.

Figs. 4 depict the better performance of the CEUDFF in the ohmic region at higher flow rate of 350 cc/min. But at higher current densities, the serpentine flow field which exhibits higher acceleration of fluid at higher flow rates, facilitates the faster removal of the product water, thus registering lower mass transport losses.

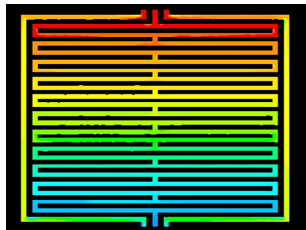


Fig. 2. Pressure distribution plot for CEUDFF from simulation

At higher current density the water can be better managed, because of under rib convection which leads to a better performance. But in the case of higher oxygen flow rates, the water removal capability of the SFF is good; so, when oxygen pushes the water over the flow path, and because of the concentration difference between the anode and cathode, there will be an effective back diffusion of water from the cathode side to the anode side, which will hydrate the membrane leading to better protonic conductivity, which is why the ohmic region extends even at higher current densities of the SFF. In the case of the CESFF the flow takes place against gravity; there may be water blockage at higher current density, where more amount of water is produced which leads to concentration losses. In the CEUDFF the

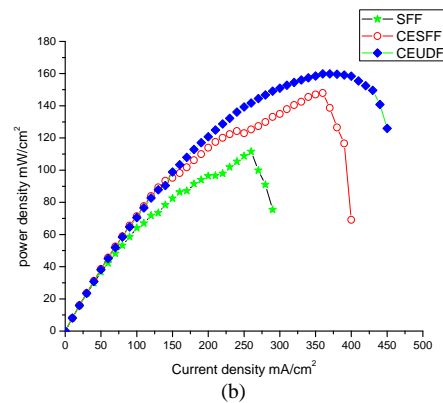
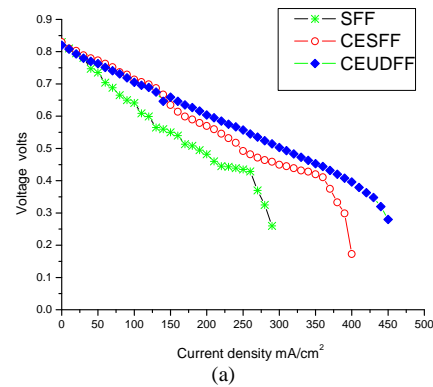
water can be better managed; so it leads to better cell performance. At a lower flow rate (275 cc/min), the CEUDFF exhibits the highest performance compared with the other two flow field designs.

The performance comparison at three different voltages is given in Table I. The current densities, at 0.4 V for the CEUDFF and CESFF are increased by about 50 % and 38 % over the serpentine flow field and at 0.6 V it is 82 % and 55%.

TABLE I
OXYGEN FLOW RATE 275 CC/MIN

| Voltage (Volts) | Current density (mA/cm ²) | | |
|-----------------|---------------------------------------|-------|--------|
| | SFF | CESFF | CEUDFF |
| 0.4 | 390 | 370 | 400 |
| 0.5 | 280 | 250 | 310 |
| 0.6 | 170 | 170 | 200 |

This performance comparison shows that in the CEUDFF even at lower flow rates of the reactant, the reactant distribution over the entire area of electrode surface is uniform and there may a better water management through under rib convection.



Figs. 3. (a) Polarization curve (b) Power density curve for cathode side reactant flow rate of 275 cc/min

At higher flow rates as seen in Table II, there is a 12% increase in the current density at 0.5V of the CESFF. In the CEUDFF, there is a 24% increase in the current density at 0.5V.

But the mass transport losses are very low in the SFF which shows the better water removal capability of the

SFF at higher current densities.

For a wide range of current densities from 330 mA/cm² to 520 mA/cm² the power density is more stable around 150 mW/cm². This shows the better water removal capability of the SFF at a higher flow rate of 350 cc/min.

TABLE II
OXYGEN FLOW RATE 350 CC/MIN

| Voltage (Volts) | Current density (mA/cm ²) | | |
|-----------------|---------------------------------------|-------|--------|
| | SFF | CESFF | CEUDFF |
| 0.4 | 260 | 360 | 390 |
| 0.5 | 190 | 250 | 300 |
| 0.6 | 110 | 170 | 200 |

IV.2. Effect of Gas Flow Orientation

From Figs. 5 in the flow configuration in which hydrogen is given from the top, and oxygen from the bottom, the performance was very poor and there was a sharp increase in ohmic loss at 50°C.

Since the oxygen is fed from the bottom the oxidant's access to the reaction sites is blocked by the product water, and hence, it exhibits the lowest performance. When oxygen is fed from the bottom the water produced at the cathode side may block the flow path.

So, when the oxygen flows against gravity it will not be distributed properly over the entire electrode area, and it will be difficult to push the water in the flow path; the drying of the membrane will also be more and this will increase the proton conduction resistance.

This leads to lower cell performance.

When hydrogen and oxygen are both fed from the bottom, because of the low density of the hydrogen, its spreading will be faster over the flow path; but at the same time, the oxygen which enters from the bottom on the cathode side against gravity, will not be distributed properly over the entire electrode area, and it will be difficult to push the water in the flow path; hence, the drying of the membrane will be there, and this will increase the proton conduction resistance.

But, still it gives 2.3 times higher maximum power density compared to the first flow configuration.

When hydrogen is fed from the bottom and oxygen from the top, the performance was the best, and the maximum power density was 3 times greater than that of the first flow configuration.

When the oxygen is given from the top, water will be produced at the lower half of the bipolar plate. At the same time, when hydrogen is fed from the bottom at dry condition, in the lower half of the MEA, because of concentration difference, back diffusion will occur, which will hydrate the membrane.

Also, there will be a uniform spreading of the reactant over the reacting area when hydrogen is given from the bottom. This gives the best performance for this flow configuration.

It is also believed that the water produced on the cathode side humidifies the oxygen, hydrates the membrane, and hence, exhibits the better performance

compared to the above configurations.

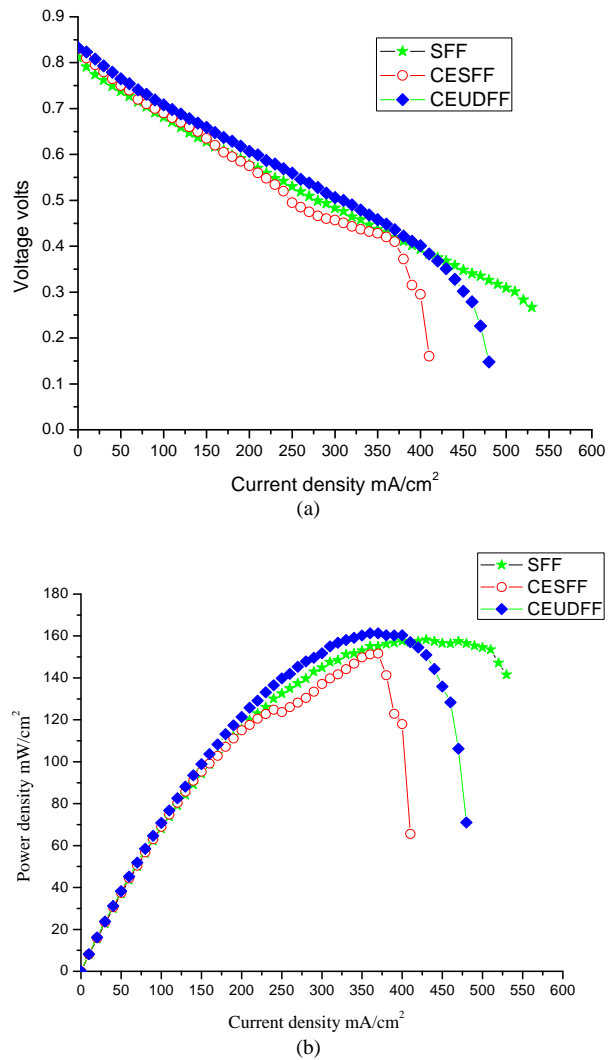
Figs. 6 show the performance curves of different gas flow orientation at 60°C.

At this higher cell temperature, the cell exhibited similar pattern of cell performance compared with 50°C performance curves. But the open circuit voltage at 60°C drops by 23% and also the when both hydrogen and oxygen were fed from top the voltage was highly fluctuating i.e. why that configuration was not included in the performance curve.

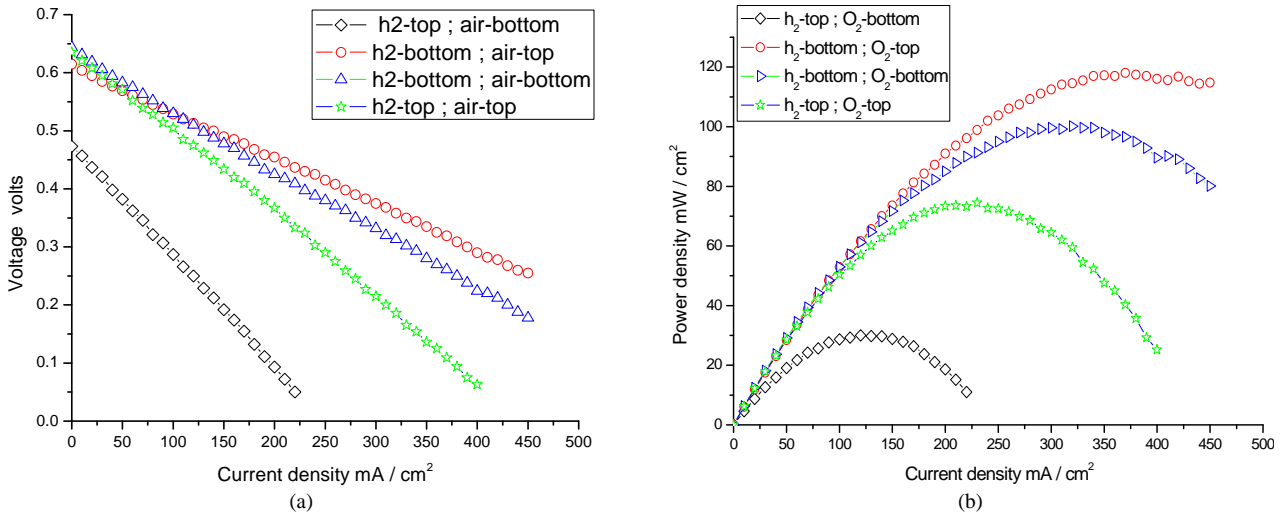
IV.3. Effect of Temperature

The effect of temperature (50°C and 60°C) on the cell performance in three different flow configurations for the hydrogen flow rate of 200 cc/min and oxygen flow rate of 350 cc/min is shown in Figs. 7.

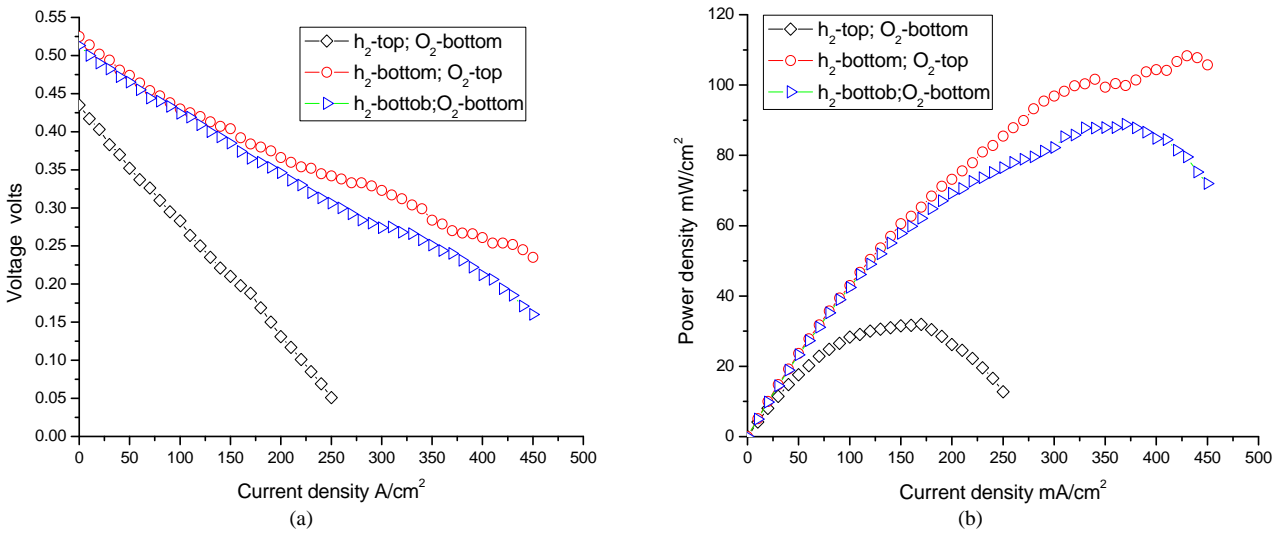
It shows that at low current densities, a lower cell temperature gives a better performance and at higher current densities, above 300 mA/cm², the higher cell temperature exhibits very low mass transport losses.



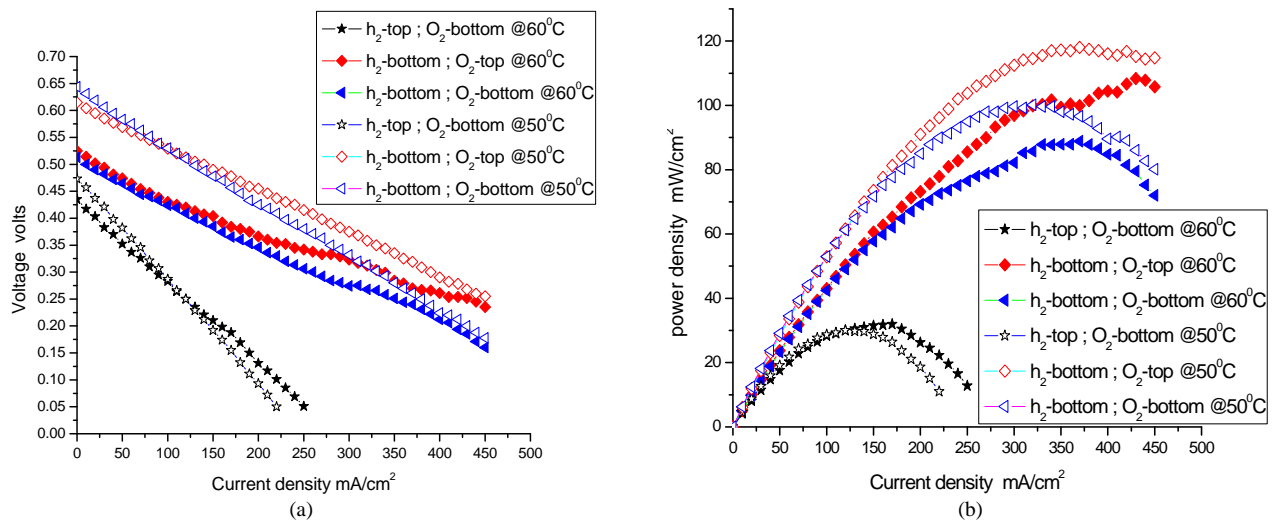
Figs. 4. (a) Polarization curve (b) Power density curve for cathode side reactant flow rate of 350 cc/min



Figs. 5. (a) polarization curve (b) Power density curve for different gas flow orientations at 50°C temperature



Figs. 6. (a) polarization curve (b) Power density curve for different gas flow orientations at 60°C temperature



Figs. 7. (a) Polarization curve (b) Power density curve for different gas flow orientation at 50°C & 60°C temperature

Normally, as the operating temperature increases, the saturation vapor pressure increases, and the surface tension between water and substrate decreases, which makes the liquid water evaporate more easily, and thus, lowers the water flooding level [10].

The liquid water appears in the anode channels mostly via a condensation mechanism, instead of liquid transport through the GDL.

This indicates that the water flooding and the mass transport resistance in the anode are not as serious as in the cathode, because liquid water does not accumulate inside the porous GDL, and block the hydrogen pathways. In contrast, liquid water in the cathode channel appears through both the condensation mechanism and liquid water transport through the GDL [11]; hence, at lower cell temperatures, the liquid water blocks the cathode flow path leading to high mass transport losses.

V. Conclusion

A new flow field design, based on uniform reactant distribution and under rib convection, has been proposed and its performance was compared with the conventional serpentine flow field and convection enhanced serpentine flow field.

At lower oxidant flow rates of 275 cc/min the new design exhibits better performance. Even at higher flow rates of 350 cc/min, the new design reveals that at lower current densities up to 400 mA/cm², the performance is better but at higher current densities the mass transport losses are comparatively higher than that of the serpentine flow field.

The effect of the gas flow orientation has also been studied experimentally at temperatures 50°C and 60°C.

The reactants used were at dry conditions. The results confirm that the gas flow orientation has a great impact on the PEMFC performance.

References

- [1] A. S. Bansode, T. Sundararajan, Sarit K. Das, Computational and Experimental Studies on the Effect of Flow-Distributors on the Performance of PEMFC, *Journal of Fuel Cell Science and Technology*, Vol.7, pp. 051014-1 - 051014-10, 2010.
- [2] Toshihiko Kanazaki, Xianguo Li, J.J. Baschuk, Cross-leakage flow between adjacent flow channels in PEM fuel cells, *Journal of Power Sources*, Vol.162, pp. 415–425, 2006.
- [3] Chin-Tsan Wang, Yuh-Chung Hu, Pei-Lun Zheng, Novel biometric flow slab design for improvement of PEMFC performance, *Applied Energy* Vol. 87, pp. 1366–1375, 2010.
- [4] K. Tüber, A. Oedegaard, M. Hermann, C. Hebling, Investigation of fractal flow-fields in portable proton exchange membrane and direct methanol fuel cells, *Journal of Power Sources* Vol.131, pp.175–181, 2004.
- [5] C. Xu, T.S. Zhao, A new flow field design for polymer electrolyte-based fuel cells, *Electrochemistry Communications*, Vol.9, pp. 497–503, 2007.
- [6] Zhou, D., Dabel, J.W., Modeling and optimization of a proton exchange membrane fuel cell based on self-hydrating coupled cathode design, (2010) *International Review of Mechanical Engineering (IREME)*, 4 (5), pp. 542-551.
- [7] J. Scholta, F. Haussler, W. Zhang, L. Kuppers, L. Jorissen, W. Lehnert, Development of a stack having an optimized flow field structure with low cross transport Effects, *Journal of Power Sources*, Vol.155, pp. 60–65, 2006.
- [8] P.V. Suresh, S. Jayanti, A.P. Deshpande, P. Haridoss, An improved serpentine flow field with enhanced cross-flow for fuel cell applications, *International journal of hydrogen energy*, Vol.36, pp.6067– 6072, 2011.
- [9] Sang-Kun Lee, Kohei Ito, Toshihiro Ohshima, Shiun Noda, and Kazunari Sasaki, In Situ Measurement of Temperature Distribution across Proton Exchange Membrane Fuel Cell, *Electrochemical and Solid-State Letters*, Vol.12, n. , pp. B126-B130, 2009.
- [10] A. Hakenjos, H. Muentner, U.Wittstadt, C. Hebling, A PEM fuel cell for combined measurement of current and temperature distribution, and flow field flooding, *Journal Power Sources* vol.131,pp 213, 2004.
- [11] M. M. Daino, Z. Lu, J. M. LaManna, J. P. Owejan, T. A. Trabold, S. G. Kandlikar, Through-Plane Water Transport Visualization in a PEMFC by Visible and Infrared Imaging, *Electrochemical and Solid-State Letters*, Vol.14, n.6, pp. B51-B54, 2011.

Authors' information



V. Savithiri is working as Associate Professor in Department of Mechanical Engineering, St. Joseph's College of Engineering, Chennai, India.

She received the B.E degree in Mechanical Engineering from Madurai Kamaraj University and M.E degree in Thermal Engineering from Anna University India in 1996 and 2005 respectively. She is currently pursuing the Ph.D degree at Anna University, Chennai. Her research interest includes Fuel cells, Heat transfer and Renewable Energy.

Ms. Savithiri is a member of Indian Society for Technical Education and the Institute of Engineers (India).



G. Nagarajan has done his doctorate in Internal Combustion Engineering discipline from Anna University, Chennai, Tamilnadu, India in 2000. He is currently working as a Professor in Department of Mechanical Engineering, College of Engineering Guindy, Anna University, and Chennai, India. He is also the Director of Admissions, Anna University, Chennai. He has published more than 100 papers in International Journals, 15 in National Journals, 37 in International Conf. Proceedings and 21 in National conf. Proceedings. Dr Nagarajan is a member of Society of Automotive Engineers (USA), Combustion Institute (USA), Indian Society for Technical Education, Indian Society for Mechanical Engineers and Quality Circle Forum of India.

Cycle Efficiency Optimization for ORC Solar Plants

A. Amoresano¹, G. Langella¹, S. Meo²

Abstract – Organic Rankine Cycle plants have been becoming an interesting chance to convert solar energy into electrical energy, when working at not very high temperature levels. Global efficiency of such plants depends on several factors, including mirror optics, receiver tube thermal losses, fluid working cycle, mechanical-electrical conversion. The paper investigates particularly about cycle efficiency and its optimization varying both organic fluid and efficiency improving techniques, as regeneration or reheat. The analysis has been performed evaluating the cycle efficiency in a lot of cases, comparing each other. Results are critically presented, offering a decisional tool when designing an ORC solar plant for medium temperature levels. **Copyright** © 2013 Praise Worthy Prize S.r.l. - All rights reserved.

Keywords: Organic Rankine Cycle, Solar Energy

I. Introduction

Within the panorama of energy conversion technologies, more and more studies and research activities have been developed in last few years about Organic Rankine cycles (ORC), due to their potential integration in future distributed generation systems and its positive characteristics to exploit low-temperature heat sources instead of conventional steam power cycles.

One of their advantages is the possibility of fitting the ORC operational parameters to the heat source characteristics by means of the selection of its working fluid among a considerable set of substances.

A typical ORC successful application is in geothermal power plants and research on this application of ORC is still being carried out.

Another interesting application of ORC regards the exploitation of waste heat and exhaust gases of gas turbines and internal combustion engines as well as power conversion unit of combined heat and power biomass plants.

In both cited cases, research activity pointed to selection of the best working fluid for the thermodynamic cycle, optimization of the ORC unit and the whole installation and analysis of possible modifications in order to increase its thermo dynamic efficiency or net mechanical power output.

A technique for the optimization of binary ORC power plants exploiting low-temperature geothermal resources takes the ratio of the total heat transfer area to total net power produced by the power plant as objective function [1]-[4]. For geothermal water temperatures between 70 °C and 90 °C, the reduced value of the thermal efficiency of the plant justifies the selection of this objective function. ORC as bottoming cycle of a combined cycle with micro-gas turbines is another possibility analyzed [5], [6] with the objective of raising the overall efficiency of the system.

Optimization of the evaporation temperature of the ORC with several working fluids is carried out taking the overall recovery efficiency as objective function.

Another heat source that can be exploited by means of ORC for mechanical power generation is solar energy. In this field, many application and research activities aimed at sea water reverse osmosis desalination plants in order to maximize the fresh water production per unit of aperture area of the solar field [7]-[10].

First studies about ORC solar plants [11]-[14] were focused on cycle efficiency optimization, skipping solar collector efficiency evaluation and optimization.

Most following [15]-[21] and actual studies aim to maximize overall efficiency of the solar power cycle, assuming it as objective function.

This is the appropriate selection because overall efficiency links the mechanical energy generated with the aperture area of the solar field.

Overall efficiency takes into account four main aspects: collector, storage, cycle and machines.

Collector efficiency regards mainly optical and thermal losses of solar energy transfer to heat transfer fluid (molten salt or thermal oil). This item is fundamental in plant energetic but especially economic evaluation due to its relative cost within the whole plant expense. The higher is the fluid temperature the more expensive is the collecting system, due to more valuable materials to be involved. Heat storage efficiency takes into account all thermal losses attributable to heat storage facility, typical of plants designed to work even in not sunny hours. Finally machines efficiency takes into account all mechanical and electrical losses related to energy conversion from cycle net work and electrical energy available at plant output. Taking into account all energy conversion processes in a global efficiency, concentrated solar power can achieve an higher value than photovoltaic plants, especially for large size plants.

The actual challenge is the reaching of interesting efficiency also in the small scale power.

The cost of solar thermal power is dropping. Experience in the US shows that today's generation costs are about 15 US cents/kWh for solar generated electricity at sites with very good solar radiation, with predicted ongoing costs as low as 8 cents/kWh in some circumstances. The technology development is on a steep learning curve, and the factors that will reduce costs are technology improvements, mass production, economies of scale and improved operation. CSP is becoming competitive with conventional, fossil-fuelled peak and mid-load power stations. Adding more CSP systems to the grid can help keep the costs of electricity stable, and avoid drastic price rises as fuel scarcity and carbon costs take effect. Hybrid plants can use concentrated solar power and fossil fuels (or bio fuels) together. Some, which make use of special finance schemes, can already deliver competitively-priced electricity. For small-scale, off-grid solar power generation, such as on islands or in rural hinterlands of developing countries, the other option is usually diesel engine generators, which are noisy, dirty and expensive to run. Several factors are increasing the economic viability of CSP projects, including reform of the electricity sector, rising demand for 'green power', and the development of global carbon markets for pollution-free power generation.

Direct support schemes also provide a strong boost, like feed-in laws or renewable portfolio standards for renewable power in some countries. Last but not least, increasing fossil fuel prices will bring the price of solar in line with the cost of conventional power generation.

Although high initial investment is required for new CSP plants, over their entire lifecycle, 80% of costs are in construction and associated debt, and only 20% from operation. This means that, once the plant has been paid for, over approximately 20 years only the operating costs remain, which are currently about 3 cents/kWh. The electricity generated is cheaper than any competition, and is comparable only to long-written-off hydropower plants.

II. ORC Features

The right selection of organic fluid has a large influence upon system efficiency and environmental impact. One of most significant thermo physical characteristic of such fluids is the slope of saturation curve in T-s diagram which falls in the following three cases: wet, isentropic and dry fluid.

For wet fluids the slope of saturation curve is negative, as represented in Fig. 1, so an isentropic expansion starting from dry saturated steam falls in the saturation area. Water is a typical wet fluid from this point of view. In case of isentropic fluid, saturation curve slope is almost vertical so an isentropic expansion starting from dry saturated steam runs along the saturation curve itself, coming out to an almost dry saturated steam condition, as in Fig. 2.

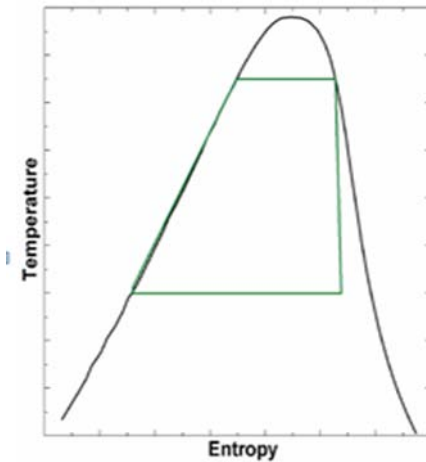


Fig. 1. T-s diagram for a wet fluid

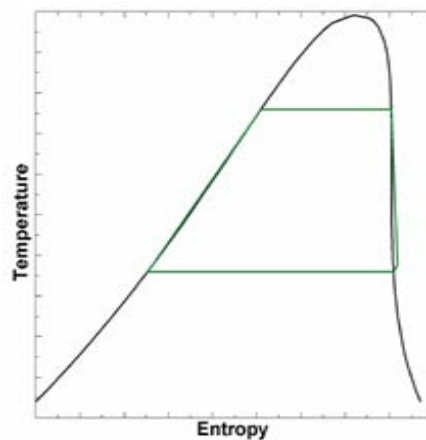


Fig. 2. T-s diagram for an isentropic fluid

Finally a dry fluid shows a negative slope for saturation curve (Fig. 3), so an isentropic expansion starting from dry saturated steam falls out of the saturation area, avoiding turbine blades erosion due to droplet formation typical of expansion in saturation area.

Isentropic or dry fluids were suggested for organic Rankine cycle to avoid liquid droplet impingent in the turbine blades during the expansion.

However, if the fluid is "too dry," the expanded vapor will leave the turbine with substantial "superheat", which is a waste and adds to the cooling load in the condenser.

The cycle efficiency can be increased using this superheat to preheat the liquid after it leaves the feed pump and before it enters the boiler.

Working fluids with relatively low critical temperatures and pressures can be compressed directly to their super critical pressures and heated to their supercritical state before expansion so as to obtain a better thermal match with the heat source.

The heating process of a supercritical Rankine cycle does not pass through a distinct two-phase region like a conventional organic Rankine cycle, resulting in a better thermal match in the boiler with less irreversibility.

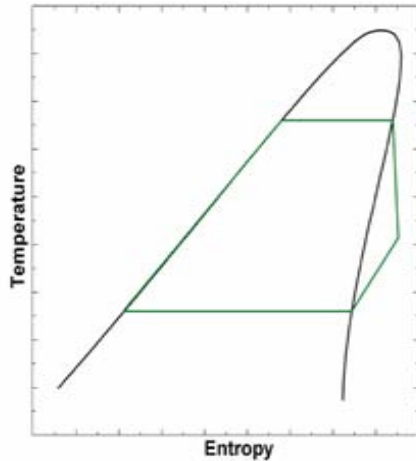


Fig. 3. T-s diagram for a dry fluid

Both the organic Rankine cycle and supercritical Rankine cycle have their own advantages.

Although the supercritical Rankine cycle can obtain a better thermal match than the organic Rankine cycle, the supercritical Rankine cycle normally needs high pressure, which may lead to difficulties in operation and a safety concern.

Moreover, organic fluids must have some important characteristic as:

- Low viscosity both in liquid and in gaseous phase in order to guarantee low friction losses and high heat exchange;
- High conductivity for an high heat exchange coefficient;
- Moderate evaporation pressure in order to reduce plant complexity and cost;
- Condensation pressure higher than atmospheric one in order to avoid air infiltration in cycle component;
- High thermal stability, avoiding chemical degradation at temperature levels of heat source;
- High safety level, including toxicity and flammability features;
- Low ozone depletion potential (ODP), lower than R11 one assumed as reference case, with ODP = 1.0;
- Low global warming potential (GWP), lower than CO₂ one assumed as reference case, with GWP = 1.0;
- Good availability and low cost.

As reported, typical power range for ORC plant is 0,5 – 5,0 MW. Within this range several benefits for expansion machines can be achieved as:

- High turbine efficiency (> 85%);
- Low mechanical stress due to low peripheral speed;
- High molecular weight allows low specific expansion work, unlike steam or gas, and so often a single stage turbine is enough;
- For dry fluid, condensation during expansion is avoided;
- Low rotational speed allows direct coupling with electrical generator without any gear reducer;
- Long lifetime of all components, up to 20 years;
- Cheap turbine due to single stage or scroll typology.

III. Cycle Optimization

Optimization of a small ORC plant, with an electrical output of 10 KW, has been carried out in the present work.

Working cycle has been modeled by ASPEN PLUS software, taking much care to modeling of working fluid characteristic and operative condition, in order to evaluate the real plant efficiency.

Ten organic fluids have been analyzed, computing for each of them the cycle efficiency with standard improvement techniques, as regeneration and reheat.

Thermodynamic properties have been evaluated by REFPROP database.

Plant scheme, as reported, shows a primary circuit for heat transfer fluid and a secondary circuit for organic fluid. The first fluid flows through solar collectors, raking thermal energy from sun and returning it back to organic fluid. Dowtherm A has been chosen as heat transfer fluid; it's an eutectic mixture of two very stable substances: biphenyl (C₆H₁₂) and diphenyl oxide (C₁₂H₁₀O).

These compounds have practically the same vapor pressures, so the mixture can be handled as if it were a single compound.

TABLE I
DOWTHERM A MAIN PROPERTIES

| PROPERTY | DATA |
|--------------------------------|--|
| Freeze point | 12,0 °C |
| Atmospheric boiling point | 257,1 °C |
| Flash point | 113 °C |
| Fire point | 118 °C |
| Autoignition temperature | 599 °C |
| Density @ 25°C | 1056 kg/m ³ |
| Surface tension in air @ 40°C | 37,6 10 ⁻³ N/m |
| Estimated critical temperature | 497 °C |
| Estimated critical pressure | 31,34 bar |
| Estimated critical volume | 3,17 10 ⁻³ m ³ /kg |
| Average molecular weight | |
| Heat of combustion | 36053 kJ/kg |

This fluid has got both chemical and physical stability, it guarantees a high maximum allowable temperature and it's easily findable on market.

In the following table, Dowtherm A main properties are reported. In the case studies proposed, thermal oil had a maximum temperature of 400 °C. In Table II Dowtherm A properties vs temperature are reported

TABLE II
DOWTHERM A PROPERTIES VS TEMPERATURE

| Temp. °C | Vapor Press bar | Visc mPa s | Specific Heat kJ/kg K | Thermcond W/mK | Density kg/m ³ |
|----------|-----------------|------------|-----------------------|----------------|---------------------------|
| 15 | 0,00 | 5,00 | 1,558 | 0,140 | 1063,5 |
| 65 | 0,00 | 1,58 | 1,701 | 0,132 | 1023,7 |
| 105 | 0,01 | 0,91 | 1,814 | 0,125 | 990,7 |
| 155 | 0,06 | 0,56 | 1,954 | 0,117 | 947,8 |
| 205 | 0,28 | 0,38 | 2,093 | 0,109 | 902,5 |
| 255 | 0,97 | 0,27 | 2,231 | 0,101 | 854,0 |
| 305 | 2,60 | 0,20 | 2,373 | 0,093 | 801,3 |
| 355 | 5,80 | 0,16 | 2,527 | 0,085 | 742,3 |
| 405 | 11,32 | 0,12 | 2,725 | 0,077 | 672,5 |

Searching for the right fluid for Rankine cycle is fundamental for looking for alternatives to pure fluid with high molecular weight, keeping low environmental impact and high safety. They also allow to use turbine “on the market” avoiding specific design.

TABLE III
ORGANIC FLUIDS INVESTIGATED

| Compound | Formula | P _c [MPa] | T _c [K] | Saturation curve |
|----------|--|-------------------------|-----------------------|---------------------|
| Acetone | C ₃ H ₆ O | 4,70 | 508,1 | wet |
| R134A | C ₂ H ₂ F ₄ | 4,06 | 374,2 | isentropic |
| R245fa | C ₃ H ₃ F ₅ | 3,65 | 427,2 | isentropic |
| R152a | C ₂ H ₄ F ₂ | 4,52 | 386,4 | wet |
| R143a | C ₂ H ₃ F ₃ | 3,76 | 345,9 | wet |
| R22 | CHClF ₂ | 4,99 | 369,3 | wet |
| R610 | C ₄ F ₁₀ | 2,32 | 386,3 | dry |
| R236fa | C ₃ H ₂ F ₆ | 3,20 | 398,1 | dry |
| R125 | C ₂ HF ₅ | 3,62 | 339,2 | isentropic |
| R600a | C ₄ H ₁₀ | 3,63 | 407,8 | isentropic |

For each fluid a Rankine and an Hirn Cycle have been considered, according to the scheme reported in Fig. 4. In all cases electrical efficiency of the plant has been calculated and so the smallest mirror surface needed for required electrical power. This has been the choice criterion for the fluid.

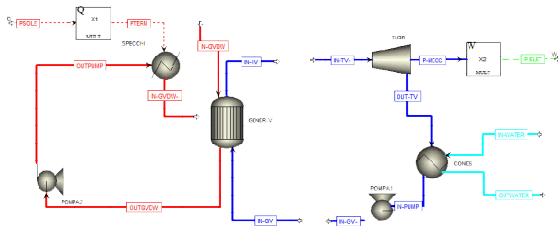


Fig. 4. Software simulation diagram for basic cases (Rankine-Hirn)

Condensation temperature has been set always to 40°C while maximum pressure and temperature have been chosen in order to reach 10 kW electrical net power in each case. The lower is condensation temperature, the higher is the cycle efficiency but expansion ratios increase, with burden on machine weight and dimension.

For all Hirn Cycle cases, boiling temperature has been kept at same value of respective Rankine case, while superheating temperature has been 250 °C in all cases, according to stability limits of fluids considered.

When lower isobar is close to the higher one, enthalpy gap for expansion is quite small and a higher fluid rate is required in order to achieve always the same electrical power output of 10 kW. This implies a higher thermal power needed and so a larger mirror surface and finally a lower cycle efficiency. Results of efficiency evaluation are reported in Figs. 5 and 6 for all examined fluids in Rankine cycle and Hirn cycle case. Best values are obtained for acetone (C₃H₆O) and pentafluoropropane (R245fa). Extension of mirror surface are outlined in Figs. 7 and 8, for Rankine and Hirn Cycles again.

Aside for lower efficiency, large mirror surface implies a higher investment cost with a longer pay back period for plant.

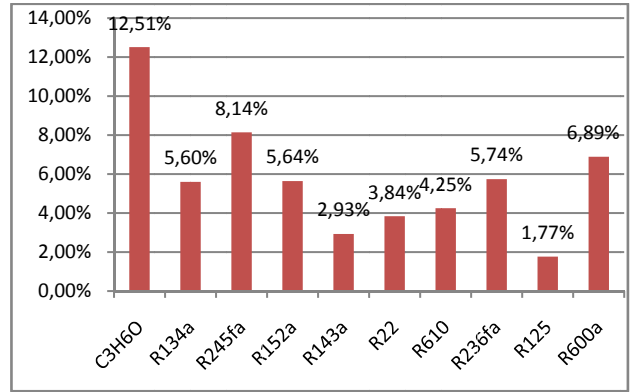


Fig. 5. Rankine cycles efficiencies

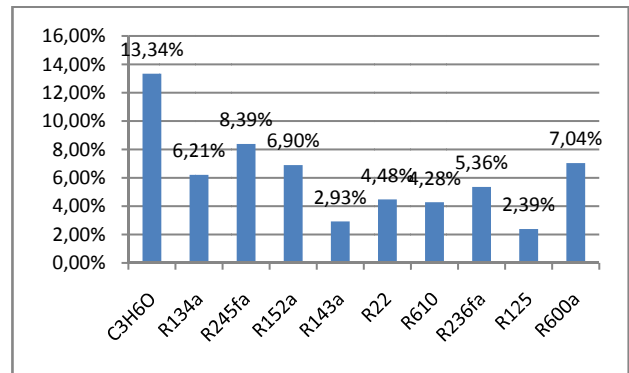


Fig. 6. Hirn cycles efficiencies

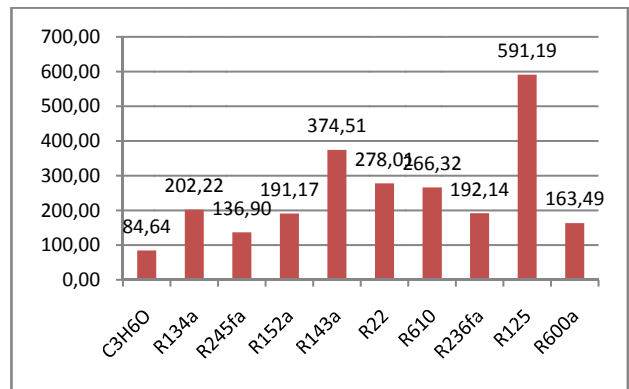


Fig. 7. Mirror surface (m²) for Rankine cycle cases

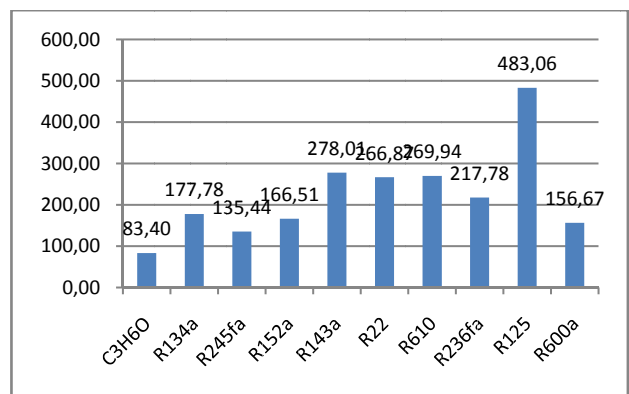


Fig. 8. Mirror surface (m²) for Hirn cycles cases

Fluids with best results from the first analysis (acetone and pentafluoropropane) have been analyzed subsequently in regeneration option, considering an heat exchange between liquid (before evaporation) and vapor out coming from expansion machine.

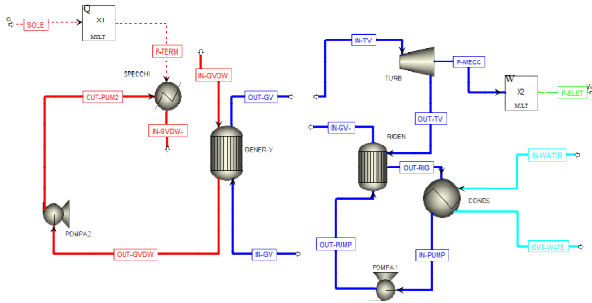


Fig. 9. Software simulation diagram for regeneration cases

Acetone has been investigated for three superheating temperature, 250°C, 300°C and 350°C; pressure at condensation has been set in order to correspond to 40 °C while higher pressure has been set to 27,58 bar.

For each superheating temperature, three regeneration factors have been considered: zero, maximum and an intermediate value.

Results are reported in Fig. 10 highlighting an efficiency increase with regeneration factor. Moreover it can be noticed that superheating temperature has a stronger effect on efficiency at higher regeneration levels.

A similar behavior has been detected for R245fa. In this case, lower pressure has been set in order to have a condensation temperature of 40°C as in previous case; upper pressure has been set to 39,5 bar. Unlike acetone, 300°C has been considered as maximum superheating level, due to thermal instability of R245fa at higher temperatures.

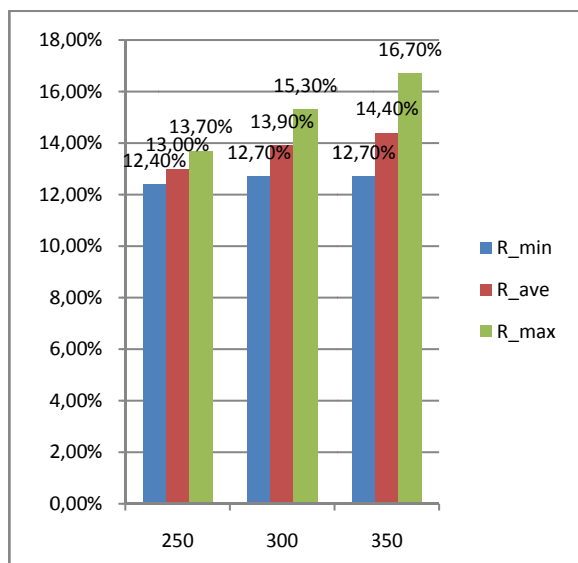


Fig. 10. Acetone cycles efficiencies in regeneration cases

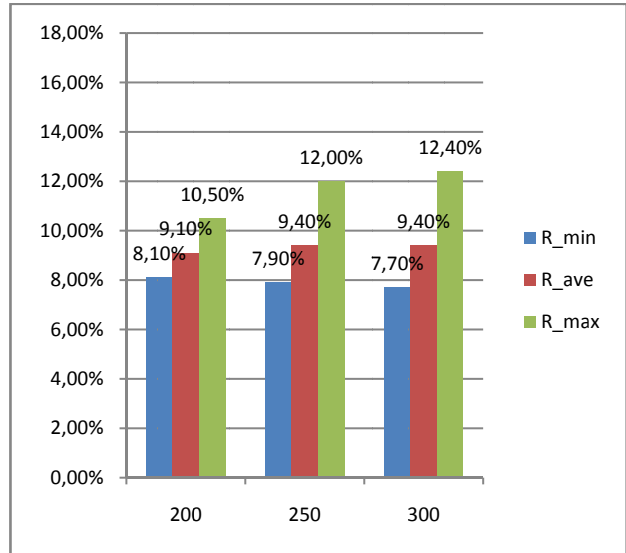


Fig. 11. R245fa cycles efficiencies in regeneration cases

Efficiency increase is less evident than acetone cases showing even a decrease in case of no regeneration.

Reheat has been analyzed too as improving technique for cycle efficiency. Acetone has been considered, as the best fluid resulting from previous analysis. A further expansion has been added, evolving from maximum pressure of 46,5 bar and 350 °C, to 27,6 bar. Reheat leads vapor to 350°C again.

As in previous case, plant has been simulated by Aspen Plus software in all main components. In the fig. 12 the relative software scheme is showed.

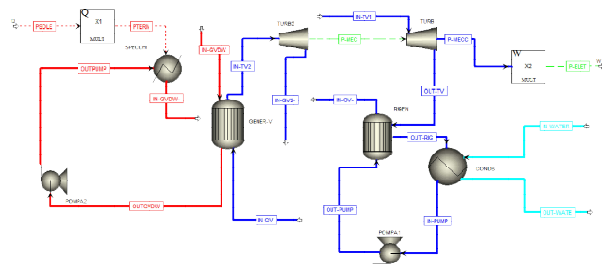


Fig. 12. Software simulation diagram for re-heat case

A 17,7% global efficiency (sun to electricity) has been calculated for this last case, which is the highest efficiency at all in the analysis carried out.

IV. Conclusion

The ORC market is growing exponentially since the beginning of the 80's, mainly in the fields of biomass CHP, geothermal energy and waste heat recovery. The compilation of the available market data shows that actual plants size is mainly limited to the MW scale.

The present work pointed out the good chance for solar energy to be exploited by ORC technology, coupled with solar radiation concentrating facilities, in case of low power size.

The thermodynamic study showed that each fluid is characterized by an optimal temperature range in terms of cycle efficiency and density. In general, the higher the critical point, the higher the optimal temperature range. Very interesting results outcome from acetone and R245fa.

Nowadays a key issue for solar ORC application regards the expanders. Positive displacement machines are preferably used for small-scale applications. At the present time, most of the employed positive displacement expanders are obtained by modifying existing compressors. Turbo machines are mainly designed for larger-scale applications and show a higher degree of technical maturity.

The experts acknowledged that not technical issues and obstacles could slow down the worldwide diffusion of solar technologies. The major barriers are the inertia of existing power plants and the unfavorable power pricing rules, which need to be addressed through ad hoc policy interventions, such as feed-in tariffs.

References

- [1] Hettiarachchi HDM, Golubovic M, Worek WM, Ikegami Y. Optimum design criteria for an organic Rankine cycle using low-temperature geothermal heat sources. *Energy* 2007;32:1698–706.
- [2] Borsukiewicz-Gozdur A, Nowak W. Maximising the working fluid flow as away of increasing power output of geothermal power plant. *ApplTherm Eng*2007;27:2074–8.
- [3] Wei D, Lu X, Lu Z, Gu J. Performance analysis and optimization of organic Rankine cycle (ORC) for waste heat recovery. *Energy Convers Manage* 2007;48:1113–9.
- [4] Liu BT, Chien KH, Wang CC. Effect of working fluids on organic Rankine cycle for waste heat recovery. *Energy* 2004;29:1207–17.
- [5] Invernizzi C, Iora P, Silva P. Bottoming micro-Rankine cycles for micro-gas turbines. *ApplThermEng* 2007;27:100–10.
- [6] Drescher U, Brüggemann D. Fluid selection for the organic Rankine cycle (ORC)in biomass power and heat plants. *ApplThermEng* 2007;27:223–8.
- [7] Delgado-Torres AM, Garcia-Rodriguez L. Preliminary assessment of solar organic Rankine cycles for driving a desalination system. *Desalination* 2007;216:252–75.
- [8] Delgado-Torres AM, Garcia-Rodriguez L. Comparison of solar technologies for driving a desalination system by means of an organic Rankine cycle. *Desalination* 2007;216:276–91.
- [9] Delgado-Torres AM, Garcia-Rodriguez L. Double cascade organic Rankine cycle for solar-driven reverse osmosis desalination. *Desalination* 2007;216:306–13.
- [10] Delgado-Torres AM, Garcia-Rodriguez L, Romero-Ternero VJ. Preliminary design of a solar thermal-powered seawater reverse osmosis system. *Desalination* 2007;216:292–305.
- [11] Wang XD, Zhao L. Analysis of zeotropic mixtures used in low-temperature solar Rankine cycles for power generation. *Solar Energy* 2009;83:605–13.
- [12] Kosmadakis G, Manolakos D, Kyritsis S, Papadakis G. Comparative thermodynamic study of refrigerants to select the best for use in the high temperature stage of a two-stage organic Rankine cycle for RO desalination. *Desalination* 2009;243:74–94.
- [13] Tchanche BF, Papadakis G, Lambrinos G, Frangoudakis A. Fluid selection for a low-temperature solar organic Rankine cycle. *ApplThermEng* 2009;29:2468–76.
- [14] Wolpert JL, Riffat SB. Solar-powered Rankine system for domestic applications. *ApplThermEng* 1996;16:281–9.
- [15] Delgado-Torres AM. Diseñopreliminar de un sistema de desalación por ósmosis inversa mediante energía solar térmica. Academic thesis, *Departamento de Física Fundamental y Experimental, Electrónica y Sistemas, Universidad de La Laguna*, 2006. ISBN 978-84-7756-740-0.
- [16] Delgado-Torres AM, Garcia-Rodriguez L. Status of solar thermal-driven reverseosmosis desalination. *Desalination* 2007;216:242–51.
- [17] Delgado-Torres AM. Solar thermal heat engines for water pumping: an update. *Renew Sustain Energy Rev* 2009;13:462–72.
- [18] OSMOSOL project website. <https://www.psa.es/webeng/projects/joomla/osmosol/> [accessed 12.09.09].
- [19] Bruno JC, Lopez-Villada J, Letelier E, Romera S, Coronas A. Modelling and optimisation of solar organic Rankine cycle engines for reverse osmosisdesalination. *ApplThermEng* 2008;28:2212–26.
- [20] POWERSOL project website. <<https://www.psa.es/webeng/projects/joomla/powersol/>>accessed 12.09.09].
- [21] Garcia-Rodriguez L, Blanco-Galvez J. Solar-heated Rankine cycles for water and electricity production: POWERSOL project. *Desalination* 2007;212:311–8.
- [22] Duffie JA, Beckman WA. Solar engineering of thermal process. 2nd ed. New York: *John Wiley*; 1991.
- [23] Wagner W, Pruss A. The IAPWS formulation 1995 for the thermodynamic properties of ordinary water substance for general and scientific use. *J PhysChem Ref Data* 2002;31:387–535.
- [24] Miyamoto H, Watanabe K. A thermodynamic property model for fluid-phasepropane. *Int J Thermophys* 2000;21:1045–72.
- [25] International Chemical Safety Cards. <<http://www.ilo.org/public/english/protection/safework/cis/products/icsc/>> [accessed 12.09.09].
- [26] Federal Register Environmental Documents. <http://www.epa.gov/EPA-AIR/>[accessed 12.09.09].
- [27] Tillner-Roth R, Baehr HD. an international standard formulation for the thermodynamic properties of 1, 1, 1, 2-tetrafluoroethane (Hfc-134a) for temperatures from 170-K to 455-K and pressures up to 70-Mpa. *J PhysChem Ref Data* 1994;23:657–729.
- [28] DuPont. http://www2.dupont.com/Directories/en_US/Products_Services_Index/index.html> [accessed 12.09.09].
- [29] WMO (World Meteorological Organization). Scientific assessment of ozone depletion: 2006. *Global ozone research and monitoring project—report*, Geneva, Switzerland; 2007.
- [30] Lemmon EW, Span R. Short fundamental equations of state for 20 industrialfluids. *J ChemEng Data* 2006;51:785–850.
- [31] Outcalt SL, McLinden MO. A modified Benedict–Webb–Rubin equation of state for the thermodynamic properties of R152a (1, 1-difluoroethane). *J PhysChem Ref Data* 1996;25:605–36.
- [32] Gas Encyclopaedia of Air Liquide. <<http://encyclopedia.airliquide.com/encyclopedia.asp?languageid=11&GasID=&CountryID=19>> [accessed12.09.09].
- [33] Tillner-Roth R, Harms Watzenberg F, Baehr HD. Eine Neue Fundamentalgleichung Für Ammoniak. *DKV-Tagungsbericht* 1993;20:167–81.
- [34] Quoilin S. Experimental study and modeling of a low temperature Rankine cycle for small scale cogeneration. Academic thesis, Thermodynamics Laboratory, Aerospace and Mechanical Engineering Department, Faculty of Applied Sciences, University of Liege; 2007.
- [35] Buckner D, Wagner W. Reference equations of state for the thermodynamic properties of fluid phase n-butane and isobutane. *J PhysChem Ref Data*2006;35:929–1019.
- [36] BOC GASES. Safety data sheet. <<http://www.bocgases.com/uk/sds/special/R245fa.pdf>> [accessed 12.09.09].
- [37] Airgas. Material safety data sheet. <<http://www.airgas.com/documents/pdf/007181.pdf>> [accessed 12.09.09].
- [38] Angelino G, Di Paliano PC. Multicomponent working fluids for organic Rankinecycles (ORCs). *Energy* 1998;23:449–63.
- [39] NIST Chemistry Webook. <http://webbook.nist.gov/chemistry/fluid/>[accessed 12.09.09].
- [40] Span R, Wagner W. Equations of state for technical applications. II. Results for nonpolar fluids. *Int J Thermophys* 2003;24:41–109.
- [41] Angelino G, Invernizzi C, Molteni G. The potential role of organic bottomingRankine cycles in steam power stations. *Proc IME J Power Energy* 1999;213:75–81.

- [42] Span R. Multiparameter equations of state. An accurate source of thermodynamic property data. 1st ed. Berlin: Springer-Verlag; 2000.
- [43] Gimelli, A., Luongo, A., Amoresano, A., Experimental data and thermodynamic analysis of biomass steam power plant with two different configurations plant, (2012) *International Review of Mechanical Engineering (IREME)*, 6 (6), pp. 1109-1116.
- [44] Di Nardo A., Langella G., Mongiello C., Numerical analysis of exhaust gas flows from GT to HRSG for post-combustion optimisation, *International Journal of Heat and Technology*, 2006, 24 (2) pp. 69-74
- [45] The solar key mark collector database. <<http://solarkey.dk/solarkeymarkdata/CollectorCertificates/solarkeymarkCollectorCertificates.aspx>>accessed 12.09.09].
- [46] Stine WB, Geyer M. Power cycles for electricity generation, in: power from the sun. <<http://www.powerfromthesun.net/chapter12/Chapter12new.htm>>

Authors' information

¹University of Naples "Federico II", Department of Industrial Engineering, Section: "Mechanics and Energetics", Via Claudio, 21, 80125 Naples, Italy.

²Electrical Engineering Department, University of Naples "Federico II", via Claudio 21, 80125 Naples, Italy.



Amedeo Amoresano was born in Naples on October 27, 1963. He took his degree in Mechanical engineering at University of Naples Federico II in 1991 by discussing a thesis concerning the analogic to digital conversion of data of a 3D PDA. In 1994 he took his PhD in Thermomechanical and Energetic Systems discussing a thesis on the fluidodynamic of two phase systems. In 1997 he became researcher of the University of Naples "Federico II" at DiME (Mechanical and Energetic Department). From 2001 he is Assistant Professor of Fluid Machinery and is an adviser for the Italian government of the Innovative Power Plant. In 2007 he was responsible of PRIN (National Research Program) "Analysis and experimental characterization of fire suppression spray". From 2009 he is Aggregate Professor of "Innovative Power Plant". His principal research fields are:

- Spray and atomization systems
- Mild and diluted combustion and gasification systems
- Optical diagnostics and thermal images processing
- Aircraft Deicing System

During his career he tutored several graduated and PhD students and gave lessons in the Italian Academy Air Force where is responsible of the experimental activity on the Wind Tunnel network of the combustion courses for chemical engineers at the University of Naples. He is author of about sixty works among the ones published on international journals, on the proceedings of international and national meeting in reduced or extended form.

E-mail: amoresan@unina.it



G. Langella (Corresponding author) was born in Naples (Italy) on May 21st 1970. He graduated cum laude in Mechanical Engineering in 1995 at University of Naples "Federico II" and he postgraduated in Thermomechanic Systems Engineering in 1999, at the same University. Since 2002 he is researcher at Department of Mechanical Engineering and Energetics of University of Naples "Federico II" Since 2004 is assistant professor of "Steam Generators and Thermal Plants" at "Federico II" University. Since 2008 is assistant professor of "Fluid Machines Management and Energy Systems" at Sannio University. Prof. Langella is author of several papers about renewable fuels use, combustion processes with specific application of computer fluid dynamics and experimental investigations, desulphurization processes of exhaust gases and ORC plants.

Tel: 0039 081 7683275

Fax: 0039 081 2394165

E-mail: giuseppe.langella@unina.it



Santolo Meo received B.S. and M.S. degrees with honours from FEDERICO II University of Naples - Italy, where currently he is an associate professor. He has actually three courses for students of Electrical and mechanical Engineering (Power Electronics, Power Electronics Laboratory and Railway Propulsion). His current research interests

include the fields of power electronics and electrical drives. He is the author of about 100 scientific publications on journals and international conferences in the power electronics field. He is Editor-in-chief of the *International Review of Electrical Engineering (IREE)* and of the *International Review on Modelling and Simulations (IREMOS)*. He is President of the Chapter Board on *Power Electronics and electrical drives* of the *World Scientific and Engineering Academy and Society*; he is member of the international scientific committee of International Conferences on Power electronics and control of electrical drives; he is reviewer for Journals and International Conferences on Power electronics and control of electrical drives; he was involved in National Research Projects financed by the Italian Minister of the Research; he has been responsible of several contracts of advice stipulated with the Researches Centre ELASIS of FIAT, on topics of power electronics for automotive applications.

E-mail: santolo@unina.it

Integrated Oil Palm Fruit Digester-Separator-Screw Press Machine

Nwankwojike B. Nduka

Abstract – An integrated digester-separator-screw press machine for digesting sterilized palm fruit, separating the digested mash into nuts and pulp before pressing only the digested pulp for palm oil extraction was developed and evaluated. This machine, designed based on the modified palm oil and nut extraction process and fabricated using locally sourced standard materials, eliminated drudgery in the loading and discharging of intermediate materials among the digestion, nut-pulp separation and pressing operations in the new process. The major components of this machine include an electric motor, feed hopper, horizontal digesting unit, cake breaking unit, auger separating unit, screw press and discharging outlets for palm nut, palm oil and pressed fibre. Performance test analysis revealed nut breakage index, average throughput and palm oil extraction efficiency of this machine as zero, 204.51kg/h and 97.44% respectively. Thus, the integrated machine constitutes a veritable option for quality palm oil and nuts production boost in small and medium scale palm fruit processing. **Copyright** © 2013 Praise Worthy Prize S.r.l. - All rights reserved.

Keywords: Digester, Drudgery, Integrated Machine, Nut Breakage, Nut-Pulp Separator, Screw Press

Nomenclature

| | | | |
|----------|--|-------------|---|
| W_{dg} | Effective weight capacity of digester, N | ρ_{pf} | Bulk density of sterilized tenera palm fruit, kg/m ³ |
| W_{sp} | Effective weight capacity of separator, N | ρ_m | Bulk density of digested palm fruit mash, kg/m ³ |
| W_{pr} | Effective weight capacity of press, N | ρ_p | Bulk density of digested pulp, kg/m ³ |
| l_1 | Length of digester cylinder, m | φ | Fill volume factor |
| r_1 | Radius of digester cylinder, m | TP | Throughput, kg/h |
| r_2 | Radius of digester shaft, m | t | Processing time, s |
| l_2 | Length of digester shaft, m | m_s | Mass of sterilized oil palm fruit processed, kg |
| l_a | Length of digester arm, m | m_o | Mass of palm oil extracted, kg |
| B_a | Breadth of digester arm, m | m_f | Mass of palm oil loss to pressed fibre, kg |
| t_a | Thickness of digester arm, m | m_n | Mass of palm oil loss to nuts, kg |
| n_a | Total number of digester arms | C | Centre distance between adjacent drive pulleys, m |
| l_s | Length of separating units upper chamber, m | D_1 | Driving pulley diameter, m |
| B_s | Breadth of separating units upper chamber, m | D_2 | Driven pulley diameter, m |
| h_s | Depth of separating units upper chamber, m | L | Length of belt, m |
| r_m | Radius of cake breaker membrane, m | d | Shaft diameter, m |
| l_m | length of cake breaker membrane, m | τ | Allowable stress for shaft with key ways provision, N/mm ² |
| r_b | Radius of beater, m | T | Maximum twisting moment, N-mm |
| l_b | Length of beater, m | M_b | Maximum bending moment, N-mm |
| n_b | Total numbers of beater | K_b | Combined shock and fatigue factor for bending |
| r_3 | Radius of press barrel, m | K_t | Combined shock and fatigue factor for twisting |
| r_p | Base radius of press shaft, m | D_G | Pitch circle diameter of meshing gears, mm |
| l_p | Length of press shaft, m | W_T | Resultant tangential load on meshing gears teeth, N |
| r_4 | Radius of press screw thread, m | W_N | Resultant normal load on meshing gears teeth, N |

| | |
|------------|---|
| C_s | Drives service factor |
| V_G | Driven gears speed, m/s |
| N_1 | Driving gear speed, rpm |
| N_2 | Idler gear speed, rpm |
| N_3 | Driven gear speed, rpm |
| T_1 | Number of driving gear teeth |
| T_2 | Number of Idler gear teeth |
| T_3 | Number of driven gear teeth |
| T_i | Tight side belt tensions, N |
| T_j | Slack side belt tensions, N |
| v | Belt speed, m/s |
| T_c | Centrifugal belt tension, N |
| T_{max} | Maximum belt tension, N |
| μ | Coefficients of friction |
| m | Mass per unit length of belts, kg/m |
| σ | Maximum safe stress of belts, N/mm ² |
| a | Cross sectional area of selected belts, mm ² |
| N_{p1} | Driving pulleys speed, rpm |
| N_{p2} | Driven pulleys speed, rpm |
| β | Groove angle of selected pulleys, ° |
| θ | Angle of lap on the drives small pulleys ° |
| W_G | Weight of gear on the digester shaft, N |
| W_m | Weight of digested palm fruit mash, N |
| W_c | Weight of cake breaker, N |
| W_{cp} | Weight of pulley on the cake breaker shaft, N |
| W_{cg} | Weight of the cake breaker driving gear, N |
| θ_g | Gear tooth pressure angle, N |
| W_a | Auger weight, N |
| W_{ap} | Weight of pulley on the auger shaft, N |
| W_{sc} | Weight of press screw, N |
| W_{pp} | Weight of pulley on the press shaft, N |
| a_f | Press screw depth at feed end, m |
| U_n | Press screw depth at discharge end, m |
| n | Number of press screw turns |
| P_r | Pressure developed by press screw thread, N/mm ² |
| θ_n | Press screw thread lift angle, ° |
| θ_p | Tapering angle of press screw thread, ° |
| h_p | Press screw depth at discharge end, m |
| d_p | Difference between successive screw depths, m |
| d_m | Press screw thread diameter, m |
| P_b | Maximum allowable pressure of press barrel, N/mm ² |
| δ_o | Yield stress of mild steel materials, N/mm ² |
| t_b | Press barrel thickness, m |
| d_i | Internal diameter of press barrel, m |
| P | Power required by each unit of the machine, W |

| | |
|-------|--|
| F_R | Resultant force of each unit drive, N |
| P_T | Total power requirement of the integrated machine, W |
| P_m | Integrated machines electric motor power rating, HP |

I. Introduction

Production of high quality palm oil and kernel, and effective recovery of these products during extraction from oil palm fruits are the primary objectives of mechanizing oil palm fruits processing apart from reducing drudgery and tedium. However no palm fruit processing mill has been able to attain these goals despite the introduction of screw press in this sector for palm oil extraction.

According to [1], broken nuts are usually as high as 10% and 15% with 9% and 10% palm oil loss to pressed fibre when screw press and auto-hydraulic press were used for palm oil extraction respectively. Also, [2] indicated 9 to 22% nut breakage depending on the type of palm fruit being processed when pressed to 8% palm oil loss to pressed fibre with screw press while an average palm oil loss to fibre of 10.7% with a screw press was also reported by [3].

In addition, [4], reported 2-3% palm oil content of pressed fibre in a small scale mechanized process but the bleachability and oxidation conservation of the extracted palm oil was negatively affected. Ref. [5], explained from the experimental records of [2], that the quality of the palm oil extracted in this process was affected because some small nuts/kernels crushed during pressing released their palm kernel oil into the palm oil. Ref.[2], revealed that as pressing pressure increases during pressing of digested palm fruit mash, nuts break and its crushed pieces fill the empty spaces created between the nuts as palm oil oozes out of press cage to permit reasonable de-oiling of the remaining mash/pressed fibre matrix. In order to combat this problem of nut breakage/crushing and its associated losses in the use of screw press for palm oil extraction effectively, [5], introduced an operation sequence modification in the mechanized palm oil and nuts extraction process by incorporating nut-pulp separator between the digester and press as shown in Fig. 1 contrary to the conventional process where nuts are subjected to compressive pressure during pressing before its separation from the pressed fibre.

This modification was based on the fact that the palm oil extracted during the pressing operation is contained in the pulp (exocarp and mesocarp) part of the palm fruit; hence, there is no reason why the nuts should be subjected to pressing. A comparative analysis of this operation sequence modified process revealed that separation of digested palm fruit mash into pulp and nuts before subjecting only the pulp to pressing in a semi-mechanized palm fruit processing improved the quality and quantity of palm oil and kernel extracted and also eliminated nut breakage during pressing and second

pressing operation in this sector [6].

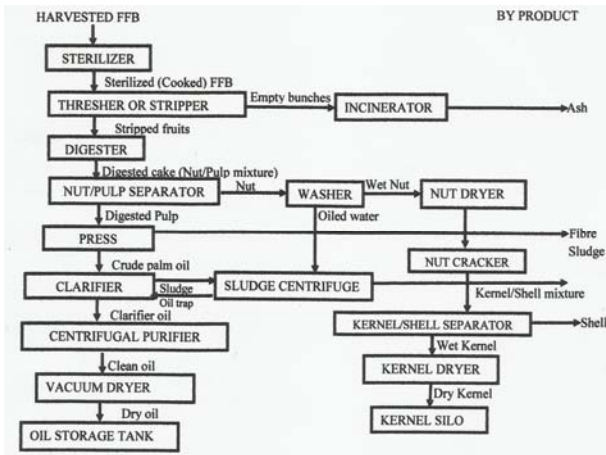


Fig. 1. Operations sequence modified mechanized palm fruit processing

Hence, [7] determined the optimal levels of some operational parameters of the nut-pulp separator in order to ensure optimal performance of the new process.

However, drudgery associated with loading and discharging of intermediate materials among the digestion, nut-pulp separation and pressing operations delays the general adoption of this latest innovative process.

The slow pace in the adoption of this innovation conceded with [4], which revealed that the current demand for palm oil mills has shifted from simple stand-alone unit operational machines to a more integrated system for easy operation and maintenance. Continuous improvement of oil palm fruit processing machineries as well as the applications of oil palm products has been acknowledged [3], [4], [8], [9] and [10].

Thus, in response to the need to reduce drudgery in this new process as well as the demand for integrated palm fruit processing systems, this work developed an integrated digester-nut/pulp separator-screw press machine for small and medium scale palm oil and nut extraction.

II. Description of the Developed Integrated Digester-Separator-Screw Press Machine

The major components of the developed integrated digester-separator-screw press machine shown in Fig. 2 include the feed hopper, digesting unit, cake breaking unit, separating unit, pressing unit, electric motor and discharging chutes for nuts and pressed fibre and palm oil. Sterilized palm fruits are feed to the machine through the feed hopper which discharges the same into the digesting unit. The hopper is a conical frustum made from 2mm thick mild steel plate with top dimensions of 520mm by 480mm and a height of 600mm.

A square aperture of 130mm at the bottom of the hopper has an adjustable valve for controlling the follow

of the fruits into the digester.

The horizontal digester mounted on top of the separator is a cylindrical structure made from 4 mm thick mild steel plate with a diameter and length of 260mm and 1432mm respectively. This digester has a 50mm diameter mild steel shaft with a length of 1500mm upon which fifteen digester arms were welded with a space of 93mm from each other in two equal spaced rows.

The digester arms are the main component of this device that macerates the sterilized fruits to mash as the shaft rotates and they also conveys the mash as it macerates from left end of the digester and discharges it into the cake breaking unit through a rectangular aperture of 200mm by 170mm at right.

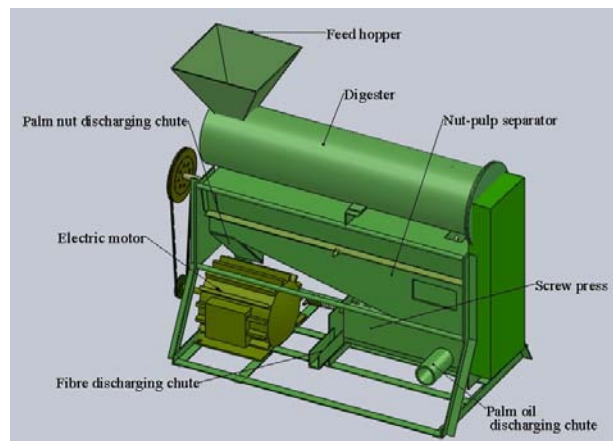


Fig. 2. Integrated palm fruit digester-separator-screw press machine

The cake breaking unit housed at the upper chamber of the separator consists of a 40mm diameter, 1600mm long mild steel shaft, cake breaker membrane of 1500mm in length made of 90mm diameter mild steel pipe and sixty-two pieces of mild steel beaters with a length of 58mm and diameter of 16mm each.

The beaters were welded vertically to the membrane in four rows at spacing of 62mm from one another with row spacing of 66.77mm. The rotary motion of the beaters slacks the fairly compacted palm fruit mash as it falls from the digester through it into the lower chamber of the separator, thereby detaching the entangled palm nuts from the pulp in order to facilitate their separation. The auger separating unit in the lower chamber performs the actual separation of the digested mash into nuts and pulp.

It consists of a pair of adjustable blade, a shaft of 1500mm in length made from a 40mm diameter mild steel rod and an auger membrane of 1377mm in length made from a 90mm diameter mild steel pipe upon which a metal of 2mm thickness was scroll welded (given an auger flight of 4.2mm with the weld) in a spiral form with a pitch of 129mm.

The lower chamber was constructed with an adjustable narrow slit at the bottom. The slit is 2.5mm wide from the right end to a length of 1000mm and 50mm wide from this point to the remaining part of the chamber. The 2.5mm slit allows only the passage of the pulp while the

nuts discharges through the 50mm-slit/nut discharging chute as the auger conveys the slacked mash from right to left end of the chamber. The nut discharging chute is a rectangular frustum with declination, length and width of 60°, 472mm and 123mm.

A hollow trapezoidal section covering the whole length of 2.5mm slit which declines at 60° into the press collates and feed the separated pulp into the screw press through a rectangular aperture of 220mm by 140mm at right end of the lower chamber.

The horizontally fixed screw press consists of a barrel with an internal diameter of 330mm and length of 730mm made of 11mm thick mild steel sheet perforated (hole of 1mm diameter) at equal spacing of 50mm.

The press screw thread is 128mm in diameter and 700mm long with thread depth and a pitch of 41mm and 120mm respectively.

The palm oil from the pulp oozes out as the screw conveys the pulp from the right end of the press to the left under pressure due to opposing cone shaped stopper at this end. The extracted palm oil discharges through the barrel perforations and is collated through the palm oil chute. The pressed fibre discharges at the left end of the press as the pressure acquired pushes the stopper (50mm height) out at regular intervals.

III. Design Analysis of Integrated Machine

III.1. Concepts and Considerations

The integrated digester-separator-screw press machine was developed based on the following considerations:

- i. The inclination of the hopper and chute through which the separated pulp discharges into the press are 30° and 60° respectively. These angles are respectively greater than angles of repose of palm fruit with steel (18.59°) and digested pulp with steel (47.91°) by more than 10° for easy flow of materials among the various units of the machine [11] and [12].
- ii. The machine was fabricated with standard components to ensure low cost of production and easy maintenance and also the internal walls of its separator were lined with score pads to prevent internal injuries to the palm nuts during cake breaking.
- iii. In order to ensure effective utilization of various units of the machine, weight capacities of the digesting, cake breaking and separating units were designed equal while that of the pressing unit goes with 75% of the separating unit capacity because the press handles only the pulp which constitutes 75% of tenera palm fruit weight.

III.2. Analysis of Unit Operations Weight Capacities

The effective weight capacity of the digester and palm nut-pulp separator were determined as 591.86N each from Eq. (1) and (2) respectively while the press capacity was computed as 443.90N using Eq. (3):

$$W_{dg} = \varphi \rho_{pf} g [\pi r_1 l_1 - (n_a l_a B_a t_a + \pi r_2 l_2)] \quad (1)$$

$$W_{sp} = \varphi \rho_m g [l_s B_s h_s - (\pi r_m^2 l_m + n_b \pi r_b l_b)] \quad (2)$$

$$W_{pr} = \rho_p g [\pi r_3 l_p + (r_4^2 - r_p^2)] \quad (3)$$

where $l_1 = 1.432\text{m}$, $r_1 = 0.168\text{m}$, $r_2 = 0.025\text{m}$, $l_2 = 1.5\text{m}$, $l_a = 0.13\text{m}$, $B_a = 0.060\text{m}$, $t_a = 0.009\text{m}$, $l_s = 1.55\text{m}$, $B_s = 0.255\text{m}$, $h_s = 0.225\text{m}$, $r_m = 0.0445\text{m}$, $l_m = 1.5\text{m}$, $r_b = 0.008\text{m}$, $l_b = 0.058\text{m}$, $r_3 = 0.165\text{m}$, $r_p = 0.025\text{m}$, $l_p = 0.8\text{m}$, $r_4 = 0.064\text{m}$, $\varphi = 0.75$, $n_a = 15$ and $n_b = 62$. ρ_{pf} , ρ_m and ρ_p were given as 656 kg/m³, 1060kg/m³ and 925 kg/m³ respectively by [2].

III.3. Drives Belts and Pulleys Selection

The integrated machine has two belt/pulley drives, electric motor/cake breaker and auger/press shafts drives.

The motor drives the cake breaker shaft which drives the digesting and separating units of this machine via gears. Due to cost, availability and performance, cast iron pulleys were selected. The respective diameters of the pulleys mounted on the electric motor, cake breaker, auger and press shafts are 65mm, 350mm, 62mm and 500mm. The centre distances between adjacent drive pulleys were determined as 272.5mm and 343mm for the motor/cake breaker and auger/press drives respectively using Eq. (4). The respective lengths of V-belts required for these drives were computed as 1271.07mm and 1708.2mm from Eq. (5) [13]:

$$C = \frac{D_1 + D_2}{2} + D_1 \quad (4)$$

$$L = 2C + 1.57(D_1 + D_2) + \frac{(D_2 - D_1)^2}{4C} \quad (5)$$

Since motor/cake breaker drive transmits more than 3.5kW and auger/press drive transmits less power, V-belts of type “B” and “A” are respectively required for the drives [14]. Based on [15], standard belts of 1339mm and 1763mm pitch lengths were selected for the motor/cake breaker and auger/press drives respectively. The exact centre distances between the pulleys of the motor/cake breaker and auger/press drives used in the development of this machine were determined as 311.1mm and 376.67mm on substituting these standard pitch lengths of the belts selected for each drive into Eq. (5).

III.4. Transmission Shafts Design

The diameters of the machine shafts, d were determined from maximum stress relations given by [13] and [14] as:

$$d = \left[\frac{16}{\pi \tau} \sqrt{(K_b M_b)^2 + (K_t T)^2} \right]^{1/3} \quad (6)$$

where $\tau = 42 \text{ N/mm}^2$. The maximum twisting moment on the digester shaft was computed as 221632.59Nmm from Eq. (7) given by [14] as:

$$T = \frac{W_T D_G}{2} \quad (7)$$

where D_G is 380mm and W_T was determined as 1166.49N from the following relation [14]:

$$W_T = \frac{P C_s}{V_G} \quad (8)$$

where $P = 1951.3\text{W}$ and $C_s = 1.25$ since light shock is involved [14]. The cake breaker drives the digester via three spur gears comprising the driver on the cake breaker shaft, the idler which only transmits rotary motion but doesn't affect the speed of the driven and the driven.

Thus, the speed of driven gear on the digester shaft was determined as 105.09rpm (2.091m/s) from the following relation [14]:

$$N_1 T_1 = N_2 T_2 = N_3 T_3 \quad (9)$$

where $N_1 = 269.29\text{rpm}$, $T_1 = 32$, and $T_3 = 82$. The twisting moments on cake breaker and auger shafts were also determined as 32837.6Nmm and 78526.4Nmm respectively from Eq. (7) where the tangential load acting on their meshing gear teeth were respectively computed as 410.47N and 923.84N using Eq. (8) since the pitch circle diameters of the gears are respectively 160mm and 170mm. The maximum twisting moment on the press shaft was determined as 505140Nmm from Eq. (10) given by [14] as:

$$T = (T_i - T_j) \frac{D_2}{2} \quad (10)$$

The tight side belt tension of motor/cake breaker and auger/press drives were determined as 387.37N and 170.04N respectively using the following relations given by [14] as:

$$T_i = T_{max} - T_c \quad (11)$$

$$T_{max} = \sigma a_c \quad (12)$$

$$T_c = m v^2 \quad (13)$$

Belt speeds for the motor/cake breaker and auger/press drives were determined from the following relationships as 4.90m/s and 0.77m/s respectively [14]:

$$v = \frac{\pi N_{p2} D_2}{60} \quad (14)$$

$$\frac{N_{p1}}{N_{p2}} = \frac{D_2}{D_1} \quad (15)$$

The slack side tensions of the belts for motor/cake breaker and auger/press drives were respectively computed as 58.99N and 33.53N using the following Equations [14]:

$$2.3 \log \frac{T_i}{T_j} = \mu \operatorname{cosec} \beta \quad (16)$$

$$\theta = 180 - 2 \left[\sin^{-1} \left(\frac{D_2 - D_1}{2C} \right) \right] \quad (17)$$

where μ , m , σ and a were respectively obtained from standard tables as 0.3, 0.193kg/m, 2.8N/mm² and 140mm² for the motor/cake breaker drive, and 0.3, 0.108kg/m, 2.1N/mm² and 81mm² for the auger/press drive [13], [14]. The motor speed (primary driver) is 1440rpm; thus, speeds of pulleys on the shafts of cake breaker, auger and press were computed as 267.43rpm, 237.72rpm and 29.48rpm respectively using Eq. (15).

Groove angle of each pulley = 38°; Angles of lap on the small pulleys of the motor/cake breaker and auger/press drives were determined from Eq. (17) as 2.04 radian and 1.76 radian respectively. The maximum bending moment on the digester shaft was determined using Fig. 3 as follows.

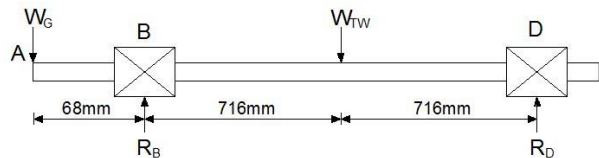


Fig. 3. Force diagram of the digester shaft

Here $W_G = 62\text{N}$ and $W_{TW} = 933.19\text{N}$ is the total load on this shaft due to its weight (231.14N) and weights of the sterilized palm fruit (591.86N) and digester arms (110.19N). The reactions at bearings R_B and R_D were computed as follows by taking moment about B:

$$\sum M_B = 0; R_D (1432) + 62 (68) = 933.19 (716)$$

$$R_D = 463.65 \text{ N}$$

also:

$$\sum F_y = 0; R_B + 463.65 = 62 + 933.14$$

$$R_B = 531.54 \text{ N}$$

Taking downward forces as negative (-) and upward forces positive (+), the shear forces and bending moments on this shaft were computed as follows:

$F_{A-B} = -62\text{N}$; $F_{B-C} = 469.54\text{N}$; $F_{C-D} = -463.65\text{N}$; $F_D = 0\text{N}$, $M_A = M_D = 0\text{Nmm}$; $M_B = 4216\text{Nmm}$; $M_C = 331974.64\text{Nmm}$.

Hence, the maximum bending moment on the digester shaft is 331974.64 Nmm. The maximum bending moments on the cake breaker was determined from its force diagrams (Fig. 4) as follows.

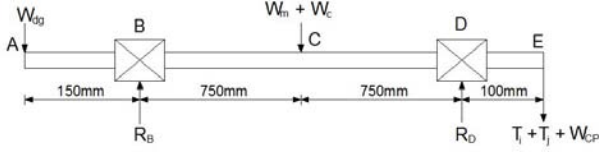


Fig. 4. Force diagram of the cake breaker shaft

Here $W_m = 591.14\text{N}$, $W_c = 204.67\text{N}$, $W_{cp} = 14.72\text{N}$ and the resultant load on this shaft due to its driving gear, W_{dg} was determined as 459.94N from Eq. (18) given by [13] as:

$$W_{dg} = \left[W_N^2 + W_{cg}^2 + 2W_N W_{cg} \cos \theta_g \right] \quad (18)$$

where $W_{cg} = 24.53\text{N}$, $\theta_g = 20^\circ$. The normal load was computed as 436.81N using the following relation [13]:

$$W_N = \frac{W_T}{\cos \theta_g} \quad (19)$$

Thus, reactions, R_B and R_D were determined as follows by taking moment about B:

$$\Sigma M_B = 0: R_D (1500) + 459.94 (150) = 461.08 (1600) + 795.81 (750)$$

$$R_D = 843.73 \text{ N}$$

also:

$$\Sigma F_y = 0; R_B + 843.73 = 459.94 + 795.81 + 461.08$$

$$R_B = 873.1 \text{ N}$$

Taking downward forces as negative (-) and upward forces positive (+), the shear forces and bending moments on this shaft were computed as follows:

$$F_{A-B} = -459.94\text{N}; F_{B-C} = 413.16\text{N}; F_{C-D} = -382.65\text{N}$$

$$F_{D-E} = 461.08\text{N}; F_E = 0 \text{ N}$$

$$M_A = 0\text{Nmm}; M_B = 68991\text{Nmm}; M_C = 240879\text{Nmm}$$

$$M_D = 46108.5\text{Nmm}; M_E = 0\text{Nmm}$$

Therefore, the maximum bending moment on the cake breaker shaft is 240879Nmm. Applying the same computational procedure the respective maximum bending moments on the auger and press shafts were also determined with aid of their force diagrams (Figs. 5 and 6) as 240447Nmm and 76727Nmm.

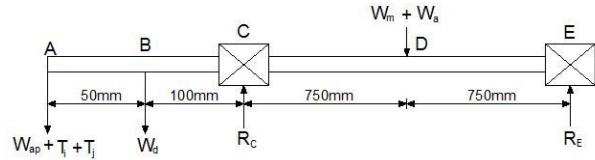


Fig. 5. Force diagram of the auger shaft

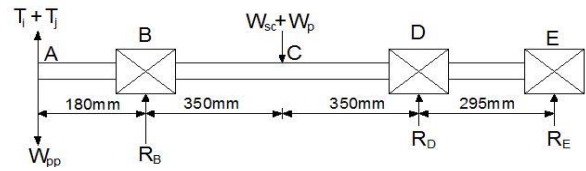


Fig. 6. Force diagram of the press shaft

Here $W_a = 147.93\text{N}$, $W_{sc} = 123\text{N}$, $W_{ap} = 14.72\text{N}$, $W_{pp} = 6.02\text{N}$. The resultant load on this shaft due to its gear, W_d was determined from Eqs. (18) and (19) as 489.37N.

Both feeding of sterilized palm fruits from the hopper into the digester and compacted digested palm fruit mash from the digester to the cake breaker are partially sudden, hence, $k_b = k_t = 1.5$ was used in the design of these shafts while $k_b = 1.5$ and $k_t = 1$ were used for the auger and press shafts design because both the flow of slacked mash from the cake breaking unit into the auger separator and separated pulp from the separator to the press are gradual and steady operations [14].

The diameters of the digester, cake breaker, auger and press shafts were determined as 43.61mm, 35.36mm, 35.51mm and 45.29mm respectively by substituting for these parameters and respective maximum bending and twisting moments of each shaft in Eq. (6). Thus, standard 50mm diameter solid mild steel shafts were selected for the operation of the digestion and pressing units while 40mm diameter shafts of the same material were selected for the cake breaking and auger separating units.

III.5. Determination of Screw and Barrel Pressure

Decreasing depth and pitch screw threading system was adopted in the design of this press screw. The difference between successive screw depths was determined as -22mm from the following relation:

$$U_n = a_f + (n-1)d_p \quad (20)$$

where $a_f = 139\text{mm}$, $U_n = 29\text{mm}$ and $n = 6$. This implies that the screw depth would be decreased consistently by 22 mm from the feed end to the discharge end of the press barrel. The pressure developed by the screw thread which expels the palm oil from the pulp was determined as 1.26N/mm^2 using Eqs. (21) and (22) derived from the following relations:

$$P_r = \frac{T(d_m \cos \alpha \tan \theta + 2\mu)}{2\pi n d_m h_p \cos \alpha (1 - \mu \tan \theta \cos \alpha)} \quad (21)$$

where:

$$\alpha = \tan^{-1}(\tan \theta_n \cos \theta) \quad (22)$$

$T = 505140\text{Nmm}$, $h_p = 29\text{mm}$, $d_m = 128\text{mm}$, $\mu = 0.10$, $\theta_n = 15^\circ$ and, $\theta_p = 9^\circ$. The maximum allowable pressure of the press barrel was determined as 4.91N/mm^2 from the relationship given by [14] as:

$$P_b = \frac{0.54t\delta_o}{d_i} \quad (23)$$

where $t_b = 15\text{mm}$, $d_i = 330\text{mm}$, and $\delta_o = 200\text{ N/mm}^2$.

Since this pressure is greater than that developed by the screw thread, the barrel can withstand the pressing pressure without bursting.

III.6. Power Requirement/Electric Motor Selection

The power required at the digesting, cake breaking, separating and pressing units were determined as 1951.30W, 1609.06W, 1566.83W and 105.11W respectively from Eq. (24) [13] and [14]:

$$P = F_R v_D \quad (24)$$

where v_D is the driving speed of each unit. Thus, the total power required by this integrated machine is 5.2323kW. The power rating of the electric motor required for the operation of this machine was determined as 6.9764kW (9.35HP) from the relationship given by [16], as follows:

$$P_m = \frac{P_T}{\eta_m} \quad (25)$$

where the load factor of the motor was taken as 0.75. Thus, a 10HP three-phase electric motor was selected for the operation of this integrated machine.

IV. Performance Test Procedure

The integrated digester-separator-screw press machine was evaluated after its fabrication using two different sets of experimental design involving ten experimental runs each. The oil palm fruits used were procured from Ariam market in Ikwuano Local Government Area of Abia state, Nigeria. In the first experimental plan, the throughput and palm oil extraction efficiency of the machine were investigated while palm oil loss to both the extracted nuts and the residual pressed fibre was analyzed in the second design. In each of the trials conducted in the first test plan, a stop watch was used to measure the time it takes the machine to process 20kg of sterilized palm fruits. The quantity of palm oil extracted was also weighed and recorded as per each run, after which the throughput, TP (kg/h) of the machine were determined using the following relation:

$$TP = \frac{m_s}{t} \quad (26)$$

Palm oil losses to the nuts and pressed fibre processed in each test were analyzed at Central Laboratory of National Root Crops Research Institute using solvent extraction gravimetric method.

The nuts and pressed fibre from each test were wrapped separately in whatman filter paper. Each wrapped sample was then placed in a soxhlet reflux flask before mounting of the flask on a weighed oil extraction flask containing 250ml of n-hexane solvent. Thereafter, the extraction flask was heated after connecting the upper end of the reflux flask to a condenser. This causes the solvent to vaporize and condense into the reflux flask to soak the wrapped sample until the flask was filled up and siphoned over, thereby carrying the refluxed oil down into a boiling flask.

This cycle of vaporization, condensation, extraction and siphon were repeated for fourteen times in each case before removing the defatted sample carefully with a pair of forceps as the solvent condensed back into the reflux flask while leaving the oil extract in the boiling flask.

The boiling flask with its content was then placed in an oven at 90° for 30 minutes, cooled in a desiccators and reweighed. The mass of oil loss to the nuts and fibre samples, W_o analyzed was computed from the difference between the mass of the flask and the oil extract, W_2 and the mass of the empty flask, W_1 (21.44g) as expressed in Eq. (27):

$$W_o = W_2 - W_1 \quad (27)$$

The palm oil extraction efficiency η (%) of the integrated machine was also determined from the experimental data of first and second test plans using the following relationship:

$$\eta = \frac{100m_o}{m_o + m_f + m_n} \quad (28)$$

V. Results and Discussion

The performance test results of this integrated digester-separator-screw press machine (Table I) indicate its average throughput, oil extraction efficiency and nut breakage index as 204.51kg/h, 97.44% and zero respectively.

This implies an average total palm oil loss to pressed fibre of 2.56% with this system which is 7.44% less than average oil loss to only pressed fibre of 10.7% associated with the conventional mechanical methods of palm fruit processing.

In addition, the machine is very easy to operate as it eliminates drudgery and tedium in feeding and collation of intermediate materials among digestion, nut-pulp separation and pressing operations in semi-mechanized palm fruit processing.

TABLE I
PERFORMANCE ANALYSIS OF THE INTEGRATED PALM FRUIT DIGESTER-SEPARATOR-SCREW PRESS MACHINE

| S/No. | Time (s) | Throughput (kg/h) | Extracted palm oil (kg) | Palm oil loss to fibre (kg) | Palm oil loss to nuts (kg) | Total palm oil loss (kg) | Oil Extraction Efficiency (%) |
|----------------|---------------|-------------------|-------------------------|-----------------------------|----------------------------|--------------------------|-------------------------------|
| 1 | 350.15 | 205.63 | 9.15 | 0.18 | 0.03 | 0.21 | 97.76 |
| 2 | 355.05 | 202.79 | 9.20 | 0.20 | 0.02 | 0.22 | 97.66 |
| 3 | 348.20 | 206.78 | 9.23 | 0.19 | 0.03 | 0.22 | 97.67 |
| 4 | 353.10 | 203.91 | 8.20 | 0.17 | 0.04 | 0.21 | 97.50 |
| 5 | 350.00 | 205.71 | 8.43 | 0.20 | 0.05 | 0.25 | 97.11 |
| 6 | 352.03 | 204.53 | 8.88 | 0.22 | 0.05 | 0.27 | 97.05 |
| 7 | 349.51 | 206.00 | 9.19 | 0.20 | 0.03 | 0.23 | 97.56 |
| 8 | 351.65 | 204.75 | 8.72 | 0.18 | 0.04 | 0.22 | 97.54 |
| 9 | 356.18 | 202.15 | 8.45 | 0.23 | 0.03 | 0.26 | 97.02 |
| 10 | 354.92 | 202.86 | 9.10 | 0.21 | 0.02 | 0.23 | 97.54 |
| Average | 352.08 | 204.51 | 8.86 | 0.20 | 0.03 | 0.23 | 97.44 |

VI. Conclusion and Recommendations

An integrated digester-separator-press machine was developed based on the latest operation sequence modified mechanical method of palm oil and nut extraction at Michael Okpara University of Agriculture, Umudike. The machine which eliminates drudgery and tedium in the feeding and collation of intermediate materials among digestion, nut-pulp separation and pressing operations in semi-mechanized palm fruit processing performed with throughput, oil extraction efficiency and nut breakage index of 204.51kg/h, 97.44% and zero respectively. This innovation of integrated digester-separator-screw press machine is recommended for adoption by small and medium scale palm fruit processors to boost quality palm oil and kernel production.

Acknowledgements

Funding received from Tertiary Education Trust Fund, Abuja under the supervision of Directorate of Research and Development of Michael Okpara University of Agriculture, Umudike is acknowledged with gratitude.

References

- [1] A. B. N. Norilia, *Report of Industrial Training at Felda Palm Industries, Mempaga Palm Oil Mill 28600 Karak, Pahangdarul Makmur, Malaysia*. pp. 18-19. 2008.
- [2] R.N. Muthurajah, *Palm Oil Factory Handbook*, Palm Oil Research Institute New Delhi. pp. 35-56. 2002.
- [3] K. A. Stephen, and S. Emmanuel. Modification in the Design of an Already Existing Palm Nut-Fibre Separator. *African Journal of Environmental Science and Technology*, vol. 3 (ii), pp. 387-398. 2009.
- [4] FAO. Small-Scale Oil Processing in Africa. *Food and Agricultural Organization (FAO) Agricultural Series* 148. 1-55. 2005.
- [5] B. N. Nwankwojike, A. O. Odukwe and C. J. Agunwamba. Modification of Sequence of Unit Operations in Mechanized Palm Fruit Processing. *Nigerian Journal of Technology*, Vol. 30, No.3. 41-49. 2011.
- [6] B. N. Nwankwojike, A. O. Odukwe and C.J. Agunwamba. Benefit Cost Analysis of Introducing Palm Nut-Pulp Separating Machine in the Mechanized Small Scale Palm Fruit Processing. *Journey of Emerging Trends in Engineering and Applied Sciences*, Vol. 3, Issue 1. pp. 38-44, 2012.
- [7] Nduka, N.B., Jonah, A.C., Okay, O.A., Application of response surface modeling in the performance optimization of a palm nut-pulp separator, (2012) *International Review of Mechanical Engineering (IREME)*, 6 (2), pp. 236-244.

- [8] Hadi, H., Tajul, L., Hussin, M.S., Zailani, Z.A., Hamzas, M.F.M.A., Bahari, M.S., Study on ability of palm oil as viscosity index improvement (VII) additive in thermal stability (base mineral oil - Cooking palm oil), (2012) *International Review of Mechanical Engineering (IREME)*, 6 (3), pp. 456-461.
- [9] Ali, O.M., Mamat, R., Faizal, C.K.M., Palm biodiesel production, properties and fuel additives, (2012) *International Review of Mechanical Engineering (IREME)*, 6 (7), pp. 1573-1580.
- [10] Mohdnor, A., Abdulmuin, M.Z., Adom, A.H., Orthogonal least squares method and its application to nonlinear modeling of automotive engine fuelled with palm oil methyl esters, (2013) *International Review of Mechanical Engineering (IREME)*, 7 (1), pp. 46-52.
- [11] O. K. Owolarafe, M. T. Olabige and M. O. Faborode. Physical and Mechanical Properties of Two Varieties of Fresh Oil Palm Fruit. *Journal of Food Engineering*, Vol. 78. pp. 1228-1232. 2007.
- [12] B. N. Nwankwojike, Angle of Repose of Digested Oil Palm Fruit Mash and Pulp on Steel. *International Journal of Innovative Technology and Creative Engineering*, Vol. 2, No.2. 12-16, 2012.
- [13] P. C. Sharma, and D.K. Aggarwal. *Machine Design* S.K. Kataria and Sons, Nai Sarak, Delhi. pp. 19-58, 483-839. 2006.
- [14] R. S. Khurmi, and J.K. Gupta. *A Textbook of Machine Design, Seventh Multi-Colour Edition*, Eurasia Publishing House Ltd, Ram Nagar, New Delhi. pp. 16-52,120-180, 509-557,624-758 and 962-1020. 2010.
- [15] IS 2494-1974 Code. *Indian Standards*. Indian Standard Institute, New Delhi. 1974
- [16] A. P. Onwualu, C. O. Akubuo and I. E. Ahaneku. *Fundamentals of Engineering in Agriculture*. Immaculate Publications Ltd, Lagos. 2006.

Authors' information



Nwankwojike, Bethrand Nduka is a Senior Lecturer in Mechanical Engineering Department at Michael Okpara University of Agriculture, Umudike, Nigeria. Born on 5th August 1975 at Ihe in Awgu Local Government Area of Enugu State, Nigeria. He earned his Bachelor of Engineering in Mechanical Engineering (Industrial and Production Technology Option) from Federal University of Technology, Owerri (2000); Masters (2005) and Doctorate (2011) Degrees in Mechanical Engineering specializing in Industrial Engineering from University of Nigeria, Nsukka. He has published many articles in learned journals in the areas of oil palm fruit processing, agro-industrial machine development for small/medium-scale production, systems modeling and optimization. His current research interests include systems analysis and integrated manufacturing systems development. Engr. Dr. Nwankwojike is a registered engineer in Nigeria and corporate member of Nigerian Society of Engineers, Nigerian Institution of Mechanical Engineers and Nigerian Institution of Agricultural Engineers.
Tel: +23480375178939
E-mail: jikeobodo@yahoo.com

Machinability Study of Biocomposite: Palm Oil Based Wax/LLDPE/Palm Oil Fiber Blends for Prototype Application

A. N. M. Khalil, M. F. M. A. Hamzas, M. S. Hussin, Z. A. Zailani, A. B. Sanuddin

Abstract – This paper is to find the possibility of developing a new blend composite in order to produce a prototype for engineering application. The new palm oil based wax is a waste material produced from palm oil refining process. Recent prototyping activity, industrial blue wax is normally used to produce part prototypes from the machining process. Hence, the tensile strength of new palm oil based wax/LLDPE/Palm oil fiber blends was investigated. The result shows that the tensile strength of new palm oil based wax/LLDPE/Palm oil fiber blend was obtained is higher compared to the existing industrial blue wax. Machinability study covered surface roughness, chip formation characteristic, dimensional consistency and cutting tool wear. The higher tensile strength of the blend was selected to proceed for the machining test. The comparison results between LLDPE/palm oil based wax/ Palm oil fiber blends and Industrial blue wax were recorded. However, since the cost of this new palm oil based wax is lower, it will be an attractive option to replace the existing industrial blue wax for prototype application. **Copyright © 2013 Praise Worthy Prize S.r.l. - All rights reserved.**

Keywords: Machinability, Palm Oil, Industrial Wax, LLDPE, Prototype

I. Introduction

Environmental awareness has been increasing globally due to waste problem, the higher of crude oil price and the processing cost of developing a sustainability concept and consider renewable resources [1]. Palm oil based wax is a new material development of machining industries where the product prototype demand has increased substantially due to more on new product development among manufacturing industries.

Therefore, this new material would substitute with existing industrial blue wax. Which is using petroleum based and high cost. Apart from that, the initiative has been taken to reduce the cost which can save a thousand of Ringgit per year by using this new palm oil based wax. Based on palm oil fatty acid waste to value added product, the research team has seen the opportunity to recycle the material and develop the product which can give benefits to industries and country as well. The aim of this research work is to investigate the strength and characterization of the new composition palm oil based wax in order to archive parallel strength compared to existing industrial blue wax Palm oil based wax is produced by a combination of stearic acid and paraffin wax with approximate composition 70/30 [2].

Existing industrial wax is an extremely hard synthetic (microcrystalline) wax that has been formulated to exhibit exceptional machining characteristics. Since it is harder and has a higher melting temperature than most other waxes, the industrial wax can be machined, cut, or shaped using standard metalworking machine. High quality surface detail and dimensional accuracy are

possible. Industrial Wax is ideal for producing product prototypes and verifying CNC machining programs. In addition, Machinable wax offers distinct advantages over other prototyping materials for some applications.

The product is environmentally friendly and the chips produced no harmful dust, odor or irritants.

The material is self lubricating and easy on tooling. Machinable wax can be recycled. The chips and unused pieces of material can be remelted and formed back into a useable material. This attribute can substantially reduce the cost of using machinable wax over other materials. The major component in Palm oil based wax is fatty acids which are chemically derived from basic Oleochemicals through a few stages of refining process [3], [4]. Oleochemicals are derived from renewable resources, as compared to petrochemicals which are obtained from exhaustible or non-renewable petroleum.

After the year. The 1980s, the oleo-chemicals found wide uses in both food and non-food, or technical applications which previously are the domains of “synthetic chemicals” derived from petroleum or better known as petrochemicals. Products derived from oleochemicals are more readily biodegradable and hence do not pose a threat to the environment. Besides that, products derived from petroleum sources use more energy and cause higher emissions of such pollutants as NO_x, SO₂, CO and hydrocarbons.

In theory, oleo-chemicals can replace petrochemicals in all their applications [4]. At the moment, oleochemicals have wide application in the manufacture of such products as food and specialty fats, soap and detergents, cosmetics and personal care products,

lubricants and greases, drying oil, surface coating and polymers, and bio-fuels.

Fiber reinforcement in composites has played major role in advance materials.

Nowadays fiber-reinforced-plastic composites are used in thousands of structural applications such as aerospace, automotive parts, sports and recreation equipment, boats and office products, machinery etc. By careful selection of reinforcing fibers, the material cost can substantially reduce. In addition, the mechanical performance of composites is mainly dependent upon the properties of the matrix and reinforcement [5].

II. Experiment Design and Material Preparation

The blends were prepared from a specific design of the experiment (Full factorial, 2³). From the first phase of experimental analysis, a full factorial design was used to screen the vital parameters and interactions.

This method is to investigate the interaction among parameters and to search the optimum point for the best matrix. Detailed parameter and interaction blends were programmed into the software and generate the results as shown in Table I for design summary. SAS JMP® 9.0.2 software, from SAS Institute Inc was used for statistical analysis. The software is specific for design of experiment analysis.

There are three factors that are considered in one specific experimental analysis such as LLDPE, fatty acids and palm fiber.

Mass percentage is set for the entire factors in order high and low. LLDPE was set in 30 % low and 70 % high. Meanwhile, the Palm oil fiber is set between 0 to 2 % high. All the optimums setting was obtained by several trials percentages of consumption on the trial and error method.

Several previous experimental results indicated that the too much fatty acids lead to too brittle and too much polymers cause the extra material cost. In addition, an inappropriate mass percentage in all factors or parameters contribute to uneconomic achievement.

The intention of this experimental study is to obtain as minimal in consumption of polymer.

TABLE I
DESIGN SUMMARY

| <i>Study Type</i> | <i>Factorial</i> | <i>Runs</i> | <i>16</i> |
|-----------------------|----------------------|---------------|-----------|
| Initial Design | 2 Level Factorial | | |
| Centre Points | 0 | | No |
| Design Model | 3FI | Blocks | Blocks |

Several tests were conducted on mass percentage of fatty acids as well. The characteristic of fatty acids is brittle and low flash point.

LLDPE was supplied in pellet form by Titan Petchem (M) Sdn Bhd, Johor. LLDPE has an MFI of 1.0 g/10 min, a molecular weight of 191 600 gmol⁻¹, a melting point of 124 °C, and a density of 0.924 g cm⁻³.

Fatty acids was used in this study which is a material waste (final refining process) and was obtained from the Malaysian Palm Oil Board (MPOB), Selangor Malaysia.

The Fatty Acid is a waste material (final refining process) which is produced by the Malaysian Palm Oil Board (MPOB). It is a paraffin wax consisting of approximately 99% of straight chain hydrocarbons and few branched chains, and it is primarily used in the candle-making industry. It has an average molar mass of 256.4 gmol⁻¹ (Fatty Acid), and a carbon distribution between C15 and C78. Its density is 0.90 g cm⁻³ and it has a melting point range around 40–60 °C. Palm fiber ash was obtained from Norstar Palm Oil Mill Sdn. Bhd, Kedah

III. The Identification of Predominance and the Setting of Upper and Lower Limits of Choosing Factors

The strength of the material is an important attribute for the desired quality of the blend for machining processes. Several elements that were considered in the composite wax blends are Palm Oil Fatty Acids wax which obtained from MPOB, Low Linear Polyethylene (LLDPE). The influences of weight percentage of each element were considered in identifying the tensile strength of the wax blend. Design of Experiment (Full factorial) has been employed in conducting the experiment. Analysis of variance (ANOVA) was used to check the validity of the model. For finding the significant parameter, t-test was used. This model can be effectively used to predict the tensile strength of the wax blends. Several trial and error blends mixing at various weight percentages were carried out. The purpose of trial and error blends mixing is to investigate and to fix the setting of lower and upper limits of the factors. Based on the several experiments and analysis, the factors were successfully identified and are discussed as follows;

- Initial studies indicated that, the strength of 70% Fatty Acid Wax/ 30% LLDPE blend was too brittle and can be easily to break. It was found that, 70% of Fatty Acid Wax and 30% LLDPE were unable to maintain its solid form (Figure 1(a)). In addition, it is also happened to composition 80% Fatty Acid Wax/ 20% LLDPE blend (Figure 1(b)). The maximum number of fatty acid wax in the blend causes the blend sample to be a brittle material.
- In the next composition blend, the experiment was conducted by increasing the percentage on LLDPE while reducing the percentage of Fatty Acid wax and 2 percent of fiber was added in the blend. The result shows, the 60% Fatty Acid Wax/ 30% LLDPE wax blend was not brittle as the 70% Fatty Acid Wax/ 30% LLDPE blend is (Fig. 2(a)). The reason of additional fiber in the blend is to investigate the influence of filler on the strength of the composition blend. Figure 2(b) depicts the 60% Fatty Acid Wax/ 40% LLDPE of the blend. The increment on the percentage of LLPDE has made the composition

blend becomes less brittle. However, the solid white fatty acid wax shows crack and easy to cause a breakdown.

- c) Cooking time and temperature were also considered in the experiment. The melting temperature was set at 250 °C and 30 minutes. Both parameters were set as a constant for the entire experiment.

IV. Tensile Strength Result

Table II represents the tensile strength results for the three responses obtained from a different matrix blend.

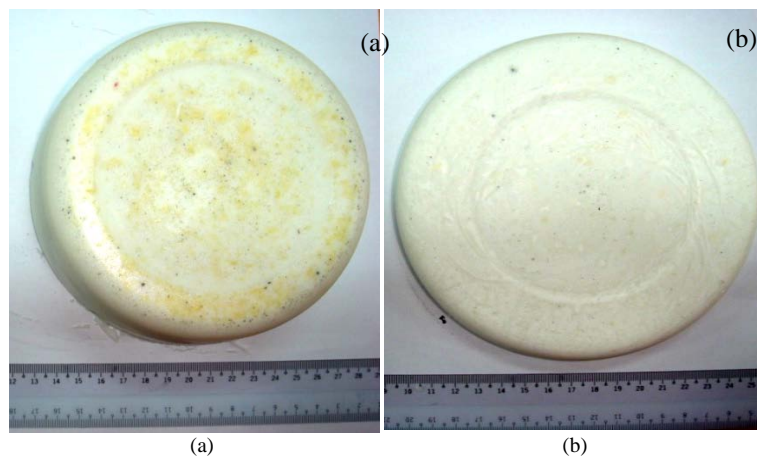
The highest value of tensile strength of the three blends matrix is 15.45 MPa, the composition between HDPE, Fatty Acids and Fiber. Meanwhile, the composition between HDPE, Palmac Fatty Acids and Fiber only achieves the highest value, 10.60 MPa. It also has the lowest value of tensile strength test which equal to zero. The composition between LLDPE, Fatty Acids and fiber only achieved 9.22 MPa. The zero value represents the test samples are too brittle and broke before the test.

Several tests were completed to investigate the reason why the several samples are too brittle and easily break before the test. The finding indicates that the cooling effect after mixing process is one of the factors that affected the test sample. Fast cooling method consequently causing the characteristics of the test sample changes to become too brittle. The results that tabulated in Table II are after considering this rerun result.

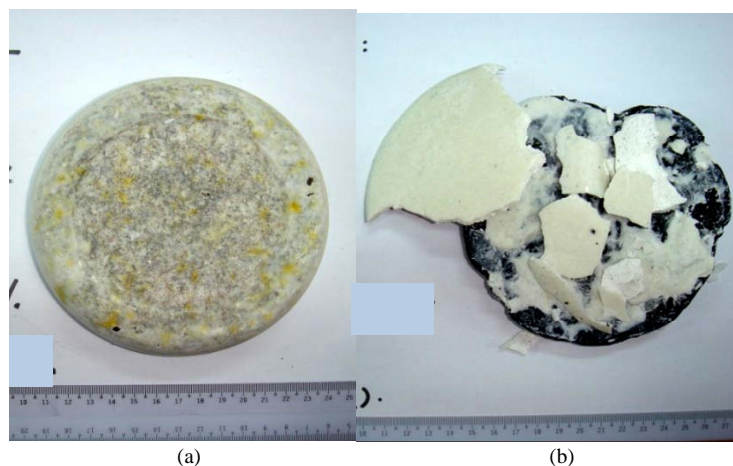
Fig. 3 shows the Tensile Strength result for blends of LLDPE/Fatty Acid/Fiber. The results show the inconsistent tensile strength for the same run composition blend.

Confirmation runs have been conducted to investigate the changes happened on the same run. Generally, the similar composition value leads to approximate close value of the tensile strength results.

Findings show that the earlier results of tensile strength are inconsistent due to fast cooling during the cooling process. Proper cooling method for the blend composition was improved by letting the specimen cool at room temperature.



Figs. 1. (a) 70% Fatty Acid Wax/ 30% LLDPE blend, (b) 80% Fatty Acid Wax/ 20% LLDPE blend



Figs. 2. (a) 60% Fatty Acid Wax/ 30% LLDPE/ 2% Fiber blend, (b) 60% Fatty Acid Wax/ 40% LLDPE blend

V. Screening Design Result for the Blend of LLDPE/Fatty Acid/Fiber

Design of Experiment (Full Factorial Method, 2³) has been employed to screen the interaction factors in the different blends.

The purpose of screening is to identify the main factor and interaction factor which affected on the tensile strength of the blend. Statistical Package that was used in the experimental analysis is SAS, JMP 9.0.2. All the experimental data and results were measured by using the SAS, JMP 9.0.2. Table III represents the result for the Blend of LLDPE/Fatty Acid/Fiber.

TABLE II
TENSILE STRENGTH RESULT

| Run | Factor A | Factor B | Factor C | Responses: Tensile Strength (MPa) | |
|-----|----------|----------|----------|-----------------------------------|-------|
| | | | | LLDPE+ FATTY+ | FIBER |
| 1 | 70 | 60 | 0 | 6.64 | |
| 2 | 30 | 20 | 2 | 5.19 | |
| 3 | 30 | 20 | 2 | 4.53 | |
| 4 | 70 | 20 | 0 | 6.08 | |
| 5 | 30 | 20 | 0 | 7.94 | |
| 6 | 30 | 60 | 0 | 9.22 | |
| 7 | 30 | 20 | 0 | 4.07 | |
| 8 | 70 | 20 | 2 | 5.21 | |
| 9 | 30 | 60 | 2 | 4 | |
| 10 | 70 | 60 | 0 | 3.85 | |
| 11 | 70 | 20 | 2 | 6.99 | |
| 12 | 30 | 60 | 2 | 5.78 | |
| 13 | 70 | 60 | 2 | 6.55 | |
| 14 | 70 | 60 | 2 | 4.68 | |
| 15 | 70 | 20 | 0 | 4.87 | |
| 16 | 30 | 60 | 0 | 6.34 | |

TABLE III
TENSILE STRENGTH RESULTS FOR THE BLEND OF LLDPE/FATTY ACID/FIBER

| LLDPE | Fatty Acid | Fiber | Tensile Strength MPa | Predicted Tensile Strength MPa |
|-------|------------|-------|----------------------|--------------------------------|
| 70 | 60 | 2 | 6.55 | 5.42875 |
| 30 | 20 | 2 | 5.19 | 4.67375 |
| 70 | 60 | 0 | 6.64 | 5.43125 |
| 70 | 20 | 2 | 5.21 | 6.28625 |
| 30 | 20 | 0 | 7.94 | 6.19125 |
| 70 | 20 | 0 | 6.08 | 5.28875 |
| 70 | 20 | 0 | 4.87 | 5.28875 |
| 30 | 60 | 2 | 4.00 | 5.07625 |
| 30 | 60 | 0 | 9.22 | 7.59375 |
| 30 | 60 | 2 | 5.78 | 5.07625 |
| 70 | 20 | 2 | 6.99 | 6.28625 |
| 70 | 60 | 2 | 4.68 | 5.42875 |
| 30 | 20 | 0 | 4.07 | 6.19125 |
| 30 | 60 | 0 | 6.34 | 7.59375 |
| 70 | 60 | 0 | 3.85 | 5.43125 |
| 30 | 20 | 2 | 4.53 | 4.67375 |

Also, the table shows the actual and predicted tensile strength for the blend.

The predicted value is obtained from the generated results from the actual value and analysis of variance (ANOVA). Table IV shows the Analysis of Variance Result for the Blend of LLDPE/Fatty Acid/Fiber. Generally, the table shows the summary results such as

Degree of Freedom, DF, Sum of Square, Mean Square and F ratio from the sources. R-Square is measured and shown in Tables V and VI. Table VII indicates the probability (P value) of the parameter and the interaction of the parameters.

From the table, the most of the P values are obtained higher than 0.05 (P >0.05). This can be defined as the individual parameter is not significant for the model as well as for the interaction parameter.

TABLE IV
ANALYSIS OF VARIANCE (ANOVA) FOR THE BLEND OF LLDPE/FATTY ACID/FIBER

| Source | DF | Sum of Squares | Mean Square | F Ratio |
|----------|----|----------------|-------------|--------------------|
| Model | 6 | 11.822750 | 1.97046 | 0.8080 |
| Error | 9 | 21.949425 | 2.43883 | Prob > F |
| C. Total | 15 | 33.772175 | | 0.5886 |

TABLE V
SUMMARY OF FIT FOR THE BLEND OF LLDPE/FATTY ACID/FIBER

| | |
|----------------------------|----------|
| RSquare | 0.350074 |
| RSquare Adj | -0.08321 |
| Root Mean Square Error | 1.561674 |
| Mean of Response | 5.74625 |
| Observations (or Sum Wgts) | 16 |

TABLE VI
LACK OF FIT FOR THE BLEND OF LLDPE/FATTY ACID/FIBER

| Source | DF | Sum of Squares | Mean Square | F Ratio |
|-------------|----|----------------|-------------|--------------------|
| Lack Of Fit | 1 | 0.555025 | 0.55503 | 0.2075 |
| Pure Error | 8 | 21.394400 | 2.67430 | Prob > F |
| Total Error | 9 | 21.949425 | | 0.6608 |
| | | | | Max RSq |
| | | | | 0.3665 |

TABLE VII
PARAMETER ESTIMATES FOR THE BLEND OF LLDPE/FATTY ACID/FIBER

| Term | Estimate | Std Error | t Ratio | Prob> t |
|---------------------------|----------|-----------|---------|---------|
| Intercept | 5.74625 | 0.390418 | 14.72 | <.0001* |
| LLDPE[70] | -0.1375 | 0.390418 | -0.35 | 0.7328 |
| Fatty Acid[60] | 0.13625 | 0.390418 | 0.35 | 0.7351 |
| Fiber[2] | -0.38 | 0.390418 | -0.97 | 0.3558 |
| LLDPE[70]* Fatty Acid[60] | -0.315 | 0.390418 | -0.81 | 0.4406 |
| LLDPE[70]* Fiber [2] | 0.62875 | 0.390418 | 1.61 | 0.1418 |
| Fatty Acid[60]*Fiber[2] | -0.25 | 0.390418 | -0.64 | 0.5379 |

However, the interaction between LLDPE and Fiber produces the lowest probability as compared to the rest of the parameter and interaction parameter. The result shows similar characteristic in Half Normal plot (Fig. 4) and Pareto plot in Fig. 5. Fig. 6 represents the set of the interaction profiles for the result of the blend of LLDPE/Fatty Acid/Fiber.

The interaction between parameter demonstrates relationships between factors. For instance, two crossing lines indicate the interaction is relying on each other.

Fig. 7 depicts the prediction profiler for the blend of LLDPE/Fatty Acid/Fiber. Maximum desirability for three parameters has been set to obtain the maximum value of the tensile strength. According to the desirability setting, the best setting for the Blend of LLDPE/Fatty Acid/Fiber is 30%/60%/0%.

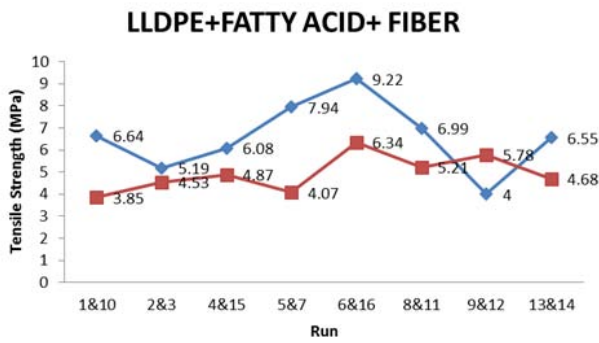


Fig. 3. Tensile Strength result for blends of LLDPE/Fatty Acid/Fiber

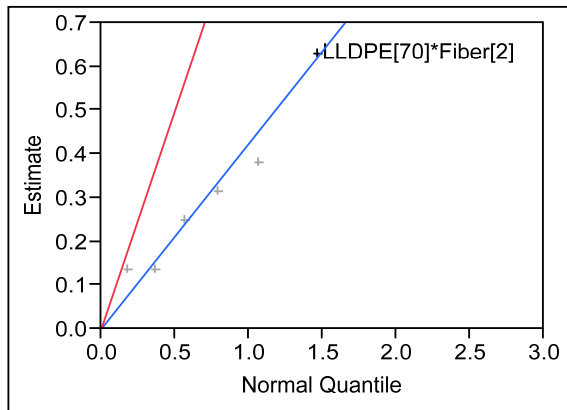


Fig. 4. Half Normal Plot for the Blend of LLDPE/Fatty Acid/Fiber

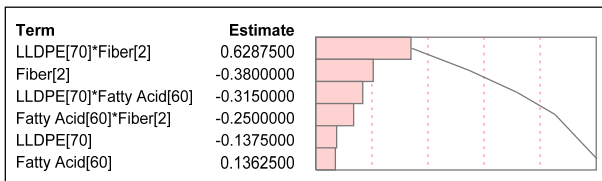


Fig. 5. Pareto Plot of Estimates for the Blend of LLDPE/Fatty Acid/Fiber

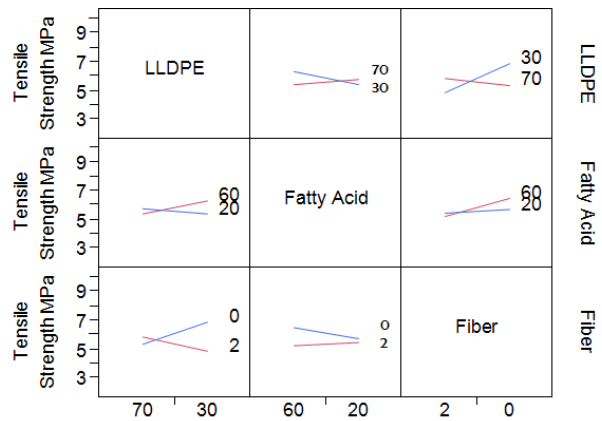


Fig. 6. Interaction Profiles for the Blend of LLDPE/Fatty Acid/Fiber

This leads to for the maximum tensile strength at 7.59375 MPa. However, the actual result for the maximum tensile strength obtained from the experiment is 9.22 MPa. The prediction profiler is used to identify the desirability of the blend. This can be set on the maximum, minimum or other special need. For the experiment, the maximum desirability has been set to determine the higher tensile strength for the blend.

The prediction profiler setting can be used as a guideline for the future experimentation or actual production purposes. The prediction expression can be expressed on the following equation:

Prediction expression for the Blend of LLDPE/Fatty Acid/Fiber:

$$\text{Tensile Strength (MPa)} = 4.6431 - 2.9631 \left[\frac{(\text{Fatty Acid} - 40)}{20} \right] + 1.7894 \left[\frac{(\text{LLDPE} - 50)}{20} \right] - 1.4531 (\text{Fiber} - 1)$$

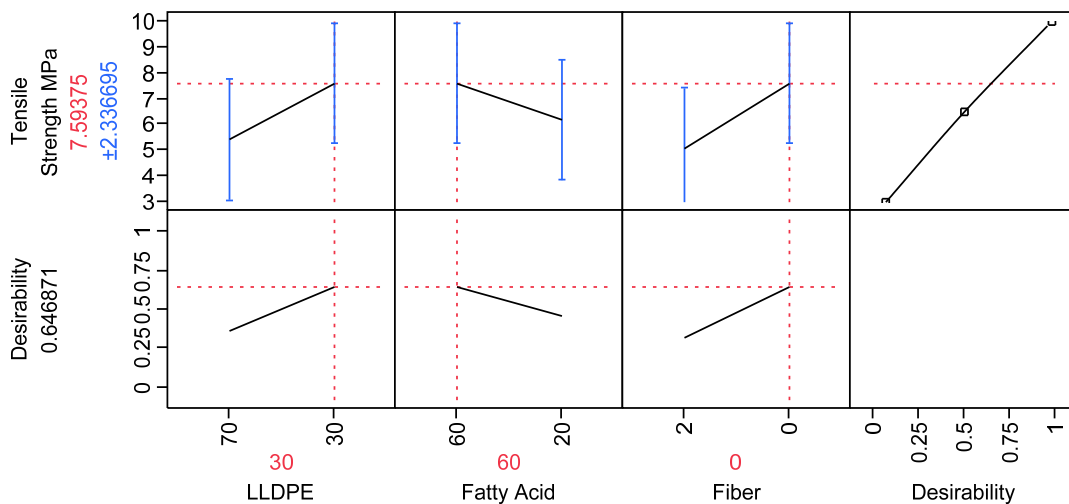


Fig. 7. Prediction Profiler for the Blend of LLDPE/Fatty Acid/Fiber

The comparison results between Industrial blue wax and Palm oil based wax/LLDPE/Palm oil fiber is shown in Table VIII. The result indicated the Palm oil based wax/LLDPE/Palm oil fiber is higher than Industrial blue wax as shown in Table VIII.

TABLE VIII
COMPARISON RESULTS OF MAXIMUM TENSILE STRENGTH FOR INDUSTRIAL BLUE WAX AND PALM OIL BASED WAX/LLDPE/PALM OIL FIBER

| | Composite Blend | Maximum Tensile Strength (MPa) |
|---|---|--------------------------------|
| 1 | Industrial Blue Wax (Renshape No. 5030) | 6.17 |
| 2 | LLDPE + Fatty Acids+ Fiber | 9.22 |

VI. Machinability Study

VI.1. Material Preparation

The machining experiment was conducted on a three-axis conventional milling and drilling machine at University Malaysia Perlis teaching factory. Chip morphology, machined surface characteristics and dimensional accuracy were the machinability measures selected to study the machinability the blends and industrial blue wax as shown in Fig. 8.

Table IX demonstrates the industrial blue wax specification. The lathe and milling machine operating speed were carried out at 3,000 and 8,000 RPM for roughing and finishing. For the three differences blend tested, the chips were carefully collected and observed.

A 0.5 inch diameter carbide two-flute end mill and drilling were used for milling and drilling operation. Tool wear is not considered on the experiments because the specimen doesn't effect on the tool wear. Only one tool is used in the experiment.



Fig. 8. Industrial blue wax

TABLE IX
INDUSTRIAL BLUE WAX SPECIFICATION

| Industrial Blue Wax | Specification |
|--|----------------------|
| Hardness Shore D | 50-55 |
| Specification Gravity | 0.92 |
| Flash Point | 575°F |
| Volumetric Shrinkage at Room Temperature | 226°F |
| Coefficient of Thermal expansion (In./in °F) | 9.5×10^{-5} |
| Colour | Blue |
| Tensile Strength | 850psi, 4MPa |

VI.2. Measurement of Surface Roughness

Surface roughness is represented by the parameter Ra, of the blend surface machined. The values of surface

roughness are the average of the three measurements taken at the middle of the surface finish of the blend.

The highest value of tensile strength and hardness were selected and the sample test were sent to milling machining process at the cutting speed of 800 rpm for roughing and 1000 rpm for finishing, a feed of 0.11 mm/rev, and a depth of cut of 0.5 mm were used.

The surface roughness test was performed using Mitutoyo Formtracer CS-3100 model F3000 with the speed rate of 0.2 mm/s.

VI.3. Dimensional Consistency

The purpose of the study is to investigate the dimensional consistency during drilling operation. The 5 cm diameter drilling tool was used in this experiment.

The average values for the 3 different drilling spots were taken into account.

VII. Surface Roughness Measurement Results

Table X summarizes the average surface roughness measurement results for different blends. Blend 1 represent composition between LLDPE, Fatty acids and fiber and blue wax represents the result for the industrial blue wax. The results indicate that surface roughness for industrial blue wax is higher compared to the surface roughness of the LLDPE, Fatty acids and fiber blends.

Fig. 9 shows the graph of the surface roughness measurement results for the three different blends. From the graph shown, it is a clear picture that blue wax is dominating on the surface roughness results. Several samples had a higher tensile strength value were selected for machinability study.

TABLE X
SURFACE ROUGHNESS RESULTS FOR DIFFERENCE BLENDS

| Composition | Surface Roughness, Ra | | | |
|---|-----------------------|-------|-------|---------|
| | Run 1 | Run 2 | Run 3 | Average |
| Blend 1: LLDPE, Fatty Acid, Fiber Blend | 2.22 | 3.83 | 2.98 | 3.01 |
| Industrial Blue Wax | 3.83 | 5.26 | 3.86 | 4.32 |

Based on the experimental results of the surface roughness measurement, the following conclusions can be mentioned:

- The higher surface roughness value, the rough the blend sample is.
- The different trend of surface roughness for the three blends and blue wax is probably due to their tensile strength and the hardness values. This is because the hardness of work piece materials is closely associates with its ductility. Ductility is an influential factor in determining the workpiece surface roughness during machining. Hardness is one of the basic mechanical characteristic for the machining materials. Hardness of the material has the advantage of being easy to measure as compared with other characteristics. Fig. 6 exhibits the hardness result for the blend. The

hardness value range between 33-45 IRD.

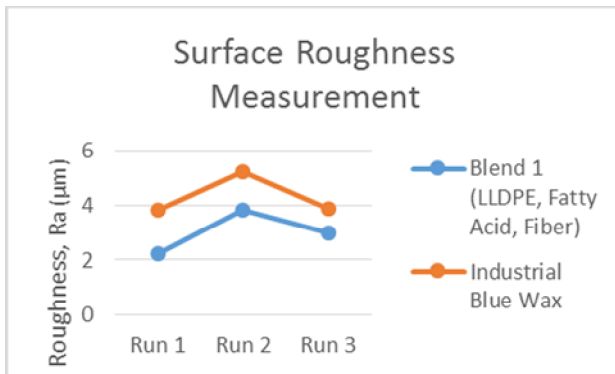


Fig. 9. Surface Roughness Measurement Results

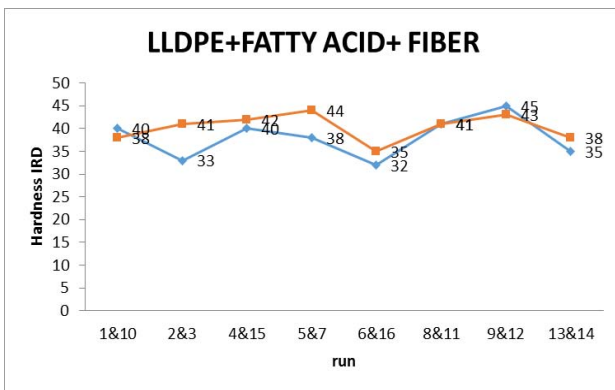


Fig. 10. Hardness Measurement Results

VIII. Chips Formation Characteristics

The mechanism of chip formation is one of the fundamental considerations to determine machinability of the material because it relates to properties, surface integrity and machining characteristics. Unlike metals, the chips formed during the machining of polymers are significantly affected by their unique characteristics like low thermal conductivity and temperature dependent mechanical properties.

The composition between LLDPE/Fatty Acids/Fiber showed good machinability in terms of chip formation produced. Continuous chips were formed over the specific cutting speed in this study. At a higher speed, chips curled slightly. A chip shape was found that it curled inwards or clockwise. This phenomenon happened because of deformation zones during the chip formation, namely the primary and the secondary zones.

Shear deformation occurs in the primary zone to accommodate the deformation caused by the change in material flow direction. In the secondary zone, plastic deformation and compressive residual stress twist the chip inwards.

Fig. 11(a) shows the drilling process on the Industrial blue wax. The purpose of the drilling process on the blend is to identify the machinability characteristics on various machining process. Figure 11(b) shows the chips formation occurred during drilling process.

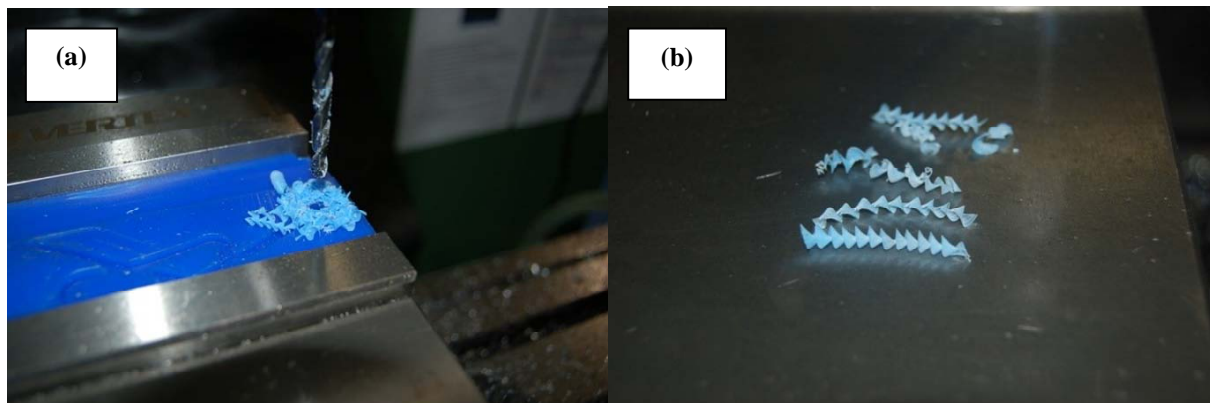
The orientation of the chips formation of the Industrial blue wax is follow thru the direction. Also, the chips produced were not sticking on the cutting tool because of the material itself is self-lubricating. Fig. 12(a) shows the drilling process for the blend of LLDPE, Fatty Acid, Fiber.

The chip was sticking on the cutting tool during the drilling process. The chips produced as shown in Fig. 12(b) can be easily broken down into small pieces. Table XI summarized the chip formation of different blends that occurred during the machining process.

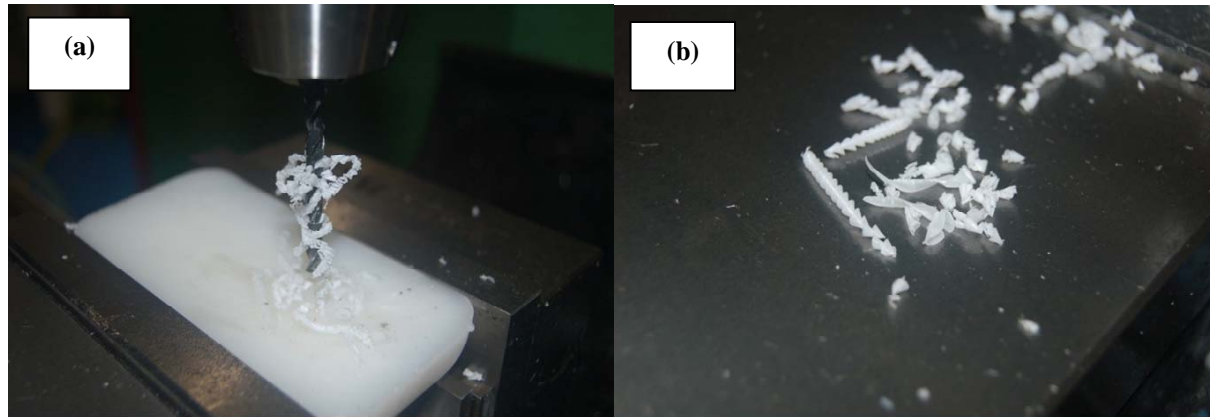
IX. Dimensional Consistency

The 5 cm diameter tool was used in this experiment. The purpose of the study is to investigate the dimensional accuracy during drilling operation. In this operation, it is easier to observe the changes on the blends and samples. All the holes measurement was taken by using vernier caliper.

The observation shows that all dimensions for the blends and blue wax holes are quite accurate. The measurement result is 4.58 cm and the tolerance is +/- 0.05 cm.



Figs. 11. Drilling process and chips formation for Industrial Blue Wax



Figs. 12. Drilling process and chips formation for Blend of LLDPE, Fatty Acid, Fiber

TABLE XI
MACHINABILITY OF DIFFERENCE COMPOSITES

| | Composite | Chips Formation |
|---|----------------------------|-----------------|
| 1 | Industrial Blue Wax | Continuous |
| 2 | LLDPE + Fatty Acids+ Fiber | Continuous |

In conclusion, all the blends and blue wax are not associated with dimensional changes. Fig. 13 shows the results for the dimensional consistency for different blends and industrial wax.

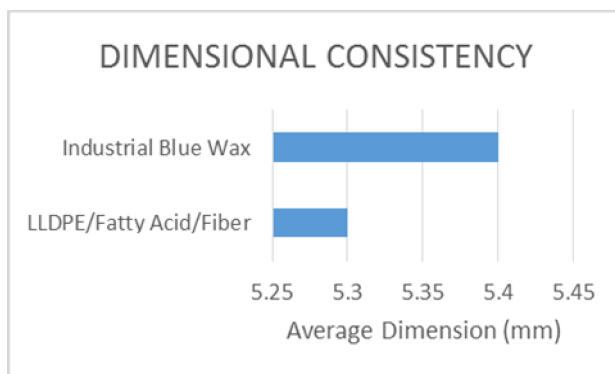


Fig. 13. Dimensional Consistency Measurement

The results are within the range of 5.2 mm and 5.4 mm and the result is still under acceptable tolerance.

The drilling process shows that the blends would not affect on the dimensional consistency.

X. Cutting Tool Wear

The Tool wear is associates with cutting condition during machining process. The heat generated on the cutting tool causes surface wear and tear to occur. In this study, infra-red gun thermometer is used to observe the heat generated during the machining of blend samples.

The infra-red gun thermometer is a non-contact infrared thermometer is supplied by ThermoWorks Company.

The temperature on the contact surface with cutting tool were measured and recorded on the graph as shown in Fig. 14. However, the temperature result would not

affect the tool wear because of the tool itself is strong enough to support the machining process.

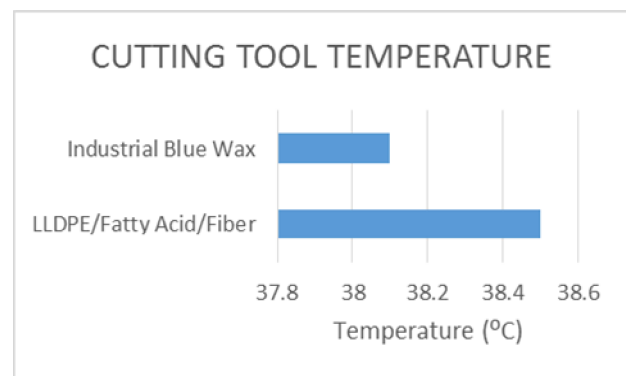


Fig. 14. Cutting Tool Temperature

XI. Conclusion

Prototype making by using low cost material is benefited to the companies and educational sector in terms of material cost saving and reusability.

Educational sector which focus on theory and practical are able to take advantage to produce product prototype more effective. The usage of excessive Palm Oil based wax help the environment to be clean and friendly. Thus, it gives the value added for the manufacturing product. Fatty acid/Palmac Fatty acid was used as main component from waste Palm oil product to improve the tensile strength of the material and machinability by adding additional ingredients such as LLDPE. The new blend of composites would give positive outcome to the manufacturing prototype industries especially in manufacturing product.

Fatty acid has the potential to mix with polymer and fiber in order to substitute existing industrial wax which is a petroleum base. This material is able to be produced

in a solid form and has good potential for engineering application. Further machining processes can be tested on turning, drilling and milling.

In brief, the development of the natural-fibers composite and Palmac Fatty Acid would make a positive impact on a global scale, especially for the product industry and educational purposes.

References

- [1] Andrzej K. Bledzki, Abdullah A. Mamun, Adam Jaskiewicz, Karsten Erdmann, Polypropylene composites with enzyme modified abaca fibre, *Composites Science and Technology*, Volume 70, Issue 5, May 2010, Pages 854-860.
- [2] Rajamony. B, Khalil. N, Hamid. F. Development of palm oil based bio-product industrial wax and its application performance study. *Journal of Life Sciences*, vol. 4(4), 2010, p. 22-27
- [3] C.C.Ho and M.C.Chow, The Effect of the Refining Process on the Interfacial Properties of Palm Oil. *JAOCS*, 2000. 77: p. 191-199.
- [4] Soon, T.K., An Overview of The Asean Oleochemical Market. *Malaysian Oil Science and Technology* 2000. 10(2).
- [5] Sreekala, M.S., et al., The mechanical performance of hybrid phenol-formaldehyde-based composites reinforced with glass and oil palm fibers. *Composites Science and Technology*, 2002. 62(3): p. 339-353.
- [6] Bledzki, A.K. and J. Gassan, Composites reinforced with cellulose based fibers. *Progress in Polymer Science*, 1999. 24(2): p. 221-274.
- [7] Aiman, A.F., Tarmizi, A.M., Bakri, B., Hussin, M.S., Hafiezal, M.R.M., Fairuz, M.A., A study on fiber glass composite hovercraft hull with different wall thickness using generative structural analysis, (2012) *International Review of Mechanical Engineering (IREME)*, 6 (6), pp. 1307-1311.
- [8] Devaki Devi, K., Naga Phani Sastry, M., Sankaraiah, G., Optimization of turning parameters on engine lathe using design of experiments, (2012) *International Review of Mechanical Engineering (IREME)*, 6 (6), pp. 1202-1208.
- [9] Ranganathan, S., Senthilvelan, T., Prediction of machining parameters of surface roughness of GFRP composite by applying ANN and RSM, (2012) *International Review of Mechanical Engineering (IREME)*, 6 (5), pp. 1068-1073.

Authors' information



Ahmad Nabil Mohd Khalil received his B.Eng in Mechanical & Manufacturing Engineering from Universiti Tun Hussein Onn and Master degree in Manufacturing Engineering from Universiti Malaysia Perlis, Malaysia. The research interest is in machining composites, product innovation, computer simulation.
E-mail: nabilkhalil@unimap.edu.my



Mohd Fidzwan Md Amin Hamzas received his BSc degree in Mechanical Engineering from Universiti Malaysia Perlis and Master's degree in Mechanical Engineering (Manufacturing) from Universiti Tun Hussein Onn, Malaysia. His main research area is in scheduling problems and engineering simulation.



Mohd Sabri Hussin received his B.Eng in Manufacturing Engineering from Universiti Malaysia Perlis and and Master degree in Innovation and Engineering Design form Universiti Putra Malaysia, Malaysia .The research interest is in modeling and control, product innovation and engineering simulation on automotive safety.



Zailani Zainal Abidin received his B. .Eng degree in Manufacturing Engineering from Universiti Malaysia Perlis, ,Malaysia and Master's degree in Manufacturing System from Universiti Putra Malaysia, Selangor, Malaysia. .The research interest is in machining technology and manufacturing system.



A. B. Sanuddin was born on 18th of March 1984. Holding Bachelors' degree in Mechanical Engineering from Universiti Putra Malaysia(UPM) and graduated in 2007. Later on He continued his study (master of science) in Mechanical Engineering at Universiti Putra Malaysia (UPM) in 2008. His research interest is related to Mechanical Engineering, Stress Analysis and Functionally Graded Materials.
E-mail: asmawi@unimap.edu.my

An Effect of Boric Acid Mixture as Solid Lubricant Towards Machining Processes

Z. A. Zailani, A. B. Sanuddin, M. S. Hussin, A. N. M. Khalil,
M. F. M. A. Hamzas, Nurliana Ahmad Mustafa

Abstract – Milling is widely used metal removal process in manufacturing industry that involves generation of high cutting forces and temperature. Lubricants become important in order to reduce the cutting force and temperature for better machining processes and performances. Conventional cutting fluid has some limitations. The applications of conventional cutting fluid create some techno-environmental problems like environmental pollution, biological problems to operators and water pollution. Application of solid lubricant in milling has proved to be a feasible alternative to the conventional cutting fluids. The present work investigates the effect of boric acid as solid lubricant towards machining performances such as tool wear and surface roughness. The results indicate that boric acid can improve the cutting processes and performance compared to conventional cutting fluid. **Copyright © 2013 Praise Worthy Prize S.r.l. - All rights reserved.**

Keywords: Milling, Cutting Fluid, Solid Lubricant, Boric Acid

I. Introduction

Machining can be defined as the process of removing material from a workpiece in the form of chips. Machining is the most important steps in manufacturing processes. In milling machining process, a rotating cutter removes material while travelling along various axes with respect to the workpiece [1]. Milling includes a number of highly versatile machining operations, taking place in a variety of configurations with the use of a milling cutter which is a multi-tooth tool that produces number of chips in one revolution.

In any metal cutting tool operations, lot of heat is generated due to plastic deformation of the work material, friction at the tool-chip interface and friction between tool and the workpiece. The heat produced in milling adversely affects the quality of products. So, it is generally considered that the heat produced during machining process is critical in terms of workpiece quality. Thus, the effective control of heat generated at the cutting zone is essential to ensure good workpiece surface quality machining [2].

Cutting fluids have been the conventional choice to deal with the problem. But, the application of conventional cutting fluids creates some techno-environmental problems like environmental pollution due to chemical disassociation of cutting fluids at high cutting temperatures, biological problems to operators, water pollution and soil contamination during disposal [3].

The use of cutting fluids needs to be eliminated. But any attempt to minimize or avoid the coolant can be dealt with only by replacing the functions normally met by the coolants with some other means.

Application of solid lubricant in machining has proved to be feasible alternative to cutting fluids, if it can be applied properly. If friction of the tool and workpiece interactions can be minimized, by providing effective lubrication, the heat generated also can be reduced to some extent. Advancement in modern tribology has identified many solid lubricants, which can sustain and provide lubricity over a wide range of temperatures.

Most of these lubricants, which include graphite, molybdenum disulphide, tungsten disulphide, and calcium fluoride, belong to a special class of materials known as lamellar solids.

Boric acid (H_3BO_3) is one of the most popular solid lubricants and has excellent lubrication properties without calling for expensive disposal techniques [4]. The most important characteristics of boric acid for use as solid lubricant are that it is readily available and environmentally safe. The Environmental Protection Agency has established that boric acid is benign and the Clean Water Act does not classify it as pollutant.

In order to produce any product with desired quality by machining, cutting parameters should be selected properly. Cutting speed, feed rate, depth of cut are the process parameters, which influence the machining process to great extent [5]. In milling, the speed and motion of the cutting tool is specified through several parameters. These parameters are selected for each operation based upon the workpiece material, tool material, tool size and more.

The selection of cutting tool materials for a particular application is among the most important factors in operations, as the selection of mold and dies materials for forming and shaping processes.

In this study, High-speed Steels (HSS) were used as cutting tool. HSS tools are so named because they were developed to machine at higher speeds than was previously possible. They can be hardened to various depths, have good wear resistance, and are relatively expensive. Because of their toughness, HSS are suitable especially for high, positive rake-angle tools, interrupted cuts, machine tools with low stiffness that are subject to vibration and chatter, and complex and single-piece tools, such as drills, reamers, taps, and gear cutters [1].

Their most important limitation (due to their lower hot hardness), is that cutting speed are low compared to those of carbide tools.

Tool wear is a major consideration in all machining operations. Tool wear adversely affects tool life, the quality of the machined surface and its dimensional accuracy, and consequently, the economics of cutting operations [1]. Moreover tool wear also can affect the tensile residual stress [6]. The rate of tool wear depends on tool and workpiece materials, tool geometry, process parameters, cutting fluids and the characteristics of the machine tool. Some general effects of tool wear include [7]:

- Increased cutting forces
- Increased cutting temperature
- Poor surface finish
- Decreased accuracy of finished part

Similar to some surface properties such as hardness, the value of surface roughness depends on the scale of measurement. Roughness is a measure of texture of a surface. It is quantified by the vertical deviations of real surface from its ideal form. If these deviations are large, the surface is rough; if they are small the surface is smooth. Roughness is typically considered to be high frequency, short wavelength component of a measured surface [8].

Characterization of surface topography is important in applications involving friction, lubrication and wear [9]. In general, it has been found that friction increases with average roughness. Roughness parameters are important in applications such as machining.

The main functions of lubricant in a metal cutting process are to lubricate or reduce friction between the tool and the workpiece and to act as a coolant by rapidly removing heat generated at the tool or workpiece interface [10]. Lubricants are used to reduce friction and wear, thus improving tool life and the surface finish of workpiece. It also cooled the cutting zone, thus improving tool life and reducing the temperature and thermal distortion of the workpiece. Besides, lubricant reduces forces and energy consumption.

Lubricants can flush away the chips from the cutting zone; therefore prevent the chips from interfering with the cutting process. Moreover, it protects the machined surface from environmental corrosion.

A solid lubricant is a material used as powder or thin film to provide protection from damage during relative movement and to reduce friction and wear. Other terms commonly used for solid lubricant include dry

lubrication and solid film lubrication. Although these terms imply that solid lubrication takes place under dry conditions, fluids are frequently used as a medium or as a lubricant with solid additives [11].

Boric Acid (H_3BO_3) is one of the most popular solid lubricants and has excellent lubrication properties without calling for expensive disposal techniques. The most important characteristics of boric acid for use as solid lubricant are that is readily available and environmentally safe [3]. The Environmental Protection Agency has established that boric acid is benign and the Clean Water Act does not classify it as a pollutant. Several studies related to the lubrication properties of boric acid are carried out over the past several decades [12]. These works have primarily focused on the performance of boric acid's unique layered inter-crystalline structure makes it very promising solid lubricant material because of its relatively high load carrying capacity and low steady state friction coefficient.

Another study focused on the use of boric acid as solid lubricant in manufacturing processes such as forming and drilling. In metal forming applications, it is shown that boric acid provided very low friction between aluminum workpiece and a steel forming tool. During the processes, the post-fabrication cleaning of boric acid was environmentally safe, non-toxic and water-soluble. In another work, drilling experiments with sapphire tools indicated that the addition of boric acid to distilled water increased the rate of drilling polycrystalline alumina by a factor of two.

In addition, boric acid was found to help in reducing friction and corrosion when mixed with cutting and grinding fluids during machining processes [4].

II. Experimentation

Experiments have been conducted under two conditions. First condition is machining by using ordinary coolant only.

The second condition is using ordinary coolant with boric acid mixture. The amounts of the boric acid are different in each sample. Sample A consist of (ordinary coolant), sample B (ordinary coolant with 50 grams boric acid), sample C (ordinary coolant with 100 grams boric acid), and sample D (ordinary coolant with 150 grams boric acid). For this experimentation, two parameters have been investigated.

The parameters are surface roughness and tool wear.

II.1. Cutting Parameters

Table I shows the details of cutting parameter used during the experiments. The cutting speed and feed rate are selected based on the tools manufacturer's recommendation.

The High Speed Steel (HSS) cutting tools are used because they were cheaper than other types of cutting tools.

TABLE I
CUTTING PARAMETER

| Cutting tool | | High speed steel (HSS) end mill 4 flute | | | | | |
|-------------------|------------------|---|-----------------------|-----------------------|------------------------|-----------------------|--------------------------|
| Material | | Mild steel (100mm×70mm×16mm) | | | | | |
| Cutting condition | | Liquid cooland, mix coolant (liquid + powder) | | | | | |
| Sample | Diameter (in mm) | Spindle speed (in rpm) | Feed rate (in mm/min) | Flow rate (in mm/min) | Length of cut (mm/min) | Depth of cut (mm/cut) | Machining time (min/cut) |
| A | 8 | 1400 | 200 | 10 | 100 | 0.5 | 0.5 |
| | 15 | 700 | 220 | 10 | 100 | 0.5 | 0.5 |
| B | 8 | 1400 | 200 | 10 | 100 | 0.5 | 0.5 |
| | 15 | 700 | 220 | 10 | 100 | 0.5 | 0.5 |
| C | 8 | 1400 | 200 | 10 | 100 | 0.5 | 0.5 |
| | 15 | 700 | 220 | 10 | 100 | 0.5 | 0.5 |
| D | 8 | 1400 | 200 | 10 | 100 | 0.5 | 0.5 |
| | 15 | 700 | 220 | 10 | 100 | 0.5 | 0.5 |

Moreover, the characteristics of HSS made it suitable for machining mild steel. The cutting tool diameters, flow rate, length of cut, depth of cut and machining time are selected based on previous researcher suggestion [13].

II.2. Surface Roughness

The measurement of surface roughness is based on roughness average (Ra). It was carried out using MAHR Perthometer PGK. The limit of tracing distance is 17.5 mm. Therefore, each slot was divided by the three point of measurement which is 5.6 mm distance each. There were three profiles taken, which are P and R profile. P profile is the largest profile peak height and the largest peak valley. Meanwhile R profile is roughness profile represents the deviation of the primary profile from the mean line.

During this experiment, three parameters had been considered. The parameters were roughness average (Ra), mean roughness depth (Rz) and maximum roughness depth (Rmax). Fig. 1 shows the analysis of surface roughness.



Fig. 1. Surface Roughness Analysis

II.3. Tool Wear

The tool wear of each cutting tools were analyzed using Leica MS 5 Stereomicroscope. Every flute is measured for each cutting tool. For 8 mm tool, the optic size used is 1.6x + 1.0x.

Meanwhile, 0.63x + 1.0x optic size is used for 15 mm tool. Fig. 2 shows the analysis of tool wear.



Fig. 2. Tool Wear Analysis

III. Results and Discussions

III.1. Tool Wear

The data for tool wear analysis was measured by using Leica MS5 Microscope. Overall results for tool wear are presented Table II.

Fig. 3 and Fig. 4 show the comparison between the total flank wear of all samples with different cutting fluid conditions. The results indicate that Sample B, C, and D have better cutting performance than Sample A due to lower total flank wear. Also, it has been observed that the more boric acid used the better cutting performance.

During machining, heat is generated at the cutting zone. The ordinary cutting fluid may not effectively reduce the heat generated because it loses its cooling properties upon film boiling temperature of ordinary cutting fluid are lower than that of biodegradable coolants means boric acid. Solid lubricant also can sustain and provide lubricity over a wide range of temperatures [14].

TABLE II
FLANK WEAR RESULTS

| Diameter | Sample | Width of flank wear (in 100µm) | | | | Total Flank Wear |
|----------|--------|--------------------------------|---------|---------|---------|------------------|
| | | Flute 1 | Flute 2 | Flute 3 | Flute 4 | |
| 8 mm | A | 19.5 | 20.4 | 18.7 | 19.3 | 77.9 |
| | B | 16.4 | 13.8 | 19.5 | 17.4 | 67.1 |
| | C | 12.3 | 20.1 | 10.9 | 22.6 | 65.9 |
| | D | 13.7 | 13.1 | 14.6 | 18.5 | 59.9 |
| 15 mm | A | 19.9 | 27.4 | 27.3 | 51.7 | 124.3 |
| | B | 20.7 | 19.5 | 16.4 | 22.1 | 78.7 |
| | C | 20.3 | 18.6 | 13.8 | 16.1 | 68.8 |
| | D | 16.6 | 12.7 | 23.1 | 5.9 | 58.3 |

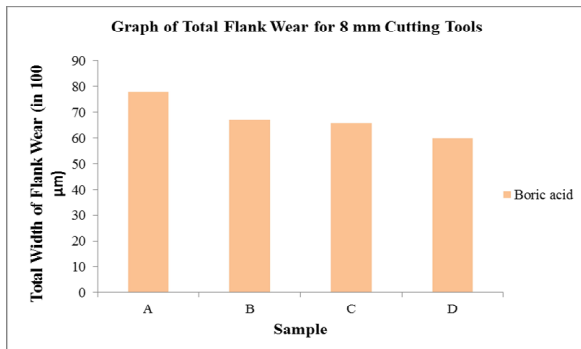


Fig. 3. Total Flank Wear for 8 mm Cutting Tools

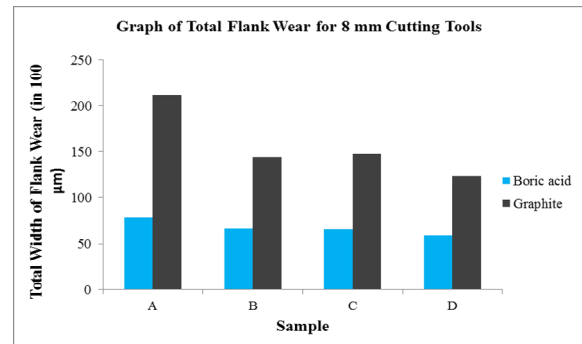


Fig. 5. Graph of Total Flank Wear for All Samples with Different Cutting Fluid

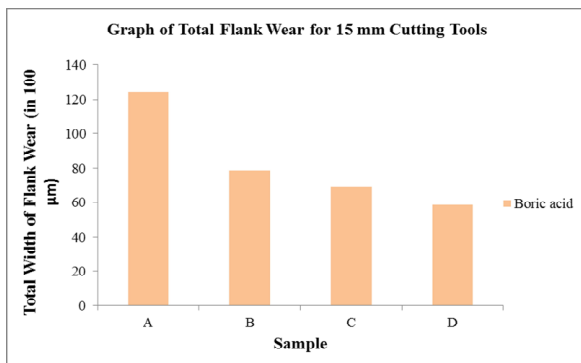


Fig. 4. Total Flank Wear for 15 mm Cutting Tools

The lubricant effectiveness in minimizing the frictional effect at the tool and workpiece interaction in case of boric acid assisted machining is evident from the reduced of total flank wear in Sample B, C and D compared to Sample A. Moreover, low coefficient of friction and sliding action when boric acid assisted machining has affected the flank wear.

Total flank wear is observed considerably less for 8 mm cutting tools compared to 15 mm cutting tools. This is because the cutting parameters used for both diameters were different.

The effectiveness of the solid lubricant in any context is strongly affected by temperature, pressure, speed, and environmental conditions. In this project, the feed rate and spindle feed used were different for both diameters.

Fig. 5 shows the comparison of flank wear with different types of solid lubricants. It has been observed that the flank wear values obtained in boric acid is less than graphite. This is due to the lubricating property of boric acid, which help the reduction of cutting force.

III.2. Surface Roughness

Table III shows the Roughness average for 8 mm and 15 mm cutting tools. The machining time was three minutes for each sample with one minute interval.

The surface roughness for nine points was taken for each sample.

A comparative performance analysis of the ordinary cutting fluid application with boric acid is done. Fig. 6 shows the comparison of Roughness average from all 8 mm cutting tools with different cutting fluid conditions.

The machining parameters such as cutting speed, feed rate and flow rate are constant. Sample A gives the highest value of Ra. The condition is same for 15 mm cutting tools as shown in Fig. 7. As mentioned before, the cutting fluid used for Sample A is ordinary coolant only. Meanwhile cutting fluids used for Sample B, Sample C and Sample D are ordinary coolant with boric acid. Results show that the better surface finished was achieved with the application of solid lubricant which is boric acid compared to ordinary coolant.

Previous study indicated that boric acid's unique layer inter-crystalline structure makes it a very promising solid lubricant material because of its relatively high load carrying capacity and low steady state friction coefficient [15]. However Sample C point out better surface finish compare to Sample D at first and second machining minutes. This may be caused by some errors that happen during surface roughness analysis.

The perthometer is very sensitive with movement or vibration because it will affect the results. It has be observed from the results that surface finish for 8 mm cutting tools are better that 15 mm cutting tools.

It is because there are some factors can influence the surface roughness during machining like tool geometry and process parameters. The feed rate used was different.

For 8 mm tools the feed rate used was 200 mm/min meanwhile for 15 mm tools the feed rate used was 220 mm/min.

The comparative Roughness average of boric acid and graphite has been carried out. As shown in Figs. 8, 9 and 10 boric acid indicate better surface roughness than graphite. The decrease in surface roughness due to boric acid can be attributed due to the inherent lubricating properties even at high temperatures [3].

TABLE III
SURFACE ROUGHNESS RESULTS

| Sample | Machining time (min) | Surface roughness | | | | |
|--------|----------------------|-------------------|------|------|------|------|
| | | Ra | 3.3 | 3.08 | 3.39 | |
| A | 8mm | 1 | 3.79 | 3.3 | 3.08 | 3.39 |
| | | 2 | 3.36 | 3.21 | 3.66 | 3.51 |
| | | 3 | 3.83 | 3.79 | 3.8 | 3.81 |
| | 15mm | 1 | 4.95 | 5.44 | 5.74 | 5.38 |
| | | 2 | 5.82 | 5.35 | 5.36 | 5.51 |
| | | 3 | 5.95 | 9.91 | 6.01 | 5.96 |
| B | 8mm | 1 | 0.75 | 0.86 | 1.33 | 0.98 |
| | | 2 | 1.24 | 1.3 | 1.51 | 1.35 |
| | | 3 | 1.12 | 1.07 | 1.41 | 1.2 |
| | 15mm | 1 | 1.12 | 1.04 | 1.1 | 1.09 |
| | | 2 | 1.38 | 1.61 | 1.06 | 1.35 |
| | | 3 | 1.07 | 0.85 | 0.88 | 0.93 |
| C | 8mm | 1 | 1.02 | 1.02 | 1.03 | 1.02 |
| | | 2 | 0.99 | 0.95 | 1.1 | 1.01 |
| | | 3 | 1.27 | 1.63 | 2.48 | 1.79 |
| | 15mm | 1 | 0.94 | 1.21 | 1.3 | 1.15 |
| | | 2 | 1.18 | 1.28 | 1.27 | 1.24 |
| | | 3 | 0.95 | 1.06 | 0.93 | 0.98 |
| D | 8mm | 1 | 1.23 | 1.14 | 1.37 | 1.25 |
| | | 2 | 2.08 | 2.05 | 1.3 | 1.81 |
| | | 3 | 1.5 | 1.5 | 1.72 | 1.57 |
| | 15mm | 1 | 1.29 | 1.19 | 1.11 | 1.2 |
| | | 2 | 0.99 | 1.12 | 1.15 | 1.09 |
| | | 3 | 1.07 | 1.97 | 1.99 | 1.68 |

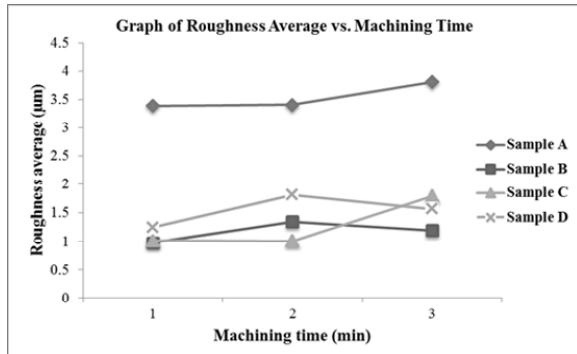


Fig. 6. Graph of Roughness Average vs. Machining Time for 8 mm cutting tools

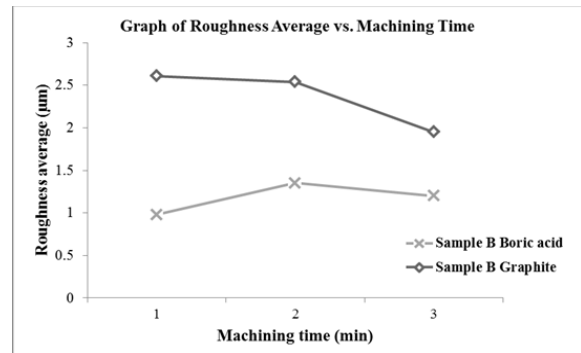


Fig. 8. Graph of Comparison Roughness Average for Boric Acid and Graphite (Sample B - 8 mm)

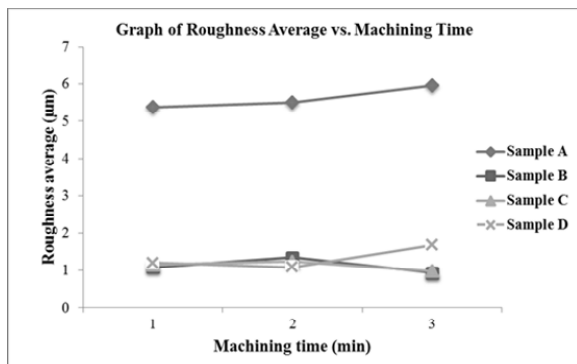


Fig. 7. Graph of Roughness Average vs. Machining Time for 15 mm cutting tools

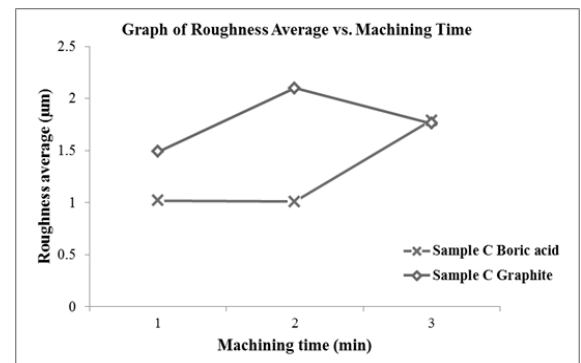


Fig. 9. Graph of Comparison Roughness Average for Boric Acid and Graphite (Sample C - 8 mm)

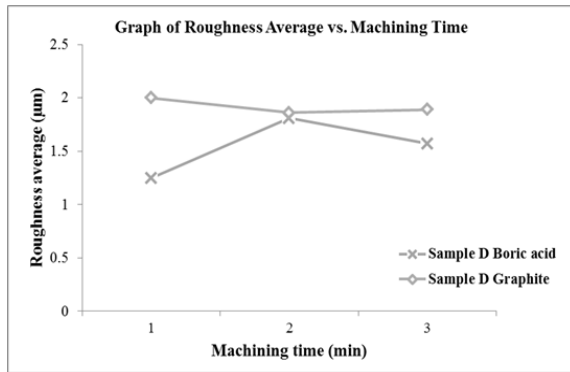


Fig. 10. Graph of Comparison Roughness Average for Boric Acid and Graphite (Sample D - 8 mm)

IV. Conclusion

The project objectives are to investigate and compare the effect of solid lubricant means boric acid to cutting parameters such as tool wear and surface roughness.

The objectives of this project are achieved successfully. The findings of the project can be concluded as follows:

1. Application of ordinary coolant may not effectively control the heat generation in milling. Besides, cutting fluids are major source pollution.
2. There is a considerable improvement in the process performance with solid lubricant assisted machining as compared to that of machining with ordinary lubricant.
3. Boric acid improved the process performance by reducing the cutting forces and tool wear. This is because of the formation of a boric acid film on the surfaces is lubricious and functioned due to its layered crystal structure and unique bond characteristics.
4. Better surface finish is achieved with the application of boric acid compared to ordinary coolant. This is because boric acid produces low coefficient of friction at the tool workpiece interface with the formation of lubricating film.
5. Boric acid is environmentally safe, non-toxic and water soluble.

References

- [1] Kalpakjian, S. & Schmid, S. *Manufacturing Engineering and Technology* (6th Edition, Pearson Prentice Hall, 2010).
- [2] Dilbag Singh, Rao P. V. *Improvement in Surface Quality with Solid Lubrication in Hard Turning*. Proceedings of the World Congress on Engineering. London, 2008.
- [3] Pasam, V. K. & Damera, N. R. Performance evaluation of solid lubricant in terms of machining parameters in turning, *International Journal of Machine Tools & Manufacturer*, 48, 1131-1137, 2008.
- [4] Damera, N. R. & Pasam, V. K. Performance Profiling of Boric Acid as Lubricant in Machining, *International Journal of Machine Tools & Manufacturer*, 3, 239-244, 2008.
- [5] Reddy, N. S. & Rao, P.V. Experimental investigation to study the effect of solid lubricants on cutting forces and surface quality in end milling, *International Journal of Machine Tools and*

Manufacture, 46 :189-198, 2005.

- [6] Dawson, T.G. & Kurfess, T. R. *Tool Life, Wear Rates and Surfaces Quality in Hard Turning*, Georgia Institute of Technology, Atlanta, Georgia, 2002.
- [7] Rao, P.N. *Manufacturing Technology- Metal Cutting and Machine Tools*, (Singapore: McGraw Hill International Edition, 2002)
- [8] Thomas, T.R., *Rough Surfaces*, 2nd ed., Imperial College Press, London (1999). Tungsten carbide, PCBN and PCD cutting tools. *Elsevier International Journal of Machine Tools & Manufacture*. 46: 482-491, 1999.
- [9] Schey, J.A. (2000). *Introduction to Manufacturing Processes* (3rd Edition, United State of America: McGraw-Hill Higher Education, 2000).
- [10] Kajdas, C., Karpinska, A. & Kulczycki, A. (2010). *Chemistry and Tecnology of Lubricants* (3rd Edition, Springer Science, 2010).
- [11] Busch, C. *Lubricants*, 9. Solid Lubricants. *Ullmann's Encyclopedia of Industrial Chemistry*, 2011.
- [12] Peterson, M.B.; Murray, S.L.; Florek, J.J, "Consideration of lubricants for temperatures above 10000F", *ASME Transactions*, Vol. 2, pp: 225-234, 1960.
- [13] Zailani, Z.A., Hussin, M.S., Hamzas, M.F.M.A., Hasnul, M.J., Sanuddin, A.B., The correlation between surface finish in milling process involving solid lubricant, (2012) *International Review of Mechanical Engineering (IREME)*, 6 (6), pp. 1262-1267.
- [14] Stachowiak, G.W. and Batchelor, A.W. *Engineering Tribology*, Butterworth-Heinenann, Woburn, 2001.
- [15] Hussin, M.S., Hamzas, M.F.M.A., Hadi, H., Sanuddin, A.B., Zailani, Z.A., Study of machining parameters of wire electrical discharge of aluminum matrix composites (AMCs) with Taguchi method, (2012) *International Review of Mechanical Engineering (IREME)*, 6 (7), pp. 1434-1440.

Authors' information



Zailani Zainal Abidin received his B. Eng degree in Manufacturing Engineering from Universiti Malaysia Perlis, Malaysia and Master's degree in Manufacturing System from Universiti Putra Malaysia, Selangor, Malaysia. The research interest is in machining technology and manufacturing system.



A. B. Sanuddin was born on 18th of March 1984. Holding Bachelors' degree in Mechanical Engineering from Universiti Putra Malaysia (UPM) and graduated in 2007. Later on He continued his study (master of science) in Mechanical Engineering at Universiti Putra Malaysia (UPM) in 2008. His research interest is related to Mechanical Engineering, Stress Analysis and Functionally Graded Materials. E-mail: asmawi@unimap.edu.my



Mohd Sabri Hussin received his B.Eng in Manufacturing Engineering from Universiti Malaysia Perlis and and Master degree in Innovation and Engineering Design form Universiti Putra Malaysia, Malaysia. The research interest is in modeling and control, product innovation and engineering simulation on automotive safety.



Ahmad Nabil Mohd Khalil received his B.Eng in Mechanical & Manufacturing Engineering from Universiti Tun Hussein Onn and Master degree in Manufacturing Engineering from Universiti Malaysia Perlis, Malaysia. The research interest is in machining composites, product innovation, computer simulation.



Mohd Fidzwan Md Amin Hamzas received his BSc degree in Mechanical Engineering from Universiti Malaysia Perlis and Master's degree in Mechanical Engineering (Manufacturing) from Universiti Tun Hussein Onn, Malaysia. His main research area is in scheduling problems and engineering simulation.

Experimental Investigation on the Performance, Emission and Combustion Characteristics of a Diesel Engine Fuelled with Polymer Oil - Ethanol Blends

Ganapathi P., Robinson Y.

Abstract – This paper describes an experimental study of using polymer oil obtained from the plastic waste as a fuel in diesel engine. In this study, the effects of using polymer oil – ethanol fuel blends [PE10, PE20] on the engine performance, exhaust emissions and combustion characteristics have been experimentally investigated. In the present work, 10% ethanol and 90% polymer oil, called here as PE10 and 20% Ethanol and 80% polymer oil called here as PE20 were used in a single cylinder four stroke, water cooled diesel engine. The engine fuelled by the blends is comparable with that fuelled by diesel. The experimental result showed that the carbon monoxide, carbondioxide, Oxides of nitrogen and smoke were significantly reduced. Unburned hydrocarbon, brake specific fuel consumption and brake thermal efficiency were found to have increased with ethanol-polymer oil blends. Copyright © 2013 Praise Worthy Prize S.r.l. - All rights reserved.

Keywords: Diesel, Polymer Oil, Plastic Waste, Ethanol, Engine Performance

I. Introduction

Plastics are used on a daily basis throughout the world. Due to their relatively low cost, versatility, durability and obduracy to water, they are used in a wide range of products. Plastics are synthetic substances produced by chemical reactions. Almost all plastics are derived from petroleum. Plastics are polymers, very long chain molecules that consist of monomers, linked together by chemical bonds. The monomers of petrochemical plastics are inorganic substances and are non-biodegradable. Hence, this leads to the soil contamination and in long term, serves as a cause for severe environmental hazards such as degradation of soil fertility, pollution of surface and subsoil water.

As per the survey conducted in India in the year 2000, nearly 6000 tonnes of plastic waste were produced on a daily basis and only 60% got recycled [1]-[2]. The remaining 40% could not be recycled. Many of the industries have developed several processes to convert waste plastics into fuels [3]-[4]. M. Murugan [5] has studied the use of pyrolysis tyre oil in the diesel engine.

The results show that the engine can produce high smoke levels and relatively low thermal efficiency due to high viscosity and carbon residue as compared to diesel. The polymer oil is derived from the plastic waste.

M. Mani [6] investigated the feasibility of using the waste plastic oil in the diesel engine. It was concluded that the waste plastic oil has properties similar to that of diesel fuel and could be used as a substitute to diesel.

CO₂, CO, NO_x and HC emissions were marginally higher than the diesel.

Using non-conventional fuels, such as vegetable oil, ethanol and methanol in internal combustion engines have the potential to reduce the dependency on petroleum fuels. Ethanol can be produced from vegetable materials such as sugarcane, corn, sugarbeets, and barley, ethanol fuels cannot be used in unmodified diesel engines because of higher volatility, lower miscibility and low cetane number [7].

Ethanol can be used in diesel engine blended with conventional diesel fuel [8]-[9]. The effect of ethanol blends with diesel fuel on the emissions of a diesel engine is found to be a decrease in CO and NO_x emission levels. THC emission increased with the use of ethanol [10]. Di et al. [11] Studied the exhaust emissions of diesel engine, using ethanol-blended diesel fuels.

The results have shown that the brake thermal efficiencies increased with an increasing amount of ethanol in blended fuels. The objective of the present study is to investigate the performance, the emission and the combustion characteristics of a diesel engine fuelled with polymer oil-ethanol blends.

II. Plastic Waste to Polymer Oil

Plastic waste material was converted into uniform size by the process of crushing, cutting and shredding in the feed system, for the purpose of handling and melting. This process of sizing and grading the waste was semi automatic.

The graded feed was stored in a hopper before feeding into the reactor by a conveyor feeder.

The dust and the other fine wastes collected from the cyclone filter are disposed through a vent with particle size monitoring system. The plastic waste was treated in a reactor along with a catalyst and maintained at a temperature of 275°C–375°C at atmospheric pressure for about 3 to 4 hours.

The outlet gas from the pyrolysis process was condensed in a series of condensers and the liquid obtained was taken as fuel. The uncondensed gases were let out into the atmosphere. Properties of diesel, polymer oil and ethanol are compared in Table I.

III. Experimental Set Up

Tests were conducted on a single cylinder, four stroke, direct injection, water cooling kirlosakar diesel engine at an engine speed of 1500 rpm. The engine has a 800cc cylinder volume. The test engine specifications are given in Table II.

The schematic arrangement of the experimental set up and photographic view are shown in Figs. 1 and 2. The test engine was directly coupled to an eddy current dynamometer for load measurement. Airflow meter was used to measure the airflow.

The fuel measuring tube (burette) was used to measure the fuel flow rate. The pressure transducer was used to measure the cylinder pressure. It was fit onto the cylinder head with a charge amplifier. AVL di-gas analyzer was used to measure NO_x/HC/CO/CO₂ emission in the exhaust gas. Exhaust gas temperature was measured with a thermo couple. AVL smoke meter was used to measure the smoke density in the exhaust.

Combustion characteristic of the engine was measured by the AVL combustion analyzer.

The fuels used in this study include diesel, polymer oil and ethanol. Diesel was obtained from Indian Petroleum Corporation. Polymer oil and ethanol were purchased from a commercial supplier.

TABLE I
FUEL PROPERTIES OF DIESEL, POLYMER OIL AND ETHANOL

| Property | Diesel (5) | Polymer oil | Ethanol |
|--------------------------------|------------|-------------|---------|
| Gross calorific value (kJ/Kg) | 46,500 | 45216 | 29800 |
| Density @30 °C in (g/cc) | 0.840 | 0.7949 | 0.789 |
| Kinematic viscosity, cst @40°C | 2.0 | 2.85 | 1.2 |
| Cetane number | 55 | 51 | 5-8 |
| Flash point (°C) | 50 | 41 | 13 |
| Fire point (°C) | 56 | 43 | 18 |
| Oxygen content (wt.%) | 0 | 0 | 34.8 |

TABLE II
SPECIFICATIONS FOR KIRLOSAKAR DIESEL ENGINE

| Parameter | Specification | Unit |
|---------------------|---------------|------|
| Power | 3.7 | Kw |
| Speed | 1500 | RPM |
| Cylinder bore | 0.08 | m |
| Stroke | 0.11 | m |
| Number of cylinders | 4 | -- |
| Number of strokes | 4 | -- |
| Type of cooling | Water | -- |

The volume percentage tested were 10%, and 20% of ethanol, with 90% and 80% of diesel fuel respectively which were named as PE10 and PE20. The fuel blends were prepared just before starting the experiment so that the fuel mixture is homogenous.

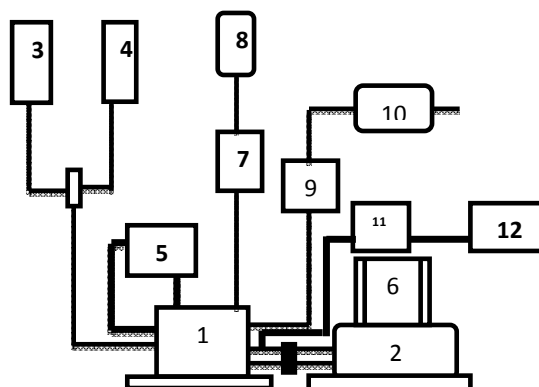


Fig 1. Experimental setup of the test engine

1. Engine
2. Dynamometer
3. Fuel Tank
4. Fuel Measuring Tube(burette)
5. Cooling Water Inlet and Outlet Thermometer
6. Control panel
7. Air flow meter
8. Air filter
9. Smoke meter
10. Exhaust gas analyzer
11. Charge amplifier
12. Monitor



Fig. 2. Photographic view of the Experimental set up

IV. Result and Discussion

The experiment was conducted in a standard diesel engine at an engine speed of 1500 rpm. A comparison of the engine performance, the emission and the combustion characteristics for the following combinations was made and the results were presented.

- Diesel fuel
- Polymer oil
- Polymer oil – ethanol blends

IV.1. Performance

IV.1.1. Brake Thermal Efficiency

The brake thermal efficiency with the engine load of polymer oil-ethanol blends is compared with the diesel and polymer oil as shown in Fig. 3.

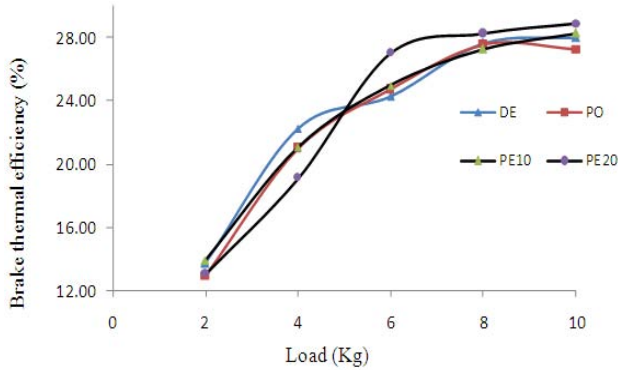


Fig. 3. Variation of brake thermal efficiency with load

It can be observed from the figure that the brake thermal efficiency of PE10 and PE20 are 28.27% and 28.84%, while those of diesel and polymer oil are 28% and 27.25%.

The brake thermal efficiency has slightly increased with the increase of ethanol in the blends. The reason may be the presence of oxygen concentrations aiding improvement in combustion especially diffusion combustion that contributes higher thermal efficiency.

Another reason may be due to the heat loss decrease in the cylinder due to lower flame temperature of ethanol than that of diesel [12].

IV.1.2. Brake Specific Fuel Consumption

Fig. 4 shows the variation of the brake specific fuel consumption with load for the tested fuels.

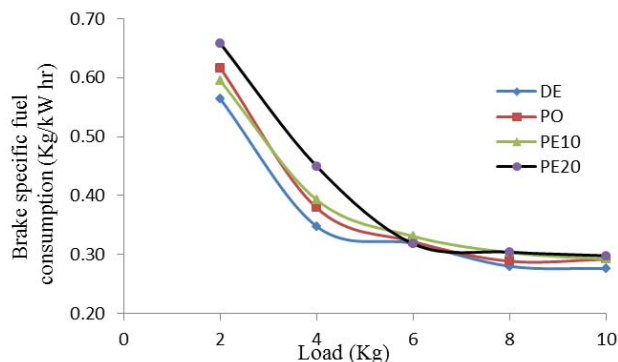


Fig. 4. Variation of brake specific fuel consumption with load

It can be observed from the figure that the brake specific fuel consumption has increased with the increase percentage of ethanol in the blends. Brake specific fuel consumption varies from 0.56kg/kWhr at 20% of load to 0.28kg/kWhr at full load for diesel and varies from

0.62kg/kWhr at 20% of load to 0.29kg/kWhr at full load for polymer oil.

In the case of polymer oil-ethanol blends, it varies from 0.59kg/kWhr and 0.66kg/kWhr at 20% of load to 0.29kg/kWhr and 0.30kg/kWhr at full load. The main reason for the increase of specific fuel consumption is due to the lower heating value of ethanol than that of diesel.

IV.2. Emission

IV.2.1. Carbon Monoxide

The variation of carbon monoxide with load is shown in Fig. 5 CO emission is toxic and must be controlled.

The concentration of CO emission varies from 0.07% at 20% of load to 0.09% at full load for diesel, It varies from 0.07% at 20% of load to 0.14% at full load for polymer oil, whereas it varies from 0.08% and 0.09% at 20% of load to 0.11% and 0.08% at full load for polymer oil-ethanol blends (PE10, PE20).

The results show that the CO emission of PE10 and PE20 blend fuels are lower than the polymer oil and PE20 blend fuel tends to produce lower exhaust CO values than the diesel at full load. An enrichment of oxygen owing to ethanol addition can be noticed and the increase in the proportion of oxygen will promote the further oxidation of CO during engine exhaust process.

IV.2.2. Unburned Hydrocarbon

The variation of unburned hydrocarbon with load for tested fuels is shown in Fig. 6.

Unburned hydrocarbons are produced when the fuels are incompletely burned. Unburned hydrocarbon varies from 32 ppm at 20% of load to 57ppm at full load for diesel. It varies from 49ppm at 20% of load to 91ppm at full load for polymer oil.

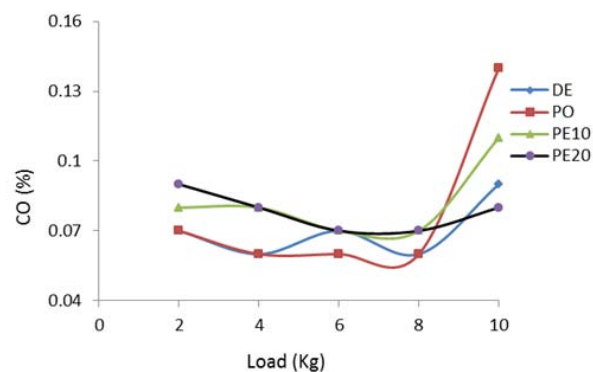


Fig. 5. Variation of carbon monoxide with load

In the case of polymer oil –ethanol blends (PE10, PE20), it varies from 54ppm and 66ppm at 20% of load to 88ppm and 85ppm at full load.

From the results, it can be noticed that the concentration of the hydrocarbon of PE10 and PE20 blend fuels are marginally lower than the polymer

oil and higher than the diesel. HC emission increase is higher with a higher percentage of ethanol in the blend.

This may be attributed to two reasons. One is that alcohols have lower cetane numbers which lead to longer ignition delays and decomposition of blended fuels [13]. The other one is that high latent heat of vaporization of ethanol tends to produce slow vaporization and mixing of fuel and air [14].

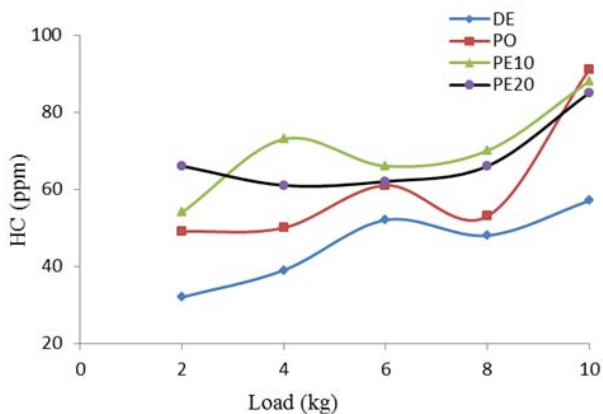


Fig. 6. Variation of unburned hydrocarbon with load

IV.2.3. Oxides of Nitrogen

The formation of NO_x is mostly dependent on oxygen concentration and cylinder temperature. Fig. 7 shows the comparison of oxides of nitrogen with load for the tested fuels. It can be noticed that the NO_x emission decreases in the polymer oil –ethanol blends. NO_x varies from 129 ppm at 20% of load to 855 ppm at full load for diesel, and from 150 ppm at 20% of load to 904ppm at full load for polymer oil.

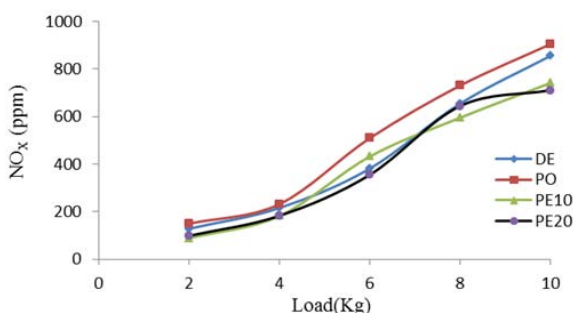


Fig. 7. Variation of oxides of nitrogen with load

In the case of PE10 and PE20, it varies from 89ppm and 99ppm at 20% of load to 741 and 711 at full load.

The reason for decreased NO_x is the cooling effect of alcohols, the dominant factor on NO emission. Higher latent heat of evaporation (840kj/kg) and lower calorific value of ethanol reduce the combustion temperature which causes reduction of NO_x emission [15].

IV.2.4. Carbondioxide

Carbondioxide occurs naturally in the atmosphere and

is a normal product of combustion[16]. Fig. 8 depicts the variation of carbon dioxide emission with load for DF, PO, PE10 and PE20 operation.CO₂ concentration varies from 2.60% at 20% load to 6.90% at full load for diesel.

It can be observed that in polymer oil, it varies from 2.82% at 20% load to 7.80 at full load.

For PE10 and PE20, it varies from 2.60 and 2.70 at 20% load to 7.20 and 6.70 at full load. From the results, it can be observed that the amount of CO₂ emissions decreases with the increase of ethanol (PE20) in the blends. The main reason of CO₂ reduction is low C/H and oxygen content of the blends [14].

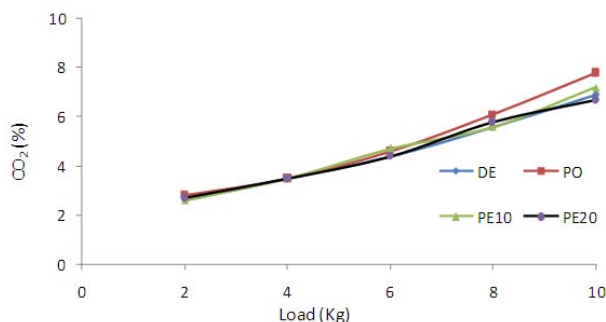


Fig. 8. Variation of carbon dioxide with load

IV.2.5. Smoke

Smoke opacity is indicative of dry soot emissions which is one of the main components of particulate matter [17]. Fig. 9 shows the comparison of smoke level with load. Smoke level varies from 1.7% at 20% load to 53.5% at full load for diesel, from 2% to 55.1% for polymer oil. It varies from 6.8% and 10.8% to 42.7% and 30.7% for PE10 and PE20.

It can be observed that the soot emitted by the polymer oil-ethanol fuel blends is significantly lower than the corresponding neat diesel and polymer oil fuel.

The presence of high oxygen content of blend fuels reduces probability of rich zones formation and aromatics fractions contribute to the reduction of smoke [18].

IV.3. Combustion Parameters

IV.3.1. Heat Release Rate

The comparison of heat release rate for diesel, polymer oil and ethanol-blends operation at full load is shown in Fig. 10. It can be observed that the maximum heat release rate of 40J/°CA is recorded for diesel, while polymer oil records its maximum heat release rate of 41J/°CA.

It can also be noticed that the maximum heat release rate is 42J/°CA for PE10 and 44J/°CA for PE20. Ethanol blends show the maximum heat release rate at full load compared to diesel. Heat released during the premixed combustion is higher for ethanol polymer oil blend than diesel due to higher ignition delay.

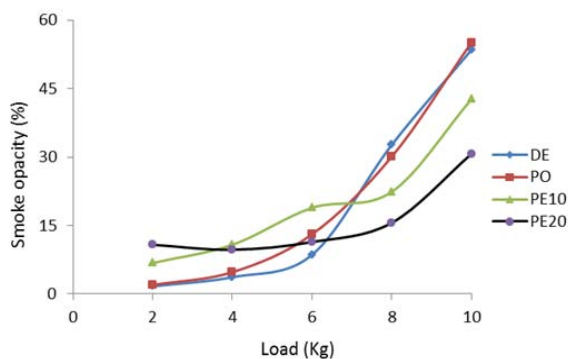


Fig. 9. Variation of smoke with load

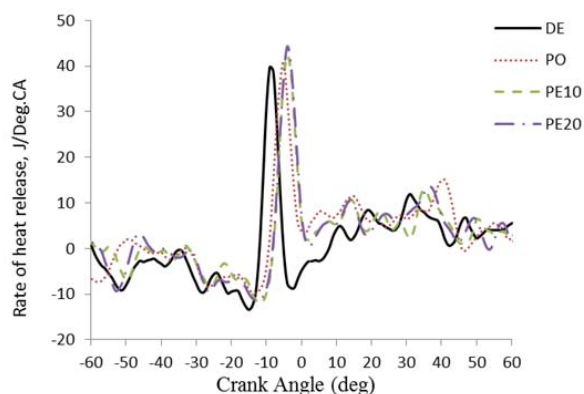


Fig. 10. Variation of heat release rate with crank angle

IV.3.2. Cylinder Pressure-Crank Angle Diagram

Fig. 11 indicates the cylinder pressure with crank angle at full load for the fuels tested. The cylinder pressure obtained at full load indicates higher value for polymer oil – ethanol blends compared to diesel and polymer oil. It can also be seen that for diesel operation, the cylinder peak pressure is about 61 bar and for polymer oil, it is 63 bar.

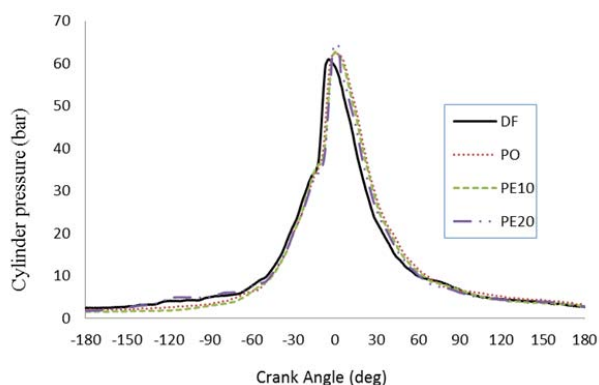


Fig. 11. Variation of cylinder pressure with crank angle

The cylinder peak pressure for PE10 and PE20 are 63 bar and 65 bar respectively. In a CI engine, the peak pressure depends on the combustion rate in the initial stages, which is influenced by the amount of fuel taking part in the uncontrolled combustion phase that is

governed by the delay period [19]-[20]-[21].

The addition of ethanol results in lower cetane number of the blended fuels and higher latent heat of evaporation, which further increases the ignition delay.

The increase in ignition delay of PE10 and PE20 results in a strong premixed burning phase and gives rise to the peak cylinder pressure.

V. Conclusion

The variations in the engine performance, the emission and the combustion parameters of a diesel engine using polymer oil-ethanol blends have been investigated. Based on the experimental results, the following conclusions are drawn.

- The soot emitted by the polymer oil-ethanol fuel blends (PE10, PE20) is significantly lower than the corresponding neat diesel and polymer oil fuel, with this reduction being higher the percentage of alcohol in the blend.
- PE20 blend fuel tends to produce lower exhaust CO and CO₂ values than the diesel and polymer oil at full load.
- The use of polymer oil – ethanol blends (PE10, PE20) caused a decrease in the emission of NO_x compared to polymer oil and diesel
- HC emission increased with use of polymer oil-ethanol blends than the diesel
- The brake specific fuel consumption and brake thermal efficiency have slightly increased with the increased percentage of ethanol in the blends.
- Heat release rate for polymer oil-ethanol blends are higher than that of diesel.
- The cylinder pressure obtained at full load indicates higher value for polymer oil – ethanol blends compared to diesel and polymer oil.

Acknowledgements

The authors sincerely thank the Government Engineering College, Bargur, for providing experimental set up to conduct the experiments.

References

- [1] PhongHai Vu, Osami Nishida, Hirotsugu Fujita, Wataru Harano, Norihiko Toyoshima, Masami Iteya, *Reduction of NOx and PM from diesel engines by WPD emulsified fuel*, SAE Technical Paper 2001-01-0152.
- [2] Sudhir Kumar, J., Subbaiah, K.V., Prasada Rao, P.V.V., Experimental studies on a DI-CI engine using blends of diesel fuel with plasti diesel derived from plastic waste, (2011) *International Review of Mechanical Engineering (IREME)*, 5 (3), pp. 540-547.
- [3] <http://www.ozmotech.com.au>
- [4] <http://www.polymerenergy.com>
- [5] S. Murugan, M.C. Ramaswamy, G. Nagarajan, *Assessment of pyrolysis oil as an energy source for diesel engines*, *Fuel Processing Technology*, 90, pp.67-74, 2009
- [6] M.Mani, C.Subash, G.Nagarajan, *performance, emission and combustion characteristics of a DI diesel engine using Waste*

- plastic oil, *Applied Thermal Engineering*, 29 pp.2738-2744,2009
- [7] Y.Ali,K.M.Eskridge,M.A.Hanna,*Testing of alternative diesel fuel from tallow and soybean oil in cummins N14-410 diesel engine*, *Bio resource Technology*, 53,pp.243-254,1995
- [8] He BQ,WangJJ,YanXG,*Study on combustion and Emission Characteristics of Diesel Engines Using Ethanol Blended Diesel Fuels*.SAE Technical paper 2003-01-0762
- [9] CorkwellKC,JacksonMM,DalyDT.*Review of exhaust Emissions of Compression Ignition Engines Operating on E Diesel Fuel Blends*. SAE Technical Paper 2003-01-3283
- [10] RakopoulosDC,RakopoulosCD,KakarasEC,GiakoumisE.*Effect of ethanol-diesel fuel blends on the engine performance and emissions on heavy duty DI diesel engine*. *Energy conversion Management*,49(11):pp.3155-3162,2008
- [11] Di Y. Cheung CS. Huang Z. *Comparison of the effect of biodiesel-diesel and ethanol-diesel on the gaseous emission of a direct-injection diesel engine*. *Atmos Environment* 43(17):pp.2721-2730,2009
- [12] Lu XC, YangJG,ZhangWG,HuangZ.*Effect of cetane number improver on heat rate and emission of high speed diesel engine fueled with ethanol-diesel blend fuel*. *Fuel* 83:pp.2013-2020,2004
- [13] Nadir Yilmaz,*Performance and Emission characteristics of a diesel engine fuelled with biodiesel-ethanol and biodiesel-methanol blends at elevated air temperatures*.*Fuel*,94,pp.440-443,2012
- [14] Bang-QuanHe,Shi-Jin Shuai,Jian-XinWang,Hong He,*The effect of ethanol blended diesel fuels on emissions from a diesel engine*. *Atmospheric Environment*,37,pp.4965-4971,2003
- [15] JinchengHuang,YaodongWang,ShuangdingLi,AnthonP.Roskilly, HongdongYu,HuifenLi.*Experimental investigation on the performance and emissions of a diesel engine fuelled with ethanol-diesel blends*. *Applied Thermal Engineering* 29 pp.2484-2490,2009
- [16] A. Pawar, R. R. Kulkarni, J. B. Sankpal, *Prediction of CO₂ in the Exhaust of C.I. Engine Using Emission Model* *International Review of Mechanical Engineering*,2007; Vol .1 n. 1 pp. 127 – 130,2007
- [17] Cenk Sayin, *Engine performance and exhaust gas emissions of methanol and ethanol-diesel blends*. *Fuel* 89,pp.3410-3415,2010
- [18] Caro, P.S,Moulounguia,Z,Vaitilingomb,G., Berge,J.C., *Interest of combining an additive with diesel-ethanol blends for use in diesel engines*. *Fuel* 80,pp.565-574,2001
- [19] Ramesh Babu, P., Prasad, V.J.J., Hari Babu, N., Appa Rao, B.V., *Combustion and performance analysis of DI-diesel engine fuelled with neat mahua methyl ester along with oxygenated fuel (DEE) as an additive*, (2012) *International Review of Mechanical Engineering (IREME)*, 6 (1), pp. 147-152.
- [20] Yoshiyuki Kidoguchi, Changlin Yang, Ryoji Kato, Kei Miwa, *Effects of fuel cetane number and aromatics on combustion process and emission of a direct injection diesel engine*, *SAE Review* 21 , pp.469-475,2000
- [21] J.B. Heywood, *Internal Combustion Engine Fundamentals*, (NewYork, McGraw Hill, 1988).

Authors' information



Mr. **P. Ganapathi** was born in 1984 in Nallipalayam, Namakkal, Tamilnadu, India. He has completed his under graduation in Mechanical Engineering from Anna University, Chennai. He obtained his Master Degree in Engineering in the field of Thermal Engineering from Anna University, Chennai in 2009. He started his carrier in 2009 as Assistant Professor in Mechanical Engineering, RVS Technical Campus, Kannampalayam, Coimbatore, Tamilnadu, India. He has participated in several conferences, seminars and workshops. His area of research is internal combustion Engine and Fuel. Currently, he is pursuing Ph.D in Mechanical Engineering under Anna University, Chennai, Tamilnadu, India.



Dr. **Y. Robison** is the Director of RVS Technical Campus, Coimbatore, Tamilnadu, India. He obtained his Bachelor of Engineering in Mechanical Engineering and Master of Engineering in Refrigeration and Air-conditioning. He has completed his Ph.D in Mechanical Engineering in the year 2006. He has more than 20 years of experience in both teaching and industry. He has published 15 research papers in the refereed journals/Conferences for his credit. Currently he is guiding 6 Ph.D Research Scholars.

Biodiesel Blend, Fuel Properties and its Emission Characteristics Sterculia Oil in Diesel Engine

P. P. Sethusundaram¹, K. P. Arulshri², K. Mylsamy³

Abstract – In the wake of current energy scenario, major research is focused on sustainable energy solution with major emphasis on energy efficiency and use of renewable energy sources. Diesel engines have proven their utility in the transportation and power sectors due to their higher efficiency and ruggedness. Depending upon the availability and production capabilities, biodiesel is derived from a large variety of oilseed. Sterculia bio fuel is identified and proved to be the best alternative to the diesel engine. Laboratory tests were carried out to determine the properties like specific gravity, kinematic viscosity, cloud point, pour point, flash point, fire point and calorific value of the fuels used. The overall performance and emission tests have given good results except for the NO_x component of the emission, which is a potential cause for smog and acid rain. This paper also focuses on the reduction of this component to a great extent with the implementation of a technique called Exhaust Gas Recirculation. In this method the water cooled exhaust of the engine is circulated back to the inlet manifold to crack the harmful NO_x. This makes the bio diesel a completely emission free alternative. Copyright © 2013 Praise Worthy Prize S.r.l. - All rights reserved.

Keywords: Bio Fuel, Sterculia Oil, Calorific Value, Emission, Exhausts Gas

I. Introduction

A large variety of alternative fuels are considered potential substitute to petroleum based diesel, however, modification, handling and transportation, ease of production, and investment cost are some of the important parameters that should be considered before using an alternative fuel in an existing diesel engine.

Several research and project in the field of internal combustion engines are being focused on reduced emission, which not only makes commercial sense but also helps benefit the environment [1]-[16].

Reducing harmful emissions from diesel vehicles not only helps improve local air quality but can also result in business benefits such as lower tax rate, increased company profile and can attract environmentally friendly business, which is now becoming increasingly important with the current focus on corporate social responsibility. Biodiesel fuel (fatty acid methyl esters), which is produced by methanolysis of triglycerides, has recently attracted considerable attention as a renewable, biodegradable, and nontoxic fuel. During the past decade, the environmental benefits of using this fuel have accelerated the development of processes for its production around the world. In the several processes so far proposed, chemical catalysts including alkalis have been employed most widely since they give a high conversion of triglycerides to methyl esters in a short reaction time.

However, processes using an alkaline catalyst have several drawbacks including the difficulty of recycling

glycerol, the need to eliminate the catalyst and salt, and their energy-intensive nature, leading to development of alternative processes.

Bio diesel, due to its biodegradable nature, and essentially no sulphur and aromatic contents, offers to reduce particulate and toxic emissions (Avinash kumar agarwal, 2001) [1]. Bio diesel when mixed with diesel fuel in small quantities also seems to improve the fuel lubricity, extend engine life and reduce fuel consumption. Sterculia oil is used as an alternative to diesel.

This oil is chosen because it has properties similar to that of diesel and mixing with the petroleum diesel would be really easy. Due to higher cetane number and lubricating properties (Gerhard Vellguth, 1983) [2], this fuel gives good performance with any diesel engine. While analyzing the emissions in Sterculia oil and comparing with that of diesel, all the components in the emission got reduced drastically except NO_x.

II. Materials and Experiments

II.1. Sterculia Foetida Oil

Sterculia is a genus of flowering plant in the mallow family, Malyaceae. It was previously placed in the now obsolete Sterculiaceae. Sterculia species are used as food plants by the larvae of some Lepidoptera species. Java olive is a soft wooded tree that grows up to 115 feet high.

The tree has smooth, grayish – white bark and a fibrous inner bark.

The woody, bright red fruit consist of 1-5 spreading follicles that are armed with stiff stinging bristle along the inner margins. Each follicle split to reveal up to 17 blue black seeds attached to inner margins (Fig. 1).



Fig. 1. Sterculia Foetida plane with fruit and seeds

II.2. Test Engine

The test engine is Kirloskar made, four-stroke, single cylinder, direct-injection, water-cooled, constant speed (1800rpm), and naturally aspirated CI engine. It has a bore of 87.5mm and stroke of 110mm. the compression ratio is 17.5:1. The combustion chamber is direct injection type with a bowl-in piston design.

II.3. Trans – Esterification Process

The trans-etherification process is carried out in order to reduce the viscosity of the oil by removing the fatty acid present in it. The materials required of the process are:

1. The OIL to be used.
2. ALCOHOL – Methanol.
3. CATALYST – sodium hydroxide.
4. WASHING AGENT - Distilled Water.
5. SEPARATING DEVICE

Initially 5.3g of NAOH is weighed and mixed with 300ml of methanol in a closed container so as to prevent the evaporation of methanol.

After mixing, 1.5 litter of raw sterculia oil is taken in a container and heated to the temperature of 40°C with constant stirring, without any swirl formation so as to enhance uniform stirring. 100ml mixture of NAOH and methanol is taken in a burette and added to the raw sterculia oil with a constant interval of 30min. during addition of the mixture the temperature should be maintained between 50°C - 60°C. If the temperature exceeds beyond this limit the oil could catch fire since methanol ignites at very low temperature.

When all the mixture of methanol and NAOH is added to the raw sterculia oil it is allowed to settle in the container for 10hrs. After this there will clear separation on glycerol and the ester which is the required oil i.e. the Biodiesel required of us. Initially Trans – esterification process was planned to do both with ethanol.

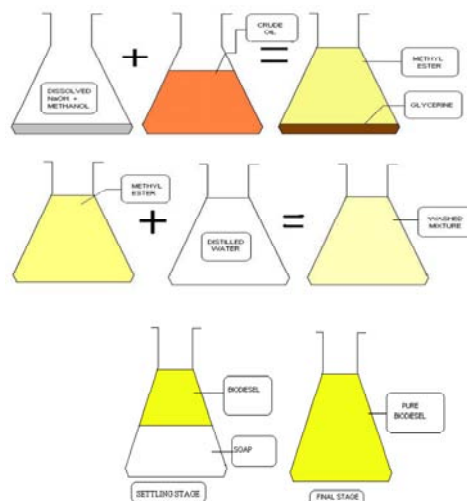


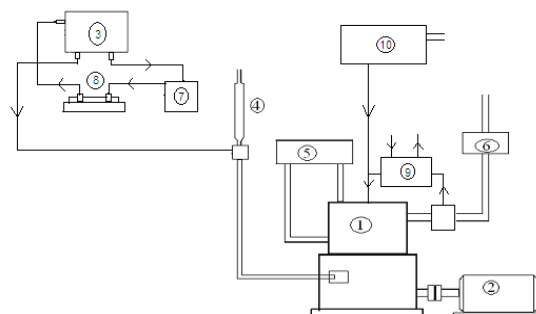
Fig. 2. The tran-esterification process and its by-products

During the process of Trans – esterification with ethanol the NAOH pilots was added to the raw sterculia oil without mixing with the ethanol. This didn't show any satisfactory chemical process. Then same quantity NAOH was added again which made all the 3 liters of oil in to soap. Learning from the mistake done with the ethanol, the Trans – esterification was done correctly with methanol. The ester was separated using an electrical centrifuge, which is as shown below: The final test which proves that the oil is undergone good Trans - esterification is by its golden colour formation and the smell which should not have any occurrence of the alcohol used in process. The picture below shows the difference between raw sterculia oil and trans- esterified oil.

II.4. Methodology Experimental Process

The following steps were followed in approaching the above said problem of emissions and scope for Sterculia oil in the future as an alternate fuel.

1. Single cylinder four stroke water-cooled electrically loaded engine with AVL five gas analyzer and AVL smoke meter was preferred for experiments.



1) Engine 2) Alternator 3) Fuel Tank 4) Fuel metering tube 5) Cooling water Thermometer 6) Exhaust Gas Thermometer 7) Fuel pump 8) Heating unit 9) EGR 10) Air box

Fig. 3. Schematic diagram of experimental setup

2. The Sterculia oil was procured and blends of 25%, 50%, 75% and 100% bio diesel were prepared for the testing purpose.
3. The performance tests and the heat balance tests have been carried out to compare the various blends and their performance with each other was carried out.
4. A comparison study between the performance of the blends and the emission comparison is also presented.

II.5. Air Flow Measurements

As the air-fuel ratio was determined by the air and fuel flow measurements, care was taken to measure the air flow accurately. A calibrated orifice meter was attached with anti-pulsating drum measures air consumption of the engine with the help of U-tube manometer. Manifold vacuum was measured using another U-tube manometer.

The anti pulsating drum fixed in the inlet side of the engine maintained a constant suction pressure, to facilitate constant airflow through the orifice meter.

II.6. Exhaust Emission Measurements

The major emissions from the four-stroke diesel engines were NOx and smoke emissions. The carbon monoxide and unburned hydrocarbon emissions were low due to the supply of excess air for combustion.

Transient exhaust smoke emission was measured using the AVL smoke meter. Oxides of nitrogen (NOx) concentration in exhaust were measured by electrochemical method using the AVL DiGas analyzer.

The CO, CO₂ and HC emissions were measured by Non-Dispersive Infra Red (NDIR) method with the same analyzer.

III. Results and Discussion

III.1. Properties of Sterculia Foetida Oil

The important properties of biodiesel blends were experimentally determined. Laboratory tests were carried out to determine the properties like specific gravity, kinematic viscosity, cloud point, pour point, flash point, fire point and calorific value of the blends using IS 15607 test methods shown in Table I.

TABLE I
PROPERTIES OF STERCVLIA FOETIDA OIL TESTED

| S.no | Properties | Sterculia oil |
|------|---------------------------------|------------------|
| 1 | Kinematic Viscosity at 40°C | 6.31 Cst |
| 2 | Flash Point (°C) | 56 |
| 3 | Fire Point (°C) | 201 |
| 4 | Cetane number | 59-65 |
| 5 | Calorific value (MJ/L) | 40.8 |
| 6 | Pour point(°C) | Minus 10 |
| 7. | Copper strip corrosion | Not worse than 1 |
| 8. | Ash content (%) | 0.009 |
| 9. | Water content (by dean & Stark) | 0.96%W/V |
| 10. | Acidity | 0.62mg of KOH/g |
| 11. | Conradson Carbon Residues (CCR) | 0.84% |
| 12. | Sediments (Hexane Insoluable) | 0.018% |

III.2. Performance and Emission Characteristics at Standard Injection Timing and Pressure

The results of engine performance, emission tests and combustion studies are presented in the following sections. The experiments were carried out in a naturally aspirated single cylinder water cooled DI diesel engine with Sterculia Foetida oil -diesel blends and the results are presented and discussed. Sterculia Foetida oil was blended with diesel fuel in various proportions on volume basis from 25% and increased by 25% volume step by step. Sterculia Foetida oil was the main fuel for the present investigation and to analyze the impact of the source of biodiesel on engine performance and emissions. The standard injection timing of 23° bTDC and standard injection pressure of 210 bar was used for testing. Owing to the differences among the calorific values and oxygen contents of the fuels tested, the comparison must be affected at the same engine load and not the same injected fuel mass or air-fuel ratio (Rakopoulos et al 2008) [3].

Although most of the literature reviewed shows a slight increase in NOx emissions when using biodiesel fuel, some works showing different effects have been found. Some of them found NOx increases only in certain operating conditions; some others did not find differences between diesel and biodiesel fuels, and others still found decreases in NOx emissions when using biodiesel. The NOx emission values have also come down drastically with the increase in the percentage of the exhaust being re-circulated into the inlet port. The emission of CO is reduced drastically with bio diesel.

Bio diesel almost completely eliminates lifecycle carbon dioxide emissions. When compared to diesel it reduces emission of particulate matter by 40%, unburned hydrocarbons by 68%, and carbon monoxide by 44%.

With the implementation of EGR the emissions of bio diesel almost remains same except for the NO_x emission which gets reduced drastically. The emission of NO_x reduced to 0.05%. This proves that with 100% bio diesel the engine can run without any trouble. The temperature reduction of the exhaust before re-circulating reduced the potential of the NO_x emission as found from engine when tested with the AVL 437C Smoke Meter.

An important observation was that the performance of the engine was not affected with the implementation of the EGR. The pressure with which the air enters into the engine depending upon the load can control the amount of exhaust gas entering in the inlet of the engine. Going for additives like orange oil, dimethyl carbonate or diethylether can improve the performance of the engine. A 20% by volume addition of these additives can give very good results. Figs. 4 - 9 prove that exhaust gas recirculation is necessary for diesel Engine to reduce NOx emission at the cost of performance characteristics. NOx is 6ppm for BD5, 5ppm for BD10, 3ppm for BD75 this drastic reduction is due to suppression of combustion temperature during diffused combustion. CO is reduced 33% from BD5 to BD75 HC also get reduced 25.92% from BD5 to BD75 these are shown in Figs. 4 to 9.

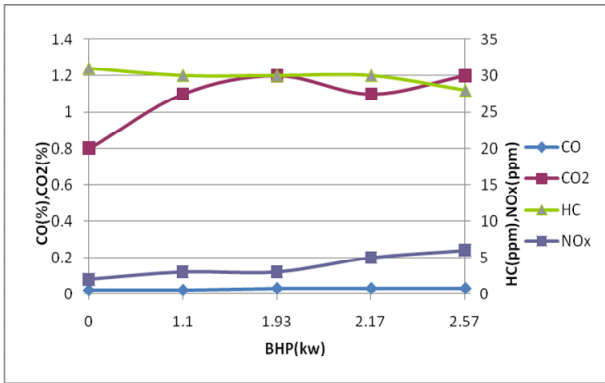


Fig. 4. Variations of Emission for BD5 with BHP

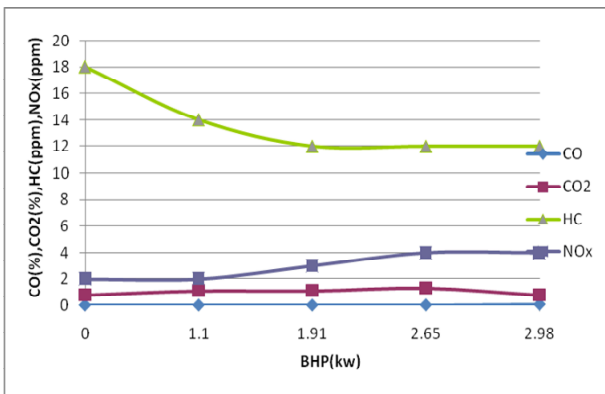


Fig. 5. Variations of Emission for BD10 with BHP

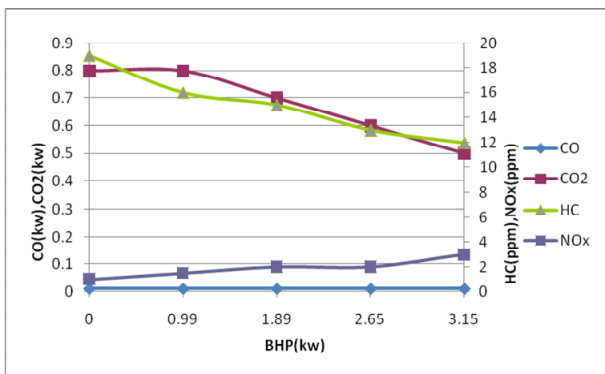


Fig. 6. Variations of Emission for BD25 with BHP

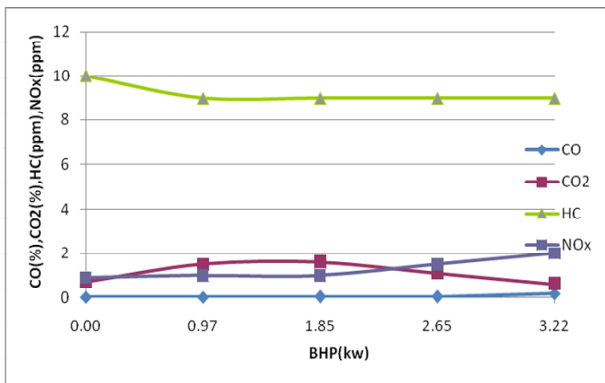


Fig. 7. Variations of Emission for BD50 with BHP

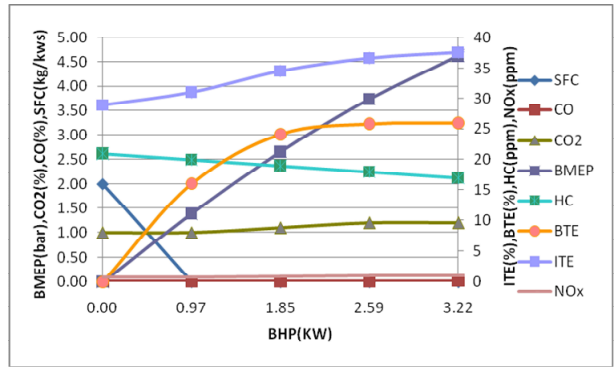


Fig. 8. Variations of Emission For BD75 with BHP

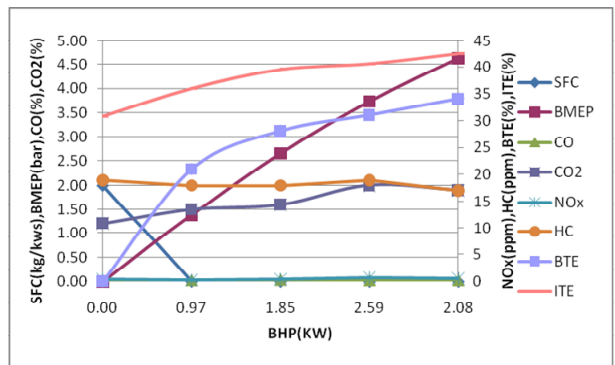


Fig. 9. Variations of Emission for EBD100 with BHP

It is known fact that biodiesel produces more NO than the diesel. Higher flame velocities also produce higher NO and that happens in case of dual fuel operation.

Fig. 9 shows that NOx, CO, CO2 & HC of EBD100 is reduce 100%, 75%, 50%, 10%, 5% respectively. This proves that EBD100 fuel is ideal. Alternative fuel for diesel engine because of reduced emission. Due to the above-mentioned reasons, the BTE was found to be lower for blends with higher concentrations of vegetable oil compared to that of base diesel fuel. As the biodiesel content was increased from 30% in the blend, a slight decrease in BTE was observed at low and mid loads.

This is due to the increased density and reduced volatility of the blend with increased quantity of biodiesel at these loads.

- When diesel employed along with Exhaust gas recirculation (EGR) sees a significant jump in Mechanical efficiency for all load values, although there is a negligible drop in the Brake power (BP). So diesel could be employed with EGR beneficially.
- When Diesel used along with Exhaust Gas Recirculation (EGR) its Specific Fuel Consumption (SFC) drops by a significant roughly, 50% points at optimal load conditions, thereby ensuring much better utilization of fuel.
- Hence, in case of the various blends, which we consider, there is practically no change with regard to the brake mean effective pressure and the indicated power.
- From the above graph, NOx is increasing up to 140 ppm in peak load in the case of hot EGR whereas in

case of ordinary diesel NO_x is nil in cold EGR. Hot EGR measurements were taken without water circulation. This has not yielded favorable results and hence the cold EGR concept was used.

- In the case of 50% bio diesel NO_x is increasing up to 30 ppm with hot EGR whereas in cold EGR NO_x is nil. Hence, 100% reduction of NO_x has been achieved.
- The figure indicates that NO_x is increasing up to 20 ppm for 100% bio diesel with hot EGR and again in the case of cold EGR it is a nil one.
- From all the above NO_x graph shows that cold EGR is giving good response compared to hot EGR.

IV. Conclusion

Following conclusions were drawn from the study:

- All the above graphs that 10% blending gives us optimum values of performance and emission characteristics.
- All the pollutants released by using *Sterculia oilare* higher as compared to diesel, except NO_x.
- Blends have lower value of Co, un burnt hydrocarbon than diesel. This is due to better combustion of fuel inside the cylinder than diesel
- The properties like density, viscosity, flash point of blends is higher and calorific value is almost 0.8 to 0.9 times that of diesel.
- There was no considerable change in the value of the brake mean effective pressure though the value of the 50% blend was closer when compared to other blends.
- The Brake thermal efficiency, brake specific fuel consumption of blends is lower and higher than diesel, this is due to higher viscosity and lower calorific value of the fuel.

References

- [1] Agarwal A. K. and Das L. M. (2001), Biodiesel development and characterization for use as a fuel in compression ignition engines', Transactions of ASME, Vol. 123, pp. 440-447.
- [2] Gerhard Vellguth, (1983) 'Performance of vegetable oils and their monoesters as fuel for diesel engines'. SAE Paper no. 831358, U.S.A.
- [3] Rakopoulos C. D., Hountalas D. T., Rakopoulos D. C., and Giakoumis E. G. and Andritsakis E. C. (2008), 'Performance and emissions of bus engine using blends of diesel fuel with biodiesel of sunflower or cottonseed oils derived from Greek feedstock', Fuel, Vol. 87, pp. 147-157.
- [4] Ashok K.Raina & B.R.Gaikwad 'Chemo-Botany of *Jatropha* species in India', Publication of Godrej soaps Research Centre, Mumbai, India
- [5] Avinsh Kumar Agarwal & Shrawan Kumar Singh (2003) 'Effects of EGR on exhaust gas temperature in CI engine', Indian Institute of Technology, Kanpur, India
- [6] Avinsh Kumar Agarwal & L.M.Das, (2002) 'Biodiesel development and characterization for use as a fuel in compression ignition engines' Indian Institute of Technology, Kanpur, India
- [7] Busch, K.W., Busch, R.E. Darling, S. (1976) 'Design of a test loop for the evaluation of magnetic water treatment devices. Process safety and environmental protection', Transactions of the Institution of Chemical Engineers

- [8] Gerhard Vellguth, (1983) 'Performance of vegetable oils and their monoesters as fuel for diesel engines', SAE Paper no. 831358, U.S.A.
- [9] Gopalkrishna K.V. and Rao P.S. 'Use of non-edible vegetable oils as alternate fuels in diesel engines', DNES Project report, I.C.Engines lab, IIT Madras, Chennai, India
- [10] Marshall, S.V., and G.G. Skitek (1987) 'Electromagnetic Concepts and applications', 2nd ed. Englewood Cliffs, N.J.: Prentice-Hall, Inc.
- [11] Mcneely, M (1994) 'Magnetic fuel treatment system designed to attack fuel-borne microbes', Diesel Progress Engines and Drives, November
- [12] Pitterson, D. J. (1966) 'Cylinder Pressure Variations - Fundamental Combustion Problem', Society of Automotive Engineers.
- [13] Ruggero Maria Santilli, (2000) 'Recycling liquid wastes and Crude oil into Magnegas and Magne Hydrogen', Hydrogen International Conference Hy2000, Munich, German, September.
- [14] Vinayak patil and Kanwarjit singh. 'Oil gloom to oil boom (*Jatropha Curcas*)' published by Agro-forestry Federation, Maharashtra, India
- [15] Proceedings of the XVIII National conference on I C engines and combustion held at College of Engineering, Thiruvanthpuram, India under the auspices of the Combustion Institute (Indian Section).
- [16] Avinsh Kumar Agarwal & Shrawan Kumar Singh (2003) "Effects of EGR on exhaust gas temperature in CI engine"- Indian Institute of Technology, Kanpur.

Authors' information

¹Assistant Professor, Department of Mechanical Engineering, M.Kumarasamy College of Engineering, Karur - 639 113, India.
Tel: +91 9486405205.
E-mail: ppsethu63@yahoo.com

²Principal, KPR Institute of Engineering and Technology, Arasur, Coimbatore- 641 407, India.

³Professor & Head, Department of Mechanical Engineering, V. S. B. Engineering College, Karur - 639 111, India.
Tel: +91 9865974859.
E-mail: mylkarthik@yahoo.com

Experimental Investigations of Silicon Carbide - Fly Ash Reinforced Aluminium Metal Matrix Composite

Vivekanandan P.¹, Arunachalam V. P.²

Abstract – Metal matrix composites are used mostly in space ships, aerospace, automotive, nuclear bio technology, electronic and sporting goods industries, but due to their high cost, experiments are usually done to reduce the cost of composites and inexpensive materials are utilized for metal matrix composites. Fly Ash is one of the most inexpensive and low density reinforcement available in large quantities as solid waste by product during combustion of coal in thermal power plants. So, composites with Fly Ash can be used to reduce the cost of the metal matrix for applications in automotive and small engine applications. It is therefore expected that the incorporation of Fly Ash particles in Aluminium alloy will promote yet another use of this low cost waste by product and at the same time has the potential for conserving energy intensive Aluminium and thereby, reducing the cost of Aluminium products. In this investigation, 10% SiC particles reinforced Al-MMC was prepared using stir casting method. The ratio of Hardness with respect to the weight fraction on the specimen was prepared. The various mechanical test via hardness & tensile test are taken to analyze the properties. The microstructure of Al-MMC's were studied in SEM microstructure. **Copyright © 2013 Praise Worthy Prize S.r.l. - All rights reserved.**

Keywords: Aluminium, SiC, Flyash, Tensile, Hardness, SEM, Wear

I. Introduction

Metal matrix composites (MMCs) particularly Aluminium matrix ceramic reinforcement composites have emerged as a potential material for automotive and aerospace industries. In this study, Fly Ash particles which are extracted from residues generated in the combustion of coal were chosen as reinforcement material. India produces about 110 million tons of Fly Ash per year from burning about 250 million tons of coal for electric power generation.

Apart from energy and cost savings, green house gases that are generated during the production of Al may be significantly reduced by decreasing the production of Al by Fly Ash substitution. Among various processing techniques, stir casting appears to be most promising route for production of Aluminium matrix composites because of simplicity and ability to manufacture composites on an industrial scale economically. In any production process, superior quality of the product can be achieved only when the process is run with the optimum parameters.

Mechanical properties of composites are affected by the size and shape of the matrix and reinforcement materials, weight fraction of the reinforcement as well as reaction at the interface. Interfacial strength between the matrix and reinforcement plays a significant role in determining the properties of MMCs. These aspects have been discussed by many researchers. Fly ash particles were incorporated into the molten Al they were observed to be floating on the molten Al surface due to the high

surface tension which leads poor wettability. Since the gas layers at the surfaces of the particles can cause the buoyant migration, mechanical stirring can be done in a semi solid state rather than in the completely liquid state in order to break away the gas layers thereby reducing surface tension.

Wet ability can be improved by increasing the surface energies of the solids, decreasing the surface tension of the liquid matrix alloy and decreasing the solid/liquid interfacial energy at the reinforcement matrix interface.

Magnesium which acts as a powerful surfactant as well as a reactive element, in the Aluminium alloy matrix seems to fulfil all the above three requirements.

Important role played by the magnesium during the composite synthesis is the scavenging of the oxygen from the dispersed surface, thus thinning the gas layer and improving wetting action with the surface of the dispersed. As concluded from previous research studies the strengthening of Aluminium alloys with a dispersion of fine particulates strongly increases their potential in tribological and structural applications.

I.1. Composite

Composite material is a material composed of two or more distinct phases (matrix phase and reinforcing phase) and having bulk properties significantly different from those of any of the constituents. Many of common materials (metals, alloys, doped ceramics and polymers mixed with additives) also have a small amount of dispersed phases in their structures, however they are not

considered as composite materials since their properties are similar to those of their base constituents (physical property of steel are similar to those of pure iron). Favorable properties of composite materials are high stiffness and high strength, low density, high temperature stability, high electrical and thermal conductivity, adjustable coefficient of thermal expansion, corrosion resistance, improved wear resistance etc.

MATRIX PHASE

1. The primary phase, having a continuous character,
2. Usually more ductile and less hard phase,
3. Holds the reinforcing phase and shares a load with it.

REINFORCING PHASE

1. Second phase (or phases) is imbedded in the matrix in a discontinuous form,
2. Usually stronger than the matrix, therefore it is sometimes called reinforcing phase.

Composites as engineering materials normally refer to the material with the following characteristics:

1. These are artificially made (thus, excluding natural material such as wood).
2. These consist of at least two different species with a well-defined interface.
3. Their properties are influenced by the volume percentage of ingredients.
4. These have at least one property not possessed by the individual constituents.

1.1.1. Classification of Composites

1. Metal Matrix Composites

Metal Matrix Composites are composed of a metallic matrix (aluminium, magnesium, iron, cobalt, copper) and a dispersed ceramic (oxides, carbides) or metallic (lead, tungsten, molybdenum) phase.

2. Ceramic Matrix Composites

Ceramic Matrix Composites are composed of a ceramic matrix and imbedded fibers of other ceramic material (dispersed phase).

3. Polymer Matrix Composites

Polymer Matrix Composites are composed of a matrix from thermoset Unsaturated polyester (UP), Epoxy or thermoplastic (PVC, Nylon, Polystyrene) and embedded glass, carbon, steel or Kevlar fibers (dispersed phase). Thus it is called polymer matrix composites.

4. Particulate Composites

Particulate Composites consist of a matrix reinforced by a dispersed phase in form of particles:

1. Composites with random orientation of particles.
2. Composites with preferred orientation of particles. Dispersed phase of these materials consists of two-dimensional flat platelets (flakes), laid parallel to each other.

5. Fibrous Composites

Short-fiber reinforced composites. Short-fiber reinforced composites consist of a matrix reinforced by a dispersed phase in form of discontinuous fibers (length <

100*diameter).

1. Composites with random orientation of fibers.
 2. Composites with preferred orientation of fibers.
- Long-fiber reinforced composites. Long-fiber reinforced composites consist of a matrix reinforced by a dispersed phase in form of continuous fibers.
3. Unidirectional orientation of fibers.
 4. Bidirectional orientation of fibers (woven).

6. Laminate Composites

When a fiber reinforced composite consists of several layers with different fiber orientations, it is called multilayer (angle-ply) composite.

1.2. Rule of Mixtures

Rule of Mixtures is a method of approach to approximate estimation of composite material properties, based on an assumption that a composite property is the volume weighed average of the phases (matrix and dispersed phase) properties.

According to Rule of Mixtures properties of composite materials are estimated as follows:

$$\text{Density } d_c = d_m \cdot V_m + d_f \cdot V_f$$

where:

d_c, d_m, d_f – densities of the composite, matrix and dispersed phase respectively;

V_m, V_f – volume fraction of the matrix and dispersed phase respectively.

Coefficient of Thermal Expansion

Coefficient of Thermal Expansion (CTE) in longitudinal direction (along the fibers):

$$a_{cl} = (a_m \cdot E_m \cdot V_m + a_f \cdot E_f \cdot V_f) / (E_m \cdot V_m + E_f \cdot V_f)$$

a_{cl}, a_m, a_f – CTE of composite in longitudinal direction, matrix and dispersed phase (fiber) respectively;

E_m, E_f – modulus of elasticity of matrix and dispersed phase (fiber) respectively.

Coefficient of Thermal Expansion (CTE) in transverse direction (perpendicular to the fibers):

$$a_{ct} = (1 + P_m) a_m \cdot V_m + a_f \cdot V_f$$

P_m – Poisson ratio of matrix

Poisson's ratio is the ratio of transverse contraction strain to longitudinal extension strain in the direction of applied force.

Modulus of Elasticity:

Modulus of Elasticity in longitudinal direction (E_{cl}):

$$E_{cl} = E_m \cdot V_m + E_f \cdot V_f$$

Modulus of Elasticity in transverse direction (E_{ct}):

$$1/E_{ct} = V_m/E_m + V_f/E_f$$

Tensile Strength:

Tensile strength of long-fiber reinforced composite in longitudinal direction:

$$\sigma_c = \sigma_m \cdot V_m + \sigma_f \cdot V_f$$

where, σ_c , σ_m , σ_f – tensile strength of the composite, matrix and dispersed phase (fiber) respectively.

Tensile strength of short-fiber composite in longitudinal direction (fiber length is less than critical value L_c):

$$L_c = \sigma_f \cdot d / \tau_c$$

where

d – diameter of the fiber;

τ_c – shear strength of the bond between the matrix and dispersed phase (fiber):

$$\sigma_c = \sigma_m \cdot V_m + \sigma_f \cdot V_f \cdot (1 - L_c / 2L)$$

where:

L – length of the fiber;

Tensile strength of short-fiber composite in longitudinal direction (fiber length is greater than critical value L_c):

$$\sigma_c = \sigma_m \cdot V_m + L \cdot \tau_c \cdot V_f / d$$

1.3. Metal Matrix Composites (MMCs)

Metal Matrix Composites are composed of a metallic matrix (Al, Mg, Fe, Cu etc) and a dispersed ceramic (oxide, carbides) or metallic phase (Pb, Mo, W etc). Ceramic reinforcement may be silicon carbide, boron, alumina, silicon nitride, boron carbide, boron nitride etc. whereas Metallic Reinforcement may be tungsten, beryllium etc.

MMCs are used for Space Shuttle, commercial airliners, electronic substrates, bicycles, automobiles, golf clubs and a variety of other applications. From a material point of view, when compared to polymer matrix composites, the advantages of MMCs lie in their retention of strength and stiffness at elevated temperature, good abrasion and creep resistance properties.

Most MMCs are still in the development stage or the early stages of production and are not so widely established as polymer matrix composites. The biggest disadvantages of MMCs are their high costs of fabrication, which has placed limitations on their actual applications.

1.3.1. Compared to Monolithic Metals, MMCs

- Higher strength-to-density ratios
- Higher stiffness-to-density ratios
- Better fatigue resistance
- Better elevated temperature properties
- Higher strength
- Lower creep rate

- Lower coefficients of thermal expansion
- Better wear resistance

1.3.2. The Advantages of MMCs over Polymer Matrix Composites

- Higher temperature capability
- Fire resistance
- Higher transverse stiffness and strength
- Higher electrical and thermal conductivities
- No out gassing
- Metalworking equipment.

1.4. Stir Casting Method

Liquid state fabrication of Metal Matrix Composites involves incorporation of dispersed phase into a molten matrix metal, followed by its Solidification. In order to provide high level of mechanical properties of the composite, good interfacial bonding (wetting) between the dispersed phase and the liquid matrix should be obtained.

Wetting improvement may be achieved by coating the dispersed phase particles (fibers). Proper coating not only reduces interfacial energy, but also prevents chemical interaction between the dispersed phase and the matrix.

The simplest and the most cost effective method of liquid state fabrication is Stir Casting.

1.4.1. Stir Casting

Stir Casting is a liquid state method of composite materials fabrication, in which a dispersed phase (ceramic particles, short fibers) is mixed with a molten matrix metal by means of mechanical stirring. The liquid composite material is then cast by conventional casting methods and may also be processed by conventional Metal forming technologies.

Fig. 1 shows the electric furnace for heating and melting it in which it is poured into casting furnace where stirring is done for proper mixing.



Fig. 1. Laboratory stir casting set up

1.4.2. *Stir Casting is Characterized by the Following Features*

Content of dispersed phase is limited (usually not more than 30 vol. %). Distribution of dispersed phase throughout the matrix is not perfectly homogeneous.

There are local clouds (clusters) of the dispersed particles (fibers);

There may be gravity segregation of the dispersed phase due to a difference in the densities of the dispersed and matrix phase. The technology is relatively simple and low cost.

1.5. *Strengthening Mechanism of Composites*

The strengthening mechanisms of the composites are different with different kind of reinforcing agent morphology such as fibres, particulate or dispersed type of reinforcing elements.

1.5.1. *Dispersion Strengthening Mechanism of Strengthened Composite*

In the dispersion strengthened composite the second phase reinforcing agents are finely dispersed in the soft ductile matrix. The strong particles restrict the motion of dislocations and strengthen the matrix. Here the main reinforcing philosophy is by the strengthening of the matrix by the dislocation loop formation around the dispersed particles. Thus the further movement of dislocations around the particles is difficult. Degree of strengthening depend upon the several factors like volume % of dispersed phase, degree of dispersion, size and shape of the dispersed phase, inter particle spacing etc. In this kind of composite

1.5.2. *Strengthening Mechanism of Particulate Composite*

In the particulate reinforced composite the size of the particulate is more than 1 μm , so it strengthens the composite in two ways. First one is the particulate carry the load along with the matrix materials and another way is by formation of incoherent interface between the particles and the matrix.

So a larger number of dislocations are generated at the interface, thus material gets strengthened. The degree of strengthening depends on the amount of particulate (volume fraction), distribution, size and shape of the particulate etc.

1.6. *Fly Ash*

Fly ash is one of the residues generated in the combustion of coal. It is an industrial by-product recovered from the flue gas of coal burning electric power plants. Depending upon the source and makeup of the coal being burned, the components of the fly ash produced vary considerably, but all fly ash includes

substantial amounts of silica (silicon dioxide, SiO_2) (both amorphous and crystalline) and lime (calcium oxide, CaO).

In general, fly ash consists of SiO_2 , Al_2O_3 , Fe_2O_3 as major constituents and oxides of Mg, Ca, Na, K etc. as minor constituent. Fly ash particles are mostly spherical in shape and range from less than 1 μm to 100 μm with a specific surface area, typically between 250 and 600 m^2/kg .

The specific gravity of fly ash vary in the range of 0.6-2.8 gm/cc . Coal fly ash has many uses including as a cement additive, in masonry blocks, as a concrete admixture, as a material in lightweight alloys, as a concrete aggregate, in flowable fill materials, in roadway/runway construction, in structural fill materials, as roofing granules, and in grouting. The largest application of Fly Ash is in the cement and concrete industry, though, creative new uses for fly ash are being actively sought like use of flyash for the fabrication of MMCs.

1.7 *Classification of Fly Ash*

1.7.1. *On the Basis of Chemical Composition*

1. *Class F Fly Ash*

The burning of harder, older anthracite and bituminous coal typically produces Class F fly ash. This fly ash is pozzolanic in nature, and contains less than 10% lime (CaO). Possessing pozzolanic properties, the glassy silica and alumina of Class F fly ash requires a cementing agent, such as Portland cement, quicklime, or hydrated lime, with the presence of water in order to react and produce cementitious compounds.

Alternatively, the addition of a chemical activator such as sodium silicate (water glass) to a Class F ash can leads to the formation of a geopolymer.

2. *Class C Fly Ash*

Fly ash produced from the burning of younger lignite or sub bituminous coal, in addition to having pozzolanic properties, also has some self-cementing properties. In the presence of water, Class C fly ash will harden and gain strength over time. Class C fly ash generally contains more than 20% lime (CaO). Unlike Class F, self-cementing Class C fly ash does not require an activator.

Alkali and sulfate (SO_4) contents are generally higher in Class C fly ashes.

1.7.2. *On the Basis of Size, Shape and Structure*

1. *Precipitator Fly Ash*

It is spherical in nature, the spheres are solid and the density is in the range of 2.0-2.5 g cm^3 .

2. *Cenosphere Fly Ash*

It is also spherical in shape but these spheres are hollow, so the density of this kind of fly ash is very less as compared to the precipitator fly ash. Here density is less than 1 gm cm^{-3} (0.3-0.6 gm/cc).

1.8. Silicon Carbide and Fly Ash as Reinforcement

1.8.1. Silicon Carbide

Silicon Carbide is a development of pure Carbon-Carbon, and can be used in automotive applications, such as components of brake systems on high performance road cars. Silicon carbide with carbon fibre and this compound is thought to be more durable than pure carbon-carbon.

1.8.2. Fly Ash

The preference to use fly ash as a filler or reinforcement in metal and polymer matrices is that fly ash is a by product of coal combustion, available in very large quantities (80 million tons per year) at very low costs since much of this is currently land filled. Currently, the use of manufactured glass microspheres has limited applications due mainly to their high cost of production. Therefore, the material costs of composites can be reduced significantly by incorporating fly ash into the matrices of polymers and metallic alloys. However, very little information is available on to aid in the design of composite materials, even though attempts have been made to incorporate fly ash in both polymer and metal matrices. Cenosphere fly ash has a lower density than talc and calcium carbonate, but slightly higher than hollow glass. The cost of cenosphere is likely to be much lower than hollow glass. Cenosphere may turn out to be one of the lowest cost fillers in terms of the cost per volume. The high electrical resistivity, low thermal conductivity and low density of fly-ash may be helpful for making a light weight insulating composites. Fly ash as a filler in Al casting reduces cost, decreases density and increase hardness, stiffness, wear and abrasion resistance. It also improves the machinability, damping capacity, coefficient of friction etc. Which are needed in various industries like automotive etc.

II. Experimental Work

Experimental Setup

For performing the stir casting operation and testing of composites the following machines/equipments were used:

1. A resistance heated muffle furnace
2. Graphite crucible
3. Brinell hardness testing machine
4. Graphite stirrer
5. C-clamp
6. Wear testing machine
7. Vernier calliper
8. Scanning electron microscope

II.1. Preparation of Samples

Pure Aluminium was melted in a crucible by heating it in a resistance furnace set at 1100°C for three to four hours.

Hardness of pure Aluminium on Rockwell Hardness testing machine was 49 HRB. The silicon carbide particles and as received dry fly ash from industry waste were preheated at 1100°C and 200°C respectively for one to three hours to make their surfaces oxidised.

The furnace temperature was first raised above the liquids temperature of Aluminium near about 750°C to melt the Al completely and was then cooled down just below the liquids to keep the slurry in semi solid state.

Automatic stirring was carried out with the help of radial drilling machine for about 20 minutes at stirring rate of 290 rpm. At this stage, the preheated SiC particles and dry fly ash particles were added manually to the vortex.

In the final mixing processes the furnace temperature was controlled within 700±10°C.

The mixture was allowed to cool down in the crucible for few hours.

The SiC particles and dry Fly Ash particles were observed to be accommodated on the boundaries. The presence of reinforcement throughout the specimen was inspected by cutting the casting at different locations and under microscopic examination. Taking the same route four specimens with different compositions of SiC and fly ash were cast.

TABLE I
COMPOSITION SPECIMEN
COMPOSITION

| Sample No. | Aluminium (gm) | FlyAsh (gm) | SiC (gm) | Remarks |
|------------|----------------|-------------|----------|---|
| 1. | 1000 | 100 | 0 | Aluminium Alloy +10 wt % Flyash |
| 2. | 1000 | 100 | 50 | Aluminium Alloy +10 wt % Flyash +5 wt % Silicon Carbide |

The above Table I deals about the composition of the alloys in terms of weight.

Here Silicon Carbide and Fly Ash are reinforced in aluminium metal matrix composites. Silicon carbide and Fly Ash are added to the aluminium according to the weight of the aluminium.



Fig. 2. Preparation of Specimen in electric furnace



Fig. 3. Specimen prepared for testing

The above Figs. 2 and 3 are the specimens for various tests. Fig. 2 shows the electric furnace for casting and Fig. 3 shows the casted specimen for testing.

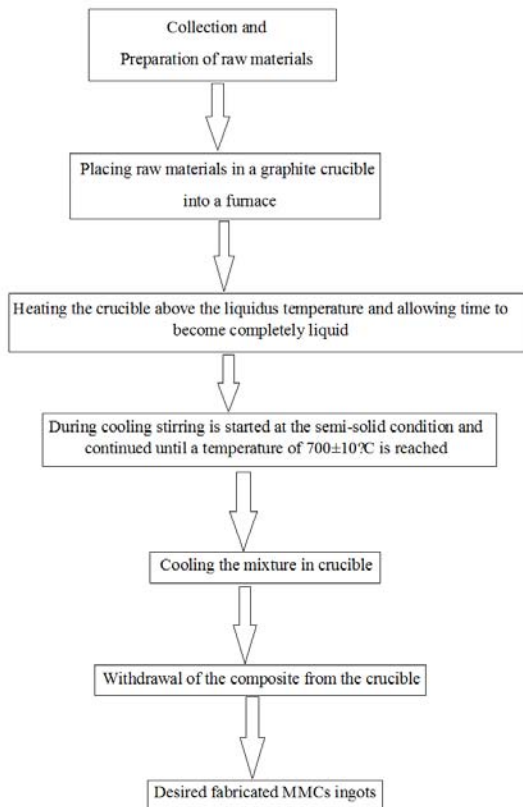


Fig. 4. Flow Chart Showing involved in Stir Casting

The above Fig. 4 shows the plan for fabricating metal matrix composites by stir casting route which is the easiest route for producing it.

III. Results and Discussion

III.1. Hardness Test

The term hardness test usually refers to static indentations made with loads not exceeding 1kgf. The testing is done on a microscopic scale with higher precision instruments. The surface being tested generally requires a metallographic finish and it was done with the help of 100, 220p, 500, 800, 800, 1000& 1500grit size emery paper.

Load used on micro hardness machine used was 200gms. Pictures of the machine on which micro hardness test was done are the following.

HARDNESS TEST

Table II shows the hardness comparison between aluminium and its alloy for different composition and the various results are obtained.

Fig. 5 shows that incorporation of fly ash particles in Aluminium matrix causes reasonable increase in hardness. The strengthening of the composite can be due to dispersion strengthening as well as due to particle reinforcements. Hence it reduces cost, decreases density and increase hardness which are needed in various industries like automotive etc.

TABLE II
HARDNESS TEST

| S.No | SAMPLE DESIGNATION | HARDNESS |
|------|--------------------|----------|
| 1. | Al | 47.5 BHN |
| 2. | Al+10%Flyash | 67 BHN |
| 3. | Al+10%Flyash+5%SiC | 68 BHN |

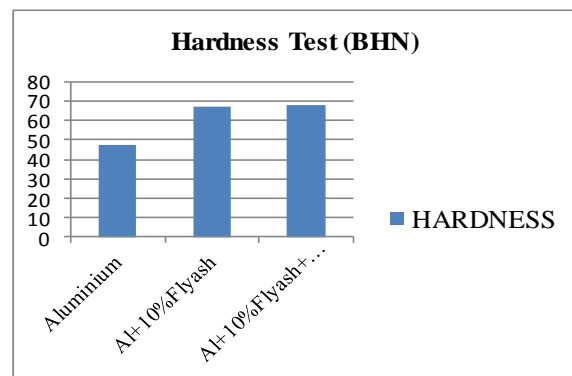


Fig. 5. Hardness test specimen

Model Calculation

$$BHN = \frac{P}{\frac{\pi D}{2} [D - \sqrt{D^2 - a^2}]}$$

P= applied Load =250kg

D= Indenter Diameter = 5mm

For sample Al+10%Flyash

d= Indentation Diameter= 2.15mm

$$BHN = \frac{250}{\frac{\pi \times 5}{2} [5 - \sqrt{5^2 - 2.15^2}]}$$

BHN= 65.5

For sample Al+10%Flyash+5%SiC

d= Indentation Diameter= 2.1mm

$$BHN = \frac{250}{\frac{\pi \times 5}{2} [5 - \sqrt{5^2 - 2.1^2}]}$$

BHN= 68.84

III.2. Tensile Test

Tensile testing, also known as tension testing, is a fundamental materials science test in which a sample is subjected to a controlled tension until failure.

The results from the test are commonly used to select a material for an application, for quality control, and to predict how a material will react under other types of forces. Properties that are directly measured via a tensile test are ultimate tensile strength, maximum elongation and reduction in area.

The most common testing machine used in tensile testing is the universal testing machine.

TABLE III
TENSILE TEST

| S.No | SAMPLE DESIGNATION | ULTIMATE TENSILE STRENGTH |
|------|--------------------|---------------------------|
| 1. | Al | 310MPa |
| 2. | Al+10%Flyash | 332MPa |
| 3. | Al+10%Flyash+5%SiC | 334MPa |

The above Table III shows the tensile strength of both aluminium and it's alloy for different composition and known that tensile strength increases with the addition of reinforcement. Results from the test are commonly used to select a material to use.

Model Calculation

Experimental Values for (Al+10%flyash)

- Load at Yield point = 18.17kN
- Breaking Load = 23.18kN
- Maximum Load= 26.12kN
- Diameter of sample rod= 10mm

CALCULATION

$$\text{Yield strength} = \frac{\text{yield load}}{\text{area}} = \frac{18.17 \times 10^3}{78.539 \times 10^{-6}} = 231 \text{ MPa}$$

$$\text{Ultimate tensile strength} = \frac{\text{ultimateload}}{\text{area}} = \frac{26.12 \times 10^3}{78.539 \times 10^{-6}} = 332 \text{ MPa}$$

Experimental Values for (Al+10%flyash+5%SiC)

- Load at Yield point =18.58 kN
- Breaking Load = 23.57kN
- Maximum Load=26.25kN
- Diameter of sample rod= 10mm

CALCULATION

$$\text{Yield strength} = \frac{\text{yieldload}}{\text{area}} = \frac{18.58 \times 10^3}{78.539 \times 10^{-6}} = 236 \text{ MPa}$$

$$\text{Ultimate tensile strength} = \frac{\text{ultimate load}}{\text{area}} = \frac{26.25 \times 10^3}{78.539 \times 10^{-6}} = 334 \text{ MPa}$$

III.3. Wear Test

Wear is the erosion of material from a solid surface by the action of another surface.

It is related to surface interactions and more specifically the removal of material from a surface as a result of mechanical action. The need for mechanical action, in the form of contact due to relative motion, is an important distinction between mechanical wear and other processes with similar outcomes.

III.3.1. Wear Test Calculation

$$\text{Volume Loss } \text{mm}^3 = \text{Height Loss} \times \text{Area}$$

$$\text{Wear Rate } \frac{\text{mm}^3}{\text{m}} = \frac{\text{Volume Loss}}{\text{Sliding Distance}}$$

$$\text{Wear Resistance } \frac{\text{m}}{\text{mm}^3} = \frac{\text{Sliding Distance}}{\text{Volume Loss}}$$

$$\text{Specific Wear Rate } \frac{\text{mm}^3}{\text{nm}} = \frac{\text{WearRate}}{\text{Load}}$$

Results of Wear Test Specimens

Specimen1

- Load 5 kg, Area 50mm²
- Sliding Distance 2000m

Model Calculation

$$\text{Volume Loss } \text{mm}^3 = \text{Height Loss} \times \text{Area}$$

$$\text{Volume Loss} = 2.20 \times 50 \times 10^{-3} \text{mm}^3 = 0.1100 \text{ mm}^3$$

$$\text{Wear Rate} = \frac{\text{Volume Loss } \text{mm}^3}{\text{Sliding Distance } \text{m}}$$

$$\text{Wear Rate} = \frac{0.1100 \text{ mm}^3}{2000 \text{ m}}$$

$$= 0.00005500 \frac{\text{mm}^3}{\text{m}}$$

$$\text{Wear Resistance} = \frac{\text{Sliding Distance } \text{m}}{\text{Volume Loss } \text{mm}^3}$$

$$\text{Wear Resistance} = \frac{2000 \text{ m}}{0.1100 \text{ mm}^3} = 18181.818 \frac{\text{m}}{\text{mm}^3}$$

$$\text{Specific Wear Rate} = \frac{\text{Wear Rate } \frac{\text{mm}^3}{\text{m}}}{\text{Load } \frac{\text{nm}}{\text{mm}^3}}$$

$$\text{Specific Wear Rate} = \frac{0.00005500 \frac{\text{mm}^3}{\text{m}}}{50 \frac{\text{nm}}{\text{mm}^3}} = 0.0000011 \frac{\text{mm}^3}{\text{nm}}$$

Specimen2

- Load 5 kg, Area 50mm²
- Sliding Distance 2000m

Model Calculation

$$\text{Volume Loss } \text{mm}^3 = \text{Height Loss} \times \text{Area}$$

$$\text{Volume Loss} = 20.02 \times 50 \times 10^{-3} \text{mm}^3 = 1.0005 \text{mm}^3$$

$$\text{Wear Rate} \frac{\text{mm}^3}{\text{m}} = \frac{\text{Volume Loss}}{\text{Sliding Distance}}$$

$$\text{Wear Rate} = \frac{1.0005 \text{ mm}^3}{2000 \text{ m}}$$

$$= 0.00050025 \frac{\text{mm}^3}{\text{m}}$$

$$\text{Wear Resistance} \frac{\text{m}}{\text{mm}^3} = \frac{\text{Sliding Distance}}{\text{Volume Loss}}$$

$$\text{Wear Resistance} = \frac{2000 \text{ m}}{1.0005 \text{ mm}^3} = 1999.0005 \frac{\text{m}}{\text{mm}^3}$$

$$\text{Specific Wear Rate} \frac{\text{mm}^3}{\text{nm}} = \frac{\text{Wear Rate}}{\text{Load}}$$

$$\text{Specific Wear Rate} = \frac{0.00050025 \text{ mm}^3}{\frac{50}{\text{nm}} \text{ nm}}$$

$$= 0.00010005 \frac{\text{mm}^3}{\text{nm}}$$

TABLE IV
WEAR TESTING OF AL+10%FLYASH

| S. No | Time (Min) | Height Loss microns | Volume Loss mm ³ | Wear Rate mm ³ /m | Wear Resistance m/mm ³ | Specific Wear Rate mm ³ /Nm |
|-------|------------|---------------------|-----------------------------|------------------------------|-----------------------------------|--|
| 1 | 3 | 2.20 | 0.1100 | 0.00005500 | 18181.8181 | 0.0000011 |
| 2 | 6 | 18.50 | 0.9250 | 0.00046250 | 2162.1621 | 0.0000092 |
| 3 | 9 | 39.27 | 1.9650 | 0.00098175 | 1018.5892 | 0.0000196 |
| 4 | 12 | 53.90 | 2.6950 | 0.00134750 | 742.1100 | 0.0000269 |
| 5 | 15 | 70.58 | 3.5290 | 0.00176450 | 566.7520 | 0.0000352 |
| 6 | 18 | 91.80 | 4.5900 | 0.00229500 | 435.7290 | 0.0000459 |
| 7 | 21 | 112.07 | 5.6035 | 0.00280175 | 356.9190 | 0.0000560 |

TABLE V
WEAR TESTING OF AL+10%FLYASH+5%SiC

| S. No | Time (Min) | Height Loss Microns | Volume Loss mm ³ | Wear Rate mm ³ /m | Wear Resistance m/mm ² | Specific Wear Rate mm ³ /Nm |
|-------|------------|---------------------|-----------------------------|------------------------------|-----------------------------------|--|
| 1 | 3 | 20.02 | 1.0005 | 0.00050025 | 1999.0005 | 0.00010005 |
| 2 | 6 | 41.45 | 2.0725 | 0.00103625 | 965.018 | 0.000020725 |
| 3 | 9 | 69.93 | 3.4965 | 0.00174825 | 572.000572 | 0.000034965 |
| 4 | 12 | 89.47 | 4.4735 | 0.00223675 | 447.077326 | 0.000044735 |
| 5 | 15 | 108.21 | 5.4105 | 0.00270525 | 369.6516034 | 0.000054105 |
| 6 | 18 | 123.42 | 6.1710 | 0.00308550 | 324.0965808 | 0.00006171 |
| 7 | 21 | 140.40 | 7.0200 | 0.00351000 | 284.9002849 | 0.0000702 |

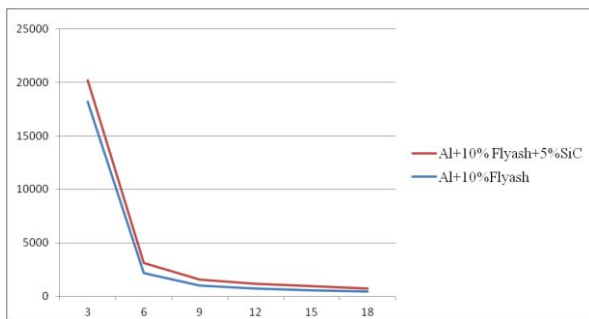


Fig. 6. Chart for Wear Test Specimen

The graph is drawn between time in X-axis and wear resistance in Y-axis. The above Fig. 6 shows the increase in wear resistance by adding Fly ash with aluminium & Fly ash with aluminium and silicon carbide.

III.4. Scanning Electron Microscope (SEM)

The scanning electron microscope is a type of electron microscope that images the sample surface by scanning it with a high energy beam of electrons in a raster scan pattern.

The electrons interact with the atoms that make up the sample producing signals that contain information about the sample's surface topography, composition and properties such as electrical conductivity.

The types of signals produced by an SEM include secondary electrons, back-scattered electron (BSE), characteristic X-rays, light (Cathodoluminescence), specimen current and transmitted electrons.

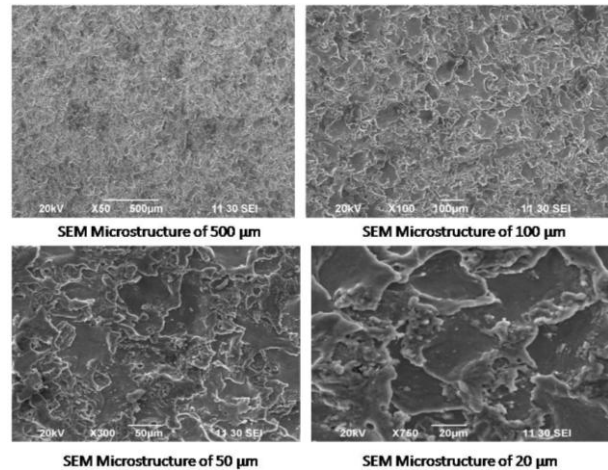


Fig. 7. SEM Micrograph of Al+10% Fly ash

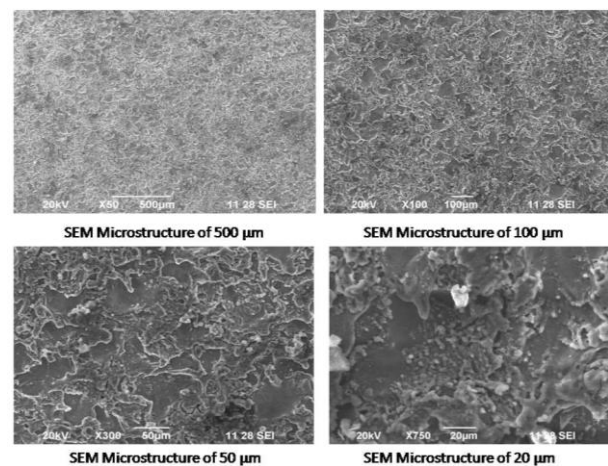


Fig. 8. SEM Micrograph of Al+10% Fly ash+5% SiC

Secondary electron detectors are common in all SEMs, but it is rare that a single machine would have detectors for all possible signals.

The signals result from interaction of the electron beam with atoms is near the surface of the sample. In the most common or standard detection mode, secondary electron imaging or SEI, the SEM can produce very high resolution images of a sample surface, revealing details about less than 1 to 5mm in size.

Due to the very narrow electron beam, SEM micrographs have a large depth of field yielding a characteristic three dimensional appearance useful for understanding the surface structure of a sample. This is exemplified by the micrograph of pollen shown to the right.

A wide range of magnifications is possible, from about 10times to more than 500,000 times, about 250times the magnification limit of the best light microscopes.

III.4.1. SEM Microstructure

SEM photographs were taken to analyze the surfaces of Al-10% fly ash and Al-10% Fly ash-5% SiC

composites. Al-Fly Ash-SiC composites were successfully produced by stirring method which ensures homogeneous particle distribution.

The Figures 7, 8 show the micrograph of Al alloy-10% wt of Fly Ash – 5%wt of SiC composites fabricated by mechanical stirring, duration of 10min with the stirring speed of 300 rpm at 630°C (in semisolid range).

It was observed that Fly Ash particles distribute homogeneously in the composites when the stirring was made in semi solid condition. The homogeneous distribution of Fly Ash particles in the Al-matrix was achieved due to smashing action of solid dendrites in semi solid state. The interface between matrix and reinforcement was almost perfectly bonded.

IV. Conclusion

From the experiments conducted following conclusions have been obtained:

Aluminium matrix composite was fabricated by Stir casting method. Hardness value of composite material was found to be 67 (Al-10% Flyash), 68 (for Al-10% Fly Ash-5% SiC). The tensile strength of aluminium matrix composite increases when compared to pure aluminium. With the addition of Fly Ash to Al-SiC the wear resistance of the composite decreased. The specimen with highest percentage of Fly Ash worn out more rapidly as compared to the other specimen during wear test. The SEM images revealed that both SiC and Fly Ash particles are well distributed in aluminium matrix.

The result of the present investigation will expand the application of aluminium-fly ash & aluminium-fly ash-silicon carbide in the field of engineering.

References

- [1] T.P.D. Rajan, R.M. Pillai, B.C. Pai, K.G. Satyanarayana, P.K. Rohatgi, Proceedings of National Conference on: Recent Advances in Materials Processing (RAMP-2001), India, 2001, pp. 327–334.
- [2] Composite Materials: Engineering and Design by F.L. Matthews and R.D. Rawlings, Chapman & Hall publication.
- [3] T. Matsunaga, J.K. Kim, S. Hardcastle and P.K. Rohatgi, Crystallinity and selected properties of fly ash particles, Materials Science and Engineering A325 (2002) 333–343
- [4] Akbulut, M. Darman, F. Yilmaz, Wear 215 (1998) 170.
- [5] S. Skolianos, T.Z. Kattamis, Mater. Sci. Engg. A163 (1993) 107.
- [6] M.K. Surappa, S.C. Prasad, Wear 77 (1982) 295.
- [7] M.J. Koczek, M.K. Prem Kumar, JOM 45 (1993) 44.
- [8] P.C. Maity, P.N. Chakraborty, S.C. Panigrahi, Scripta Metall. Mater. 28 (1993) 549.
- [9] M.K. Aghajanian, R.A. Langensiepen, M.A. Rocazella, J.T. Leighton, C.A. Andersson, J., Mater. Sci. 28 (1993) 6683–6690.
- [10] T.W. Clyne, P.J. Withers, An Introduction to Metal Matrix Composites, Cambridge University Press, Cambridge, UK, 1993, pp. 166–217.
- [11] E.A. Feest, Composites 25 (1994) 75–86.
- [12] T.P.D. Rajan, R.M. Pillai, B.C. Bai, J. Mater. Sci. 33 (1998) 3491–3503.
- [13] L. Cao, Y. Wang, C.K. Yao, The wear properties of an SiC-whisker reinforced aluminium composite, Wear 140 (1990) 273–277.
- [14] B.N. Pramila Bai, B.S. Ramashesh, M.K. Surappa, Dry sliding wear of A356-Al-SiCp composites, Wear 157 (1992) 295–304.
- [15] Manish Narayan, M.K. Surappa, B.N. Pramila Bai, Dry sliding

- wear of Al alloy 2024–Al₂O₃ particle metal matrix composites, Wear 181–183 (1995) 563–570.
- [16] A. Ravikiran, M.K. Surappa, Oscillations in coefficient of friction during dry sliding of A356 Al-30% wt. SiCp MMC against steel, Scripta Mater. 36 (1997) 95–98.
- [17] S. Bandyopadhyay, T. Das, and P.R. Munroe, Metal Matrix Composites - The Light Yet Stronger Metals For Tomorrow, A Treatise On Cast materials, p-17-38.
- [18] T.W. Clyne, (2001), Metal Matrix Composites: Matrices and Processing, Encyclopedia of Materials : Science and Technology, p- 8
- [19] T. Matsunaga, J.K. Kim, S. Hardcastle and P.K. Rohatgi, Crystallinity and selected properties of fly ash particles, Materials Science and Engineering A325 (2002) 333–343
- [20] 2004 Coal combustion product (CCP) production and use survey, American Coal Ash Association. ([http://www.aaaa-usa.org/PDF/2004_CCP_Survey\(9-9-05\).pdf](http://www.aaaa-usa.org/PDF/2004_CCP_Survey(9-9-05).pdf)).

Authors' information

¹Associate Professor & Head, Mechatronics Engineering, SNS college of Technology, Coimbatore, India – 641035.

²Principal, SNS College of Technology, India.
E-mail: aanand_23@rediffmail.com



Prof. **P. Vivekanandan** received his Bachelor of Engineering degree in Mechanical Engineering from Maharaja Engineering College, Bharathiar University, Coimbatore, India in 1998, Master of Engineering degree in Engineering Design from Maharaja Engineering College, Anna University, Chennai, India in 2004. He is currently a Research Scholar in the department of Mechanical Engineering, Anna University, of Technology - Coimbatore, India. He has long academic career of 14 years of experience at various capacities from Lecturer to Associate Professor. Currently he is working as an Associate Professor and Head in the department of Mechatronics Engineering, SNS College of Technology, Coimbatore, India. He has published 4 papers in International Journals and 6 papers at National and International conferences.



Dr. **V. P. Arunachalam** received his Bachelor of Engineering degree in Mechanical Engineering from Coimbatore Institute of Technology, Coimbatore, University of Madras., India in 1971, Master of Engineering degree in Machine Tool Engineering from PSG College of Technology, Coimbatore, University of Madras., India in 1973, Ph.D degree in Mechanical Engineering from Government College of Technology, Coimbatore, India in 1988. He is a Life member of ISTE & IE. He had more than 35 years of academic experience at various capacities. Currently he is serving as a principal in SNS College of Technology, Coimbatore. He published 32 International Journals, 13 National Journals and presented 63 papers at National and International Conferences. He has been guiding 15 Research scholars and his areas of interest are Production Engineering, Quality Management, and Maintenance Managements etc.

Development of Empirical Models of Polyfelt Fibrous Materials for Acoustical Applications

L. Egab, X. Wang, S. K. Mazlan, M. L. Choo

Abstract – In this study, new empirical models for predicting the airflow resistivity, sound absorption coefficient of polyfelt fibrous materials have been developed. The empirical models were presented as simple power-relations by least square best fitting method of impedance tube and flow bench test data over a set of 14 samples. Two coefficients were identified for a new empirical formula to predict the airflow resistivity from the mass density and thickness of polyfelt materials and eight coefficients were identified for a new empirical formula to predict the characteristic acoustic impedance, propagation coefficients and sound absorption coefficient from the airflow resistivity. For the given mass density and thickness of a polyfelt fibrous material, the outcome proposed in this paper enables a quick and accurate evaluation of the acoustic properties of the material such as the airflow resistivity and sound absorption coefficient without a further requirement of flow bench and impedance tube tests. This is because that the predicted results from the new empirical models are closer to the measured results in the frequency range of interest than the other models in the previous work in the published literatures. **Copyright © 2013 Praise Worthy Prize S.r.l. - All rights reserved.**

Keywords: Polyfelt Fibrous Materials, Absorption Coefficient, Characteristic Acoustic Impedance, Propagation Coefficient, Airflow Resistivity

Nomenclature

| | |
|-------|--|
| A | Area of the tested sample, m^2 |
| h | Thickness of the tested sample, m |
| q_v | Airflow rate through the sample, m^3s^{-1} |
| Z_c | Characteristic acoustic impedance |
| K_c | Propagation coefficient |
| Re | Real part of Z_c |
| X | Imaginary part of Z_c |
| c_0 | Speed of sound |
| Z | Normal acoustic impedance |

Greek symbols

| | |
|----------------|---|
| Δp | Pressure drop, N/m^2 |
| σ | Airflow resistivity, $N.s/m^4$ |
| $\rho(\omega)$ | Effective density |
| $c(\omega)$ | Complex wave velocity |
| ω | Natural frequency |
| ρ_m | Bulk density of porous material, kg/m^3 |
| ρ_0 | Mass density of air, kg/m^3 |
| α | Attenuation coefficient |
| β | Phase constant |
| α_n | Sound absorption coefficient |
| α_m | Measured sound absorption coefficient |
| α_p | Predicted sound absorption coefficient |

I. Introduction

Accurate modeling of the acoustical properties of porous materials is of considerable interest to acoustic and noise engineers and material manufacturers. Hence, there are many theoretical and empirical models which have been developed to predict the characteristic acoustic impedance and propagation coefficient of these materials.

These models may be divided into three categories: empirical, phenomenological, and microstructural models.

Empirical models do not require detailed knowledge of the internal structure of the material nor are they derived from theoretical considerations.

Delany and Bazley [1] showed that the values of the characteristic acoustic impedance and propagation coefficient for a range of fibrous materials, normalized as a function of frequency divided by flow resistivity, which could be presented as simple power law functions. The models were based on numerous impedance tube measurements and were good for determining the bulk acoustic properties at the frequencies higher than 250 Hz, but not at the low frequencies [2], [3].

The validity of this model for the lower and higher frequencies was further extended by Bies and Hansen [4]. Dunn and Davern [5] calculated new regression coefficients of characteristic acoustic impedance and propagation coefficient for the low airflow resistivity values of polyurethane foams and multilayer absorbers.

Qunli [6] later extended this work to cover a wider range of flow resistivity values by considering porous plastic open-cell foams. Miki [7] generalized the empirical models developed by Delany and Bazley for the characteristics acoustic impedance and propagation coefficient of porous materials with respect to the porosity, tortuosity, and the pore shape factor ratio. Moreover, he showed that the real part of surface impedance computed by the Delany's model converges to negative values at low frequencies.

Therefore, he modified the model to give it real positive values even in wider frequency ranges. Other empirical models include those of Allard and Champoux [8]. These models are based on the assumption that the thermal effects are dependent on frequency. The models work well for the low frequencies. The Voronina model [9] is another simple model that is based on the porosity of a material. This model uses the average pore diameter, frequency and porosity of the material for defining the acoustical characteristics of the material. Voronina [10] further extended the empirical model developed for porous materials with rigid frame and high porosity, and compared it with that of Attenborough's theory.

A significant agreement was found between their empirical model and Attenborough's theoretical model. Recently, Gardner et al. [11] used neural networks to implement an empirical model for polyurethane foams with easily measured airflow resistivity. The algorithm embedded in the neural networks substitutes the usual power-law relations.

The phenomenological models are based on the essential physics of acoustic propagation in a porous medium such as their universal features and how these can be captured in a model [12]. Biot [13] established the theoretical explanation of saturated porous materials as equivalent homogeneous materials. His model is believed to be the most accurate and detailed description till now. Among the significant refinement made to Biot theory, Johnson et al. [14] gave an interpolation formula for "Dynamic tortuosity" of the medium based on limiting behavior at zero and infinite frequency.

The dynamic tortuosity employed by Johnson et al. is equivalent to the structure factor introduced by Zwikker and Kosten [15] and therefore represent a surrogate form of the complex effective fluid density. Johnson et al. interpolate between zero and infinite frequencies by the use of characteristic length, which is unambiguously related to the geometry, though difficult to calculate or measure exactly for practical types of materials.

Champoux and Allard [16] extended this work and showed that an additional characteristic length was required in order to obtain an expression for the dynamic bulk modulus of the fluid in the pores. Allard and Champoux [8] later applied this approach to bulk fibrous materials and compared their prediction with those using the empirical power law of Delany and Bazley. They found that for random fibrous materials, the characteristic lengths could not easily be measured and some degree of approximation was inevitable.

Work by Pride et al. [17] showed that at low frequencies the effective density of the fluid given by Johnson et al. should be modified. This was because Johnson's model did not give the correct low-frequency behavior as ω tends to zero. Therefore, they suggested five possible functions that can connect the low and high frequency limits, but they are also complicated expressions and difficult to interpret.

The microstructural models are developed by calculating the exact solution for propagation in pores of constant, usually circular cross-section, and then tuning the equations to accommodate more complicated geometries using shape factors [12]. Attenborough [18], [19] derived rigid frame models that require five parameters, including the static and dynamic shape factors for more complicated pore microstructures. He also showed that these models can be applied to both the fibrous and granular materials. Champoux and Stinson [20] later proposed another five parameters model, including two different shape factors accounting for viscous and thermal effects.

They verified their model on various porous materials having an exactly known geometry. Wilson [12] developed a general three parameter model by matching relaxation characteristics of viscous and thermal properties and compared it with previous models.

Although microstructural models are advantageous over other models owing to their adequacy for various high and low range frequencies and types of materials, they suffer from the disadvantage of being complicated and the need for determining about three to five parameters.

The main objective of this work is to develop new empirical acoustic absorption models of polyfelt fibrous materials for noise control engineering. The new empirical models are highly advantageous as they enable to accurately predict the airflow resistivity and sound absorption coefficient from easily measured material property parameters such as the mass density and thickness without a further requirement of flow bench and impedance tube tests.

II. Methodology

II.1. Materials

Polyfelt fibrous material is a very commonly used sound absorber. It is often made from 100% recycled P.E.T fibers.

Table I details the fourteenth polyfelt samples used in the experiment. The samples were prepared and cut out with pressure by a hydraulic device.

The bulk density of each material was at the nominal value.

II.2. Airflow Resistivity Measurements

The airflow resistivity of a porous material is one of the significant acoustic performance parameters.

TABLE I
VALUES OF THICKNESS, BULK DENSITY AND AIRFLOW RESISTIVITY
OF 14 SAMPLES OF POLYFELT FIBER MATERIAL

| Material type | Thickness (mm) | Bulk density (kg/m ³) | Measured Airflow resistivity (Pa.s/m ²) |
|---------------|----------------|-----------------------------------|---|
| Felt_1 | 3.7 | 140.7 | 180137.73 |
| Felt_2 | 3.97 | 123.5 | 183145.75 |
| Felt_3 | 19.18 | 58.89 | 33900.30 |
| Felt_4 | 19.65 | 52.31 | 33478.40 |
| Felt_5 | 5 | 96.6 | 147581.76 |
| Felt_6 | 4.8 | 94.4 | 148141.87 |
| Felt_7 | 19 | 52.75 | 37329.3 |
| Felt_8 | 19.2 | 54.2 | 37073.4 |
| Felt_9 | 12.3 | 130.3 | 54393.94 |
| Felt_10 | 12.2 | 130.9 | 58343.08 |
| Felt_11 | 20 | 54.3 | 35231.41 |
| Felt_12 | 19.2 | 52.79 | 35694.95 |
| Felt_13 | 10.74 | 142.8 | 66145.05 |
| Felt_14 | 11.75 | 132.7 | 60521.31 |

It is defined as the ratio of the pressure drop to the volume flow rate of air through a unit thickness porous material:

$$\sigma = \frac{\Delta p}{q_v} \frac{A}{h} \quad (1)$$

where A is the sample area, h is the sample thickness, Δp is the pressure drop across the sample, q_v is the volume airflow rate through the sample.

Experimental measurements of airflow resistivity were performed according to the direct airflow method described in ASTM C522-3 standard [21].

Fig. 1 shows the airflow resistivity testing system. The sample holder of the system comprises of two sections with a 100 mm diameter transparent tube for a good visibility to avoid material sample compression during the test.

The upper section of the material holder is a thin plastic screen disk attached to a screw mechanism which is able to adjust the height of this section to hold the material in place with a corresponding thickness. The bottom section of the material holder consists of a circular honeycomb disk where the material sample is placed on.

The circular honeycomb disk also maintains the flow to be laminar. Adjustable airflow pump allows user to control the airflow to avoid the high velocity turbulent flow enter the test tube. Measurements were conducted for ten different air flow values with three sequential repeated tests for every sample to get an average airflow resistivity. The measured values of airflow resistivity are given in Table I.

II.3. Sound Absorption Measurements

The normal incidence sound absorption coefficients of the samples were measured using Bruel & Kjaer impedance tube, following the two-microphone broadband method in accordance with ASTM E1050-08 standards [22]. This method involves the decomposition of broadband stationary random signal into its incident and reflected components.

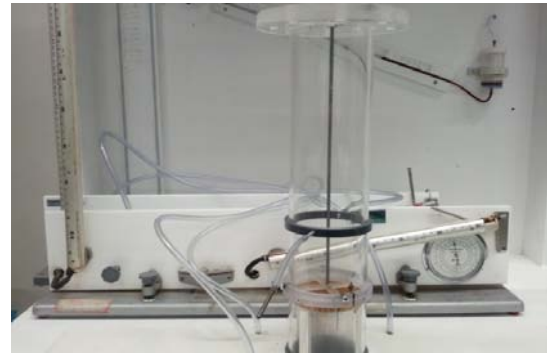


Fig. 1. Airflow resistivity measurement system

The signal is generated by a sound source and the incident and reflected components are determined from the acoustic pressure measured by microphones at two locations of the tube. 100 mm and 29 mm diameter samples were cut and the measurements were done inside the large tube set up with the valid frequency range of 50 Hz - 1.6 kHz and small tube set up with the valid frequency range of 500 Hz - 6.4 kHz.

The microphone and the tube correction factors were considered and compensated throughout the measurements. At least two co-related results were picked up for averaging and combining low and high frequency plots, with the cross-over frequency range of 500-1.6 kHz. The experimental set up in Fig. 2 consists of: Bruel & Kjaer impedance tube type 4206, ¼ in Bruel & Kjaer 4187 condenser microphones cartridge with Bruel & Kjaer 2670 preamplifier, and Bruel & Kjaer 2716 C power amplifier, and Bruel & Kjaer PULSE software, the multi-analyzer system type 3560.



Fig. 2. Impedance tube set up

II.4. Calculation of Characteristic Acoustic Impedance and Propagation Coefficient

The acoustical properties of the characteristic acoustic impedance Z_c and the propagation coefficient K_c were calculated by the two cavity methods [23].

The characteristic acoustic impedance was calculated by Eq. (2) while the propagation coefficient was calculated by Eq. (3). When the air gap thickness behind the material sample was set to L , the normal acoustic

impedance Z_0 on the surface of the material and the impedance Z_0' at the rear of the sample were measured.

Similarly, when the thickness of the air gap behind the material was changed to L' , the normal acoustic impedance Z_1 on the surface of the material and the impedance Z_1' at the rear of the material sample were measured. The thickness of the sample is given by h :

$$Z_c = \pm \left[\frac{Z_0 Z_0' (Z_1 - Z_1') - Z_1 Z_1' (Z_0 - Z_0')}{(Z_1 - Z_1') - (Z_0 - Z_0')} \right]^{\frac{1}{2}} \quad (2)$$

$$K_c = \frac{i}{2jh} \ln \left(\frac{Z_0 + Z_c}{Z_0 - Z_c} \frac{Z_1 - Z_c}{Z_1 + Z_c} \right) \quad (3)$$

The measured values of the effective density $\rho(\omega)$ and the bulk modulus $K(\omega)$ were derived from the above characteristic acoustic impedance Z_c and propagation coefficient K_c .

Eq. (4) shows the relationship among the characteristic impedance Z_c , the effective density $\rho(\omega)$, and the bulk modulus $K(\omega)$. While Eq. (5) shows the relationship between propagation coefficient K_c and the complex wave velocity $c(\omega)$. Eqs (6) and (7) can be derived from Eqs. (4) and (5), respectively:

$$Z_c = \rho(\omega)c(\omega) = [K(\omega)\rho(\omega)]^{1/2} \quad (4)$$

$$K_c = i \left[\frac{\omega}{c(\omega)} \right] \quad (5)$$

$$\rho(\omega) = \frac{Z_c K_c}{i\omega} \quad (6)$$

$$K(\omega) = \frac{Z_c^2}{\rho(\omega)} \quad (7)$$

III. New Models

III.1. A New Resistivity Model

There is a close relationship between the airflow resistivity, the bulk density and the diameter of the porous materials. Based on this relationship, Bies and Hansen [4], [26] and later Garai and Pompoli [24] derived one variable empirical equation to estimate the airflow resistivity for the fibrous materials as follows:

$$\sigma = A\rho_m^B \quad (8)$$

The above equation is only valid for uniform fiber diameter (<15 μm for fiber glass and <33 μm for

polyester fibers) with a small quantity of binder. Hence, the straight forward application of the above equation to predict the airflow resistivity of polyfelt materials gives a large underestimation from the measured one.

Therefore, in the context of this study, the authors proposed a new empirical equation based on two variables of the bulk density and thickness of polyfelt materials as following:

$$\sigma = A\rho_m^B h^{-C} \quad (9)$$

The optimum values of A, B, and C are shown in Table II which are obtained by least square best-fitting of the airflow resistivity measured data. The discrepancies between the measured and predicted airflow resistivity is about 3%. this is a good indication that new airflow resistivity model with two variables provide very accurate prediction results for the airflow resistivity of the polyfelt materials from a known thickness and bulk density.

TABLE II
OPTIMUM COEFFICIENT VALUES OF A, B, AND C FOR VARIOUS
EMPIRICAL RESISTIVITY MODELS

| Model | Material type | A | B | C |
|-------------------|---------------|---------|----------|--------|
| Bies and Hansen | Fiber glass | 2.920 | 1.53 | - |
| Garai and Pompoli | Polyester | 25.989 | 1.404 | - |
| New model | polyfelt | 627.057 | 0.004315 | 1.0186 |

III.2. A New Impedance Model

The new predictive empirical model for the characteristic acoustic impedance Z_c and propagation coefficient K_c can be presented as simple power-law functions by [1], [24]:

$$Z_c = Re + jX \quad (10)$$

$$K_c = \alpha + j\beta \quad (11)$$

$$Re = \rho_0 c_0 \left[1 + C_1 \left(\frac{\rho_0 f}{\sigma} \right)^{-C_2} \right] \quad (12)$$

$$X = -\rho_0 c_0 \left[C_3 \left(\frac{\rho_0 f}{\sigma} \right)^{-C_4} \right] \quad (13)$$

$$\alpha = \left(\frac{\omega}{c_0} \right) \left[C_5 \left(\frac{\rho_0 f}{\sigma} \right)^{-C_6} \right] \quad (14)$$

$$\beta = \left(\frac{\omega}{c_0} \right) \left[1 + C_7 \left(\frac{\rho_0 f}{\sigma} \right)^{-C_8} \right] \quad (15)$$

The above equations depend mainly on analysis frequency and flow resistivity of the porous materials.

The normal impedance and sound absorption coefficient can be obtained:

$$Z = Z_c \coth(K_c h) \tag{16}$$

$$\alpha_n = 1 - \left| \frac{Z - \rho_0 c_0}{Z + \rho_0 c_0} \right|^2 \tag{17}$$

Several researchers have noted that predictions made using Delany and Bazley’s original coefficients are not accurate when applied to porous sound absorbing materials and have obtained different set of coefficients [5], [7]. In this work, the characteristic acoustic impedance, propagation coefficient and airflow resistivity of the polyfelt materials were measured experimentally. The methodology described by Delany and Bazley was then applied to derive the unknown coefficients C_1 to C_8 for these particular polyfelt materials. It is possible to obtain the value of the coefficients $C_1 \dots C_8$ in the above equations by the least square best-fitting method. The coefficients and power coefficients that were obtained are presented in Tables III and IV, respectively. It can be seen that the coefficients are significantly different from the Delany and Bazley’s [1] and Garai and Pompoli’s [24] coefficients. These differences support the previous findings that predictions made using the original Delany and Bazley coefficients are not especially accurate when applied to poroelastic materials [5], [6], [25] and that the coefficients would be unique to each type of porous material [18].

TABLE III
THE COEFFICIENT VALUES OF THE TERMS
($\rho_0 f / \sigma$) FOR VARIOUS MATERIALS

| Material type | C1 | C3 | C5 | C7 |
|--|--------|--------|--------|--------|
| Rockwool/fiberglass Delany & Bazley | 0.0571 | 0.087 | 0.189 | 0.0978 |
| Polyester | 0.078 | 0.074 | 0.159 | 0.121 |
| Garai & Pompoli Polyfelt | 0.0612 | 0.2508 | 0.2507 | 0.0167 |
| New Model | | | | |

TABLE IV
THE POWER COEFFICIENT VALUES OF THE TERMS ($\rho_0 f / \sigma$)
FOR VARIOUS MATERIALS

| Material type | C2 | C4 | C6 | C8 |
|--|-------|-------|-------|-------|
| Rockwool/fiberglass Delany & Bazley | 0.754 | 0.732 | 0.595 | 0.70 |
| Polyester | 0.623 | 0.660 | 0.571 | 0.530 |
| Garai & Pompoli Polyfelt | 0.78 | 0.556 | 0.557 | 0.779 |
| New Model | | | | |

IV. Results and Discussions

IV.1. Values of Coefficients and Power Coefficients of the New Model

The airflow resistivity of polyfelt fibrous materials was utilized in Eqs (10) - (15) to calculate the characteristic acoustic impedance and propagation

coefficient up to 6400 Hz. These two parameters constituted the surface impedance relation of polyfelt materials in Eq. (16) which was implemented to calculate absorption coefficients in Eq. (17).

To validate the new model equations for polyfelt materials, normalized real and imaginary parts of characteristic acoustic impedance and propagation coefficient against parameter ($\rho_0 f / \sigma$) are shown in Figs. 3. Graphs show that ($\rho_0 f / \sigma$) is between 0.01 and 0.1 for the majority of normalized real and imaginary components of z_c and k_c . It is worth mentioning that the characteristic acoustic impedance of test samples correlates well with airflow resistivity, producing the correlation coefficients between 0.97 and 0.99. The propagation coefficient of the test samples also correlates well, producing the correlation coefficients between 0.98 and 0.99. Hence, the new empirical relations are reliable.

IV.2. Prediction of Sound Absorption Coefficients

The predicted normal sound absorption coefficients for polyfelt material samples by three models of the Delany and Bazley, the Garai and Pompoli, and the new model are compared with measurement results.

Fig. 4 shows for the same sample with bulk density 54.3 kg/m³ and thickness 19.2 mm the comparison between the measured values of the normal sound absorption coefficients and the predicted values using the Delany and Bazley, Garai and Pompoli and the new model. All models are used with the measured value of the airflow resistivity. The absorption coefficients predicted by the new model are closer to measured one.

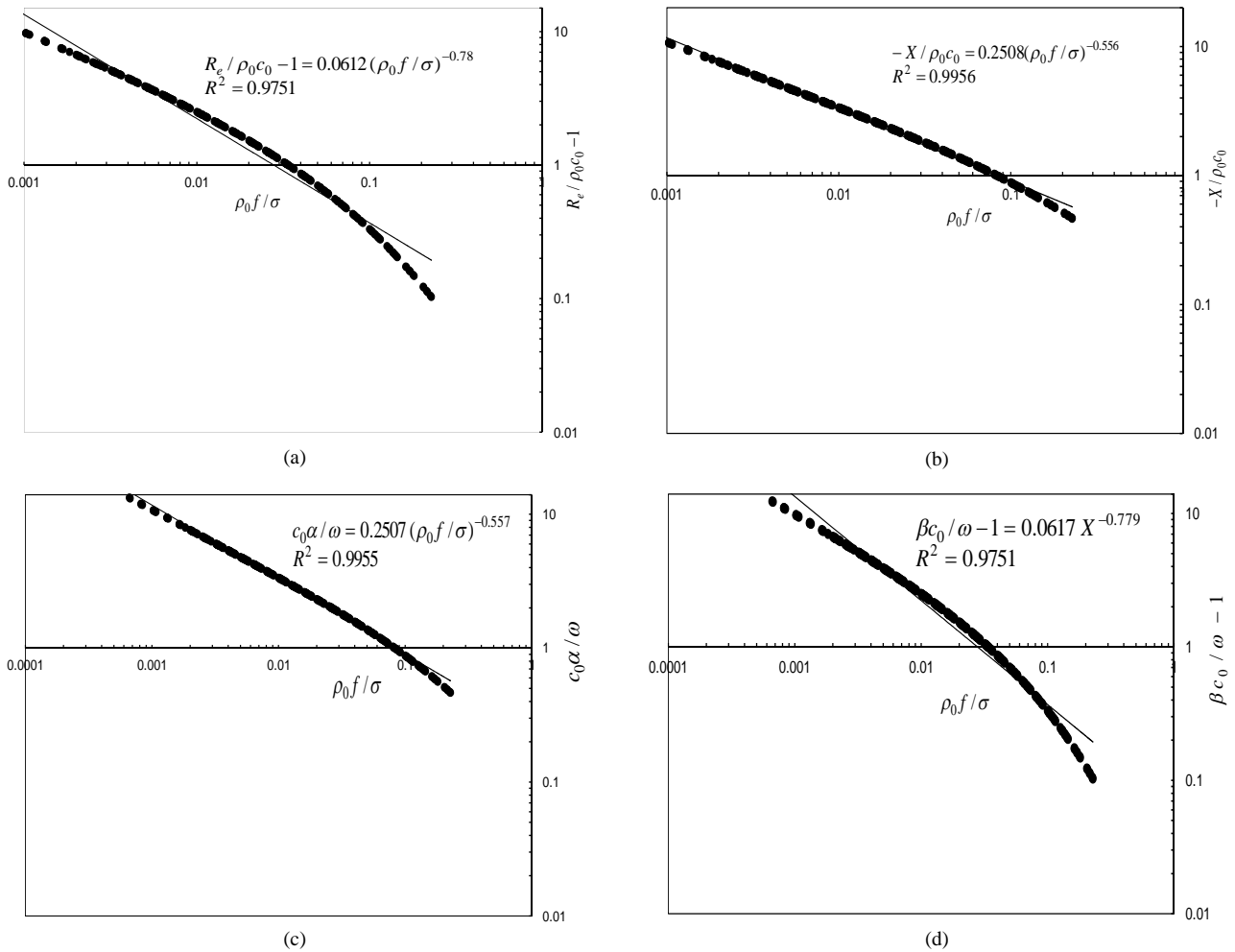
This suggests that the new model of impedance is suitable to describe the sound absorption characteristic of polyfelt materials in the frequency range of interest. Slight deviation only occurring at low frequencies could be caused by the measurement errors.

The discrepancies between the predicted and measured absorption coefficients have been calculated using Eq. (18):

$$100 \times \frac{|\alpha_m - \alpha_p|}{\alpha_m} \tag{18}$$

Table V shows the mean deviation between the measured values of the normal sound absorption coefficients and the calculated values using the Delany and Bazley, Garai and Pompoli and the new model for the samples of Fig. 4. Fig. 5 shows the same comparison for another sample with density 96.6 kg/m³ and thickness 5 mm. it can be seen that the new model gives better prediction of the normal sound absorption coefficients both at low and high frequencies.

Fig. 6 shows comparison of the measured sound absorption coefficient values of the same sample of Fig. 4 and those predicted by the new model where the airflow resistivity was calculated from the new resistivity model in Eq. (9) and Table II and from Delany-Bazley and Garai-Pompoli models.



Figs. 3. (a) Normalized real component of characteristic acoustic impedance, (b) normalized imaginary component of characteristic acoustic impedance, (c) normalized real component of propagation, coefficient, and (d) normalized imaginary component of propagation coefficient

TABLE V
 THE MEAN DEVIATION BETWEEN THE MEASURED VALUES OF THE NORMAL SOUND ABSORPTION COEFFICIENTS AND CALCULATED USING THE DELANY - BAZLEY, GARAI – POMPOLI AND THE NEW MODEL

| Model | Mean deviation between measured and calculated α values (%) |
|-------------------|--|
| Delany and Bazley | 39.36 |
| Garai and Pompoli | 21.3 |
| New model | 15.3 |

It is clearly the Delany-Bazley and Garai-Pompoli models give large underestimations of the airflow resistivity because they were developed for other kind of fibrous sound absorbing materials and not for polyfelt fibrous materials, which led to the evident underestimations of the sound absorption coefficient. It is seen from Eq. (9) and the coefficients in Table II, for the given thickness and mass density of a polyfelt material, airflow resistivity and sound absorption coefficient can be predicted using the empirical formulae developed in this paper, which enables a quick evaluation of the acoustic properties of the polyfelt materials without a further requirement of the time consuming flow bench and impedance tube tests.

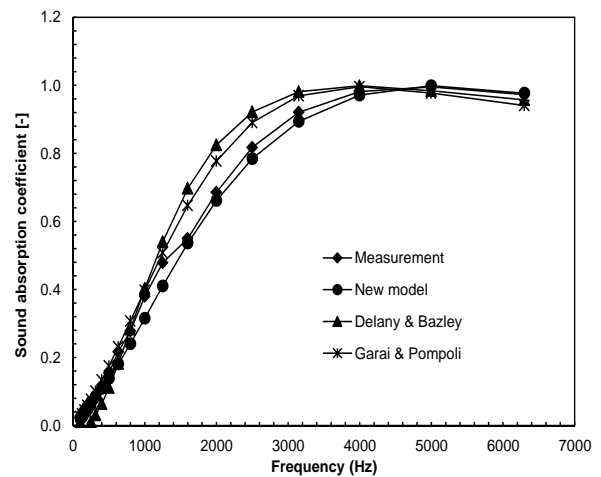


Fig. 4. Comparison among the measured sound absorption coefficients and those predicted by the new model, Delany and Bazley, and Garai and Pompoli of polyfelt fibrous material with Bulk density 54.3 kg/m³ and thickness 19.2 mm

The predicted airflow resistivity and sound absorption coefficients by the new models developed here are closer to the measured results than the models developed by the previous work in the literatures.

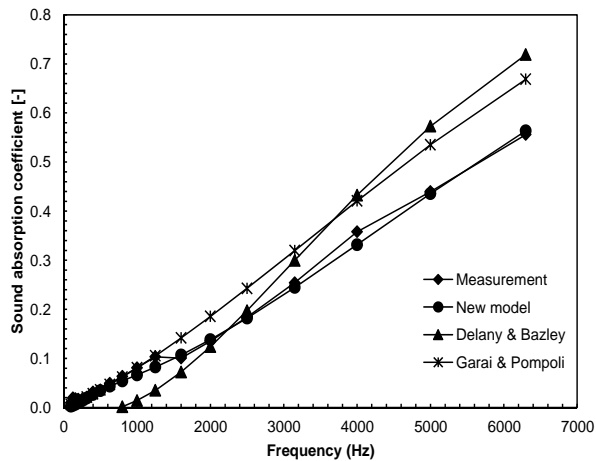


Fig. 5. Comparison among the measured sound absorption coefficients and those predicted by the new model, Delany and Bazley, and Garai and Pompoli of polyfelt fibrous material with Bulk density 96.6 kg/m^3 and thickness 5 mm

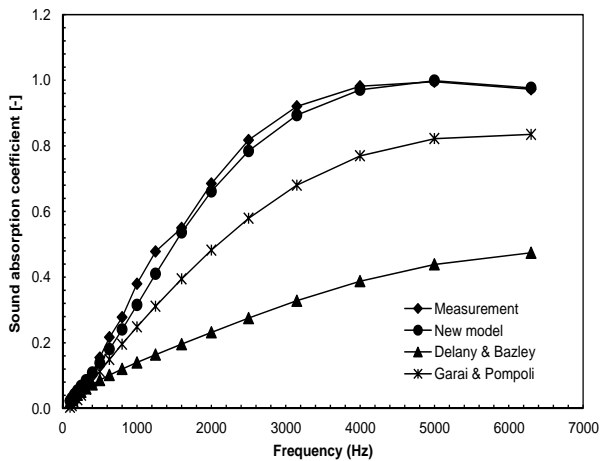


Fig. 6. Comparison among the measured sound absorption coefficients and those predicted by the new model with the airflow resistivity calculated from the new resistivity model, by Delany and Bazley model with the airflow resistivity calculated from Bies and Hansen resistivity model, by Garai and Pompoli model with the airflow resistivity calculated from Garai and Pompoli resistivity model for a polyfelt fibrous material with Bulk density 54.3 kg/m^3 and thickness 19.2 mm

V. Conclusion

This paper proposes simple empirical acoustic models that can be used to predict the airflow resistivity and sound absorption coefficients of polyfelt fibrous materials which enable an efficient tool for practical acoustic applications of polyfelt fibrous materials. At last, the airflow resistivity, characteristic acoustic impedance, propagation coefficient, and sound absorption coefficients calculated by the new models have been compared with the measured results.

By comparison, it is shown that the values calculated by the new models fit the measured ones better in particular at low and high frequencies than the other models in the literatures. Future work should be focused on the validation of the proposed model for multi-layered polyfelt materials.

Acknowledgements

The authors would like to thanks Mr. Peter Tkatchyk, NVH lab supervisor for his permanent assistance and guidance.

References

- [1] M. Delany, E. Bazley, Acoustical Properties of Fibrous Acoustical materials, *Applied Acoustics*, Vol. 3, pp. 105-116, 1970.
- [2] R. Del Ray, J. Alba, J. P. Arenas, and V. J. Sanchis, An empirical modelling of porous sound absorbing materials made of recycled foam, *Applied Acoustics*, Vol.73 (6-7), 604-609, 2012.
- [3] M.H. Fouladi, MD. Ayub, MJ. Mohd nor, Analysis of coir fiber acoustical characteristics, *Applied Acoustics*, Vol. 72, pp. 35-42, 2011.
- [4] D. Bies, C. Hansen, Flow Resistance Information for Acoustical Design, *Applied Acoustics*, Vol. 13, pp. 357-391, 1980.
- [5] I. P. Dunn, W. A. Davern, Calculation of Acoustic Impedance of Multi-layer Absorbers, *Applied Acoustics*, Vol. 19, pp. 321-334, 1986.
- [6] Q. Wu, Empirical Relations between Acoustical Properties and Flow resistivity of Porous Plastic Open-cell Foam, *Applied Acoustics*, Vol. 25, pp. 141-148, 1988.
- [7] Y. Miki, Acoustical properties of porous materials-Modification of Delany – Bazley models, *J. Acoust. Soc. Japan*, Vol. 11, pp. 19-28, 1990.
- [8] J.F. Allard, Y. Champoux, New empirical equations for sound propagation in rigid frame fibrous materials, *Journal of the Acoustical Society of America*, Vol.91, pp.3346–3353, 1992.
- [9] N. Voronina, Acoustic properties of Fibrous materials, *Applied Acoustics*, Vol. 42, pp. 165-174, 1994.
- [10] N. Voronina, An empirical model for rigid frame porous materials with high Porosity, *Applied Acoustics*, Vol.51, pp.181–98, 1997.
- [11] G.C. Gardner, M. E. O'Leary, S. Hansen, J. Q. Sun, Neural network for prediction of acoustical properties of polyurethane foams, *Applied Acoustics*, Vol. 64, No.2, 229–42, 2003.
- [12] D.K. Wilson, Simple, Relaxation Models for the Acoustical Properties of Porous Media, *Applied Acoustics*, Vol. 50, No. 3, pp. 171-188, 1997.
- [13] M.A. Biot, Theory of propagation of elastic waves in a fluid saturated porous solid. I. Low-frequency range, *Journal of the Acoustical Society of America*, Vol.28, No.2, pp.168–178, 1956.
- [14] D.L. Johnson, J. Koplik, R. Dashen, Theory of dynamic permeability and tortuosity in fluid-saturated porous media, *Journal of Fluid Mechanics*, Vol.176, pp.379–402, 1987.
- [15] C. Zwikker and C.W. Kosten, *Sound absorbing materials*, Elsevier, New York, 1949.
- [16] Y. Champoux, J. F. Allard, Dynamic tortuosity and bulk modulus in air-saturated porous media, *Journal of Applied Physics*, Vol.70, pp. 1975-1979, 1991.
- [17] S. R. Pride, F. D. Morgan, F. A. Gangi, Drag forces of porous media acoustics, *Physical Review B* 47, pp. 4964-4975. 1993
- [18] K. Attenborough, Acoustical characteristics of porous materials, *Physics reports*, Vol. 82, pp.179-227, 1982.
- [19] K. Attenborough, Acoustical characteristics of rigid fibrous absorbents and granular materials, *Journal of the Acoustical Society of America*, Vol. 73:785–799, 1983.
- [20] Y. Champoux, M. R. Stinson, Experimental investigation of models of sound wave propagation in air saturated porous media, *Journal of the Acoustical Society of America*, Vol.88 (Suppl.):121, 1990.
- [21] ASTM C522-03, Acoustics-materials for acoustical applications-determination of airflow resistance, 2003.
- [22] ASTM E1050-08, Standard test method for Impedance and Absorption of Acoustical Materials using a Tube, Two Microphones and A Digital frequency Analysis System, 2008.
- [23] H. Utsuno, T. Tanaka, T. Fujikawa, A. F. Seybert, Transfer function method for measuring characteristic impedance and propagation constant of porous materials, *J Acoust Soc Am*, Vol. 86, pp. 637-643. 1989.

- [24] M. Garai, F. Pompili, A simple empirical model of polyester fibre materials for acoustical applications, *Applied Acoustics*, Vol.66, pp. 1383-1398, 2005.
- [25] M. K. Ling, Technical note-Impedance of polyurethane foams, *Appl. Acoust.*, Vol. 34, pp. 221-224, 1991.
- [26] D.A. Bies, and C. H. Hansen, *Engineering noise control: Theory and practice*, Fourth ed., Spon press, London and New York.2009.
- [27] T. Komatsu, improvement of the Delany - Bazley and Miki models for fibrous sound absorbing materials, *Acoust. Sci. & Tech.*, Vol. 29(2), pp. 121-129, 2008.

Authors' information

RMIT University
School of Aerospace, Mechanical and Manufacturing Engineering
Bundoora East, Victoria, Australia.
Tel.:+61 399256028
Fax: +61 3 99256108



Mr. **L. N. Egab** was born on 6 February, 1980 in Iraq. He received his Bachelor degree in Mechanical Engineering from Basrah University in 2003. Then he received his Master degree in RMIT University, Australia in 2010. He has been a Ph.D. student of School of Aerospace, Mechanical and Manufacturing Engineering, RMIT University and His Ph.D. research topic

is: Acoustical characterization of porous sound absorbing materials for vehicle interior,

E-mail: laith.egab@student.rmit.edu.au



A/Prof **Xu Wang** (Corresponding author) was born on 6 August, 1964, in China. He received his Bachelor and Maser degree in Tianjin University (China) in 1985 and 1988. Then he received his Ph.D. degree in Monash University, Australia in 1994. He conducted his post-doctor research work in Department of Mechanical and Manufacturing Engineering, University of Melbourne and was awarded 1997 SAE-A Automotive Engineering Excellence Award for his research work on the CMC Scotch Yoke Engine Technology "SYTech". He has been Associate Professor of School of Mechanical, Manufacturing Engineering, RMIT University and Fellow members of Institute of Engineers, Australia and Society of Automotive Engineers since 2013. His research interests include ambient vibration energy harvesting, acoustics and vibration. He completed his research leave in Lin Lab of Berkeley Sensor and Actuator Centre, University of California, USA between 12 November 2012 and 12 February 2013.

E-mail: xu.wang@rmit.edu.au



Ms. **S. K. B. Mazlan** was born on 23 March, 1989 in Malaysia. She received her Bachelor degree in Automotive Engineering from School of Aerospace, Mechanical and Manufacturing Engineering, RMIT University, Australia in 2012. She has been a Ph.D. student of School of Aerospace, Mechanical and Manufacturing Engineering, RMIT University and Her Ph.D.

research topic is: Investigation and optimization of direct injection gaseous fuel vehicle.

E-mail: kelly_myboo@yahoo.com



Mr. **M. L. Choo** was born on 20 February, 1990 in Malaysia. He received his Bachelor degree in Automotive Engineering from School of Aerospace, Mechanical and Manufacturing Engineering, RMIT University in 2012. His final year undergraduate project topic is: A Study of Air Flow Resistivity of Polyfelt in Vehicle Interior Trim Sound Package.

E-mail: mingliang0220@gmail.com

Workability Behaviour of Al-SiC Matrix P/M Composite Under Triaxial Stress State Condition

J. Bensam Raj, P. Marimuthu, M. Prabhakar, V. Anandakrishnan

Abstract – Workability is concerned with the scope to which a material can be deformed in a specific metalworking process without the initiation of cracks. The ductile fracture of components is the most common mode of cracks in any metalworking processes. Workability is the complex technological concept, depends upon the ductility of the material and the details of the process parameters. The purpose of this paper is to illustrate the workability behaviour of the Al-SiC during cold upsetting. In the present study three types of sintering temperature and time have been considered to evaluate the effect of P/M preforms of Al-SiC composite on workability studies. The material studied in this paper is Aluminium with SiC reinforcement. SiC content has been varied from 0 to 20 percent. The experimental results were analyzed for workability under triaxial stress state condition as a function of the relative density. The formability stress index (β_σ) and stress ratio parameters namely $\sigma_\theta/\sigma_{eff}$ was obtained. These phenomena have shown tremendous variations for different kind of sintering temperature and time. **Copyright © 2013 Praise Worthy Prize S.r.l. - All rights reserved.**

Keywords: Aluminium Metal Matrix Composites, Powder Metallurgy, Workability Plastic Behaviour

Nomenclature

| | |
|----------------------------------|--|
| F | Force applied on the cylindrical preform for deformation |
| h_0 | Initial height of the cylindrical preform |
| h_f | Height of the barreled cylinder after deformation |
| D_0 | Initial diameter of the preform |
| D_B | Bulged diameter of the preform after deformation |
| D_{TC} | Top contact diameter of the preform after deformation |
| D_{BC} | Bottom contact diameter of the preform after deformation |
| α | Poisson's ratio |
| σ_z | True stress in the axial direction |
| σ_θ | True stress in the hoop direction |
| σ_r | True stress in the radial direction |
| σ_{eff} | True Effective stress |
| σ_m | True Hydrostatic or mean stress |
| β_σ | Formability Stress Index |
| ρ_0 | Initial preform density of the preform |
| ρ_f | Density of the preform after deformation |
| ρ_{th} | Theoretical density of the fully dense material |
| $R(or) \frac{\rho_f}{\rho_{th}}$ | Relative density |
| K | Strength Coefficient value |
| n | Strain hardening index value |

h_0/D_0

Aspect Ratio

I. Introduction

Powder metallurgy (P/M) is a highly developed method of manufacturing precision metal parts. Over the last seven decades, the technology has matured from making self-lubricating bearings for autos to complex carrier gear set in automobile transmissions and high strength powder-forged connecting rods in engines.

Powder forging is attractive due to its ability to produce the products with no wastage of material and its ability to fabricate high quality, complex parts to close tolerances in an economical manner [1]. Powder forged parts are performing with high strength along with the absolutely uniform grained microstructure. Particles reinforced Aluminium alloy matrix composite is one of the best materials to substitute the conventional structural alloys.

The sintering is also difficult in some cases which is not giving satisfactory densifications [2] due to improper sintering temperature and time. Similarly we can get better corrosion resistant materials through these sintering variations [3]. Sintering is one of the important consolidation processes, which is very essential for cold compaction processes, due to very low strength of the green compact. Press-and-sinter fabrication technique is one of the oldest methods to produce good quality P/M products. In a powder metallurgical forging process the sintering effect has been modeled by few of the authors

to evaluate the effect of sintering in a forging processes [4], [5] Selecka et al. studied the behaviour of liquid phase sintering effect on the specimen sintering at 1200°C for 60 min in hydrogen for Ni, Mo and Cr alloyed structural elements with boron. They identified the increase of specimen density and formation of a new microstructure type.

Sintering of powder is the root cause for the establishment and growth of bonds between the particles of powder at their areas of contact and migration of the grain boundaries formed at the bonds. The spheroidization of the pores between the particles, and the elimination of small pores (and possibly the growth of larger pores) were also caused by the sintering effects. As the sintering temperature increases, porosity decreases and shrinkage increases [6]. Bonds form between the particles during sintering, and the number of particle bonds increase as the temperature increases.

As generally agreed by the results presented in several previous works [7], [8] successful sintering of aluminium alloys can only be carried out through the formation of a liquid phase able to disrupt the extremely stable aluminium oxide film always covering the aluminium particles. Such liquid phase must be able to penetrate the oxide film, through the discontinuities created during cold pressing. Thus facilitating material transport and hence the development of adequate bonding by the formation of necks between particles. Khairaldien et al. have studied the sintering effect of Al-SiC composites fusion behaviour and weldability behaviour of the composite and found that the weldability behaviour is reducing, if the aluminium picks oxygen during the sintering and also he found that the increase in sintering temperature is reducing the weldability problems [9].

Workability is to which a material can be deformed in a specific metal working process without the initiation of cracks [10]. Abdel-Rahman et al., [11], presented the effect of relative density on the forming limit of P/M compacts during upsetting. They have proposed the criteria called formability stress index (β) for describing the effect of the mean stress and the effective stress with the help of two theories, proposed by Kuhn-Downey and Whang-Kobayashi.

Narayanasamy et al. [12] investigated some of the important criteria generally used for the prediction of workability. They have done tremendous experimental work on workability behaviour of Aluminium [13], [14], Al-Al₂O₃ [15] – [20], Al-Fe [21], [22], Fe [23], Fe-TiC [24] and Al-SiC [25], [30] composites during cold upsetting.

The previous literature are not dealing with the effect of sintering temperature and sintering time on workability under triaxial stress state condition and the work hardening behaviour on Al-SiC porous composite.

The present investigation is an attempt to evaluate the effect of the sintering temperature and sintering time on particle size on the workability parameter under triaxial stress state condition and work hardening effects in porous Al-SiC composite during upsetting at room

temperature. The relationships between the various stress ratios namely $\sigma_{\theta}/\sigma_{eff}$ and σ_z/σ_m , and the relative density and its effect on the sintering effect are also attempted in this work.

II. Experimental Details

II.1. Compacts Preparation

Atomized Aluminium powder of -100 μ m was used for analysis of its purity. The purity level of the powder was found to be 99.7 percent and insoluble impurities to be 0.3 percent. The flow rate, apparent density and particle size distribution of Aluminium powder was studied.

Al-10%SiC and Al-20%SiC powder mix were blended on a pot mill to obtain a homogeneous powder blend. The particle size of Silicon carbide powder mixed was 50 μ m. Green compacts of the powder blend was prepared on a 1.0 MN capacity hydraulic press using suitable punch and die assembly as shown in Fig. 1.

The compact pressure was maintained for all composition of SiC composites to maintain the 92% relative density level.

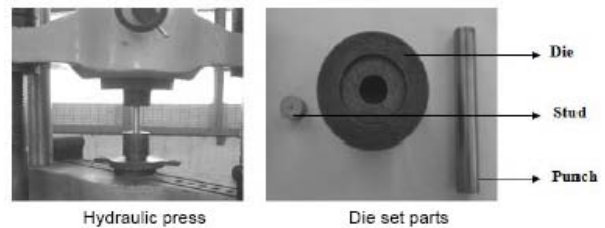


Fig. 1. Photographs of hydraulic press and parts of compacting die tool

The green compact surfaces were coated with an indigenously developed ceramic mixture [21] and dried under room-temperature conditions for a period of 9 hours.

A second coating was applied at a direction of 90° to the direction of first coating and was allowed to dry for a further period of 9 hours under the same conditions as stated above.

II.2. Sintering

The ceramic-coated compacts were sintered in an electric muffle furnace in the temperature range of 600±10°C for a period of 120 minutes and allowed to be cooled to room temperature in the furnace itself.

The sintered preforms of pure aluminium and aluminium-SiC composites prepared.

The microstructure of sintered Al-SiC composites with sintering temperature of 605°C at 3 hrs is shown in Fig. 2.

The ceramic coatings applied over specimen were removed by machining. The aspect ratio was maintained as 0.90 for all compositions of composites.

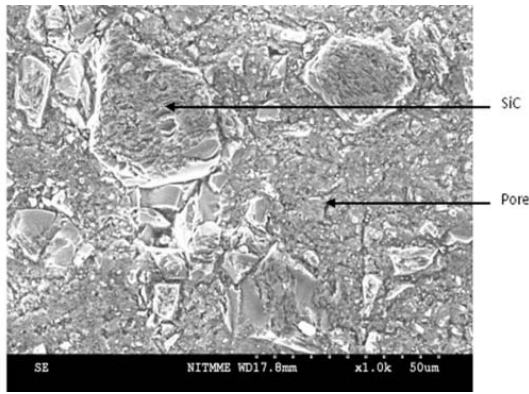


Fig. 2. The SEM photograph of as sintered Al-20% SiC at 605°C at 3 hrs

II.3. Deformation Test

Initial diameter (D_0), initial height (h_0) and the initial preform relative density (ρ_0) of the specimen were measured and recorded. Each compact was subjected to the incremental compressive loads of 0.01 MN and the upsetting was carried between two flat, mirror finished open dies on a hydraulic press of 1.0 MN capacity.

The deformation was carried out until the appearance of the first visible crack on the free surface. After each interval of loading, dimensional changes in the specimen such as height after deformation (h_f), top contact diameter (D_{TC}), bottom contact diameter (D_{BC}), bulged diameter (D_B) and density of the preform (ρ_f) were measured. The schematic diagram showing the various parameters measured before and after deformation is provided in Fig. 3.

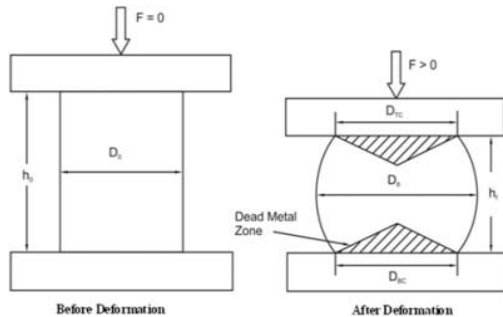
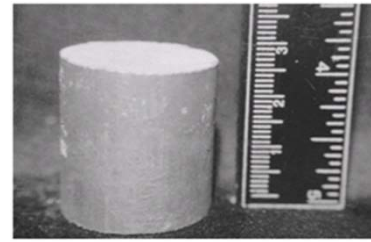


Fig. 3. Schematic of upset test of perform (before and after deformation)

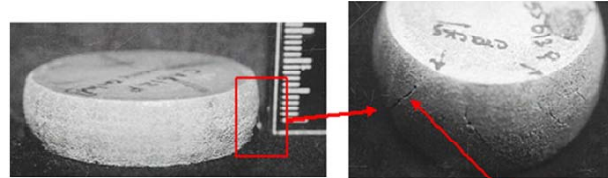
Using the Archimedes principle, the density of upset performs was also determined after every loading interval. The deformation test is continued until the fracture occurs at outer surface of the specimen as shown in Figs. 4 (a) and (b).

III. Theoretical Investigations

In a triaxial stress state condition pertains to actual stresses developed during cold upsetting of cylindrical preform with friction and barreling.



(a) Before deformation



(b) after deformation

Figs. 4. Photographs showing preform – before and after deformation test

Here the axial stress is compressive in nature, the hoop and the radial stresses are tensile in nature.

In order to simplify the plasticity theory, the radial stress can be taken as equivalent to the hoop stress. Narayanasamy et al., [26], reported the state of stress in a triaxial stress condition is as follows:

The relationships between stress and strain increment for an ideal plastic solid, where the elastic strains are negligible, are called flow rules or Levy-Mises equations.

The relationship between the strain increment and stresses for triaxial stress state condition for a porous material is written as follows [26], α , which is nothing but the ratio of the hoop strain increment to the axial strain increment. Say:

$$\alpha = \left(\frac{A}{B} \right) \quad (1)$$

where

$$A = \left[(2 + R^2) \sigma_\theta - R^2 (\sigma_z + 2\sigma_\theta) \right]$$

$$B = \left[(2 + R^2) \sigma_z - R^2 (\sigma_z + 2\sigma_\theta) \right]$$

- α is Poisson's Ratio
- R is Relative Density
- σ_z is the axial stress and
- σ_θ is the hoop stress

In triaxial stress condition for the known values of Poisson's ratio (α), relative density (R) and axial stress (σ_z), the Hoop stress component (σ_θ) can be determined as explained elsewhere [27], is as follows:

$$\sigma_\theta = \left(\frac{2\alpha + R^2}{2 - R^2 + 2R^2\alpha} \right) \sigma_z \quad (2)$$

In the above Eq. (2), the relative density (R) plays a major role in determining the hoop stress component (σ_θ).

The hydrostatic stress for axi-symmetric upset forging condition is given by:

$$\sigma_m = \frac{(\sigma_z + \sigma_r + \sigma_\theta)}{3} \quad (3)$$

Since $\sigma_r = \sigma_\theta$ for axi-symmetric or cylindrical upsetting, the above equation can be written as:

$$\sigma_m = \frac{(\sigma_z + 2\sigma_\theta)}{3} \quad (4)$$

The effective stress can be determined from the following expression in terms of cylindrical coordinates for axi-symmetric upset forging condition as explained [28]:

$$\begin{aligned} & \left[\sigma_1^2 + \sigma_2^2 + \sigma_3^2 - R^2 (\sigma_1\sigma_2 + \sigma_2\sigma_3 + \sigma_3\sigma_1) \right] = \\ & = (2R^2 - 1) \sigma_{eff}^2 \end{aligned} \quad (5)$$

The above Eq. (5) can be written in terms of cylindrical coordinates as follows:

$$\sigma_{eff}^2 = \frac{\left[\sigma_z^2 + \sigma_\theta^2 + \sigma_r^2 - R^2 (\sigma_z\sigma_\theta + \sigma_\theta\sigma_r + \sigma_r\sigma_z) \right]}{2R^2 - 1} \quad (6)$$

Since $\sigma_\theta = \sigma_r$, for axi-symmetric or cylindrical upsetting, the Eq. (6) can be modified as:

$$\sigma_{eff} = \left(\frac{\left[\sigma_z^2 + 2\sigma_\theta^2 - R^2 (\sigma_\theta^2 + 2\sigma_z\sigma_\theta) \right]}{2R^2 - 1} \right)^{1/2} \quad (7)$$

In the above Eq. (7), for the known values of σ_z , σ_θ and R , the effective stress σ_{eff} can be determined.

The stress ratio parameters, namely $(\sigma_\theta / \sigma_{eff})$ and (σ_z / σ_m) are calculated from the above equations.

III.1. Formability Stress Parameter

The formability stress index parameter (β_σ) can be determined for triaxial stress state condition.

As an evidence of experimental investigation implying the importance of the spherical component of the stress state on fracture, Vujovic and Shabaik [29], proposed a parameter called a Formability Stress Index ' β_σ ' given by:

$$\beta_\sigma = \left(\frac{3\sigma_m}{\sigma_{eff}} \right) \quad (8)$$

where, σ_m is the mean or hydrostatic stress component and σ_{eff} is the effective stress component can calculate through the Eqs. (4) and (8). This index determines the fracture limit as explained in the reference [26].

IV. Results and Discussions

The workability of metals is one of the most important parameters that must be considered in the design of forming an operation. A preform with high relative density is at a relatively greater stress, while a preform with low relative density is at a relatively smaller stress.

The application of a compressive hydrostatic stress will close the pore and will increase the relative density.

Similarly the application of tensile hydrostatic stress will increase the size of the pores and reduces the relative density. Bulk forming is a process that reflects the complicated workability of materials. It is very important to guide the production practice according to the forming limits.

Figs. 5(a)-(c) have been plotted between the relative density and the true axial strain (ϵ_z) for Aluminium containing different Silicon carbide percentage and for three different sintering time namely at 1.5, 3 hrs and 4.5 hrs with sintering temperature of 560°C, 605°C and 630°C. It is observed that the relative density increases with increasing amount of SiC added in the Al-SiC composite. For any given composition of composite, as the sintering time increases, the relative density increases. From these Fig. it is understood that the relative density and axial strain are affected by the amount of SiC content and sintering behavior.

The same behaviour has been observed when the sintering temperature increases. As a SiC content and sintering temperature increases, the porosity level decreases and the relative density increases for the same compacting pressure.

This may be one of the reasons for the increasing stresses for higher amount of SiC content.

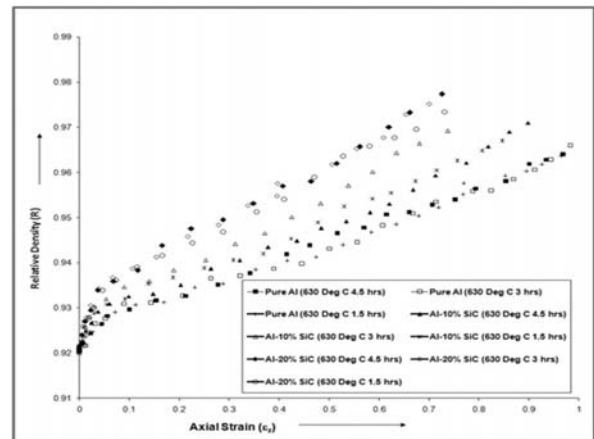


Fig. 5(a). The variation of Relative Density (R) with respect to the True Axial strain (ϵ_z) for the sintering temperature of 630°C at various time intervals

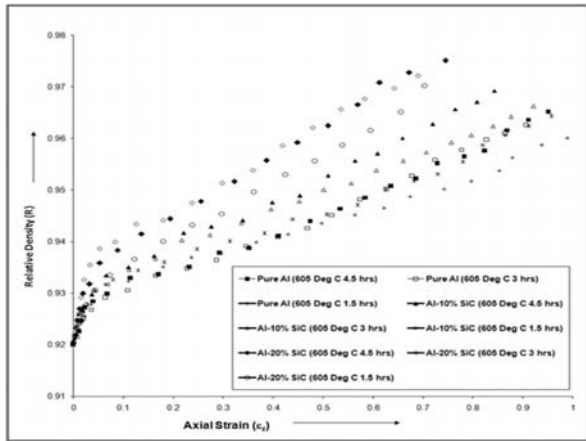


Fig. 5(b). The variation of Relative Density (R) with respect to the True Axial strain (ϵ_z) for the sintering temperature of 605°C at various time intervals

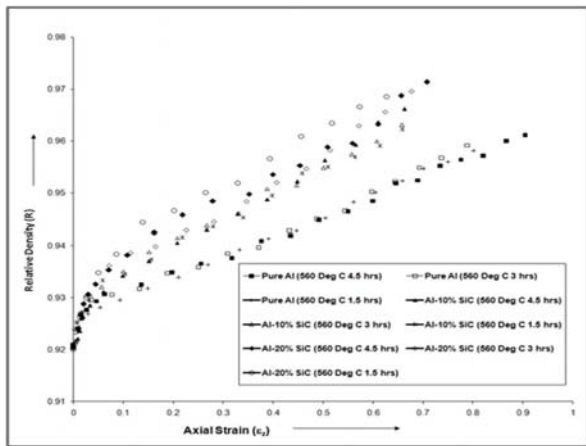


Fig. 5(c). The variation of Relative Density (R) with respect to the True Axial strain (ϵ_z) for the sintering temperature of 560°C at various time intervals

Further, as the amount of SiC content in the composites increases, the SiC particulates impede the motion of dislocations and hence the stress required for further plastic deformation increases. Due to these reasons all stresses increase with increasing amount of SiC. Figs. 6 (a)-(c) have been plotted between the formability stress index (β_σ) and the true axial strain (ϵ_z) for Aluminium containing different SiC percentage and for three different sintering time namely at 1.5, 3 hrs and 4.5 hrs with sintering temperature of 560°C, 605°C and 630°C. Table I provides the maximum value of the formability stress index (β_σ) for various sintering time and temperature increment in the Al-SiC composites.

It is observed that as the Sintering temperature increases, the formability stress index (β_σ) also increases.

The reason is that as the Sintering temperature increases the relative density also increases and porosity decreases. This may be the reason that the formability stress index increases with increasing sintering temperature. It is further observed that as the sintering time increases the formability stress index also increases.

The reason may be due to increase in relative density with increasing sintering time. Therefore, the formability stress index (β_σ) also increases with sintering time.

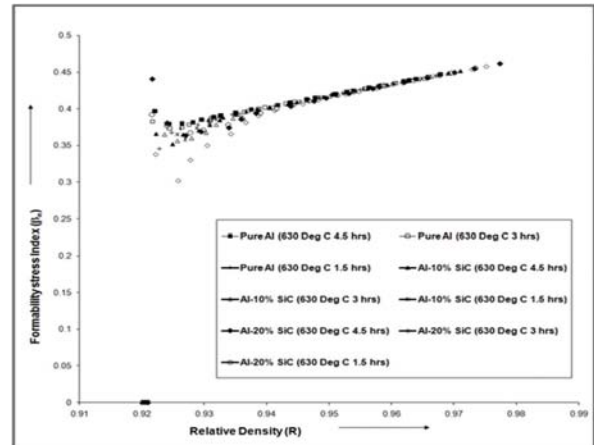


Fig. 6(a). The variation of Formability stress index (β_σ) with respect to the Relative Density (R) for the sintering temperature of 630°C at various time intervals.

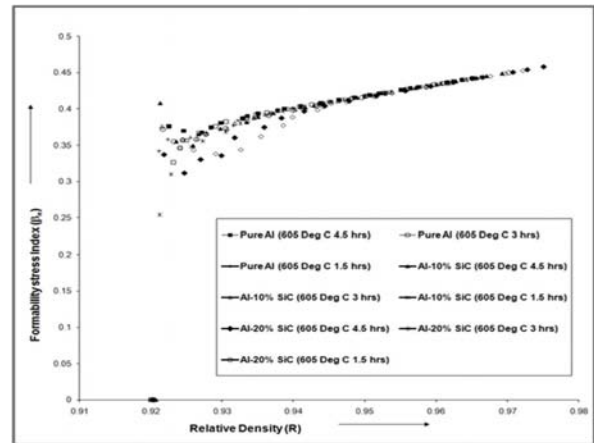


Fig. 6(b). The variation of Formability stress index (β_σ) with respect to the Relative Density (R) for the sintering temperature of 605°C at various time intervals

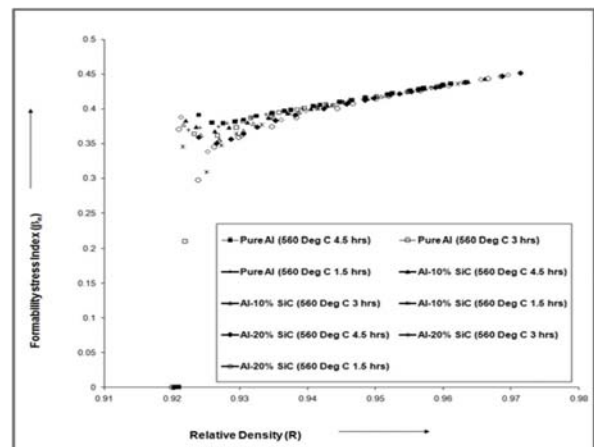


Fig. 6(c). The variation of Formability stress index (β_σ) with respect to the Relative Density (R) for the sintering temperature of 560°C at various time intervals

TABLE I
THE VALUES OF MAXIMUM FORMABILITY STRESS INDEX (β_σ) FOR VARIOUS SINTERING TEMPERATURE AT VARIOUS TIME INTERVALS

| Sintering temperature (°C) | Sintering time (h) | SiC percentage | Maximum formability stress index (β_σ) | |
|----------------------------|--------------------|----------------|---|----------|
| 630°C | 4.5 | Pure | 0.446836 | |
| | | aluminium | 0.443675 | |
| | 3 | 10 | | 0.439983 |
| | | | | 0.45157 |
| | 4.5 | 20 | | 0.448334 |
| | | | | 0.445154 |
| | 3 | 10 | | 0.461532 |
| | | | | 0.457743 |
| | 4.5 | 20 | | 0.455177 |
| | | | | 0.455177 |
| 605°C | 4.5 | Pure | 0.442314 | |
| | | aluminium | 0.438017 | |
| | 3 | 10 | | 0.434278 |
| | | | | 0.448685 |
| | 4.5 | 20 | | 0.44397 |
| | | | | 0.440895 |
| | 3 | 10 | | 0.457744 |
| | | | | 0.452944 |
| | 4.5 | 20 | | 0.449793 |
| | | | | 0.449793 |
| 560°C | 4.5 | Pure | 0.436033 | |
| | | aluminium | 0.432671 | |
| | 3 | 10 | | 0.431117 |
| | | | | 0.443209 |
| | 4.5 | 20 | | 0.438334 |
| | | | | 0.436747 |
| | 3 | 10 | | 0.451693 |
| | | | | 0.448707 |
| | 4.5 | 20 | | 0.446709 |
| | | | | 0.446709 |

The same behaviour has been observed irrespective of the sintering temperature in the Al-SiC composite.

Further it can be understood that the true mean stress (σ_m) also increases with increasing sintering temperature and sintering time to the true effective stress (σ_{eff}).

Therefore the formability stress index increases with increasing sintering temperature. As the sintering time increases, the formability stress index also increases. The reason is due to the association of fine pores in higher sintering temperature. The same behaviour has been observed in the case of stress ratio parameter ($\sigma_\theta/\sigma_{eff}$) is plotted against the relative density as shown in Figs. 7(a)-(c).

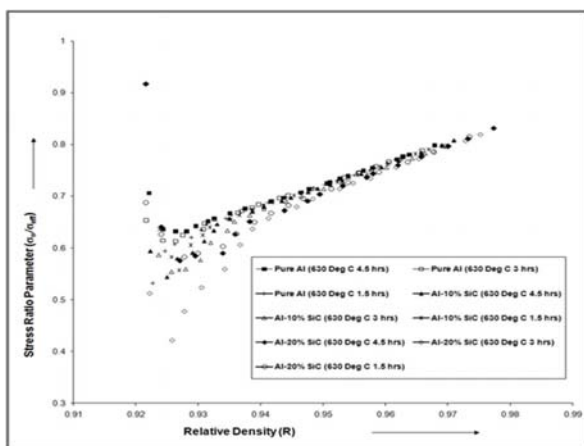


Fig. 7(a). The variation of Stress Ratio Parameter ($\sigma_\theta/\sigma_{eff}$) with respect to the Relative Density (R) for the sintering temperature of 630°C at various time intervals.

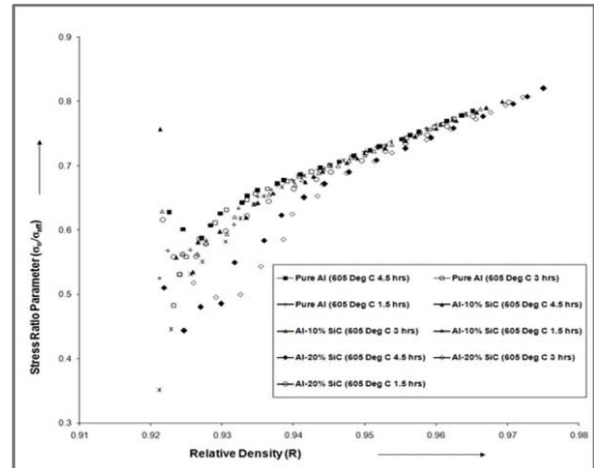


Fig. 7(b). The variation of Stress Ratio Parameter ($\sigma_\theta/\sigma_{eff}$) with respect to the Relative Density (R) for the sintering temperature of 605°C at various time intervals

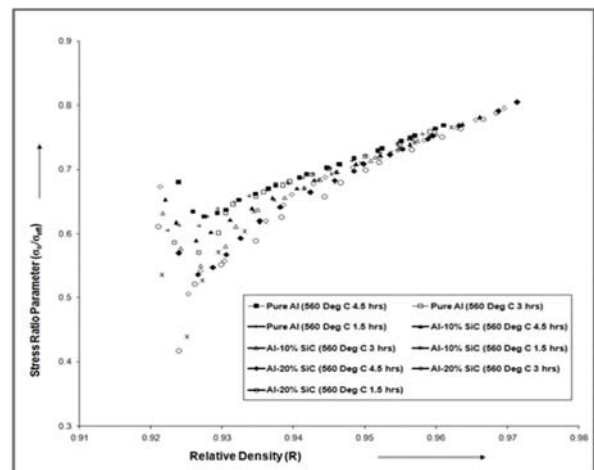


Fig. 7(c). The variation of Stress Ratio Parameter ($\sigma_\theta/\sigma_{eff}$) with respect to the Relative Density (R) for the sintering temperature of 560°C at various time intervals

V. Conclusion

The following conclusions can be drawn from the above results and discussions.

- As the Sintering temperature increases the pore size becomes smaller. As the pore size becomes smaller, the formability stress index value (β_σ) increases.
- 20% SiC added composites show higher formability stress index value (β_σ) compared to other composite because of better densification.
- The stress ratio parameter ($\sigma_\theta/\sigma_{eff}$) is found to be higher for Al-SiC composites compared to pure Aluminium because of better densification.
- For preforms with higher percentage addition of SiC, the initiation of crack exhibits at lower fracture strain.
- Higher sintering temperature initiates cracks with higher fracture strain.
- Higher sintering time given composites initiate crack at higher fracture strain.

References

- [1] George E. Dieter, Howard A. Kuhn and S. Lee Semiatin, Handbook of Workability and process design, *ASM International, Metals Park, OH 44073-0002*, 1984.
- [2] ASM International; *Powder Metal Technologies and Applications*, ASM Handbook, 2002.
- [3] Metal Powder Industries Federation, (1994) *Material Standards for P/M Structural Parts*, Standard 35
- [4] H.Lippmann, R.Iankov, (1997) Mathematical modeling of sintering during powder forming processes, *International Journal of mechanical sciences*, Vol.39, No.5, pp. 585-596.
- [5] M.Selecka, A.Salak, H.Danninger, (2003) The effect of boron liquid phase sintering on properties of Ni-, Mo- and Cr- alloyed structural steels, *Journal of materials processing technology* Vol. 141, pp. 379-384.
- [6] W.B. James, G.T.West, *Production Sintering Practices*, in: *Powder Metal Technologies and Applications*, ASM Handbook, ASM International, Vol. 07, pp. 468-503, 2002.
- [7] Lumley, R.N., G.B. Schaffer, The effect of solubility and particle size on liquid phase sintering, *Scripta Mater.*, Vol.35, No. 589, 1996.
- [8] Lumley, R.N., G.B. Schaffer, The effect of additive particle size on the mechanical properties of sintered Aluminium-Copper alloys, *Scripta Mater.*, Vol.39, pp.1089, 1998.
- [9] Khairaldien. W. M., A. A. Khalil and M. R. Bayoumi, Production of Aluminum-Silicon Carbide Composites Using Powder Metallurgy at Sintering Temperatures Above the Aluminum Melting Point, *Journal of Testing and Evaluation*, Vol. 35, No.6, pp. 1-13.
- [10] George.E. Dieter, Hand book on workability analysis and applications, *ASM publications, USA*, .2000.
- [11] M.Abdel-Rahman, M.N.El-Sheikh, Workability in forging of powder metallurgy compacts, *J. Mater. Process Technol.* Vol.54 , pp.97-102, 1995.
- [12] R. Narayanasamy, R. Ponalagusamy, K.R. Subramanian, Generalized yield criteria of porous sintered powder metallurgy metals, *J. Mater. Process Technol.* Vol. 110 , pp. 182-185, 2001.
- [13] R. Narayanasamy, T. Ramesh, K.S. Pandey, Some aspects of workability studies in cold forging of pure aluminium powder metallurgy compacts, *Mater. Sci. Technol.* Vol. 21, No. 8 , pp. 912-916. 2005.
- [14] K. Manisekar , R. Narayanasamy, Effect of friction on barrelling in square and rectangular billets of aluminium during cold upset forging, *Materials and Design*, Vol. 28 , pp.592-598, 2007.
- [15] R.Narayanasamy, T.Ramesh, K.S.Pandey, An investigation on instantaneous strain hardening behaviour in three dimensions of aluminium-iron composites during cold upsetting, *Mater. Sci. Eng. A* , Vol. 394 ,pp. 149-160, 2005.
- [16] R. Narayanasamy, K.S. Pandey, Some aspects of work hardening in sintered aluminium-iron composite preforms during cold axial forming, *J. Mater. Process. Technol.* Vol. 84 , pp.136-142, 1998.
- [17] R. Narayanasamy , T. Ramesh , K.S. Pandey, An experimental investigation on strain hardening behaviour of aluminium - 3.5% alumina powder metallurgy composite preform under various stress states during cold upset forming, *Mater. Des.* Vol. 28, pp. 1211-1223, 2007.
- [18] Narayanasamy, R., Anandakrishnan, V., Pandey, K.S., Effect of geometric work-hardening and matrix work-hardening on workability and densification of aluminium-3.5% alumina composite during cold upsetting, *Mater. Des.* Vol. 29, pp. 1582-1599, 2008.
- [19] R. Narayanasamy, N. Selvakumar, K.S. Pandey, Phenomenon of instantaneous strain hardening behaviour of sintered Al-Fe composite preforms during cold axial forming, *Mater. Des.*, Vol. 28 , pp.1358-1363, 2007.
- [20] R. Narayanasamy , T. Ramesh , K.S. Pandey, Some aspects on strain hardening behaviour in three dimensions of aluminium-iron powder metallurgy composite during cold upsetting, *Mater. Des.* Vol. 27 , pp.640-650,2006.
- [21] R. Narayanasamy, T. Ramesh, K.S. Pandey, Some aspects on workability of aluminium-iron powder metallurgy composite during cold upsetting, *Mater. Sci. Eng. A*, Vol.391, pp. 418-426, 2005.
- [22] N.Selva kumar, R.Narayanasamy, Deformation Behavior of Cold Upset Forming of Sintered Al-Fe Composite Preforms, *J. of Eng. Mater. Technol.*, Vol.127, pp. 251- 256, 2005.
- [23] R. Narayanasamy, V. Senthilkumar, K. S. Pandey, Workability studies on powder metallurgy pure iron preforms during hot forging under triaxial stress state condition, *Int. J. Mech. Mater. Des.* Vol. 3, pp.175-184,2006.
- [24] R. Narayanasamy, V. Senthilkumar, K. S. Pandey, Some aspects of workability studies on P/M sintered high strength 4% Titanium carbide composite steel preforms during cold upsetting, *Int. J. Mech. Mater. Des.* Vol.3, pp.39-57,2006.
- [25] R. Narayanasamy, T. Ramesh, M. Prabhakar, Effect of particle size of SiC in aluminium matrix on workability and strain hardening behaviour of P/M composite, *Materials Science and Engineering A*, Vol. 504 , pp.13-23, 2009.
- [26] R. Narayanasamy, T. Ramesh and K.S. Pandey , Some aspects on workability of aluminium-iron powder metallurgy composite during cold upsetting, *Mater. Sci. Eng. A*, Vol.391, pp.418-426. 2005.
- [27] Narayanasamy, R, T. Ramesh and K.S. Pandey, Workability studies on cold upsetting of Al-Al₂O₃ composite material, *Mater. Des.*, Vol. 27, No. 7, pp. 566 - 575, 2006.
- [28] Doraivelu, S.M., H.L. Gegel, J.S. Gunasekaran, J.C. Malas, and J.T. Morugan, A new yield function for compressible P/M materials, *Int. J. Mech. Sci.* Vol. 26, No. 9, pp. 527-535, 1984.
- [29] Vujovic, V. and A.H. Shabaik, A New workability criteria for Ductile Metals, *Journal of Engineering Materials and Technology*, Vol. 108, pp. 245 -249, 1986.
- [30] C. Dhavamani, T. Alwarsamy, Optimization of Cutting Parameters for Aluminum and Silicon Carbide Composite Using Taguchi's Techniques, *International Review of Mechanical Engineering*, Vol. 6, No.6, pp. 1361-1365.

Authors' information



J. Bensam Raj (Corresponding author) was born on July 10th, 1978 in Nagercoil (India). He received his B.E degree in Mechanical Engineering from Madurai Kamaraj University in 1999. Then he received his M.E degree in Thermal Engineering from Annamalai University in 2000. He is currently doing Ph. D. in Anna University, Chennai. His research activities include workability studies of composite materials. He is an Assistant Professor in The Rajaas Engineering College Vadakkankulam. He has co - authored four Engineering Books.
Tel.: 9442076893
E-mail: bensmech@yahoo.co.in



Dr. P. Marimuthu, obtained his Bachelor degree in Mechanical Engineering and Master Degree in Production Engineering from Thiagarajar College of Engineering, Madurai. He obtained his Ph.D., in the area of Machining of Metal Matrix Composite from Anna University, Chennai. He had served in many Institutions at various positions as Lecturer, Assistant Professor, Professor, Head of the Department and Principal. Now he is working as a principal in Syed ammal Engineering College, Ramanathapuram. He had published more number of papers in refereed International Journals and Conferences. Presently he is board of study member for PG course at Anna University of Technology, Madurai. He is also Life member in Indian Society for Technical Education. He received "RASTRIYA VIDYA SARASWATI PURASKAR AWARD" during March 2010 for his achievement and remarkable role in the field of education, honored by the International Institute of Education and Management, New Delhi. His research areas include Manufacturing, Composites, Machining Science, Modeling and optimization. He is guiding PhD scholars in different areas. He is active Doctoral committee member for PhD scholars, Question paper setter and Examiner for various autonomous Institutions and Universities.



Dr. **M. Prabhakar** received his engineering degree in Mechanical Engineering from Bharathidasan University in 1996. Then he received his M.E degree in Thermal Power Engineering from Bharathidasan University in 2001 and Ph.D., Degree from National Institute of Technology, Tiruchirappalli in 2010. Currently he is doing Post doctoral work in

National University of Singapore. He has 16 years of teaching experience. He has co-authored 16 conference papers and 11 international journals. His research interest is Composite materials.



V. Anandkrishnan was born on January 3, 1977 in Karaikudi (India). He received his B.E. degree in Mechanical Engineering from Bharathidasan University (India) in 1999. Then, he received his M.E. degree in Production Engineering from Annamalai University (India) in 2001. Then, he received his Ph.D. in Production Engineering from National Institute

of Technology Tiruchirappalli (India) in 2010. Since 2008, he has been an Assistant Professor at National Institute of Technology Tiruchirappalli (India). His R&D activities include the development and investigations on metal matrix composites. He has authored and co-authored many refereed articles most concentrating on manufacturing possibilities of metal matrix composites.

E-mail: krishna@nitt.edu

Experimental and Emission Analysis of Rubber Seed Oil and Jatropha Oil Blends with Diesel in Compression Ignition Engine

S. Mahalingam¹, B. R. Ramesh Babu²

Abstract – In the fast growing world of automobiles, the demand for petroleum products is increasing day by day. Many of renewable energies are used to full fill that demand. One of the best alternatives is the use of biodiesel. In this study a dual fuel blend with pure diesel in a single cylinder direct injection constant speed diesel engine was analyzed by varying the power outputs with different proportions of the fuel blends. In the dual fuel operation, the rubber seed oil and jatropha oil blends with diesel. The proportions of 20% and 40% blend have been investigated on volume basis. In this dual fuel operation is observed that they have higher emission of hydrocarbon (HC) and carbon monoxide (CO) emissions than the ester, diesel blend. The ignition delay was reduced using dual fuel blend with diesel and efficiencies were improved. The proportion, B20 (20% of biodiesel) is gives the optimum efficiency with low emission. **Copyright © 2013 Praise Worthy Prize S.r.l. - All rights reserved.**

Keywords: Rubber Seed Oil, Jatropha Oil, Emission, Performance

I. Introduction

In rural area, a variety of unused seeds are available. They are processed in different ways to obtain oil for medical purpose. In an alternative thing where so many research works are done, that the oils are being mixed with the diesel or petrol to reduce the petroleum demands. But if vegetable oil is used in an internal combustion engine, viscosity of the oil is a major problem which affects complete combustion, increasing carbon deposits, smoke density etc. Using different esterification process, any vegetable oil can be esterified by which viscosity is reduced and also reducing the ester. The different proportions of rubber seed oil were blended with diesel and studied for performance factors such as calorific value, flash point, fire point and kinematic viscosity. Emission of rubber seed oil were studied and compared with that of the diesel.

Ramadhas et al., [1] conducted 50-80% of rubber seed blended with diesel and showed higher carbon deposits inside the combustion chamber than the diesel fueled engine. The rubber seed oil was directly used without any modifications of diesel engine and then concluded that, by using the rubber seed oil from 50-80%, there was a higher brake thermal efficiency and reduction of specific fuel consumption. For 80% of blends, the carbon deposits are increased. So it was found that the rubber seed oil is most suitable for power generation.

Ramadhas et al., [2] investigated the main properties of methyl esters of rubber seed that were compared with other esters and diesel.

The rubber seed oil with diesel were analyzed and studied for the different emission characteristics of the engine at different load conditions.

Also concluded that the viscosity and density of methyl ester of rubber seed oil are very close to that of the diesel fuel and the calorific value of rubber seed oil is slightly lower than that of diesel.

The flash and fire point temperatures were higher than that of diesel. The lower concentration of rubber seed oil such as 5-10% were used in the diesel engine to improve brake thermal efficiency and reduce specific fuel consumptions with different load conditions. When high concentration of refined rubber seed oil was used, smoke density and NO_x formation also increased.

Edwin et al., [3] analyzed a single cylinder diesel engine, using rubber seed oil methyl ester blend with a rated output of 4.4 kW at a constant speed of 1500 rpm.

By varying the hydrogen quantity of rubber seed oil and rubber seed oil methyl ester it was concluded the maximum thermal efficiencies were 28.12%, to 31.62%.

The smoke level by using rubber reed oil was increased, but in rubber seed oil methyl ester, smoke density was reduced from 5.5 to 3.3 BSU. With the increase of peak pressure and combustion, from emission test, HC and CO were considerably low for all load conditions and NO_x was considerably high at 6.9 g/kWh to 10.76 g/kWh for rubber seed oil. By using of rubber seed oil methyl ester, NO_x is increased to a maximum of 11.67% g/kWh due to increase in exhaust temperatures. Jincheng Huang et al., [4] analyzed an engine with two different oil as pistache oil and jatropha oil blended with diesel. The brake thermal efficiency and specific fuel consumption of engine were increased. In emission analysis the CO percentage was reduced at full load conditions and hydrocarbon (HC) and Nitrogen oxides (NO_x) are also controlled in different load conditions. It was concluded that, by using the pistache oil, the

performance and emissions were similar to the jatropha oil blended with biodiesel fuel.

Senthil Kumar et al., [5] experimentally studied a single cylinder constant speed engine using transified jatropha oil and methanol blend with diesel. The brake thermal efficiency increased as 27.4%-29% in different load conditions. The smoke was reduced in vegetable oil operations to an extent that the emission values were 4.4 Bosch Smoke Units (BSU) and with jatropha blended with methyl ester it was reduced to 4.1 BSU to 4BSU. In dual operation smoke again reduced up to 3.5 BSU. The nitric oxide (NOx) was very low using jatropha with methanol and hydrocarbon (HC), carbon monoxide (CO) and ignition delay were increased using the dual fuel of jatropha with methanol.

Pi-qiang Tan et al., [6] studied the regulated and unregulated emissions, were in jetropha blended with diesel fuel at different proportions such as 5%, 10%, 20%, 50%, and 100% by volume. The regular emissions are carbon monoxide, nitrogen oxide, unburned hydrocarbon, smoke, and another four unregulated emissions: acetaldehyde, acetone, formaldehyde and toluene. In the emission with biodiesel, there was no change in NOx emission for various load conditions, but the CO emission was increased from low load condition onwards. The Hydro carbon emission was continuously reduced in different blended biodiesel ratios. It was concluded that, the acetaldehyde and formaldehyde emission were higher than that of pure diesel fuel at 5% of biodiesel. But in B100 fuel, the same was lower than that of the pure diesel fuel at no load and medium load conditions. The acetone emission was higher in different biofuel from B5 to B100 when compared to that of the diesel fuel. Shyam Pandeyetal., [7], analyzed to find the performance parameters such as fuel consumption, thermal efficiency, exhaust gas temperature and emissions like CO, NOx, HC and smoke, of a Direct Injection (DI) engine fueled with a variety of blended fuels and the parameters were compared with that of diesel fuel. The different blends were studied as B0%D95%E5%, B0%D90%E10%, B15%D70%E15% and B20%D60%E20%. The fuel was stable for 17days at room temperature and the Physiochemical properties were studied to improve the fire points of the fuels. The experimental results showed that the B0%D95%E5% biofuel was given the maximum thermal efficiency and least amount of brake specific fuel consumption (BSFC) at full load condition. In addition to that for the B0%D90%E10%, blended fuel, the emission characteristics were excellent when compared to other blended fuels. In this experimental work mixing of two bio fuels namely jatropha oil and rubber seed oil blended with the diesel fuel and studied at the normal engine condition and analyzed for the various performance and emission characteristics.

II. Experimental Setup and Procedure

The experimental setup considered in this study was

fueled with two vegetable oils blended with diesel. The direct injection, four stroke, single cylinder, constant speed (1500 rev/min), air cooled engine was used to study the performance and emission characteristic of the dual fuel diesel engine.

TABLE I
PROPERTIES OF FUELS

| Property | Diesel | Rubber seed oil | Jetropha oil | Dual Fuel |
|--|--------|-----------------|--------------|-----------|
| Sp. Gravity | 0.74 | 0.82 | 0.96 | 0.90 |
| Viscosity at 400C (mm ² /s) | 4.15 | 70.2 | 4.4 | 4.2 |
| Calorific Value (kJ/kg) | 42000 | 37000 | 38500 | 39500 |
| Carbon residues% | 0.12 | 0.19 | 0.61 | 0.26 |
| Iodine value | 0.067 | 133.46 | 120.5 | 133.32 |

Without any major modification, a constant pressure at 220 bar and 24⁰ BTDC ignition timing was maintained to run the engine. The engine was tested for the thermal efficiency and brake specific fuel consumptions. An AVL model gas analyzer was used to observe the emissions like smoke, CO, HC, NOx and CO₂.

The test engine was attached with an electric dynamometer to control the test engine with different load conditions and a smoke meter was attached to it.

A diesel engine of the following specifications have been used for the experimental analysis for the given dual fuel biodiesel with pure diesel fuel:

| | |
|---------------------|---------------------------------------|
| No. of stroke | : 4 stroke |
| Bore | : 87.5mm |
| Stroke | : 110.0mm |
| Speed | : 1500 (Constant Speed) |
| Compression ratio | : 17.5:1 |
| Rated power | : 4.4 kW |
| Number of cylinders | : One |
| Type of cooling | : Air cooled-eddy current Dynamometer |
| Injector opening | : 240 BTDC |
| Pressure | : 220 bar |

III. Results and Discussions

III.1. Carbon Monoxide Emission

Fig. 1 shows the variations of Carbon monoxide (CO) emissions at different loads with constant speed of 1500 rev/min under 20% and 40% of biodiesel blended with pure diesel.

Due to incomplete combustion of fuel, carbon monoxide was formed in the engine. From the survey of the past research, increasing of complete combustion of fuel were done by changing of injection pressures in cylinder, injection timings and preheating of fuels etc.

From Fig. 1 it was found that the diesel only mode of running the engine emitted a lowest carbon monoxide, even at full load condition when compared to that of the other two blended proportions. For the two blended fuels, the CO emission was nearly equal, as they are from 0.06 ppm to 0.07 ppm for the variation of different loads from no load (zero loads) to 75% of load.

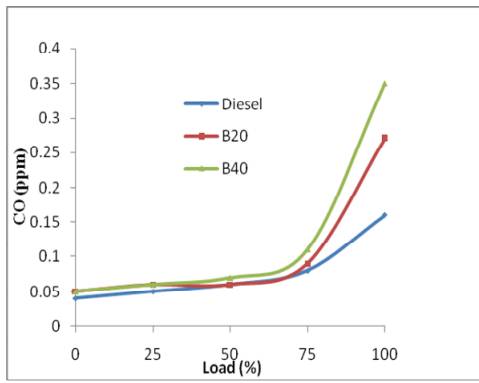


Fig. 1. Variations of Carbon monoxide with changing load Conditions

But for the full load condition, the emission was increased from 0.28ppm to 0.42 ppm for B20 and B40 respectively. Hence from the emission characteristics test, that the biodiesel B20 emits little more than the diesel fuel and also the blend B40 emits more than that of B20 and diesel.

III.2. Hydro Carbon Emission

As shown in Fig. 2, the HC was reduced by increasing the oxygen content which leads to the complete combustion of the fuel. In addition, increasing of the cetane number of different blends minimizes the combustion delay period.

Fig. 2 shows, for the diesel fuel, the Hydro Carbon percentage varied from 10 ppm to 19 ppm which was released in the exhaust without modifying the pressure (220 bar) at various load conditions. It was found that for B20 zero load conditions, the amount of HC released is higher. If the 50% of load is given to the engine, the HC emission was reduced then gradually increased.

For another bio-fuel of B40 it was gradually increased from zero load condition to full load conditions as 15 ppm and 25 ppm respectively.

But as the load on the engine increases, the amount of HC's released increases drastically when the injection pressure is 220 bar. Hence the amount of HC's released for the B20 blend was comparatively less than other bio-fuel, and suitable for the environmental emission limit.

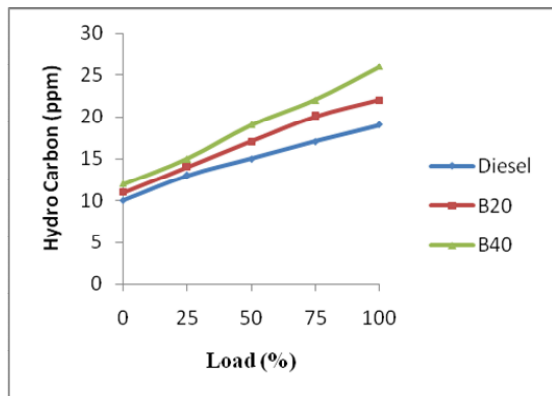


Fig. 2. Variations of Hydro Carbon with changing load conditions

III.3. Carbon Dioxide Emission

From Fig. 3, the CO₂ emissions were approximately the same for all pure diesel and blended dual fuel at constant speed of 1500 rev/min from the no loads to 75% of load conditions. The intake air amount was constant throughout the engine test at full load condition. Due to low oxygen content in the bio-fuel, the fuel to air ratio decreased and hence CO₂ emission increased at full load (100% loads) condition. The CO and CO₂ emissions were higher than that of fossil diesel as higher amounts of the vegetable oils were burned for the tested engine. In addition, it is feasible that the higher oxygen content in the vegetable oils supported to combust the rubber seed oil and jatropa oil and caused higher CO₂ emission than with pure diesel fuel.

It was found that the CO₂ emission when compared to pure diesel fuel and blend fuels there is no change, but for different load from no load to 75% of the load condition for biodiesel it was same as that of the diesel fuel. In full load condition, for B20 blend the emission was reduced. From the graph, for the dual fuel of rubber seed oil and jetropha oil blended with the pure diesel there is no change in the emission.

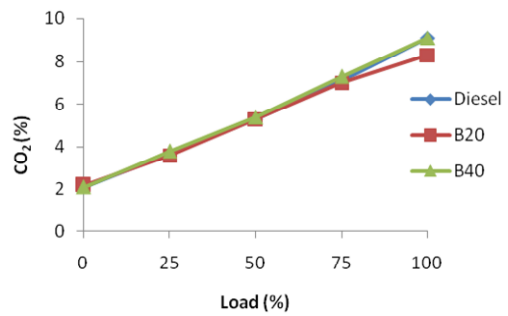


Fig. 3. Variations of Carbon dioxide with changing load conditions

III.4. Nitric Oxide Emission

The NO_x emissions for rubber seed oil and jetropha oil and its blends with 20% and 40% to diesel fuel are shown in Fig. 4.

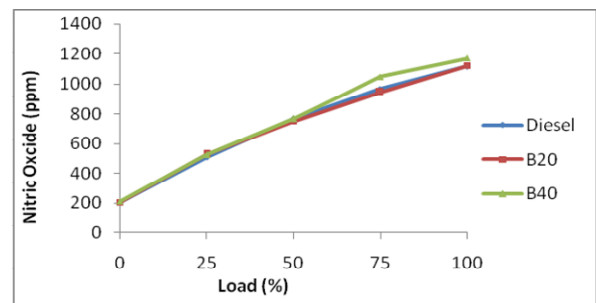


Fig. 4. Variations of Nitric oxide with changing load conditions

The increasing combustion temperature with the different loads in diesel only mode, the amount of NO_x was increased. The most significant factor for the emissions of NO_x is the combustion temperatures in the

CI engines and chemically corrects mixture. For this study, from the no load condition to 50% load, the NO_x emission was same for all fuels such as pure diesel and blended fuels.

The NO_x emissions of biodiesel of B40 varied and increased from the pure diesel fuel as 967 ppm for 75% load to 1086 ppm for 100% load it increased in 1117 ppm to 1210 ppm respectively. The NO_x emissions takes place in diesel engines is mainly a function of flame temperature, which is closely related to the peak cylinder pressure. Hence the temperature of the higher concentration of biodiesel compared to pure diesel fuel with the increased injection pressure, results in the release of a higher amount of fuel at the same injection setting conditions. For that reaction, the engine cannot cool and no heat transfer takes place so that the formation of NO_x was associated in the biodiesel.

It is found that for biodiesel of B20 the NO_x formation was not changed from zero load condition to full load condition as compared to that of the pure diesel fuel.

III.5. Brake Specific Fuel Consumption

The viscosity and density are the two important factors of the biodiesel. The Specific Fuel Consumption (SFC) will be increased and low discharge of fuel pump will occur due to the increase in of density of the fuel.

Using esterification process the viscosity and density of fuel can be lowered and used in the engine to improve the efficiency which in turn reduces the BSFC then controlling the emission.

Fig. 5 shows that the brake specific fuel consumption of pure diesel fuel and its blended fuels with different load conditions. It is found that the SFC of rubber seed oil and jatropha oil blends was little higher than that of the pure diesel fuel. For the pure diesel fuel, the BSFC was decreased from no load condition to full load conditions as 0.16 kg/kW-h. By using the biodiesel of B40 the same is varied from no load to 100% of load condition as 0.24 kg/kW-h which varies as 0.8 kg/kW-h from the pure diesel fuel.

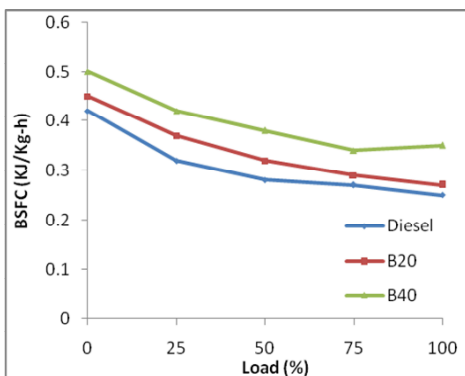


Fig. 5. Variations of Brake Specific Fuel consumption with changing load conditions

In the case of biodiesel of B20 from no load to full load condition where up to 50% load was same as that of

B40 but at 100% of full load condition it is varied as 0.02 kg/kW-h. On comparison of pure diesel fuel, it is increased as 0.06 kg/kW-h.

So it is concluded that, by using dual fuel blend there was not a major difference from the pure diesel fuel in SFC. In the pure diesel mode the heating value was increased, hence the brake thermal efficiency also increased. The dual fuel of rubber seed oil and jatropha oil leads to low heat released rate when compared to that of the diesel fuel.

III.6. Brake Thermal Efficiency

The variation in thermal efficiency for the different load conditions of the engine is presented in Fig. 6.

The maximum brake thermal efficiency of single cylinder constant speed engine at 1500 rev/min was 30.2% at 25% of load condition after that it was decreased up to 27% in full load condition.

From the result BTE of B20 at no load condition was 16% and on further increase in the engine load, BTE also increased up to 50% of load then decreased to 24% of full engine load condition. For the B40 of biodiesel when started from no load condition the BTE was 16% then it increased up to 50% load condition as 26%.

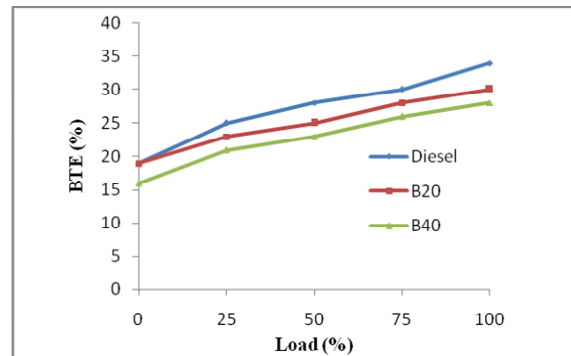


Fig. 6. Variations of Brake thermal efficiency with changing load conditions

Then it gradually reduced to 24% at full load condition. From the experimental study, the blend B20 gives higher thermal efficiency as compared to the biodiesel of B40 blended with the pure diesel fuel.

IV. Conclusion

From the investigational analysis of the single cylinder constant speed engine following results were concluded:

1. The brake thermal efficiency by using dual fuels namely rubber seed oil and jatropha oil, B20 and B40 were compared to that of the pure diesel, B20 gave higher efficiency than B40. The maximum value of efficiency was 30.1% in B20.
2. The Brake Specific Fuel Consumption (BSFC) of test engine for B20 was a little higher than that for the pure diesel fuel as 0.04 kg/kW-h in full load

condition. For B40 it was also increased at the rate of 0.06 kg/kW-h.

3. In CO emission characteristics test for the biodiesel of B20, the CO emission percentage was approximately nearer to that of the diesel fuel. For B40 it was higher when compared to that of the diesel fuel. The variations of different loads from no load (zero loads) to 75% of load, the CO emission was same as from 0.06 ppm to 0.07 ppm. But in the full load condition it was increased from 0.21ppm to 0.42 ppm compared to that of the diesel fuel.
4. The hydrocarbon (HC) emissions characteristics from the bio diesel at B20 was little lower than that of diesel fuel. At full load condition it varied from 0.21ppm to 0.42 ppm but biodiesel B40 at engine no load to full load, the HC emissions are similar to that of the diesel.
5. From the result of CO₂ emission, at zero load to 75% of engine load condition, pure diesel and blended biodiesel was approximately same at the rate of 8% to 9% .In the case of B20 it was little decreased from that of the base fuel. So it is concluded that the dual fuel of rubber seed oil and jetropha oil blended with the pure diesel there are no changes in CO₂ emission.
6. From the no load condition to 50% load condition, the NO_x emission was same for all fuels such as pure diesel and blended fuels. The NO_x emissions of biodiesel of B40 was increased from that of the pure diesel fuel varied as in 967 ppm at 75% load to 1086 ppm and 100% of load correspondingly to 1117 ppm and 1210ppm.

References

- [1] Ramadhas A.S., Jayaraj S., , Characterization and effect of using rubber seed oil as fuel in the compression ignition engines, Fuel, Vol.84, pp. 335–340, 2005.
- [2] Ramadhas A.S., Muraleedharan C., Performance and emission evaluation of a diesel, engine fueled with methyl esters of rubber seed oil, Renewable Energy, Vol.30, pp. 1789–1800, 2005.
- [3] Edwin Geo V., Nagarajan G., Experimental Investigations to study the characteristics of Rubber-Seed-Oil-Fueled Diesel Engine Supplemented with Diethyl Ether, Energy & Fuels ,vol. 23, pp. 533–538. 2009.
- [4] Jincheng Huang ,Yaodong Wang, Comparative study of performance and emissions of a diesel engine using Chinese pistache and jatropha biodiesel, Fuel processing and technology, vol.91, pp. 1761-1767, 2010.
- [5] Senthil Kumar M., Ramesh A., An experimental comparison of methods to use methanol and Jatropha oil in a compression ignition engine, Biomass and Bioenergy, vol. 25, pp. 309 – 318, 2003.
- [6] Pi-qiang Tan ,Zhi-yuan Hu, Exhaust emissions from a light-duty diesel engine with Jatropha biodiesel fuel, Energy, vol.39, pp. 356-362, 2012.
- [7] Shyam Pandey 1, Amit Sharma, Experimental investigation on the performance and emission characteristics of a diesel engine fuelled with ethanol, diesel and jatropha based biodiesel, International Journal of Advances in Engineering & Technology, IJAET, ISSN:2231-1963, 2012.

Authors' information

¹Research Scholar, Department of Mechanical and Production Engineering, Sathyabama University, Chennai, India.
E-mail: mahathermal@gmail.com.

²Dean (R&D), Chennai Institute of Technology, Chennai, India.



Mahalingam S. (Corresponding author) is a research scholar in the Department of Mechanical and Production Engineering at Sathyabama University, Chennai, India. He received his Master degree in Thermal Power Engineering, Annamalai University. His field of interest is Thermal engineering and I.C engines. He published more than 10 research papers in

journals and conference proceedings.

A Review of Localised Time-Frequency Features Classification Associated to Fatigue Data Analysis

M. F. M. Yunoh¹, S. Abdullah¹, Z. M. Nopiah², M. Z. Nuawi¹

Abstract – The paper presents a review of the rational to perform the localised time-frequency fatigue damage feature classifications, which can be categorised as an alternative approach for fatigue life prediction that is relatively new in this research field. It is a good need to have a study in fatigue feature classification that lead to the formation of a new guideline and enable a design to the same reference level as well as high reliability towards the maximum usage. Consequently, this review paper emphasis on the concentration for performing the localised time-frequency feature classification approach as a scientific and engineering knowledge advancement in about fatigue of material and structures. Hence, related approaches to be said as the subject contents, i.e. fatigue life prediction models, signal processing approaches, the implementation of segmentation and clustering methods towards fatigue data, as well as data classification that lead for pattern recognition technique. It is known from the literature about the selection of the appropriate approaches which were often based on the analyst's experience and preferences. By predicting the structure fatigue life, which needs only several variable and will automatically calculate, classify and optimise the severity of fatigue damage through the significant mathematical and experimental findings, leading to cost and time saving. **Copyright** © 2013 Praise Worthy Prize S.r.l. - All rights reserved.

Keywords: Clustering, Fatigue, Features Classification, Review, Signal Processing

Nomenclature

| | | | |
|-----------|---|-----------------|--|
| A | Wavelet scale | S_{min} | Minimum stress amplitude [MPa] |
| A | Material constant for the ESD strain-life model [MPa] | S_u | Ultimate strength of a material [MPa] |
| B | Material constant for the ESD strain-life model | t | Time [s] |
| $C.F.$ | Crest factor | T_p | Period [s] |
| D | Fatigue damage parameter | $W_\psi(a, b')$ | Wavelet coefficients for continuous wavelet transform |
| E | Modulus of elasticity [MPa] | $W_\psi(m, n)$ | Wavelet coefficients for discrete wavelet transform |
| f_0 | Cyclic frequency [Hz] | \bar{x} | Mean value [mm, microstrain, etc.] |
| j | Number of point in time series | $X(\omega)$ | Amplitude of Fourier transform in frequency distribution |
| K | Kurtosis | σ | Stress [MPa] |
| n | Number of data points | σ_a | Stress amplitude [MPa] |
| N | Number of samples in time series | σ'_f | Fatigue strength coefficient |
| N_f | Fatigue life [Number of cycles or blocks to failure] | σ_{max} | Maximum stress [MPa] |
| N_{fi} | Number of constant amplitude cycles to failure | σ_{min} | Minimum stress [MPa] |
| N_i | Number of applied cycles | ASTM | American Society for Testing and Materials |
| N_T | Number of blocks to failure | CA | Constant amplitude |
| $r.m.s.$ | Root-mean-square [microstrain] | CWT | Continuous wavelet transform |
| S | Skewness | DFT | Discrete Fourier transform |
| SD | Standard deviation [microstrain] | DWT | Discrete wavelet transform |
| S_e | Fatigue limit or endurance limit of a material [MPa] | FFT | Fast Fourier transform |
| S_i | Intrinsic stress limit under VA loading [MPa] | HCF | High-cycle-fatigue |
| S_{max} | Maximum stress amplitude [MPa] | IDFT | Inverse Discrete Fourier transform |
| | | IFFT | Inverse Fast Fourier transform |
| | | LCF | Low-cycle-fatigue |
| | | OWT | Orthogonal wavelet transform |

| | |
|------|------------------------------|
| PSD | Power spectral density |
| PV | Peak-valley |
| S-N | Stress-life |
| STFT | Short time Fourier transform |
| VA | Variable amplitude |
| WBE | Wavelet Bump Extraction |

I. Introduction

Various approaches have been used to calculate the life calculations of modern structural design based on a comprehensive theoretical analysis. However, the structural failures gave significant effects to the performance which lead to the loss of human life, loss of properties and pollution of the environment [1], [2].

Components such as machinery, vehicles, and structures are subjected to cyclic loading produce a stress that can lead to microscopic damage to the materials. At the fluctuating service loads below the yield strength of the materials, the microscopic damage expands with the continuous loads and forms the crack that will lead to the components failure. This kind of phenomenon is known as fatigue, and this failure contributes to the major loss in industrial applications [3], [4].

Due to the long period required for fatigue crack growth, from the beginning to the end of failure, there is enough time to detect fatigue damage and perform an appropriate improvement. With the current advances technology, there is a strong interest to apply the digital signal processing in the fatigue life prediction [5].

For many years, the global statistical parameters such as Root Mean Square (r.m.s) and kurtosis, has emerged as a good indicator of fatigue damage [6]. However, the frequency information in the time domain analysis is usually not available.

Analysis that relates to the frequency is very important in determining the identity of the frequency components [7]. Methods like Discrete Fourier Transform (DFT), Fast Fourier Transform (FFT) and Power Spectral Density (PSD) is widely used. Frequency analysis method has a striking weakness because it only produces frequency information and not time information, it causing a bit impossible to know the effect of the event happen. So that, Time-Frequency analysis has been introduced and widely used to solve the engineering problems included fatigue damage because it can produce the information of frequency and time [8].

The methods that widely used are Short-Time Fourier Transform (STFT), Wavelet Transform and S-Transform (S-T). Fatigue data editing technique has been developed for the acceleration during fatigue durability testing in order to increasing the frequency, increasing the amplitude and low amplitude cycles and eliminate the loading time series [9].

Fatigue data editing, which is defined as a method for omitting the small amplitude cycles which provide a minimal contribution to the overall fatigue damage, while retaining the high amplitude cycles which are the most damaging sections.

Practically, any fatigue data editing technique must reduce the testing period and be technically valid.

In fatigue damage analysis, global signal statistics, Wavelet and data correlation required parameters for the data classification. Therefore, the fatigue data analysis techniques based on signal classification have been developed to ensured that the segments of high amplitude can be detected and removed from the original signal, and at the same time maintain the fatigue damage. Clustering is the classification of data into different groups. In other words, the data sets are mapped to a small group, so that the data in each cluster can share some common properties according to the defined measured distance [10], [11]. In general, clustering methods can be categorised into two types, namely, hierarchical algorithms and restrictions.

There were some works of fatigue feature classification to industrial structure such as marine structure and building structure, but none of them can be used, or have been developed for the automotive applications. Most of researchers had found very intensive method to detect and prevent structures failure but there is not much research on finding a scale/indices/index of failure [12]. This situation and observation has led to the indication for the researchers to explore the development of a computational-based algorithm for the fatigue feature classification in the scope of automotive component/material failure. Currently, it can be said that many techniques have been used to assess fatigue failure, but the development of a real-time fatigue feature classification to monitoring fatigue failure still under investigation which needs more research. This issue is very important in order to produce components or a system that has a good durability in term of their design, as well as high reliability towards the maximum usage [13] [14]. Using the propose fatigue feature classification technique, it is easier to predicting structure fatigue life, which needs only several variable and will automatically calculate, classify and optimise the severity of fatigue damage through the significant mathematical and experimental findings, leading to cost and time saving.

II. Fatigue Life Assessment

II.1. Historical Overview

A fundamental step regarding fatigue as a material problem was made in the beginning of the 20th century by Ewing and Humfrey in 1903. They carried out a microscopic investigation which showed that fatigue crack nuclei start as microcracks in slip bands. Much more evidence about fatigue as a material phenomenon was going to follow in the 20th century [15]. Mechanical failure due to fatigue has been studied more than 180 years ago. However, the first fatigue research was performed by the German engineer, named Wilhelm Albert in 1829. He imposed the cyclic loading on the iron chains in order to prove the relationship between the strain loads on the durability of materials. Ten years

later, the term of 'fatigue' was introduced in in a book of mechanics by a French researcher, i.e. J. V. Poncelet.

Due to the technology expansion, fatigue studies continued in the middle of the 1800's by individuals on the basis of failure of components such as railway axles, shafts, gears, beams and girders of the bridge [4].

A piece of metal can fail if the cyclic load is applied at a lower stress than the yield strength of the static load. Between 1852 and 1870, a German engineer, August Wöhler carries out experiments of fatigue on the axle of the train, as reported by [16]. Two railways were suspended from the ends of the axles and the axles rotated till failure. He was then plotted the nominal stress versus the numbers of rotation to failure on what has become known as the stress-life (S-N) diagram. According to Wöhler, a fatigue failure depends on the stress range given and not the value of maximum stress [4]. This research is considered as the first fatigue research until he was known as the "father" in fatigue research.

Other researchers strengthen the effort and statement by Wöhler. For example, in 1874, H. Gerber studies the influence of the mean stress, and in 1899 J. Goodman suggested that the easier theory of mean stress concentration [4], [17]. In beginning of the 1900's, microscopic has been used in mechanism of fatigue studies [18], [19], until the micro-cracks formation factor can be carried out. In 1921, A.A. Griffith published the calculation results the brittle fracture of glass. H. J. Gough and H.V. Pollard was in 1935 has studied the effects of bending and torsion on fatigue mechanisms [20]. Then in 1930, C.R. Soderberg develops a simple stress limit diagram [21].

Strain life (e-N) approach assumes that the plastic deformation occurred in the localised area of fatigue cracks began under the influence of the mean stress. This approach is often used for ductile materials at relatively short fatigue life.

This approach is also used where there is little plasticity at long fatigue life. Therefore, this is a comprehensive approach that can be used in place of the stress-based approach. Therefore, it is normal that the service loadings can cause by machinery and vehicles are determined using a strain-life fatigue damage approach [4], [23], [24].

II.2. Stress-Based Life Assessment

Stress-life (S-N) approach, methods for characterising fatigue life are based on work performed by Wöhler (1860). In order to determine the fatigue life parameters of the stress-life approach, smooth specimens with cylindrical gauge length were normally tested under CA loading conditions with in-plane bending, rotational bending, uniaxial compression-tension or tension-tension cyclic loading.

The S-N analysis is seems to be valid when the load is applied between the transition and the endurance limit, i.e. at approximately 10^6 and 10^7 cycles.

Above the endurance limit, the slope of the curve reduces dramatically and as such this is often referred to as the 'infinite life' region. Several effects are notable about the approach. At below the transition point (approximately 1000 cycles), the S-N curve is not valid because of the nominal stresses are in the elastic-plastic condition. This plateau stress amplitude is known as the fatigue limit or endurance limit (S_e).n. The fatigue limit for a smooth specimen of a material is defined as [25]:

$$S_e = 0.5S_u \quad (1)$$

where S_u is the ultimate strength.

In general, the fatigue limit for a notched specimen is lower than the fatigue limit of a smooth specimen. For notched specimens, the fatigue life can be expressed in terms of the fatigue notch factor K_f by the expression:

$$S_{e(notched)} = \frac{S_{e(Smooth)}}{K_f} \quad (2)$$

where the fatigue notch factor K_f is determined from the stress concentration factor K_t and the notch sensitivity q :

$$K_f = 1 + q(K_t - 1) \quad (3)$$

In the case of a notch that is relatively deep and sharp, it can be assumed that the notch is already cracked and the fatigue life can be predicted using the fracture mechanics approach [18], [26]. Most of designs try to avoid using the sharp edges because this area contributes the stress concentration that will lead to the failure.

The development in S-N analysis, Low Cycle Fatigue terms established (LCF, $N = 104 \dots 105$ cycles) and High Cycle Fatigue Largest (FSTB, $105 < N < 107$ cycles) the term Very High Cycle Fatigue (VHCF, $N > 107$ cycles) was introduced. In VHCF, the region failure occurs depending on materials, design, manufacturing and special failure mechanisms can emerge. Although the research interest in VHCF region was increased in the last years there are a few experiments data to separate the different influences on fatigue behaviour. Data scatter is large because microstructure effects and statistical evaluation fatigue strength is still a research topic [27], [28].

Fatigue testing for mechanical structure is widely implemented in all industries as one part of the design process. In real applications, fatigue loading services such as stresses on the car wheels, bending moment on stub axle car, insists on the back passenger car axle and the other is variable amplitude history [29].

The History often contains large percentage of small amplitude cycles and fatigue damage of the cycle can be small.

Therefore, in many cases of fatigue loading history was edited using signal processing, segmentation and classification order to produce a representative and meaningful economic test [30], [31].

II.3. Strain-Based Life Assessment

The strain-life approach can be used proactively for a component during early design stages. The local strain-life approach is preferred if the loading history is irregular and where the mean stress and the load sequence effects are thought to be of importance.

The strain-life approach involves the techniques for converting the loading history, geometry and materials properties (monotonic and cyclic) input into a fatigue life prediction [32]. Strain-life ($\epsilon-N$) approach is considered as a more accurate approach for fatigue failure analysis because it is associated to the occurrence of plastic deformation that exist in the localised area, and also under the condition of fatigue loading with the mean stress effects [21].

This approach is often applied for the analysis of ductile materials with a low fatigue life, also for materials with some plasticity at high fatigue life.

Therefore, this approach is a general method that can be used to replace the stress-life approach. In practices, this $\epsilon-N$ approach is generally been applied to evaluate the imposed load that caused by machinery and vehicles [23], [24], [33].

Similar to the stress-based approach, the development of strain-life curve requires the information that obtained from the displacement controlled fatigue experiments with constant amplitude loading [34]. For this reason, the uniaxial cyclic load has been applied to the smooth surface testing specimen at the amplitude ratio of -1.

The procedure to plot strain-curve life can be referred in ASTM E739-91 (1998)³⁵ and in Williams et al., (2003)³⁶. An example of the general plot of a strain-life curve is shown in Fig. 1.

For high fatigue life region, the elastic strain is dominant and the plastic strain is relatively small, and is called high-cycle fatigue. When there is the case of the plastic strain is greater than the elastic strain, it is then called a low-cycle fatigue.

In the centre life, there is a point located at similar position of the elastic and plastic strain, and it is defined as the transition life [37].

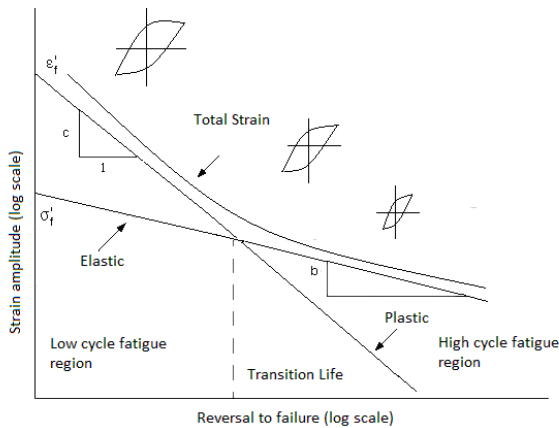


Fig. 1. A typical strain-life curve for most of metallic materials [37]

In order to determine the life produced from the analytical works, the Coffin-Manson relationship was introduced by L.F. Coffin in 1954 and Manson in 1965, which is the basis for strain-life approach [21]. This model assumes the fatigue damage at zero mean stress but in the real situation the fatigue data have a mean stress effect [38]. The foundation of the strain-life approach is the Coffin-Manson relationship and it is defined as the following equation:

$$\epsilon_a = \frac{\sigma'_f}{E} (2N_f)^b + \epsilon'_f (2N_f)^c \quad (4)$$

where $a\sigma$ is the stress amplitude, N_f is the number of cycles to failure, σ'_f is the fatigue strength coefficient, b is the fatigue strength exponent, ϵ'_f is the fatigue ductility coefficient, c is the fatigue ductility component and E is the modulus of elasticity. The mean stress effect contributes to the major damage failure and it is an important aspect in the fatigue studies. , and it has been reported by A. Bannantine [39]. The components that imposed with high stress ratio reach the critical point first than low stress ratio and lead to initial crack. Various effects of mean stress have been explained for various types of materials and experimental techniques that produce a variety of mean stress theory. Two strain-life models for application that involve the mean stress effect is the Morrow model [40] and the Smith-Watson-Topper (SWT) model that was develop by N. Smith and colleagues [41]. The Morrow model was developed based on the modification to the baseline strain-life curve which accounted for the effect of the mean stress by modifying the elastic part of the strain-life curve. The Morrow's strain-life model is mathematically defined by:

$$\epsilon_a = \frac{\sigma'_f}{E} \left(1 - \frac{\sigma_m}{\sigma'_f} \right) (2N_f)^b + \epsilon'_f (2N_f)^c \quad (5)$$

For loading sequences that are predominantly tensile, the SWT approach is more conservative and therefore recommended. In a case of the loading being predominantly compressive, particularly for wholly compressive cycles, the Morrow model provides more realistic life estimates [4], [37]. The SWT strain-life model is mathematically expressed by:

$$\epsilon_a \sigma_{mak} = \frac{\sigma'_f{}^2}{E} (2N_f)^{2b} + \sigma'_f \epsilon'_f (2N_f)^{b+c} \quad (6)$$

For continuous tension loading which are more suitable rules for use are SWT. For cases where the overall load of the compression cycle, Morrow is a more realistic model to apply. Morrow approach gives better results for the steel material, while the SWT approach is likely to provide a wider selection of materials and a good choice for general use [4]. Morrow equation was used to apply for carbon steel hardened by Wehner&Fatemi [42].

III. Fatigue Life Assessment

III.1. Type of Signals

A time series typically consists of a set of observations of a variable being taken at equally spaced intervals of time. Signal is derived from a variety of information sources obtained from the measurement results and use some method of recording as a function of time. Many signals in nature exhibit random or nondeterministic characteristics which provide a challenge to analyse using feature extraction techniques [43]. A signal representing a random phenomenon can be characterised as either stationary or nonstationary. A stationary signal is characterised by values of the global signal statistical parameters, such as the mean, variance and root-mean-square (r.m.s), which are unchanged across the signal length. In the case of nonstationary signals the global signal statistical values are dependent on the time of measurement. Nonstationary signals can be divided into two categories, i.e. mildly nonstationary and heavily nonstationary.

A mildly nonstationary signal is defined as a random process with a stable mean, variance and root-mean-square values for most of the record, but with short periods of changed signal statistics due to the presence of transient behaviour. A heavily nonstationary signal is defined as being similar to a mildly nonstationary signal, but with the presence of transient events over a large interval of the time history. In the case of fatigue signal, the signal consists of a measurement of the cyclic loads, i.e. force, strain and stress against time. This measured signal commonly consists of variation of amplitude, frequency, phase and energy. Fatigue signal was commonly found as a nonstationary behaviour [44] and many vibration responses can be adequately classified as stationary periodic time histories [45].

For the fatigue damage monitoring studies, small microstructural changes occurring inside the material during the initial stages of fatigue damage cause attenuation and distortion of transmitted waves at the receiver end. The anomaly detection algorithm is based on time series analysis of ultrasonic, strain or vibration data and is built upon the principles of symbolic dynamics, information theory and statistical signal processing [46], [47]. The random distribution of defects in identically manufactured structural components leads to different behavioural patterns of time series signal for fatigue damage [46], [48], [49]. Consequently, the analysis of time series data from available dedicated sensors is essential for monitoring the developing fatigue damage in real time.

III.2. Global Statistical Analysis for Strain Data

Global signal statistical parameters are frequently used to classify random signals and monitor the pattern of analysed signals. For a fatigue signal, the calculation of the r.m.s. and the kurtosis values are important in order to retain a certain amount of the signal amplitude range

characteristics [50]. The r.m.s. value is the signal 2nd statistical moment used to quantify the overall energy content of the oscillatory signal and 3rd statistical moment, skewness is used for measuring asymmetry of the signal [51]. In engineering field, the kurtosis (also known as the 4th statistical moment) is used as a measure of nongaussianity for detection of fault symptoms since it is highly sensitive to spikiness or outlier signal among the instantaneous values [52], [53].

In some definitions of the kurtosis, a deduction of 3.0 is added to the definition in order to maintain the kurtosis of a Gaussian distribution to be equal to zero. For clarity and convenience, in this study the original definition of the kurtosis, where the Gaussian distribution has a kurtosis value is approximately 3.0, was used for the analysis. Therefore, a kurtosis value of higher than 3.0 indicates the presence of more extreme values than the one that should be found in a Gaussian distribution [53]; [54]. It indicates the fatigue damage is higher than Gaussian stresses due to higher amplitude fatigue cycles [55], [56], [57].

By analysing the data using statistical parameter on the time series data, we may identify trends and patterns of data scattering based on critical statistical parameters.

From the scattering of data we may acknowledge which parts of the data made significant contribution and which did not [58], [53]. Finally based on our findings we may eliminate or exclude certain parts of the data in order to make further study and analysis of the signal much faster and more efficient without significant loss of data. Statistical analysis and fatigue damage calculation was made on each segment of the time series and patterns of data scattering were identified based on the plots of relationship between segmental damage and its corresponding kurtosis and/or r.m.s. The scatter of the kurtosis produced better and more evident data scattering than that of r.m.s. The information gained from the data scattering could then be made useful for fatigue data scattering and editing [53].

Integrated Kurtosis-based Algorithm for Z-notch Filter (I-kaz) is a method that was developed by Nuawi, 2008 [59] based on the two relevant statistical parameters which is kurtosis and standard deviation. This method was divided to two parts which is I-kaz coefficient calculation and three dimension (3D) graphic displays, for which the I-kaz analysis is used to find the key variables that control the system. In addition, the I-kaz graphic represent reduce of dimension of relationship and observation of sample. The main contribution of the statistical analysis is to find the effect and make a conclusion for fluctuating effect of non-constant variables to constant variables.

Abdullah et al., in 2010 [60] then explores the correlation between the strain signal resulted from displacement and vibration response when subjected to the variable amplitude loading. This comparative study was implemented using fatigue damage assessment, (ϵ -N) and Hybrid Integrated Kurtosis-based Algorithm for Z-notch filter Technique (Hybrid I-kaz).

The total fatigue damage and Hybrid I-kaz coefficients for each signal of the different frequency were compared in order to correlate the relationship and it was found that the strain signal was linear proportionally related to the vibration responses [60], [61].

III.3. Signal Analysis in the Frequency Domain

Signal processing is a non-destructive process that converts the input signal to the information that would give the signal source and predict the pattern. This processing is to determine the information contained in the signal that cannot be analysis through the direct observation.

One of the signals processing technique is the analysis of time series data in the frequency domain. The frequency analysis is performed for converting a time domain signal into the frequency domain. The algorithm used to split the time history into its constituent sinusoidal components is the Fourier transform.

A commonly used form of Fourier transformation is the discrete Fourier transform (DFT). This algorithm transforms a time-domain sample sequence into a frequency-domain sequence which describes the spectral content of the signal [62]. The DFT is defined as:

$$X_k = \frac{1}{N} \sum_{t=0}^{N-1} x_j e^{-i(2\pi kt/N)} \quad (7)$$

$$j, k = 0, 1, 2, 3, \dots, (N-1)$$

The frequency information obtained from the DFT can be reverted back into the time domain using the inverse discrete Fourier transform (IDFT) which is defined as:

$$x(n) = \sum_{k=0}^{N-1} X(k) e^{jk\omega n} \quad 0 \leq n \leq N-1 \quad (8)$$

The most commonly used forms of Fourier transform, however, is the fast Fourier transform (FFT) algorithm which was introduced in order to have a faster DFT calculation of the time series [63]. Various FFT algorithms were developed. The algorithm introduced by Cooley and Turkey is the most commonly used because of its simplicity and fast computing time [63]. This algorithm produced the N frequency spectra corresponding to the N data points of a time domain signal which is calculated using the log format or \log_2^N . To permit the fatigue analysis class of data, a series of computational algorithms based on Fourier analysis techniques has been developed.

The principle underlying these algorithms is the use of an FFT to transform the frequency spectrum to an equivalent time series suitable for cycle counting [64].

The technique of short time FFT could be used to detect the phenomena of fatigue crack propagation, such as crack initiation, propagation, arrest and re-propagation under the cyclic loading.

Also the technique of long time FFT could be used to detect the phenomena of dislocation such as pileup and removing before crack nucleation. This technique can be applied for strain, acoustic emission and vibration data [65]; [66]. A power spectrum density (PSD) is a normalised density plot describing the mean square amplitude of each sinusoidal wave with respect to its frequency.

The PSD presents the vibrational energy distribution of the signal across the frequency domain. Each frequency step value of the PSD is characterised by amplitude, A_k , defined as:

$$A_k = \sqrt{2\Delta f \cdot S(f_k)} \quad (9)$$

where $S(f_k)$ is the underlying PSD of the signal and f_k is the harmonic frequency.

A vibration analysis is usually carried out to ensure that potentially catastrophic structural natural frequencies or resonant modes are not excited by the frequencies present in the applied load. It is often easier to obtain a power spectral density (PSD) of stress rather than a time history. The designer can carry out a frequency response analysis on the finite element (FE) model to determine the transfer function between load and stress in the structure. Using this, simply multiplied the PSD of load by the transfer function to arrive at the PSD of stress [67].

PSD approach was then used for the energy based observation and a signal was converted from the time domain to the frequency domain using the fast FFT method. The comparison between experimental findings with related parameters such as of different materials, strain signals pattern, FFT, PSD and statistical approach, were always correlated and discussed in fatigue data analysis [66], [67].

Since the corresponding combined spectra can be estimated at low computational costs, damage could be estimated by using the narrow-band approximation on them, but in practice that method is over conservative by a large amount [68].

Frequency band the history cover on PSD graph in the sense that as the irregularity factor approaches to one, the process gets closer to narrow band process, and as the irregularity factor approaches to zero, the process gets closer to broadband process. In other words, a value of one corresponds to a narrow band signal which means that the signal contains only one predominant frequency while a value of zero implies that the signal contains an equal amount of energy at all frequencies [69].

A better approach is to approximate PDF directly from the PSD without using the narrow band approach as a starting point because PDF of rainflow stress ranges is the issue controlling fatigue life [70]. Dirlik's method has been found to be very accurate for damage estimation in the frequency domain. Previous studies have demonstrated the usefulness of Dirlik's method for ocean engineering and wind turbines but few have shown how well Dirlik performs in automotive applications.

This study compares Dirlik's method with the rainflow cycle counting and with other frequency domain methods [71].

III.4. Signal Analysis in the Time-Frequency Domain

III.4.1. Short Time-Frequency Transform (STFT)

The simple time-frequency analysis is Short-time Fourier transform (STFT) method, a technique which adapted the Fourier transform for analysing a small section of the signal at one specific time [8];[72]. STFT is performed by dividing the signal into small sequential or overlapping data frames. Then, fast Fourier transform (FFT) has been applied to each data frame [73]. During the calculation process, the signal is truncated into short data frames by multiplying it by a window so that the modified signal is zero outside the data frame. In order to analyse the whole signal, the window is then translated into a time and reapplied to the signal.

The STFT is composed by the local spectra of segments of the primary function, as viewed through a translating window of fixed shape. The local spectra at all points on the primary time axis constitute the STFT. The general expression is:

$$STFT(t, f) = \int_{-\infty}^{\infty} h(t)w(t-\tau)exp(-2\pi if\tau)d\tau \quad (10)$$

where h is the primary function, τ is the time and f is the frequency. The position of the translating window w is determined by t , which has the same units as τ . If w is replaced with the value of 1 in Eq. (7), the STFT reduces to H , i.e. the Fourier transform of h . The modulus of the STFT is also known as the spectrogram.

In fatigue data analysis, the capability of STFT localisation method can be used as the features extraction for determination of fatigue damage events for automotives, biomedical, renewable energy and oil and gas field [74]; [75]; [76]. STFT localisation plot can presented some of higher mapping found across the signal length the it can showed the occurrence of fatigue damage events at those areas because of the type of roads in automotive research [75]. STFT also was used to determine the deformation of wind turbine. In this study, the rotor speed, generator torque and gear torque are investigated as a result of possible blade fault at wind turbine by creating a wind turbine model. Based STFT analysis, a result of frequency components of healthy and faulty blade structures are identified successfully [77].

III.4.2. Wavelet Transforms

STFT technique has limited precision localisation due to fix window size and was not the proper method to analyse transient based data. Another alternative is multi-resolution analysis, which is the common time-frequency analysis, known as wavelet. A wavelet is a small wave with a signal energy concentrated in time [78], on the

condition of admissibility condition. The wavelet transform (WT) is defined in the time-scale domain and is a significant tool for analysing time-localised features of a signal. It represents a windowing technique with variable-sized region. The harmonic form of the wavelet transform can be derived from the Fourier transform in the phase form, i.e.:

$$W_{(\psi)}(a, b') = \int_{-\infty}^{+\infty} x(t)\psi\left(\frac{t-b'}{a}\right)dt \quad (11)$$

This approach is said to be a recent solution to overcome some uncertainties in analysing nonstationary signals [50]. The WT is being applied in general time series analysis by cutting a time domain signal into various frequency components via the compromise between the simultaneous time and frequency signal view in a more useful form [77]; [78].

The WT analysis is started with a basic function scaled, known as a mother wavelet, and is then translated to represent the analysed signal [79]. The transform shifts a window along the signal and calculates the spectrum for every position. The process is repeated many times with a slightly shorter (or longer) window for every new cycle, representing a signal with different resolutions.

Wavelet transforms change the window along the signal and calculate the spectrum for each position. This process is repeated several times with a little shorter or longer window for each new round. Size window used is determined the resolution obtained [80].

Different windows sizes are used as the signal at low frequencies can be analysed using a wider window size, initiating a slower oscillations at high frequencies that required wide small window [81]. For width window, it provides a good frequency resolution but it can affect the resolution time, while contradictory applies to the smaller window size. The advantage of wavelet transform is the ability to analyse local wave area or also known as the local analysis [8].

The main advantages of wavelets is that they have a varying window size, being wide for slow frequencies and narrow for the fast ones, thus leading to an optimal time-frequency resolution in all the frequency ranges [82]. It has been frequently used in the field of vibration diagnostic and fault detection. Oh, [83] has investigate the used of Wavelet transform to editing a fatigue history. From the finding, the wavelet transform technique can be applied in fatigue data editing, especially denoising spike removal and compression of data set. The use of wavelet transform has proven to be better tool for crack detection the appearance of subcritical peaks is an indication of crack in the system [84].

A wavelet transform can be classified as either a continuous wavelet transform (CWT) or a discrete wavelet transform (DWT) depending on the discretisation of the scale parameter of the analysing wavelet. CWT conducted at all reasonable scale, resulting in more data and used to determine the value of

a continuous decomposition in order to build the signal accurately. It is easy to interpret all the information and adequate to reconstruct the signal accurately [8]. It has suitable properties for signals analysis and provides freedom in the selection of wavelet functions. One of the families in the CWT category is the Morlet wavelet. CWT described by [85]:

$$CWT_{(a,b)} = \int_{-\infty}^{+\infty} f(t)\psi_{a,b}(t)dt \quad (12)$$

An example of the use of the CWT for the purpose of fatigue damage detection in the study of a gearbox system was performed by [86]. In this study, the CWT wavelet function was used to analyse the cracking of a gear tooth that was caused by fatigue failure. Using the technique, the transient events that caused the damage of the geared system were detected and extracted from the acceleration input signal. Most of the early studies used either 1D or 2D CWT for predict crack and the crack indicators are both time as well as frequency dependent [84]; [87]. The use of 2D CWT transform (which is time vs. amplitude) may detect the frequency component but it cannot indicate the frequency component quantitatively. Nagaraju, in 2009 [88] overcome the above problem a new wavelet plot called 3DCWT has been applied which clearly shows the time-frequency-amplitude. Using the above 3D plots the crack features can be quantitatively as well as qualitatively detected.

Not all DWT decomposition value is needed to rebuild the original signal accurately and more efficient and accurate analysis [8]. DWT is derived from discrete CWT, and it is shown as the following expression [85]:

$$DWT_{(j,k)} = \frac{1}{\sqrt{2^j}} \int_{-\infty}^{+\infty} f(t)\psi\left(\frac{t-2^j k}{2^j}\right)dt \quad (13)$$

where a and j are the scale factor, both b and k are the position and Ψ is the mother wavelet.

The DWT based on such wavelet functions is called the orthogonal wavelet transform (OWT). Orthogonal wavelet transforms are normally applied for the compression and feature selection of signals. Wavelet types used in OWT analysis include the Haar wavelet which is the simplest type of wavelet [89], and the Daubechies wavelet [90] which is a more complex wavelet [89]; [91]. The 30 Daubechies wavelet, which was developed by Ingrid Daubechies [90], has orthogonal basis functions based on iteration procedure. Daubechies wavelets are commonly used for damage detection [92]-[94] and fatigue damage analysis [83]; [95].

The discrete wavelet transform is one of the most popular tools used for power signal time series disturbance classification today due to its multi-resolution capabilities and fast calculation of its coefficients. The feature vectors used for classifying the power signal time series events usually involve performing some kind of transformation on the DWT

coefficients, comparing between the DWT coefficients of the disturbance signal with the DWT coefficients of a pure signal, compressed DWT coefficients, and the direct use of the DWT coefficients [96].

Among the many applications of the wavelet transform, Wavelet Bump Extraction (WBE) is an algorithm that was developed by Abdullah [50] in order to identify fatigue features or bumps, so as to extract them from the original time history. Using the WBE procedure the total damage produced by the combination of the extracted fatigue features was close to that of the original data set. From the finding it is suggested that are a potential and better approach of using the orthogonal wavelet transform (the 12th order of the Daubechies wavelet) to identify and extract fatigue features in variable amplitude fatigue loadings.

III.4.3. S-Transform

S-transform is an effective method to analyze non-stationary signals, and has been applied widely in many diverse fields, such as biomedical instrumentation, geophysics, electrical engineering [97]-[99].

The S-Transform (S-T) can be used to replace the Fourier spectrum with maintaining the value of the absolute phase of each frequency component. This function is a product of the Fourier transform with window function, which is depends on the frequency [100]. As a wavelet transform, the S-T applies various sizes of window in the signals analysis. In addition, the window size should be determined in order to control the time-frequency domain resolution.

The S-T utilised the windowed Fourier analysis similar to the STFT but performs multi-resolution analysis on the signal because the present of varieties window size. It is a time localised Fourier spectrum method that maintains the absolute phase of each localized frequency component. The expression of the S-T is [100]:

$$S(\tau, f) = \int_{-\infty}^{\infty} u(t)w(\tau-t, f)e^{-i2\pi ft} dt \quad (14)$$

with S denote the S-T u, f is the frequency and τ and t are time variables. τ is the centre time of the window, w . In this case the Gaussian window was used since one simultaneously achieves an optimal time and frequency resolution [101]. The mathematical equation for Gaussian window is:

$$w(\tau-t, f) = \frac{|f|}{k\sqrt{2\pi}} e^{-\frac{f^2(\tau-t)^2}{2k}}, k > 0 \quad (15)$$

where k is the scaling factor which controls the number of oscillations in the window. The k parameter permits to control the time-frequency resolution. That is, the frequency resolution increases with k on costs of the time resolution whenever the increased windows sample more

of the investigated signal. A high precision in both, time and frequency, cannot be obtained due to the uncertainty principle. An increased frequency resolution can be useful for the separation of time interfering signals [100].

S-transform based methods are showing promising results in the area of multiple pattern recognition and data mining of time series data from an electricity supply network. Further the approach of utilizing wavelets and soft computing methods [102] for pattern recognition of non-stationary time series data is a general one and can be applied to medical, financial, engineering and other types of temporal data [103].

In fatigue data editing, the S-T spectrum were utilised to identify damaging segment in the fatigue signal due to the high S-T spectrum magnitude. The magnitudes of S-T spectrum in time-frequency domain were transposed into time representation in order to trace the time location of damaging segment. The magnitudes of time domain S-T spectrum were obtained from the accumulation of S-T magnitude distribution along the frequency band for at each time interval.

Thus the S-T spectrum in time representation was gained and this signal was used to detect the presence of damaging event in the fatigue signal. S-T based fatigue data editing can successfully remove the low amplitude cycles with respect to the S-T spectrum distribution. The S-T spectrum shows relatively adequate with damage event in the fatigue signal and is a very useful tool for damage detection in the fatigue signal [74].

IV. Fatigue Life Assessment

Fatigue data editing is a technique to remove small amplitude cycles that lead to minimal fatigue damage was introduced by Frost et al. in 1974 (Nizwan, 2007)[9].

In this approach, large amplitude events needs to extract for further investigation which produced the majority of damage are retained, so as to produce a shortened loading for accelerated fatigue tests [23]; [104]; [83]; [50]. Using this technique, there is a process to remove low amplitude segments, which are theoretically contributes to minimal or no fatigue damage to the components.

Using the time domain editing approach, the damage signal is divided into a number of time segments. Fatigue damage is then calculated for each time-window containing a short segment of time history. Windows having minimal damage are removed, so as to retain the windows containing the majority of the fatigue damage.

These windows are assembled together in order to produce a shortened signal for the purpose of the durability analysis [37]; [105]. In the frequency domain, fatigue loading time histories are often low-pass filtered in order to reduce small amplitudes located in the high frequency region of PSD distribution [104].

The idea behind the method is that small amplitude events do not cause much fatigue damage. Unfortunately, the low pass filter does not reduce the length of the signal, but almost certainly reduces the fatigue damage.

Therefore, the frequency domain editing technique is not recommended, as the time series regenerated from a frequency spectrum does not produce the same fatigue life [50]. For editing in the time-frequency, there not many researcher studies of STFT, wavelet and S-Transform based fatigue data editing. There is a study conducted by Oh, [83] using a VA loading measured on light railway train component. Abdullah et al. and Nizwan [50]; [75] using a VA loading measured on automobile component. The wavelet and STFT based fatigue data editing using the vibration, strain signal and comfort mission synthesis algorithm was performed.

In an automotive-related strain data, a difference of 10% was used as the cut-off criteria in selecting the fatigue damaging events, which lead to a production of a new shortened signal. For this case, a 10% difference is a measure of a change in fatigue damage and the global signal statistics (i.e. r.m.s. and kurtosis) between the original signal and the newly shortened signal [50].

The purposes of laboratory experiments which involve the acceleration of fatigue durability test show that time to test durability component is shorter than the original data, but have the same potential of fatigue damage. Due to conventional fatigue damage experiment takes a long time to run on, the feature extraction method is very useful in reducing the time fatigue test. Because using a shorter signal, the experimental time required is shorter.

As an example for a case study presented by Nizwan et al., in 2007 [9], using STFT method, if a signal with 60 seconds long and repeat 60,000 block requires until the specimens fail, the time required is 1,000 hours. But if the signal can be reduced up to 50% of the original length without affecting the contents of fatigue damage, the time required to obtain the results can be reduced up to 50% or about 21 days. Indirectly, the use of extraction methods can also reduce the fatigue characteristics of the operating costs of equipment.

In research by Abdullah et al., in 2010 [106], they performed fatigue data editing technique in time-frequency domain by using the STFT and Morlet wavelet methods for VA loading collected from automobile component. Overall, based on the simulation analysis, the findings suggested that the Morlet wavelet was more suitable for the fatigue data editing. The Morlet wavelet-based edited signal contained at least 94 % of the original fatigue damage in the 59 second edited signal, i.e. only 37 % of the original signal time length. Whereas the STFT-based edited signal contained 94 % of the original fatigue damage in the 124 second edited signal, i.e. 78 % of the original signal time length.

Bahera, 2011 [96] compared the DWT and the S-transform for feature extraction for power quality monitoring. Then the extracted features are classified with neural classifiers such as multilayered perceptron network (MLP) for pattern classification, data mining and subsequent knowledge discovery. From the finding, the window of the ST varying inversely with the frequency provides good frequency localization, better time and frequency resolution at low frequencies and

higher time resolution at high frequencies. These characteristics of the ST along with its linearity make it a good choice for time frequency analysis.

V. Multi-Variate Analysis for Time Series Data

Multivariate time series (MTS) data are widely available in different fields including medicine, finance, science and engineering. Modelling MTS data effectively is important for many decision-making activities [107].

Multivariate time series analysis is used when one wants to model and explain the interactions and movements among a group of time series variables.

There are concerned with the recognition of recurring patterns within multivariate time series, which capture the evolution of multiple parameters over a certain period of time. The separates time series into segments that can be considered as situations, and then clusters the recognized segments into groups of similar context.

The time series segmentation is established in a bottom-up manner according the correlation of the individual signals. Recognized segments are grouped in terms of statistical features using agglomerative hierarchical clustering [108]; [109].

V.1. Data Segmentation

Segmentation is the most frequently used subroutine in both clustering and classification of time series. In the literature, the segmentation methods can be categorized into two classes: online and offline. The offline methods segment the whole data sequence, and the online methods produce segments based on the data seen so far [110]. The representation error of offline methods is usually lower than that of the online methods since offline methods take a global view of the time series. In time series, segmentation approach allows the time series data divided and organised into a several sections that have the same criteria for each of them [111].

In recent years, many methods have been created to segment the data as accurate as possible. It is important for researchers to find a method to divide the data into the specific parts and analyse each part to the optimum [112]. The outcome of segmentation can be further used to support indexing, clustering, and classification tasks in time series mining [113].

Segmentation method has own name and applications, but most of algorithms for segmentation in time series can be divided into three main types sliding window, top-down and bottom-up [114]. Sliding Window Method is divided into two which is Feasible Space Window (FSW) and Stepwise Feasible Space Window (SFSW). FSW reduces the number of segments to find the farthest end point in the time series. SFSW is a combination between FSW and phased strategy. This method refines the segment points with consider the impact of new points of entry so that the representation error can be reduced [113].

Top-down is a recursively division of time series data, which is almost the same for each reduction until some of limiting criteria that set from the beginning of the analysis are met [115]. It works by considering each of the time series and allocate it to the best cuts.

Bottom-up the best method in the process of signal segmentation. From the total length of the time series of n , it forms a best approximation of the time series until the segment cuts $n / 2$. Starting from the best approximation, the segments enlarged until one reached the limiting criteria [114].

Each segmentation algorithm divided the data signal to the homogeneous length which is suitable to the characteristics in signal analysis. Homogeneous section may be expressed in the form of average or based on specific characteristics. Line approximation is obtained in at least two methods that linear interpolation and linear regression as shown in Fig. 2. Due to the PLR approximation to the data series using the straight-line, the linear regression is usually used.

For linear interpolation, the approximation line for sub-segment of time series is a straight line which is connecting the first data point in the sub-segment with the last point in the same segment. Linear regression considers the straight line best fitting least squares [114].

For linear interpolation, the approximating line for a subsection of the time series is the straight line connecting the first datapoint in the subsection to the last datapoint in the same subsection:

$$y = y_a + (x + x_a) \frac{y_b - y_a}{x_b - x_a} \quad (16)$$

Eq. (16) defines the approximating line in a Cartesian plane that connects the first datapoint in the segment (x_a, y_a) to the last datapoint in the same segment (x_b, y_b).

This method is simple, fast and requires relatively less calculations. However, it produces a comparatively poor least squares approximation.

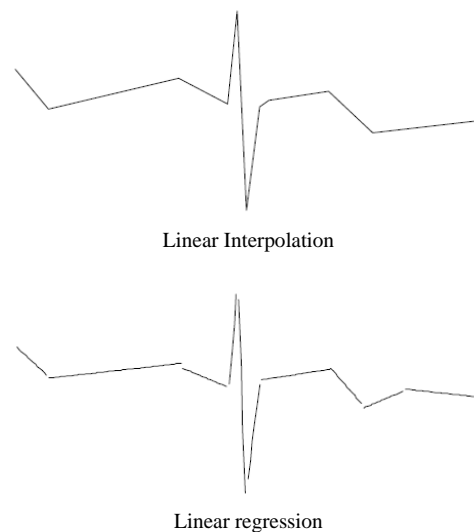


Fig. 2. Approximation time series [114]

The approximating line for a subsection of the time series is the best fitting straight line in the least squares sense. The fitted simple linear regression model is defined as:

$$\hat{y} = \hat{\beta}_0 + \hat{\beta}_1 x \tag{17}$$

where the least-squares estimators and computed as:

$$\hat{\beta}_0 = \bar{y} - \hat{\beta}_1 \bar{x} \tag{18}$$

$$\hat{\beta}_1 = \frac{\sum_{i=1}^n y_i (x_i - \bar{x})}{\sum_{i=1}^n (x_i - \bar{x})^2} \tag{19}$$

where, in terms of time series, x_i is the i -th timepoint (the independent variable) and y_i is the i -th datapoint, \bar{x} is the mean of the timepoints x and \bar{y} is the mean of the data y .

The residual or the difference between the data (y_i) and the fitted value (\hat{y}_i), is defined as:

$$e_i = y_i - \hat{y}_i = y_i - (\hat{\beta}_0 + \hat{\beta}_1 x_i) \tag{20}$$

For the i -th data in the segment [116]. Linear interpolation produces a smooth, connected PLR, while linear regression can produce a very disjointed PLR, depending on the time series dataset.

However, the approximating lines produced using the linear regression approach is superior in terms of Euclidean distance [114].

For the fatigue studies, the segmentation algorithm selected is able to provide varies kurtosis and fatigue damage [47]. Piecewise linear representation (PLR) is an approximation to the time series, T for length, n with K-line basis. Number of segments derived from the PLR will be reduced to one obtained the limiting criteria [115].

V.2. Data Clustering

Clustering is the unsupervised classification of patterns (observations, data items, or feature vectors) into groups (clusters). Clustering is useful in several exploratory pattern-analysis, grouping, decision-making, and machine-learning situations, including data mining, document retrieval, image segmentation, and pattern classification.

Normally, the distance formula is required in determining the clusters that need to be merged next for adjacent locations or clusters which needs to be divided because of the position that rare or dense. Among the distance formula commonly used is the Euclidean distance formula [117]:

$$d(x, y) = \sqrt{(a_1 - b_1)^2 + (a_2 - b_2)^2 + \dots + (a_n - b_n)^2} \tag{21}$$

where $d(x,y)$ is the distance of x and y , a is the first point position, b is the second point position and n is the dimension of data.

Clustering algorithm can be divided into two which is hierarchical and restrictions [10]; [109]. Hierarchical algorithms find the successive clusters using previously established clusters. This group consists of agglomerative (from bottom to top) or breakdown (from top to bottom).

The agglomerative algorithm begins with each element as separate cluster and merges into larger clusters in a row. Breaking algorithm starts with a whole and process to be divided into smaller groups in a row.

Restrictions Algorithm is to determine the entire group immediately. This algorithm is divided into three types, namely k-means, Fuzzy and the quality threshold (high threshold / QT). The K-means algorithm divided each point to the nearest centre cluster (also called centroid). Centroid is the mean of all points in a cluster, which is the mean arithmetic of the coordinates for each dimension separately for all points in the group.

The main advantage of this algorithm is simplicity and speed which allows be used on large data sets.

The disadvantage is that it does not give the same result in each analysis, as the group generated depends on the initial random assignment [10]. K-means can define:

$$J_h = \sum_{j=1}^k \sum_i^c ||x_i^{(j)} - c_j||^2 \tag{22}$$

where $||x_i^{(j)} - c_j||^2$ Distance between data points $x_i^{(j)}$ center group c_j . The K-means clustering algorithm is thus a simple to understand, fairly intuitive method by which we can divide the available data into sub-categories

In fuzzy clustering, each point has a coefficient that gives the degree in one group. This algorithm has a similar problem as the K-means, where the results are depending on the number of group selection.

The data points can belong to more than one cluster, and associated with each of the points are membership grades which indicate the degree to which the data points belong to the different clusters [118]. Fuzzy clustering method is offered to construct clusters with uncertain boundaries, so this method allows that one object belongs to some overlapping clusters to some degree. In other words, the essence of fuzzy clustering is to consider not only the belonging status to the clusters, but also to consider to what degree do the objects belong to the clusters [119]. QT clustering is a method of alternative data partition, which is designed for clustering of genes. It requires more computing power than the K-means, but does not required the determination of the clusters number, and always give the same result when analysed in several times [120].

V.3. Data Classifications

Data classification method use set of features or parameters to characterise each object, where these features should be relevant to the application.

The consideration methods for classification, meaning that a human expert both has determined into what classes an object may be categorized and also has provided a set of sample objects with known classes. Classification technique is used in many areas such as in medical, finance, optimization and quality control analyses of production processes in various energy applications, determination of the endurance of construction materials, determination of achievement status of students in education, weather forecast, and classification of drugs [121].

Some data are selected as training data during the process of applying classification, and the algorithm is operated on both this training data set and the other data set with unknown classification so as to determine which group this test data belongs to. The common classification models are Decision Trees (DT), Regression Trees, Support Vector Machine (SVM) [121]; [122]. Besides these models, classification also uses artificial intelligence techniques such as artificial neural networks [123].

Decision tree is a hierarchical structure comprised of decision knots (for determining to which branch data is going to be directed) and leaves (including labels for revealing the class of data at the end of those branches) [121]. Decision tree model is also defined as rule based learning. In establishing this model, a root node is designated at the beginning, and then sub-nodes are generated based on the decision taken according to the status of the quality chosen at each node. When each node is minimized to a single quality status, it is called a leaf, and a class is thus determined at the end of this node. This transaction continues recursive until a class is determined at the end of each node [124].

Classification by regression trees also includes obtaining sub-nodes and leaves from a root node as in decision trees. Nevertheless, in regression trees, each node proceeds only by being divided into two sub-nodes: left and right. CART, Twoing, and Gini are among algorithms developed for this technique [125].

SVM method is based on estimation of the most appropriate function for separating data [121]. The SVM method aims at finding a special linear line separating between classes. There is a possibility to draw this linear line more than once during the classification. The SVM identifies the farthest line to both classes, and thus maximum error tolerance is determined. Upon identification of training data and the border line, test data is classified based on their places in reference to the border [126]. Suppose a set of data $T = \{x_i, y_i\}_{i=1}^m$ where $x_i \in R^n$ denotes the feature vectors, $y_i \in \{+1, -1\}$ stands for two classes, and m is the sample number, if two classes are linearly separable, the hyperplane $f(x) = 0$ can be determined such that separates the given feature vectors:

$$f(x) = w \cdot x + b = \sum_{k=1}^m w_k \cdot x_c + b = 0 \quad (23)$$

where w and b denote the weight vector and the bias term, respectively. The position of the separating hyperplane is defined by setting these parameters. Thus the separating hyperplane satisfy the following constraints:

$$y_i f(x_i) = y_i (w \cdot x + b) \geq 1, \quad i = 1, 2, \dots, m \quad (24)$$

Neural networks are composed of simple elements operating in parallel. These elements are inspired by biological nervous systems. As in nature, the connections between elements largely determine the network function.

Neural networks can be trained to perform a particular function by adjusting the values of the connections (weights and biases) between elements. Generally, neural networks are adjusted, or trained, so that a particular input leads desired target output. The network is adjusted, based on a comparison of the output and the target, until the network output matches the target. Usually, many such input/target pairs are needed to train a network. Neural networks have been trained to perform complex functions in various fields, including pattern recognition, identification, classification, and speech, vision, and control systems [122]; [123].

Then The Probabilistic Neural Network (PNN) was first proposed in [123]; [127]. The development of PNN relies on the Parzen window concept of multivariate probability estimates. The PNN combines the Baye's strategy for decision-making with a non-parametric estimator for obtaining the Probability Density Function (PDF) [123]; [127]. The PNN architecture includes four layers; input, pattern, summation, and output layers. The input nodes are the set of measurements. The second layer consists of the Gaussian functions formed using the given set of data points as centers. The third layer performs an average operation of the outputs from the second layer for each class. The fourth layer performs a vote, selecting the largest value. The advantage of this technique is training process very fast; inherent parallel structure and training pattern can be added or removed without extensive retraining [128].

V.4. Pattern Recognitions and Feature Selection

Pattern recognition is the science of making inferences from perceptual data, using tools from statistics, probability, computational geometry, machine learning, signal processing, and algorithm design. Pattern recognition is the recognition of an output value for input value according to some specific algorithm. The common pattern recognition is the output of the data classification techniques, namely the division of each input value to the one of a certain class [129].

The description and classification tasks work together to determine the most accurate label for each unlabelled object analysed by the pattern recognition system. Feature extraction is a critical stage because it reduces the dimension of input data to be handled by the classifier.

The features which truly discriminate among groups will assist in identification, while the lack of such features can prevent the classification task from arriving at an accurate identification. The final result of the description task is a set of features, commonly called a feature vector, which constitutes a representation of the data [122]; [128].

The selection methods provide useful information about advantage of selected features, advantage of feature selection strategy and the relation between the useful features and the desired feature size [130].

Generally feature selection that always use is for filtering is correlation function method. A correlation function is the correlation between random variables at two different points in space or time, usually as a function of the spatial or temporal distance between the points. If one considers the correlation function between random variables representing the same quantity measured at two different points then this is often referred to as an autocorrelation function being made up of autocorrelations.

The most familiar measure of dependence between two quantities is "Pearson's correlation." It is obtained by dividing the covariance of the two variables by the product of their standard deviations. The population correlation coefficient $\rho_{X,Y}$ between two random variables X and Y with expected values μ_X and μ_Y and standard deviations σ_X and σ_Y is defined as [131]:

$$P_{x,y} = \text{corr}(X,Y) = \frac{\text{cov}(X,Y)}{\sigma_x \sigma_y} = \frac{E[(X - \mu_x)(Y - \mu_y)]}{\sigma_x \sigma_y} \quad (25)$$

where E is the expected value operator, cov means covariance and, corr a widely used alternative notation for Pearson's correlation. The Pearson correlation is +1 in the case of a perfect positive (increasing) linear relationship (correlation), -1 in the case of a perfect decreasing (negative) linear relationship (anticorrelation), and some value between -1 and 1 in all other cases, indicating the degree of linear dependence between the variables.

As it approaches zero there is less of a relationship (closer to uncorrelated). The closer the coefficient is to either -1 or 1, the stronger the correlation between the variables. Some feature can be selected from feature space based on the obtained correlation coefficient of potential features.

Wrapper based methods use a search algorithm to seek through the space of possible features and evaluate each subset by running a model on the selected subset. Wrappers usually need huge computational process and have a risk of over fitting to the model.

One of the methods is Genetic algorithms (GA). GA belong to the larger class of Evolutionary Algorithms (EA), which generate solutions to optimization problems using techniques inspired by natural evolution, such as mutation, selection, and crossover. Commonly, the algorithm terminates when either a maximum number of

generations has been produced, or a satisfactory fitness level has been reached for the population [132]. The chromosomes are encoded with {0,1} binary alphabet. In a chromosome, "1" indicates the selected features while "0" indicates the unselected ones. For example, a chromosome defined as:

$$\{1\ 0\ 1\ 0\ 1\ 1\ 0\ 0\ 0\ 1\} \quad (26)$$

Specifies that the features with index 1, 3, 5, 6, and 10 are selected while the others are unselected. The fitness value corresponding to a chromosome is usually defined as the classification accuracy obtained with the selected features.

To generate index, the identification process should be carried out first. Both are closely interlinked each other's.

The studies regarding to this matter can be seen in the environmental field. The air pollution index produced by the classification of air quality data obtained. The water quality index is obtained by classifying the water content [133]. In the field of forensics, the index of human fingerprints is used to segment the fingerprint data on a number of patterns [134]. In the study of fatigue, fatigue failure index is a new study. But for this index epoxy, pattern recognition process by clustering method can still be used to get the desired output.

Many algorithms have been proposed for detection and classification of. Pattern recognitions schemes are very popular solution for engineering application data.

The combinations of signalprocessing and classification tools have been widely applied in detection methods. The most useful features are extracted by analysis of signals and then they are discriminated by using a classifier or by definition of a properindex [122].

VI. Multi-Variate Analysis for Time Series Data

This review has discussed the concepts and approaches which form the basis of this study. Several aspects have been discussed in the field of fatigue background such as fatigue loadings, fatigue life behaviour, fatigue life prediction and fatigue data editing. It common that the loads measure on the component of structures are analysed for fatigue life using crack growth approaches. It is important to predict the crack initiation in order to avoid the fatigue failure. A fatigue life estimation based on the strain-life is usually used in these cases.

The Relevant method or techniques for localised time-frequency features classification for fatigue data analysis have been defined. Many of analysis for non-stationary characteristic signal provide a challenge for research. Using the Fourier transform the frequency component of an entire signal can be analysed, but not possible to locate at what point in time that frequency component occurred or it duration. To overcome this problem, the time-frequency localised signal processing technique such as STFT or wavelet can be used.

In order save the time and cost for fatigue analysis, large amplitude events needs to extract for further investigation which produced the majority of damage are retained, so as to produce a shortened loading for accelerated fatigue tests. Using fatigue data editing technique, there is a process to remove low amplitude segments, which are theoretically contributes to minimal or no fatigue damage to the components.

Multivariate time-series analysis is important in order to explain the interactions and movements among a group of time series variables. There are concerned with the recognition of recurring patterns within multivariate time series, which capture the evolution of multiple parameters over a certain period of time. Segmentation, clustering, data classification and pattern recognition technique is the relevant analysis in fatigue data. It is known from the literature about the selection of the appropriate approaches which were often based on the analyst's experience and preferences. By predicting the structure fatigue life, which needs only several variable and will automatically calculate, classify and optimise the severity of fatigue damage through the significant mathematical and experimental findings, leading to cost and time saving.

Acknowledgements

The authors would like to express their gratitude to UniversitiKebangsaan Malaysia(UKM-GUP-2011-069) for supporting this research.

References

- [1] S. G. Hellevik, I. Langen & J. D. Sørensen, Cost Optimal Reliability Based Inspection and Replacement Planning of Piping Subjected to CO2 Corrosion. *International Journal of Pressure Vessels and Piping*, Vol. 76, pp. 527-538, 1999.
- [2] E. Acar, R. T. Hafitka & N. H. Kim, Effect of Structural Tests on Aircraft Safety, *AIAA Journal*, Vol. 48, No. 10, pp. 2235-2248, 2010.
- [3] H. O. Fuchs & R. I. Stephens, *Metal Fatigue in Engineering* (John Wiley & Sons, New York, 1980).
- [4] N. E. Dowling, *Mechanical Behaviour of Materials: Engineering Method for Deformation, Fracture, and Fatigue* (Prentice Hall, New Jersey, 1999).
- [5] Y. Nadot, & V. Denier, Fatigue Failure of Suspension Arm: Experimental Analysis and Multiaxial Criterion, *Engineering Failure Analysis*, Vol. 11, pp. 485-499, 2004.
- [6] V. Pakrashi, B. Basu & A. O' Connor, Structural Damage Detection and Calibration Using a Wavelet-Kurtosis Technique. *Engineering Structures*, Vol. 29, pp. 2097-2108, 2007.
- [7] Y. L. Lee, J. Pan, R. Hathaway & M. Barkey, *Fatigue Testing and Analysis: Theory and Practice* (Elsevier Butterworth-Heinemann, Oxford, 2005).
- [8] M. Misiti, Y. Misiti, G. Oppenheim & J. M. Poggi, *User's Guide: Wavelet Toolbox TM 4. MA* (The Math Works, Inc, 2008).
- [9] C. K. E. Nizwan, S. Abdullah, M. Z. Nuawi & F. Lamin, A Study of Fatigue Data Editing Using Frequency Spectrum Filtering Technique. *Proceedings of World Engineering Congress*, pp.372-378, 2007.
- [10] A.K. Jain, M. N. Murty & P. J. Flynn, Data Clustering: A Review, *ACM Computing Surveys*, Vol. 31, pp. 264-323, 1999.
- [11] Matlab. 2008b. User's Guide: Statistics Toolbox™ 6. MA: The Math Works, Inc.
- [12] G. V. Tsybanev & S. L. Ponomarev, Fatigue of Low-Carbon and Low-Alloyed Steels for the Automotive Industry, *Strength of Materials*, Vol. 33, n.1,2001.
- [13] N. A. Kadhim, S. Abdullah & A. K. Ariffin, Effect of The Fatigue Data Editing Technique Associated With Finite Element Analysis on The Component Fatigue Design Period, *Materials and Design*, Vol. 32, No.2, pp.1020-1030, 2011
- [14] N. A. Kadhim & S. Abdullah, Effective Strain Damage Model Associated With Finite Element Modelling and Experimental Validation, *International Journal of Fatigue*, Vol. 36, n. 1, pp. 194-205, 2012.
- [15] J. Schijve, Fatigue of Structure and Materials in 20th Century and The State of Art, *International Journal of Fatigue*, Vol. 25, pp. 679-702, 2003.
- [16] K. J. Miller, Metal Fatigue-Past, Current and Future. *Proceedings of the Institution of Mechanical Engineers. Part C: Journal of Mechanical Engineering Science*, Vol. 205, n. 5, pp. 291-304, 1991.
- [17] R. I. Stephens, A. Fatemi, R. R. Stephens & O. F. Henry, *Metal Fatigue in Engineering* (John Wiley & Sons, Inc., New York, 2001).
- [18] D. Taylor & G. Wang, The Validation of Some Methods of Notch Fatigue Analysis. *Fatigue Fracture Engineering Materials Structure*, Vol. 23, pp. 387-394, 2000
- [19] R. C. Juvinall & K. M. Marshek, *Fundamentals of Machine Component Design*, (Fourth Ed. John Wiley & Sons, Inc, New Jersey, 2006).
- [20] M. Shariyat, A Fatigue Model Developed by Modification of Gough's Theory, for Random Non-Proportional Loading Conditions and Three-Dimensional Stress Fields, *International Journal of Fatigue*, Vol. 30, pp. 1248-1258, 2008.
- [21] E. Zahavi, *Fatigue Design: Life Expectancy of Machine Parts* (CRS Press, Inc, Florida, 1996).
- [22] S. D. Downing & D. F. Socie, Simple Rainflow Counting Algorithms. *International Journal of Fatigue*, Vol. 4, pp. 31-40, 1982
- [23] F. A. Conle & C. C. Chu, Fatigue Analysis and The Local Stress-Strain Approach in Complex Vehicular Structures, *International Journal of Fatigue*, Vol. 19, n. 1, pp. S317-S323, 1997
- [24] C. C. Chu, Multiaxial Fatigue Life Prediction Method in The Ground Vehicle Industry, *International Journal Fatigue*, Vol. 19, n. 1, pp. S325-S330, 1998.
- [25] S. Suresh, *Fatigue of Materials* (Cambridge University Press, Cambridge, 1991).
- [26] M. Ciavarella & G. Meneghetti, On Fatigue Limit in the Presence of Notches: Classical vs. Recent Unified Formulations. *International Journal of Fatigue*, Vol. 26, pp. 289-298, 2004.
- [27] C. M. Sonsino, Course Of SN-Curves Especially in The High-Cycle Fatigue Regime With Regard To Component Design And Safety, *International Journal of Fatigue*, Vol. 29, n. 12, pp. 246-2258, 2007
- [28] B. Pyttel, D. Schwerdt, I. Brunner & C. Berger, Fatigue Strength And Failure Mechanisms In The VHCF-Region, *Anales de Mecanica de la Fractura*, Vol. 28, n. 1, pp. 1-8,2011
- [29] C. M. Sonsino, Fatigue Testing Under Variable Amplitude Loading, *International Journal of Fatigue*, Vol. 29, n. 6, pp. 1080-1089, 2006.
- [30] R. I. Stephens, P. M. Dindinger & J. E. Gunger, Fatigue Damage Editing for Accelerated Durability Testing Using Strain Range and SWT Parameter Criteria. *International Journal of Fatigue*, Vol. 19, pp. 599-606, 1997.
- [31] M. F. M. Yunoh, S. Abdullah, Z. M. Nopiah, M. Z. Nuawi & N. Ismail, Fatigue Geature Classification for Automotive Strain Data, *IOP Conf. Series: Materials Science and Engineering*, Vol. 36 (2012), pp. 012301, 2012
- [32] M. M. Rahman, K. Kadirgama, M. M. Noor, M. R. M. Rejab & S. A. Kesulai, Fatigue Life Prediction Of Lower Suspension Arm Using Strain-Life Approach, *European Journal of Scientific Research*, Vol. 30, n. 3, pp. 437-450, 2009
- [33] M. H. Hafezi, N. N. Abdullah, J. F. O. Correia & A. M. P. De Jesus, An Assessment Of A Strain-Life Approach For Fatigue Crack Growth, *International Journal of Structural Integrity*, Vol. 3, n. 4, pp. 344-376, 2012

- [34] ASTM E606, Standard Recommended Practice for Constant-Amplitude Low-Cycle Fatigue Testing, 1980.
- [35] ASTM E739-91, Standard Practice for Statistical Analysis of Linear and Linearised Stress-Life (S-N) and Strain-Life (E-N) Fatigue Data, American Society for Testing and Materials, 1980.
- [36] C. R. William, Y. L. Lee, & R. T. Rilly, A Practical Method For Statistical Analysis Of Strain-Life Fatigue Data, *International Journal Fatigue*, Vol. 25, pp. 427-436, 2003.
- [37] nSoft® User Manual, nSoft V5.3 Online Documentation, nCode International Ltd., Sheffield, 2001.
- [38] W. D. Callister & D. G. Rethwisch, *Fundamentals of Materials Science and Engineering: an Integrated Approach*, (Third Ed, John Wiley & Sons, Inc, New Jersey, 2008)
- [39] J. A. Bannantine, J. J. Comer & J. Handrock, *Fundamentals of Metal Fatigue Analysis* (Prentice-Hall, New Jersey, 1990)
- [40] D. J. Morrow, *Fatigue Properties of Metal Fatigue Design Handbook*, (Society of Automotive Engineers, 1968).
- [41] K. N. Smith, P. Watson & T. H. Topper. A Stress-Strain Function for the Fatigue of Metals. *Journal of Materials (JMLSA)*, Vol. 5, n.4, pp. 767-778, 1970.
- [42] T. Wehner & A. Fatemi, Effects of Mean Stress on Fatigue Behaviour of Hardened Carbon Steel. *International Journal of Fatigue*, Vol. 13, pp. 241-248, 1991
- [43] J. Giacomini, A. Steinwolf & W. J. Staszewski, A Vibration Mission Synthesis Algorithm For Mildly Nonstationary Road Data. *ATA 6th Int. Conf. on the New Role of Experimentation in the Modern Automotive Product Development Process, Florence, Italy*, 17-19 November, 1999
- [44] I. Djurovic, L. Stankovic, M. Rupp & L. Shao, Robust Processing of Nonstationary signals, *EURASIP Journal on Advances in Signal Processing*, pp. 1-3, 2010
- [45] M. D. Spiridonakos & S. D. Fassois, Parametric Identification of a Time-Varying Structure Based on Vector Vibration Response Measurements, *Mechanical Systems and Signal Processing*, Vol. 23, pp. 2029-2048, 2009.
- [46] S. Gupta, A. Ray & E. Keller, Symbolic Time Series Analysis of Ultrasonic Signals For Fatigue Damage Monitoring In Polycrystalline Alloys, *Measurement Science Technology*, Vol. 17, pp. 1963-1973, 2006
- [47] Z. M. Nopiah, M. I. Khairir, S. Abdullah, C. K. E. Nizwan & M. N. Baharin, Peak-Valley Segmentation Algorithm for Kurtosis Analysis and Classification of Fatigue Time Series Data. *European Journal of Scientific Research*, Vol. 29, n.1, pp.113-125, 2009
- [48] A. Khatkhate, A. Ray, E. Keller, S. Gupta & S. C. Chin, Symbolic Time-Series Analysis For Anomaly Detection in Mechanical Systems, *IEEE/ASME Transactions on Mechatronics*, Vol. 11, n.4, pp. 439-447, 2006.
- [49] A. Lennie, S. Abdullah, Z. M. Nopiah & M. N. Baharin, Behavioural Investigation Of Fatigue Time Series Using Statistical Approach, *Journal of Applied Sciences*, Vol. 10, pp. 1714-1722, 2010.
- [50] S. Abdullah, J. C. Choi, J. A. Giacomini & J. R. Yates, Bump Extraction Algorithm For Variable Amplitude Fatigue Loadings, *International Journal of Fatigue*, Vol. 28, n.7, pp. 675-691, 2006
- [51] D. P. Doane & L. E. Seward, Measuring Skewness: A Forgotten Statistic?, *Journal Of Statistics Education*, Vol. 19, n.2, pp. 1-18, 2011
- [52] X. Niu, L. Zhu & H. Ding, New Statistical Moments For The Detection of Defects in Rolling Element Bearings, *International Journal of Advance Manufacturing Technology*, Vol. 25, pp. 1268-1274, 2005
- [53] Z. M. Nopiah, M. I. Khairir, S. Abdullah, C. K. E. Nizwan, & M. N. Baharin, Peak-Valley Segmentation Algorithm for Kurtosis Analysis and Classification of Fatigue Time Series Data, *European Journal of Scientific Research*, Vol. 29, n.1, pp. 113-125, 2009.
- [54] J. A. Ghani, M. Rizal, A. Sayuti, M. Z. Nuawi, R. Ramli, B. Deros & C. H. C. Haron, Online Tool Wear Monitoring Using Portable Assistant (PDA), *International Journal of the Physical Sciences*, Vol. 6, n. 16, pp. 4064-4069, 2011.
- [55] A. Steinwolf & S. A. Rizzi, Non-Gaussian Analysis of Turbulent Boundary Layer Fluctuating Pressure on Aircraft Skin Panels, *AIAA Journal of Aircraft*, Vol. 43, n.6, pp. 1662-1675, 2006
- [56] A. Przekop, S. A. Rizzi, & K. A. Sweitzer, An Investigation of High-Cycle Fatigue Models for Metallic Structures Exhibiting Snap-Through Response, *International Journal of Fatigue*, Vol. 30, n.9, pp. 1579-1598, 2008.
- [57] S. A. Rizzi, M. N. Behnke & P. Przekop, The Effect of a Non-Gaussian Random Loading on High-Cycle Fatigue of a Thermally Post-Buckled Structure, *Structural Dynamics: Recent Advances, Proceedings of the 10th International Conference, Paper 26, Southampton, UK*, July 12-14, 2010
- [58] S. Abdullah, J. A. Giacomini & J. R. Yates, A Mission Synthesis Algorithm For Fatigue Damage Analysis, *Proceeding Institute Mechanical Eng. Part D. Journal Automotif Eng*, Vol. 218 (D3), pp. 243-258, 2004.
- [59] M. Z. Nuawi, M. J. Nor, N. Jamaluddin, S. Abdullah, F. Lamin & C. K. E. Nizwan, Development of Integrated Kurtosis-Based Algorithm for Z-Filter Technique. *Journal of Applied Sciences* Vol. 8, n.8, pp. 1541-1547, 2008.
- [60] S. Abdullah, N. Ismail, M. Z. Nuawi, Z. M. Nopiah, & A. Ariffin, Using the Hybrid Kurtosis-Based Method to Correlate Strain and Vibration Signals. *Journal of WSEAS Transactions on Signal Processing*, Vol. 6, n.3, pp. 79-90, 2010.
- [61] M. M. Padzi, S. Abdullah, M. Z. Nuawi, & A. Shamsudeen, Fatigue Failure Assessment of Variable Amplitude Loading (VAL) on Carbon Steel AISI 1045 Using I-Kaz Approach, *International Review of Mechanical Engineering (I.R.E.M.E)*, Vol. 6, n.3, pp. 578-582, 2012.
- [62] S. D. Stearns & R. A. David, *Signal Processing Algorithms in FORTRAN and C* (Prentice-Hall, New Jersey, 1993).
- [63] S. W. Smith, *The Scientist and Engineer's Guide to Digital Signal Processing* (2nd Edition, California Technical Publishing, San Diego, 1999)
- [64] H. J. Sutherland, Frequency Domain Analysis of The Fatigue Loads on Typical Wind Turbine, *Journal of Solar Energy Engineering, Transactions of ASME*, Vol. 118, pp. 204-211, 1996.
- [65] M. Shiwa, Y. Furuya, H. Yamawaki, K. Ito & M. Enoki, Fatigue Process Evaluation of Ultrasonic Fatigue Testing in High Strength Steel Analysed by Acoustic Emission and Non-Linear Ultrasonic, *Materials Transactions*, Vol. 51, n. 8, pp. 1404-1408, 2010.
- [66] M. B. Ali, S. Abdullah, M. Z. Nuawi, M. M. Padzi, & K. Z. Zakaria, Experimental Analysis of an Instrumented Charpy Impact Using Statistical Study Based Data Analysis, *International Journal of Mechanical and Materials Engineering (IJMME)*, Vol. 6, n.2, pp. 260-268, 2011.
- [67] M. M. Rahman, K. Kadirgama, M. M. Nor, M. R. M. Rejab & S. A. Kesulai, Fatigue Life Prediction of Lower Suspension Arm Using Strain-Life Approach, *European Journal of Scientific Research*, Vol. 30, n. 3, pp. 437-450, 2009.
- [68] M. Olagnon & Z. Guede, Rainflow Fatigue Analysis for Loads With Multimodal Power Spectral Densities, *Marine Structures*, Vol. 21, n.2-3, pp. 160-176, 2008.
- [69] T. Tanaka & Y. Izawa, Detection Method of Fatigue Damage in Carbon Steel Using Laser Ultrasonics, *Journal Nuclear Science Technology*, Vol. 39, n.5, pp. 514-519. 2002.
- [70] T. Dirlik, *Application of computers in Fatigue Analysis*, Ph.D. Thesis, University of Warwick, 1985.
- [71] J. P. Quiley & Y. L. Lee, Assessing Dirlik's Fatigue Damage Estimation Method for Automotive Applications, *SAE International Journal of Passenger Cars- Mechanical Systems*, Vol. 5, n.2, pp. 911-920, 2012.
- [72] S. J. M. Rosvall, M. J. Honeychurch, D. M. Elton, & A. M. Bond, A Practical Approach to Applying Short Time Fourier Transform Methods in Voltammetric Investigations, *Journal Electroanalytical Chemistry*, Vol. 515, pp. 8-16, 2001.
- [73] M. K. Kiyimik, I. Guler, A. Dizibuyuk & M. Akin, Comparison Of STFT and Wavelet Transform Methods in Determining Epileptic Seizure Activity in EEG Signal For Real-Time Application, *Computer in Biology and Medicine*, Vol. 35, pp. 603-616, 2005.
- [74] D. Maclsaac, P. A. Parker & R. N. Scott, The Short-Time Fourier Transform and Muscle Fatigue Assessment in Dynamic Contractions, *Journal Electromyogr. Kinesiol*, Vol. 11, n. 6, pp. 439-449. 2001.

- [75] S. Abdullah, C. K. E. Nizwan & M. Z. Nuawi, A Study of Fatigue Data Editing Using The Short-Time Fourier Transform (STFT). *American Journal of Applied Sciences*, Vol. 6, n. 4, pp. 565-575, 2009.
- [76] S. V. Nese, O. Kilic & T. C. Akinci, Analysis of Wind Turbine Blade Deformation With STFT Method, *Energy Education Science and Technology Part A: Energy Science and Research*, Vol. 29, n.1, pp. 679-686, 2012.
- [77] D. V. Percival & A. T. Walden, *Wavelet Methods for Time Series Analysis* (Cambridge University Press, Cambridge, UK, 2000).
- [78] P. S. Addison, *The Illustrated Wavelet Transform* (Handbook, Institute of Physics Publishing, London, 2002).
- [79] S. Berry, Practical Wavelet Signal Processing for Automated Testing. *Proceedings of IEEE Systems Readiness Technology Conference*, pp. 653-659, 1999
- [80] B. S. Kim, S. H. Lee, M. G. Lee, J. Ni, J. Y Song & C. W. Lee, A Comparative Study on Damage Detection in Speed-Up and Coast-Down Process of Grinding Spindle-Typed Rotor-Bearing System. *Journal of Materials Processing Technology*, Vol. 187-188, pp. 30-36. 2007.
- [81] Z. Leonowicz, T. Lobos & K. Woźniak, Analysis of Power Quality Disturbances Using the S-Transform. *Proceedings of International Conference on Fundamentals of Electronics and Circuit Theory*, 2007
- [82] O. Rioul & M. Vetterli, Wavelet and Signal Processing. *IEEE Signal Processing Magazine*, Vol. 8, n.4, pp.14-38, 1991.
- [83] C. S. Oh, Application of Wavelet Transform in Fatigue History Editing, *International Journal of Fatigue*, Vol. 23, pp. 241-250, 2001.
- [84] S. Prabhakar, A. S. Sekhar & A. R. Mohanty, Detection and Monitoring of Cracks in a Rotor-Bearing System Using Wavelet Transforms. *Mechanical Systems and Signal Processing*, Vol. 15, n.2, pp. 447-450, 2001.
- [85] V. Purushotham, S. Narayanan & S. A. N. Prasad, Multi-fault Diagnosis of Rolling Bearing Elements Using Wavelet Analysis and Hidden Markov Model Based Fault Recognition. *NDT & E International*, Vol. 38, pp. 654-664, 2005.
- [86] D. Boulahbal, M. F. Golnaraghi & F. Ismail, Amplitude and Phase Wavelet Maps for The Detection of Cracks in Geared Systems, *Mechanical Systems and Signal Processing*, Vol. 13, n.3, pp. 423-436, 1999.
- [87] A. S. Sekhar, Crack Detection Through Wavelet Transform For a Run Up Rotor. *Journal Sound and Vibration*, Vol. 259, n.2, pp. 461-472, 2003.
- [88] C. Nagaraju, K. Narayana Rao & K. Mallikarjuna Rao, Application of 3D Wavelet Transforms for Crack Detection in Rotor Systems, *Sadhana*, Vol. 34, n.3, pp. 407-419, 2012.
- [89] J. S. Walker, *A Primer on Wavelets and Their Scientific Applications* (Chapman & Hall/CRC, Boca Raton, USA 1999).
- [90] I. Daubechies, *Ten Lectures on Wavelets* (SIAM, Philadelphia, 1992).
- [91] A. Graps, An Introduction to Wavelets, *IEEE Computational Science and Engineering*, Vol. 2, n. 2, pp. 50-61, 1995.
- [92] W. J. Staszewski, Structural and Mechanical Damage Detection Using Wavelets, *The Shock and Vibration Digest*, Vol. 30, n. 6, pp. 457-472, 1998.
- [93] L. Li, Study of Data Mining Algorithm Based on Decision Three, *International Conference on Computer Design and Applications (ICCD A China)*, 2010.
- [94] J. Lin & M. J. Zuo, Gearbox Fault Diagnosis Using Adaptive Wavelet Filter, *Mechanical Systems and Signal Processing*, Vol. 17, n. 6, pp. 1259-1269, 2003.
- [95] S. Abdullah, J. A. Giacomini, J. R. Yates, A Mission Synthesis Algorithm For Fatigue Damage Analysis, *Proceeding Institute Mechanical Engineering: Part D Journal Automotive Engineering*, Vol. 218 (D3), pp. 243-258, 2004.
- [96] L. K. Bahera, M. Nayak & S. Mohanty, Discrete Wavelet Transform and S-Transform Based Time Series Data Mining Using Multilayer Perception Neural Network, *International Journal of Engineering Science and Technology (IJEST)*, Vol. 3, n.11, pp. 8039-8046, 2011.
- [97] C. R. Pinnegar & L. Mansinha, The S-Transform With Windows of Arbitrary and Varying Shape. *Geophysics*, Vol. 68, n. 1, pp. 381-385, 2003.
- [98] C. C. Huang, S. F. Liang, M. S. Young & F. Z. Shaw, A Novel Application of The S-Transform in Removing Powerline Interference From Biomedical Signals, *Physiol Measurement*, Vol. 30, pp. 13-27, 2009.
- [99] L. Ai, J. Nan & J. Shen, Application of S-Transform To Driving a Fatigue in EEG Analysis, *Intelligent Computing and Intelligent Systems (ICIS)*, Vol. 1, pp. 814-817, 2010.
- [100] R. G. Stockwell, L. Mansinha & R. P. Lowe, Localization of the Complex Spectrum: the S Transform. *IEEE Transactions on Signal Processing*, Vol. 44, pp. 998-1001, 1996.
- [101] M. Shimmel & J. Gallart, The Inverse S-Transform in Filters with Time-Frequency Localization. *IEEE Transactions on Signal Processing*, Vol. 53, pp. 4417-4422, 2005.
- [102] Y. Yin, L. Zhang, M. Jin & S. Xie, Wavelet Packet and Generalized Gaussian Density Based Textile Pattern Classification Using BP Neural Network, *Lecture Notes in Computer Science*, Vol. 6146, pp. 540-547, 2010.
- [103] M. Nayak & B. S. Panigrahi, Advanced Signal Processing Techniques For Feature Extraction in Data Mining, *International Journal of Computer Applications*, Vol. 19, n.9, pp. 31-37, 2011.
- [104] D. Morrow & H. Vold, Compression of Time Histories Used for Component Fatigue Evaluation, SAE930403 in PT-67, in *Recent Developments in Fatigue Technology*, edited by Chernenkoff, R. A. and Bonnen, J. J., Society of Automotive Engineers (SAE), USA, 1997.
- [105] W. El-Ratal, M. Bennebach, X. Lin & R. Plaskitt, Fatigue Life Modelling and Accelerated Test for Components Under Variable Amplitude Loads, in *Symposium on Fatigue Testing and Analysis Under Variable Amplitude Loading Conditions, Tenth International Spring Meeting of SF2M, Tours, France, 29-31st May, 2002*.
- [106] S. Abdullah, T. E. Putra, M. Z. Nuawi, Z. M. Nopiah, A. Arifin & L. Abdullah, Extracting Fatigue Damage Features Using STFT And CWT, *WSEAS Transactions on Signal Processing*, Vol. 3, n.6, pp. 91-101, 2010.
- [107] R. D. Peng, A Method for Visualizing Multivariate Time Series data, *Journal of Statistical Software*, Vol. 25, pp.1-17, 2008.
- [108] J. Abonyi, B. Feil, S. Nemeth & P. Arva, Modified Gath-Geva Clustering for Fuzzy Segmentation Of Multivariate Time-Series, *Fuzzy Sets System*, Vol. 149, pp. 39-56, 2005.
- [109] S. Spiegel, J. Gaebler & A. Lommatzsch, Pattern Recognition and Classification for Multivariate Time Series, *Sensor KDD San Diego, CA, USA*, 2011
- [110] E. Keogh et al., *Segmenting Time Series: A Survey and Novel Approach, Data Mining in Time Series Databases* (second ed. World Scientific, 2003).
- [111] D. Lemire, 2007. A Better Alternative to Piecewise Linear Time Series Segmentation. Université du Québec à Montréal (UQAM).
- [112] D. S. Jeffrey, Joint Segmentation of Multivariate Astronomical Time Series: Bayesian Sampling with a Hierarchical Model, *IEEE Transaction on Signal Processing*, Vol. 55, pp. 414-420, 2007.
- [113] X. Liu, Z. Lin & H. Wang, Novel Online Methods for Time Series Segmentation. *IEEE Transactions on Knowledge and Data Engineering*, Vol. 20, n. 12, pp. 1616-1626. 2008.
- [114] E. Keogh, C. Selina, H. David & M. Pazzani, *Segmenting Time Series: A Survey and Novel Approach* (University of California, USA, 2001).
- [115] Z. M. Nopiah, S. Abdullah & M. I. Khairir, Segmentation and Scattering of Fatigue Time Series Data by Kurtosis and Root Mean Square. *International Conference on Signal Processing System*, pp. 64-68, 2008.
- [116] D. C. Montgomery, E. A. Peck & G. G. Vining, *Introduction to Linear Regression Analysis* (Wiley Interscience Publications, New York, 2001).
- [117] W. Pedrycz, *Knowledge-Based Clustering: From Data to Information Granules* (John Wiley and Sons Inc, New Jersey, 2005).
- [118] J.C. Bezdek. *Pattern Recognition with Fuzzy Objective Function Algorithms* (Plenum Press, New York, 1981).
- [119] R. Dave, Fuzzy Shell-Clustering and Applications to Circle Detection of Digital Images, *International Journal of General*

- Systems, Vol. 16, n.4, pp. 343–355, 1990
- [120] Matlab. 2008. User's Guide: Statistics Toolbox™ 6. MA: The Math Works, Inc.
- [121] H. Ibrahim & U. Ozkan, Comparison of classification technique used in machine learning as applied on vocational guidance data, 10th International Conf. on Machine Learning and Applications, 2011.
- [122] JZ. Moravej, A. A. Abdoos & M. Pazoki, Detection and Classification of Power Quality Disturbances Using Wavelet Transform and Support Vector Machines, *Electric Power Components and Systems*, Vol. 38, pp. 182–196, 2010.
- [123] W. Mao, I. Rychlik & G. Storhaug, Safety Index of Fatigue Failure for Ship Structure Details Department of Mathematical Science Chalmers University of Technology, University of Gothenburg, 2008.
- [124] L. Li, Study of Data Mining Algorithm Based on Decision Tree, *International Conference on Computer Design and Applications (ICCCA)*, China, 2010.
- [125] W. Y. Loh, Classification and regression tree methods, *Encyclopedia of statistics in Quality and Reliability*, Ruggeri, Kenett and Faltin (eds), pp. 315-323, 2008.
- [126] A. C. Steinwart, *Support Vector Machines* (Springer, New York, 2008).
- [127] D. F. Specht, Probabilistic Neural Network. *Neural networks*, Vol. 1, pp. 109-118, 1990.
- [128] Z. Moravej, A.A. Abdoos, M. Pazoki M, New Combined S-transform and Logistic Model Tree Technique for Recognition and Classification of Power Quality Disturbances, *Electric Power Components and Systems*, Vol. 39, n. 1, pp. 80-98, 2011.
- [129] N. W. Bishop & F. Sherratt, Finite Element Based Fatigue Calculations, *The International Association for Engineering Analysis Community, NAFEMS. Farnham*, 2006
- [130] S. Gunal, O. N. Gerek, D. G. Ece & R. Edizkan, The Search for Optimal Feature Set in Power Quality Event Classification. *Expert Systems with Application*, Vol. 36, pp. 10266–10273, 2009.
- [131] J. L. Rodgers & W. A. Nicewander, Thirteen Ways to Look At the Correlation Coefficient, *The American Statistician*, Vol. 42, pp. 59–66, 1988.
- [132] J. Yang & V. Honavar, Feature Subset Selection Using a Genetic Algorithm. *IEEE Intelligent Systems and their Applications*, Vol. 2, pp. 44–49, 1988
- [133] M. Nazmi, *Kajian Indeks Kualiti Air*. Universiti Teknologi MARA, Malaysia, 2009
- [134] Muslim, Fingerprint Pattern Recognition Using Distance Method Algorithm. *Proceeding. Of Regional Conference on Mathematics, Statistics and Applications*, 2006

Authors' information

¹Department of Mechanical and Materials Engineering, Faculty of Engineering and Built Environment, Universiti Kebangsaan Malaysia, 43600 UKM Bangi, Selangor, MALAYSIA.

²Fundamental Studies of Engineering Unit, Faculty of Engineering and Built Environment, Universiti Kebangsaan Malaysia, 43600 UKM Bangi, Selangor, MALAYSIA.



Mohd Faridz Mod Yunoh was born in Malaysia, in 1984. He completed his B.Eng in Universiti Teknikal Malaysia Melaka (2007) and M.Sc in Universiti Kebangsaan Malaysia, Malaysia (2012). Currently, he is a PhD candidate in Department of Mechanical and Materials Engineering, Universiti Kebangsaan Malaysia. His major fields of study are fatigue life assessment, structural integrity and durability of semiconductor packaging.



Shahrum Abdullah was born in Malaysia, 13th August 1971. He completed his B.Eng in Universiti Kebangsaan Malaysia, Malaysia (1995), M.Sc in Loughborough University, U.K (1997) and Ph.D in The University of Sheffield, U.K (2005). Currently, he is a professor in Department of Mechanical and Materials Engineering, Universiti Kebangsaan Malaysia, Malaysia. His major fields of study are fatigue life assessment, engineering design and data analysis for automotive application. Dr. Abdullah previous publications were fatigue strain analysis.



Mohd Zaki Nuawi is an associate professor in the Department of Mechanical and Materials Engineering, Faculty of Engineering and Built Environment, Universiti Kebangsaan Malaysia. (UKM). He received his Bachelor in Industrial Engineering and Msc in Industrial Engineering from INSSET, France and his PhD from Universiti Kebangsaan Malaysia in 2008. His research interests include acoustic and vibration, condition monitoring and applied ultrasonic. Assoc. Prof. DrNuawi is a member in the Malaysian Non Destructive Testing.



Zulkifli Mohd Nopiah is an associate professor at Fundamental Studies of Engineering Unit, Faculty of Engineering and Built Environment, Universiti Kebangsaan Malaysia. (UKM). He received his BSc in Mathematics, University of Minnesota, USA (Ogos 1991). Masters of Science (M.Sc in Operational Research), University of Southampton, United Kingdom (1995) and Doctor of Philosophy (PhD) University of Portsmouth, United Kingdom, Title : “The use of Goal Programming and its Extensions for Portfolio Problems” (1998). His research interest is Multiobjective Optimisation- Goal Programming, Genetic Algorithms, Linear Programming.

Strength of the Weld Line and Warpage Defects on the Molded Parts in Injection Molding Process

S. M. Nasir^{1,2}, K. A. Ismail¹, Z. Shayfull^{1,2}, N. A. Shuaib^{1,2}

Abstract – Strength at weld the line location and warpage problem in injection molding plastic component were not new problems in injection molding industries. Many researchers had emerged with several improvement techniques to reduce these problems that been applied to a verity of customer products that injected with various types of polymers. This paper reviewed the improvement techniques previously studied to maximize strength at weld line location and minimize warpage or deflections of the molded parts. From the review, it can be seen that by using mechanical and thermal assistance during injection molding process, and the optimization of machine parameters for stated problems can be improved. However, there was lack on the multi objectives optimization which should be apply to ensure the weld line and warpage were improved together to get the best quality products. **Copyright © 2013 Praise Worthy Prize S.r.l. - All rights reserved.**

Keywords: Injection Molding, Weld line Strength, Warpage, Optimization

I. Introduction

Plastics material is commonly used in variety of consumer products as well as industries. Nowadays, plastic become popular for all types of products such as foods, agricultures, automotive, aerospace and so on. In the automotive industry most of components are made from plastic especially for internal components are very tangible and popular. The demand for the thermoplastic product is very high in the market alongside a wide variety of shapes can be produced using the injection molding process.

However, they are some problems of using thermoplastic product during manufacturing process such as warpage, sink mark, short shot, weld line which affecting the quality of products.

The weld line will affect the mechanical strength by causing the poor appearance of the molded parts and consequently will decrease the part quality. Many researches about this problem has been done lately due to the of the ever-growing technologies for the quality of injection molded parts [1]. However, without modifying the part geometry, the weld lines formation was not possible to be eliminated completely. Eventually some improvement regarding the weld line problem had been studied such as by trial and error experiments and model prediction methods [1].

Basically, the weld line formation happens when plastic melt splits and then recombines at some location during the injection molding process [2]. The classifications of weld line formation are shown in Figure 1. The first type of the weld line was formed when resin flow through the difference wall thickness of a component as shown in Fig. 1(a).

Fig. 1(b) shows the weld line formed when material flow through a holes and meet together after it passed the hole. Moreover, in Fig. 1(c), weld line will happen when two or more gates used on the molded parts. Lastly, the weld lines occurred when the material flow at difference route and meet together at end of filing as shown in Fig. 1(d). Different cases will cause difference properties of the parts. Strength of component at location of weld line formation was become a serious problem in plastic injection molding process especially for the parts which required strength for functionality.

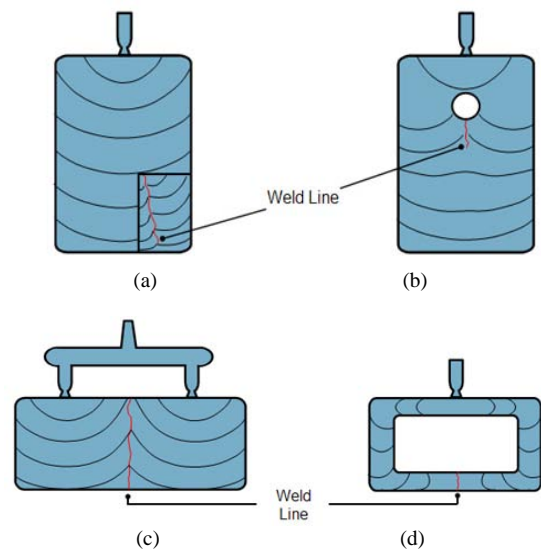


Fig. 1. Types of weld line formation, when; (a) Differential wall thickness, (b) Material flow through a holes, (c) Multi gates used, and (d) Material meet together at the end of filling

In order to increase the mechanical strength at the critical location on this parts, many researchers had used some techniques such as using mechanical assistance [3]-[4], thermal assistance [5]-[6] and using material additives method such adding some filler to a parent material or blended with two or more materials [7]-[8].

On the other hand, parameters optimization method was widely used as a technique for machine setup in order to get a quality product [9]-[10].

Many researchers worldwide including companies and academicians had studied in this issue [11]-[12]. Warpage formation will affect the quality of plastic injection molding products.

Mostly, the warpage problem had been reduced by parameter optimization method such as Taguchi method, PSO, ANN, GA and RSM where some parameters was adjusted to the suitable value in order to get a minimum value of warpage. Some researchers also used more than one optimization method to minimize a warpage value that called hybrid optimization method [13]-[14].

A few cases have used optimization method to improve more than one objective, such as combination of warpage and shrinkage as the objectives of optimization.

This technique called multi objectives optimization method [15].

The classification of improvement have been done by the previous researches can be divided into four categories such as mechanical assistance, thermal assistance, material additive and parameters optimization method.

II. Improvement of Weld Line Strength and Warpage Using Mechanical Assistance Method

The improvement techniques of weld line strength as well as mechanical strength in plastic injection molding products such as Vibration Assisted Injection Molding (VIAM), Ejector Pins Compression System (EPCS) and Ultrasonic as shown in Table I.

Strengthen of the product especially at location of weld line formation by mechanical assistance are founded in early 1980 by Tom et al. [3] in studied of Vibration Assisted Injection Molding (VAIM) method using Atactic Polystyrene (PS) as a molded material. The concept of VAIM indicates where vibrational forces were induced to polymer flow melts during the filling and packing phases of injection molding process as shown in Figure 2. This vibration forces need to be controlled to enhance and change the structures of the melt material at weld line location to strengthen the part. As results, the thermal, mechanical, aesthetic, and optical properties of plastic molded part have been improved significantly.

VIAM also used by Kikuchi et al. [4]-[5], and Li and Shen [17] who studied the weld line strength of molded parts. This technique was similar with Tom et al. [3] who apply the mechanical vibration to polymer melt using motion of the injection screw during the filling and packing stages of injection molding process.

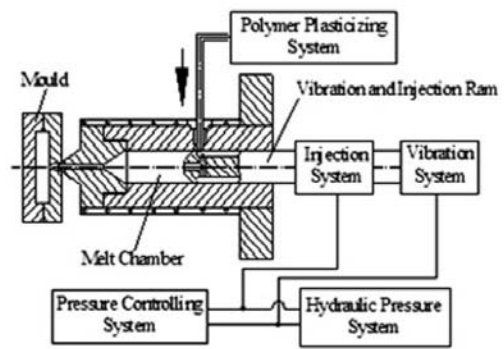


Fig. 2. Schematic diagram of VAIM [17]

The experiment was tested using PS material. In this study, the strength of the molded part was tested using tensile experiments and birefringence measurements and the results were compared with conventional injection molding process. As much as 18.7% - 28% of tensile strength had improved significantly.

Moreover, Nian and Huang [18], recommends a Ejector Pins Compression System (EPCS) in injection molding process to strengthen the weld lines on molded parts. Two ejector pins are positioned intentionally near the weld lines location as shown in Fig. 3. These pins are initially dipped below the cavity surface to allow the molten plastics flowed and filled the cavity. Then, the molten plastics were compressed by movement of ejector pins for disordering the molecular orientation at location of weld line formation. From the verification experiment, an EPCS was effectively changing the orientation of the plastic molecules parallel to the weld line in order to improve the mechanical strength of the molded part. As results, the strength of the molded part has been increased between 100% - 200% compared to conventional injection molding process.

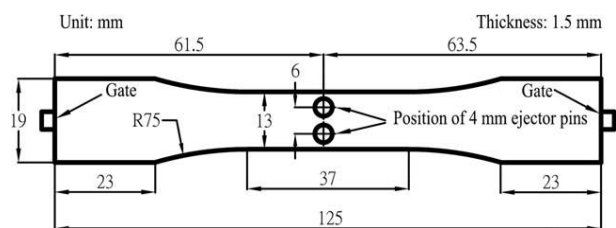


Fig. 3. Location of EPCS on Specimen [18]

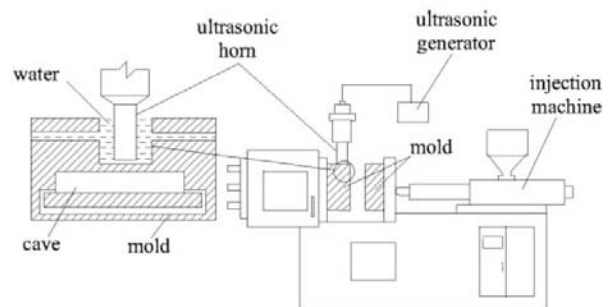


Fig. 4. Schematic Diagram of Ultrasonic Oscillations system in Injection Molding Machine. [19]

TABLE I
THE RESEARCHES ON IMPROVEMENT OF WELD LINE STRENGTH USING MECHANICAL ASSISTANCE

| No. | Authors | Improvement Method | Output | Results |
|-----|-------------------------------|---|-----------------------|--|
| 1 | Tom <i>et al.</i> [3] | Vibrational Assisted Injection Molding (VAIM) | Tensile strength | The tensile strength was increased about 20% using PS material |
| 2 | A. Kikuchi <i>et al.</i> [16] | VAIM | Tensile strength | The addition of vibration to the otherwise optimized molding conditions gave rise to significant product strength improvements to all materials used |
| 3 | Li and Shen [17] | VAIM | Mechanical Properties | Tensile properties, Young modulus and impact strength were increased with the vibration frequency and pressure vibration amplitude |
| 4 | Nian and Huang [18] | Ejector-pins compression system (EPCS) | Mechanical strength | EPCS was an efficient method to strengthen the weld line of the molded part |
| 5 | C. Lu <i>et al.</i> [19] | Ultrasonic Improvement | Weld line strength | The strength of the molded part has been increased between 100% - 200% compared to conventional injection molding process |

Lu *et al.* [19] applied an ultrasonic oscillations technique as shown in Fig. 4 to improve strength at weld line. Ultrasonic signal from ultrasonic generator was induced to a core side of mold via ultrasonic horn. Ultrasonic signal are divided into two modes, Mode I and Mode II.

For Mode I, ultrasonic oscillations were induced into the mold at the entire phases while for Mode II ultrasonic oscillations were induced into the mold after filling phase of injection molding process. As a result, the ultrasonic oscillations using Mode II more effective to enhance the weld line strength of PS and PS/ High density polyethylene (HDPE) blends. In addition, Lu *et al.* [20] utilized the same equipment to improve the mechanism of ultrasonic oscillations that can increase the molecular diffusion across weld line. Consequently, these combinations of melts at the skin results of increasing the mechanical strength at weld line location.

Although these techniques of improvement were used by many researchers to improve the mechanical strength and weld line strength of injection molded products, all researchers did not focus on improvement of warpage problem.

The weld line strength improvement using mechanical assistance was applicable to be used in industries. Nevertheless, although this technique was developed in past 20 years, almost industries were not applied using this improvement because of high setup cost and a complicated design to setup the equipment. Therefore, further development should be study in these techniques in order to reduce the setup cost with a simple design to setup the equipment.

III. Improvement of Weld Line Strength and Warpage Using Thermal Assistance

Thermal assistance in injection molding process has become a popular technique to improve mechanical properties and aesthetic properties of the molded products. From reviewed summary in Table II, the most famous method for thermal assistance is Rapid Heat Cycle Molding (RHCM) that was raised to be investigated and used in years 2009 until now to improve of weld line strength and surface defects.

The concept of RHCM was shown in Fig. 5 where heaters were placed inside a mold along with cooling channel to heat and cold the mold rapidly [5]-[6], [21]-[22]. RHCM can greatly improve the aesthetic property of molded parts such as silver mark, weld line mark, flow mark, jetting mark, and swirl mark, and also improve the dimensional accuracy and gloss finish by maintaining the cycle time [22].

Wang *et al.* [22] studied on mechanical and aesthetic properties of the molded part by investigated on effects of the cavity surface temperature during filling phase injection molding process using RHCM. The materials used were PS, Acrylonitrile Butadiene Styrene (ABS), Polypropylene (PP), ABS/Polymethylmethacrylate (ABS/PMMA), Glass Fiber Reinforced Polypropylene (FRPP) and ABS/ PMMA/nano-CaCO₃. The result shows RCHM technique can improve the weld strength as well as suitable for all types of material compare to conventional method.

TABLE II
THE RESEARCHES ON IMPROVEMENT OF WELD LINE STRENGTH AND SURFACE QUALITY USING THERMAL ASSISTANCE

| No. | Authors | Improvement Method | Output | Results |
|-----|-------------------------|--------------------|--|---|
| 1 | Zhao <i>et al.</i> [5] | RHCM | Improve surface quality of large LCD TV panels | The surface appearance of the LCD TV panels was improved and the surface marks were absolutely removed. |
| 2 | Wang <i>et al.</i> [6] | RHCM | Mechanical and aesthetic properties | RHCM process can greatly increase the surface gloss of the part and the weld line factor can be improved with RHCM process both for ABS/PMMA and the 20% glass fiber-reinforced PP. |
| 3 | Wang <i>et al.</i> [22] | RHCM | Mechanical and aesthetic properties | RHCM technique can improve the weld strength as well as suitable for all types of material compare to conventional method. |
| 4 | Li <i>et al.</i> [21] | RHCM | Uniform temperature distribution on the cavity surface | The temperature distribution uniformity on cavity mold insert cavity surface was improved. |

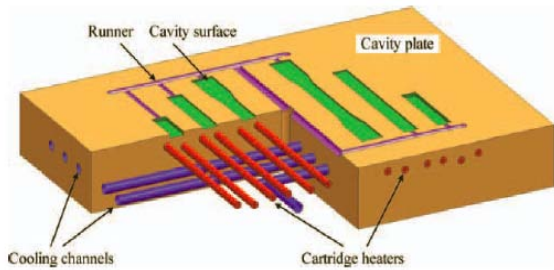


Fig. 5. Location for heaters and cooling line in RHCM [6]

Wang *et al.* [6] also applied RHCM to study on mechanical property which is tensile strength and aesthetic property which is surface appearance of the molded part. Mold was designed to allow the rapid heat function applied to the mold as shown in Fig. 5. The results show that surface appearance as well as weld line and jetting mark were absolutely improved, and the tensile strength of the molded parts were slightly increase.

Moreover, Zhao *et al.* [5] investigated an efficiency of electric heating technology applied to heat the mold surface during RHCM process. Two different of mold structures with and without separate cooling plate for a large LCD TV panel were designed and compared as shown in Figs. 6 and 7. As a result, the mold with separate cooling plate was better on heating efficiency compared to the mold without cooling plate. Furthermore, the surface appearance of the LCD TV panels was improved and the surface marks were absolutely removed.

Li *et al.* [21] had optimized the uniformity of temperature distribution on cavity surface of mold insert for RHCM mold. Latin Hypercube design of experiment method has used to identify the experiment samples for calculating the objective function. The distance between cooling channel centers were selected as design variable and optimized using Genetic Algorithm (GA) method.

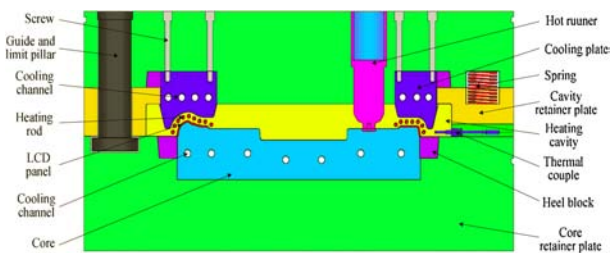


Fig. 6. Mold Structure with Separate Cooling Plate [5]

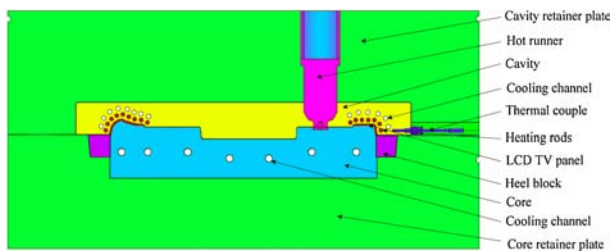


Fig. 7. Mold Structure without Cooling Plate [5]

After optimization, the temperature distribution uniformity on the stationary mold insert cavity surface was significantly improved.

Thermal assistance by using RHCM was an alternative for increasing product quality by enhancing its mechanical and aesthetic properties. More research on this technique need to be explored to get reliable and optimum results. The complex mold setup and requirement an extra cost need to be conceded for mold fabrication and injection process.

IV. Improvement of Weld Line Strength and Warpage Using Material Additive Method

The weld line strength has been investigated using material additive method where some additive material was mixed with hosts like fillers or other types of materials [7]-[8], [23]-[24]. The examples of fillers are talc, glass fiber, carbon nano fiber and TiO₂ nano particles were used for investigation. Summarized of review on this technique is shown in Table III.

The strength of weld lines was also studied by Ersoy *et al.* [23] with the new approach of filler addition onto incompatible polymer blend composites. PP, PA-6 and PP/PA-6 blend were used as injected materials in injection molding process. The mold was fabricated to commit the tensile, flexural and impact test specimen.

The weld line occurred was correspondingly observed by Scanning Electron Microscope (SEM). From the result, the strength of weld line for PP and PA-6 were decreased when some fillers were added.

The strength of weld line also was investigated by Seldan [24] using experimental design method using five types of thermoplastic material consist of PP with 40% talc, PPS with 40% Glass Fiber (GF), PA-6 with 35% GF, ABS, and PPO. Melt and mold temperatures, packing pressure, injection velocity were four parameters that focused in this experiment. The strength at location of weld line was measured using flexural and impact tests, and the weld line factor for each tests were calculated. The weld line factor was defined as strength of specimen with weld line divided by strength of specimen without weld line.

From the result, unfilled materials obtained the highest weld line factors with combination of high packing pressure and melt temperature, but low mold temperature. Pure PPO and ABS materials used resulted higher strength at weld line compare to glass fiber-reinforced and talc-filled materials that obtained the lowest. The weld line factor was not varied although some parameters were changed.

Furthermore, Xie and Ziegmann [7] studied of strength improvement at weld line location were used PP which blended respectively with Titanium Dioxide (TiO₂) nano particles and CNFs at difference weight fractions such as 10%, 20%, 30% and 35% mixed by co-screws internal mixing.

TABLE III
THE RESEARCHES ON IMPROVEMENT OF WELD LINE STRENGTH USING MATERIAL ADDITIVE METHOD

| No. | Authors | Improvement Method | Output | Results |
|-----|----------------------|--|--------------------|---|
| 1 | Ersoy and Nugay [23] | Addition of talc as inorganic filler to PP and Polyamide (PA)-6 | Weld line strength | When tact filler added to PP and PA-6, the strength of weld line decreased with the filler content. |
| 2 | Selden, R [24] | Addition of glass fiber and talc to some polymers. | Weld line strength | The used of pure PPO and ABS materials has resulted a higher strength at weld line compare to glass fiber-reinforced and talc-filled materials that obtained the lowest. The weld line factor was not varied although some parameters were changed. |
| 3 | Lu et al. [8] | Polymers blended with SMA | Weld line strength | The neat materials gave better results of weld line strength compare to blended polymers. |
| 4 | Xie and Ziegmann [7] | PP was compounded respectively with 10%, 20%, 30% and 35% of carbon nano fibers (CNFs) as well as TiO ₂ nano particles. | Weld line strength | CNFs or TiO ₂ were filled higher than 10% for nano composites samples, the strength of weld line was lower compared to the neat PP material. |

The mixed materials were produced using micro injection molding technique and then the tensile experiments were conducted in order to find the strongest blended materials. The results show the strength of specimens with weld lines blended with TiO₂ as well as CNFs, become lower than neat of PP when the CNFs was blended higher than 10%.

Lu et al. [8] focused on strength and morphology of weld line for PS/PA-6 blended with Poly (Styrene-co-maleic Anhydride) (SMA). The tensile and Izod impact strengths were conducted for PS, PS/PA-6 as well as PS/PA-6 blended with 2.5% and 7.5% of SMA materials after molded with injection molding process. As results, neat PS material shows the highest strength followed by PS/PA-6 blended with 7.5% SMA and the least was PS/PA-6. Although the additional of SMA to PS/PA-6 shown a better weld line strength, but the strength still lower compared to neat PS. Therefore, the neat material resulted better weld line strength compare to blended polymers.

Many researchers had founded that additive supplementary like filler did not improve the strength of molded part. From Table III, the trend was shows indicated that when some fillers have been added, the weld line strength will decrease. Effect of warpage deflection by using this method was not studied. So, this method of improvement for weld line strength is not suitable because strength of weld line was not improved when fillers added to the host materials.

V. Improvement of Weld Line Strength Using Parameters Optimization Method

Optimization of parameters method has been widely implemented in order to improve the mechanical strength at weld line location and surface quality in injection molding process. Therefore, many researchers had analyzed these problems and initiated various solutions to improve the strength of the molded parts [9]-[10], [25]-[30] as summarized in Table IV.

Liu et al. [25] studied the optimization on strength at weld line location. Taguchi method was used as an optimization tool for maximizing the strength.

Melt and mold temperatures, injection and packing pressures, injection speed and obstacle geometry were the selected parameters which had been chosen in the research. Location of the obstacle and tensile bar are shown in Fig. 8. The strength of the weld line was measured using a tensile tester. From the result, the weld line property of injection molded parts was significantly affected by melt and mold temperatures, as well as the size of the obstacles. The sizes of the obstacle were directly proportional to the strength of weld line on injection molded parts.

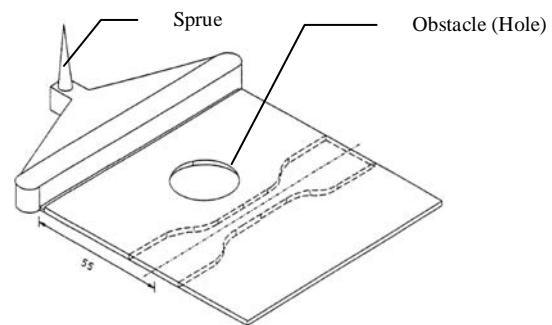


Fig. 8. Location of tester bar and obstacle [25]

Effect of weld line is not only at the strength, but also the appearance of the molded parts. Taguchi method was used by Li et al. [26] to investigate the weld lines formation by adjusting the parameters on molding process. Fig. 9 shows a sample of the molded part which is the right door of a copying machine used to obtain and improve the weld line. Adobe Photoshop and Matlab software were used to calculate a hue value of the sample after the pictures taken by digital camera.

From analysis, injection velocity, melt temperature, and injection pressures were founded as the main factors that affect the weld lines formation.

Taguchi also was applied by Ozcelik [9] to maximize the strength of the molded parts that have a weld line using PP as a thermoplastic material. The mold was constructed to form a weld line on the specimen as shown in Fig. 10. Effects on the mechanical strength of the molded parts with and without weld lines formation were studied on parameters set up such as packing and injection pressures, as well as melt temperature.

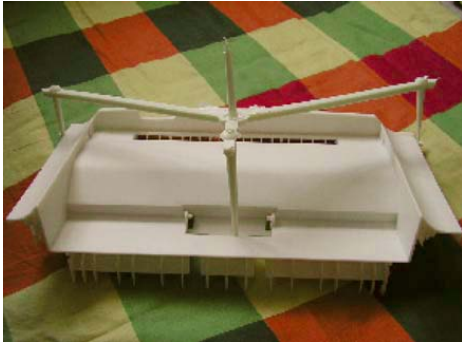


Fig. 9. Product with Injection System [26]

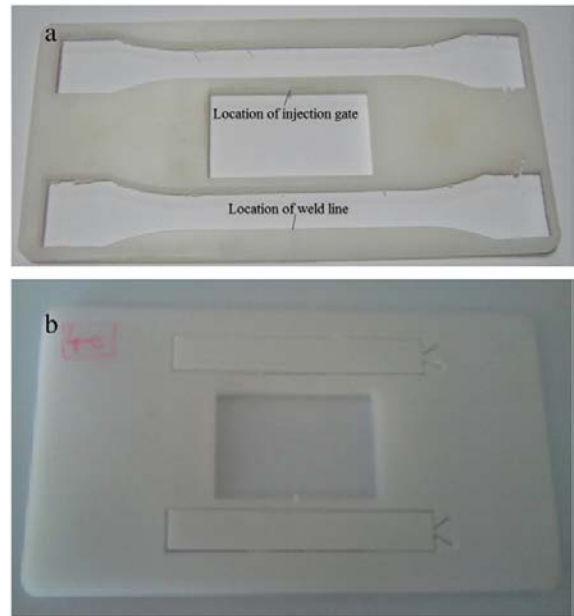
Charpy impact strength, maximum tensile load and extension at break were tested to obtain the mechanical properties of the molded part.

As a result, injection pressure was found as the most significant parameter affecting the maximum tensile load as well as extension at break, followed by melt temperature for molded part with and without weld line. Moreover, for Charpy impact strength, melt temperature and injection pressure molded with and without weld line was found as the significant parameters.

Furthermore, Wu and Liang [27] examined the injection molding parameters to increase the strength at weld line using Taguchi method. The molded parts were designed with different cross sections as shown in Fig. 11. HDPE and PP materials were used in the study. Six factors were selected to be investigated such as injection velocity, packing pressure and time, mold and melt temperatures and injection acceleration. From the analysis, speed of injection, mold and melt temperatures, and packing pressure found to be the most significant parameters affected the strength of the weld line.

Deng et al. [28] proposed two approaches for designing and applying of an optimization technique in order to minimize the total length of weld line formation, and arranging the weld line as far away as possible from specified critical regions on the molded part surface. Injection time, mold and melt temperatures, and gate location were factors used for the optimization.

The model of objective function was developed from the simulation results. Then, GA optimization method was applied to the modeled equation. The result shows that GA optimization method was the most effective method in optimizing the gate location and process parameters in order to minimize the length and position of the weld lines.



Figs. 10. Test specimen for (a) Tensile test, and (b) Impact test [9]

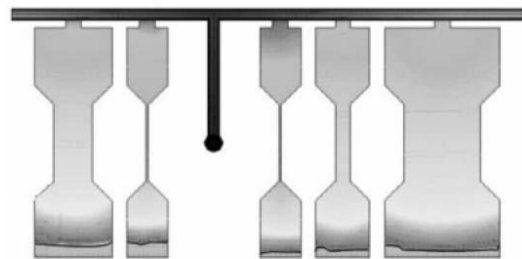


Fig. 11. Five difference geometry specimens for tensile test [27]

TABLE IV
The Researches On Improvement Of Weld Line Strength Using Parameters Optimization Method

| No. | Authors | Improvement Method | Output | Results |
|-----|-------------------|--------------------|---|---|
| 1 | Liu et al. [25] | Taguchi method | Weld line strength | The properties of weld line on the molded part was mostly affected by melt and mold temperatures setting |
| 2 | Li et al. [26] | Taguchi method | Appearance of weld lines | The main factors which influence the appearance of weld lines were injection velocity, melt temperature and injection pressure |
| 3 | B. Ozcelik [9] | Taguchi method | Mechanical properties | Extension at break and maximum tensile load were significantly affected by melt temperature and injection pressure for both of the molded part with and without weld line |
| 4 | Deng et al.[28] | GA method | Minimizing weld line length and by re-positioning the weld line | GA optimization method was the most effective method in optimizing the gate location and process parameters in order to minimize the length and position of weld lines. |
| 5 | Wu and Liang [27] | Taguchi method | Strength and appearance of weld lines | Injection speed, melt and mold temperatures, and packing pressure found to be the most significant parameters affected the strength of the weld line. |

GA also used by Wu et al. [10] as an optimization tool to increase the strength at weld line location. This research was focused on weld line behaviors by enhanced GA, called Distributed Multi-Population Genetic Algorithm (DMPGA).

A dominance-based constraint-handling technique and a master-slave distributed architecture were combined with optimization algorithm and simulation software to produce DMPGA. A digital photo outer frame of as shown in Fig. 12 was used as an optimization example to illustrate the capability of DMPGA. The result shows that weld line constraint was effectively decrease by using DMPGA technique.

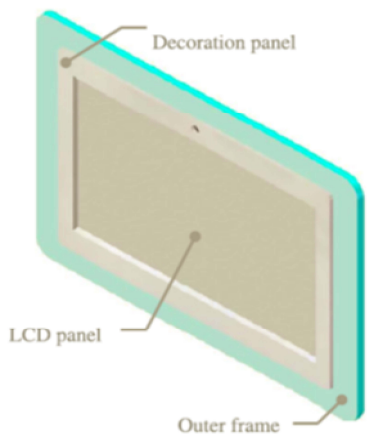


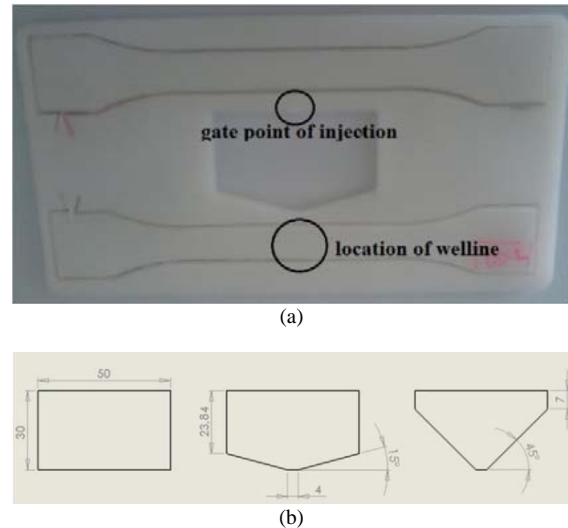
Fig. 12. Geometry of a Digital Photo Frame [10]

Weld line strength also studied by Ozcelik et al. [29] by adjustment of injection molding parameters and angles of obstacle geometry molded by PP material.

Figs. 13(a) and (b) show the obstacles position at the center of mold, and the obstacles edge angle of 0° , 15° and 45° respectively, which are designed to produce weld line. Izod impact (notched) and tensile strength on the specimens were measured in order to evaluate the mechanical properties of molded part.

Finite Element Analysis (FEA) also applied to study the mechanical properties of the molded part which effected by molecular orientation. As a result, an injection molded specimens that have the Obstacle Edge Angle (OEA) of 15° acquired higher tensile strength compared to the other obstacle angles.

Chen et al. [31] explored on effect of molding parameters on the strength of weld line for thin-wall plastic parts molded with ABS material. The related parameters include the melt and mold temperatures, injection speed and packing pressure were used to investigate the strength of specimen at different thickness which is 1.0mm, 1.2mm and 2.5mm. The geometry of tensile specimen was shown in Fig. 14. The tensile strength of single and double gates molded parts was compared. The result from Regression analysis shows that higher melt and mold temperatures, lower packing pressure and faster injection speed produced higher mechanical strength for specimen with and without weld line formation.



Figs. 13. (a) Location of obstacles, and (b) Obstacles design [29]

At that moment, the diffusion of molecular chains will tighten the surface bonding at the weld line location when higher melt and mold temperatures applied. Conversely, high packing pressure was applied to reduce the molecular bonding rate as well as increase the residual stress.

In addition, the thickness of the molded parts also shows significant effect on weld line strength.

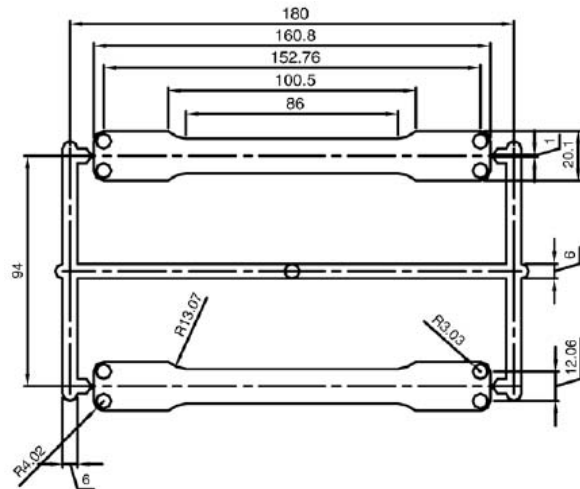


Fig. 14. Mold geometry of tensile test specimen [31]

Chun [32] analyzed the characteristic of the filling cavities in plastic injection molding process in order to study the formation of bubbles and weld lines. All experiments were conducted at mold and melt temperatures of 50°C and 260°C respectively, as well as injection time were specified at 1.5s for each experiment. Six different wall thicknesses were investigated.

The simulation model is shown in Fig. 15. Results from the analysis shows the long visible of weld line and a bubble formation for the mold designed and the part studied. By referring to Fig. 15, when the lip and side wall were modified to same thickness, the weld line

formation almost can be eliminated due to simultaneous filling pattern formed. Moreover, the locations of gate also influence the filling pattern and should be relocated to gate position number 2 as shown in Fig. 15, in order to get the uniform filling of the cavities. Chun [32] also founded, when thickness of floor and side wall were increased, the flow of polymer in the side wall relative to the lip area become smooth and air was allowed to vent naturally at the top. The molded parts should have a good mechanical property and free from defects in order to increase the quality of parts produced. Othman et al. [33] used a numerical simulation (Cadmould) which employed to investigate the influence of gate sizes as well as the injection molding parameters towards the formations of weld lines using ABS material.

Double gates mold was used to present the weld line defects as shown in Fig. 16. The result shows that the smaller gate size produced less weld line in plastic parts, which was verified through simulation process.

The optimal parameter setting that produced good tensile strength specimens was validated experimentally in this research. The improvement on the weld lines defects by optimizing injection molding parameters have been summarized in Table IV. There are several improvement methods can be selected to improve the strength of the weld line in order to optimize the quality of the product produced. This improvement technique had been also applied to solve the warpage issues [11]–[14], [30]–[41].

VI. Improvement of Warpage Problem Using Parameters Optimization Method

Warpage is one of common defect in plastic injection molded parts. Warpage of a product is measured in x-axis, y-axis, z-axis or all direction depending on requirement of the product used. Warpage defect was categorized in aesthetic properties in injection molding process [3].

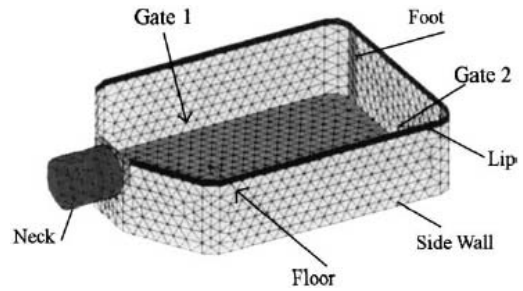


Fig. 15. Terminology of the component used [32]

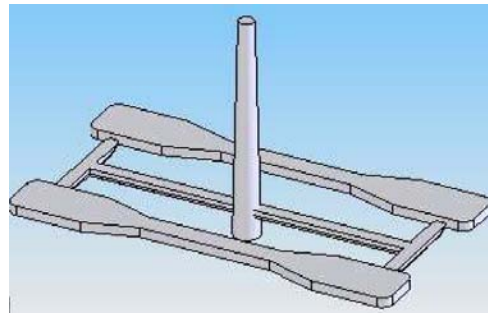


Fig. 16. Double gates mold that used by Othman et al. [33]

The aesthetic properties were important in order to show the appearance of a product developed as well as to ensure the product ability to be assembled well. The researches on improvement of warpage using parameters optimization method were summarized in Table V.

Previous researchers proved that the value of warpage on the molded parts can be reduced by optimization of the injection molding parameters.

One of the optimization method which widely used in injection molding process is Taguchi method [37]–[40], [42]–[43]. This method is used to get the best combination parameters in order to minimize the warpage. Tang et al. [39] used Taguchi method in order to improve warpage by optimizing a set of parameters selected for thin plate plastic component.

TABLE V
SUMMARY OF IMPROVEMENT OF WARPAGE USING PARAMETERS OPTIMIZATION METHOD

| No. | Authors | Improvement Method | Output | Results |
|-----|-----------------------------|--|---|---|
| 1 | Tang et al. [39] | Taguchi method | Reducing warpage | Melt temperature found as the most significant factor on warpage formation. |
| 2 | Shayfull et al. [40] | Taguchi method | Reducing warpage | The cavity and core mold temperatures were the most significant factor affecting the warpage in ultra-thin shell part. |
| 3 | Erzurumlu and Ozelik [37] | Taguchi method | Warpage and sink index | Warpage and sink index were improved after been optimized using Taguchi method for all material used varied from 7.1% to 69.2%. |
| 4 | Yin et al. [35] | Back Propagation Neural Network (BPNN) | Prediction and optimization of Warpage | Warpage improved as much as 32.99% from initial value 2.358 mm after optimized by BPNN method. |
| 5 | Gao and Wang [34] | Kriging model | Reducing warpage | After optimization base on Kriging model, the result shows that warpage value was reduced from 0.811mm to 0.134mm. |
| 6 | Ozelik and Erzurumlu [11] | Artificial Neural Network (ANN) and GA | Reducing warpage | Warpage was improved by about 51% after been optimized using ANN and GA method. |
| 7 | Kurtaran and Erzurumlu [36] | RSM and GA | Reducing warpage | Warpage was improved by about 46% after been optimization of bus ceiling lamp product |
| 8 | Deng et al. [12] | Mode-Pursuing Sampling (MPS) method and GA | Minimization of injection molding warpage | Mold and melt temperatures, injection time and packing pressure were applied as 69°C, 280°C, 0.8s and 70% respectively to obtain the lowest warpage 0.81mm. |

From the experiment results, melt temperature was found as the most effective factor on formation of warpage while filling time was slightly influenced. Erzurumlu and Ozcelik [37] also applied Taguchi to minimize warpage and sink index on thin shell plastic component. The selected materials were PC/ABS, POM, and PA66. Orthogonal arrays of Taguchi, the Signal-to-Noise (S/N) ratio as well as ANOVA were applied to improve the aesthetic properties of the molded part that were warpage and sink index by optimizing the process condition of injection molding.

Validation analyses with the optimal levels of process parameters were tested in order to evaluate the result from Taguchi analysis. As a result, warpage and sink index were improved after been optimized using Taguchi method for all material used varied from 7.1% to 69.2%.

Shayfull et al. [40] used Taguchi and ANOVA methods to improve the warpage on ultra-thin shell parts using a three plate mold with a pin point gating system as shown in Fig. 17. Experiments were simulated using Autodesk Moldflow Insight (AMI) software in order to evaluate warpage with and without considering the difference effect on mold temperatures on the ultra-thin shell molded parts. PC/ABS was used as a thermoplastic material of the molded parts. Results showed that the mold temperature was the most significant factor that affected the warpage while the temperature difference on the core and cavity plates was not significant.

Furthermore, Ozcelik and Sonat [41] also studied on thin shell design of product using PC/ABS thermoplastic material to reduce the warpage that affected by injection molding parameters as well as types of material used on the molded part using Taguchi method.

In addition, the forces that specified at the top surface of the cell phone cover were analyzed using general structural analysis.

Moldflow plastic insight (MPI) 4.0 software and CATIA V5R12 were used to determine the warpage and force result respectively. Packing pressure found as the most important parameter on the warpage. Results from structural analysis show that the strongest materials are 15% carbon fiber reinforced PC/ABS followed by 15% carbon fiber reinforced ABS, PC, PC/ABS and ABS. The most critical point on the molded part was at point 2 as shown in Fig. 18. Taguchi method also used by Huang and Tai [44] to investigate a thin shell from PC/ABS thermoplastic material to determine the best setup of injection molding parameters with the intention of eliminated warpage. C-MOLD software has been used as an experimental tool to simulate the warpage on injection processes.

The design of part completed with feed system and cooling line are shown in Fig. 19.

After optimization, packing pressure has been identified as the most influence factor toward warpage which shows 15.59%, followed by mold and melts temperatures, and lastly was packing time at 9.61%.

Nevertheless, gate dimension and filling time were slightly influence the warpage on the molded part.

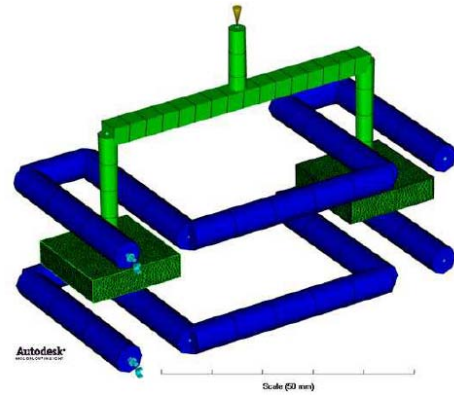


Fig. 17. Ultra-thin shell part in three-plate mold [40]

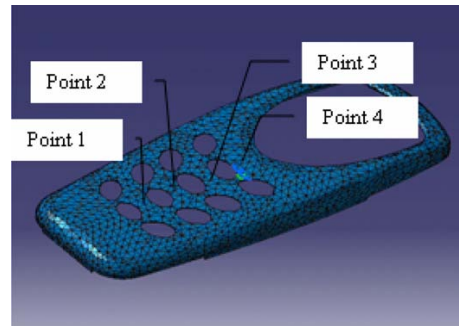


Fig. 18. Critical point at Cell thin shell phone cover [41]

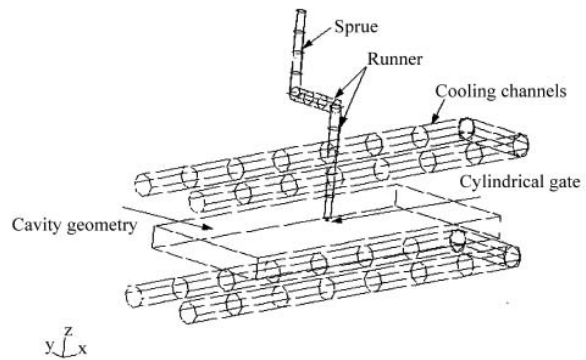


Fig. 19. Plastic part design complete with cooling line and feed system [44]

Fathullah et al. [38] also used Taguchi and ANOVA method to improve warpage issue on thin shallow plastic parts as shown in Fig. 20. Three types of polymer materials are selected for experimentations such as PP, ABS/PC and ABS, that molded with three plate mold using pin point gate. The result shows that packing time was the most significant factor for all materials but packing pressure found to be the least significant factor for warpage formations.

On the other work, Yin et al. [35] applied a BPNN method for prediction of model and optimization on warpage for main variables of processing parameters including mold and melt temperatures, packing pressure and time, and cooling time that had been analyzed using AMI software. Automobile glove compartment cap was developed as a part and modeled as shown in Fig. 21.

From the results, BPNN method has a capability to predict a mathematical model relationship between input parameters and warpage as an output within minimum of 2% errors. The warpage then optimized by 32.99% compared to before optimization process was 2.358mm and reduced to 1.58mm. Furthermore, cooling time was also been shortened by 50% from 20s to 10s compared to initial result. In addition, Gao and Wang [34] investigated the relationship between warpage and the injection molding parameters based on model of prediction that build by using Kriging model. AMI software was operated to analyze the warpage on a cellular phone cover as shown in Fig. 22.

Mold and melt temperatures, packing pressure and injection time, were considered as the design variables.

After optimization base on Kriging model, the result shows that warpage value was reduced from 0.811mm to 0.134mm and the injection time has the most important factor effect on warpage of the molded part.

Ozcelik and Erzurumlu [11] studied on warpage minimization using Artificial Neural Network (ANN) that interfaced with an effective GA for thin shell plastic product as shown in Fig. 23. Packing and cooling times, mold and melt temperatures, packing pressure, runner type and gate location had been selected as the variables parameters and was simulated using AMI software.

The most important process parameters contributing to warpage were determined using finite element analysis and ANOVA methods. The result from ANOVA indicates that packing pressure was the most influence factor for warpage by 33.7% followed by mold and melt temperatures that 21.6% and 20.5% respectively, and the least was gate location by 1.3%.

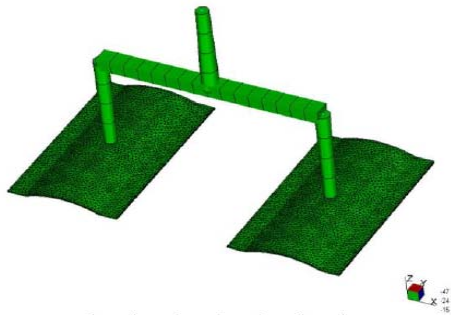


Fig. 20. Thin shallow plastic parts [38]

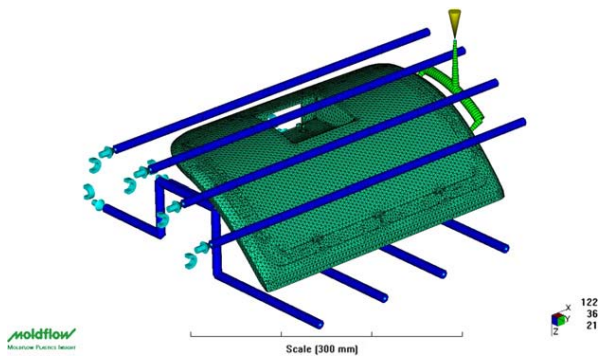


Fig. 21. FE model of the automobile glove compartment cap [35]

ANN model also predict that packing pressure was the most influence parameter follow by mold and melt temperatures. The warpage has improved about 51% after optimized the injection molding parameters using GA. Chen and Lin [13] also used ANN and GA method to analyze the warpage of multi-cavity plastic injection molding parts. The results indicate that the value of warpage were slightly lower than the traditional GA method and CAE simulation. Example of FE component used for the study was shown in Fig. 24.

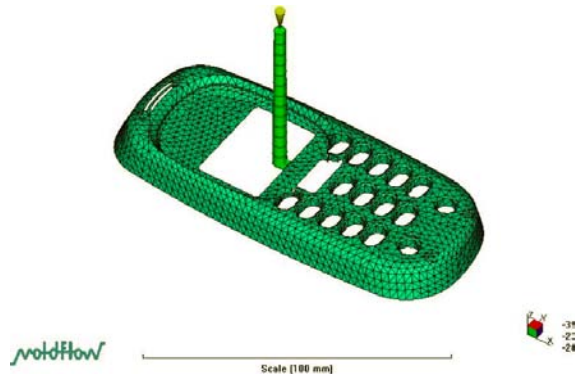


Fig. 22. FE for Cellular phone cover [34]

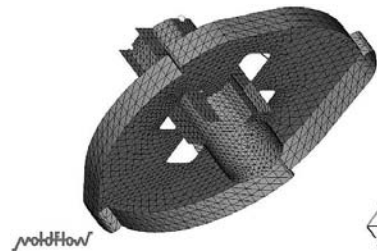


Fig. 23. Thin shell button base for washing machine component [11]

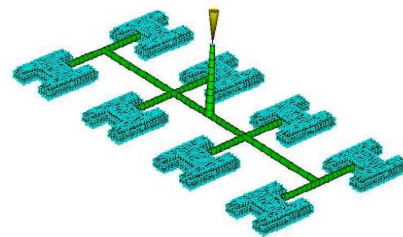


Fig. 24. Multi-cavity plastic components [13]

Kurtaran and Erzurumlu [36] focused on minimization of warpage on thin shell plastic parts by integrating statistical DOE, RSM and GA methods using Finite Element Analysis (FEA).

Optimum process condition parameters were determined to reach the minimum warpage of bus ceiling lamp as shown in Fig. 25. Packing and cooling times, mold and melt temperatures and packing pressure were considered as input factors. A relationship model between input factors and warpage as an output was created using RSM technique. Afterward, GA method was applied to find the optimum value of input parameters.



Fig. 25. Dimensions of bus ceiling lamp [36]

Together, ANOVA method was used to determine the most important process parameters influencing warpage.

Results from ANOVA indicates that the most significant process parameter that influence warpage was packing pressure followed by mold and melt temperatures, packing time, and cooling time. GA has reduced 46% the warpage of the initial model that created using RSM.

VII. Improvement of Warpage Problem and Weld Line Strength Using Multi Objective of Parameters Optimization Method

Nowadays, multi objectives optimization method has become popular for engineering application in over the world. The main objectives of product optimization was to produce quality products by minimizing the part defects [45]. Multi objectives optimization was occasionally used in injection molding process. The multi objectives method may be used for optimizing more than one output such as warpage and weld line, by a set of same input parameter. Table 6 shows the previous researches using multi objective optimization in injection molding process.

Yin et al. [14] investigated the warpage and clamp force as the objectives to be optimized using BP and GA methods. A BP model was developed base on orthogonal experimental method that had been run by Moldflow software. Mold and melt temperature, packing and cooling times, and packing pressure were considered as input parameters.

Plastic cover as shown in Figure 26 was considered as a plastic part to be optimized. The study proves that the proposed optimization method was able to suggest the process parameters accurately and effectively to minimize the warpage on the molded parts.

Furthermore, Wang et al. [15] studied on temperature uniformity, heating efficiency and mold strength using RSM integrated with Particle Swarm Optimization (PSO) multi objective methods on RHCM. Three factors describing layout and scale of the heating channels, and three levels of Box-Behnken experiment was used in this study. ANSYS software comprising thermal and structural analyses were carried out to obtain the corresponding values of the objectives for flat television frame as shown in Fig. 27. RSM was utilized to analyze the effect of the design parameters and construct the mathematical models to describe the relationship between input parameters and objectives by regression analysis. After optimization, the cavity surface temperature uniformity was improved by 80.97% and at the same time required heating time was reduced by 61.70% as well as the structural strength of the cavity block was also improved.

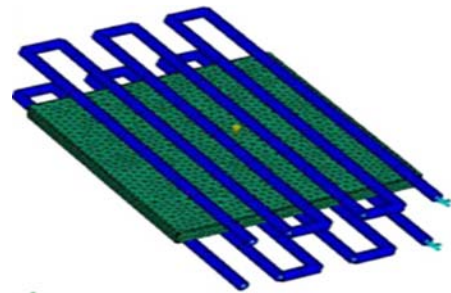


Fig. 26. FE model of plastic cover [14]

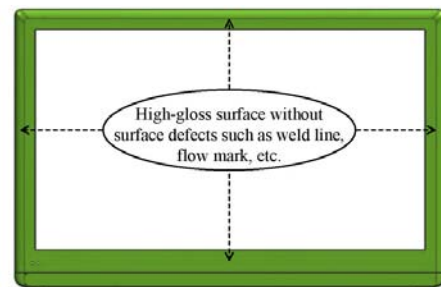


Fig. 27. Flat television frame model [15]

TABLE VI
SUMMARY OF IMPROVEMENT OF WARPAGE USING MULTI OBJECTIVES OF PARAMETERS OPTIMIZATION METHOD

| No. | Authors | Improvement Method | Output | Results |
|-----|--------------------|---|--|---|
| 1 | Yin et al. [14] | Back Propagation (BP) neural-network and GA | Warpage and clamp force | The proposed optimization method can adjust the process parameters accurately and effectively to satisfy the demand of real manufacture. |
| 2 | Wang et al. [15] | RSM and particle swarm optimization | Heating efficiency, temperature uniformity and mold strength | Thermal efficiency and temperature uniformity of the RHCM mold can be greatly improved with the optimum design variables for the layout of the heating/cooling channels. |
| 3 | Farshi et al. [46] | Sequential simplex method | Warpage and shrinkage | Compromise recommendation can be offered for a near optimum shrinkage in combination with optimum warpage involving low cycle time and low residual stresses simultaneously |

Farshi et al. [46] also used a multi objectives optimization by examined warpage and shrinkage defects of plastic injection molding parts using sequential simplex optimization method. Moldflow software had been used to simulate the molding experiments for an automotive venti duct grid as shown in Fig. 28.

Variables parameter used in this experiment were mold and melt temperatures, pressure switch-over, packing pressure, packing time, and coolant inlet temperature.

The result shows that the warpage and shrinkage were minimized up to 2,086mm and 5.81 simultaneously. At the same time, optimizations have shortened the cycle time and less residual stresses.

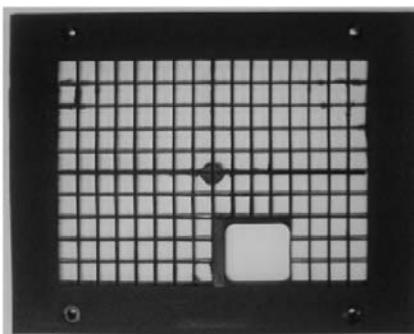


Fig. 28. Design for Automotive venti duct grid [46]

The optimization using multi objectives to improve warpage as well as strength at weld line were never studied by other researchers in order to improve quality of the molded part. As the plastic injection parts are categorized as a finish product before assembly, the aesthetic and mechanical properties of products are very important.

Thus, optimization for warpage (aesthetic properties) and strength at weld line (mechanical properties) should be investigated.

VIII. Conclusion

From the review have been done, it can be seen that, there are many methods have been used to improve the strength of the weld line and the warpage of the molded parts such as mechanical assistance, thermal assistance, material additive and optimization of injection molding parameters. Mechanical and thermal assistance in injection molding process was a successful technique to improve the strength of molded parts as well as strength at weld line position but the warpage problem has not been considered in these types of improvement.

The disadvantages of these techniques are higher setup cost, complex mold design and require higher knowledge during operation. Thus, these techniques were not widely used. The additive supplementary such as filler did not improve the strength of molded parts and the previous researches have founded that when some filler have added, the weld line strength was decreased. Effect of warpage not been studied using this method.

Thus, is not appropriate to apply this method in order to improve the strength of the weld line. The weld line improvement by optimizing the injection molding parameters was an alternative technique as well as simply and easy to be implemented. There are many optimization tools that can be selected to improve the strength of weld line as well as warpage in order to optimize the product quality by using single and multiple objectives. The improvement on the strength of weld lines and warpage of the molded parts should be done parallel especially for the part which required the strength for functionality and it is never studied by other researches in order to improve component quality.

Because of plastic injection molding parts were categorized as a finish component before assembly, the aesthetic and mechanical properties of product are very important. Thus, optimization for both warpage (aesthetic properties) and strength at weld line (mechanical properties) should be further investigated.

References

- [1] J. G. Kovács and B. Sikló, "Experimental validation of simulated weld line formation in injection moulded parts," *Polymer Testing*, vol. 29, no. 7, pp. 910–914, Oct. 2010.
- [2] T. A. O. C. Chang and E. Faison, "Optimization of Weld Line Quality in Injection Molding Using an Experimental Design Approach," vol. 3, no. 2, pp. 61–66, 1999.
- [3] A. M. Tom, A. Kikuchi, and J. P. Coulter, "Experimental Determination of Optimized Vibration-assisted Injection Molding Processing Parameters for Atactic Polystyrene," *Special Molding Techniques*, pp. 245–252, 1980.
- [4] A. Kikuchi, J. P. Coulter, D. Angstadt, and A. Pinarbasi, "Localized Material and Processing Aspects Related to Enhanced Recycled Material Utilization Through Vibration-Assisted Injection Molding," *Journal of Manufacturing Science and Engineering*, vol. 127, no. 2, p. 402, 2005.
- [5] G. Zhao, G. Wang, Y. Guan, and H. Li, "Research and application of a new rapid heat cycle molding with electric heating and coolant cooling to improve the surface quality of large LCD TV panels," *Polymers for Advanced Technologies*, vol. 22, no. 5, pp. 476–487, May 2011.
- [6] G. Wang, G. Zhao, and Y. Guan, "Thermal response of an electric heating rapid heat cycle molding mold and its effect on surface appearance and tensile strength of the molded part," *Journal of Applied Polymer Science*, p. n/a–n/a, Jul. 2012.
- [7] L. Xie and G. Ziegmann, "Mechanical properties of the weld line defect in micro injection molding for various nano filled polypropylene composites," *Journal of Alloys and Compounds*, vol. 509, no. 2, pp. 226–233, Jan. 2011.
- [8] C. Lu, S. Guo, L. Wen, and J. Wang, "Weld line morphology and strength of polystyrene/polyamide-6/poly(styrene-co-maleic anhydride) blends," *European Polymer Journal*, vol. 40, no. 11, pp. 2565–2572, Nov. 2004.
- [9] B. Ozelcik, "Optimization of injection parameters for mechanical properties of specimens with weld line of polypropylene using Taguchi method," *International Communications in Heat and Mass Transfer*, pp. 7–12, May 2011.
- [10] C.-Y. Wu, C.-C. Ku, and H.-Y. Pai, "Injection molding optimization with weld line design constraint using distributed multi-population genetic algorithm," *The International Journal of Advanced Manufacturing Technology*, vol. 52, no. 1–4, pp. 131–141, May 2010.
- [11] B. Ozelcik and T. Erzurumlu, "Comparison of the warpage optimization in the plastic injection molding using ANOVA, neural network model and genetic algorithm," *Journal of Materials Processing Technology*, vol. 171, no. 3, pp. 437–445, Feb. 2006.

- [12] Y.-M. Deng, Y. Zhang, and Y. C. Lam, "A hybrid of mode-pursuing sampling method and genetic algorithm for minimization of injection molding warpage," *Materials & Design*, vol. 31, no. 4, pp. 2118–2123, Apr. 2010.
- [13] W. J. Chen and J. R. Lin, "Design of Optimization Parameters with Hybrid Genetic Algorithm Method in Multi-Cavity Injection Molding Process," *Advanced Materials Research*, vol. 463–464, pp. 587–591, Feb. 2012.
- [14] F. Yin, H. Mao, and L. Hua, "A hybrid of back propagation neural network and genetic algorithm for optimization of injection molding process parameters," *Materials & Design*, vol. 32, no. 6, pp. 3457–3464, Jun. 2011.
- [15] G. Wang, G. Zhao, H. Li, and Y. Guan, "Multi-objective optimization design of the heating/cooling channels of the steam-heating rapid thermal response mold using particle swarm optimization," *International Journal of Thermal Sciences*, vol. 50, no. 5, pp. 790–802, May 2011.
- [16] a. Kikuchi, J. P. Coulter, and R. R. Gomatam, "Assessing the effect of processing variables on the mechanical response of polystyrene molded using vibration-assisted injection molding process," *Journal of Applied Polymer Science*, vol. 99, no. 5, pp. 2603–2613, Mar. 2006.
- [17] Y. Li and K. Shen, "Improving the Mechanical Properties of Polypropylene via Melt Vibration," *Journal of Applied Polymer Science*, vol. 109, pp. 90–96, 2008.
- [18] S.-C. Nian and M.-S. Huang, "Enhancement of weld line mechanical strength using a novel ejector-pins compression system," *Journal of Applied Polymer Science*, p. n/a–n/a, Jul. 2012.
- [19] C. Lu, X. Yu, and S. Guo, "Ultrasonic improvement of weld line strength of injection-molded polystyrene and polystyrene/polyethylene blend parts," *Polymer Engineering & Science*, vol. 45, no. 12, pp. 1666–1672, Dec. 2005.
- [20] C. Lu, X. Yu, and S. Guo, "The Mechanism of Ultrasonic Improvement of Weld Line Strength of Injection Molded Polystyrene and Polystyrene / Polyethylene Blend Parts," *Journal of Polymer Science*, vol. 44, pp. 1520–1530, 2006.
- [21] X.-P. Li, G.-Q. Zhao, Y.-J. Guan, and M.-X. Ma, "Optimal design of heating channels for rapid heating cycle injection mold based on response surface and genetic algorithm," *Materials & Design*, vol. 30, no. 10, pp. 4317–4323, Dec. 2009.
- [22] G. Wang, G. Zhao, and X. Wang, "Effects of cavity surface temperature on mechanical properties of specimens with and without a weld line in rapid heat cycle molding," *JOURNAL OF MATERIALS&DESIGN*, vol. 46, pp. 457–472, 2013.
- [23] O. G. Ersoy and N. Nugay, "A new approach to increase weld line strength of incompatible polymer blend composites: selective filler addition," *Polymer*, vol. 45, no. 4, pp. 1243–1252, Feb. 2004.
- [24] R. Selden, "Effect of Processing on Weld Line Strength in Five Thermoplastics," vol. 37, no. 1, 1997.
- [25] S.-J. Liu, J.-Y. Wu, J.-H. Chang, and S.-W. Hung, "An experimental matrix design to optimize the weldline strength in injection molded parts," *Polymer Engineering & Science*, vol. 40, no. 5, pp. 1256–1262, May 2000.
- [26] H. Li, Z. Guo, and D. Li, "Reducing the effects of weldlines on appearance of plastic products by Taguchi experimental method," *The International Journal of Advanced Manufacturing Technology*, vol. 32, no. 9–10, pp. 927–931, Apr. 2006.
- [27] C.-H. Wu and W.-J. Liang, "Effects of geometry and injection-molding parameters on weld-line strength," *Polymer Engineering & Science*, vol. 45, no. 7, pp. 1021–1030, Jul. 2005.
- [28] Y.-M. Deng, D. Zheng, B.-S. Sun, and H.-D. Zhong, "Injection Molding Optimization for Minimizing the Defects of Weld Lines," *Polymer-Plastics Technology and Engineering*, vol. 47, no. 9, pp. 943–952, Aug. 2008.
- [29] B. Ozcelik, E. Kuram, and M. M. Topal, "Investigation the effects of obstacle geometries and injection molding parameters on weld line strength using experimental and finite element methods in plastic injection molding," *International Communications in Heat and Mass Transfer*, vol. 39, no. 2, pp. 275–281, Feb. 2012.
- [30] B. Sun and Z. Wu, "Optimization of injection molding process parameters based on Response Surface Methodology and genetic algorithm," *2010 2nd International Conference on Computer Engineering and Technology*, pp. V5–397–V5–400, 2010.
- [31] C.-S. Chen, T.-J. Chen, R.-D. Chien, and S.-C. Chen, "Investigation on the weldline strength of thin-wall injection molded ABS parts," *International Communications in Heat and Mass Transfer*, vol. 34, no. 4, pp. 448–455, Apr. 2007.
- [32] D. H. Chun, "Cavity filling analyses of injection molding simulation: bubble and weld line formation," *Journal of Materials Processing Technology*, vol. 90, no. 89–90, pp. 177–181, 1999.
- [33] M. H. Othman, S. Shamsudin, S. Hasan, and M. N. A. Rahman, "The Effects of Injection Moulding Processing Parameters and Mould Gate Size towards Weld Line Strength," *Advanced Materials Research*, vol. 488–489, pp. 801–805, Mar. 2012.
- [34] Y. Gao and X. Wang, "An effective warpage optimization method in injection molding based on the Kriging model," *The International Journal of Advanced Manufacturing Technology*, vol. 37, no. 9–10, pp. 953–960, Jun. 2007.
- [35] F. Yin, H. Mao, L. Hua, W. Guo, and M. Shu, "Back Propagation neural network modeling for warpage prediction and optimization of plastic products during injection molding," *Materials & Design*, vol. 32, no. 4, pp. 1844–1850, Apr. 2011.
- [36] H. Kurtaran and T. Erzurumlu, "Efficient warpage optimization of thin shell plastic parts using response surface methodology and genetic algorithm," *The International Journal of Advanced Manufacturing Technology*, vol. 27, no. 5–6, pp. 468–472, Apr. 2005.
- [37] T. Erzurumlu and B. Ozcelik, "Minimization of warpage and sink index in injection-molded thermoplastic parts using Taguchi optimization method," *Materials & Design*, vol. 27, no. 10, pp. 853–861, Jan. 2006.
- [38] M. Fathullah, Z. Shayfull, N. A. Shuaib, and S. M. Nasir, "Optimal Process Conditions of Warpage with Thin-Shallow Features Molded with Pin-Point Gating System II . Design III . Materials and Methods," *International Review of Mechanical Engineering*, vol. Volume 5, no. Issue 7, November 2011, pp. 1295–1301, 2011.
- [39] S. H. Tang, Y. J. Tan, S. M. Sapuan, S. Sulaiman, N. Ismail, and R. Samin, "The use of Taguchi method in the design of plastic injection mould for reducing warpage," *Journal of Materials Processing Technology*, vol. 182, no. 1–3, pp. 418–426, Feb. 2007.
- [40] Z. Shayfull, M. Fathullah, S. Sharif, S. M. Nasir, and N. A. Shuaib, "Warpage Analysis on Ultra-Thin Shell by Using Taguchi Method and Analysis of Variance (ANOVA) for Three-Plate Mold," vol. 5, no. September, pp. 1116–1124, 2011.
- [41] B. Ozcelik and I. Sonat, "Warpage and structural analysis of thin shell plastic in the plastic injection molding," *Materials & Design*, vol. 30, no. 2, pp. 367–375, Feb. 2009.
- [42] Y.-K. Yang, J.-R. Shie, H.-T. Liao, J.-L. Wen, and R.-T. Yang, "A Study of Taguchi and Design of Experiments Method in Injection Molding Process for Polypropylene Components," *Journal of Reinforced Plastics and Composites*, vol. 27, no. 8, pp. 819–834, Jan. 2008.
- [43] H. Oktem, T. Erzurumlu, and I. Uzman, "Application of Taguchi optimization technique in determining plastic injection molding process parameters for a thin-shell part," *Materials & Design*, vol. 28, no. 4, pp. 1271–1278, Jan. 2007.
- [44] M.-C. Huang and C.-C. Tai, "The effective factors in the warpage problem of an injection-molded part with a thin shell feature," *Journal of Materials Processing Technology*, vol. 110, no. 1, pp. 1–9, Mar. 2001.
- [45] R. T. Marler and J. S. Arora, "Survey of multi-objective optimization methods for engineering," *Structural and Multidisciplinary Optimization*, vol. 26, no. 6, pp. 369–395, Apr. 2004.
- [46] B. Farshi, S. Gheshmi, and E. Miandoabchi, "Optimization of injection molding process parameters using sequential simplex algorithm," *Materials & Design*, vol. 32, no. 1, pp. 414–423, Jan. 2011.

Authors' information

¹School of Manufacturing Engineering, Universiti Malaysia Perlis, Malaysia.

²Green Design and Manufacture Research Group, Center of Excellence Geopolymer and Green Technology (CEGeoGTech), School of Materials Engineering, Universiti Malaysia Perlis, 01000 Kangar, Perlis, Malaysia.



S. M. Nasir is a Teaching Engineer in Universiti Malaysia Perlis (UniMAP), Malaysia. He obtained his Bachelor Degree in Mechanical Engineering from Universiti Sains Malaysia (USM), Malaysia and currently undergoing a postgraduate research in UniMAP in the field of injection molding process. He is an expert in teaching and doing research in the field of

injection molding processes and simulations. S.M.Nasir also actively involves with Engineering Professional Bodies in Malaysia such as Board of Engineers, Malaysia (BEM) and Institution of Engineers, Malaysia (IEM) until today.

Design of a Fuzzy Logic Approach for Optimization of Fracture Length in Hydrofracturing Technique

B. Guruprasad, A. Ragupathy, T. S. Badrinarayanan, E. Sambath

Abstract – This paper presents the application of a fuzzy logic controller and Response surface methodology in developing the fracture length as a mechanical property in hydrofracturing technique. In this study, a fuzzy logic controller was used to explore functional relationships between variables to determine the effect of operating parameter, and to achieve optimal process conditions. In addition, the most relevant input variables are identified through analysis of variance using Design expert software (version 8.0) and implemented in the construction of an appropriate fuzzy logic controller model. The experimental results indicate that the combination of response surface methodology and a fuzzy logic controller makes a robust, effective and efficient approach using Matlab / Simulink tool box software. **Copyright © 2013 Praise Worthy Prize S.r.l. - All rights reserved.**

Keywords: Fuzzy Logic Control, RSM, Hydro Fracturing; Fracture Length, Analysis of Variance

I. Introduction

The analysis of the hydro-mechanical behavior of rock masses remains an important topic in rock mechanics, due to it being a critical phenomenon in ongoing challenging issues such as tunneling under high groundwater pressures, extraction of hydrocarbons from deep, pressurized petroleum reservoirs, and underground nuclear waste disposal.

Despite continuing and extensive efforts, such analysis continues to be difficult. Hydro-mechanical response in a rock mass is identified as the interaction between the solid phase of the rock materials and any interstitial fluid [1]. This technique involves pumping a fluid under pressure into a borehole. This pressurized fluid introduced into the borehole produces stress concentration in the surrounding rock causing the development of fractures due to micro mechanical effects [2]. Because of the heterogeneity of the material properties, rock structure and in situ stress state, the hydraulic fracturing process is highly complex [3]. A common difficulty in the hydraulic fracturing process in the real time is in observation and measurement of the fractures that develop beneath of the earth. Generally, the induced fracture geometry is measured by cutting the sample after the test [4]-[6] or by using an acoustic monitoring system [7]-[8]. This method gives valuable results but limitations are there. The final results are observed by cutting the samples after the test.

The resolution of the acoustic method is currently insufficient to capture details of the fracture propagation process.

As a result, laboratory experiments on hydraulic fracturing in transparent materials have also been performed. These studies allowed the visualization in real time of the developing geometry of the fracture [9]-[10]

and the direction of fracture propagation [11]-[13].

Commonly used transparent geometrical analogues for fracturing are poly methyl methacrylate (PMMA, acrylic) [14]-[15].

Since, the Fracture behavior is hard to predict because the relationship between stress and permeability is complex and highly dependent on pressure, temperature and Injection hole diameter.

The previous works mainly focused on identification and quantification of hydro fracturing process. Due to its nature, variations, it is common if a fracture length in hydro fracturing process appears to be nonlinear. The hydro fracturing process is a special process driven by numerous operating parameters that are interrelated for many of them and that have to be controlled in order to get maximize the fracture length as a mechanical property. It is ideal to find optimized process parameters in hydro fracturing technique with a low cost and good performance for a precise output; it is very difficult to find it among conventional methods.

However, searching for a suitable mathematical model to connect input and output variables is not easy. Hence, the development of a systematic model is needed.

Traditionally, controllable variables for hydro fracturing process are implemented through trial and error but the consumption cost does not permit the reaching of optimized values.

Moreover, in order to maximize the fracture length by numerical modeling of involved physical phenomena is complex and complicated. Recently, several techniques [16]-[26] such as design of experiment, artificial neural network and fuzzy logic control, etc can be implemented to reach this goal. of the hydro fracturing process, fuzzy logic control has seldom being in use while characterizing the nature of responses.

In this paper, a fuzzy logic control with design of experiments will be developed to maximize the fracture length and productivity in the hydro fracturing process. The Response surface methodology of experiments was the preferred approach to develop a means of applying orthogonal arrays of statistically designed experiments to efficiently obtain the results with the fewest possible experiments [27]-[29]. Additionally, a fuzzy logic control has been used to model complicated and uncertain problems. It is a knowledge-based methodology, which has several advantages in developing improvements in quality and productivity for the hydro fracturing process. Its applications can be seen in decision-making automatic control, and manufacturing systems.

The objective for the project is to determine the best model for the hydro fracturing process so that the fracture length can be predicted near the perfect idea. This paper proposes obtaining good predictions of fracture length in rock as a mechanical property in the hydro fracturing process using a fuzzy logic control approach. It is well known that the input of hydro fracturing process parameters play a major role in determining the fracture length. As the process facts have not been disclosed so far, the selection of input parameters to find the fracture length (mm) is very difficult. A common difficulty in the hydraulic fracturing process in the real time is in observation and measurement of the fractures that develop beneath of the earth.

Hence, the problem of getting optimized hydro fracturing process parameters to attain maximum fracture length is attempted in this investigation. In addition, functional relationships between inputs and outputs will be analyzed and discussed.

II. Experiment Work

II.1. Fabricating the Experimental Set Up

Figs. 1-3 show, a container for storing the fluid of SAE 140 oil which is having viscosity 40 centipoises, a commercially available feed pump to feed pressurized fluid to the inner casing pipe provided in the PMMA test sample is shown in the experimental set up in Fig. 1. The PMMA test samples prepared for the experiment was 20 nos. The length of a PMMA test sample was 300mm and its outside diameter was 150mm.

The material in which the inner casing pipe made up of stainless steel and it has 6 to 10mm of an inner diameter. The applied pressure can be varied by the adjustment of the two control valves which is provided in the experimental set up and the range of pressure can be 4 to 8 N/mm².

The adjustment of the flow control valves ensured the required pressure which was applied in the inner casing tube, before starting the experiment. A bypass line was provided separately in the experimental setup which helps to achieve the required pressure for the same. To control the pressurized fluid rate with respect to the time, say 5 s to 15 mins, a 555 IC timer is provided for feed

pump.

For heating the PMMA test sample in the range of 40 to 60°C, it is placed over the heater. The material in which the heater control unit made up of Nichrome and it has the capacity of 400W.

The input to the heater was varied by the provision of the Dimmerstat 0-2A, Single phase, open type and the voltmeter and ammeter helps in the measurement of input. The digital range of voltmeter was 0 to 200V AC, the digital range of ammeter was 0 to 2A AC, the temperature indicator was digital 0 to 199.9°C. AC single phase, 230V earthed stabilized current was the electrical supply for the experimental setup. The heat input at the desired value for the desired temperature on PMMA sample was adjusted by varying the Dimmerstat.

The temperature was measured through the temperature gauge by the commercially available thermocouples that are embedded to the PMMA test sample.

The experimental table and Stand was made up of MS square hollow pipe and angle. The fracture length was measured by using a measuring scale [30].

II.2. Finding the Limits of the Experiments Test Parameters

From the literature, the predominant factors that have a greater influence on the Fracture rate of Hydro fracturing process had been identified.

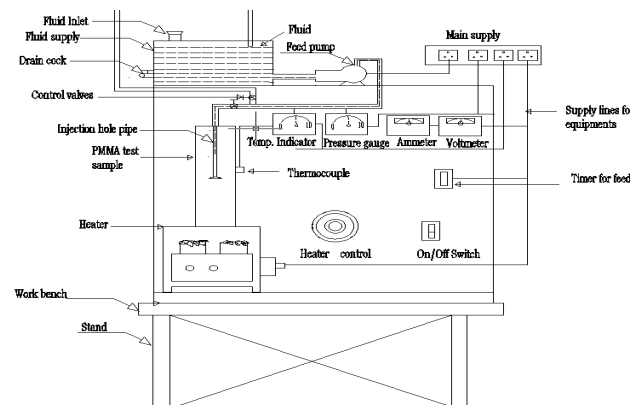


Fig. 1. Experimental set up for Hydrofracturing process



Fig. 2. Front view of Experimental set up



Fig. 3. PMMA test specimen

They were: (i) Pressure applied in N/mm^2 (ii) Temperature in $^{\circ}C$ (iii) Injection hole diameter in mm. large numbers of trial experiments were conducted to identify the feasible testing conditions for obtaining the Fracture length of Hydro fracturing process. The following inferences were obtained:

1. Based on the field trials the pressure applied is limited to 4 to 8 N/mm^2 .
2. From the literature survey, the temperature and the injection hole diameter is limited to the range of 40 to 60 $^{\circ}C$ and 6 to 10 mm respectively.
3. Further the Maximum with stand temperature of the PMMA samples is to be Less than 100 $^{\circ}C$, hence the temperature range is fixed to 40 to 60 $^{\circ}C$ only [31].

Table I shows the factors and their levels set in this study; Table II lists the experimental settings in each run. The three factors and five levels were used for the experimental study. The orthogonal arrays maintain not only themselves but also mutual balances and provide

enough experimental information with the least number of experiments conducted.

III. Analysis of Variance (ANOVA)

The purpose of using ANOVA is to determine the significant factors in the Hydro fracturing process. To evaluate the performance of experiments, each trial is replicated six times. The results and signal-to-noise ratio (SNR), using a formula that suits nominal-is-better characteristics [32].

From the ANOVA Table III, the value of coefficient of variation is also low as 8.85% indicate that the deviations between experimental and predicted values are low. Adeq precision measures the signal to noise ratio.

A ratio greater than 4 is desirable. In this investigation, the ratio is 17.344, which indicates an adequate signal. This model can be used to navigate the design space.

TABLE I
IMPORTANT FACTORS AND THEIR LEVELS

| S. No | Factor | Unit | Notation | Levels | | | | |
|-------|-------------------------|-------------|----------|--------|------|------|------|--------|
| | | | | -1.682 | -1 | 0 | +1 | +1.682 |
| 1 | Pressure applied | N/mm^2 | A | 4.0 | 5.0 | 6.0 | 7.0 | 8.0 |
| 2 | Temperature | $^{\circ}C$ | B | 40.0 | 45.0 | 50.0 | 55.0 | 60.0 |
| 3 | Injection hole Diameter | mm | C | 6.0 | 7.0 | 8.0 | 9.0 | 10.0 |

TABLE II
DESIGN MATRIX AND EXPERIMENTAL RESULTS

| Ex. No | Coded values | | | Actual Values | | | Fracture length (mm) |
|--------|----------------------|-----------------|-----------------------------|----------------------|-----------------|-----------------------------|----------------------|
| | Pressure applied (A) | Temperature (B) | Injection hole diameter (C) | Pressure applied (A) | Temperature (B) | Injection hole diameter (C) | |
| 1 | -1 | -1 | -1 | 5.00 | 45.00 | 7.00 | 21.0 |
| 2 | +1 | -1 | -1 | 7.00 | 45.00 | 7.00 | 25.0 |
| 3 | -1 | +1 | -1 | 5.00 | 55.00 | 7.00 | 20.0 |
| 4 | +1 | +1 | -1 | 7.00 | 55.00 | 7.00 | 40.0 |
| 5 | -1 | -1 | +1 | 5.00 | 45.00 | 9.00 | 24.0 |
| 6 | +1 | -1 | +1 | 7.00 | 45.00 | 9.00 | 35.0 |
| 7 | -1 | +1 | +1 | 5.00 | 55.00 | 9.00 | 36.0 |
| 8 | +1 | +1 | +1 | 7.00 | 55.00 | 9.00 | 58.0 |
| 9 | -1.682 | 0 | 0 | 4.32 | 50.00 | 8.00 | 22.0 |
| 10 | +1.682 | 0 | 0 | 7.68 | 50.00 | 8.00 | 46.0 |
| 11 | 0 | -1.682 | 0 | 6.00 | 41.59 | 8.00 | 21.0 |
| 12 | 0 | +1.682 | 0 | 6.00 | 58.41 | 8.00 | 41.0 |
| 13 | 0 | 0 | -1.682 | 6.00 | 50.00 | 6.32 | 26.0 |
| 14 | 0 | 0 | +1.682 | 6.00 | 50.00 | 9.68 | 42.0 |
| 15 | 0 | 0 | 0 | 6.00 | 50.00 | 8.00 | 39.0 |
| 16 | 0 | 0 | 0 | 6.00 | 50.00 | 8.00 | 42.0 |
| 17 | 0 | 0 | 0 | 6.00 | 50.00 | 8.00 | 42.0 |
| 18 | 0 | 0 | 0 | 6.00 | 50.00 | 8.00 | 35.0 |
| 19 | 0 | 0 | 0 | 6.00 | 50.00 | 8.00 | 43.0 |
| 20 | 0 | 0 | 0 | 6.00 | 50.00 | 8.00 | 33.0 |

It is easy to see that factors A,B,C are the three most important factors in terms of process robustness and of the three process parameters investigated, the applied pressure (N/mm^2) found to have greater influence on Fracture length (mm) followed by Temperature ($^{\circ}C$) and Injection hole diameter(mm).

The normal probability of the Fracture length shown in Fig. 4 reveals the residuals were falling on the straight line, which meant that the errors were distributed normally.

All of this indicated an excellent suitability of the regression model. Each of the observed values compared with the experimental values shown in Fig. 5. A larger SNR indicates a better hydrofracturing performance. The estimated SNRs are analyzed with an ANOVA to determine significant factors.

The significant factors identified though ANOVA were considered later in the optimization of the fuzzy logic control model.

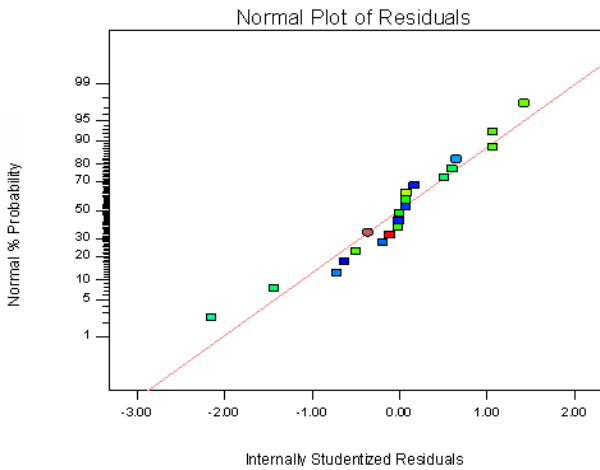


Fig. 4. Normal probability plot

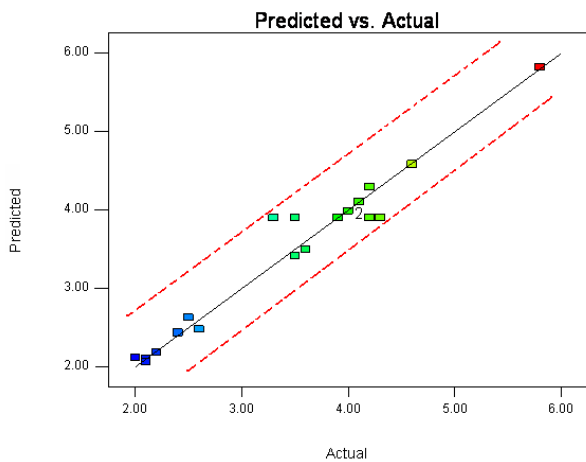


Fig. 5. Correlation graph for response (Fracture length)

TABLE III
ANOVA TEST RESULTS

| Source | Sum of squares | df | Mean square | F Value | p-value prob.>F | |
|---------------------------|----------------|----|-------------|---------|-----------------|-----------------|
| Model | 1933.36 | 9 | 214.82 | 22.95 | < 0.0001 | significant |
| A-Pressure | 694.12 | 1 | 694.12 | 74.16 | < 0.0001 | |
| B-Temperature | 500.02 | 1 | 500.02 | 53.43 | < 0.0001 | |
| C-Injection hole diameter | 399.98 | 1 | 399.98 | 42.74 | < 0.0001 | |
| AB | 91.13 | 1 | 91.13 | 9.74 | 0.0109 | |
| AC | 10.13 | 1 | 10.13 | 1.08 | 0.3228 | |
| BC | 55.13 | 1 | 55.13 | 5.89 | 0.0356 | |
| A ² | 47.89 | 1 | 47.89 | 5.12 | 0.0472 | |
| B ² | 119.82 | 1 | 119.82 | 12.80 | 0.0050 | |
| C ² | 47.89 | 1 | 47.89 | 5.12 | 0.0472 | |
| Residual | 98.59 | 10 | 9.36 | | | |
| Lack of Fit | 7.59 | 5 | 1.52 | 0.088 | 0.9907 | not significant |
| Pure Error | 86.00 | 5 | 17.20 | | | |
| Cor.Total | 2026.95 | 19 | | | | |

Std. Dev. 3.06
 Mean 34.55
 C.V. % 8.85
 PRESS 186.33
 R-Squared 0.9538
 Adj R-Squared 0.9123
 Pred R-Squared 0.9081
 Adeq Precision 17.344
 df -degrees of freedom, CV- coefficient of variation,
 F- Fisher's ratio, p- probability

The Fig. 6 shows the highest fracture length of 58.0 mm was observed at a pressure 7 N/mm², temperature of 55°C and injection hole diameter of 9 mm during the experimental procedure.

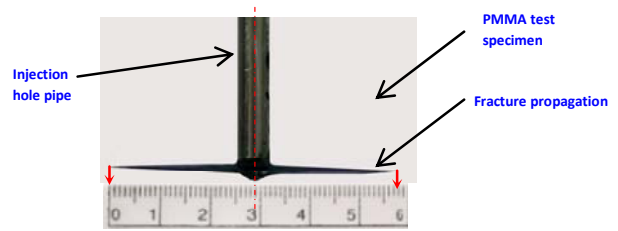


Fig. 6. Fracture propagation

IV. Design of Fuzzy Logic

IV.1. The Fuzzy Logic Analysis

Fuzzy logic analysis, introduced by Dr. Zadeh in 1965 [33], is an efficient way to handle ambiguous and vague problems.

Its ability in handling uncertainties has led to it been widely applied in engineering control systems. Using fuzzy rules in the “if- then” statements, fuzzy logic maps inputs to outputs in a non-linear way.

IV.2. Fuzzy Logic Control Structure

A fuzzy logic control (FLC) is a knowledge-based system that converts human linguistics into its knowledge base using fuzzy rules and membership functions. It consists of a fuzzifier, an inference engine containing one database and one rule base, and a defuzzifier. As a crisp input enters, the fuzzifier allocates it to a fuzzy set. Fuzzy rules in the rule base produce fuzzy conclusions and the defuzzifier converts these conclusions into crisp outputs.

This process is shown in Fig. 7. Based on the fuzzy rules, the Mamdani implication method for the fuzzy inference reasoning is adopted.

IV.3. Development of Fuzzy Logic Control

FLC system can be applied to all kind of processes.

The development of fuzzy logic control consists of the following steps:

1. Specify the range of controlled variable and manipulated variables
2. Divide these ranges into fuzzy sets and attach linguistic labels which can be used to describe them
3. Determine the rules (rule base), which relate the manipulated variable and controlled variable, to specify control action
4. Application of a suitable defuzzification method.

The number of necessary fuzzy sets and their ranges were designed based upon the experience gained on the process.

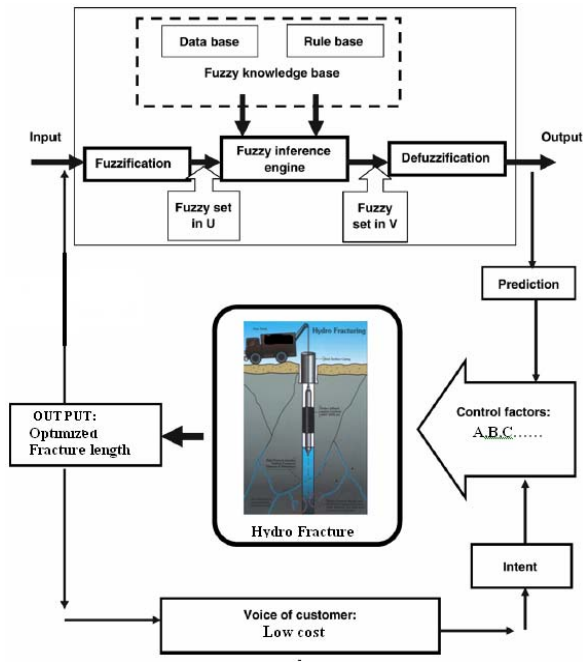


Fig. 7. FLC process

IV.4. Architecture a Fuzzy Control Using Inference Engine

The settings for variables are results from ANOVA. A FLC with fuzzy rules will be constructed and used to predict the outputs. The input variables Pressure applied (N/mm²), Temperature (°C), Injection hole diameter (mm) shown in Figs. 8(a)-(b)-(c). The range of the input will be partitioned into three sets, S, M, and L, which stand for “small”, “medium”, and “large”; the range of outputs are separated into nine parts, L4,L3,L2,L1,M,M1,M2,M3 and M4 which denote “small small”, “very small”, “small”, “small medium”, “medium”, “medium large”, “large”, “very large”, and “large large” shown in Fig. 9. The centroid method is used to defuzzify the output membership functions. The rule-based array for FLC is illustrated in Fig. 10.

When the three inputs enter, they will be transformed into linguistic values. Apply the logic rules along with the Mamdani inference, the linguistic and membership values for the outputs can be obtained.

The Fig. 11 shows the SIMULINK model developed for chosen fracture length (mm) for FLC.

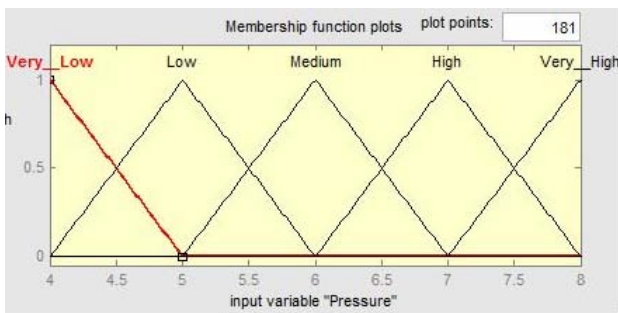


Fig. 8(a). Membership functions for input variables for Pressure

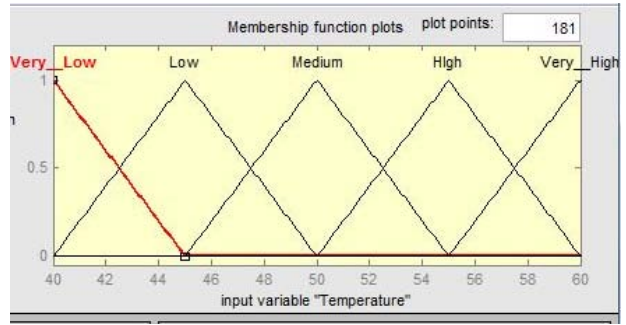


Fig. 8(b). Membership functions for input variables for Temperature

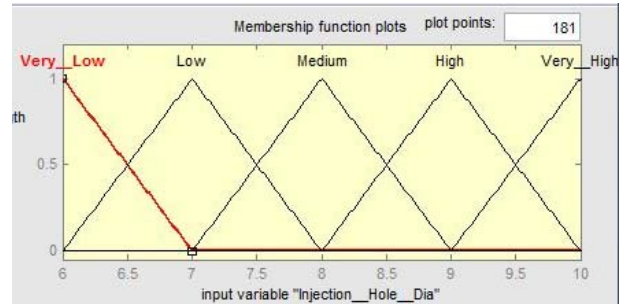


Fig. 8(c). Membership functions for input variables for Injection hole diameter

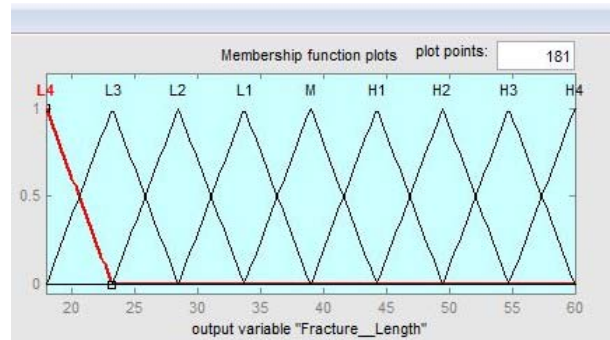


Fig. 9. Membership function for the Fracture length

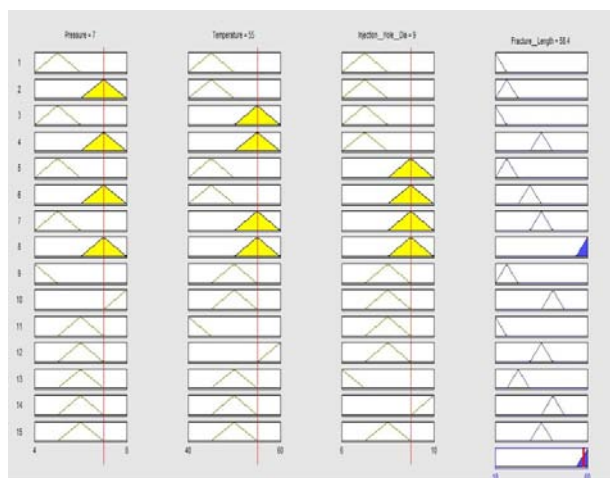


Fig. 10. Rule-based array for FLC

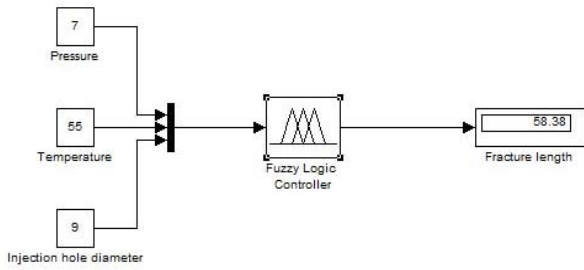


Fig. 11. SIMULINK model

IV.5. Decision Making Stage

This stage consists of fuzzy control rules which decide how the fuzzy logic control works. This stage is the core of the fuzzy control and is constructed from expert knowledge and experience. The fuzzy logic control rule will be of the following type:

IF (condition) AND (condition) AND (condition)
THEN (action)

The rules can be interpreted as follows and then similarly other rules can be interpreted in the same way.

IF Pressure is Low AND Temperature is Low AND Injection_hole_dia is High Then Fracture_length is L3.

IV.6. Inference Surface for Hydrofracturing Process

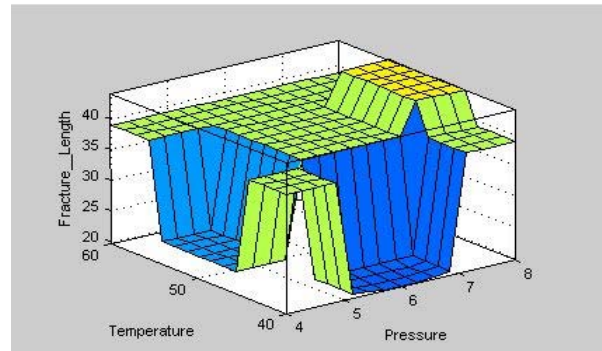
Figs. 12(a)-(c) show response surface plots for Pressure applied (N/mm^2), Temperature ($^{\circ}C$), Injection hole diameter (mm).

Fig. 12(a) shows that when the applied fluid pressure was more, maximum fracture length was observed. Since fluid is compressed between the injection hole pipe and surface of the test sample.

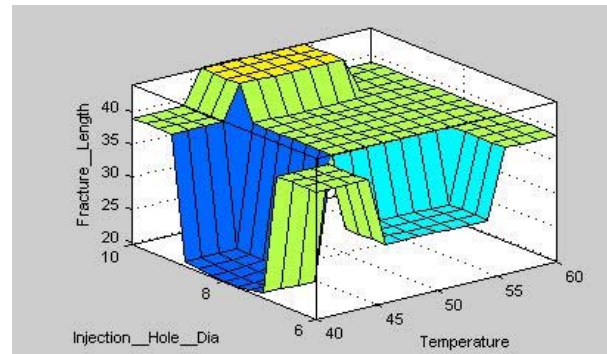
This energy can be stored in or released from the test medium to the surrounding area subjected to internal pressure which induces the elastic strain energy before the fracture occurs at the peak pressure. If the internal energy exceeds the limit that the material can withstand, the energy release will occur to re-establish the internal energy level within a tolerable limit. The excess of energy is dissipated with the growth of micro cracks during process.

The micro mechanical factor which influences the new crack and porosity generation is heavily influenced by the high pressure. The fracture propagation stops when the elastic strain energy releases over the surface of the test sample. Hence maximum fracture length was observed during the experimental study [34]. Fig. 12(b) shows that when the Temperature was more, maximum fracture length was obtained.

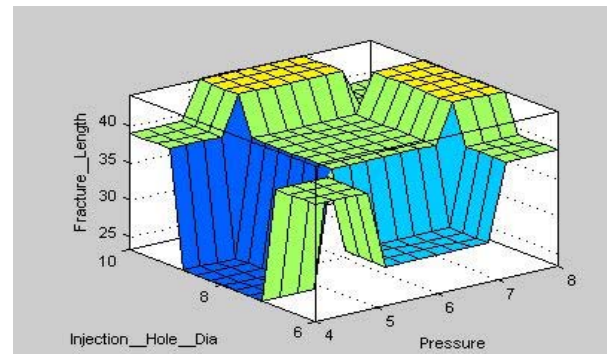
Because of heating the test sample, the deformation resulting from thermal expansion or contraction is non uniform along the radial and axial directions.



(a)



(b)



(c)

Figs. 12. The response plots for the yield of fracture length using a fuzzy logic controller inference result

This induces the thermal stresses in the sample. For example, under heating condition, the material close to the periphery tends to expand more than the material closer to the axis. Consequently, this produces an outer ring of compression and an inner core of tension. Since fractures in tensile stress fields tend to grow in a plane that is perpendicular to the maximum principle stress, it is expected that loading the sample hydraulically would create a fracture that is oriented perpendicular to the sample axis. Hence highest fracture length was observed when the temperature was at its maximum [35].

Fig. 12(c) indicates that at higher injection hole diameter, maximum fracture length was observed. Since the fluid which is being impinges on the test sample exert a large internal pressure on the perimeters of underground structures of the test sample and this pressure develops an internal fracture within the sample.

The sample with fractures with large apertures is susceptible to deformation enabling to produce large stresses that induces a further cracking through hydraulic fracturing. Hence highest fracture length was observed when the injection hole diameter was at its maximum [36]. Therefore, it is clear from the figures that these response plots can easily predict the relationship between responses and variables, as well as determine the nature of a desired area and provide other information regarding the process of hydrofracturing process.

V. Concluding Remarks

It is shown that with the combination of Design of experiment and FLC, a clear demonstration of the efficiency and robustness of hydrofracturing process is achieved. The condition that results in the optimal result is also achieved through FLCs. Based on the experimental results; conclusions can be drawn as follows:

1. The most significant variables affecting the hydrofracturing processes identified from analysis of variance in hydrofracturing process incorporating parameters at 95% confidence level. Of the three process parameters investigated, the applied pressure (N/mm^2) found to have greater influence on Fracture length (mm) followed by Temperature ($^{\circ}\text{C}$) and Injection hole diameter (mm).
2. A maximum Fracture length (mm) of 58.4 mm could be attained under the maximum value of pressure of 7 N/mm^2 , Temperature of 55°C and Injection hole diameter of 9 mm using FLC.
3. It is easier to predict the relationship between input and output variables with the aid of FLC. This also aids in providing information regarding the nature of the hydrofracturing process.
4. To increase the robustness, effectiveness and efficiency to understand the prediction of the process at any area of the experimental domain, the artificial intelligence like neural network, fuzzy logic and generic algorithms can be used.
5. The supremacy of the integrated fuzzy logic control was analyzed through computer simulation using Matlab / Simulink software appears was encouraging.

Acknowledgements

This work was supported by Tamil Nadu Water Supply and Drainage Board (TWAD), Tamil Nadu, India through their reference No. 1313/AHG2/HG/2010/ Dated 24.05.2011 and M/s. Poly lab Engineering equipments, Miraj, Maharashtra, India for their support to develop the experimental set up.

References

[1] Rutqvist J, Stephansson .O, The role of hydro mechanical coupling in fractured rock engineering *Hydrogeology Journal* , vol.11, issue 1, pp. 7–40. 2003.

[2] B.Guruprasad, A. Ragupathy, T.S. Badrinarayanan, K.B. Rajkumar, The Stress Impact On Mechanical Properties Of Rocks In Hydro Fracturing Technique, *International Journal of Engineering Science and Technology* (IJEST), ISSN : 0975-5462, Vol. 4 ,n.2 , pp. 571-580, 2012.

[3] Germanovich, L. N., D. K. Astakhov, M. J. Mayerhofer, J. Shlyapobersky, and L. M. Ring , Hydraulic fracture with multiple segments – I: Observations and model formulation, *International journal of rock mechanics*, Mineral science, vol.4, n.471,1997.

[4] Murdoch, L. C, Hydraulic fracturing of soil during laboratory experiments: part I Methods and observations, *Geo technique*, vol.43, pp. 255– 265,1993.

[5] de Pater, C. J., L. Weijers, M. Savic, K. H. A. A. Wolf, P. J. van den Hoek, and D. T. Barr , Experimental study of nonlinear effects in hydraulic fracture propagation, *SPE production & facilities journal*, vol.9, pp. 239– 246,1994.

[6] Abass, H. H., S. Hedayati, and D. L. Meadows , Non planar fracture propagation from a horizontal wellbore: Experimental study, *SPE production & facilities journal*, vol.11, pp. 133– 137,1996.

[7] de Pater, C. J., L. Weijers, M. Savic, K. H. A. A. Wolf, P. J. van den Hoek, and D. T. Barr , Experimental study of nonlinear effects in hydraulic fracture propagation , *SPE production & facilities journal*, vol.9, pp. 239– 246,1994.

[8] Groenenboom, J., and D. B. van Dam, Monitoring hydraulic fracture growth: Laboratory experiments, *Society of Geophysics*, vol.65, pp. 603–611,2000.

[9] Rummel, F., Fracture mechanics approach to hydraulic fracturing stress measurements in Fracture Mechanics of Rock, edited by B. K. Atkinson, pp.217– 239, *Elsevier*, New York ,2000.

[10] Bunger, A. P., R. G. Jeffrey, and E. Detournay, Toughness dominated near-surface hydraulic fracture experiments, paper presented at Gulf Rocks 2004, 6th NARMS: Rock Mechanics Across Borders and Disciplines, *American rock Mechanics association*, Houston, Texas,2004,pp. 5 – 9.

[11] Hubbert, M. K., and D. G.Willis, Mechanics of hydraulic fracturing, *Journal of petroleum technology*, vol.9,pp .153– 166,1957.

[12] Takada, A., Experimental study on propagation of liquid-filled crack in gelatin: Shape and velocity in hydrostatic stress condition, *Journal of geophysical research: solid earth*, vol.95, pp.8471– 8481,1990.

[13] Bakala, M., *Fracture propagation in sediment-like materials*, M.S. thesis, pp. 83 , University of Oklahoma, Norman,1997.

[14] Rummel, F, Fracture mechanics approach to hydraulic fracturing stress measurements, in Fracture Mechanics of Rock, edited by B. K. Atkinson, pp. 217– 239, *Elsevier*, New York,1987.

[15] Cooke, M. L., and D. D. Pollard, Fracture propagation paths under mixed mode loading within rectangular blocks of Poly methyl methacrylate, *Journal of geophysical research: solid earth*, vol.1, pp. 3387– 3400, 1996.

[16] F. Martin, P. Christer.W. Jan, *Surface coating technology*,2001,115-141.

[17] R.O. Kuehl, *Design of Experiments: Statistical Principles of Research Design and Analysis*, Duxbury Press at (Brooks/Cole Publishing Company, 511 Forest Lodge Road Pacific Grove, CA USA, 2000, p. 391).

[18] S.H. Park, *Robust Design and Analysis for Quality Engineering*, (Chapman & Hall, 2–6 Boundary Row, London, UK, 1996, p. 42).

[19] S. Sharafat, A. Kobayashi, Y. Chen, M. Ghoniem, *Vacuum* 65, vol.65, Issues 3–4, Pages 241-570,2002

[20] T.J. Ross, *Fuzzy Logic with engineering applications*, (John-Wiley and Sons,The Atrium, Southern Gate, Chichester, West Sussex PO198SQ, UK, 2004, pp. 90).

[21] A.J. Wal, *Fuzzy Sets Systems*. Vol.74, pp.33-41,1995

[22] G.E. D'Errico, *Journal matrial process technology*, vol.109, pp.38-43.2001

[23] H. Ying, *Automatica* , vol.39, pp.1171-1184,200

[24] K. Hirota, W. Pedrycz, *Fuzzy Sets Systems*. 70, (1995) pp.287-301.

[25] R. Wachter, A. Cordery, *Diamond Related Materials*, , vol. 6, n.5-7, pp. 537-541,1997.

[26] I.Choudhury, M.El-Baradie,*Journal of Materials Processing*

- Technolog*, vol. 67,n.1-3,pp.55,1997
- [27] H. Ying, *Automatica* , vol.40, n.9,pp. 1551–1559,2003.
- [28] K. Hirota, W. Pedrycz, *Fuzzy Sets Systems*. 70, (1995) pp.287-301.
- [29] S. Gara, W. Bouzid, M. Hbaieb, M. Ben Amar, Cutting Speed Optimization in High Speed Turning, *International Review of Mechanical Engineering (IREME)*, Vol .1 n. 3, pp. 237 – 244,2007.
- [30] B. Guruprasad , A. Ragupathy, T.S. Badrinarayanan, R.Venkatesan Estimation of Fracture Length as a Mechanical Property in Hydrofracturing Technique using an Experimental Setup *International Journal of Engineering and Technology (IJET-UK)*, ISSN 2049- 3444, vol.2, n.12, pp. 1921-1925, 2012.
- [31] B. Guruprasad , A. Ragupathy, T.S. Badrinarayanan, R.Venkatesan Estimation of Fracture Length as a Mechanical Property in Hydrofracturing Technique using an Experimental Setup *International Journal of Engineering and Technology (IJET-UK)*, ISSN 2049- 3444, vol.2, n.12, pp. 1921-1925, 2012.
- [32] S.H. Park, *Robust Design and Analysis for Quality Engineering*, (Chapman & Hall, 2–6 Boundary Row, London, UK, 1996, p. 42.
- [33] K. Hirota, W. Pedrycz, *Fuzzy Sets Systems*. 70, (1995), pp.287-301.
- [34] B. Guruprasad , A. Ragupathy, T.S. Badrinarayanan, R.Venkatesan Estimation of Fracture Length as a Mechanical Property in Hydrofracturing Technique using an Experimental Setup *International Journal of Engineering and Technology (IJET-UK)*, ISSN 2049- 3444, vol.2, n.12, pp. 1921-1925, 2012.
- [35] Ruiting Wu, Leonid N. Germanovich, Peter E. Van Dyke, and Robert P. Lowell, *Thermal technique for controlling hydraulic fractures*, *Journal of Geophysical research*, vol.112, B05209, 2007.
- [36] B. Guruprasad , A. Ragupathy, T.S. Badrinarayanan, R.Venkatesan Estimation of Fracture Length as a Mechanical Property in Hydrofracturing Technique using an Experimental Setup *International Journal of Engineering and Technology (IJET-UK)*, ISSN 2049- 3444, vol.2, n.12, pp. 1921-1925, 2012.

Authors' information



B. Guruprasad, is currently working as an Assistant professor since 2004 in Department of Mechanical Engineering, Annamalai University, Annamalai Nagar, Tamilnadu, India. He received his B.E. degree in Mechanical Engineering (1998) and M.E. degree in Energy Engineering (2007) from Annamalai University, Annamalai Nagar, Tamilnadu, India. He has got 5 years of industry experiences in R&D in Automobile field. He is presently doing his Ph.D research work in the area of Fluid Mechanics. He is a life member of ISTE. His research interests are in fluid mechanics, finite element analysis.



A. Ragupathy received his B.E. degree in Mechanical Engineering (1989), M.E. degree in Thermal Engineering (1994) and Ph.D. in Mechanical Engineering (2008) from Annamalai University, Annamalai Nagar, Tamilnadu, India. He is working as Professor in the Department of Mechanical Engineering cum The Controller of Examinations, Annamalai University since 1992. He is a life member of ISTE. His research interests are in heat and mass transfer, thermodynamics, HVAC.



T. S. Badrinarayanan is currently a Geoscientist, B² Geo Tech Services, Kollidam, Sirkali, Tamilnadu, India. He received his MSc.,(Geology) Degree from Annamalai University, Annamalai Nagar, Tamilnadu, India during the year of 1979. He has published more than 25 research papers in national and international journals. His research interests are in Geo mechanical, Mineral exploration, Hydro fracturing, and Geotechnical investigations.



E. Sambath obtained his Diploma in EEE with Distinction from Muthiah Polytechnic, Annamalai nagar, India and B.E (Electronics and Instrumentation), M.E (Process Control & Instrumentation) from Annamalai University, Annamalai Nagar, India. He is currently working as a Assistant Professor in the Department of Instrumentation Engg., Annamalai University, since 2005, He is at present pursuing his Ph.D degree in the field of power electronics from the Department of Instrumentation Engg., Annamalai University. His research interests are in Power Electronics, Multilevel Inverters, Embedded systems.



Praise Worthy Prize



1970-8742(201307)7:5;1-N